Organic complexation in karst cave systems: implications for transition metal incorporation into speleothems

A thesis

submitted in fulfilment

of the requirements for the degree

of

Doctor of Philosophy in Earth Sciences

at

The University of Waikato

by

Sebastian Niels Höpker

THE UNIVERSITY OF
WAIKATO
Te Whare Wānanga o Waikato

2024

To my family.
For your continuing inspiration, love, and support.
I am forever grateful.

Abstract

The accurate prediction of future climate scenarios heavily relies on the robust understanding of the magnitude and drivers of past climate variability. Amongst the various materials used to study historic climate beyond the instrumental record, secondary cave carbonate deposits, or speleothems, have proven to present particularly valuable archives of numerous environmental processes over a range of temporal and spatial scales. In this context, trace elements included in speleothems are increasingly used to bolster speleothem-based records of past climates and environments (often primarily based on stable isotope proxies), with Mg/Ca and Sr/Ca ratios presenting the most widely interpreted elemental signatures indicative of hydrological processes in the karst. More recently, however, a novel proxy system based on the concentrations of first-row transition metals in stalagmites has been proposed to potentially offer a first means to quantitatively reconstruct past cave drip rates, and hydroclimate by extension. The transport from the surface to the site of speleothem formation of transition metals, such as Co, Ni, or Cu, is understood to be largely governed by the formation of organic metal complexes (OMCs) with ligands present in natural organic matter (NOM). This organic association can evidently facilitate the deposition of organically-complexed metals in response to strong infiltration events, however, has also been suggested to enable a mechanistically distinct and largely undefined inclusion pathway for metals into calcite. Specifically, the availability of transition metals at speleothem surfaces for partitioning into the crystal phase may arguably be driven by the rate-dependant dissociation (or 'decay') of OMCs, which is in turn predicted to depend on their residence time at speleothem surfaces. OMC decay kinetics may thus present a potentially viable link between metal concentrations in stalagmites, and the residence time of OMCs at their surfaces. This thesis further investigates these interactions between selected first-row transition metals (Co, Ni, Cu) with NOM, aiming to advance the applicability of respective metal signatures in speleothems to palaeoclimatic reconstructions.

In the first research chapter, the decay of OMCs is characterised in a first comparative study of in-cave OMC dissociation kinetic signatures by means of competitive ligand exchange experiments. Performed on water samples and soil extracts from eight Aotearoa New Zealand caves, the findings demonstrated that natural organic ligands decisively limit transition metal availability (by example of Co, Ni, Cu) at the dripwater-speleothem interface, whereas alkaline earth metals (here: Mg, Sr) are essentially unaffected by organic interactions in solution. OMC stability was found to occur in the hierarchy of Cu $\approx$ Co $>$ Ni, with a variable fraction of all three metals bound very strongly to effectively inert complexes. OMC stability was overall enhanced

in soil extracts, presumably due to higher organic content and aromaticity. The study further uses empirical estimates of OMC decay rate constants to assess the time-dependent release of metals at stalagmite surfaces in a simple forward model. This exercise predicted that the decay of transition metal complexes was most sensitive on time-scales relevant to typical cave drip points (up to ca. 40 drips min^{-1}), and increasingly so towards lower flow rates.

The second research chapter comprises experimental and field-based measurements of the inclusion rates of Co, Ni, Cu, as well as Mg, Sr. Firstly, a set of ten cave-analogue experiments were aimed to test for kinetic signatures in transition metal concentrations linked to the decay of OMCs during calcite precipitation. Performed at a range of drip rates and with variable concentrations of organic ligands in solution (Suwannee River Fulvic Acid (SRFA) and nitrilotriacetic acid (NTA)), however, the experimental calcite precipitates primarily depicted a direct inclusion of OMCs without prior dissociation. This was particularly pronounced for metal-SRFA complexes due to a considerable degree of co-precipitation of SRFA. Signatures attributable to OMC decay were in turn not discernible, presumably due to experimental conditions preventing their resolution. The study further yielded new estimates of inorganic partition coefficients for Co (≈1.8), Ni (≈0.4), Mg (≈0.04), Sr (≈0.09), and Cu (≈13 on average, but up to ca. 57), with the latter showing a pronounced positive dependency on drip rate. In the second part of this study, a wide range of new and previously published datasets on experimental and in-cave metal partitioning were compiled, which collectively allowed for the establishment of a conceptual framework around hypothesised system-specific conditions determining the dominant drivers of transition metal concentrations in dripwater and stalagmites.

The final research chapter explores elemental systematics in two caves on the South Pacific island of Niue, aiming to utilise modern field observations to corroborate stalagmite-based palaeoclimate reconstructions of Holocene climate variability. Intermittent cave monitoring between September 2019 and November 2022 in principle supported the assumption that stalagmites from these caves record environmental conditions in their chemistry and binary lamination. Although reliable chronologies could not be established for the two stalagmite samples analyses in this study, their trace elemental and reconnaissance stable isotope measurements suggested that the most pronounced elemental signal of Mg/Ca ratios reflected a combined control of water-rock interactions, prior calcite precipitation (both indicative of rainfall amount), and marine aerosol inputs. The analysis further implied that Ni/Ca (and Cu, Co, and Zn to a lesser extent) also primarily reflected local hydrology, predominantly exhibiting behaviour consistent with that expected for a pervasive kinetic drip rate control. Based on preliminary interpretations, OMC decay presented the primary driver of transition metal concentrations in the deposits from Anapala Cave, while short-lived 'soil-flushing' peaks in various elemental concentrations in response to heavy rainfall events only sporadically defined the record.

Collectively, albeit warranting further investigation, the results of this thesis provide new systematic insights into the role of organic complexation for transition metal incorporation into calcite speleothems, thereby presenting important precedent for the further development of a novel (semi-)quantitative class of hydrological proxies.

Acknowledgements

HTB! Foremost, I would like to sincerely thank my chief supervisor Adam Hartland for the opportunity to be involved in this fascinating and diverse project. It's been a long time since an unassuming video call from the Pyrenees about caves and ligands, which quite frankly, didn't mean much to me at the time! Thank you for an amazing PhD project and overall experience. I am extremely grateful for the many opportunities of amazing fieldwork near and far, the attendance of conferences and summer schools, lab visits, involvement with the development of Syp, and the chance to gain experience in academia beyond the thesis research. I highly appreciate your availability and advice when needed, your patience, dad jokes, and friendship. I am also thankful to my second supervisor Megan Grainger, for your helpful discussions, encouragement, and problem solving. Thank you for being there when needed, your constructive feedback on various drafts and ideas, and friendly chats. I am also very grateful to Bedartha Goswami, for hosting me at the Potsdam Institute of Climate Impact Research early on during my PhD, and getting me started with computational aspects of the project. I further thank Pauline Treble and James Baldini for the examination and constructive review of my thesis.

A huge 'thank you' also goes to the Waikato Environmental Geochemistry (WEG) lab group for making me feel very welcome. Brittany and Cole – I can't thank you both enough for taking Jess and I in when we first arrived in Hamilton. I'd like to also specifically thank Thomas, Huma, Mahdie, and Amir for help around the lab, Ingrid for help with GeoMic and lab equipment, and Amanda for ICP-MS analyses and method development. Thank you also Louis Schipper and Dave Campbell for providing a comfortable work environment and interesting group meetings. I was fortunate to have many (too many to list!) helping hands come join me for fieldwork, but like to specifically thank Travis Cross for guiding and sharing his experience on several field campaigns around Aotearoa New Zealand. I would also like to acknowledge Jeff Lang for your exceptional helpfulness, positivity, and friendship, which have helped to achieve ambitious fieldwork goals.

I am further thankful that I was able to work alongside the QUEST (QUantitative palaeoEnvironments from SpeleoThems) team, who also initiated fieldwork on Niue. Specifically, thanks to Seb Breitenbach, Max Hansen, Ola Kwiecien, and Cinthya Nava-Fernandez for making the first trip to Niue extra special. Thank you, Seb, for carrying out isotope analyses, and the helpful discussions throughout my PhD. Max, thank you for advice on cave-analogue experiments, and the many friendly chats. I am further grateful to John Hellstrom and Denis Scholz for carry-

ing out the dating of speleothem samples, and Fernando Gázquez for water isotope analysis. Thank you, Sophie Warken for collaborative research and hosting me at the University of Heidelberg, and Niklas Lehto for helpful discussions and training in COMSOL.

I am grateful for permission to visit and work in various caves of Aotearoa New Zealand. Specifically, I thank the Glenn family for permitting research in Majumba Cave. Thank you, Darden King, Richard NiaNia, and the Pōhaturoa Ahuwhenua Trust, for access and exciting collaborative research in Te Reinga Cave. I further thank the Department of Conservation for permission to conduct ongoing research in Hodge Creek Cave and Dave's Cave, and access to all other Aotearoa New Zealand caves discussed in this thesis.

I would also like to acknowledge the S4 committee, namely Elizabeth, Hege, Nela, Mojgan, Marie, Marcela, Jon, and Jess. It was an absolute pleasure to work with you from 2019 (after meeting in Cluj-Napoca, Romania) to late 2022, and our events S4 Online (January - February 2022) and Mini-S4 in Innsbruck (July 2022) with all of you were definite highlights during my PhD.

A big 'thank you' also goes to all the School of Science technical staff who have helped me along the way. Specifically, I'd like to thank Jenny Stockdill for putting up with my at times (always) crowded lab space and dirty cave equipment, Annie Barker for banter, help with lab problems, and help with navigating MPI restrictions, Steve Newcombe for help with speleothem processing and glass work, Kirsty Vincent, Noel Bates, and Holly Harvey-Wishart for help with rock and soil processing, Danielle Blackwell for elemental analyses, Helen Turner for training on the SEM, and Fiona Petchey for supporting the import of my samples from overseas. Thank you, Peter Jarman, for your help with just about anything technical, and GeoMic, in particular. Thank you also, Warrick Powrie, for helping to establish connections and facilitating fieldwork on Niue. I also thank Dean Sandwell for putting together the cave monitoring station based in Anapala Cave. Finally, my gratitude extends to the Sci Admin team who on numerous occasions were quick to help with urgent or unusual travel or postage requests. Thank you, Fiona Martin, Vicki Smith, Janice McAulay, and Gloria Edwards.

I am further grateful for the fantastic opportunity to participate in experiments at the Australian Synchrotron in Melbourne. My sincere thanks to Daryl Howard and Andrew Langendam for their support in three remote experiments, and finally, one experiment in person. I thank the New Zealand Synchrotron Group for financially supporting each of these experiments.

A very warm word of gratitude goes to the people on Niue who I was lucky enough to meet and work with during three (and counting) wonderful field campaigns. Foremost, I thank Daryn Magatogiia for showing us around Ulupaka Cave and permitting our research. Thank you also for your help, patience, and friendly chats during visits, even when the drips were taking their time! I also extend my gratitude to the Government of Niue for granting us permission to carry out our research. Thank you Rossy Mitiepo for the kind support of our activities and discussion of meteorological data. I thank Moira Enetama for encouraging discussions and the opportunity to share our findings with Tāoga Niue. My sincere gratitude also goes to the Hon. Mititaiagimene Young Vivian and Hakupu village council for permitting our research in

Anapala Cave and Chasm. Finally, I'd also like to thank the many people who helped out to overcome the various challenges of fieldwork: Willie S. for your help with equipment repairs and taking us to Vaikona Chasm, Helena and the Jessop family for the above and beyond hospitality (and safe-guarding during the tsunami evacuation), the community and Crazy Uga team for support during a Covid-19 isolation. I kindly thank the National Geographic Society for providing financial support for the fieldwork on Niue through an Early Career Grant.

I would also like to thank my friends near and far, for the many laughs, adventures, and pep-talks. Thank you, in particular, Andy, Steph, John, Claire, Chris, Dori, Tuan, and Katha for your friendship and support when needed.

Mum, Dad, and Martin, I am forever grateful for your love and encouragement. You have always supported my passions, even when that meant living far apart. I cannot express how thankful I am for the opportunities you provided for us, your positivity, and unconditional support. Finally, I couldn't have done this without you, Jess. You have been my partner in life for over ten years now, and have over the course of this project become my wife and the mother to our little Finn. I thank you with all my heart for your incredible patience and understanding, optimism, constant support and encouragement, help on numerous field campaigns, and keeping me sane even during the most hectic of times. To many more adventures!

Table of contents

List of Figures

List of Tables

List of common terms and abbreviations

3D EEM . . . . Three-dimensional excitation emission matrix

AA . . . . . Ammonium acetate

AAO . . . . . Antarctic Oscillation (alternative name for the Southern Annular Mode; SAM)

AD . . . . . Anno Domini

ADBL . . . . . Apparent diffusive boundary layer

AdCSV . . . . . Adsorptive cathodic stripping voltammetry

ASV . . . . . Anodic stripping voltammetry

BP . . . . . Before present (by convention, relative to 1950 AD)

Chelex-100 . . Chelex® 100 ion exchange resin

CLE . . . . . Competitive ligand exchange

DCF . . . . . Dead carbon fraction

DDC . . . . . Dark dense calcite

DGT . . . . . Diffusive gradients in thin-films

DI . . . . . Deionised water (used synonymously with terms Milli-Q and 'ultrapure' water)

DIC . . . . . Dissolved inorganic carbon

DL . . . . . Detection limit (sometimes referred to as limit of detection; LOD)

DOC . . . . . Dissolved organic carbon

DOM . . . . . Dissolved organic matter

D_X . . . . . Partition coefficient for an element or species X as defined in Equation 4.1

EC . . . . . Electrical conductivity

EDTA . . . . . Ethylenediaminetetraacetic acid

ENSO . . . . . El Niño-Southern Oscillation

FA . . . . . Fulvic acid

GeoMic . . . . . 'Geological Microclimate'; controlled atmosphere setup at the University of Waikato used for cave-analogue experiments

GMWL . . . . . Global meteoric water line

GNIP . . . . . Global Network of Isotopes in Precipitation

HA . . . . . Humic acid

HEPES . . . . . N-hydroxyethylpiperazine-N'-2'-ethanesulphonic acid

ICD . . . . . Incongruent calcite dissolution

ICP-MS . . . . . Inductively-coupled plasma mass spectrometry

ID . . . . . Identifier (with respect to sample names)

IPO . . . . . Interdecadal Pacific Oscillation

IPWP . . . . . Indo-Pacific Warm Pool

IRMS . . . . . Isotope ratio mass spectrometry

ITCZ . . . . . Inter-tropical Convergence Zone

k_d . . . . . Complex dissociation rate constant

LA-ICP-MS . . . Laser ablation inductively-coupled plasma mass spectrometry

MAT . . . . . Mean annual temperature

MC-ICP-MS . . Multi-collector inductively-coupled plasma mass spectrometry

M:L . . . . . metal:ligand ratio

NIST . . . . . National Institute of Standards and Technology

NOM . . . . . Natural organic matter

NTA . . . . . Nitrilotriacetic acid

OM . . . . . Organic matter

OMC . . . . . Organic metal complex

PARAFAC . . . PARAllel FACtor analysis; statistical analysis relevant to 3D fluorescence measurements

PCA . . . . . Principal component analysis

pCO_2 . . . . . Partial pressure of CO_2

PCP . . . . . Prior calcite precipitation

PES . . . . . Polyethersulfone

PPC . . . . . Pale porous calcite

R_{acc} . . . . . Rate of calcite accumulation (observed parameter)

$R_{acc\text{-}norm}$ . . . . Same as R_{acc}, but normalised to area of crystal coverage (Equation 4.2)

RH . . . . . Relative humidity

R_{prec} . . . . . Rate of calcite precipitation (theoretical parameter; Equation 4.5)

SAM . . . . . Southern Annular Mode

SD . . . . . Standard deviation of the mean

SEM . . . . . Scanning electron microscopy

SfM . . . . . Structure-from-motion

$SI_{Calcite}$ . . . . . Calcite saturation index

SLP . . . . . Sea level pressure

SOI . . . . . Southern Oscillation Index

SPCZ . . . . . South Pacific Convergence Zone

SPMWL . . . . South Pacific meteoric water line

SPSD . . . . . South Pacific Subtropical Dipole

SRFA . . . . . Suwannee River Fulvic Acid

SR-μXRF . . . . Synchrotron radiation micro x-ray fluorescence

SST . . . . . Sea surface temperature

$SUVA_{254}$ . . . . Specific UV absorbance at 254 nm wavelength

SV-DGT . . . . Small-volume diffusive gradients in thin-films (type of DGT design)

TIC . . . . . Total inorganic carbon

TOC . . . . . Total organic carbon

UV . . . . . Ultraviolet

UV-Vis . . . . . Ultraviolet-visible

VPDB . . . . . Vienna Pee Dee Belemnite

VSMOW . . . . Vienna Standard Mean Ocean Water

v/v . . . . . Volume/volume

w/v . . . . . Weight/volume

XFM . . . . . X-ray fluorescence microscopy

Chapter 1

Introduction

1.1 Significance of research

The study of environmental conditions throughout the geological record plays a major role in advancing our understanding of the Earth's climate system, and its sensitivity to natural and anthropogenic forcings. Evidence derived from a wide range of palaeoenvironmental archives, *i.e.*, natural or human-made materials that record and store information on environmental variables through time, therein serve to inform climate models in both reconstructing and predicting climatic processes. Amongst the various archives used to study past environments, secondary cave carbonate deposits, or speleothems, have gained increasing attention in recent decades after being previously largely ignored due to their complex formation pathways (Fairchild & Baker, 2012). However, comprehensive studies regarding their fundamental characteristics, along with significant methodological and technological advances, have rendered cave carbonates exceedingly promising deposits to extract information on past environmental conditions over a range of temporal and spatial scales.

The inference of past environments is achieved via so-called proxies, which are essentially measurable quantities in a given archive that vary systematically with certain environmental processes or conditions. By extension, they thereby allow to approximate their environmental controls through time well beyond instrumental records. For instance, the widely applied analysis of stable oxygen isotope ratios ($\delta^{18}O$) preserved during the growth of speleothems allow for estimations of past rainfall and temperature variability, in addition to providing information on several other atmospheric and karst processes (Lachniet, 2009). However, despite substantial progress in understanding karst systems, unambiguous interpretations of many existing speleothem-based proxies in terms of a specific environmental parameter remain complicated. Most proxies are controlled by multiple factors, demanding careful considerations and assumptions to confidently delineate the primary origin of a measured signal at a given study site. In order to improve our capability to study past climate variations, new tools need to be developed that can complement and elaborate on information extractable with existing techniques.

In this context, speleothem trace metal concentrations present a promising alternative (Fairchild & Treble, 2009). Conventionally, studies of trace metals in speleothems and dripwaters have focussed on alkaline earth metals, particularly Sr and Mg, the relative abundances of which are considered to primarily reflect certain processes in the karst system. However, a wide range of other elements are likewise incorporated from dripwater into carbonate minerals, but have received little attention to date. As a consequence, their role in the karst system, as well as possible climatic signals encoded in their abundances in speleothems, remain poorly constrained. It is now clear, however, that divalent first-row transition metals, such as Ni, Cu, Co, and Zn, are strongly controlled by natural organic matter (NOM) present in dripwater, which appears to largely govern their transport to the site of speleothem deposition due to the formation of metal-NOM complexes (Hartland et al., 2012). Indeed, Blyth et al. (2016) note that these strong interactions of transition metals with organic matter in so-called organic metal complexes (OMCs) may very well present the most promising avenue in developing new tools for studying OM quality and quantity in (ancient) dripwaters, and associated environmental drivers.

In this regard, the few existing experimental and applied studies suggest that the dissociation of OMCs at the water-stalagmite interface likely occurs in a predictable manner, and as a function of time. These observations have led to the recognition of the opportunity to develop a novel quantitative proxy of past drip rates based on the dissociation of OMCs at the stalagmite surface, and corresponding metal concentrations preserved in the speleothem (Hartland & Zitoun, 2018).

This thesis aims to elaborate on these findings and further explore the cave dripwater and carbonate chemistry of a suite of divalent first-row transition metals. Through a number of experimental and field-based studies, the thesis seeks to further substantiate the underlying concepts of quantifying drip rates from speleothem trace metal concentrations, and increase confidence in the interpretation of transition metal systematics in karst systems.

1.2 Overarching research aims

Considering the strong evidence for dominant NOM-mediated supply of certain transition metals for the incorporation into calcite (the mineral of interest throughout this thesis) during speleothem deposition, and the arguably predictable relationship of OMC dissociation at the speleothem-water interface with dripwater residence time, fundamental precedent exists for developing a speleothem-based quantitative proxy for cave drip rates (Hartland & Zitoun, 2018; Sliwinski et al., 2022). Through the integration of experimental and field-based approaches, this thesis aims to elaborate on these observations, and at large seeks to provide a mechanistic foundation for developing this novel class of palaeoclimate proxies in stalagmites based on the kinetic interactions of first-row transition metals with ligands present in NOM. More specifically, the thesis addresses three primary objectives:

(I) Quantitatively assess OMC dissociation kinetics of selected trace metals in natural cave waters

(II) Test for 'kinetic signatures' during the inclusion of transition metals into calcite under cave-analogue experimental conditions and in natural cave environments

(III) Assess the systematics of trace elements (and first-row transition metals, in particular) in modern cave environments with view to applying a novel class of hydrological proxies to stalagmite palaeoclimate records

1.3 Thesis outline

This thesis is structured into 6 chapters, with chapters 3 to 5 comprising the core research findings. The research focus of this thesis and each chapter is conceptualised in Figure 1.1.

Chapter 1 – The first chapter serves to introduce the broader thesis topic and significance of research.

Chapter 2 – The second chapter provides a review of the literature and state-of-the-art in speleothem science, aqueous chemistry, and Holocene climate history.

Chapter 3 – The third chapter comprises an experimental study aimed to characterise and quantify the kinetic dissociation (or 'decay') of OMCs in a range of cave waters from Aotearoa New Zealand. This chapter serves to assess the characteristics of in-cave organic metal complexation and the rate-dependent availability of selected first-row transition metals (Co, Ni, Cu) in cave waters at the water-calcite interface.

Chapter 4 – This chapter investigates the role of organic complexation and OMC decay kinetics in the incorporation process of selected transition metals (Co, Ni, Cu) and alkaline earth metals (Mg, Sr) into calcite. To a first point, this study reports on 10 cave-analogue laboratory experiments, in which various inorganic and organic synthetic drip solutions are used to precipitate calcium carbonate, mimicking the formation of stalagmites at variable drip rates. Experimental estimates of apparent partition (distribution) coefficients are integrated with a large range of datasets obtained from various caves around Aotearoa New Zealand and the South Pacific (this study), as well as a comprehensive compilation of previously published studies. With view to utilising the rate-dependent metal release from OMCs (see Chapter 3) as a palaeoclimatic proxy system applicable to stalagmites, this chapter tests for the preservation of 'kinetic signals' due to OMC decay during metal inclusion into calcite.

Chapter 5 – With insights from Chapter 3 and Chapter 4, the final research chapter comprises results from an ongoing case study of trace elemental systematics in modern cave

environments on the South Pacific island of Niue, and two preliminary Holocene stalagmite records derived from these. Located at ca. 19 °S, Niue is geographically predestined for the study of several major climatological phenomena, while numerous limestone caves provide premise to add valuable new speleothem-based information to the otherwise sparsely covered Southern Hemisphere climate record. This chapter serves to build up a comprehensive cave monitoring dataset to support palaeoclimatic interpretation of annually-laminated stalagmites from these caves.

Chapter 6 – The final chapter presents overarching conclusions on the findings of this thesis, and provides recommendations for future avenues of research.

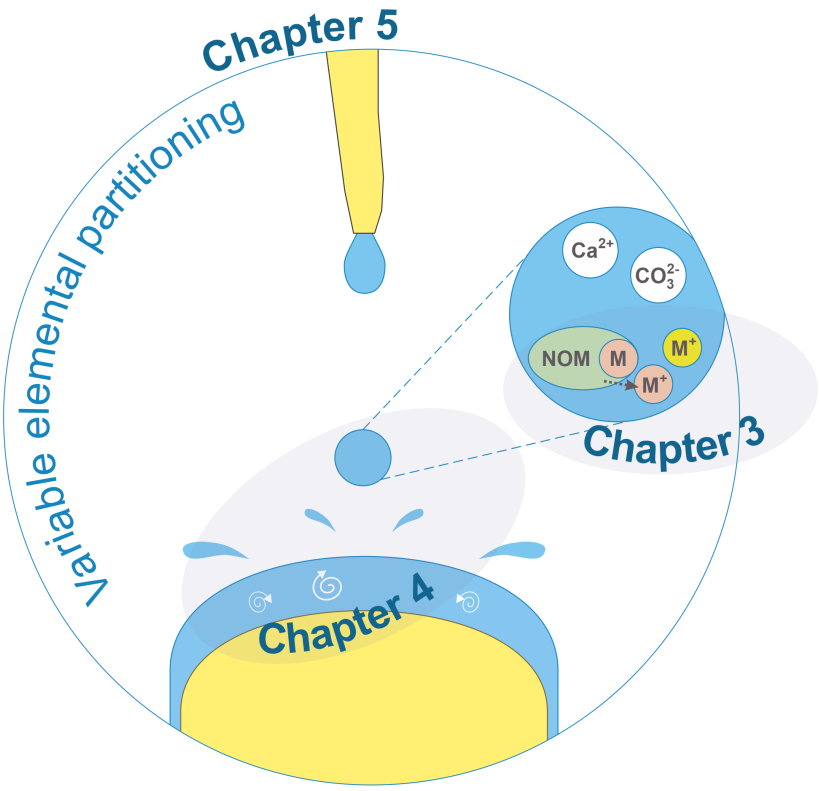

Figure 1.1: Illustration of thesis research topic and chapter-wise foci. The first research chapter (Chapter 3) focusses primarily on processes in the dripwater, namely the decay of organic metal complexes (OMCs). Chapter 4 investigates the incorporation of trace metals into calcite at the dripwater-calcite interface. Chapter 5 assesses these processes in the wider context of natural karst systems.

Chapter 2

Literature review

2.1 Introduction

This thesis links aspects of speleothem science, aqueous and carbonate chemistry, and palaeoclimatology. This chapter serves to review the literature of each field with relevance to this project, starting with an overview of karst and cave systems (Sections 2.2.1 and 2.2.2), and processes driving the formation and chemical composition of speleothems (Section 2.2.3). Their role and potential as environmental archives are reviewed in Section 2.3. Section 2.4 describes the current application of trace metals in speleothem science. Key principles of metal speciation and complexation are reviewed in Section 2.5, along with a brief overview of different techniques used to assess the dissociation of organic metal complexes (Section 2.5.2). Using examples, Section 2.5.3 describes the major factors controlling aqueous metal complex stability. Section 2.6 outlines the current state of knowledge of transition metal behaviour in karst systems, and the most relevant recent findings that encourage their use as palaeoenvironmental proxies. Finally, the dominant drivers of modern (Section 2.7.1) and Holocene (Section 2.7.2) climate in the study regions of Aotearoa New Zealand and the South Pacific are briefly described.

2.2 Cave systems and speleothems

2.2.1 Caves as archives of natural processes and human activity

Caves are subterranean cavities of highly diverse morphology and origin, examples of which have been found on all continents, including Antarctica (Sawagaki et al., 2008; Tebo et al., 2015). Their limited connection to atmospheric conditions and processes has led to the evolution of unique ecosystems and numerous niche-adapted species (Barton & Northup, 2007). Many caves have held considerable sociocultural significance as places of refuge, habitation and domestic activities, burial, and ceremony and worship, for both ancient and modern soci-

eties (Goldberg & Sherwood, 2006; Roebroeks & Villa, 2011; Tomkins, 2009). Consequently, caves have long been at the focus of archaeological studies as archives of human activity, recorded through human-made modifications to caves, such as wall paintings (Valladas et al., 2001) and burning (Karkanas et al., 2007), artefacts found in the cave (Goldberg & Sherwood, 2006), or human remains. A prominent recent example of the latter is the discovery of Late Pleistocene elements of a possibly new species of the genus *Homo* in a cave in the Philippines, presenting significant new information on the human evolution and dispersal (Détroit et al., 2019). Similarly, caves traditionally play a central role in the study of prehistoric fauna due to their inherent function as both natural shelters and traps (Lundelius, 2006), with numerous palaeontological studies benefiting from the high preservation potential of caves for the remains of ill-fated animals (Black et al., 2010; Worthy, 1997). A large variety of different types of caves exists across a range of landscapes and climatic regimes, the most abundant of which are solution caves formed in terrains dominated by carbonate rocks (*e.g.*, limestone, dolomite, and marble). Another type of the latter is found in gypsum deposits, which host some of the longest known examples of solution caves (Klimchouk, 2005).

With regards to the formation of carbonate solution caves, Ford and Williams (2007) suggested a set of favourable criteria, including the presence of abundant bedrock of pure and hard calcium carbonate with pronounced secondary porosity (see Section 2.2.2), hilly or mountainous terrain with local relief, and significant rainfall. Since this study is concerned with carbonate deposits as found in solution caves, the following sections are focussed on their development in particular, and carbonitic karst environments at large. The processes involved in the formation of speleothems, *i.e.*, cave deposits, are outlined in Section 2.2.3

2.2.2 Karst hydrology and surface-to-cave processes

Continuous weathering of carbonate rocks by meteoric water gives rise to so-called karst landscapes, often characterised by ragged and high-relief topography. Given that rainwater is naturally acidic with a pH ranging from ca. 4.5 to 5.6 (Charlson & Rodhe, 1982), the infiltration of meteoric water into carbonate bedrock produces pronounced dissolution features.

The capacity for drainage and storage is largely dictated by the porosity and permeability of the bedrock. In a broader sedimentological context, it is generally distinguished between primary and secondary porosity, where spaces in the sediment or rock originating from the time of deposition define the former. In contrast, secondary porosity describes any subsequently generated cavities. However, these terms are less definitive with regards to carbonate deposits. In carbonates, secondary porosity derives from the extension of existing spaces, and the dissolution and removal of less resistible components. In addition, spaces may be generated amongst secondary crystals, such as dolomite, that form in place of primary host phases during diagenesis (Ford & Williams, 2007).

Variable degrees of weathering, and resulting structural properties, allow for the broad subdivision of typical karst systems into a vadose (aerated or unsaturated) and a phreatic (satu-

rated) zone (Figure 2.1). The vadose zone comprises the soil (if present), the epikarst, and a lower transmission zone that is characterised by the downward flux of water through fissures and conduits under absence of significant storage. The epikarst denotes the uppermost zone of the vadose carbonate terrain, which is typically marked by more intense weathering than underlying bedrock (Williams, 2008). Strongly weathered epikarst is typically less permeable and porous than lower regions of the vadose zone due to complex structural modifications, and often functions as an aquifer by retaining and storing infiltrating surface waters. As such, the epikarst is critical in controlling the residence time of water along its flow path through a karst system (in the order of days to 10s of years), and hence in modulating environmental signals eventually captured by speleothems (Poulain et al., 2018). The thickness of each zone in the karst system can vary substantially, and soil and epikarst (with respect to its hydrological function) may be completely absent (Williams, 2008). The underlying phreatic zone refers to the part of the karst system below the water table, where pore spaces are saturated with water, and storage dominates (J. Perrin, 2003).

Depending on local porosity and permeability, the migration of water through karst systems occurs as a mixture of different end-member modes, namely via fracture flow or matrix / seepage / diffusive flow. Fracture flow along fissures or conduits can be dominant in layers of high porosity and permeability (*e.g.*, in parts of the transmission zone), and is generally comparably quick. Slow diffusive flow is most significant where bedrock exhibits a low porosity (*e.g.*, in the epikarst), and presents the primary mechanism for storage (Markowska et al., 2015). Accordingly, cave drip points primarily fed by fracture flow tend to show a stronger sensitivity and responsiveness to recharge, whereas the temporal variability in the latter may effectively be smoothed or lagged when diffusive flow is dominant. For instance, the slow movement of diffusive flow often persists even over periods of droughts, whereas fracture flow is more likely to cease in response to diminishing surface recharge. In general, however, hydrological routing at a given cave drip point can be expected to involve various flow regimes along a spectrum between fracture and diffusive flow, and signals captured by speleothems consequently carry information integrated over the entire flow path (Poulain et al., 2018).

As water enters the soil zone, natural organic matter (NOM) is detached and mobilised. For simplicity, organic matter (OM) herein synonymously refers to naturally occurring organic matter, *i.e.*, excluding anthropogenic material and living organisms. Organic matter is by convention categorised into three operationally-defined size fractions based on the separation by filtration, namely the dissolved (DOM, size $<$1 nm), colloidal (solids between 1 nm and 1 µm), and particulate (solids of $>$1 µm) fractions. At large, organic matter deposited in speleothems can be assumed to be either derived from the overlying media (primarily from soil and vegetation) or from microbial activity within the cave. The former is for the most part produced by the degradation of plant-litter and remnants of soil fauna. During its transport through the soil zone, and potentially beyond, OM is further broken down by microbial activity (Lehmann & Kleber, 2015). The relative contribution of different size fractions depends to a large extent on the dominant flow mode, given that larger particles require more energy to be mobilised and retained in motion. However, differences in the leaching potential of OM also exist within size

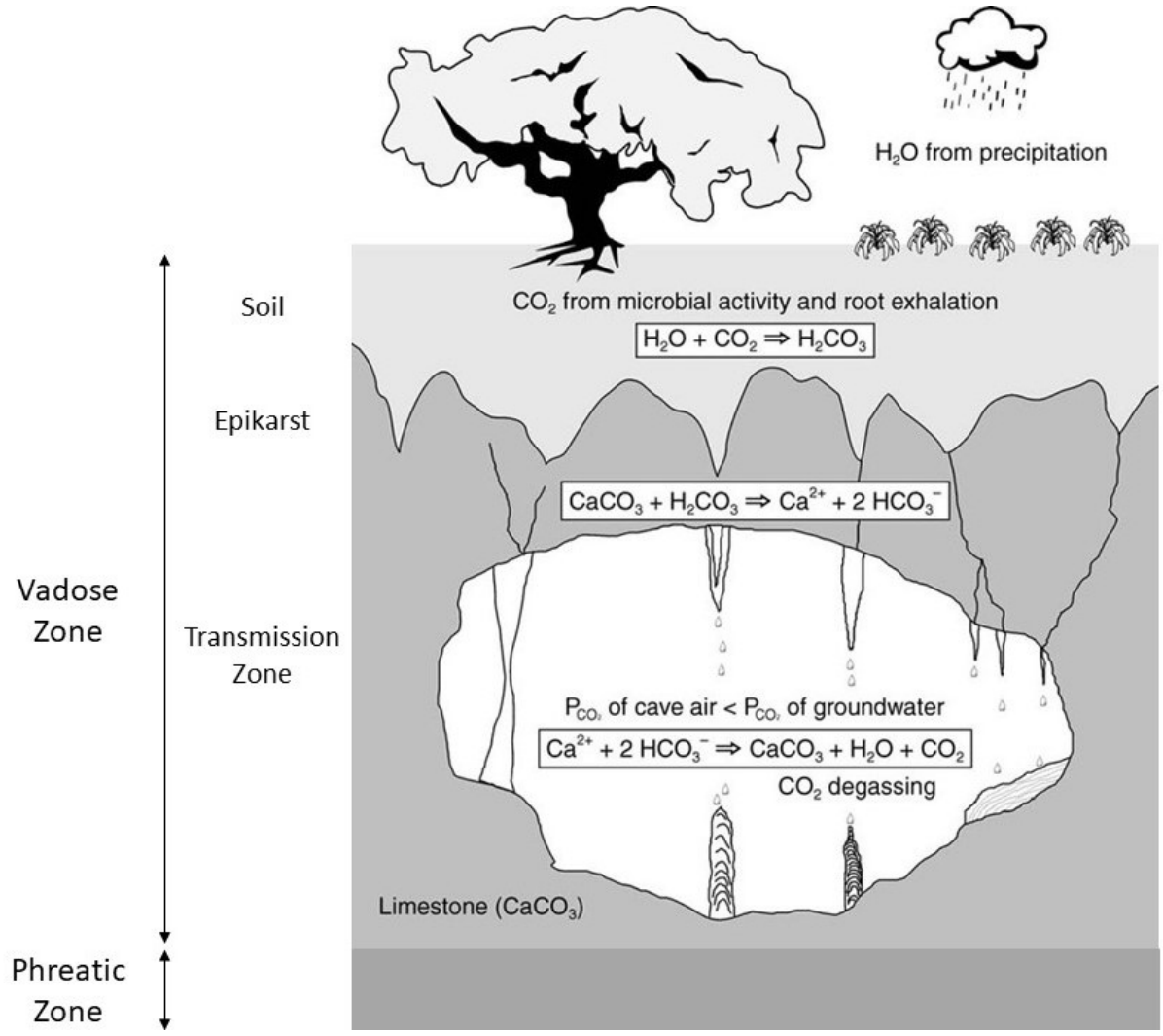

Figure 2.1: Schematic overview of typical karst system components and processes. Speleothem formation is at large driven by varying pCO_2 levels encountered by percolating water on its way from the surface to the cave, favouring calcite dissolution in the epikarst, and precipitation in the deeper karst and in caves. The figure is modified from Fleitmann et al. (2004).

classes due to the composition. For instance, hydrophilic compounds (*e.g.*, carboxylic acids and amino acids) are more readily transported in water than the hydrophobic fraction of DOM (*e.g.*, *n*-alkanes, lignin and derived products). However, transport of the latter may in turn be facilitated to some extent by the mobilisation of colloidal matter (Blyth et al., 2007).

The second main source of OM is provided by microbial communities within the cave. These communities vary greatly in their composition between different cave systems (Barton & Northup, 2007; Epure et al., 2014), likely owing to some capacity to adapt to specific rock types. Their preservation nowadays presents an important aspect in cave conservation and management efforts (Northup, 2011). Microbes are present in cave sediments, dripwaters, and on cave surfaces, which renders their contribution to OM incorporated in speleothems very likely (Baker et al., 2016; Blyth & Frisia, 2008; Blyth et al., 2014; Tomczyk-Żak & Zielenkiewicz, 2016; Yang et al., 2011; Yun et al., 2015), albeit the latter may well be indistinguishable from allochthonous OM inputs in many cases. This in turn may complicate the interpretation of certain proxy signals derived from speleothem-bound OM (Yang et al., 2011). To some extent, the relative contributions of allochthonous and autochthonous OM may be related to the flow time of water from the surface environment to the speleothem, *i.e.*, the residence time of water within the soil and vadose zone where significant degradation occurs. Accordingly, a larger time window for the breakdown of OM during prolonged transport is likely to result in a proportionally larger contribution of autochthonous OM, whereas allochthonous OM is more likely to be preserved and present in larger proportions when the residence time is short. However, Blyth et al. (2016) also note the potential limitations for autochthonous OM contributions due to a limited supply of energy sources for microbial activity when allochthonous inputs are small.

2.2.3 Speleothem formation

The formation of speleothems (derived from the ancient Greek words *speleux* for "cave", and *them* for "deposit") is ultimately driven by the dissolution of calcareous rocks by meteoric waters. Rainwater is naturally acidic due to the dissolution of atmospheric CO_2, and the resulting formation of the weak acid H_2CO_3 (carbonic acid, Equation 2.1). As water percolates through the upper vadose zone, it encounters relatively high pCO_2 in the soil due to plant root exhalation and microbial degradation of organic matter. As a consequence, more CO_2 can be dissolved, which in turn increases the capacity for the dissolution of calcareous bedrock (Figure 2.1, Fairchild & Baker, 2012).

As dripwater enters cave environments, where pCO_2 levels are typically lower than in the epikarst, the equilibration of dripwater with ambient pCO_2 conditions drives the degassing of dissolved CO_2 (Treble et al., 2015). This reduction in CO_2 results in the super-saturation of the drip solution with respect to calcite, driving Equation 2.4 towards the consumption of Ca^{2+} and HCO_3^-, and the precipitation of $CaCO_3$ (M. Hansen et al., 2013). The degassing of CO_2 and the precipitation of $CaCO_3$ occur at a stoichiometry of 1:1. The key chemical reaction steps responsible for speleothem formation can be described as follows:

$$H_2O + CO_2 \rightleftharpoons H_2CO_3 \tag{2.1}$$

$$H_2CO_3 \rightleftharpoons HCO_3^- + H^+ \rightleftharpoons CO_3^{2-} + 2H^+ \tag{2.2}$$

$$2H^+ + CaCO_3 \rightleftharpoons 2HCO_3^- + Ca^{2+} \tag{2.3}$$

$$2HCO_3^- + Ca^{2+} \rightleftharpoons CaCO_3 + CO_2 + H_2O \tag{2.4}$$

Calcite may, however, already precipitate from a solution along its flow path before it reaches the cave, a process termed prior calcite precipitation (PCP). This occurs primarily in the vadose (unsaturated) zone, when the percolating fluid is allowed to equilibrate with lower $p\mathrm{CO}_2$ conditions (Fairchild et al., 2000). Importantly, PCP may result in a substantial evolution of the dripwater chemistry prior to reaching the cave, and may consequently present a dominant control on the ultimate concentrations of certain elements in speleothems formed from these (see Section 2.4). The extent of PCP in a given system may in turn vary substantially over time (Treble et al., 2015), and is particularly pronounced during droughts (McDonald et al., 2004; Owen et al., 2016).

The dependency of calcite precipitation on the equilibration of percolating water with variable ambient $p\mathrm{CO}_2$ conditions also defines cases where cave settings do not allow for the precipitation of calcite, or may in fact drive its dissolution instead. For instance, Genty et al. (2003) noted that altered soil $p\mathrm{CO}_2$ levels during glacial periods temporarily inhibited the deposition of speleothems in Villars Cave (France). In a more general sense, any undersaturated, acidic, or otherwise aggressive water films forming on speleothem surfaces may promote calcite dissolution, for which various mechanisms have been described (*e.g.*, condensation corrosion). Corrosion of cave surfaces is often particularly pronounced near entrances, where conditions are less stable (Baker & Genty, 1998; James, 2005).

In addition to chemical controls on calcite deposition, a shear lack of water supply will also prevent speleothem formation. This may locally be related to changes in hydrological routing or the cease of recharge, both of which are often associated with significant environmental processes (*e.g.*, permafrost or glacial coverage that prevents surface water from entering the karst system). In the context of palaeoclimate reconstructions, growth cessations (manifest in a hiatus) are thus important features of speleothem records, both in terms of chronology, as well as an indication of environmental change during the time of the hiatus (Spötl & Mangini, 2007).

Although the underlying chemical processes of formation are essentially the same in most caves (examples of exceptions include hyperalkaline settings, such as Poole's Cavern, UK; Hartland et al., 2011), speleothems come in a large variety of shapes and sizes. Broadly, they

are differentiated into three main categories depending on their morphology, namely stalagmites (growing upwards), stalactites (growing from the ceiling), and flowstones (growing from fluid flow). Each of these can be further described according to more specific geometrical properties (*e.g.*, Curl, 1972, 1973; Gams, 1981; Hill & Forti, 1995), and several models to characterise the speleothem architecture based on growth-determining factors have been put forward (*e.g.*, Dreybrodt, 2008; Kaufmann, 2003; Romanov et al., 2008). In addition to their shape, speleothems further may differ in their mineralogy (*e.g.*, calcite versus aragonite; Frisia et al., 2002), crystal development, and crystal fabrics (Frisia et al., 2000, 2022). Speleothem morphologies and chemical properties can additionally be altered after their deposition, for instance due to chemical and mechanical weathering, ground-shaking, or human and faunal activities.

A crucial property and key incentive to study speleothems in a palaeoclimatic context is their accretionary growth, *i.e.*, the effectively continuous deposition of calcite over time. In certain settings, for instance with a high seasonality in climate and karst processes driving speleothem formation, clear annual layers may be distinguishable (Baker et al., 1993, 2008; Tan et al., 2006; Fairchild & Treble, 2009), as first demonstrated by Broecker et al. (1960). These are typically composed of a darker and lighter growth band corresponding to seasonal variations in recharge and dripwater composition (including OM content). Laminae may, however, also reflect different time scales, and examples of both sub-annual and super-annual (including centennial) frequency of growth layers are known, but mechanistically less well understood (Baker et al., 2008; Fairchild & Baker, 2012).

2.3 Speleothem-based environmental reconstructions: an overview of selected proxy systems

The conceptual situation of speleothems at effectively the end of meteoric water flow paths from atmosphere and surface through complex soil and bedrock systems gives rise to a wealth of information potentially stored in them on various environmental, climatic, and anthropogenic processes (Fairchild, Smith, et al., 2006) on local to global spatial scales (Bar-Matthews et al., 1999; Mariethoz et al., 2012). Various other terrestrial environmental archives exist, including tree rings (Babst et al., 2018) and sediment records (*e.g.*, from lakes (Bichet et al., 2014; Zolitschka et al., 2015), peatlands (Swindles et al., 2012), loess or palaeosol deposits (Schaetzl et al., 2018)), all of which have certain advantages and disadvantages. In this regard, however, speleothems generally show highly favourable characteristics, rendering them particularly powerful recorders of environmental conditions. Cave deposits may grow continuously for 1000s to 10,000s of years, and incremental growth layers are not typical subject to mechanical disturbances (Gałuszka et al., 2017). Depending on their growth rates, individual speleothems may record information at temporal resolutions in the order of days to a million years, a range that is otherwise only matched by ice cores (Battarbee & Binney, 2008; Fairchild & Baker, 2012). Moreover, speleothems are typically well-datable using radiometric techniques, and their inter-

nal structures further facilitate the establishment of robust chronologies. The ^{230}Th-U method allows for accurate dating up to approximately 500,000 years BP (Richards & Dorale, 2003; Scholz & Hoffmann, 2008), while the more recent development of the U-Pb method has made dating up to ca. 4 million years BP possible (Richards et al., 1998; Woodhead et al., 2006, see Section 2.3.2 for a more detailed overview of dating procedures for speleothems). With the exception of Antarctica, speleothem-bearing caves have been found on all continents, and cover numerous climate regimes from low to high latitudes.

Nonetheless, the unique nature of each speleothem sample requires careful and thorough interpretation of proxy records for a given site and sample, and the exact origin of measured signals may be ambiguous. To some extent, these challenges may be approached by an increased integration of various proxy records within and amongst individual speleothems, as well as other, contextually related environmental archives (*e.g.*, Fairchild & Baker, 2012; C. L. Smith et al., 2006). Here, a brief overview is given of the most common techniques and proxy systems applied to speleothem-based environmental reconstructions, as well as selected examples of novel developments.

2.3.1 Collection of speleothem samples

Given the individuality of each speleothem, careful planning prior to the collection of samples for (palaeo)environmental studies is critical to facilitate the extraction of meaningful information in subsequent analyses. While the specific research question typically pre-defines desirable sample material in terms of its age and internal structure (*e.g.*, presence and quality of growth bands), however, such criteria cannot be readily assessed in the field. Similarly, the preservation state (*i.e.*, the degree of diagenetic alteration) presents a critical requirement that cannot be accurately determined *in-situ*. Although speleothems are typically less susceptible to chemical and physical transformations compared to many other archives (Fairchild & Baker, 2012), significant diagenesis may occur even under seemingly stable conditions (Martín-García et al., 2009), or in microscopic, highly confined areas within a sample (Bajo et al., 2016). This in turn can considerably change original features and the geochemical composition of a sample, and the analysis of unknowingly altered material may lead to considerable chronological errors and misinterpretations of proxy signals (Bajo et al., 2016; C. Perrin et al., 2014; Scholz & Hoffmann, 2008; Martín-García et al., 2009). Additional factors may influence the choice of speleothem sample to be obtained, including accessibility and permission, as well as conservation policy. As speleothems receive increasing attention as desirable archives of past environments, the rising demand for sample material from these slowly-forming structures adds to more obvious conservation challenges surrounding cave systems, such as tourism, and environmental modifications (Gillieson, 2011).

In order to increase the chance of success in obtaining suitable samples, and thereby minimise the removal of potentially unsatisfactory material, Frappier (2008) proposed a step-wise screening protocol based on various *in-situ* and subsequent laboratory-based observations

with emphasis on well-defined research objectives and expectations. For palaeoenvironmental studies, initial targeted sampling at the base of a stalagmite, for example, can provide preliminary age constraints on extractable records, and thereby inform whether any further sampling would be reasonable (Frappier, 2008). Moreover, long-term palaeoenvironmental records can be established using either whole specimens or cores drilled along the growth axis of a deposit (*e.g.*, Hellstrom et al., 1998). Core sampling can often present a less destructive and at times more practical alternative, however, requires rather symmetric growth. Depending on the research question, well-preserved and datable loose specimens previously detached from their original position (*e.g.*, during earthquakes or prior human or faunal activity) may also be considered to avoid the removal of intact material (*e.g.*, Columbu et al., 2019; M. C. Meyer et al., 2008). All sampling is naturally subject to permission from respective landowners and custodians, and community engagement should be practised to ensure respectful and culturally appropriate practices.

2.3.2 Dating of speleothems

One of the most significant advantages of speleothems over many other environmental archives is their exceptional suitability for radiometric dating and the establishment of robust chronologies (Spötl & Boch, 2019; Zhao et al., 2009). Since the first efforts to determine the ages of speleothems, and extract meaningful environmental information from them, techniques to date these deposits have substantially improved. In particular, speleothems are well-suited for uranium-thorium dating.

The uranium-thorium (U-Th) radiometric dating technique, also known as U-series or U-series disequilibrium dating, amongst other names, utilises the radioactive decay of ^{238}U (with a half-live $t_{1/2} \approx 4.469 \times 10^9$ years) to the stable ^{206}Pb. This occurs via a series of intermediate daughter products, including ^{234}U and ^{230}Th. The dating is based on the disruption of a secular equilibrium, which describes the state in which the activities of all parent and daughter isotopes in the decay chain are equal (Richards & Dorale, 2003). The radiometric "clock" is started by a disequilibrium in the ^{238}U–^{234}U–^{230}Th series, in the course of which U is differentiated from Th. In the speleothem context, this is established by the precipitation of calcite from water due to the contrasting solubility of U and Th (highly insoluble) in natural aqueous systems. The much more mobile U is readily incorporated into calcite, whereas essentially no Th is included (Grenthe et al., 1992). Reliable dating is now possible for ppb to ppm concentrations of U and concurrent negligible initial and detrital Th contents in the sample, and provided that the system remained closed after disequilibrium, excluding post-depositional exchange of parent or daughter isotopes (Dorale et al., 2004).

The first major methodological breakthrough with regards to U-Th dating was the development of thermal ionisation mass spectrometry in the 1980s (TIMS) (Edwards et al., 1987, 1988; Ludwig et al., 1992), which replaced the original α-counting method. The introduction of TIMS methods significantly improved the resolvable age range due to considerably lower

instrumental detection limits from ca. 350,000 to 500,000 years, yielded unprecedented precision in the order of 1–2% for interglacial speleothems and corals, and substantially reduced the necessary sample size (Zhao et al., 2009).

From the 1990s, the U-Th technique saw further significant advancements with the development of multi-collector inductively coupled plasma mass spectrometry (MC-ICP-MS) (*e.g.*, Hellstrom, 2003; McCulloch & Mortimer, 2008) and high-resolution sector field ICP-MS methods (*e.g.*, Shen et al., 2008), which yet again improved precision, required sample sizes, and sample throughput, relative to the capacities of TIMS analyses. Importantly, the increased sensitivity of ICP-MS and lower detection limits have allowed for robust dates beyond 500,000 years BP and up to ca. 4 million years BP using the U-Pb technique (Richards et al., 1998; Woodhead et al., 2006, 2019), while Cheng et al. (2013) report U-Th ages of up to 800,000 years. With view to the proposed project, well-preserved Holocene samples of ca. 12,000 years of age may now be constrained with errors as low as $\pm$10 years (Cheng et al., 2013). MC-ICP-MS has recently been furthermore coupled with laser ablation, exploring the feasibility of *in-situ* high spatial resolution dating to detect potential small-scale age inversions (Y. Lin et al., 2017).

Altogether, the latest improvements in dating methods present perhaps the most significant advances in the field of speleothem science in recent years, giving rise to the possibility of soon extending high-resolution environmental proxy records well into the Quaternary (Woodhead et al., 2010). Nonetheless, dating of younger carbonates (10s to 100s of years of age) remains challenging despite these developments, largely due to the low concentrations of measurable ^{230}Th, and associated much smaller achievable precisions (Cobb et al., 2003; Shen et al., 2008).

Radiocarbon (^{14}C) dating, although routine for many carbonate and non-carbonate archives with ages resolvable up to ca. 50,000 years, is less commonly applied to speleothem samples. While several studies have successfully used radiocarbon in speleothems (*e.g.*, Fohlmeister et al., 2017; Genty & Massault, 1999; Hua et al., 2012, 2017), especially for younger material spanning recent millennia, a few factors often complicate its application to secondary carbonate deposits. The major challenge lies in the characterisation of reservoir effects in a given system, which arise from the "dead carbon fraction" (DCF). The latter denotes carbon that derives from sources other than atmospheric CO_2, such as the bedrock or old organic matter stored in the soil zone, which may bear little or no ^{14}C due to its age (Griffiths et al., 2012). Since reservoir effects are variable with time, and not readily quantifiable, radioactively "dead" carbon incorporated into speleothem $CaCO_3$ may result in significant errors in derived ^{14}C dates. Finally, the temporal variability in atmospheric ^{14}C needs to be considered, which can be achieved using a number of calibration curves developed for this purpose (Reimer et al., 2013). Efforts to increase the applicability of ^{14}C dating of speleothems continue to be made (*e.g.*, Columbu et al., 2019; Fohlmeister & Lechleitner, 2019), stressing its importance for cases where insufficient ^{238}U (or pronounced detrital thorium) contents in sample materials preclude U-series dating (Hua et al., 2017).

Based on the incremental growth of stalagmites, the manual or automated counting of

growth laminae can help to affirm and improve age-depth relationships (*e.g.*, Baker et al., 2008; Faraji et al., 2021). This is particularly useful in samples that are not amenable to radiometric dating methods, or have formed at sufficiently high rates that allow for the identification of annual growth increments. Importantly, these are not always visible in hand samples or standard optical microscopy, but may for instance be manifest in trace elemental cycles (*e.g.*, Borsato et al., 2007; Faraji et al., 2021; McMillan et al., 2005; Roberts et al., 1998). A combination of lamina counting and high-resolution radiometric dating has in the case of recent stalagmites from the tropical Cook Islands, for instance, yielded age models with uncertainties as low as a few years (Faraji et al., 2023).

2.3.3 Stable oxygen isotopes (δ^{18}O)

Stable oxygen isotope records present the most common proxies applied in speleothem-based studies, and are of particular use to trace regional to global (hydro)climate variability and teleconnections (J. Chen et al., 2016; Cruz et al., 2006; Vuille & Werner, 2005; X. Wang et al., 2004; Treble et al., 2022; J. U. L. Baldini et al., 2021). The stable oxygen isotope ratio δ^{18}O of a sample, expressed in units of ‰, is defined as the ratio of ^{18}O and ^{16}O in the sample material, relative to this ratio in a known standard:

$$\delta^{18}O = \frac{(^{18}O/^{16}O)_{Sample} - (^{18}O/^{16}O)_{Standard}}{(^{18}O/^{16}O)_{Sample}} \times 1000 \tag{2.5}$$

Analytical procedures are well established for the measurement of δ^{18}O in a range of materials, and little sample is needed to achieve robust results. Moreover, the technique is relatively inexpensive, allowing for very highly resolved records. Efforts to compile the rapidly growing body of published speleothem-based δ^{18}O (and δ^{13}C) records have recently culminated in the SISAL database (Atsawawaranunt et al., 2018).

The application of δ^{18}O values as a proxy for environmental conditions is due to pronounced equilibrium and kinetic fractionation, with the latter being the result of the relatively large mass difference between the stable isotopes ^{16}O and ^{18}O. Within the speleothem-forming system, the final δ^{18}O composition as measured in carbonates carries signals derived from dripwater and rainwater evolutions, as well as conditions within the cave during calcite precipitation (Lachniet, 2009). Figure 2.2 provides an overview of the major processes involved.

The oxygen isotopic composition of precipitation ($\delta^{18}O_{Precipitation}$), the primary source of speleothem-forming dripwater, is controlled by several processes that collectively shape the $\delta^{18}O_{Precipitation}$ value before this water enters the soil and karst system. The most determinant processes generating $\delta^{18}O_{Precipitation}$ values include effects related to the moisture source, precipitation amount, topography, and temperature (Dansgaard, 1964; Siegenthaler, 1979). The relative contribution of these in turn varies greatly both spatially and temporally, and needs to be taken into careful consideration for a given location.

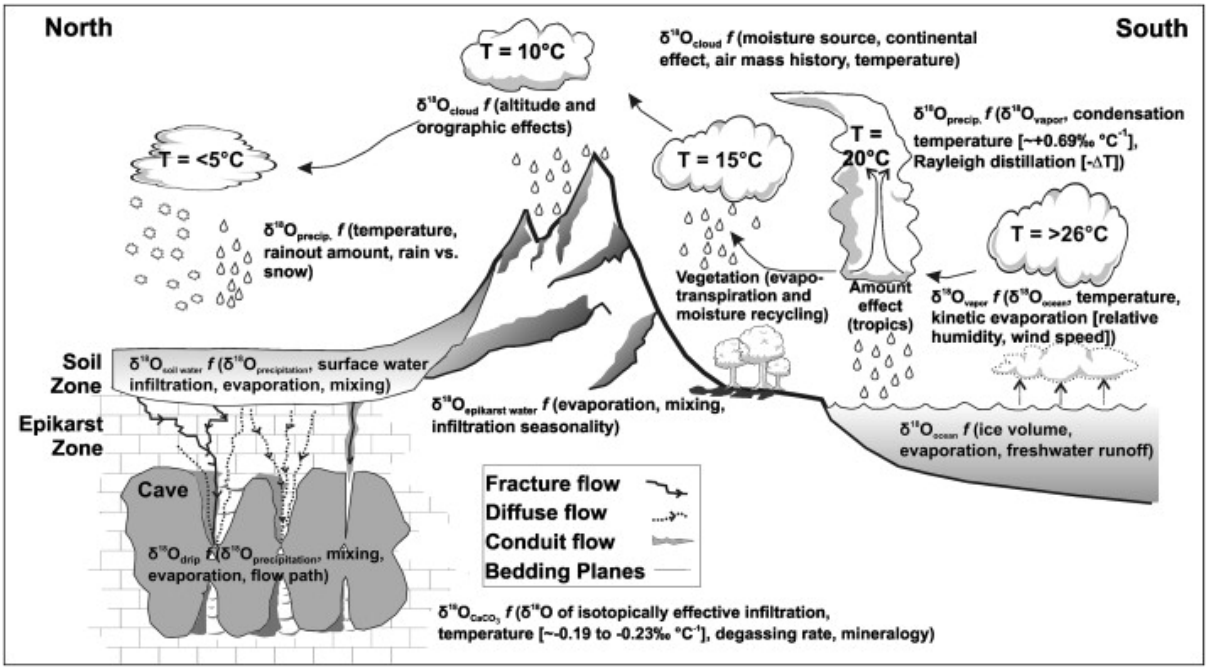

Figure 2.2: Schematic overview of the major processes that collectively shape δ^{18}O values measured in speleothems. Kinetic and/or thermodynamic fractionation of δ^{18}O occurs between meteoric H_2O phases in the atmosphere, soil, and epikarst, and between dripwater and $CaCO_3$ as a function of cave conditions. The figure is adopted from Lachniet (2009).

At a larger scale, the evolution of $\delta^{18}O_{Precipitation}$ can be understood in terms of a Rayleigh-type distillation process, which essentially describes the continuous isotopic fractionation of water vapour and derived phases as they are transported from the tropics (the primary source of water vapour) to higher latitudes (Dansgaard, 1964). As water vapour condenses, $H_2{}^{18}O$ is preferentially precipitated due to its greater mass, resulting in a progressive decrease in δ^{18}O of the remaining water vapour and subsequent precipitates with distance from the vapour source. This phenomenon is enhanced towards the poles due to increased fractionation at lower temperatures.

With view to the strong temperature dependence of δ^{18}O in many marine environmental archives, most early speleothem-based studies attempted to demonstrate similar relationships between air temperature at a given location and local $\delta^{18}O_{Speleothem}$ values (*e.g.*, Duplessy et al., 1970; Emiliani, 1971). A certain control of temperature on $\delta^{18}O_{Precipitation}$ is indeed evident, given that condensation from a vapour mass is enhanced as temperatures decrease, which contributes to many of the processes driving isotopic fractionation in the hydrological cycle (Dansgaard, 1964). However, it is now recognised that in the vast majority of cases, air temperature is likely not the primary driver of speleothem δ^{18}O values (Lachniet, 2009).

For instance, when extensive precipitation occurs over a specific region, the so-called amount effect essentially accelerates the Rayleigh distillation process, and precipitation in these areas exhibits particularly low δ^{18}O values (Lachniet & Patterson, 2009). This effect is a direct result of the shear amount of precipitation, and is thus especially pronounced in tropical monsoonal regions. Moreover, the initial δ^{18}O value of precipitation largely depends on the

moisture source of the respective air mass (the so-called source effect), which can vary considerably between locations (Cole et al., 1999; Friedman, 2002). The $\delta^{18}O$ values of a given air mass in turn reflect its history, the temperature of the moisture source, and regional patterns in oceanic $\delta^{18}O_{Water}$ (Lachniet, 2009; LeGrande & Schmidt, 2006).

Apart from the source and its composition, the pathway of moisture transport also poses a significant control on the water isotopic composition. The continental and orographic effects describe the influence of landmass and topography on the isotopic evolution of moisture, linked to both the distance travelled across land, and altitude experienced by a vapour mass (Liu et al., 2010). Continental precipitation generally tends to exhibit increasingly depleted $\delta^{18}O$ values with distance from the coast due to progressive rainout, however, significant spatial and indeed temporal differences in the degree of this effect are observed (Liu et al., 2010; Salati et al., 1979). This phenomenon is closely associated with, and often amplified by the altitude effect. The latter arises from enhanced condensation and precipitation as vapour rises and is subjected to decreasing air temperatures at higher elevations (Siegenthaler, 1979). In principle, $\delta^{18}O$ values of precipitation consequently decrease with altitude (Vogel et al., 1972), although in some circumstances additional factors, such as mixing of different air masses, may mask this trend (Gat et al., 2001).

The isotopic composition of meteoric water is furthermore modified by a number of processes upon entering the soil and karst system. Shifts in $\delta^{18}O_{Water}$ values from the precipitation may already occur at the soil surface, for instance due to pooling or run-off when the soil is saturated, or an enrichment in $\delta^{18}O_{Water}$ as a result of excessive evaporation (Lachniet, 2009). Within the karst system, the hydrological routing and recharge of water is furthermore critical for its isotopic evolution, as mixing and storage may significantly alter the original composition. Indeed, karst hydrology has recently been shown to exert a pervasive control on speleothem $\delta^{18}O$ that may dominate isotopic ratios in some systems (Treble et al., 2022).

Finally, isotopic fractionation also occurs during the precipitation of $CaCO_3$ at speleothem surfaces, typically with both an equilibrium and a kinetic component. The former is at large temperature-dependent, and predictable if equilibrium conditions are provided. This may be the case when the cave atmosphere is stable with a high relative humidity, and calcite precipitation is driven by slow degassing of CO_2 from the dripwater (particularly in deep caves, Hendy, 1971). In contrast, factors including cave ventilation or low relative humidity often create a disequilibrium between dripwater and speleothem, resulting in rapid CO_2 degassing. Under such circumstances, kinetic effects may superimpose on the thermodynamic fractionation, wherein the favoured precipitation of ^{18}O produces elevated $\delta^{18}O_{Speleothem}$ values.

Considering the various intricately related factors determining $\delta^{18}O_{Speleothem}$, it is clear that their interpretation in terms of specific environmental processes is extremely complicated. A powerful tool to aid in delineating particular environmental signals is the use of multiple proxy systems, of which the respective controls are ideally mechanistically distinct. With view to this project, the concentrations of most trace metals in dripwater and speleothems are not influenced by many of the processes driving $\delta^{18}O_{Speleothem}$, thus presenting an opportunity to com-

plement and support δ^{18}O records.

2.3.4 Stable carbon isotope (δ^{13}C)

Stable carbon isotopes are routinely analysed alongside stable oxygen isotopes, and δ^{13}C (in ‰) is defined analogously to δ^{18}O as:

$$\delta^{13}C = \frac{(^{13}C/^{12}C)_{Sample} - (^{13}C/^{12}C)_{Standard}}{(^{13}C/^{12}O)_{Sample}} \times 1000 \tag{2.6}$$

Given the analytical practicality, multiple studies have assessed the applicability of $\delta^{13}C_{Speleothem}$ as palaeoenvironmental proxies. In many other environmental archives, the significance of δ^{13}C values is at times challenged, primarily because biological processing of carbon results in substantial and often highly variable kinetic fractionation (*e.g.*, Halverson, 2013; Watanabe et al., 2002). Similarly, a vast number of factors are known to affect δ^{13}C values of speleothem-forming dripwaters along their flow path from the surface to the cave.

Carbon derived from plants and their products in the soil is mobilised by percolating water, and ultimately presents a significant fraction of the carbon available for the incorporation into $CaCO_3$. To a large extent, speleothem δ^{13}C values are thus considered to reflect the overlying vegetation regimes, which in turn are governed by climatic conditions. Consequently, any process that affects the vegetation above the cave effectively also contributes to δ^{13}C signals captured by speleothems, albeit indirectly.

For instance, fluctuations in atmospheric pCO_2 over geological time-scales have been shown to potentially exert a major control of speleothem δ^{13}C, accounting for more than half of the signal's variance (Wong & Breecker, 2015). Differences in the isotopic composition are therein attributed to the pCO_2-controlled relative abundance of C3 and C4 vegetation types, which are known to be favoured under higher and lower pCO_2 conditions, respectively (Flores et al., 2009). Linked to differences in their photosynthetic pathways, C3 plants typically exhibit significantly lower δ^{13}C values in the range of approximately -40 to -20‰, opposed to ca. -17 to -9‰ observed for C4 plants (Staddon, 2004). Moreover, temporal variability in plant respiration, for example due to seasonal differences in temperature and precipitation, may result in significant changes in the relative contributions of isotopically light soil CO_2 and atmospheric CO_2 (comparably enriched), both of which are dissolved in the infiltrating water (Genty et al., 2001).

However, it has also been recognised that aged organic matter and (to a lesser extent) bedrock dissolution likely contribute to the calcite δ^{13}C (Genty et al., 2001; Oster et al., 2010), with some evidence suggesting that old organic matter in the epikarst could in fact present the primary source of carbon for speleothems (Noronha et al., 2015). In addition, carbon isotopes are kinetically fractionated during CO_2 degassing from water in the epikarst and caves, and during the subsequent precipitation of $CaCO_3$. This in turn is strongly modulated by the degree

of cave ventilation. Isotopic equilibrium is generally disrupted by strong ventilation, which accelerates CO_2 degassing and favours the enrichment of ^{13}C in the calcite precipitate (K. W. Meyer et al., 2014). Conversely, in-cave kinetic effects are minimal under stable cave conditions.

Despite these complexities, comprehensive efforts to constrain $\delta^{13}C$ systematics in karst environments continue to promote their establishment as routine speleothem-based proxies (Fohlmeister et al., 2020; Lechleitner et al., 2021).

2.3.5 Fluid inclusions

As calcite precipitates from the thin water films sitting on speleothems, some of the water may essentially be trapped in voids between calcite crystals. Such fluid inclusions present potential windows into the dripwater composition and its environmental controls at the time of precipitation (Harmon et al., 1979; Schwarcz et al., 1976), provided that fluids can be extracted without any significant chemical alterations. This critical first step has proven technically and analytically difficult (Matthews et al., 2000; Vonhof et al., 2006), however, and only recent methodological advances have allowed for more reliable applications of geochemical proxies to fluid inclusions, such as $\delta^{18}O$ or δD (*i.e.*, $\delta^{2}H$) measurements (*e.g.*, Affolter et al., 2014, 2019; Uemura et al., 2016; Demény et al., 2021; Warken, Weißbach, et al., 2022). Although extraction techniques continue to be refined (Affolter et al., 2019), the majority of fluid inclusion studies are now achieved using crushing systems coupled to the respective analytical instrument (*e.g.*, Isotope Ratio Mass Spectrometers). Various additional components, such as cold traps, have been introduced to the set-ups, intended to prepare the sample for analysis while minimising any post-extraction alterations of chemical signals of interest. Nonetheless, inconsistencies between different crushing and analytical set-ups remain, and the reproducibility of fluid inclusion analyses needs to be observed (Arienzo et al., 2013).

2.3.6 Organic proxies

The quantity and quality of organic matter found in dripwaters and speleothems is governed by climatic and ecological processes occurring at all stages of OM production and transport, and a range of palaeoenvironmental proxies based on OM found in cave settings has been explored. A recent review of the state-of-the-art of speleothem-based organic proxies is provided by Blyth et al. (2016), including a discussion of the use of NOM-associated trace metals, which bears direct relevance to this thesis (see Section 2.6). Indeed, the development of new speleothem-based organic proxy systems is considered particularly promising, as the integration of multiple inorganic and organic proxy signals in single speleothem samples could provide exceptionally comprehensive accounts of past climatic conditions, as well as landscape dynamics (*e.g.*, vegetation changes).

Early work involving organic matter in speleothems has focussed primarily on the fraction of OM that fluoresces upon excitation. These measurements thereby provide information on

the quality of OM and possibly associated palaeoclimatic and -environmental signals (Baker et al., 1998; Quiers et al., 2015). The method is essentially based around the principle that different OM components show variable susceptibility to excitement by higher energy, ultraviolet (UV) light, and visible light, and in turn emit fluorescence at different wavelengths in response. For instance, electrons weakly bound to aromatic groups in OM are readily excited, resulting in relatively pronounced emissions at wavelengths of ca. 360 to 450 nm (longwave UV and blue-violet). In contrast, some fractions of NOM emit at shorter (UV) wavelengths in the range of ca. 300 to 350 nm, particularly those with fewer aromatic groups. Generally, decreasing aromaticity and increasing hydrophilicity of OM appear to correspond with lower emission wavelengths (McKnight et al., 2001; Quiers et al., 2015). Importantly, this provides a basis for evaluating OM processing through the karst systems, as biological breakdown of OM in the soil is considered to produce fluorescent DOM that emits at shorter wavelengths compared to fresher OM (Cumberland & Baker, 2007). Fluorescence measurements are also of interest to this proposed study as a relatively simple means to characterise OM present in dripwater (Hartland et al., 2012), and aid in interpreting kinetic experiments.

Other promising new approaches include targeted chemical analyses of OM, such as compound-specific $\delta^{13}C$ measurements (Blyth et al., 2013), or the analysis of plant-derived biomarkers (*e.g.*, Glycerol Dialkyl Glycerol Tetraethers, GDGTs, or n-alkanes, Blyth et al., 2007; Blyth & Schouten, 2013). However, more fundamental work is needed to allow for reliable interpretations of these proxies in speleothems, and the targeted chemical analysis remains challenging due to the need for isolating sufficient quantities of the substances of interest from the calcite, and subsequent chemical separation and extraction.

2.4 Trace elements in dripwater and speleothems: established applications

As calcite is precipitated, minor and trace elements present in the dripwater may additionally be incorporated into the speleothem structure. Given their same valence and similar atomic size, elements such as Mg and Sr can readily substitute for Ca, and occupy the same site in the carbonate crystal lattice (Fairchild & Treble, 2009; Gascoyne, 1983). Experimental studies, including via 'cave-analogue' setups that simulate cave conditions (Day & Henderson, 2013; Huang & Fairchild, 2001), have shown that this partitioning of Mg and Sr into calcite is comparably predictable (Fairchild & Treble, 2009), and can be described in terms of the partition (or 'distribution') coefficient, D_X, where X denotes a divalent metal cation (*e.g.*, Mg^{2+} or Sr^{2+}):

$$D_X = \frac{\left(\frac{X}{Ca}\right)_{Crystal}}{\left(\frac{X^{2+}}{Ca^{2+}}\right)_{Solution}} \tag{2.7}$$

Trace element concentrations, typically normalised to Ca contents, present common proxy

systems for many environmental archives, and Sr and Mg abundances are likewise frequently reported in speleothem-based studies. While Sr/Ca and Mg/Ca ratios respond rather well with ambient environmental conditions during the formation of several primary materials (*e.g.*, as palaeothermometers in corals or foraminifera, Henderson, 2002), the controls on trace elements in dripwater and speleothems are more diverse. Several early studies attempted to similarly demonstrate a thermal control of trace metal incorporation into speleothems (Gascoyne, 1983; Goede & Vogel, 1991), and experiments indeed showed correlations between temperature and Mg partitioning into calcite under cave-analogue conditions (Huang & Fairchild, 2001; Wassenburg et al., 2020). In most cave settings, however, the effect of temperature on the incorporation of alkaline earth metals into calcite appears subordinate compared to other factors or noise, and the notion to use Mg/Ca in speleothems as a palaeothermometer has largely been dismissed (Fairchild & Treble, 2009). Exceptions exist, however, including the sub-aqueous samples presented by Drysdale et al. (2019), which proved amenable for temperature reconstructions. Nonetheless, trace elements in speleothems at large rather reflect the geochemical evolution of the dripwater, which in turn is a function of numerous processes at the surface and in the karst (J. U. L. Baldini et al., 2006; Fairchild & Treble, 2009), in addition to specific local properties. Amongst others, factors that influence trace element concentrations in dripwater include their origin (*e.g.*, precipitation, dust, marine aerosols, bedrock, and soil; Dredge et al., 2013; Fairchild et al., 2000), landscape processes above the cave (*e.g.*, fires or deforestation; Borsato et al., 2007; Campbell et al., 2023; Treble et al., 2016), interactions with and mobilisation of soil components (see Section 2.6, Hartland et al., 2012), water mixing and hydrological routing, dissolution of host rock, or prior calcite precipitation (PCP) (Fairchild et al., 2000; Sinclair et al., 2012).

Indeed, one of the most prominent applications of speleothem Sr/Ca and Mg/Ca ratios today is the use as a diagnostic tool for PCP (Figure 2.3), which is important to consider when interpreting speleothem-based proxies, such as $\delta^{13}C$ (Fairchild, Smith, et al., 2006). Given that D_{Mg} and D_{Sr} are <1, both Sr and Mg preferentially remain in solution during calcite precipitation, while Ca ions tend to go into the solid phase much more readily (Fairchild & Treble, 2009). As a consequence, PCP results in an enrichment of Sr and Mg in residual dripwater (and ultimately in speleothems) relative to Ca, which is reflected in a systematic concurrent increase in the ratios Mg/Ca and Sr/Ca (McMillan et al., 2005; Sinclair et al., 2012). Simultaneously, however, Sr and Mg are also preferentially released from calcite when the latter is dissolved (McGillen & Fairchild, 2005), causing a fractionation of Mg and Sr with respect to Ca in the same direction. Sinclair (2011) cautioned therefore that incongruent calcite dissolution in karst system may consequently yield similar signals in the elemental record as PCP, proposing a mathematical approach to delineate the two contrasting processes. These considerations were followed by the suggestion that a relatively distinct degree of covariance between stalagmite Mg and Sr contents (specifically, the slope of ln(Sr/Ca) versus ln(Mg/Ca) being $\approx$0.9) should be diagnostic of dominant PCP controls Sinclair et al., 2012. However, it has since been shown that these criteria were too stringent (Wassenburg et al., 2020), and that with consideration of mixed bedrock compositions and other variables, significant PCP may be reflected

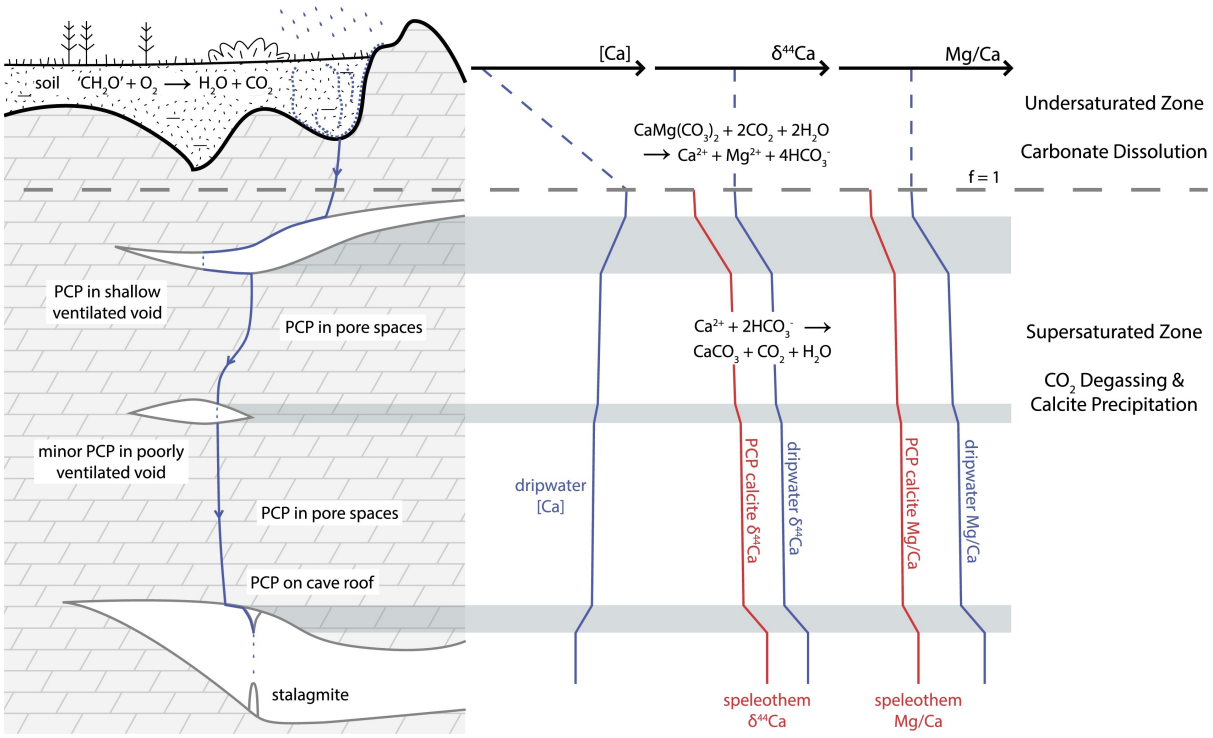

Figure 2.3: Schematic overview of prior calcite precipitation (PCP) and its implications for Ca concentrations, Ca isotope ratios, and Mg/Ca. PCP is generally enhanced, where ventilation facilitates degassing of CO_2 from CO_2-rich percolating water. The figure is adopted from Owen et al. (2016).

in a much larger range of slopes in logarithmic Sr/Ca versus Mg/Ca coordinates (ca. 0.709 to 1.45; Wassenburg et al., 2020).

Based on the observation that PCP is facilitated by enhanced CO_2 degassing, the relative abundances of Mg and Sr have been used as indicators of hydroclimate variability (Jo et al., 2010; Tadros et al., 2016), particularly for the identification of droughts (McDonald et al., 2004; Treble et al., 2003). Relationships between dry conditions and PCP have been observed in many locations (but with exceptions, *e.g.*, Tooth & Fairchild, 2003), and are supported by other records, such as Ca isotope ratios ($\delta^{44/42}$Ca), which have recently been proposed as additional indicators of PCP in Heshang Cave, Central China (Owen et al., 2016).

While the incorporation of divalent trace elements, such as Mg and Sr, from solution into calcite is typically considered to occur according to the partition coefficient as given in Equation 2.7, it is important to note that in reality additional factors influence how much of an element is included in the solid phase in substitution for Ca (Fairchild & Treble, 2009). Particularly in aragonite, which often develops in various forms with different crystal faces, trace elements are preferentially bound at certain sites, leading to a spatially heterogeneous distribution in concentrations (so-called sector zoning, Reeder & Grams, 1987). This is generally less pronounced in calcite speleothems, in which the unit rhombohedral form tends to dominate. Nonetheless, given that crystal development is in part dependent on growth rate, variations in Mg and, more notably, Sr contents in calcite with growth rate have been observed in some studies (Gabitov & Watson, 2006; Treble et al., 2005), although not in others (Huang & Fairchild, 2001).

Apart from alkaline earth metals, such as Mg, Sr, or Ba, a wide range of other elements are also incorporated into calcite, however, they have received little attention to date. Early studies based on speleothems from the Grotta di Ernesto (Italy) demonstrated that concentrations of various trace metals exhibit a strong spatial coherence with fluorescent laminae, suggesting a potential association of certain elements with organic matter within the speleothem (Borsato et al., 2007; Huang et al., 2001). In particular, first-row transition metals from vanadium (V) to zinc (Zn) measured in the speleothem showed distinct layers of enrichments in presence of OM, which was attributed to periodic influx of soil-derived colloidal and dissolved OM during periods of strong rainfall (Borsato et al., 2007). Notably, the findings of Borsato et al. (2007) depicted a hierarchy of covariance between trace metals and fluorescent layers in the order of Y $>$ (Zn, Cu, Pb) $>$ P, Br, implying that some elements (*e.g.*, Y) are more tightly coupled with particular OM fractions than others (*e.g.*, P, Br). Subsequent studies assessing first-row transition metals in dripwaters supported this interpretation (Hartland et al., 2012), and it is now clear that the transport of these elements through the karst system is to a significant degree mediated by the binding of metals by natural organic matter, particularly by the colloidal fraction (Hartland et al., 2014; Hartland & Zitoun, 2018). Importantly, the supply of metals bound to NOM to caves has been shown to be sensitive to hydrological processes in the karst (J. U. L. Baldini et al., 2012; Hartland et al., 2012; Rutlidge et al., 2015), while also carrying information on the OM composition in the dripwater (Hartland et al., 2012).

The following sections provide an overview of concepts and techniques regarding aqueous metal speciation and complexation (Section 2.5, Section 2.5.2, and Section 2.5.3), and a more detailed discussion of the interactions between selected divalent first-row transition metals and NOM in cave waters and during speleothem deposition (Section 2.6).

2.5 Principles of metal speciation and complexation in natural waters

In addition to their total concentrations, the chemical speciation of metals in water is a major determinant variable for their bioavailability and toxicity (Filella et al., 2002; Sigg et al., 2006). The study of speciation in natural waters (here with focus on freshwaters), however, is challenging. Essentially all elements are present in extremely varied chemical forms, and often in low concentrations below 10^{-6} M or even 10^{-10} M. Similarly, the sizes of aquatic compounds range from a few Å to 1 µm or more, which influences their reactivity, mobility, and other properties. The large range of methods used to assess speciation in natural waters can in principle be differentiated into two main categories (Filella et al., 2002). Techniques are either designed to measure total metal concentrations following certain pre-treatments, or to detect operationally-defined fractions. The latter requires prior separation of the solution, for instance based on size (filtration), size and charge (*e.g.*, dialysis, ion exchange, solvent extraction), or complex stability (*e.g.*, fluorescence, spectrophotometry, cathodic or anodic stripping voltammetry).

Due to their tendency to achieve the highest energetic stability, metal cations (generalised as M^{n+}) are readily coordinated to other species in water and are found in a large variety of different forms, which in turn govern their chemical reactivity (*e.g.*, with respect to acid-base, precipitation, and redox reactions), bioavailability, and toxicity. In their simplest ("free") form, metal cations are hydrated, which can be described as $M(H_2O)x^{n+}$. In reality, however, metals are readily bound by NOM, and only a minor fraction of the total metal content exists as hydrated ions (Lead & Wilkinson, 2006). Species that bind metal ions are generally termed ligands, where the case in which a ligand binds at two or more sites to a metal is referred to as chelexation. Another terminology used to describe metal binding is that of denticity, which refers to the number of atom donor groups ($\sim$binding sites) of a ligand involved in binding a metal (*i.e.*, complexes may be monodentate, bidentate, etc.).

In natural waters, the dominant class of complexing agents is formed by humic substances, *i.e.*, materials derived from the decomposition of vegetation. Humic substances are in turn composed of the three principal operationally-defined components, namely fulvic acids, humic acids, and humin. Their capacity for binding metals is primarily due to their range of functional groups, of which the acidic carboxyl and phenolic OH groups are most important for complexation (Güngör & Bekbölet, 2010; Town, 2008). Fulvic acids (FA) form the fraction of humic substances that is soluble in water at any pH level, and are hence sometimes referred to as the acid-soluble fraction. They are comparably small compounds, and typically constitute the largest proportion of NOM in freshwaters with ca. 40 – 80% (Tang & Johannesson, 2003). Humic acids (HA) present the fraction that is not soluble in water under acidic conditions ($pH < 2$), however, are typically soluble at higher pH. Humic acids are generally much larger structures of high molecular weight, tend to possess fewer oxygen-containing functional groups, and typically present $<$5 – 20% of aquatic NOM in freshwater (Tipping, 2002). The third type of humic substance is humin, which is defined as the insoluble fraction in aqueous base following alkali extraction procedures. The proportions of HA and FA in natural waters (including cave dripwaters) may vary considerably (Hartland et al., 2012), which in turn has significant implications for metals present in the solution.

2.5.1 Kinetics of aqueous metal complexation

The kinetics of metal complexation in aqueous systems are typically described in terms of the Eigen mechanism (Eigen & Wilkins, 1965; van Leeuwen & Buffle, 2009; Town et al., 2012), which involves two fundamental steps. Firstly, an initial outer-sphere complex $M(H_2O)L$ is formed. In the second, rate-determining step, water is released from the inner sphere of the metal ion, and a coordination bond with the ligand forms (*i.e.*, a complex ML). Given that the rate of complex formation is dictated by the rate of loss of a water molecule, where each metal cation has a specific rate constant (Eigen & Wilkins, 1965), the dissociation rate for a simple metal complex is inversely proportional to the complex stability constant K_i (Morel & Hering, 1993, Equation 2.9). At large, the Eigen model presents a basis for estimating rates of complex formation based on metal properties (*e.g.*, electron configuration, oxidation state of the metal),

the charge and size of the ligand, and ligand concentrations in solution.

Considering the heterogeneous composition of NOM, it can be assumed that *n* binding sites are available for M^{2+}, denoted as L_i. Metal complexation can be described as:

$$M + L_i \underset{k_{d,i}}{\overset{k_{f,i}}{\rightleftharpoons}} ML_i \tag{2.8}$$

, where charges are omitted for simplicity. $k_{d,i}$ and $k_{f,i}$ present the dissociation rate constant and formation (association) rate constant, respectively. $k_{d,i}$ can be expressed in terms of the equilibrium constant of reaction Equation 2.8, K_i, as:

$$k_{d,i} = \frac{k_{f,i}}{K_i} \tag{2.9}$$

, with

$$K_i = \frac{[ML]}{[M][L]} \tag{2.10}$$

It can be noted from the denominator in Equation 2.9 that the dissociation rate constant $k_{d,i}$ is inversely proportional to the ML complex stability, suggesting that stronger bonds are expected to be kinetically more inert (Amery et al., 2010; Rate et al., 1993). Conversely, as $k_{d,i} \to \infty$, the complex is increasingly labile (Warnken et al., 2007). Using the same notation as in Equation 2.8, metal ligand exchange reactions in a system with ligands L and L′ can be described using the following equation (Hering & Morel, 1990):

$$ML + L' \underset{}{\overset{fast}{\rightleftharpoons}} LML' \overset{slow}{\longrightarrow} L + ML' \tag{2.11}$$

2.5.2 Measuring kinetic properties of trace metals in aqueous solutions

In order to assess processes and possible implications of metals in the environment, it is critical to quantitatively understand their interactions with NOM in natural waters. The kinetic properties of organic metal complexes (OMCs) are of particular interest, given that they at large dictate the degree and timing of how metals are bound, transported, and released by organic ligands. As with studies of metal speciation, characterising complex dissociation kinetics is complicated due to species being operationally-defined by a given method, a sensitivity to pretreatments, time frames, potential contamination, and other factors (Amery et al., 2010; Sigg et al., 2006). Here, a few more commonly applied methods to measure dissociation kinetics of aqueous OMCs with relevance to this study are outlined.

Competitive ligand exchange method

In the competitive ligand exchange (CLE) method, a test solution containing OMCs of interest is augmented with a strong competing ligand (*e.g.*, Chelex-100 cation exchange resin or 4-(2-Pyridylazo)resorcinol; PAR), which readily binds metals to form strong complexes (Amery et al., 2010; Lam et al., 1999; Sekaly et al., 1999). Dissociation kinetics using this approach are either assessed in terms of the rate at which metal concentrations decrease in the solution, or alternatively by monitoring the concentration of metals accumulating in the competitive phase. Importantly, measured dissociation kinetics are sensitive to the quantity and type of the competing ligand, requiring the latter to be well-characterised and carefully prepared to achieve comparable experimental conditions (Yapici et al., 2009). Variations to the experimental setup for this method exist, from using relatively simple and often improvised stand-alone reactors from which sub-sampling is achieved manually (*e.g.*, Amery et al., 2010), to directly coupling reactors to analytical systems for essentially continuous, online measurement of elemental concentrations over time (*e.g.*, Sekaly et al., 1999, 2003). Additional techniques to characterise metal speciation can be coupled to CLE approaches. For instance, anodic stripping voltammetry (ASV; Lam et al., 1999; R. Wang & Chakrabarti, 2008) or adsorptive cathodic stripping voltammetry (AdCSV; van Leeuwen & Jansen, 2005; Gerringa et al., 2021; Moffett, 1995; A. J. Smith et al., 2022) have been used in conjunction with CLE. The applicability of these methods may, for instance, vary depending on the choice of competing ligand or detection window, for which reliable analysis of kinetic parameters is possible (R. Wang & Chakrabarti, 2008; Bruland et al., 2000). In its simplest form, CLE nonetheless provides a relatively robust and reproducible approach to kinetic measurements (Amery et al., 2010), and lends itself to characterising basic kinetic parameters in test solutions without the need for specialised equipment.

Diffusive gradients in thin-films (DGT) technique

The diffusive gradients in thin-films (DGT) technique uses relatively simple and robust devices that can be deployed *in-situ* for the measurement of labile metal species (Davison & Zhang, 1994; Zhang & Davison, 1995). Put simply, the devices are designed to accumulate metals upon their diffusion through a well-characterised diffusive gel layer over a known period of time. Owing to their small size, versatile applicability, and cost-efficient assemblage, DGTs are increasingly used for the assessment of metal behaviour and fate in various aquatic environments. DGT devices as described in Davison and Zhang (1994) are based on two principal operational components, namely a diffusive layer, which allows for diffusion prior to binding (*e.g.*, using a hydrogel), placed on top of a binding layer, which selectively binds desired solutes (the setup of a conventional DGT device is illustrated in Figure 2.4). The binding medium is chosen depending on the targeted species, with different agents enabling the measurement of a large range of solutes, including various trace metals (Davison & Zhang, 1994), other cations (Dahlqvist et al., 2002), uranium (Gregusova & Docekal, 2011), or radium (Leermakers et al., 2009). In addition, DGT assemblages commonly contain a membrane filter with diffusion

properties comparable to the diffusive medium, which forms the top of the diffuse layer to prevent potential clogging (Zhang & Davison, 1995). The different components are stacked on a plastic piston-shaped base, and fixed by a windowed-cap that allows solutions to be in contact with the diffusive layer. The technique revolves around Fick's First Law of Diffusion, given in Equation 2.12:

$$J = \frac{D\delta C}{\delta x} \tag{2.12}$$

, where the diffusive flux J (*i.e.*, the transport of mass by diffusion per area per time) is defined as the product of the concentration gradient of the dissolved ion in the hydrogel ($\frac{\delta C}{\delta x}$) and the diffusion coefficient (D, in m^2/s). D accounts for the effects of temperature, fluid viscosity, and particle size on diffusion (Yapici et al., 2008). Given that cations that diffuse to the binding layer are readily fixed, and provided that the binding resin is not saturated, it can be assumed that the concentration of cations at the interface of the diffusive and binding layer is essentially nil. Consequently, δC may be taken to equal the cation concentration C in the solution. Provided the solution is well-mixed, the thickness of the diffusive boundary layer is negligible, and the thickness of the diffusive layer (δx) may be taken as the combined thickness (Δg) of the filter membrane and the diffusive hydrogel. Equation 2.12 thus simplifies and rearranges to Equation 2.13:

$$C = \frac{J\Delta g}{D} \tag{2.13}$$

Equation 2.13 can be rewritten in terms of the mass of accumulated metal in the binding layer M to give Equation 2.14, considering that $J = M/At$, where A is the area of the diffusive layer exposed to the solution, and t is the exposure time.

$$C = \frac{M\Delta g}{DtA} \tag{2.14}$$

Based on the same principles as conventional DGT probes, a number of adapted DGT methods have been developed to serve specific applications (see below). By changing the kinetic window of DGT devices (*i.e.*, changing the thickness of diffusion layers), it is furthermore possible to estimate complex dissociation rate constants (Scally et al., 2003; Warnken et al., 2007), an approach that could also be adapted to modified DGT probes.

Small-volume (SV-)DGT probes (Welikala et al., 2018) allow for the assessment of the relative kinetic limitations of different metals in a solution (*i.e.*, metal A versus metal B, relative to a spiked control solution). These devices comprise a thin binding gel layer (*e.g.*, Chelex-100) cast in flat-bottomed sample vials, overlain by a diffusive layer, and optionally a filtration layer (absent in the set-up used in Welikala et al., 2018). SV-DGT probes would be suitable to confirm the relative kinetic limitation of various metals in different cave dripwaters under controlled experimental conditions. It is noted, however, that for some modified DGT devices,

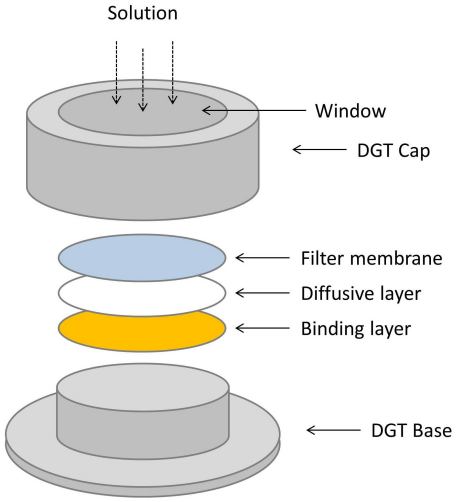

Figure 2.4: Schematic view of a conventional diffusive gradients in thin-film (DGT) assembly. The figure is redrawn from Yao et al. (2017).

the pH range of cave waters has not been tested yet (SV-DGT, only up to pH of 6.5), and that swelling of hydrogels under alkaline conditions may compromise measurements (Niklas Lehto, personal communication). Prior to applying these devices to dripwater samples, further testing would thus be required.

DGT channel probes have been developed by the Waikato Environmental Geochemistry group at the University of Waikato, and are specifically designed for the deployment beneath cave drip points. The device consists of a 30 cm long, ca. 1 cm wide channel lined with a diffusive and a binding layer. The end of the probe is positioned under a drip point at a known angle to collect dripwater, which subsequently slowly flows through the channel, in which metals can diffuse to the binding layer. The binding layer can finally be cut into regular pieces (*e.g.*, every 1 cm) perpendicularly to the flow direction, enabling the measurements of accumulated metals in the binding layer as a function of distance (and time) travelled from the drip point.

Isotope exchange technique

The isotope exchange technique to characterise dissociation is based on the spiking of a sample solution with dissolved elements in exchangeable form (*e.g.*, free ions) of a distinctly different isotopic composition to the sample (Larive et al., 1996; Sivry et al., 2006). The spiked sample is allowed to equilibrate for a given time during which exchanges between spike and natural ions can take place. Finally, the solution is fractionated, for instance by ultrafiltration, Donnan dialysis, or resin purification (Amery et al., 2010). Differences in observed isotopic ratios of free ions and the total solution from isotopic equilibrium can finally be interpreted in terms of the degree of exchange that occurs, and conversely, how much of an element is bound in non-exchangeable forms (Sivry et al., 2006).

2.5.3 Kinetic behaviour and controls of selected transition metals

While only few studies have specifically addressed cave waters, the kinetic properties of transition metal complexes in aqueous solutions have been the focus of various experimental and field studies. In order to facilitate comparison and reproducibility, many of these studies utilise artificial solutions with known quantities of well-characterised complexing agents, such as isolated humic acids (HA) and fulvic acids (FA), nitrilotriacetic acid (NTA), or ethylenediaminetetraacetic acid (EDTA). The use of specific ligands has the advantage of reducing the number of variables affecting complexation and dissociation, and thus enable a more targeted study of kinetics under certain conditions. Natural waters, however, are highly heterogeneous in terms of the quantity and quality of organic ligands, and comparably few kinetic data are available of metals in natural systems (examples include Warnken et al. (2007) and Shafaei Arvajeh et al. (2012)). Given the diverse physical and chemical make-up of NOM, the number and distribution of binding sites and respective affinities for different metal cations likewise vary substantially (Town, 2008). In NOM, metal complexation is primarily attributed to carboxylic and phenolic functional groups, both of which can form various bidentate and tridentate sites of varying binding strengths (Shi et al., 2016). Generally, carboxylic groups provide weaker binding sites, whereas phenolic sites tend to bind metals more strongly (Warnken et al., 2007). Model results based on various experimental datasets presented in Shi et al. (2016) show that under most conditions (primarily with respect to pH and metal concentrations), bidentate complexes of Cu, Cd, Ni, Pb, and Zn likely dominate. In contrast, monodentate binding was found to be typically negligible (except potentially at low pH of ca. 5), while tridentate binding was increasingly observed at a pH of ca. 7 – 8. Importantly, the strong control of NOM binding sites on complex stability, and consequently metal dissociation, renders the assumption of single representative values of kinetic parameters (such as k_d values) a significant oversimplification (Warnken et al., 2007). Rather, a large range of respective values needs to be anticipated for each metal depending on the NOM quantity and composition (Tipping, 2002; Town, 2008). Nonetheless, studies of both manufactured and natural solutions have identified a number of common controls on kinetic properties of aqueous metal-ligand complexes, which superimpose on the ligand properties.

Likely the most significant factor controlling metal binding to organic ligands is considered to be the pH of the solution (Bradl, 2004; Stern et al., 2007; Tipping, 2002). In an early study investigating the sensitivity of Cu-HA dissociation kinetics in synthetic solutions to varying conditions, Rate et al. (1993), for example, observed a greater fraction of slowly dissociating Cu-HA complexes as pH was increased (measured at pH values of 5.0, 6.0, and 7.0). Their findings were consistent with similar observations of Ni-FA complexes (Cabaniss, 1990; Lavigne et al., 1987) at the time, while various experimental and modelling studies have since confirmed a strong control of pH on metal binding (Shi et al., 2016; Stern et al., 2007). Model results of Shi et al. (2016) show in the pH range of 5.0 to 8.0 that the proportion of tridendate binding sites increases towards alkaline conditions, whereas monodentate (*i.e.*, weaker) binding sites were observed in notable proportions only at low pH (ca. 5). Enhanced binding of transition

metals was also evident in hyperalkaline cave dripwaters (pH of ca. 11) of Poole's Cavern, UK (Hartland et al., 2011), compared to that observed under pH more typical for caves (pH of ca. 8).

Another major control on complex stability is the ratio of metals to ligands (Guthrie et al., 2003; Yapici et al., 2009), which is understood to reflect changes in the degree of binding site occupation (Town, 2008). Rate et al. (1993) noted that an increase of Cu concentrations relative to HA yielded faster dissociation, which was coherent with earlier findings of Lavigne et al. (1987) and Cabaniss (1990) for Ni-FA, and Hering and Morel (1990) for Cu-HA. Conversely, when fewer metal cations are present relative to available ligands, the lower metal loading allows for the formation of more polydentate, stable complexes (Shi et al., 2016). This typically entails a decrease in free metal cations and the fraction of very labile complexes, resulting in overall reduced dissocation rates (Guthrie et al., 2003). This effect is also seen over time, for instance, as metal cations are stripped from the solution, dissociation rates progressively decrease in response to increasing complex stability (Town, 2008).

Rate et al. (1993) furthermore noted a decrease in Cu-HA dissociation rates when the pre-dissociation equilibration time was increased, *i.e.*, the time window in which equilibration was allowed to occur without complex dissociation. An increase from 24 to 96 hours resulted in altogether slower dissociation and a larger proportion of slow or non-dissociating Cu. Most likely, formation of more thermodynamically stable complexes is favoured over time, suggesting that complex formation may still be significant even after several days (Amery et al., 2010; Rate et al., 1993).

In a fourth experiment conducted by Rate et al. (1993), electrolyte concentrations were adjusted, demonstrating a positive relationship between the ionic strength of the solution and Cu-HA dissociation rates. However, while dissociation was altogether enhanced with increased electrolyte concentrations, this dependence was most significant in the more rapidly dissociating fraction, consistent with observations for Ni-FA (Cabaniss, 1990). It is now widely recognised that ionic strength presents an important factor that can reduce complex stability, and needs to be taken into consideration in experimental designs (Sekaly et al., 2003; Shafaei Arvajeh et al., 2012).

Various studies additionally provide (semi-)quantitative estimates of kinetic limitation and parameters, such as the dissociation rate constant k_d of complexes (Equation 2.9), which is a key variable in the proposed drip rate proxy. Most kinetic studies use artificial solutions and complexing agents that cannot be expected to accurately represent kinetics of complexes found in dripwaters, however, a number of examples of natural freshwaters exist. Warnken et al. (2007), for example, deployed DGT probes to obtain *in-situ* measurements of trace metals in river water from NW England. Based on DGT deployment time and the concentration of accumulated metals using different thicknesses of the diffusive layer, the authors estimated the thickness of the apparent diffusive boundary layer (ADBL), and computed k_d and k_f values for a suite of metals. The ADBL was found to be indicative of kinetic limitation. A thin ADBL was observed for Cd, Zn, and Pb, which showed fast formation rates and fast dissociation

($\sim$no kinetic limitation) in accordance with the Eigen mechanism. Slower formation rates were reported for Mn, Co, and Ni, while Cu, Al, and Fe were strongly bound (evident in a very thick ADBL). This sequence of ADBL thickness is coherent with findings of Burba (1994), who reported dissociation rates from natural aqueous humic substances when binding to synthetic chelate in the order of Mn $<$ Co $<$ Ni $<$ Cu $\ll$ Al $<$ Fe. For the metals most relevant to this project (kinetically limited elements), k_d values were found to be 4.1×10^{-2} s^{-1} for Mn, 3.1×10^{-3} s^{-1} for Co, 6.6×10^{-4} s^{-1} for Ni, and 6.1×10^{-2} s^{-1} for Cu (Warnken et al., 2007).

The ADBL determined by DGT was also used to characterise kinetic signatures of various transition metals complexed to FA (Levy et al., 2012). Their experiment demonstrated substantial kinetic limitation for Cu, Pb, and Ni (at a pH of ca. 7), whereas none was observed for Cd, Co, and Mn (in part contrasting the findings of Warnken et al., 2007 for Co and Mn). Accordingly, complexes between FA and Cu, Pb, or Ni, are expected to dissociate relatively slowly at circum-neutral pH conditions. In part, similar patterns were evident in the experimental study of Welikala et al. (2018), in which SV-DGT probes were used to assess the relative kinetic limitation of Ni, Cd, and Zn in soil leachates and synthetic solutions with NTA and EDTA. A common elevated kinetic limitation was observed for Ni compared to Zn, and both Ni and Cd were very strongly bound by EDTA. In composts and peat samples (*i.e.*, solutions with heterogeneous ligand compositions), Ni likewise exhibited a relatively strong kinetic limitation, whereas Cd and Zn were considerably more labile.

Another study using natural water samples was carried out by Amery et al. (2010) based on DGT and the CLE method. k_d values computed for different Cu-DOM complexes were found to be in the order of ca. 10^{-3} s^{-1} on average. The dissociation was considerably faster for Cu-DOM complexes than for Cu-HA in synthetic solutions, presumably because HA has overall larger affinities for Cu than samples with natural and more heterogeneous DOM compositions (Amery et al., 2008). In addition to humic and fulvic acids, natural DOM also contains components that are less humified, for example, small organic acids, amino acids, and carbohydrates. Their presence likely renders overall dissociation kinetics faster than those observed in experimental solutions that only contain Cu-HA or Cu-FA complexes (Amery et al., 2010), although contrasting results were found by Sivry et al. (2006) in an hour-long isotopic exchange experiment.

The study of metal complexes with well-characterised humic and fulvic acid, despite omitting various other components found in natural aqueous solutions, provide information of relevance to cave studies. For example, Shafaei Arvajeh et al. (2012) used modified DGT devices and geochemical modelling to characterise dissociation of Ni-Fa and Ni-HA complexes in synthetic solutions. At comparable conditions (with respect to ionic strength, pH, and metal-ligand ratios), Ni-HA complexes were shown to be more kinetically limited (*i.e.*, dissociated more slowly) than Ni-FA complexes (Shafaei Arvajeh et al., 2012), consistent with other studies (Guthrie et al., 2003). Calculated k_d values were in the order of 2.5×10^{-3} s^{-1} and 3.4×10^{-4} s^{-1} for Ni-FA and Ni-HA, respectively. These findings bear implications for natural systems, where the relative proportions of HA and FA, and thus binding affinities to a given metal, vary over time.

2.6 Transition metals in dripwaters and speleothems: towards new organic proxies

Following initial observations of apparently systematic associations of a range of alkaline and first-row transition metals with OM in stalagmite samples from Grotta di Ernesto (Borsato et al., 2007; Huang et al., 2001), several studies attempted to further characterise relationships between elements and NOM, and their dependence on hydrological processes in karst systems (Hartland et al., 2012, 2014; Hartland & Zitoun, 2018). Altogether, it is now recognised that NOM in dripwater plays a determinant role in the transport of such metals from the surface to caves, and hence may present an important vector for the availability of these elements for the incorporation into calcite during speleothem formation (Fairchild et al., 2010; Hartland & Zitoun, 2018; Jo et al., 2010). Thus, a mechanistic understanding of processes involved in determining measurable metal concentrations in speleothems would not only provide a novel means to characterise the composition and quantity of OM in dripwater over time, but in light of laser-ablation techniques for elemental analyses, also facilitate the establishment of highest-resolution palaeoenvironmental records (Blyth et al., 2016). Moreover, recent methodological advances in measuring aqueous transition metal concentrations in the high-Ca matrices of limestone cave waters provide additional means for a more routine assessment of these elements (Warken, Kuchalski, et al., 2022).

2.6.1 Precedent for a sensitivity to sporadic infiltration events

The applicability of first-row transition metals as potential proxies has been proposed to be twofold (Blyth et al., 2016). Firstly, metal:metal ratios have been suggested to possibly provide insights into the composition of OM in dripwaters. This notion is largely based on the findings of Hartland et al. (2012), who showed that Cu:Ni data of dripwaters and soil leachates collected from Poole's Cavern (UK), Lower Balls Green Mine (UK), and Grotta di Ernesto (Italy) exhibit distinct linear trends that correspond to poorly-soluble (≈humic acid-like) and acid-soluble (≈fulvic acid-like) dissolved OM end-members (data are also presented in Blyth et al., 2016). These variations in Cu:Ni were attributed to distinct distributions of functional groups in each end-member, and consequently specific binding affinities for given elements.

Similar observations of competitive binding were also previously reported. Mandal et al. (1999a), for example, demonstrated in natural freshwater samples that under the absence of Cu and Co cations in solution, Ni had the tendency to occupy strong binding sites of humic substances to form strong and essentially inert complexes. However, when Cu and Co concentrations were sufficient, strong binding sites were primarily occupied by these elements, whereas Ni associated with weaker sites in less stable, labile complexes. Both Co and Cu can thus successfully compete with Ni for binding sites, and their concentrations likely exert a control on the lability of Ni-NOM complexes. Of the two elements, Cu was found to be particularly competitive in binding strong sites when present, which is in good agreement with the

Cu:Ni dripwater data of Hartland et al. (2012). The same tendency, although with a particularly enhanced competitiveness of Cu over both Co and Ni, was also observed in an analogous experimental study using model solutions with a well-characterised fulvic acid as the complexing agent (Mandal et al., 1999b).

Differences in Cu:Ni observed in Hartland et al. (2012) were furthermore linked to the prevailing size of organic matter transported in dripwaters, depicting distinct elemental trends for high and low fluxes of NOM in dripwaters of the hyperalkaline Poole's Cavern (UK). During periods of high dripwater supply, larger concentrations of coarse colloidal and particulate NOM were mobilised, which corresponded with altogether elevated concentrations of Ti, Mn, Fe, Cu, and Ni. Lower fluxes were characterised by low contents of fine and dissolved NOM, and overall lower metal concentrations (primarily V, Co, and Ti, with minor Cu and Ni). Differences in Cu:Ni ratios between high and low fluxes were primarily attributed to the presumably preferential binding of Cu and Ni to stronger binding sites (*e.g.*, phenolic groups) that are proportionally more abundant in coarser OM (>100 nm) compared to small, humic-like colloids (Tipping, 2002). These findings are in line with previous notions that a certain competition for binding exists between particulates, colloidal, and dissolved NOM (Nimmo & Fones, 1997; Pédrot et al., 2008; Warnken et al., 2007). While this was not observed in this study, however, it is noted that fine colloidal particles (<25 nm) can often dominate trace metal partitioning over larger fractions (Lyvén et al., 2003; Stolpe et al., 2005), likely due to their greater specific surface area (Buffle et al., 1998). It is reasonable to expect that a control of the size of NOM on trace metals is likely particularly pronounced in regions with a strong seasonality in precipitation, presumably resulting in elemental abundances associated with particulate NOM being mobilised by intense flows (Hartland et al., 2012). The latter has more recently been corroborated by the observations of Warken, Kuchalski, et al. (2022) in dripwaters from Puerto Rico, who were able to link transition metal concentrations to extreme rainfall associated with tropical cyclones.

2.6.2 Precedent for a sensitivity to drip rate variability

The second proposed application of first-row transition metals is based on the concentrations of individual elements measured in speleothems, which have been suggested to depend to a significant degree on the residence time of dripwater in the thin-film from which calcite precipitates, the rate at which labile OMCs therein dissociate, and the stability of OMCs adsorbed during calcite precipitation (Hartland & Zitoun, 2018; Lindeman et al., 2022). In their study, Hartland and Zitoun (2018) argued for a conceptual "aqueous sink" and a "solid phase sink" for transition metals (demonstrated by the example of Cu) in dripwater and at the speleothem surface, respectively (Figure 2.5). In dripwater samples collected from five caves in Aotearoa New Zealand, effectively all Cu was found to be complexed by organic ligands with only a minor fraction of "free" Cu^{2+} in concentrations several magnitudes lower than the total Cu in the solution. Given that the fraction of bioavailable Cu furthermore increased only slightly in response to rising overall Cu concentrations, the overriding control of metal-binding by ligands was suggested a pervasive property of dripwaters. Consistent with experimental evidence from

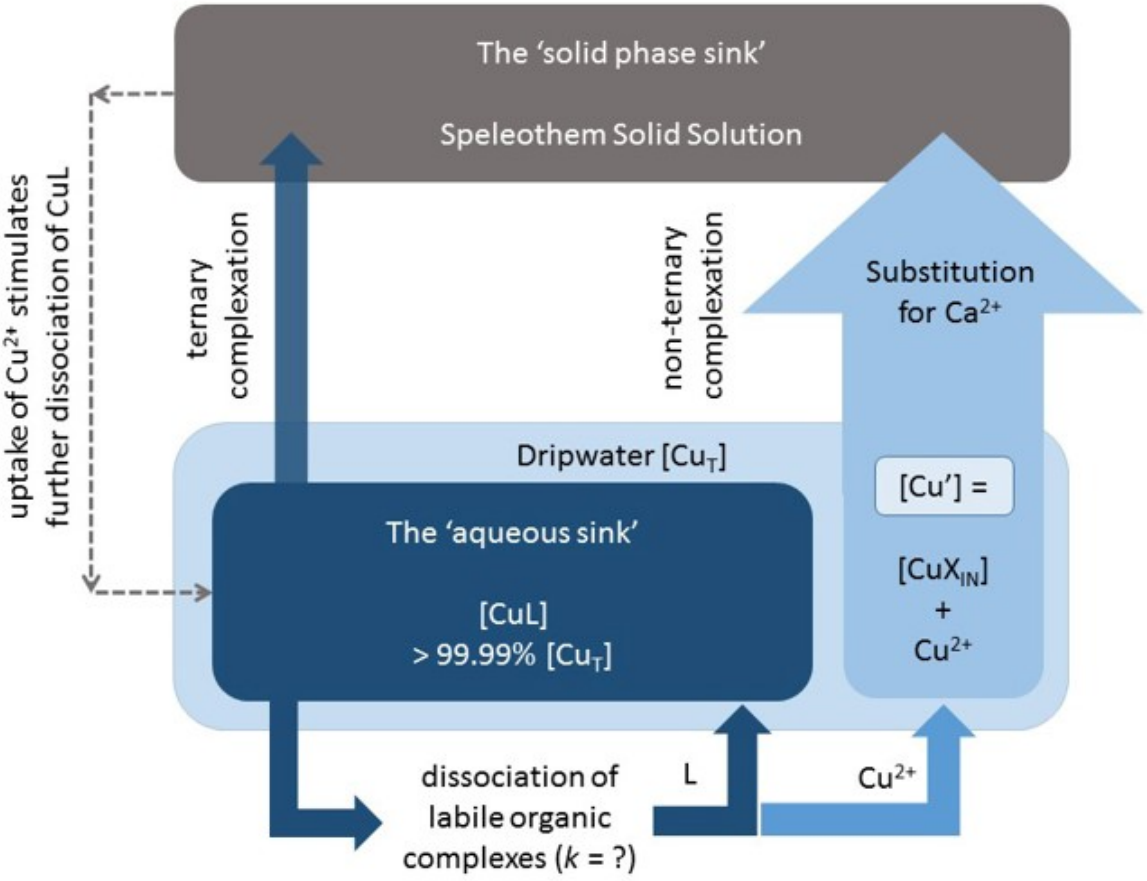

Figure 2.5: Conceptual diagram of NOM-mediated transport of Cu to the water-calcite interface, and its incorporation into speleothems. Rapid aqueous metal complexation creates an "aqueous sink" for Cu and other transition metals, while the instantaneous sorption of newly dissociated cations in the dripwater thin-film to calcite serves as a "solid phase sink". The latter likely enhances the further OMC dissociation. This model presents the basis for estimating drip rates based on accumulated metals, given that the time-dependent OMC decay is assumed to largely determine speleothem metal concentrations. The figure is adopted from Hartland and Zitoun (2018).

Lee et al. (2005), an "aqueous sink" of Cu was proposed due to the ready binding of Cu by aqueous complexes in solution, which essentially inhibits the generally favoured adsorption of Cu to calcite (Elzinga & Reeder, 2002). A "solid phase sink" was in turn suggested to exist for metals released from complexes at the water-calcite interface, where the momentarily free cations are rapidly adsorbed to calcite. The uptake of cations by calcite may in turn favour further dissociation of labile OMCs in the thin-film (Hartland & Zitoun, 2018).

Although the exact mechanisms of how NOM-associated metals are incorporated into the speleothem structure are not fully understood yet, it has been suggested to involve the formation of ternary complexes at the calcite surface (Blyth et al., 2016), which can be described according to Equation 2.15.

$$\equiv SOH^{0}_{(s)} + L - M^{(l^- + m^+)}_{(aq)} + H^{+}_{(aq)} \longleftrightarrow \equiv S - L - M^{(m-l+1)}_{(s)} + H_2O_{(aq)} \tag{2.15}$$

, where $\equiv S$ is a generic metal cation (S), which is crystallographically bound at the surface-

water interface, and $L - M_{(aq)}^{(l^- + m^+)}$ is an organic acid-cation complex in solution (Blyth et al., 2016; Fein, 2002). Ternary complexation may be understood as the concurrent adsorption of complexed metals and organic ligands at the same mineral surface site. This is considered to be favoured when OMCs exhibit partition coefficients in the vicinity of 1, which implies that metal:ligand ratios are consistent between solution and solid (Hartland et al., 2014). However, information on ternary complexes between OMCs and calcite is extremely sparse, and experimental conditions in the most applicable study in this regard by Lee et al. (2005) were not representative of those found in natural freshwater. Their findings suggest that the presence of HA at the water-calcite interface may in fact impede Cu(II) sorption to calcite, and do not provide conclusive evidence of ternary complexation. The authors argue that elevated HA concentrations in solution reduce the uptake of Cu(II) by calcite likely due to the formation of aqueous Cu-HA complexes, and largely discard an alternative interpretation that surface-bound HA competitively occupies sites for Cu(II) sorption (Lee et al., 2005).

In a speleothem context, the possible formation of ternary complexes has been discussed in Hartland et al. (2014), however, was considered to be likely of subordinate significance in most cave systems. Between the hyperalkaline dripwaters (pH of ca. 11) and speleothems of Poole's Cavern (UK), metal:NOM ratios for V, Ni, and Cu increased considerably in correspondence to calculated partition coefficients between 24 and 150. A peculiar exception in Poole's Cavern was observed for Co, which was found to be bound exceptionally strongly in disagreement with model predictions and existing evidence of generally weaker complexation of Co to NOM compared to Cu and Ni (Warnken et al., 2007). Given the very slow dissociation of aqueous Co-NOM complexes and an apparent partition coefficient of ca. 1 (0.9), it is reasonable to assume that ternary complexation may occur under certain conditions, but presumably not under most (Blyth et al., 2016; Hartland et al., 2014). The capacity of Co to form extremely stable and potentially inert complexes with NOM in natural freshwaters has likewise been observed by R. N. Collins and Kinsela (2010), who reported substantial ranges in calculated dissociation rate constants from 3.1×10^{-1} to 10^{-11} s^{-1}, translating into Co dissociation half-lives of few minutes to over 2000 years.

Nonetheless, with the exception of Co, the elemental measurements in Poole's Cavern strongly suggest the absence of significant ternary complexation. Rather, dominant inorganic or otherwise non-ternary pathways were suggested, possibly including the inorganic substitution of divalent metals for Ca according to Equation 2.7 (Hartland et al., 2014). Importantly, this assumption has the critical implication that the supply of Cu that can be incorporated into calcite is essentially determined by the dissociation of OMCs (Hartland & Zitoun, 2018; Warnken et al., 2007), and thus depends on time. Based on these considerations, it may in turn be argued that the time window available for complex dissociation is effectively dictated by the residence time of the drip solution at the water-calcite interface. It follows that if dissociation kinetics are well-characterised, certain metal concentrations in calcite may allow for the estimation of dripwater residence time at the speleothem surface, which is taken to be a direct function of the cave drip rate (Hartland & Zitoun, 2018).

Convincing precedent for this proposed sensitivity of stalagmite transition metal concentrations to drip rate exists also in stalagmite records. Most recently, Sliwinski et al. (2022) demonstrated by example of yttrium (present as Y^{3+}) a highly similar behaviour to that predicted under a kinetic organic control. The authors were able to inversely link Y inclusion into recent stalagmite deposits to drip rate, which they attributed to the residence (or 'retention') time of Y-NOM complexes in the water film at the stalagmite surface. This retention time was taken to be largely defined by the interval of incoming drips as consistent with the reasoning of Hartland and Zitoun (2018), suggesting that the impact of fresh drops mechanically removes and replenishes OMCs at the stalagmite surface. Furthermore, a suite of transition metal concentrations in the Indian stalagmite DHAR-1 presented by Giesche et al. (2023) showed a pronounced positive correlation with periods of major droughts during the mid-Holocene and the 4.2-kiloyear event, implying transition metals were able to accumulate in the carbonate fabric due to the prolonged release of metals from OMCs.

With view to potentially using kinetic properties of aqueous OMCs as a first quantitative means to reconstruct cave drip rates, however, it is clear that the large number of factors influencing the kinetic behaviour of metals in natural waters necessitates the thorough characterisation of the dripwater chemistry at a given study site. Based on compiled information on kinetic properties of transition metals in natural and artificial aqueous solutions in presence of organic ligands, and preliminary analyses of dripwater and stalagmite records from Heshang Cave, China (Hartland et al., unpublished data), Ni and Co show particular promise for the use as proxies of palaeoclimatic drip rates. This is presumably due to (1) their kinetic properties in transient conditions that favour dissociation over relevant time-scales for cave drip points at circum-neutral pH conditions, and (2) their inorganic partitioning coefficients, which are estimated to be close to 1 (Y. Wang & Xu, 2001; Lindeman et al., 2022). Importantly, the latter implies a subordinate control on their concentrations in dripwater and calcite of PCP (cf., elements like Mg and Sr; Wassenburg et al., 2020), which would otherwise compromise the proxy signal captured by speleothems.

2.7 Climate variability in Aotearoa New Zealand and the South Pacific

2.7.1 Modern climate

Aotearoa New Zealand is located within the influence of several large-scale oceanic-atmospheric circulation patterns and climate modes, including the El Niño-Southern Oscillation (ENSO), the Interdecadal Pacific Oscillation (IPO), the South Pacific Subtropical Dipole (SPSD), and the Southern Annular Mode (SAM), which collectively shape Aotearoa New Zealand's intra- and inter-annual climate variability (Fauchereau et al., 2018).

The influence of the different drivers varies across the latitudinal gradient covered by Aotearoa

New Zealand's North and South Islands, and additionally corresponds with topographic features. Particularly on the South Island, the mountain ranges extending along the length of the island result in sharp climatic contrasts due to dominant westerly winds. Substantial orographic precipitation renders the western coast of the South Island Aotearoa New Zealand's wettest region, whereas the eastern side of the mountains is the driest (Figure 2.6). For the most part, climate is temperate and maritime (type "Cfb" according to the Köppen classification scheme Kottek et al., 2006), but includes subtropical zones in the very north of the North Island, and severe alpine conditions in the high mountains. Aotearoa New Zealand's diverse topography furthermore gives rise to numerous microclimates on both the North Island and South Island, for instance the anomalously mild and dry climate found in the eastern Tasman Region at the otherwise wet northern tip of the South Island.

In the South Pacific (with a particular emphasis on the region around Niue, ca. 19°00'S, 169°50'W), the location of the Intertropical Convergence Zone (ITCZ) and South Pacific Convergence Zone (SPCZ; Figure 2.7), along with modal changes in ENSO are the dominant controls of inter-annual climate variability, primarily manifest in the amount of precipitation. Islands in the South Pacific are furthermore subject to tropical cyclones and associated extreme rainfalls, which commonly form during the months from November to the end of April with variable intensities and spatial extents (Diamond et al., 2013). Severe cyclones are not uncommon, and may have devastating socio-economic impacts, particularly on low-lying islands.

A brief overview of the key climatic processes governing climate in Aotearoa New Zealand and the South Pacific is provided in the following.

El Niño-Southern Oscillation (ENSO)

The El Niño-Southern Oscillation (ENSO) presents the most pronounced and globally coherent oceanic-atmospheric climate phenomenon, the mode and strength of which largely determine inter-annual climate variability in large parts of the tropics and beyond (M. Collins et al., 2010; C. Wang et al., 2016). The prevailing state of the equatorial Pacific is characterised by a prominent zonal asymmetry in sea surface temperatures (SST, ca. 5°C difference; Figure 2.8), and the depth of the mixed layer. Essentially the result of a westward equatorial current that is generated by the easterly trade winds, the western Pacific and the so-called Indo-Pacific Warm Pool (IPWP) experience relatively warm surface waters with a deep thermocline at depths of 200 to 400 m, whereas the eastern Pacific exhibits comparably lower SSTs and a shallow thermocline at ca. 50 m (Ravelo et al., 2006). The associated zonal gradient in sea level pressure (SLP) initiates a low westward flow of dry air from the cooler eastern Pacific (high SLP) towards the central IPWP convective regime, contributing to the Pacific component of the Walker Circulation; a conceptualised cycle of easterly trades, descending air over the eastern high SLP region, and the deep atmospheric convection above the IPWP. For most of the time, stabilising air-sea feedbacks retain a strong Walker Circulation, as well as cross-basin SST, SLP, and thermocline differences, thereby favouring these La Niña-like conditions as the mean mode of the equatorial Pacific (Ravelo et al., 2006). In irregular intervals of 2 to 7 years, however, the

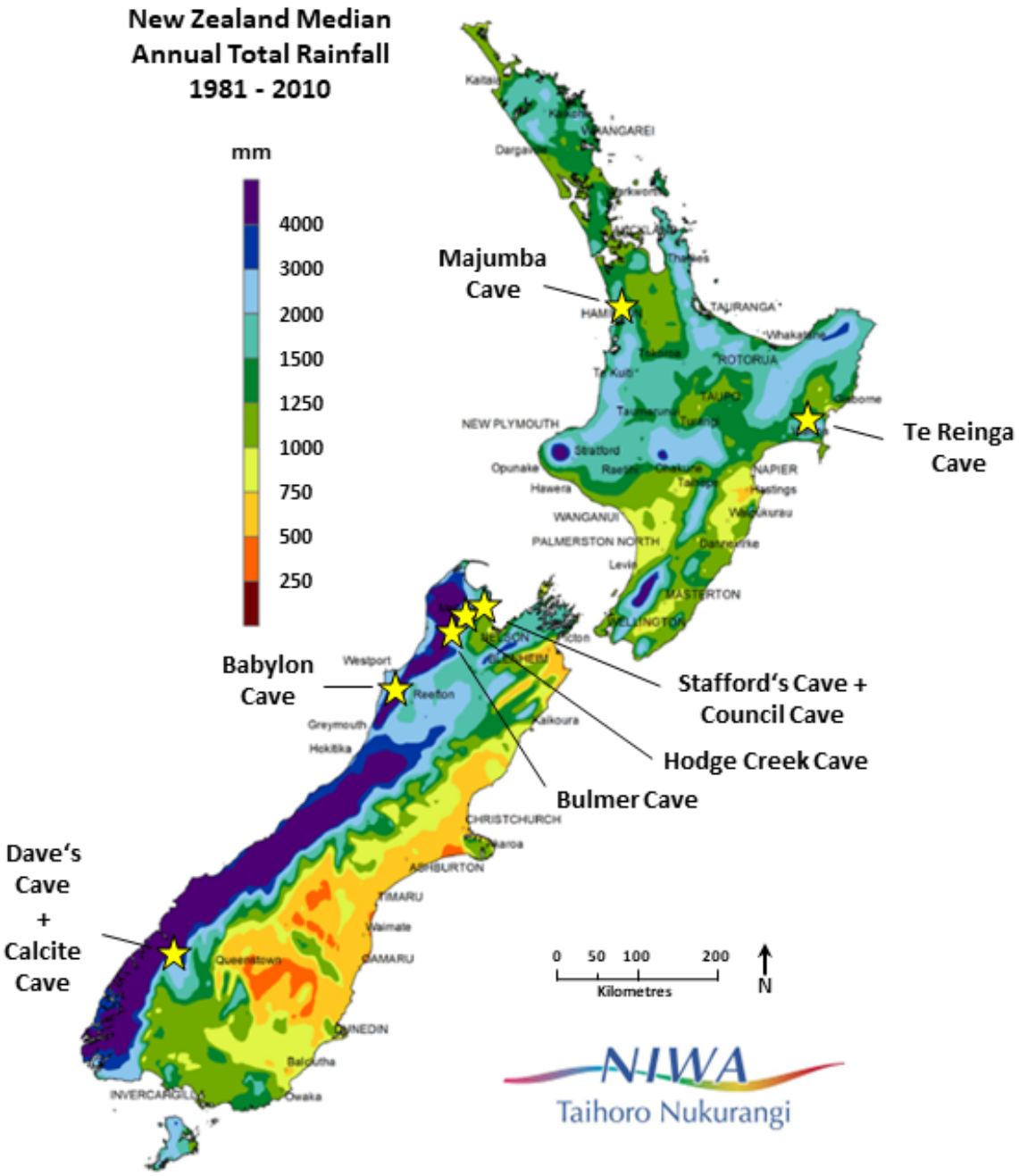

Figure 2.6: Median annual total rainfall in Aotearoa New Zealand over the 30-year period from 1981 to 2010. Approximate locations of all Aotearoa New Zealand caves discussed in this thesis are indicated by yellow star symbols. The figure is modified from Macara (2018).

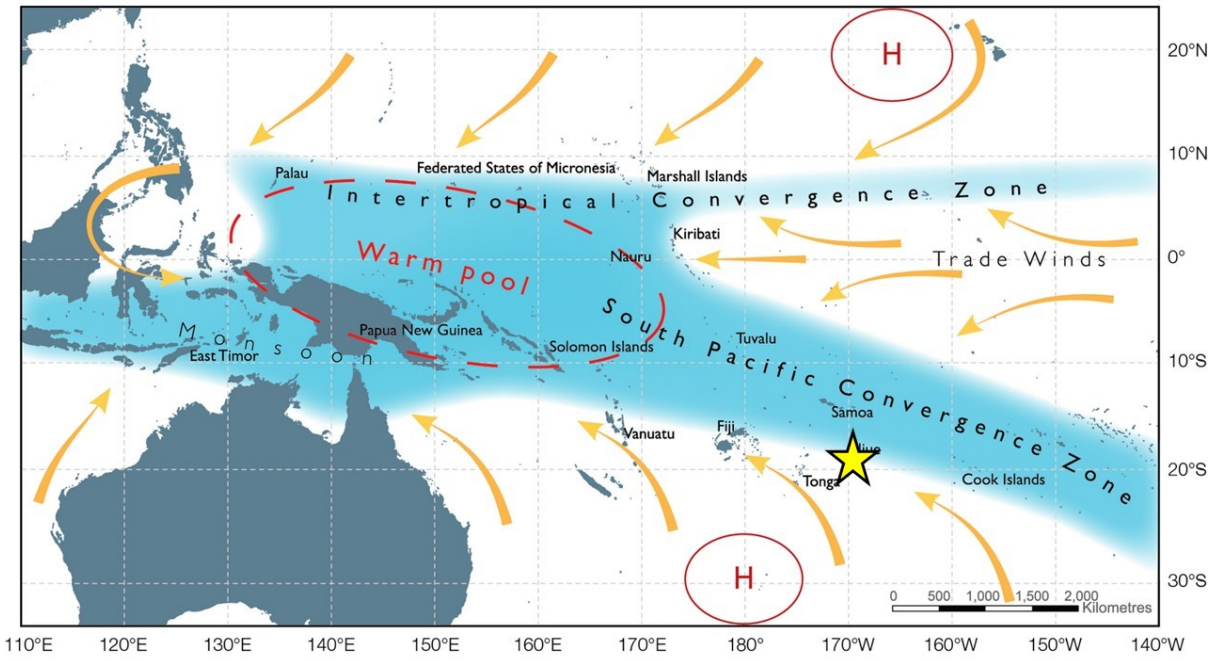

Figure 2.7: Overview of the primary atmospheric and oceanographic features governing climate variability in the western and southern Pacific. Niue (indicated by the yellow star symbol) is directly affected by latitudinal migrations of the monsoonal trough associated with the South Pacific Convergence Zone (SPCZ). The position of the SPCZ on an inter-annual time scale in turn largely depends on the El Niño-Southern Oscillation (ENSO). The figure is modified from Perkins et al. (2012).

east-west SST gradient slackens, causing a temporary break-down of the asymmetrical conditions, along with a weakening of the Walker Circulation (M. Collins et al., 2010). The onset and development of such an El Niño event is facilitated by the positive Bjerknes feedback loop, which effectively couples SST and the strength of the easterly trades in the eastern and central Pacific (Bjerknes, 1966). El Niño events typically evoke an eastward shift of rainfall, imparting generally cooler and drier conditions on large parts of the Western Pacific with peak intensities during the austral summer, whereas the Eastern Pacific becomes relatively warmer and wetter. Conversely, prevailing La Niña conditions favour the location of the deep atmospheric convection above the central IPWP, and are consequently characterised by warmer and wetter, and cooler and drier conditions in the Western and Eastern Pacific, respectively.

Although ENSO originates in the equatorial Pacific, related climatic anomalies are propagated well beyond the tropics. With regards to the South Pacific, the low-level South Pacific Convergence Zone (SPCZ) branches off from the IPWP and the ITCZ, and extends towards French Polynesia, reaching as far as the Cook Islands. Positional changes of the SPCZ largely dictate seasonal monsoonal precipitation in the South Pacific, while inter-annual migrations of the convergence zone are strongly correlated with ENSO (Juillet-Leclerc et al., 2006; Kidwell et al., 2016). In principle, ENSO modal shifts in the South Pacific are manifest in similar climate anomalies (although primarily in terms of precipitation) as those in the Western Pacific. Accordingly, El Niño events are typically associated with relatively dry conditions, whereas pronounced La Niña modes commonly entail enhanced rainfall (Wheeler & Aharon, 1997).

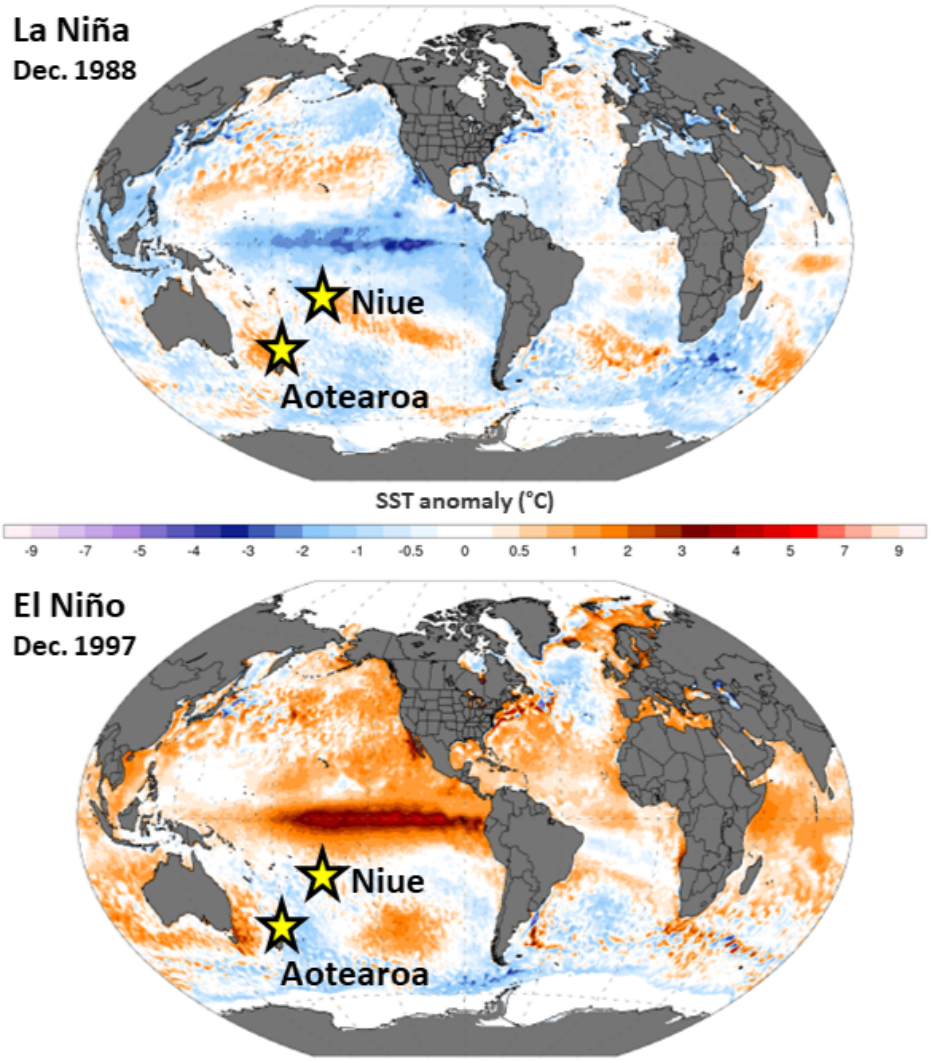

Figure 2.8: Sea surface temperature (SST) anomalies during La Niña (negative SOI; example of December 1988, top panel) and El Niño (positive Southern Oscillation Index, SOI; example of December 1997, lower panel) conditions. The southeast-ward extension of SST anomalies from the western Pacific and Indo-Pacific Warm Pool largely corresponds with the South Pacific Convergence Zone, which primarily modulates South Pacific precipitation. The locations of Niue and Aotearoa New Zealand (North Island) are indicated as yellow stars. The figure was created using the 'Climate Reanalyzer" online toolkit (https://climatereanalyzer.org/), based on the NOAA OISST V.2.1 dataset with 1971 – 2000 climatology baseline (retrieved Feb. 2024).

In Aotearoa New Zealand, the degree and nature of ENSO-induced climate anomalies vary considerably with location, however, are generally less pronounced. Across most of Aotearoa New Zealand, less than 25% of the inter-annual variance in rainfall and temperature is attributed to ENSO. During peak El Niño conditions in the austral summer, enhanced westerly winds often cause drier than normal conditions on the eastern coasts, whereas precipitation increases on the western sides of major mountain ranges, particularly on the South Island. The impacts of La Niña episodes are variable, but generally result in wetter conditions in the northeast of the North Island, while rainfall is decreased in large parts (particularly southern and southwestern regions) of the South Island (Macara, 2018)

Given the significance of ENSO for climate variability, an understanding of its sensitivity to changing boundary conditions through geological history is highly relevant to aid in predicting potential future alterations to the system under anthropogenic climate forcings. In this regard, ENSO is considered as one of the so-called potential tipping elements of Earth's climate system, which could change dramatically and relatively quickly under current warming trends (Lenton et al., 2008). Severe El Niño conditions could potentially occur more frequently, along with larger-scale changes in monsoon dynamics linked to modified oceanic-atmospheric circulation patterns (W. Cai et al., 2014).

Interdecadal Pacific Oscillation (IPO)

On a scale of several decades, a dominant driver of Aotearoa New Zealand and South Pacific climate is the Interdecadal Pacific Oscillation (IPO), the phases of which last ca. 20 to 30 years. The IPO at large denotes episodic SST anomalies similar to ENSO, which in turn result in abnormal precipitation patterns. During positive IPO phases, SSTs are higher and lower than normal in the tropical and sub-tropical Pacific, respectively, while contrasting patterns are observed during negative modes. The spatial distribution of SST anomalies broadly resembles that caused by ENSO, and the degree of association between the two oscillations has been a matter of considerable debate (Newman et al., 2016). Recent reanalyses of the phenomena, however, rather support the notion that they are indeed mechanistically distinct, and may not be as closely coupled as previously thought (Dong et al., 2018). Nonetheless, the impacts on regional climate of Aotearoa New Zealand and the South Pacific remain comparable to those of ENSO, where positive IPO phases coincide with drier and wetter periods in the east and west of Aotearoa New Zealand, respectively. In contrast, negative phases tend to enhance precipitation in the northeast of Aotearoa New Zealand, similarly to La Niña conditions. At a larger scale, precipitation is generally increased and reduced northeast and southwest of the SPCZ during positive IPO phases, respectively (Jiang et al., 2012).

South Pacific Subtropical Dipole (SPSD)

Only recently, inter-annual SST variability in the South Pacific has been mechanistically described in terms of the so-called South Pacific Subtropical Dipole (SPSD), a seasaw of SST

anomalies orientated in northeast-southeast direction in large areas of the central Pacific basin between ca. 20 °S and 60 °S (Guan et al., 2014; Morioka et al., 2013). Much of the South Pacific inter-annual variability has since been attributed to the SPSD, including up to 15% and 40% of seasonal rainfall and temperature variation in Hawke's Bay on the eastern coast of Aotearoa New Zealand's North Island (Fedaeff & Fauchereau, 2015). Models furthermore suggest a strong coupling with the Southern Annual Mode (described below), and potentially with ENSO (Guan et al., 2014). However, the exact extent to which the SPSD affects climate variability in the study sites is not clear.

Southern Annual Mode (SAM)

With regards to Aotearoa New Zealand study locations, another important driver of climate variability is the Southern Annular Mode (SAM), also known as the Antarctic Oscillation (AAO). This circular zone of pressure variations around the South Pole operates on short time-scales in the order of weeks, and is primarily associated with the position of the westerly surface winds (Swart et al., 2015). Seasonality of the SAM is strongest at the latitudes coinciding with the extent of Aotearoa New Zealand (ca. 40 °S – 50 °S), resulting in stronger and weaker westerlies in the austral winter and summer, respectively. During SAM positive phases, winds are generally weaker, whereas the negative mode is typically associated with intensified westerly winds and altogether more turbulent conditions. These effects are generally more pronounced on the South Island than on the North Island of Aotearoa New Zealand, given that the epicentre of the causal air pressure anomalies is situated over central Antarctica (Ummenhofer & England, 2007). Although the SAM primarily drives variability in winds, Aotearoa New Zealand's complex topography and associated orographic effects render its climate highly sensitive to changes in wind speed and direction. Consequently, both positive and negative phases in the SAM have been linked to seasonal rainfall variability across large parts of Aotearoa New Zealand, with each causing drier and wetter conditions in certain parts of the country (Kidston et al., 2009; Ummenhofer & England, 2007).

2.7.2 Holocene climate

The Holocene epoch within the Quaternary era (the last ~2.6 million years) denotes the last approximately 12,000 years until the present, and is characterised by relatively stable climate conditions in the geological context. It is noted that the momentous impacts of humans on the environment and climate in recent centuries have led to increasing calls for the proclamation of a new geological era, the Anthropocene (*e.g.*, Lewis & Maslin, 2015). However, a formal definition according to traditional identification conventions of geological time periods has not yet been agreed upon, and herein, the Holocene continues to refer to the current geological era. Although considered comparably stable, the Holocene still experienced significant climatic fluctuations, including several pronounced global events. A synthesis of major climatic changes from the mid-Holocene (ca. 6000 cal. years BP) to the pre-industrial (ca. 1700 AD) is given in

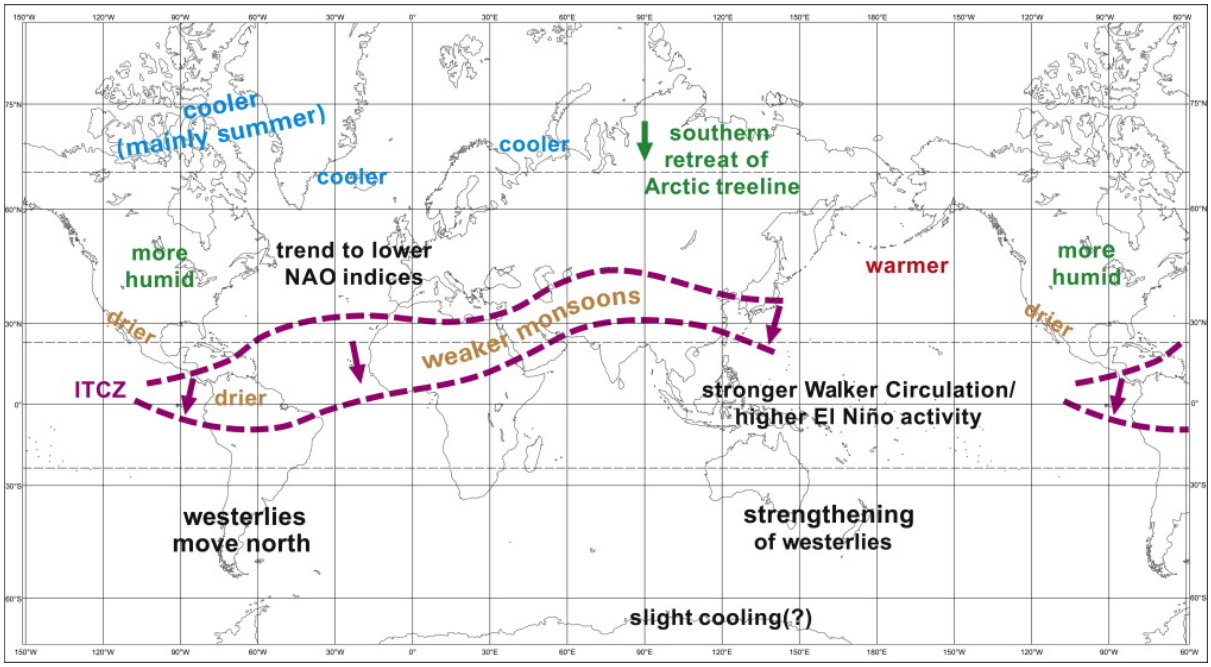

Figure 2.9: Summary of global climate changes from the mid-Holocene (ca. 6000 cal. years BP) to the pre-industrial (ca. 1700 AD). Notably, the ITCZ shifted southwards in response to weakening Northern Hemisphere summer insolation, resulting in a reduction in Afro-Asian monsoon intensities. A number of proxy records furthermore suggest a reduced frequency and/or intensity of ENSO during the mid-Holocene, and a subsequent strengthening towards the modern state. While the figure indicates broad trends in major climate phenomena, however, it is noted that proxy and model evidence shows that changes were spatially and temporally heterogeneous, and considerable uncertainties remain in many cases (Wanner et al., 2014). The figure is adopted from Wanner et al. (2008).

Figure 2.9.

A prominent set of Holocene phenomena is seen in the Bond Cycles (Bond, 1997), which describe a series of a total of nine ca. 1,500 year-long cycles in the advance and retreat of glaciers. These were originally identified by distinct layers of ice-rafted debris in deep-sea sediment cores from the North Atlantic, which have since been correlated with various environmental signals, including SST anomalies off West Africa (deMenocal, Ortiz, Guilderson, & Sarnthein, 2000), Chinese loess deposits (F. H. Chen et al., 1997), European speleothems (Niggemann et al., 2003), or lake records in southern Australia (Kemp et al., 2012). Comparable signals have not been recorded from Aotearoa New Zealand or the South Pacific, with the possible exception of a stalagmite from Hollywood Cave (northeast South Island of Aotearoa New Zealand), which shows indications of a ∼1,500 year cyclicity (Whittaker, 2008). The Bond Cycles were initially linked to the Pleistocene Dansgaard-Oeschger oscillations (Dansgaard et al., 1993), but are now widely understood to operate independently from the dominant glacial-interglacial modes. Nonetheless, we still lack a clear mechanistic understanding of these cold events and the extent of their influence on global climate (Debret et al., 2007; Wanner et al., 2011).

An important overriding control on Holocene climate variability was exerted by contrasting hemispheric changes in the summer solar insolation in response to variations in Earth's orbital parameters, with decreasing and increasing energy inputs in the Northern and South-

ern hemisphere, respectively (Wanner et al., 2014). To a large extent, solar forcing and associated migrations of the ITCZ have been attributed to the modification of several major monsoonal systems. Specifically, this included the mid-Holocene southward shift of the West African Monsoon, manifest in the termination of the (North) African Humid Period (deMenocal, Ortiz, Guilderson, Adkins, et al., 2000), an early to mid-Holocene (ca. 11,000 – 5,500 years BP) weakening of the South American Monsoon (Novello et al., 2017), and enhanced Asian Monsoon at ∼6,000 years BP (Hu et al., 2008). In addition, various proxy and modelling studies have postulated far-reaching physical correlations (teleconnections) between different systems based on Pleistocene and Holocene palaeoclimate data, suggesting for instance a pronounced influence of North Atlantic processes on the Asian Monsoon (Goswami et al., 2006; Gupta et al., 2003).

High-resolution palaeoenvironmental reconstructions, as well as climate models, furthermore suggest significant variability in ENSO regimes during the Holocene. Notably, proxy-based evidence rather consistently indicates a reduced intensity of the oscillation between around 6,000 – 6,500 years BP (Gagan, 2009; Liu et al., 2000; McGregor & Gagan, 2004; Tudhope, 2001), which was followed by a transition towards the modern ENSO state punctuated by periods of stronger intensities and/or higher periodicity (Gagan, 2009; Moy et al., 2002). However, more highly-resolved records are clearly necessary to further constrain past ENSO modulations, to which purpose speleothems from South Pacific could play an important role (*e.g.*, Nava-Fernandez et al., 2022; Aharon et al., 2006; Rasbury & Aharon, 2006; Tremaine et al., 2016).

The Holocene is of significant interest to understanding present and potential future climate variability on various time-scales, given that many boundary conditions (*e.g.*, global ice volume) were similar to today, while important climate drivers, particularly the orbital configuration and greenhouse gas concentrations, underwent distinct changes. A comprehensive review of Holocene climate variability and likely controls is provided by Wanner et al. (2014), who emphasise the considerable under-representation of the Southern Hemisphere in terms of existing palaeoclimate records (particularly data with a high temporal resolution).

Chapter 3

Characterising the decay of organic metal complexes in speleothem-forming cave waters

Chapter notes: At the time of publication of this thesis, the content of this chapter is in altered form under review for publication in *Geochimica et Cosmochimica Acta*. Elemental analyses presented in this chapter were performed by Claudine Stirling (ca. 95%; University of Otago) and Danielle Blackwell (ca. 5%; University of Waikato).

Abstract

Ligands associated with natural organic matter (NOM) dictate metal speciation, mobility, and bioavailability in aquatic environments by binding metals in organic metal complexes (OMC). To assess their environmental relevance, a quantitative understanding of OMC stability is thus essential. In the context of limestone caves, it has been shown that OMCs largely govern the transport of various first-row transition metals (*e.g.*, Co, Ni, Cu) from the surface to sites of cave carbonate (speleothem) precipitation. Importantly, the time-sensitive dissociation (or 'decay') of OMCs in the thin water film at speleothem surfaces has been argued to potentially define the availability of complexed metals to co-precipitate. OMC decay kinetics may thus present a potentially viable link between metal concentrations in stalagmites, and the residence time of OMCs at their surfaces. To provide a first comparative characterisation of in-cave OMC dissociation kinetic signatures, competitive ligand exchange (CLE) experiments were performed on water samples and soil extracts from eight Aotearoa New Zealand caves. This approach corroborated that natural organic ligands critically limit transition metal availability at the dripwater-speleothem interface, suggesting a hierarchy of complex stability of Cu $\approx$ Co $>$ Ni, and virtual absence of stable organic complexation of the alkaline earth metals Mg and Sr. Systematic variations of OMC stability with NOM characteristics were not observed amongst water sam-

ples, whilst enhanced complexation was clearly evident in the comparably organic-rich soil extracts. However, based on empirical estimates of the time-dependent release of metals at stalagmite surfaces, the decay of transition metal complexes was predicted to be most sensitive on time-scales relevant to typical cave drip points ($<$1 to ca. 40 drips min^{-1}), although noting that kinetic metal release is likely insignificant at faster flow rates ($>$40 drips min^{-1}). At large, this study encourages further examination of OMC decay kinetics *in-situ* and in controlled experiments, particularly with view to testing for the presence of kinetic imprints on metal concentrations during calcite precipitation.

3.1 Introduction

The speciation, mobility, and bioavailability of trace metals in aquatic environments are tightly governed by the interactions of metals with ligands present in natural organic matter (NOM) (H. B. Allen & Hansen, 1996; Sigg & Behra, 2005). At a pH of 8 – 9 as typical for karst waters, NOM ligands typically bind $>$90% of the total pool of Cu, Co, and Ni (*e.g.*, Hartland & Zitoun, 2018; Xue et al., 2000), leaving a marginal labile (available) fraction consisting of hydrated 'free' cations and simple inorganic metal complexes (IMCs) (Hoffmann et al., 2007; Lead & Wilkinson, 2006). In consequence, organic metal complexes (OMCs) effectively control transition metal transport from the surface to caves (Hartland & Zitoun, 2018), where infiltrating waters deposit speleothems (secondary cave carbonates).

The kinetic inhibition of transition metals imposed by organic ligands complicates the apparent partitioning (estimated as the ratio of $(M/Ca)_{solid}$ and $(M/Ca)_{solution}$, where M and Ca are concentrations of a metal and calcium, respectively) between dripwater and speleothems (Lindeman et al., 2022). This stands in contrast to alkaline earth metals (Mg, Sr, Ba), which exhibit comparably predictable partitioning that allows these elements to routinely serve as palaeoenvironmental proxies in speleothems (*e.g.*, Fairchild & Treble, 2009; Huang & Fairchild, 2001; Wassenburg et al., 2020). As demonstrated by example of Cu, the 'aqueous sink' for transition metals created by organic complexation effectively moderates their availability for substitution into Ca^{2+} sites in the calcite lattice at the dripwater-calcite interface. Thus, the dissociation, or decay of OMCs is expected to determine respective metal concentrations in the speleothem (Hartland & Zitoun, 2018; Sliwinski et al., 2022). Considering that the residence time of the water thin-film on top of a stalagmite is essentially governed by the impact of incoming drips, a systematic understanding of OMC dissociation kinetics may offer an opportunity to quantitatively relate stalagmite metal concentrations to the drip rate. The interactions between a metal M and a ligand L_i are defined by the equilibrium describing the formation and dissociation of ML complexes (*i.e.*, OMCs; Equation 3.1):

$$M + L_i \underset{k_{d,i}}{\overset{k_{f,i}}{\rightleftharpoons}} ML_i \tag{3.1}$$

, where the dissociation rate constant ($k_{d,i}$) is proportionate to the ratio of the formation

rate constant ($k_{f,i}$) and the stability constant K of the equilibrium reaction for a given ligand (Equation 3.2):

$$k_{d,i} = \frac{k_{f,i}}{K_i} \tag{3.2}$$

For the quantitative analysis of dissociation kinetics, the concentration of metal-ligand complexes in solution over time is commonly described in terms of an exponential decay with k_d as the rate determining variable. To best account for the large number of heterogeneous binding sites in NOM (Rate et al., 1992), the total concentration of a metal due to dissociation at any given time t (C_t) can be expressed as a function of a continuous distribution of k_d (opposed to discrete values)(Equation 3.3):

$$C_t = C_0 \int_{-4\sigma}^{+4\sigma} f(\ln k_d) \times e^{(-k_d \times t)} d(\ln k_d) \tag{3.3}$$

, where C_0 denotes the initial metal concentration, and $f(\ln k_d)$ describes the normal distribution of $ln(k_d)$ with mean μ and standard deviation σ (Equation 3.S5; see details in Section 3.4). One approach to study complex dissociation kinetics is the competitive ligand exchange (CLE) method, in which dissociation is induced by the introduction of a competing, typically very strong and well-characterised ligand to a test solution (*e.g.*, Chakrabarti et al., 1994; Sigg et al., 2006). Consequently, the equilibrium in Equation 3.1 favours the formation of metal complexes with the introduced ligand, in turn driving the decay of native OMCs. Rate constants describing this process can be estimated by monitoring the removal of metals from the sample solution over time.

In this study, a set of quantitative estimates of OMC dissociation rate constants (k_d) are provided for Ni, Cu, and Co in waters and extracts of overlying soils from eight Aotearoa New Zealand cave systems through competitive ligand exchange experiments and kinetic modelling. Based on this information, it is aimed to elaborate on the hypothesis of a hydrological control of the concentrations of these metals in cave waters and speleothems as proposed by Hartland and Zitoun (2018), and move towards extracting meaningful and well-constrained palaeoenvironmental information from these.

3.2 Materials and methods

3.2.1 Sample solutions

Test solutions for kinetic experiments were obtained from eight Aotearoa New Zealand cave systems with various soil and vegetation cover, and distinct climatic regimes (see Table 3.S2 for details). Cave water samples were collected by placing acid-clean screw-cap Nalgene© HDPE bottles directly under drip points (n = 7) or sampling stream water (n = 1). Following

transfer to the laboratory, samples were filtered (0.45 µm) and stored frozen in the dark until analysis. Remote sampling locations and/or shipment of some samples prevented consistent pre-treatment, but analyses were carried out within three weeks of sample collection. Native concentrations of transition metals in cave waters are typically close to instrumental quantitation limits (often $<$0.1 µg L^{-1} for Ni, Cu, Co), rendering the study of dissociation kinetics in untreated samples analytically challenging. Defrosted cave waters were therefore augmented with 5 µg L^{-1} of Ni, Cu, and Co to facilitate quantification of these elements. From three of the studied caves (Table 3.1), representative soil samples from ca. 10 cm depth were dried at 40 ℃ for 48 hours, manually homogenised, and finally sieved (2 mm). Soil extracts were prepared by shaking soil sub-samples at a 1:10 (*w/v*) ratio in 0.01 M $CaCl_2$ for 2 hours, followed by centrifuging for 10 minutes at 3000 rpm, and finally filtering the supernatant (0.45 µm). 400 mL of the soil extracts and spiked cave waters were adjusted to a concentration of 0.005 M HEPES and a pH of 8.5 to facilitate direct comparison of kinetic parameters. This pH was chosen based on the median of all dripwater samples (ca. pH 8.52), which varied between 8.25 and 8.70. Similarly, 3 M KCl was used to adjust the ionic strength of cave water solutions to ca. 0.018 M, whereas soil extracts were measured at their original ionic strength of ca. 0.044 M (HC-Soil and MAJ-Soil) and 0.087 M (Babylon-Soil). While the *in-situ* ionic strength (derived from measurements of electrical conductivity) of water samples lay between 0.005 M and 0.008 M (291 – 509 µS/cm), the adjustment accounted for added ions during pH buffering to create comparable conditions between experiments. *In-situ* water temperatures (between 6.8 ℃ and 15.9 ℃) were not attempted to be replicated in this study but are expected to be of minor importance (cf., Rieuwerts et al., 1998). Native metal concentrations varied only slightly between water samples with all three transition metals of interest near instrumental detection limits (Table 3.1), and the addition of 5 µg L^{-1} is regarded to equally affect all aqueous samples. Treated test solutions were stirred in the dark in sealed acid-cleaned 1000 mL Nalgene© HDPE bottles that served as reactors, and were allowed to equilibrate at experimental temperature for 24 hours prior to the experiment.

3.2.2 Competitive ligand exchange (CLE) experiments

M-NOM decay kinetics were studied via CLE, which was considered suitable given its established application for kinetic studies, and comparably limited dependence on specialised equipment. The competing ligand was prepared by suspending Chelex-100 ion exchange resin (see Section 3.4 for details on reagents) in an excess volume of 0.1 M HEPES buffer solution (adjusted to pH 8.5 with 1 M or 0.1 M NaOH) for at least 24 hours in the dark using a Teflon-coated magnetic stir bar to stabilise the pH of the resin to that of the test solutions. Prior to the pH equilibration of the resin, the buffer solution was purified by stirring 5% Chelex-100 (*w/v*) for 12 hours, and subsequently removing and discarding the resin by filtration (0.45 µm). The preconditioned resin was extracted shortly before each experiment by centrifuging the mixture for 20 minutes at 3000 rpm, and subsequently extracting the supernatant buffer solution. Each experiment was initiated with the addition of 1% (wet weight/volume; *i.e.*, 4 g for 400 mL solution)

Table 3.1: Overview of CLE test solutions and experimental conditions. Dissolved organic carbon (DOC), indicative parameters of NOM quality, and native metal concentrations were determined using filtered (0.45 µm) aliquots of otherwise unaltered water samples and $CaCl_2$ soil extracts.

Test solution	Experimental conditions			Selected properties of untreated test solutions								
	pH	Ionic strength	Temperature	DOC	$SUVA_{254}$	E_3/E_4	S_R	[Co]	[Ni]	[Cu]	[Mg]	[Sr]
	median	mol L^{-1}	average, °C	mg L^{-1}	L mg^{-1} m^{-1}	a(300)/a(400)		µg L^{-1}	µg L^{-1}	µg L^{-1}	µg L^{-1}	µg L^{-1}
Cave waters												
Babylon Cave	8.48	0.016	22.3	2.1	153.5	2.17	2.91	<0.01	<0.01	0.10	1560.0	39.1
Bulmer Cave	8.53	0.017	22.5	4.8	29.3	0.08	0.62	<0.01	<0.01	0.15	1120.0	24.6
Calcite Cave	8.48	0.019	22.2	1.4	116.2	0.13	0.67	0.01	<0.01	0.18	1340.0	63.5
Dave's Cave	8.48	0.017	22.2	2.9	161.6	0.15	0.40	0.00	<0.01	0.00	39.7	2.0
Hodge Creek Cave	8.46	0.019	22.1	4.1	197.4	0.70	1.01	0.01	<0.01	0.19	1210.0	77.4
Majumba Cave	8.53	0.023	21.7	6.8	85.1	1.49	0.44	0.01	0.08	0.21	5340.0	365.0
Stafford's Cave (stream)	8.49	0.016	21.9	2.5	325.7	0.49	1.20	<0.01	0.28	0.08	1160.0	77.7
Te Reinga Cave	8.54	0.017	22.3	2.9	194.1	0.34	0.90	<0.01	0.06	0.08	2250.0	340.0
All water experiments	8.49	0.018 ± 0.002	22.1 ± 0.3									
Soil extracts												
Babylon Cave	8.50	0.087	22.4	60.5	540.8	6.78	0.96	0.34	2.82	7.01	76237.7	1108.0
Hodge Creek Cave	8.45	0.043	22.5	17.9	331.5	3.37	1.36	0.07	0.94	6.18	7649.6	499.5
Majumba Cave	8.48	0.044	21.7	9.2	651.8	2.95	1.06	0.09	1.05	4.19	20938.8	754.0
All soil extract experiments	8.48	0.058 ± 0.025	22.2 ± 0.4									

of pre-treated resin to the stirred test solution. Including one sub-sample collected just prior to the start of the experiment, a total of 12 aliquots were taken in time intervals evenly distributed in log-space ranging from 10 s to 7200 s following Chelex-100 addition. This duration of kinetic experiments was determined based on preliminary experiments under equivalent conditions, which indicated little to no change in the undissociated fraction over 72 hours. The sub-samples were drawn from the reactor and immediately filtered using syringes equipped with 0.45 µm PES filters and Tygon® Inert tubing, thus separating the test solution from the resin. Aliquots of sub-samples were immediately acidified to 2% (volume/volume) with double-distilled HNO_3 for the analysis of elemental concentrations. The solution pH across all experiments was maintained at 8.5 and varied by less than 0.3 pH units over the duration of individual experiments. Solution temperature was kept at 22.2 °C ± 0.3, with an ionic strength of 0.018 M ± 0.002 for water samples (variable for soil extracts). An overview of experiments and information on test solutions is presented in Table 3.1.

3.2.3 Kinetic data analysis

Continuous distributions of conditional dissociation rate constants (k_d) for each CLE experiment were estimated based on the measured total metal concentrations normalised to respective initial concentrations (*i.e.*, C_t / C_0). This was achieved by numerically integrating Equation 3.3 and subsequently fitting μ and σ in $f(\ln k_d)$ (see Equation 3.S5) as proposed in Rate et al. (1992). The same datasets were also fitted to discrete site models. Details on both modelling approaches are found in the Supplement.

3.3 Results and discussion

3.3.1 Kinetic signatures of OMC decay in cave water and soil solutions

To characterise OMC dissociation kinetics for Ni, Co, and Cu in typical cave environments, dissociation rate constants (k_d) were estimated for eight cave water samples and three soil extracts via competitive ligand exchange experiments. An exponential decay of OMCs as commonly assumed was universally evident but distinct between different metals and samples. Estimates of μ for the normal distribution of $ln(k_d)$ in cave waters varied from ca. -1.1 s^{-1} to -8.3 s^{-1} ($k_d = 3.3\times10^{-1} - 2.5\times10^{-4}$ s^{-1}) and -4.1 s^{-1} to -10.5 s^{-1} ($k_d = 1.7\times10^{-2} - 2.8\times10^{-5}$ s^{-1}) for Ni and Co, respectively (Figure 1), suggesting an overall stronger kinetic limitation for Co. At the end of CLE experiments (*i.e.*, after 2 hours), between 30% and 60% of initial Co remained undissociated in cave water solutions (referred to here as the 'inert' fraction, or $\%M_{2h}$), whereas only 15% to 25% of Ni-NOM complexes persisted. The tendency of Co to form more stable complexes coincided with a generally more heterogeneous kinetic behaviour. While distributions of $ln(k_d)$ were comparably well constrained for Ni (*i.e.*, smaller fitted values of σ), a larger range in k_d values was required to adequately describe the decay of Co-NOM complexes. However, the ≈asymptotic evolution of Ni and Co concentrations in most water samples after ca. 15 minutes of exposure to Chelex-100 attested to a relatively large proportion of both metals occupying weaker NOM binding sites. Although the latter may be exaggerated in this study due to procedurally increased M:NOM ratios by elemental spiking, a release of up to ca. 80% and 64% of Ni and Co was observed within ca. 2 minutes, respectively. The average k_d (4.0×10^{-3} s^{-1} as derived from fitted μ) for Co-NOM was highly comparable to that found by Warnken et al. (2007) in stream waters at a comparable pH ≈ 8 (3.1×10^{-3} s^{-1}), whereas Ni-NOM dissociation rate constants in their study (6.6×10-4 s^{-1}) suggested considerably more stable complexation than implied here by an average k_d for Ni-NOM of 1.1×10^{-1} s^{-1}. Ni dissociation curves in turn compared well with those for a Ni:Fa of 0.25 and pH 7.6 modelled by Shi et al. (2016), who compiled CLE experimental data from various previous studies.

The kinetic behaviour of Cu was less distinct, with several experiments exhibiting an unexpected increase in dissolved Cu following its initial rapid uptake by the resin. Despite preconditioning containers, this may be due to desorption from the reactor walls, or alternatively be linked to more intricate processes and interactions with other metals at the binding sites of NOM ligands (*e.g.*, site competition; Mandal et al., 1999a). Regardless, while showing an overall exponential decay as expected, the complicated behaviour immediately after experiment initiation precluded adequate kinetic models for most samples. Fits yielded values of μ translating to k_d in the order of 9×10^{-4} to 7×10^{-3} s^{-1}, while between 30% and 80% of initial Cu remained undissociated. This magnitude of k_d for Cu-NOM complexes is similar to that reported by Warnken et al. (2007) (ca. 6.1×10^{-2} s^{-1}), while reflecting lower complex stability than in solutions with anthropogenic contributions as expected (cf. Baken et al. (2011), but not

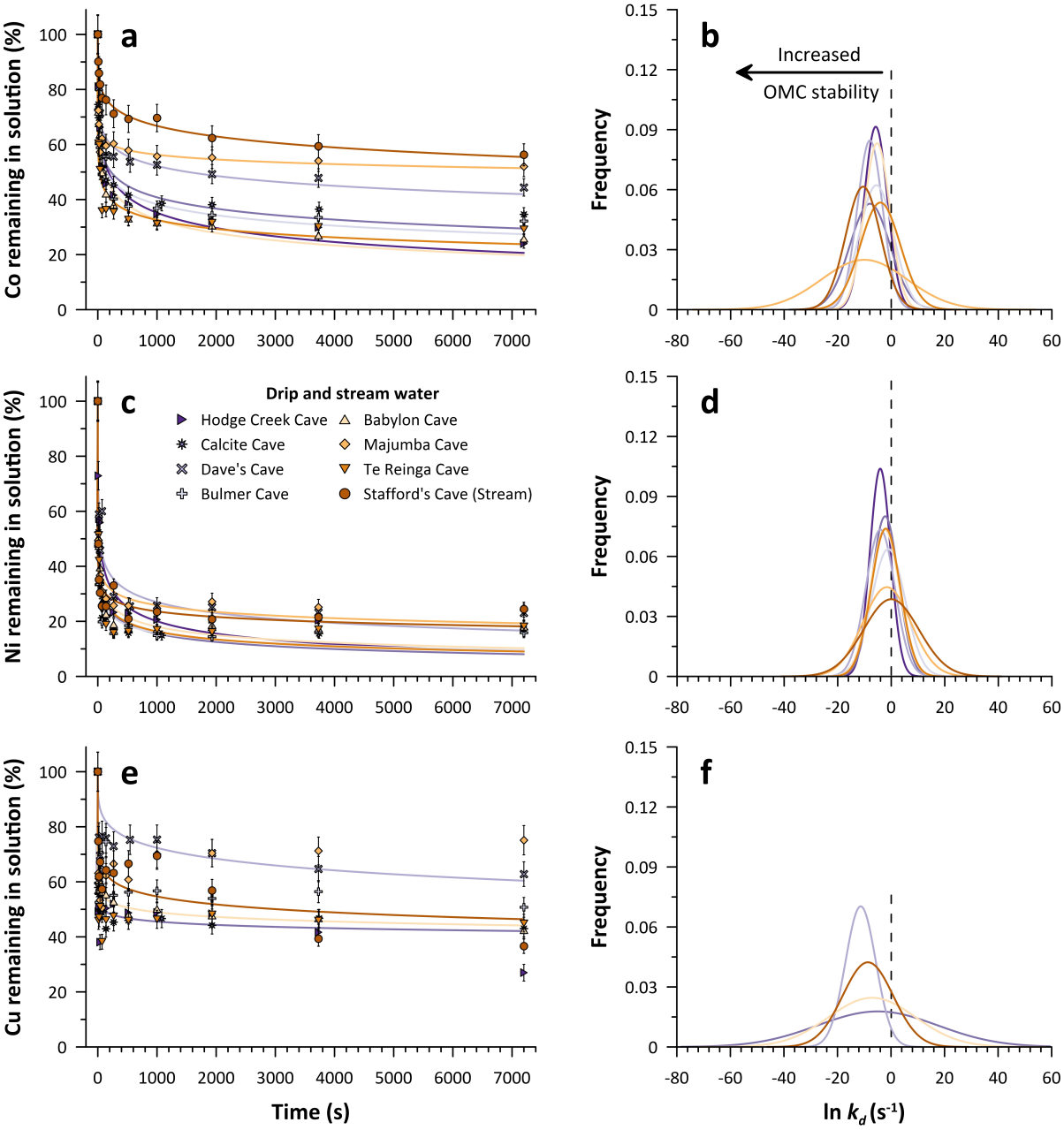

Figure 3.1: OMC decay curves and corresponding fitted log-normal distributions of k_d for transition metals in CLE experiments of cave waters. Sub-plots in the left column show the measured evolution of metal concentrations in solution (symbols) and corresponding log-normal model fits (solid lines) according to Equation 3.3 (Rate et al., 1992). Vertical error bars denote propagated standard deviations (1 SD). The right column depicts the respective frequency distributions (site densities) of $ln(k_d)$ based on fitted values of μ and σ. Note that fitted values for σ produce excessively large distributions of $ln(k_d)$. Where only symbols are shown, no adequate model fit was obtained. Values of $ln(k_d) > -2$ cannot accurately be distinguished from the decay of metal-aqua complexes.

Amery et al. (2010)). Based on fitted values of μ (Table 3.2) and an assessment of comparative metal binding throughout experiments (Figure 2), the data thus depict a stronger binding affinity of Cu and Co to NOM than Ni across cave water samples, which is partly at odds with the predicted hierarchy of Cu $>$ Ni $>$ Co according to the Irving-Williams series (Irving & Williams, 1953). However, these findings are in turn supported by observations of M. Collins et al. (2010) and Hartland et al. (2014), who reported exceedingly stable complexation of Co in natural freshwater systems.

Mg and Sr present the most widely assessed trace elements in speleothems and other carbonate archives. In these experiments, both metals were readily removed from solution upon Chelex-100 addition to below detection limit in most water samples, with negligible fractions ($<$2.0%) of initial concentrations remaining undissociated in two experiments (Table 3.S1). Despite the initially linear rapid removal slowing after ca. 3 minutes (Figure 3.3), these results demonstrate the effective absence of ligand binding of Mg and Sr, and its arguably inconsequential contribution to observed partitioning coefficients in cave environments (Chapter 4). Dissociation was highly consistent for Mg and Sr with estimated values for μ between -3.8 s^{-1} and -5.0 s^{-1} (k_d = 2.4$\times10^{-2}$ – 7.2$\times10^{-3}$ s^{-1}), and -3.7 s^{-1} and -4.9 s^{-1} (k_d = 2.2$\times10^{-2}$ – 6.7$\times10^{-3}$ s^{-1}), respectively. Values of μ were strongly correlated between Mg and Sr (r = 0.98, $p <$ 0.0001, n = 8) but not between any other metal pairs. This may suggest that the source for the observed minimal kinetic limitation of Mg and Sr may be attributable to the HEPES buffer or equilibrium constraints rather than heterogeneous binding sites of natural organic ligands.

The stability of OMCs depends on several factors, the most determinant of which are pH, ionic strength (I), metal:ligand ratios, and the quality of ligands (*e.g.*, Sanders & Bloomfield, 1980; Rate et al., 1993. Empirically derived values of kinetic parameters are thus inherently conditional and sensitive to the specific experimental design. One such methodological constraint for the quantitative interpretation of derived kinetic parameters is the analytical timescale τ, which is defined by the experimental duration. Specifically, the duration of 2 hours during which OMC decay was monitored imposes a threshold for the resolvable 'kinetic window' with limit τ^{-1} (Amery et al., 2010). For τ = 2 hours this translates to a threshold $k_d \approx$ 1.4$\times10^{-4}$ s^{-1}, which may serve to operationally differentiate 'labile' and 'inert' fractions for $k_d > \tau^{-1}$ and $k_d < \tau^{-1}$, respectively. Accordingly, complexes thereby deemed 'labile' are expected to be mostly dissociated after 2 hours, whereas 'inert' species remain largely complexed beyond the experimental duration (also reflected by $\%M_{2h}$). In case of the latter, k_d values are effectively extrapolated, limiting confidence in their absolute magnitude. A second limit exists as $t \rightarrow 0$. Adopting the threshold identified by Fasfous et al. (2004) for an equivalent kinetic window, decay constants of $k_d > 10^{-2}$ s^{-1} cannot reliably be attributed to OMCs because the fast dissociation rate approaches that of metal-aqua complexes. This limit further accounts for time required for the Chelex-100 to mix in solution. Interestingly, these constraints suggest that a considerable fraction of Ni was very weakly complexed, with fitted values of k_d indicating mostly 'labile' behaviour of most Ni complexes within the analytical time-frame. However, $>$20% of Ni was persistently characterised as more stable and/or 'inert' in discrete models, which was also reflected by similar fractions of $\%Ni_{2h}$ (Table 3.2). On the other hand, Mg was not detectable

Table 3.2: OMC decay characteristics for transition metals in cave waters and soil extracts determined in CLE experiments. Values of μ and σ were fitted using the continuous (log-normal) kinetic model described by Rate et al. (1992) (Equation 3.3). The discrete model is shown in Equation 3.S4 and was solved for 1 to 3 kinetic components (*i.e.*, C_1, C_2, C_3, expressed as fractions) with corresponding dissociation rate constants. $\%M_{2h}$ denotes the fraction of initial metal that remained undissociated after two hours. Data are only shown where adequate model fits were obtainable ($R^2 > 0.75$). The threshold k_d (τ^{-1}) was 1.4×10^{-4} for all transition metal fits. Kinetic parameters obtained for Mg and Sr are found in Table 3.S1.

		Continuous kinetic model				Discrete kinetic model							
	Test solution	$\mu \pm 1$ SD	$\sigma \pm 1$ SD	k_d	R^2	C_1	C_2	C_3	$k_{d,1}$	$k_{d,2}$	$k_{d,3}$	R^2	$\%M_{2h}$
		$ln(k_d)$	$ln(k_d)$	s^{-1}		%	%	%	s^{-1}	s^{-1}	s^{-1}		%
	Cave waters												
Ni	Babylon Cave	-2.4 ± 0.5	5.4 ± 0.9	9.2×10^{-2}	0.96	42.3	39.8	17.9	2.5	1.8×10^{-2}	6.2×10^{-7}	1.00	18.0
	Bulmer Cave	-1.1 ± 0.8	6.3 ± 1.1	3.4×10^{-1}	0.96	60.7	23.1	16.2	1.8×10^{-1}	1.5×10^{-2}	6.2×10^{-6}	0.99	15.8
	Calcite Cave	-2.3 ± 0.6	5.0 ± 0.9	1.0×10^{-1}	0.95	78.1	19.0		6.2×10^{-2}	3.2×10^{-5}		0.97	17.1
	Dave's Cave	-4.1 ± 0.6	5.4 ± 1.3	1.7×10^{-2}	0.90	86.9	25.6	6.5	2.6×10^{-2}	1.6×10^{-5}	4.1×10^{-3}	0.75	23.0
	Hodge Creek Cave	-4.1 ± 0.4	3.8 ± 0.7	1.6×10^{-2}	0.92	57.7	22.6	19.8	2.1×10^{-2}	3.7×10^{-5}	2.1×10^{-1}	0.99	17.1
	Majumba Cave	-1.6 ± 0.8	8.9 ± 1.7	2.0×10^{-1}	0.96	42.1	32.0	25.8	2.2	2.5×10^{-2}	7.8×10^{-6}	1.00	24.2
	Stafford's Cave (stream)	No model				73.8	26.0		1.1×10^{-1}	2.5×10^{-5}		0.98	24.5
	Te Reinga Cave	-2.1 ± 0.7	5.4 ± 1.1	1.3×10^{-1}	0.94	79.8	18.4		5.6×10^{-2}	1.1×10^{-5}		0.98	18.2
Co	Babylon Cave	-5.3 ± 0.2	4.8 ± 0.5	5.1×10^{-3}	0.97	42.9	33.8	23.3	1.2×10^{-2}	4.5×10^{-5}	2.3	1.00	25.7
	Bulmer Cave	-5.6 ± 0.2	6.4 ± 0.8	3.9×10^{-3}	0.96	40.5	35.6	24.1	1.1×10^{-1}	1.4×10^{-5}	4.1×10^{-3}	0.98	32.2
	Calcite Cave	-6.0 ± 0.2	6.3 ± 0.7	2.5×10^{-3}	0.96	42.2	37.2	20.6	3.2×10^{-5}	1.7×10^{-2}	3.1×10^{-1}	0.99	34.6
	Dave's Cave	-7.9 ± 0.3	7.5 ± 1.2	3.6×10^{-4}	0.93	57.8	53.8		2.6×10^{-2}	2.9×10^{-5}		0.87	44.4
	Hodge Creek Cave	-5.8 ± 0.2	4.4 ± 0.4	3.1×10^{-3}	0.96	42.9	39.2	17.9	1.4×10^{-2}	7.3×10^{-5}	1.4×10^{-1}	1.00	24.0
	Majumba Cave	-10.0 ± 0.8	16.0 ± 2.8	4.4×10^{-5}	0.96	59.1	40.7		2.1×10^{-5}	1.0×10^{-1}		0.98	52.0
	Stafford's Cave (stream)	-10.5 ± 0.2	6.5 ± 0.5	2.7×10^{-5}	0.98	62.1	22.8	14.5	1.4×10^{-5}	4.4×10^{-2}	8.8×10^{-4}	0.99	56.2
	Te Reinga Cave	-4.1 ± 0.5	7.5 ± 1.3	1.7×10^{-2}	0.94	62.9	34.7		4.8×10^{-2}	3.0×10^{-5}		0.97	29.2
Cu	Babylon Cave	-7.1 ± 0.2	16.2 ± 1.7	8.5×10^{-4}	0.99	49.9	40.8	9.3	2.2×10^{-5}	2.6	4.7×10^{-3}	0.99	42.4
	Calcite Cave	-5.0 ± 0.6	22.5 ± 5.5	6.9×10^{-3}	0.97	45.5	37.3	17.2	4.6×10^{-6}	3.1	3.1×10^{-2}	0.99	43.0
	Stafford's Cave (stream)	-8.6 ± 0.9	9.4 ± 2.9	1.8×10^{-4}	0.77	65.4	23.9	10.9	8.8×10^{-5}	1.6×10^{-1}	1.6×10^{-1}	0.91	36.6
	Soil extracts												
Ni	Babylon Cave	-8.3 ± 0.2	5.0 ± 0.6	2.5×10^{-4}	0.95	45.8	33.8	20.0	8.9×10^{-18}	2.5×10^{-2}	9.1×10^{-4}	0.99	46.5
Cu	Babylon Cave	-11.7 ± 0.3	5.5 ± 0.8	8.0×10^{-6}	0.96	75.2	16.4	8.4	3.1×10^{-5}	3.3×10^{-3}	9.3×10^{-2}	0.98	61.5
	Hodge Creek Cave	-11.0 ± 0.4	4.9 ± 1.1	1.7×10^{-5}	0.90	74.8	22.5		4.7×10^{-5}	5.6×10^{-3}		0.96	55.0
	Majumba Cave	-10.0 ± 0.6	4.3 ± 1.0	4.7×10^{-5}	0.87	77.7	19.0		1.0×10^{-4}	5.9×10^{-3}		0.96	39.4

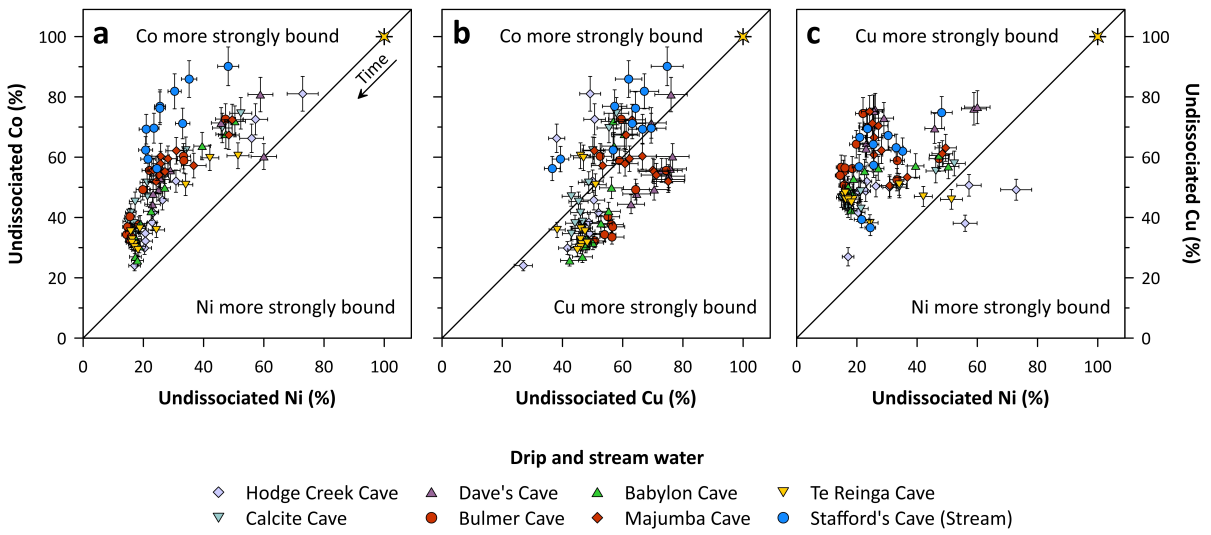

Figure 3.2: Comparative transition metal fractions bound to OMCs over the course of CLE experiments. Organic complexes of Co and Cu consistently decayed more slowly than those of Ni, but exhibited variable binding affinities between samples and with progressive dissociation. Error bars denote propagated standard deviations (1 SD), and are for clarity omitted for the common initial metal fraction of 100% (yellow star symbol).

beyond ca. 5 to 10 minutes of sub-sampling in most experiments, and $\%Sr_{2h}$ was consistently $<$2%. Despite their fitted values of μ comparable to those of transition metals, their kinetic signatures in light of τ and estimated proportions of kinetic components altogether thus depict expected negligible or absent organic binding largely indistinguishable from metal-aqua complexes.

Notwithstanding the caveats on absolute kinetic parameters, this study primarily aimed to compare complexation characteristics of various cave waters representative of a range of cave environments. Regarding factors driving complex stability, the experimental pH of 8.5 was therefore selected to represent most limestone cave waters that typically vary in pH between 7.5 and 9, although noting that significantly more alkaline systems with distinct complexation regimes are known (*e.g.*, Poole's Cavern; Hartland et al., 2011). Likewise, *I* was fixed but similar to that found in caves. Consequently, the observed variability in kinetic signatures is interpreted primarily as a function of ligand quality and quantity, which are expected to present the dominant variables driving OMC stability in most karst systems.

Following the interpretation of spectral absorption ratios (E_3/E_4) of Artinger et al. (2000), DOM in most samples was dominated by components resembling humic acid, opposed to fulvic acid (Figure 3.S1A). On the other hand, clear trends were absent between samples with regards to molecular weight or aromaticity based on parameters derived from UV-Vis spectra, suggesting that DOM properties were not sufficiently distinct for such characterisations. Perhaps because of this, there was no pronounced relation between fitted values for $ln(k_d)$ and DOC, nor between the former and $SUVA_{254}$ or other indices of NOM quality derived from UV-Vis spectra (all relationships $p > 0.05$; Figure 3.S1). These observations are coherent with a lack of correlation between ligand concentration and DOM content observed in dripwaters by Hartland and Zitoun (2018), however, stand in contrast to several studies relating kinetic

parameters to proxies of NOM properties. For instance, Amery et al. (2010) and Baken et al. (2011) noted a pronounced positive relationship of $SUVA_{254}$ with the fraction of non-labile Cu (undissociated after 8h) and metal binding affinity (Ni, Cu, Co, Zn), respectively. Similarly, Welikala et al. (2018) observed that Ni in soil amendments was complexed more strongly by DOM of higher aromaticity (see also Baker et al., 2008). However, the discrepancies with many previous published datasets are not altogether surprising, given the often substantially greater metal and/or DOM contents and ranges of test solutions in other studies. For instance, natural stream water analysed *in-situ* by Warnken et al. (2007) had significant organic contributions from peat, and consequently possessed DOC contents (ca. 11 – 15 mg L^{-1}) that were 2 to 6 times higher than those of cave waters studied here. The DOC content of agricultural and urban test solutions presented by Amery et al. (2010) in turn measured 19 – 144 mg L^{-1} DOC, clearly challenging direct comparisons with typical cave waters regarding kinetic parameters and their relationships with organic components. Thus, cave waters measured here possibly vary insufficiently in NOM quality and quantity for noticeable effects on complex kinetics to eventuate. This narrow range of DOM characteristics in cave waters may itself reflect discriminative processes that NOM in dripwater is subject to (*e.g.*, adsorption, filtration, or co-precipitation).

This notion was supported by CLE experiments performed on $CaCl_2$ soil extracts from three of the studied caves, which contained considerably higher metal and DOM concentrations than water samples (Table 3.1). These experiments yielded four adequate kinetic models (Figure 3), while the remaining transition metal patterns precluded reliable model fits. Soil extracts were not augmented with elemental stock given their far greater native elemental content compared to water samples. Despite this, only Cu consistently dissociated from M-NOM complexes during the experiments as evident in monotonous Cu uptake by Chelex-100. In soils from Hodge Creek Cave and Majumba Cave, both Ni and Co measurements were unreliable and varied incoherently over the course of 2 hours, implying limited complex dissociation and/or reassociation. These differences between Ni and Co compared to Cu are likely explained by the much higher native concentrations of Cu (ca. 4.2 – 7.0 µg L^{-1} compared to 0.1 – 0.3 µg L^{-1} and 0.9 – 2.8 µg L^{-1} for Co and Ni, respectively), translating to considerably higher M:DOC ratios for Cu that are predicted to result in increased lability of Cu. Compared to dripwater solutions, however, fitted distributions of k_d altogether indicated a larger stable fraction for Cu-NOM complexes (39% – 61%). Similarly, 32% – 60% of Ni and 80% – 91% of Co remained complexed in soil extracts after 2 hours, attesting to substantially greater Ni-NOM and Co-NOM stability than in any water sample. Indeed, relative to drip water solutions these stronger complexation regimes of soil extracts coincided with higher aromaticity, lower degrees of humification, as well as greater fraction of fulvic acids as estimated by UV-spectral parameters (Figure 3.S1).

However, in this study, bounds of σ (Equation 3.S5) were not adequately estimated by the log-normal model, yielding the unrealistically large distributions around μ. Fitted values of μ were in turn consistent with estimates from comparable environments (*e.g.*, 10^{-5} to 10^{-3} s^{-1} for Cu, Shi et al., 2016; order of 10^{-5} s^{-1} for Co in river water; Fasfous et al., 2004), suggesting that the excessive values of σ were in fact computational artefacts (cf. magnitude of $0.1 < \sigma < 2.2$ in Amery et al., 2010). As a compromise, k_d values were additionally approximated based

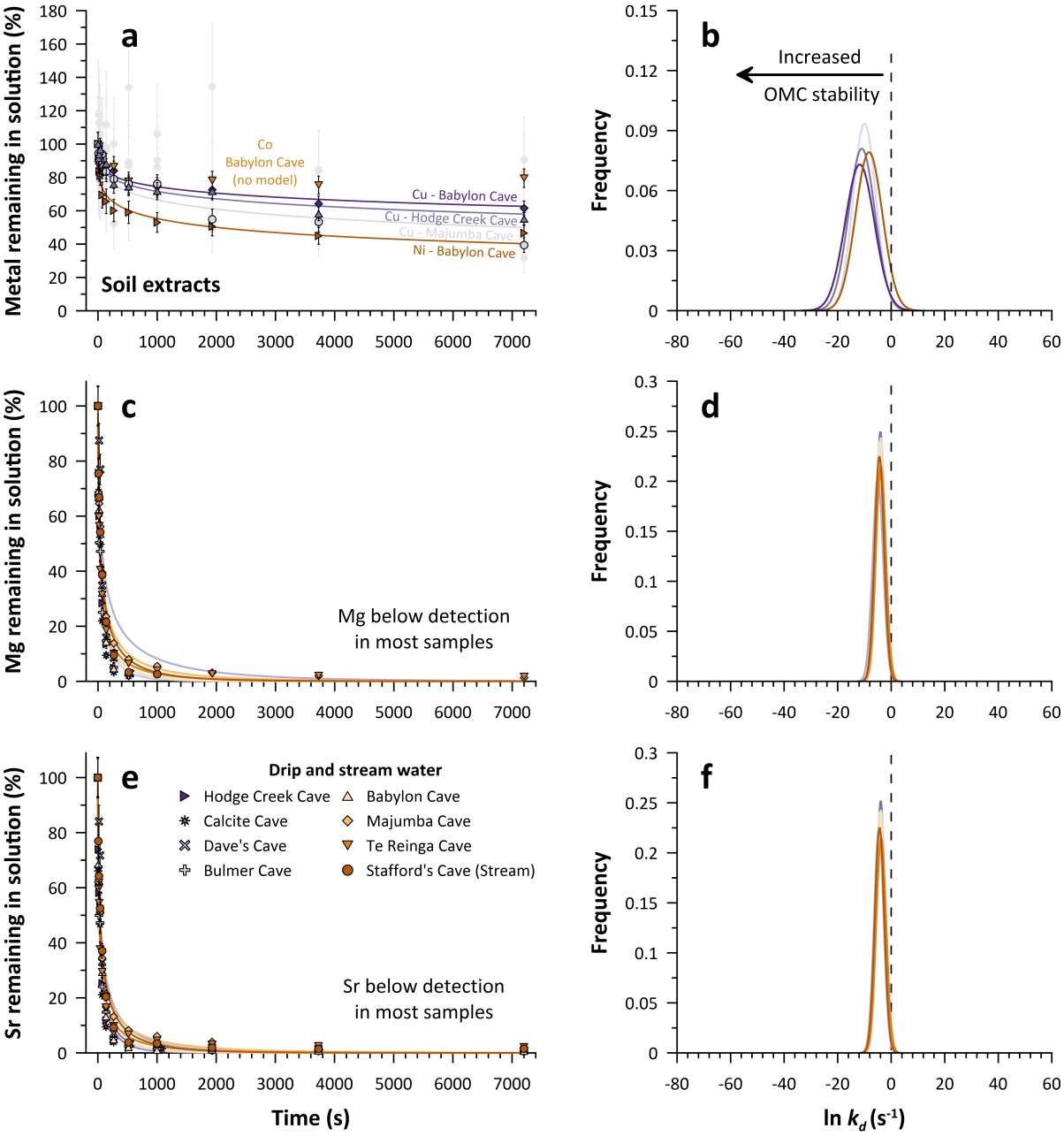

Figure 3.3: OMC decay curves and corresponding fitted log-normal distributions of k_d for metals in CLE experiments of cave waters and soil extracts. Sub-plots in the left column show the measured evolution of metal concentrations in solution (symbols) and corresponding log-normal model fits (solid lines) according to Equation 3.3 (Rate et al., 1992). Vertical error bars denote propagated standard deviations (1 SD). The right column depicts the respective frequency distributions (site densities) of $ln(k_d)$ based on fitted values of μ and σ. Note that fitted values for σ produce excessively large distributions of $ln(k_d)$. Where only symbols are shown, no adequate model fit was obtained. For clarity, the highly inconsistent measurements of Ni and Co in Majumba Cave and Hodge Creek Cave are shown as light grey symbols. Values of $ln(k_d) > -2$ cannot accurately be distinguished from the decay of metal-aqua complexes.

on the conventional model depicted in Equation 3.S4), which numerically reduces ligand action to a discrete number of binding sites. For most test solutions, the best fits were obtained when assuming either two or three kinetically distinguishable components (*i.e.*, fractions of distinct lability) (Table 3.2). In their magnitude, these estimates of the dominant component were generally in good agreement with those obtained for μ, but were inconsistently related. Although discrepancies between the models are to be expected due to their distinct underlying assumptions, they also highlight the complexity kinetic characterisations, as well as their high sensitivity to both method and data analysis (*e.g.*, Fasfous et al., 2004; Rose & Waite, 2003; Sigg et al., 2006). Solely based on fitted values of k_d, for instance, the CLE data implied that Ni was bound more weakly than Mg and Sr in several test solutions (Table 3.2; Table 3.S1). In this example, the fitted dissociation rate constants do not account for the virtually complete removal of Mg and Sr from solution over the course of experiments (*i.e.*, effectively variable τ), whereas significant remnant undissociated Ni fractions and considerable 'inert' components of Ni in all solutions attest to stronger complexation. Given methodological and computational caveats encountered here, it may be necessary to adopt an alternative empirical approach to improve confidence in quantitative estimates of in-cave OMC decay kinetics. In this regard, diffusive gradients in thin-films (DGT) may present a feasible option to help circumvent analytical challenges related to low native metal concentrations, given their capacity to accumulate metals over time (*e.g.*, Sigg et al., 2006). A well constrained DGT setup could potentially be deployed *in-situ* to allow for more representative characterisation of OMC decay (*e.g.*, Hartland et al., 2011). Nonetheless, the data obtained from CLE experiments provide insights into the heterogeneous nature of metal binding in cave waters with indicative quantifications that enable an assessment of potential implications for metal inclusion into speleothems.

3.3.2 OMC decay during speleothem formation

OMC decay is driven by the availability of a competitive sink for metal cations. In limestone caves, such a sink is provided by calcium carbonate precipitating from infiltrating waters. The partitioning of Co in the absence of ligands (*i.e.*, under 'inorganic' experimental conditions) occurs with slight preference for the crystal phase (inorganic partition coefficient (k_p) for calcite $\approx$ 4), whereas even a small degree of carbonate precipitation would effectively remove all Cu from solution ($k_p > 40$) (Lindeman et al., 2022). While ligand action in natural systems is thus arguably essential for the presence of Cu in speleothems in measurable quantities, the underlying substantial control of prior carbonate precipitation (PCP) along the dripwater flow path complicates the use of Cu as a proxy based on OMC decay alone. Importantly, the susceptibility to PCP is less pronounced for Co and negligible for Ni with an empirical k_p value of ca. 1 (Lindeman et al., 2022; Y. Wang & Xu, 2001), indicating a largely indiscriminate incorporation of Ni in carbonate relative to Ca. Thus, the net measured distribution of these metals between water and associated carbonate precipitate in natural systems is expected to be foremost controlled by the dissociation of OMCs serving as the source of metals available for inclusion into carbonate.

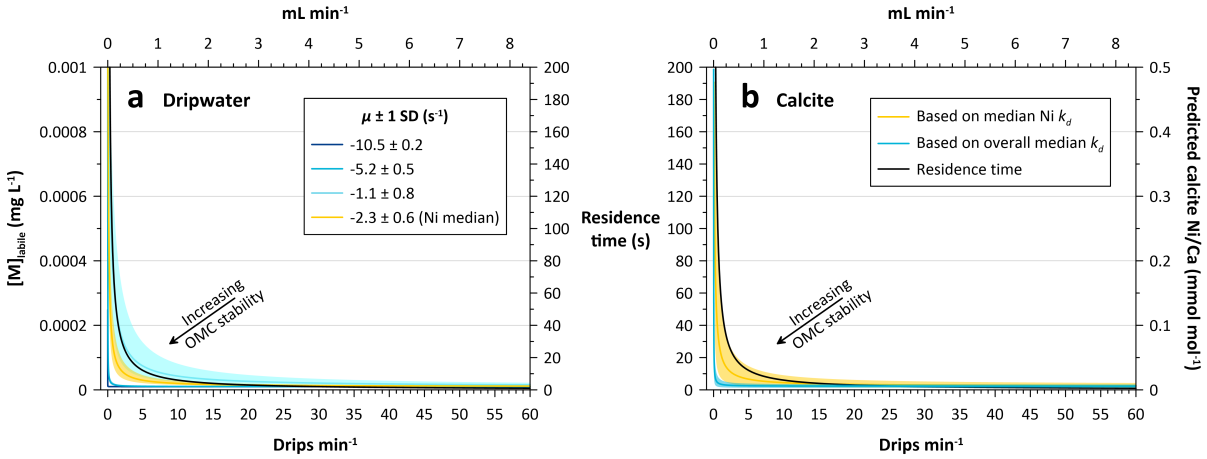

Figure 3.4: Theoretical supply of labile metals to stalagmite surfaces as a function of drip rate and OMC decay. a) Simple forward model of metal release from OMCs at the dripwater-calcite interface based on empirical minimal, median, and maximal estimates of μ for transition metal datasets. Uncertainty envelopes denote the respective error margin (1 SD) of μ as determined by the fitting routine. **b)** Example prediction of theoretical Ni/Ca in a calcite stalagmite (orange line and shading) based on the empirical median $k_{d,\ Ni\text{-}NOM}$ shown in **a** and assuming an inorganic partition coefficient of Ni into calcite of 1.1 $\pm$ 0.5 (Lindeman et al., 2022). The blue line and shaded area depict the same calculation but using the overall median k_d, reflecting higher overall OMC stability. Both parts of the model suggest a maximal sensitivity of OMC-driven metal supply for ca. $<$30 drips min^{-1}. The conversion of drip rate (bottom x-axes) to an approximate flow rate in mL min^{-1} (top x-axes) in both sub-plots assumes a single drop volume of 0.14 mL (*e.g.*, Genty & Deflandre, 1998). Black solid lines in both sub-plots denote the approximate residence time as a function of drip rate, which approaches infinity with ceasing drips. Details on model assumptions and calculations are found in the Supplement (Section 3.4).

The available metal fraction as a function of drip rate can be estimated based on the time-dependent decay of M-OMC complexes parameterised by μ and associated fit uncertainties (Figure 3.4A). Across the range of empirical k_d values based on the log-normal model, the labile (taken to be 'available') metal fraction is most sensitive within time windows relevant for typical cave drip points (*i.e.*, ca. $<$1 – 30 drips min^{-1}; see for instance Baker et al., 1997b), although reaching an asymptote from ca. 40 drips min^{-1}. At very high drip rates (*e.g.*, $<$60 drips min^{-1}), residence time is thus insufficient for OMC decay to contribute significantly to the labile metal pool, whereas the contribution increases exponentially towards longer drip intervals (*e.g.*, order of few drips per hour or day).

The modelled relationship of $[M]_{\text{labile}}$ with drip rate was most distinct for stable complexation regimes observed in CLE experiments, while test solutions with μ closer to 0 imply that OMC decay would be essentially indistinguishable from the dissociation of aqua complexes (cf. Amery et al., 2010). However, considering that the fitted uncertainties of μ used in the model were greatly exceeded by the range of values of k_d implied by the presumably mischaracterised (and hence ignored) distribution parameter σ, it is reasonable to assume that the metal supply by OMC decay is altogether underestimated. Indeed, discrete site models suggest substantially more stable kinetic components present in many samples to varying extent (Table 3.2), which would increasingly contribute to the labile metal pool at longer drip intervals. By example of Ni (using the median empirical estimate) and assuming a realistic aqueous Ni/Ca (here, 0.01 mmol mol^{-1}), the model can be extended to make a simplistic prediction of the impact on calcite Ni/Ca as a function of drip interval (Figure 3.4B).

Using an inorganic partition coefficient of Ni of ca. 1.1 (Lindeman et al., 2022) with a conservative uncertainty of $\pm$0.5, and accepting negligible influence of other processes on partitioning, the same initial data support that metal supply to stalagmite tips through OMC decay likely occurs on relevant time-scales and across measurable magnitudes. By extension, these findings thus imply that under favourable circumstances (*i.e.*, OMC decay dominates metal supply), the concentration of Ni and potentially other transition metals may indeed allow for reconstructions of dripwater residence times, and ultimately flow rates. Where complex stability is very high, however, OMC decay may occur at insufficient rates and only imprint on carbonate M/Ca at very long drip intervals. In this regard, however, the variability in k_d observed between samples and metals in both continuous and discrete kinetic models illustrates that empirical estimates are not sufficiently constrained or generalisable for reliable quantitative models. To achieve the latter, system-specific calibration of kinetic parameters through cave monitoring may be required to inform an appropriate distribution of k_d.

Regardless, the data at large support two key notions for the interpretation of trace element concentrations in dripwaters and speleothems. Firstly, it is corroborated that binding of transition metals by organic ligands is universal to dripwaters and thus presents a critical rate-dependent control for the distribution of affected cations between aqueous and crystal phases. Subject to further characterisation, the latter may be quantified to link speleothem metal concentrations with the dripwater residence time at stalagmite vertices, during which metals dissociate from the 'aqueous sink' and are captured by the 'carbonate sink' as conceptualised in Hartland and Zitoun (2018). Based solely on kinetic signatures derived in this study, empirical estimates of $k_{d,\ Ni\text{-}NOM}$ suggest a resolvable release of labile Ni for $<$40 drips min^{-1}, which is predicted to be imprinted in calcite Ni/Ca measurements. In absence of detrital contamination, (*e.g.*, due to flushing events that may mobilise trace metals associated with colloidal or particulate fractions and cause accumulations of these elements in the speleothem fabric), it is argued that OMC equilibrium kinetics may thus present a major driver of net inclusion of similarly behaving first-row transition metals and possibly some rare earth elements (Sliwinski et al., 2022). Secondly, the experiments illustrate the effective absence of kinetic limitation by ligands on alkaline earth metals such as Mg and Sr, arguing for their more straightforward inclusion pathway from dripwater to speleothems. This observation in turn supports the use of different elemental concentrations as mechanistically independent and complementary proxies, which can greatly enhance interpretive power of speleothem trace element datasets.

3.4 Conclusions

Organic complexation pervasively governs the speciation of many trace metals in cave dripwaters, imparting kinetic constraints on their availability to speleothems. Competitive ligand exchange experiments performed in this study demonstrate considerable variability in OMC decay kinetics between transition metals in natural dripwaters and soil extracts, depicting a hierarchy of OMC stability of Cu $\approx$ Co $>$ Ni $\gg$ Mg, Sr. However, in absence of distinct covariation

between derived OMC dissociation rate constants with proxies of NOM properties, the variability of dripwater OMC decay rates was largely unpredictable. The ambiguity of controlling factors of kinetic signatures was exacerbated by a problematic model description of log-normal distributions of k_d as implemented herein. However, additional discrete site models provided further confidence, depicting a range of site stabilities with considerable 'inert' fractions for transition metals, and lack of the latter for Mg and Sr. Although these findings emphasise a pronounced sensitivity of kinetic properties to methodology, empirical parameters suggested favourable kinetic time-scales of OMC decay to potentially dominate metal supply at typical cave drip rates ($<$1 to ca. 40 drips min^{-1}). With precedent provided by Lindeman et al. (2022), this observation in turn raises the question whether kinetic signals could be reliably distinguished in calcite deposits, which requires experimental investigation into OMC decay kinetics and metal inclusion into calcite analogous of stalagmite growth.

Supplementary information

Supplementary figures and tables

Table 3.S1: OMC decay characteristics for Mg and Sr in cave waters determined in CLE experiments. Values of μ and σ were fitted using the continuous (log-normal) kinetic model described by Rate et al. (1992) (Equation 3.3). The discrete model is shown in Equation 3.S4 and was solved for 1 to 3 kinetic components (*i.e.*, C_1, C_2, C_3, expressed as fractions) with corresponding dissociation rate constants. $\%M_{2h}$ denotes the fraction of initial metal that remained undissociated after two hours. Data are only shown where adequate model fits were obtainable ($R^2 > 0.75$). Note that Mg concentrations in many test solutions were below detection (shown as <DL) after ca. 5 minutes of exposure to Chelex-100. Discrete models were not solved in those cases.

		Continuous kinetic model					Discrete kinetic model							
	Test solution	**Threshold k_d (τ^{-1})**	**μ ± 1 SD**	**σ ± 1 SD**	**k_d**	**R^2**	**C_1**	**C_2**	**C_3**	**$k_{d,1}$**	**$k_{d,2}$**	**$k_{d,3}$**	**R^2**	**$\%M_{2h}$**
		s^{-1}	$ln(k_d)$	$ln(k_d)$	s^{-1}		%	%	%	s^{-1}	s^{-1}	s^{-1}		%
	Cave waters													
Mg	Babylon Cave	3.7×10^{-3}	-4.2 ± 0.3	1.7 ± 0.1	1.5×10^{-2}	0.98	No model							<DL
	Bulmer Cave	1.9×10^{-3}	-3.8 ± 0.2	1.6 ± 0.1	2.2×10^{-2}	0.99	62.9	37.2	0.0	1.4×10^{-1}			0.99	<DL
	Calcite Cave	1.9×10^{-3}	-4.0 ± 0.3	1.6 ± 0.2	1.8×10^{-2}	0.97	84.1	14.1	1.7	1.7×10^{-2}	5.7	3.3×10^{-7}	0.99	<DL
	Dave's Cave		No model				No model							<DL
	Hodge Creek Cave	3.7×10^{-3}	-4.2 ± 0.3	1.7 ± 0.2	1.5×10^{-2}	0.97	81.5	18.6	0.0	1.9×10^{-1}			0.99	<DL
	Majumba Cave	1.4×10^{-4}	-4.4 ± 0.2	1.9 ± 0.1	1.3×10^{-2}	0.99	64.8	25.6	9.6	1.0×10^{-2}	1.0×10^{2}	4.9×10^{-4}	1.00	1.3
	Stafford's Cave (stream)	1.0×10^{-3}	-4.4 ± 0.3	1.8 ± 0.1	1.2×10^{-2}	0.98	71.5	21.1	7.3	1.1×10^{-2}	1.5×10^{-1}	1.2×10^{-3}	1.00	<DL
	Te Reinga Cave	1.4×10^{-4}	-3.8 ± 0.1	1.9 ± 0.1	2.1×10^{-2}	0.99	54.8	37.2	7.8	1.2×10^{-2}	1.3×10^{-1}	4.5×10^{-4}	1.00	1.8
Sr	Babylon Cave	1.4×10^{-4}	-4.1 ± 0.3	1.7 ± 0.1	1.6×10^{-2}	0.98	77.7	20.3	2.0	1.4×10^{-2}	9.5×10^{2}	2.6×10^{-4}	1.00	0.6
	Bulmer Cave	1.4×10^{-4}	-3.8 ± 0.2	1.6 ± 0.1	2.2×10^{-2}	0.99	62.2	33.3	4.6	1.4×10^{-2}	1.6×10^{-1}	9.7×10^{-4}	0.99	0.6
	Calcite Cave	1.4×10^{-4}	-3.9 ± 0.3	1.6 ± 0.1	2.0×10^{-2}	0.98	19.6	80.4	5.0	1.6×10^{-2}			1.00	0.9
	Dave's Cave		No model				No model							<DL
	Hodge Creek Cave	1.4×10^{-4}	-4.1 ± 0.3	1.6 ± 0.2	1.7×10^{-2}	0.98	80.2	17.8	2.1	1.5×10^{-2}	2.2×10^{-1}	1.6×10^{-4}	1.00	0.8
	Majumba Cave	1.4×10^{-4}	-4.1 ± 0.2	2.0 ± 0.2	1.7×10^{-2}	0.99	68.3	31.7	0.0	3.0			0.98	1.9
	Stafford's Cave (stream)	1.4×10^{-4}	-4.4 ± 0.2	1.8 ± 0.1	1.3×10^{-2}	0.99	68.0	28.1	4.0	1.0×10^{-2}	9.4×10^{-2}	2.3×10^{-4}	1.00	1.5
	Te Reinga Cave	1.4×10^{-4}	-3.7 ± 0.1	1.9 ± 0.1	2.4×10^{-2}	0.99	48.4	44.6	6.8	1.1×10^{-2}	9.5×10^{-2}	2.6×10^{-4}	1.00	2.2

Table 3.S2: Overview of sample locations for CLE experiments. Soil characteristics denoted with an asterisk are inferred from (Informatics - Manaaki Whenua Landcare Research, 2020). All caves were formed in bedrock primarily consistent of shallow marine limestone of Oligocene origin, with exception of Bulmer Cave, which partly developed in marble. In-cave mean annual temperatures (MAT) are based on own cave monitoring datasets with exception of Bulmer Cave (Holden, 2018).

Origin of test solutions	Latitude	Longitude	MAT (°C)	Soil characteristics	Vegetation cover	Further information	Comments
Babylon Cave	42°02'54.8"S	171°29'33.2"E	N/A	Orthic podzol*	Mixed primary native species, including emergent rata, nikau, and kahikatea, dense understorey	(Worthy & Holdaway, 1993)	Approximate location
Bulmer Cave	41°33'29.9"S	172°31'7.7"E	ca. 4	Orthic podzol*	Dominant beech forest; sub-alpine grasses and tussock above tree line	(Holden, 2018)	
Calcite Cave	45°23'14.6"S	167°37'10.4"E	4.8	Peaty, organic-rich	Tussock and other alpine species (above tree line)	(Heidke et al., 2021)	Located close to Dave's Cave
Dave's Cave	45°23'14.6"S	167°37'10.4"E	4.8	Peaty, organic-rich	Tussock and other alpine species (above tree line)	(Heidke et al., 2021)	Monitored cave
Hodge Creek Cave	41°10'12.6"S	172°41'12.7"E	6.3	Litter organic, orthic gley, orthic podzols	Mature beech forest with native emergent species	(Heidke et al., 2021)	Monitored cave
Majumba Cave	37°37'26.6"S	174°50'39.3"E	14.6	Clay loam, orthic brown*	Grazed pastureland	N/A	Monitored cave (discontinued)
Stafford's Cave (stream)	40°45'57"S	172°37'38"E	N/A	Pākihi among barren rock	Dominant scrub and bushland, abundant mānuka	(Densem, 2017)	
Te Reinga Cave	38°49'32.2"S	177°32'18.6"E	11.3	Orthic podzol, clay*	Pine forestry with native emergent species	(Crossley, 1988)	Monitored cave

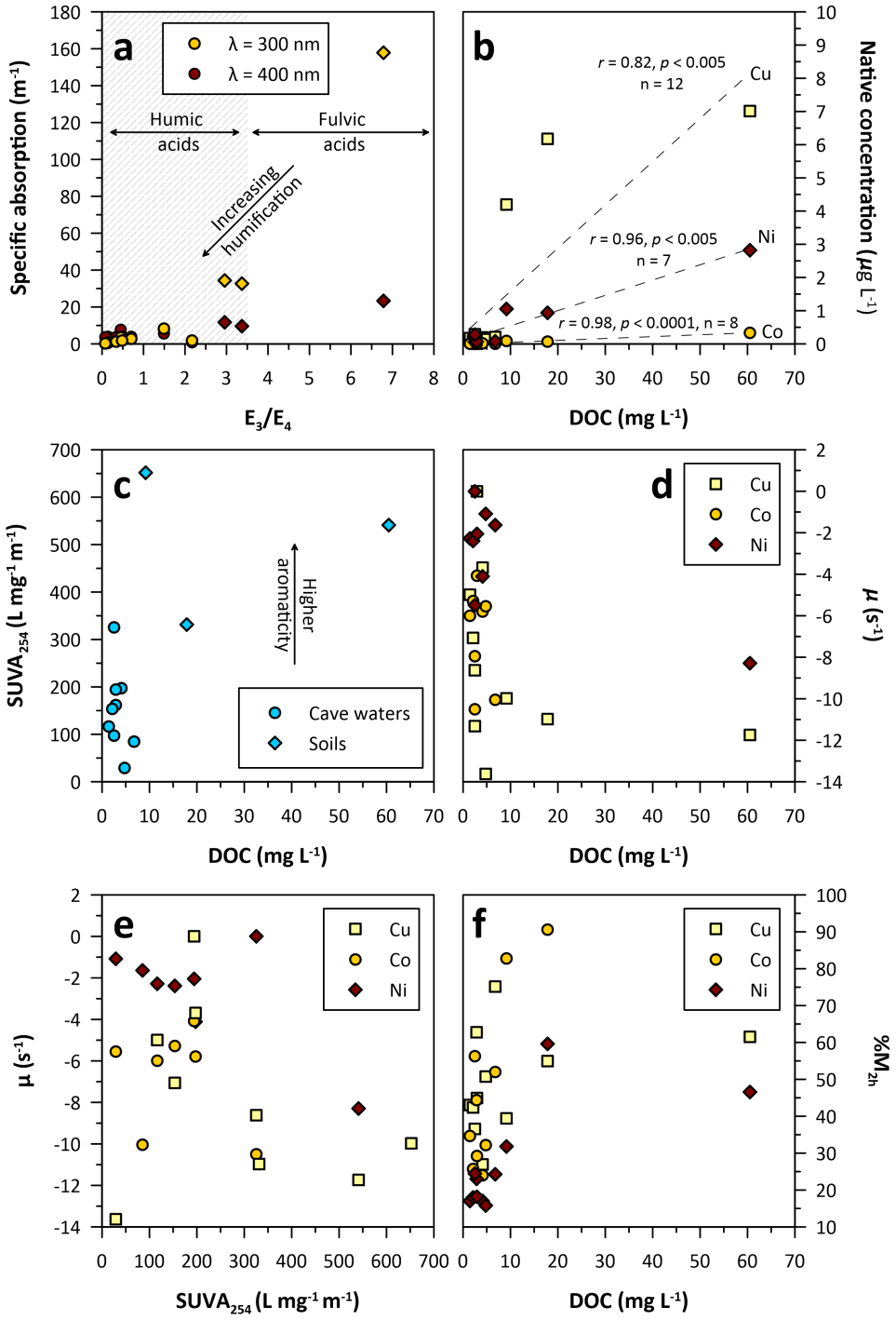

Figure 3.S1: Selected relationships between OMC decay characteristics and indices of NOM quantity and quality. a) E_3/E_4 denotes a spectral absorption ratio indicative of the relative presence of humic and fulvic acid components (Artinger et al., 2000), while the relationship of the latter with the specific absorption at wavelengths 300 nm and 400 nm reflects the degree of humification. Dashed lines in **b** represent linear regressions between concentrations of dissolved organic carbon (DOC) and transition metals in unaltered samples. **c)** A higher value of the specific UV absorbance at 254 nm ($SUVA_{254}$) typically implies a higher fraction of aromatic functional groups (Weishaar et al., 2003). Sub-plots **d**, **e**, and **f** exemplify that covariation between kinetic parameters (fitted values of μ, and metal fraction remaining undissociated after 2 h ($\%M_{2h}$) and NOM indices was largely absent between water samples, but distinct for soil extracts in some cases.

Supplementary methodology

Reagents

Chelex® 100 resin (Bio-Rad Laboratories, Inc., USA; Na-form, 200 – 400 mesh; herein Chelex-100) was used as the competing ligand in all experiments. The selection of buffer (HEPES; N-hydroxyethylpiperazine-N'-2'-ethanesulphonic acid, Sigma-Aldrich, USA) was a compromise between metal complexation properties and suitable pH range representative of *in-situ* values (Ferreira et al., 2015). Although some measurable complexation of Cu by ligands present in the HEPES buffer solution has been reported (*e.g.*, Mash et al., 2002), this effect is assumed to be negligible in relation to complexation by natural ligands, and is expected to be of the same magnitude in all experiments. Solution spiking was carried out using single-element standards produced by British Drug House (BDH) Limited, UK ($NiCl_2 \cdot 6H_2O$, $CuCl_2 \cdot 2H_2O$, $CoCl_2 \cdot 6H_2O$). HNO_3 (65%) and HCl (37%) were provided by EMSURE®, Germany. NaOH solutions were prepared using NaOH pellets (Sigma-Aldrich, USA). All solutions were prepared with ultrapure water (resistivity of 18.2 MΩ cm) obtained directly from a Milli-Q® Reference Water Purification System (Millipore, USA).

Cleaning procedures

All containers and consumables were thoroughly rinsed with ultrapure water before being soaked for at least 24 h in a 10% HCl solution. This was followed by further rinsing with deionised water and soaking for at least 24 h in a 10% HNO_3 (double-distilled) solution, and a subsequent final rinsing (10 times) with deionised water.

Competitive ligand exchange control solution

In addition to natural samples, a control solution without natural ligands was prepared by augmenting ultrapure water (sparged for 1 hour with O_2-free N_2 to remove DIC) with 5 µg L^{-1} of Ni, Cu, and Co. The pH and ionic strength of the control solution were adjusted in accordance with the test solutions. However, this experiment was inadvertently compromised by the use of HEPES buffer to stabilise the pH, which did appear to act as a sink for the added metals in absence of any other complexing agents (cf. Ferreira et al., 2015; Mash et al., 2002). This was implied by low pre-experiment metal concentrations. Presumably due to the already depleted aqueous metal concentrations, an expected near-linear uptake upon addition of Chelex-100 was not observed. Rather, metal concentrations remained minimal and varied indistinctly. In consequence, no empirical estimates of specific metal-aqua complex dissociation rates were obtained. This is largely unproblematic for the purpose of this study, however, given that the resolvable range in k_d is ultimately dictated by the analytical time-scale.

Elemental analysis

Filtered and acidified (2% volume/volume with double-distilled HNO_3) aliquots of sub-samples taken before and during experiments were analysed for elemental concentrations on an Agilent 7900 quadrupole inductively-coupled plasma mass spectrometer (q-ICP-MS) at the Centre for Trace Element Analysis, University of Otago, Dunedin, Aotearoa New Zealand. Sample introduction occurred via an Agilent SPS 4 Auto-sampler and Agilent Integrated Sample Introduction System (ISIS 3), coupled with a glass concentric MicroMist nebuliser, a quartz spray chamber with quartz torch of 2.5 mm diameter injector and Ni interface cones. Analyses were performed in He collision mode. Data acquisition consisted of 3 replicate measurements with 50 sweeps and an integration time of 0.1 s. Calibration was achieved using NIST traceable Agilent multi-element standards, with calibration curves for each element consisting of a calibration blank and at least 3 calibration levels. A cocktail of 7 internal standards containing Be, Sc, Ge, Rh, In, Tb and Bi was added online to correct for matrix effects and instrumental drift. ^{43}Ca and ^{63}Cu were reported, while ^{44}Ca and ^{65}Cu were used as confirmation masses.

Dissolved organic carbon analysis

The total organic carbon (TOC) concentrations of original (untreated) samples were determined on an Aurora 1030W TOC Analyser (OI Analytical, Texas, USA) by means of wet chemical oxidation. Due to filtration (0.45 µm) of aliquots prior to analysis, the measured TOC effectively equates to dissolved organic carbon (DOC). Samples were reacted with freshly prepared 5% phosphoric acid (H_3PO_4) and 0.84 M sodium persulfate ($Na_2S_2O_8$), using a commercial carbon standard (potassium hydrogen phthalate; Ajax-Finechem, Australia) for quantification.

Characterisation of natural organic matter

Filtered (0.45 µm) aliquots of cave waters and soil extracts were analysed by UV-Vis absorbance spectroscopy prior to treatment for CLE experiments. UV-Vis spectroscopy is widely used either separately or in tandem with additional techniques to assess the quality and quantity of organics in aqueous samples (*e.g.*, Kowalczuk et al., 2005). UV-Vis absorbance spectra of cave water solutions were obtained using a Cary 300 UV-Vis spectrometer (Agilent Technologies, USA) with a 1 cm quartz cuvette over the range of 200 – 600 nm in 1 nm intervals against Milli-Q as reference. Averaged absorbance spectra of bracketed Milli-Q measurements were subtracted from spectra collected for samples to account for interference of Raman water peaks. Likewise, raw absorbance spectra of soil extracts were corrected against a 0.01 M $CaCl_2$ reference matrix. Absorbance values (A(λ); arbitrary units) for a given wavelength λ (nm) were converted to Napierian absorption coefficients a(λ) (m^{-1}) using Equation 3.S1 (Helms et al., 2008):

$$a(\lambda) = \frac{2.303A(\lambda)}{l} \tag{3.S1}$$

, where *l* denotes the length of the cell used in the analysis (m). Absorption coefficient data of water and soil extract samples were fitted to Equation 3.S2 by optimising values for S_e and *c* using non-linear regression:

$$a(\lambda) = a(\lambda_{ref}) \times e^{-S_e(\lambda - \lambda_{ref})} + c \tag{3.S2}$$

, where λ_{ref} is a reference wavelength, S_e is the spectral slope parameter (nm^{-1}), and *c* (m^{-1}) is a correction parameter accounting for baseline shifts due to scattering (Stedmon et al., 2000). Spectral slopes as estimated by S_e describe the decrease in absorption with wavelength, and are indicative of average characteristics of NOM largely irrespective of NOM concentration (Brown, 1977). $S_{275\text{-}295}$ (*i.e.*, the spectral slope obtained for the region of wavelengths 275 nm to 295 nm) has been found characteristic of DOM composition and molecular weight (*e.g.*, Helms et al., 2008), whereas the degree of humification may be approximated by $S_{350\text{-}400}$ (A. M. Hansen et al., 2016). The latter may also be assessed through the spectral absorption ratio E_3/E_4, calculated as the ratio of *a(300)* and *a(400)*. Values of E_3/E_4 greater than ca. 3.5 correspond to dominant fulvic acids, whereas values smaller than 3.5 indicate dominant humic acids with greater aromaticity and molecular size (Artinger et al., 2000). The ratio of $S_{275\text{-}295}$ and $S_{350\text{-}400}$ (S_R) provides a further (inversely related) metric of molecular weight, independent of DOM concentration (Xiao et al., 2013). In addition, the specific UV absorbance at 254 nm ($SUVA_{254}$; L mg^{-1} m^{-1}) was calculated as Equation 3.S3:

$$SUVA_{254} = \frac{a(254)}{DOC} \times 100 \tag{3.S3}$$

, where DOC is the measured dissolved organic carbon concentration (mg L^{-1}). $SUVA_{254}$ provides a measure of the aromaticity of organic matter, with higher and lower values indicating greater and smaller percent aromaticity, respectively (Weishaar et al., 2003).

Additional information on kinetic data analysis and forward model

Estimation of discrete values and continuous distributions of k_d

The estimation of k_d in terms of a log-normal distribution around a mean and standard deviation (*i.e.*, Equation 3.3 in the main text) extends on the more widely utilised discrete sites model (Equation 3.S4):

$$C_t = \sum_{i=1}^{n} C_{0,i} \times e^{(-k_{d,i} \times t)} \tag{3.S4}$$

, where the total concentration of a metal due to dissociation at any given time (*t*) is given as C_t and $C_{0,i}$ denotes the initial concentration of the *i*th complex. Typically, kinetic data are fitted to Equation 3.S4 for one to three terms, denoting different kinetically distinguishable compo-

nents whose relative contribution can be estimated (*e.g.*, Yapici et al., 2009). While convenient, however, the selection of the number of terms is in essence arbitrary and oversimplifies the heterogeneity of binding sites present in NOM. The latter may be reconciled by approximating the sum of exponential terms in Equation 3.S4 as a continuous distribution of k_d as shown in Equation 3.3 (see main text), where $f(\ln k_d)$ is the normal distribution of *ln(k_d)* with mean μ and standard deviation σ (Equation 3.S5):

$$f(\ln k_d) = \frac{1}{\sigma\sqrt{2\pi}} \times e^{\left(-\frac{(\ln k_d - \mu)^2}{2\sigma^2}\right)} \tag{3.S5}$$

This log-normal model provided the best agreement between observed and modelled kinetic data out of several approaches assessed in Rate et al. (1992). Both the discrete and continuous kinetic models make the implicit assumptions that all metal will eventually dissociate, and that the rate of reaction between metal cations and competing ligand (*i.e.*, the formation of M-Chelex) is much faster than OMC formation and dissociation equilibrium reactions. The latter assumption is critical to ensure that OMC decay is the rate-determining step and correctly characterised by derived kinetic parameters. The models further require that OMCs do not adsorb to Chelex-100 resin (*i.e.*, without dissociation), and that the fraction of free metal is minimal compared to complexed species (Fasfous et al., 2004). Non-linear regression analysis to obtain discrete values was carried out using the Levenberg-Marquardt method and solving for one, two, and three terms representative of kinetic components.

Forward model of OMC metal supply to drip solution and calcite

The forward model depicted in Figure 3.4 describes the release of labile (here, 'available') metal cations to the drip solution thin-film via OMC decay based on empirical values of $k_d \pm 1$ SD. The release is described as Equation 3.S6:

$$[M]_{labile} = \left(\left(1 - \lambda_{fast}\right)\left(1 - e^{-\frac{k_d}{v}}\right) + \lambda_{fast}\right) \times [X]_{total} \tag{3.S6}$$

, where λ_{fast} denotes the assumed fraction of very fast dissociation (≈free) cations in solution, v is the drip rate in drips min^{-1}, and $[M]_{total}$ is the total available aqueous metal pool. For λ_{fast}, a value of 0.01 was selected, assuming that virtually all transition metals are complexed by NOM (*e.g.*, Hartland & Zitoun, 2018), while $[M]_{total}$ was selected as 1 µg L^{-1}. The estimation of calcite Ni/Ca is based on the experimentally determined inorganic partition coefficient of Ni from Lindeman et al. (2022) (ca. 1.1 ± 0.5), which denotes the unitless ratio of M/Ca$_{calcite}$ and M/Ca$_{solution}$. The aqueous concentration of Ni in this example was taken to be 2×10^{-5} mmol L^{-1}, which translates to a Ni/Ca$_{aqueous}$ of ca. 0.01 mmol mol^{-1} when assuming a typical karst water Ca concentration of ca. 0.002 mol L^{-1}.

Chapter 4

Trace metal incorporation into calcite in caves and cave-analogue experiments: assessing the role of organic complexation

Chapter notes: The content of this chapter is unpublished. Elemental analyses presented in this chapter were performed at the University of Waikato by Danielle Blackwell (ca. 70%) and Amanda French (ca. 30%).

Abstract

Trace elements are increasingly used to bolster speleothem-based records of past climates and environments. Given the complexity of the sources, transport, and fate of elements in karst systems, however, the exact environmental controls on trace elements in dripwater and speleothems are often obscure. In this regard, the alkaline earth metals (particularly Mg and Sr) have historically been the most widely interpreted trace elements in speleothem science, owing to their comparably predictable incorporation into calcite. Although increasingly utilised as additional hydrological proxies, the systematics of first-row transition metals are far less constrained. Notably, their transport from the surface to the site of speleothem formation is understood to be largely dictated by the formation of organic metal complexes (OMCs) with ligands present in natural organic matter. While this pervasive organic association has been shown to facilitate capture of organically-complexed metals in response to strong infiltration events, however, the decay of OMCs at speleothem surfaces may present a mechanistically distinct inclusion pathway. Specifically, it has been hypothesised that the availability of transition metals at speleothem surfaces for partitioning into the crystal phase may be driven by the rate-dependant decay of OMCs, which is in turn predicted to depend on their residence time at

speleothem surfaces.

To provide new systematic insights into the complicated implications of OMCs for transition metal concentrations in speleothems, this study assessed the apparent partitioning of selected transition metals (Ni, Cu, Co) and alkaline earth metals (Mg, Sr) in cave-analogue calcite precipitation experiments as a function of drip rate and organic complexation. Inorganic experiments supported the previously reported hierarchy of affinity for calcite in the order of Cu $\gg$ Co $>$ Ni, with average inorganic $D_{Cu} \approx 13$, $D_{Co} \approx 1.8$, and $D_{Ni} \approx 0.4$. Similarly, empirical inorganic values of D_{Mg} (ca. 0.04) and D_{Sr} (ca. 0.09) were highly consistent with the previous estimates. Contrary to a hypothesised time-dependent release of transition metals through the decay of OMCs, however, organic experiments revealed a pronounced positive relationship between Cu inclusion and drip rate. Attributable to the extreme affinity of Cu for the crystal phase, this correlation akin to 'soil flushing' signals was only muted at very high ligand concentrations. The behaviour of Ni and Co was altogether less distinct in organic experiments due to an inadvertently uncharacteristic complexation by selected ligands, but a kinetic inhibition of their partitioning was nonetheless evident. These observations implied that ternary complexation (adsorption) of OMCs without prior dissociation was likely favoured under these experimental conditions, thereby presumably masking any potential contribution of transition metals through the decay of OMCs. Nonetheless, the compilation of a wide range of new and previously published datasets on experimental and in-cave metal partitioning altogether supported the notion of a pervasive control of organic complexation on the speciation of transition metals, while corroborating a relatively predictable ($\approx$inorganic) behaviour of Mg and Sr. Further, the prevailing controls on transition metal inclusion into speleothems are argued to be likely system-specific, requiring further experimental and *in-situ* investigation.

4.1 Introduction

Cave carbonate deposits (speleothems) present extremely valuable terrestrial archives of past climates and environments (Fairchild & Baker, 2012; Wong & Breecker, 2015). While stable oxygen isotopes remain the most interpreted geochemical property of speleothems, measurements of elemental concentrations are increasingly used to bolster palaeoclimate reconstructions (*e.g.*, Fairchild & Treble, 2009; Wassenburg et al., 2020; Stoll et al., 2012). Albeit not without its challenges, elemental analysis is encouraged by the comparably fast and affordable acquisition of high-resolution records (see Table 4.1 in Fairchild, Smith, et al. (2006) for an overview), and the ability to simultaneously quantify the concentrations of a vast suite of elements.

Most minor and trace elements found in speleothems are predominantly derived from the overlying soil zone and bedrock, where the slightly acidic infiltrating meteoric water dissolves minerals and leaches organic soil components. Mg and Sr are normally the dominant cations substituting for Ca in the carbonate crystal lattice due to compatible ionic radii and valence. In most cave settings, Mg and Sr, like Ca, are primarily sourced from bedrock dissolution and

weathering. Most of the elemental mobilisation occurs in the area of maximal pCO_2 either within the soil or unsaturated zone, coinciding with the highest rates of dissolution of bedrock or fragments thereof (Fairchild & Treble, 2009). As such, elemental patterns in cave waters can vary considerably according to the bedrock composition (*e.g.*, dolomite versus limestone) and soil/vegetation cover (*e.g.*, clay contributions), and may also be decisively affected by specific features above the cave (*e.g.*, calcitic veins in Tartair Cave; Roberts et al., 1998). To variable extent, most trace elements are also associated with the soil, where leaching and mobilisation of organic and inorganic components initiates their transport through the karst (*e.g.*, Hartland et al., 2011, 2012).

In coastal proximity, sea spray can present another significant source of certain elements, particularly Cl, Na, Br, but also Mg (Tremaine et al., 2016). Likewise, wildfires (Campbell et al., 2023; McDonough et al., 2022), volcanic eruptions (particularly S; *e.g.*, Frisia et al., 2008), anthropogenic emissions (particularly S; Borsato et al., 2015), land-use (Baker et al., 1998), and potentially seismic activity (Wood et al., in prep), can regionally dominate the concentrations of some elements in dripwater and/or precipitates. Similarly to the source of elements, their fate can vary depending on system-specific conditions. For instance, dripwater chemistry (particularly pH) exerts a critical control on elemental speciation and interactions, and can in some cases substantially modify mobilisation, transport, and deposition processes (*e.g.*, stabilising complexes in hyperalkaline systems; Hartland et al., 2014). Additionally, conditions during speleothem formation and the resulting microstructural properties of speleothems are known to critically affect the spatial distribution of elements within a carbonate fabric (Borsato et al., 2007), resulting in phenomena such as sectoral zoning (Paquette & Reeder, 1995). Naturally, chemical species preserved in speleothems are further subject to secondary alteration processes, such as recrystallization (Ortega et al., 2005), which may produce significant and potentially cryptic changes to their original attributes (*e.g.*, Bajo et al., 2016).

Arguably due to this complexity of sources, transport, and fate of elements in karst systems, their interpretation in speleothem studies often relies heavily on statistical approaches to infer potential environmental controls (*e.g.*, via principal component analysis). Where elements can be more directly linked to distinct sources, such as bedrock dissolution (*e.g.*, Mg, Sr; Fairchild & Treble, 2009) or marine aerosols (*e.g.*, Cl, Br; Tremaine et al., 2016), mixing lines between empirical or theoretical end-members (*e.g.*, the bulk elemental composition of the bedrock or seawater) may provide additional confidence in interpretations. However, while undoubtedly insightful, statistical approaches often do not allude to the likely mechanisms or specific chemical conditions producing the observed signals. Moreover, the ultimate inclusion of any element present in speleothems occurs at the interface of dripwater and speleothem, effectively decoupled from sources and transport. A chemical species' behaviour in the thin water film at the crystalline growth surface may thus be decisive for the final concentration of the element in the carbonate, potentially overriding preceding controls.

These defining processes at the speleothem surface are captured by the concept of elemental partitioning (or distribution) between solution and crystal phases. For divalent metal cations substituting for Ca, this is conventionally described in terms of partition coefficients

(D_X) of dilute ideal solid-solutions (Equation 4.1; Morse & Bender, 1990):

$$D_X = \frac{\left(\frac{X}{Ca}\right)_{Crystal}}{\left(\frac{X^{2+}}{Ca^{2+}}\right)_{Solution}} \tag{4.1}$$

, where X and Ca are the respective molar concentrations of a trace element X and calcium in the crystal phase, and X^{2+} and Ca^{2+} are the respective concentrations of free cations in solution. Dimensionless ratios for each phase are specified by the subscript. Accordingly, a $D_X > 1$ implies that the element X preferentially distributes into the crystal phase relative to Ca. Conversely, X tends to remain in solution if $D_X < 1$, thus resulting in a progressive enrichment of X in the solution as precipitate is formed. First-order thermodynamic and kinetic principles can be used to predict D_X (*e.g.*, Rimstidt et al., 1998; Curti, 1999; Watson, 2004; Y. Wang & Xu, 2001). More frequently, however, values for D_X are empirically estimated based on elemental measurements for a given couplet of parent solution and precipitate according to Equation 4.1 (*e.g.*, Lorens, 1981; Huang & Fairchild, 2001). To account for all possible modes of elemental inclusion in the precipitate, empirical D_X are more appropriately termed 'apparent' partition coefficients (used herein), although other terminology (*e.g.*, 'speleothem distribution coefficient'; Frisia et al., 2012) and mathematical definitions (*e.g.*, Hartland et al., 2014) exist.

While numerous studies on calcite crystal growth typically initiate subaqueous precipitation by solution mixing (*e.g.*, Lorens, 1981; Rimstidt et al., 1998; Morse & Bender, 1990; Gabitov & Watson, 2006), these growth conditions are often not directly comparable to the processes involved in speleogenesis. A few purpose-built experimental setups have more recently allowed the simulation of more representative 'cave-analogue' growth conditions to address this caveat, under which crystals are precipitated due to the degassing of CO_2 from growth solution thin-films (*e.g.*, Huang & Fairchild, 2001; Day & Henderson, 2011; M. Hansen et al., 2013). Although most of these studies target isotopic processes (*e.g.*, M. Hansen et al., 2013; Day & Henderson, 2011; Reynard et al., 2011; EL-Shenawy et al., 2020), trace element partitioning has been the focus of some (Huang & Fairchild, 2001; Day & Henderson, 2013; Magiera, 2018; Lindeman et al., 2022). Given their greater significance for palaeoenvironmental applications, partitioning of Mg and Sr has received particular attention, revealing significant controls on D_{Mg} and D_{Sr} by temperature (*e.g.*, Gascoyne, 1983; Wassenburg et al., 2020), precipitation rate (Lorens, 1981; Gabitov & Watson, 2006), and solution chemistry (*e.g.*, Mg/Ca effects on D_{Mg}; Riechelmann et al., 2014). Their altogether relatively predictable behaviour has also allowed for the establishment of (semi-)quantitative models applicable to speleothem records (Stoll et al., 2012), which serve to constrain potential signals and controls of prior calcite precipitation (Fairchild & Treble, 2009).

In contrast, the systematics of first-row transition metals in karst systems are far less understood, and the subject of few experimental studies with conditions relevant to speleothem science (*e.g.*, Lindeman et al., 2022; Magiera, 2018). Consequently, their potentially valuable signatures in speleothem records are often largely ignored for interpretation. The transport

of these elements from the surface to the cave is strongly controlled by the binding to natural organic matter (NOM) present in infiltrating waters (Hartland & Zitoun, 2018; Hartland et al., 2014; Chapter 3), which limits the fraction of labile metals that can readily distribute into speleothems (Lindeman et al., 2022). The ubiquitous association of transition metals with organic metal complexes (OMCs) has previously been tied to 'soil flushing' or infiltration signals observed in dripwaters (Warken, Kuchalski, et al., 2022; Wynn et al., 2014) and speleothems (Borsato et al., 2007; Fairchild et al., 2001), primarily characterized by sharp and disproportionately large increases in various trace metal concentrations (Sliwinski et al., 2022). These interpretations are corroborated by imaging of organic inclusions in speleothem fabrics (*e.g.*, Baker et al., 2000; Sliwinski & Stoll, 2021), attesting to the potential for a preservation of NOM and associated metals in precipitates via adsorption or entrapment.

However, an additional mechanism for metal inclusion may be facilitated by the prior dissociation (or 'decay') of these OMCs at the dripwater-stalagmite interface, which has been proposed as potentially determinant for the availability of associated metals to stalagmites (Hartland & Zitoun, 2018; Lindeman et al., 2022). In the hypothesised pathway, the rate-dependent decay of OMCs (*e.g.*, Cabaniss, 1990; Levy et al., 2012; Town et al., 2012) releases metals to the water thin-film at a stalagmite's surface, where the momentarily labile metal cations are available to partition into calcite. The initial dissociation of metals from OMCs occurs due to competition of organic ligands with another metal sink, which causes the complexation equilibrium to favour the disintegration of OMCs (Davranche et al., 2008). The temporal OMC decay window is thought to be effectively limited by the water residence time, and renewed with the impact of incoming drips that replenish the thin water film and OMCs within. Under the assumption of an OMC decay pathway, the incorporation efficiency of complexed metals into the precipitate as estimated by apparent partition coefficients is thus predicted to be inversely related with drip rate. Importantly, the link between OMC decay and metal availability for deposition in turn presents an opportunity to quantitatively relate respective carbonate metal concentrations to the time available for OMCs to decay and release metals.

Evidence for these proposed implications of organic complexation for trace metal partitioning is thus far largely founded on inferences from cave water analyses (*e.g.*, Hartland et al., 2014; Hartland & Zitoun, 2018), supporting implicit experimental observations (Lindeman et al., 2022; Chapter 3), and theoretical considerations. However, detailed investigations of yttrium (Y) in dripwater and modern stalagmites provide new key precedent for the hypothesised pathway (Sliwinski et al., 2022). Specifically, the authors attribute peak carbonate Y concentrations to a combination of inclusion mechanisms, including a kinetic release of Y from organic complexes adsorbed to active calcite surfaces.

To contribute to the systematic understanding of these interactions between trace metals with NOM in karst systems and their applicability to speleothem science, this study sets out to further assess the mechanistic controls of the inclusion of selected trace metals into calcite in controlled and natural environments. Specifically, this study firstly aims to experimentally test the hypothesis that the decay of OMCs may pose a time-dependent control on metal availability at the tip of stalagmites. To this effect, a set of ten calcite precipitation experiments

are presented, mimicking the development of stalagmites under cave-analogue conditions. These experiments serve to quantify apparent partitioning of transition metals (Ni, Cu, Co) and alkaline earth metals (Mg, Sr) as a function of drip rate and organic complexation. In addition, experimental datasets are complemented by a range of estimates of in-cave metal partition coefficients based on modern carbonate precipitates and dripwater samples obtained from alpine to tropical cave systems of Aotearoa New Zealand and Niue. Finally, data from this study are integrated in a synthesis of previously published empirical and theoretical datasets on metal partitioning in calcite.

4.2 Materials and methods

4.2.1 Chemicals

Experimental solutions were prepared using analytical grade $CaCO_3$ (Sigma-Aldrich, USA), $CaCl_2$ (Sigma-Aldrich), $NiCl_2{\cdot}6H_2O$ (British Drug House (BDH) Ltd., UK), $CuCl_2{\cdot}2H_2O$ (BDH), $CoCl_2{\cdot}6H_2O$ (BDH), $MgCl_2$ (Sigma-Aldrich), and $SrCl_2{\cdot}6H_2O$ (BDH). In ligand experiments nitrilotriacetic acid (NTA; BDH) and Suwannee River Fulvic Acid (SRFA; Standard II, International Humic Substances Society) were used. Industrial grade CO_2 (code 169) and N_2 (code 152) were obtained from the British Oxygen Company Ltd. (UK). The pH and conductivity meters were calibrated against commercial buffer and ion solutions provided by Merck KGaA (Germany) and HORIBA Advanced Techno Co., Ltd. (Japan), respectively.

Table 4.1: Overview of cave-analogue experimental solution and atmospheric properties. M:L represents the ratio of the total concentration of all complexed metals (Co, Ni, Cu) to that of the ligand. EC, $SI_{Calcite}$, DOC, and RH denote electrical conductivity, calcite saturation index, dissolved organic carbon, and relative humidity, respectively.

	Initial solution composition									Initial solution properties				Target atmospheric properties			Comment
Experiment	**$CaCO_3$ (mM)**	**Mg (µM)**	**Sr (µM)**	**Co (µM)**	**Ni (µM)**	**Cu (µM)**	**SRFA (µg L_{-1})**	**NTA (µM)**	**M:L (molar)**	**pH**	**EC (µS cm^{-1})**	**$SI_{Calcite}$**	**DOC (M)**	**Temp. (℃)**	**pCO_2 (ppmv)**	**RH (%)**	
1 (Inorganic)	5.0	41.15	1.14	0.085	0.085	0.079	-	-	-	6.30	823	-0.22	0.02025	20	1000	>90	
2 (NTA)	5.0	41.15	1.14	0.085	0.085	0.079	-	5.23	0.05	6.43	839	-0.09	0.01760	20	1000	>90	
3 (SRFA)	5.0	41.15	1.14	0.085	0.085	0.079	1989.7	-	0.25	6.51	828	-0.01	0.01632	20	1000	>90	
4 (Inorganic)	5.0	41.15	1.14	0.085	0.085	0.079	-	-	-	6.52	1025	-0.01	0.01632	21	-	-	Open experiment
5 (NTA)	5.0	41.15	1.14	0.085	0.085	0.079	-	0.50	0.50	6.52	1138	-0.01	0.01632	22	700	>90	Loss of atmospheric control
6 (SRFA)	5.0	41.15	1.14	0.085	0.085	0.079	663.2	-	0.75	6.40	893	-0.12	0.01814	22	1000	>90	
7 (SRFA)	5.0	41.15	1.14	0.085	0.085	0.079	994.9	-	0.50	6.44	908	-0.08	0.01743	22	1000	>90	
8 (SRFA)	5.0	41.15	1.14	0.085	0.085	0.079	497.4	-	1.00	6.48	882	-0.05	0.01693	22	1000	>90	
9 (Inorganic)	5.0	41.15	1.14	0.085	0.085	0.079	-	-	-	6.45	877	-0.07	0.01726	22	1000	>90	
10 (NTA)	5.0	41.15	1.14	0.085	0.085	0.079	-	0.50	0.50	6.50	876	-0.02	0.01647	22	1000	>90	

4.2.2 Preparation of experimental drip solutions

For each cave-analogue experiment, a 10 L reservoir solution with 5 mM $CaCO_3$ (*i.e.*, 5.0043 g) was prepared with view to mimic typical cave dripwater characteristics, while facilitating feasible carbonate precipitation rates and analyses (see Table 4.1 for an overview of experiments). Given the focus of this study on the first-row transition metals Ni, Cu, and Co, only these elements were included in the solution at a target concentration of 5 µg L^{-1} alongside the dominant matrix elements Mg (1000 µg L^{-1}) and Sr (100 µg L^{-1}). This was to minimise potential competing effects, which would compromise the study of specific controls. Concentrations of each element were selected to resemble their abundances in relation to each other in natural dripwaters. All elements were added from single-element stock solutions. Similarly, stock solutions of nitrilotriacetic acid (NTA) and Suwannee River Fulvic Acid (SRFA) were used to spike reservoir solutions for organic experiments.

NTA is a relatively simple, widely utilised synthetic complexing agent (*e.g.*, Elliott & Brown, 1989; Hering & Morel, 1990), known to form stable complexes with Ni (log $K_{Ni\text{-}NTA} \approx 11.5$), Cu (log $K_{Cu\text{-}NTA} \approx 12.9$), and Co (log $K_{Co\text{-}NTA} \approx 10.4$) (values from Anderegg, 1982). Given the good agreement with stability constant estimates for Cu-NOM in natural caves (log $K_{Cu\text{-}NOM}$ between ca. 13.5 and 15.5; Hartland & Zitoun, 2018), NTA is considered to adequately simulate the complexing strength of natural ligands (Lindeman et al., 2022). The commercially available SRFA standard was chosen to reflect the structural complexity and diversity of binding characteristics of NOM. Although not strictly analogous given the required extraction procedures, SRFA is frequently used in kinetic studies as a relatively well-characterised representation of fulvic acids in aqueous and soil environments (*e.g.*, Cabaniss, 1990; Leenheer et al., 1998; Levy et al., 2012; Town et al., 2012). The ligand concentrations to achieve comparable complexation regimes to those observed in natural freshwater systems (*e.g.*, Hartland & Zitoun, 2018) were informed using the speciation code Visual MINTEQ (ver. 3.1; Allison et al., 1991) to predict the equilibrium species distribution for initial reservoir solutions (Table 4.2).

In experiments with NTA at an M:L of 0.5, ca. 97% and 82% of total Cu and Ni were complexed, respectively, whereas Co-NTA accounted for only ca. 27% of total Co. Approximately 50% of Co was predicted to be present as free cations. At an M:L of 0.05, the fraction of complexed Co increased to nearly 85%, while virtually all of Cu and Ni were predicted to be bound to NTA. Speciation modelling indicates that only Cu was significantly complexed by SRFA (Cu-SRFA comprising 41% – 87% of total Cu; Table 4.2), whereas ca. 57% and 69% of Ni and Co, respectively, were predicted to exist as free cations irrespective of M:L. This predicted, stark preferential complexation by SRFA had previously been noted by Lindeman et al. (2022), who purposefully excluded Co and Ni from their SRFA experiment. For consistency, however, the complete suite of trace metals was included in all experiments herein. Complexed species of Mg and Sr accounted for less than 0.1% in all organic experiments.

PHREEQC (Interactive ver. 3.7.3; Parkhurst & Apello, 1999) was used to approximate the required solution pH to achieve a calcite saturation index of 0, based on the solution chemistry

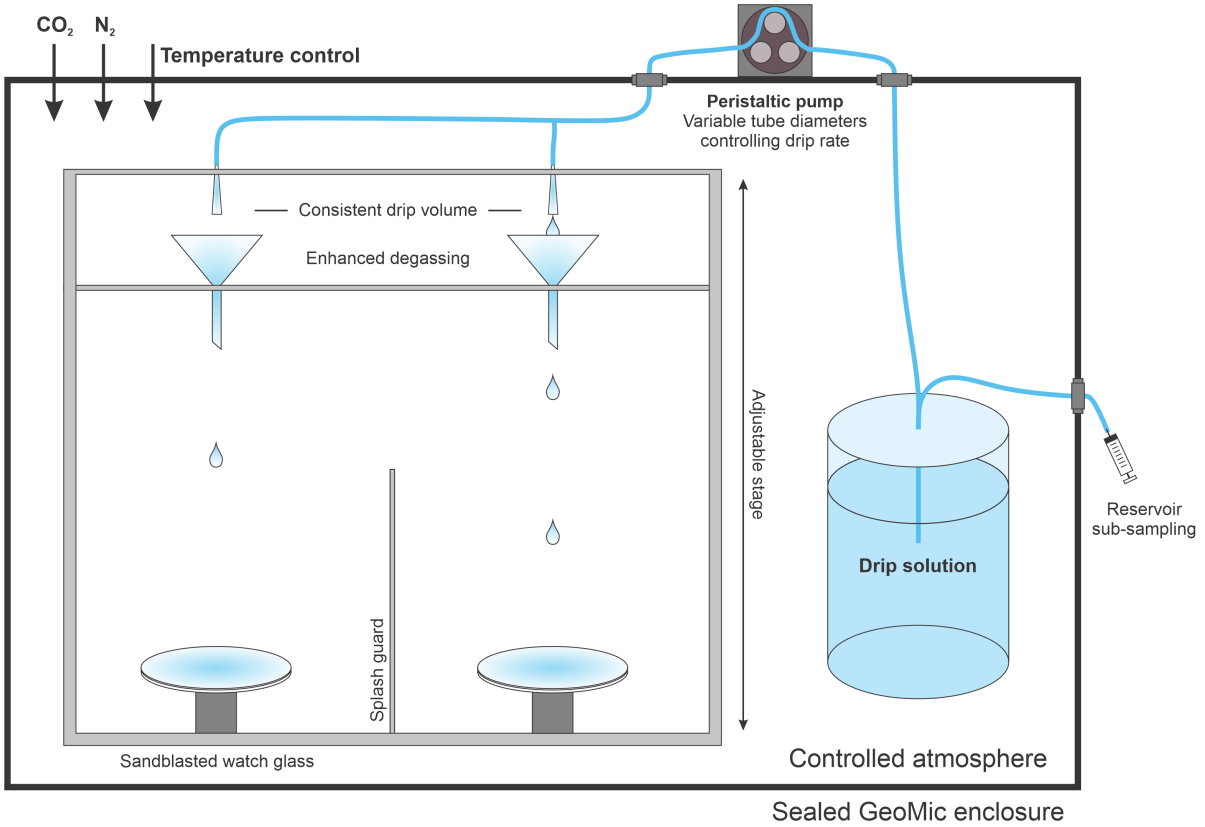

Figure 4.1: Schematic and photo of purpose-built GeoMic controlled atmosphere and experimental setup. Four to five drips of experimental solution were delivered to the enclosure at different drip rates in each experiment using a high-precision peristaltic pump. Drips are delivered through upturned 1 mL pipette tips to achieve a consistent drop volume. Precipitate is collected on sandblasted watch glasses that mimic the roughness of natural stalagmites. Glass funnels were introduced from Experiment 4 onwards to enhance CO_2 degassing and increase the yield of precipitate. Splash guards between watch glasses prevent cross-contamination.

Table 4.2: Distribution of major chemical species in cave-analogue reservoir solutions predicted by Visual MINTEQ equilibrium speciation code. For SRFA experiments, M-SRFA includes both fulvic acid components distinguished by Visual MINTEQ. All data are reported in % of the total concentration.

Component	Species name	Exp. 1 %	Exp. 2 (M:L 0.05) %	Exp. 3 (M:L 0.25) %	Exp. 4 %	Exp. 5 (M:L 0.5) %	Exp. 6 (M:L 0.75) %	Exp. 7 (M:L 0.50) %	Exp. 8 (M:L 1.00) %	Exp. 9 %	Exp. 10 (M:L 0.5) %
Cu^{2+}	Cu^{2+}	55.45	0.03	2.27	38.78	0.41	10.20	6.77	10.65	43.88	0.42
	$CuOH^{+}$	2.00	-	-	2.31	-	-	-	-	2.22	-
	$CuCO_{3\,(aq)}$	37.70	0.10	9.93	54.61	2.04	36.01	25.61	43.69	49.36	1.77
	$CuHCO_3^{+}$	4.82	-	0.79	4.21	0.15	3.70	2.41	3.75	4.47	0.15
	Cu-SRFA	-	-	86.83	-	-	49.44	64.74	41.07	-	-
	$CuNTA^{-}$	-	99.86	-	-	97.35	-	-	-	-	97.63
Co^{2+}	Co^{2+}	90.11	10.49	68.96	87.80	49.64	68.43	68.73	68.99	88.52	50.28
	$CoCO_{3\,(aq)}$	0.20	0.12	0.98	0.40	0.80	0.78	0.84	0.92	0.32	0.69
	$CoHCO_3^{+}$	9.66	4.46	29.59	11.76	22.12	30.62	30.18	29.95	11.12	21.51
	Co-SRFA	-	-	0.33	-	-	0.11	0.16	0.08	-	-
	$CoNTA^{-}$	-	84.93	-	-	27.42	-	-	-	-	27.50
Ni^{2+}	Ni^{2+}	85.15	0.85	57.20	81.87	10.60	57.33	57.49	58.00	82.89	10.72
	$NiCO_{3\,(aq)}$	0.37	0.02	1.58	0.73	0.33	1.28	1.37	1.50	0.59	0.29
	$NiHCO_3^{+}$	14.47	0.58	38.90	17.38	7.48	40.66	40.00	39.91	16.51	7.27
	Ni-SRFA	-	-	2.20	-	-	0.69	1.08	0.55	-	-
	$NiNTA^{-}$	-	98.55	-	-	81.59	-	-	-	-	81.72
Mg^{2+}	Mg^{2+}	98.48	94.21	93.92	98.11	94.14	94.05	94.11	94.23	98.22	94.36
	$MgCO_{3\,(aq)}$	-	0.04	0.05	0.02	0.06	0.05	0.05	0.05	0.01	0.05
	$MgHCO_3^{+}$	1.51	5.72	5.75	1.88	5.79	5.81	5.70	5.65	1.76	5.57
	Mg-SRFA	-	-	0.10	-	-	0.03	0.05	0.02	-	-
Sr^{2+}	Sr^{2+}	97.96	92.34	92.09	97.45	91.78	91.70	91.81	91.94	97.61	92.09
	$SrCO_{3\,(aq)}$	-	0.03	0.04	0.01	0.05	0.03	0.04	0.04	0.01	0.04
	$SrHCO_3^{+}$	2.04	7.63	7.67	2.53	8.17	8.20	8.05	7.97	2.38	7.87
	Sr-SRFA	-	-	0.04	-	-	0.01	0.02	-	-	-
Ca^{2+}	Ca^{2+}	98.22	93.17	93.02	97.77	92.98	92.94	93.02	93.13	97.91	93.25
	$CaCO_{3\,(aq)}$	0.02	0.09	0.11	0.04	0.12	0.09	0.09	0.10	0.03	0.11
	$CaHCO_3^{+}$	1.77	6.65	6.69	2.20	6.88	6.91	6.78	6.72	2.06	6.63
	Ca-SRFA	-	-	0.02	-	-	-	0.01	-	-	-
	$CaNTA^{-}$	-	0.09	-	-	-	-	-	-	-	-
CO_3^{2-}	CO_3^{2-}	-	-	0.01	0.01	0.01	-	-	0.01	-	0.01
	$CaCO_{3\,(aq)}$	0.02	0.02	0.03	0.04	0.04	0.02	0.03	0.03	0.03	0.03
	$CaHCO_3^{+}$	1.76	1.85	2.03	2.20	2.15	1.88	1.94	2.02	2.06	2.07
	HCO_3^{-}	47.17	54.77	58.92	59.19	61.79	53.75	56.04	58.18	55.45	59.17
	$H_2CO_{3\,(aq)}$	51.03	43.33	39.00	38.55	35.99	44.32	41.98	39.75	42.44	38.70

and temperature. The solution was then slightly undersaturated through the addition of CO_2 to minimise untimely calcite precipitation, which would affect estimates of partition coefficients. Once the desired SI (between -0.01 and -0.22) was achieved via incremental pH adjustments by means of N_2 and CO_2 sparging, the reservoir was sealed and allowed to equilibrate at experimental temperature inside the GeoMic enclosure for at least 12 hours. A syringe attached to tubing allowed for sub-sampling of the reservoir throughout the experiment and monitoring of pH, electrical conductivity, and temperature.

4.2.3 Cave-analogue experiments

Cave-analogue experiments were carried out using the controlled atmosphere setup GeoMic ('Geological Microclimate') at the School of Science, University of Waikato, Aotearoa New Zealand (Figure 4.1; first described in Lindeman et al. (2022)). Adopting the design by M. Hansen et al. (2017), GeoMic comprises a hermetically sealed enclosure (1.6 m $\times$ 0.6 m $\times$ 0.6 m), in which pCO_2 concentration, air temperature, and relative humidity can be tightly controlled. The

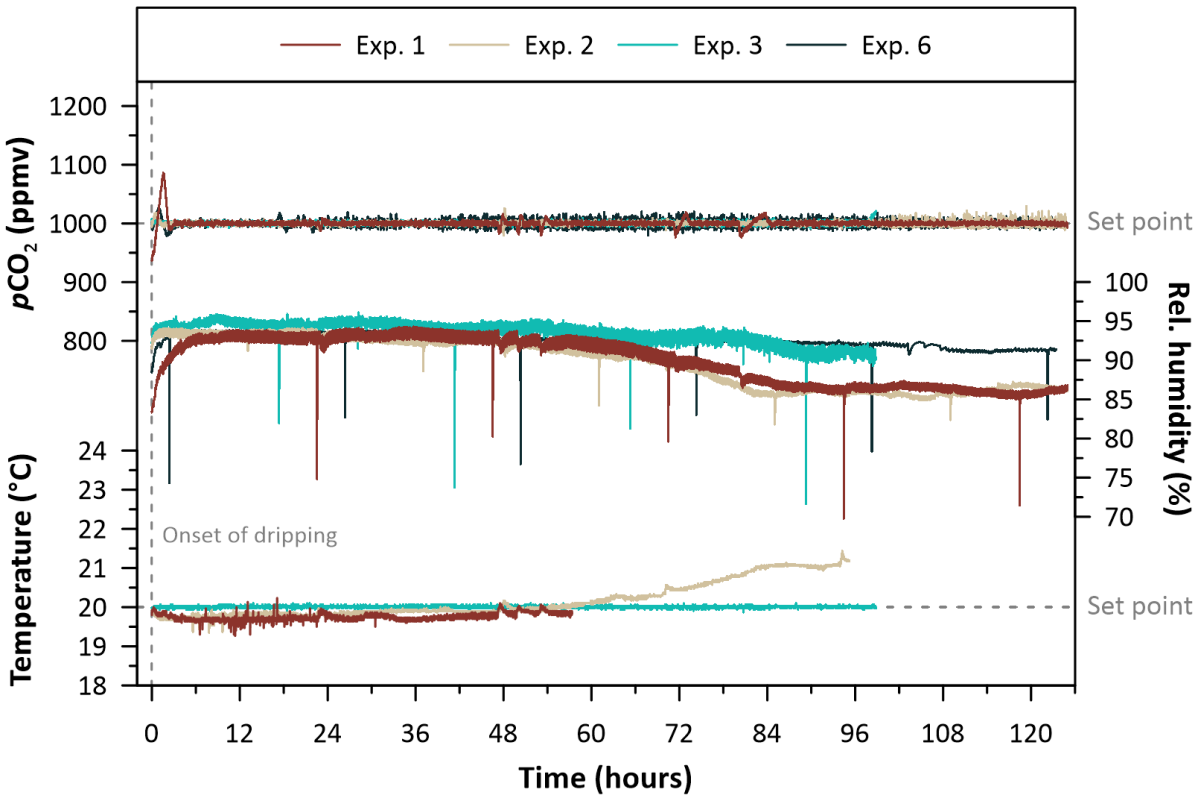

Figure 4.2: Example atmospheric conditions of four experiments. Logged data of pCO_2 (ppmv), relative humidity (%), and air temperature (°C) inside the GeoMic enclosure during Experiments 1, 2, 3, and 6. Data were logged every minute. Temperature in Experiment 6 was likewise ca. 20 °C but logger data were corrupted. Conditions of other experiments are shown in Supplementary Figure 4.S1 and Figure 4.S2.

pCO_2 is regulated by opening and closing of magnetic valves to release small pulses of either CO_2 or N_2 bubbled through ultrapure water. A Vaisala GMP252 CARBOCAP® (Vaisala, Finland) carbon dioxide sensor records CO_2 in real-time (±40 ppm CO_2 reported accuracy), and the automatic gas release is adjusted accordingly. Air temperature is measured by 3 negative temperature coefficient thermistors, in response to which a liquid-to-liquid recirculating chiller unit (Model 6000 series; PolyScience, USA) operates to achieve the desired temperature. Relative humidity is retained at above 90% by bubbling air through a water reservoir, and maintaining a constant volume of water inside the basin of the drip stage. Measurements of relative humidity are taken by a Vaisala HMP7 relative humidity and temperature sensor (±0.8% RH, ±0.1 °C reported accuracy; Vaisala, Finland). Fans circulate air through the enclosure to ensure homogenous conditions. Data logging and control of the system occurs through a LabVIEW (Version 2015 SP1; National Instruments, USA) interface. An example of atmospheric conditions during experiments is presented in Figure 4.2.

A Hei-FLOW Heidolph Precision (Heidolph Instruments, Germany) peristaltic pump with a four-channel pump head delivers drips from a 10 L reservoir solution. Different drip rates are achieved by adjusting the inner diameter of peristaltic tubing at a constant pump rate of 5 rpm, while 1 mL pipette tips inserted tip-first into the end of each tube maintain a consistent drip volume across different drip rates of ca. 0.11 mL (estimated gravimetrically). A bespoke adjustable stage ensures consistent drip heights and a drip impact central to watch glasses that

are positioned beneath each drip. Watch glasses (4 per experiment, with exceptions of 3 and 5 glasses used in Experiments 1 and 10, respectively) were sandblasted and wiped with ethanol before experiments to reduce surface tension and mimic the roughness of natural stalagmites to aid with nucleation. Due to supply constraints, watch glasses used in experiments varied in diameters between 70 mm (Experiments 1 and 2) and 90 mm (Experiments 3 to 10), but were deployed consistently where possible. However, glass size is not expected to affect chemical measurements due to sufficient space in the centre of all glasses to allow for consistent calcite growth without any effects on flow caused by the glass edges. Likewise, potential miniscule differences in glass curvature are not regarded to be consequential for chemical observations.

The drip height was initially set to ca. 15 cm for Experiment 1 to minimise splashing, and the drip solution was dripped onto glasses directly from the transfer tubing. This experiment yielded low total accumulated masses of $CaCO_3$ (1.5 – 50 mg per glass), possibly due to limited dispersal of the thin-film and consequently insufficient degassing. Subsequent experiments were therefore adjusted to enhance precipitation by increasing the drip height to 30 cm (to increase thin-film dispersion). In Experiments 4 – 10, the drip solution was allowed to further degas by initially dripping onto the inside of acid-clean glass funnels placed directly under the pipette tip delivering the drip solution. The solution flowed through the funnel stems (inner diameter of 0.5 cm), yielding drip intervals and drop volumes consistent with those obtained from the tubing. This approach considerably increased the mass of calcite precipitating on glasses, and generally $<$3% of total precipitate formed in the funnels. However, significant funnel deposition of 10% to 14% occurred at 4 drip points, each coinciding with the lowest drip rates of the experiment.

Faster drips were stopped sequentially before the end of experiments to account for the varying volumes of reservoir solution transferred at different drip rates. Each experiment lasted 7 – 8 days, including ca. 2 days for equilibration and resting of glasses at experimental conditions after stopping the drips. Watch glasses were left to dry under experimental conditions for at least 12 hours, before being oven-dried at 30 °C, and weighed. Information on individual experimental glass deployments can be found in Supplementary Table 4.S1.

All experiments were carried out with a target pCO_2 of 1000 ppmv and constant temperature at 20 – 22 °C, with exceptions of Experiments 4 and 5. Experiment 4 was performed at ambient room pCO_2 (ca. 420 ppmv) and temperature, without actively controlling these parameters. These conditions reflect an open system, akin to a well-ventilated or near-entrance cave location. Experiment 5 was carried out at a pCO_2 of 700 ppmv in an attempt to further enhance accumulation rates, but all subsequent experiments were once more performed at a pCO_2 of 1000 ppmv.

Upon completion of Experiments 4 to 10, the tubing used to transfer the drip solution was pumped dry, and then briefly rinsed with deionised water to remove excess reservoir solution. The tubing was subsequently flushed with a known volume of dilute (2% v/v) double-distilled HNO_3 in order to estimate the degree of $CaCO_3$ precipitation within the tubing as approximated by the mass of Ca retrieved. The maximal mass of Ca collected by the acid in Experiments 6

to 10 was 135 µg (on average 51 µg), but up to 350 µg and 1100 µg of Ca were removed from tubing used in Experiments 5 and 4, respectively. For experiment 4, this equates to up to ca. 0.3% of total dissolved Ca moved through the tubing. All tubing was finally rinsed again with ca. 1 L of ultrapure water.

4.2.4 Sample collection in natural caves

In addition to $CaCO_3$ growth experiments, modern carbonate precipitates were collected on a total of 32 sandblasted watch glasses deployed under active drip points in five caves in Aotearoa New Zealand and Niue. Diameters of deployed glasses were subject to availability (ranging between 70 and 90 mm), with drip height varying likewise. Where feasible, glasses were mounted on Stalagmate® acoustic drop counters (Driptych, UK) to record drip rate throughout the growth period. Corresponding water samples were collected using acid-clean polypropylene Falcon™ tubes during each visit, along with a record of *in-situ* observations of environmental variables. Upon retrieval, watch glasses were allowed to dry and subsequently stored in individual softly lined clean containers, before being oven-dried in the laboratory at 30 °C. In an additional attempt to survey in-cave partition coefficients, a total of 76 small samples (ca. 1 – 5 mg) of carbonate from active stalagmites were collected from various locations around Aotearoa New Zealand and Niue using a Teflon-coated scalpel and acid-clean 2 mL glass vials. Samples were oven-dried at 30 °C at the laboratory for 24 hours. Details of glass deployments and surficial $CaCO_3$ sampling are provided in Supplementary Table 4.S2 and Table 4.S3.

4.2.5 Characterisation of carbonate precipitates and growth rates

Prior to any physical treatment, standardised digital photographs were taken of all glasses, followed by an assessment of carbonate growth coverage, as well as crystal properties by optical microscopy and scanning electron microscopy. Spatial growth coverage on glasses was characterised following a similar approach to Day et al. (2021), which is based on the automated identification of crystals on watch glasses using photography and optical microscopy. The characterisation of $CaCO_3$ coverage was achieved using the threshold function of the image-processing software ImageJ (Rasband, 2012), which returns the percentage of pixels in a greyscale image that fall within a user-defined range of intensity values (ranging from 0 to 255, black to white). Glass coverage was differentiated into areas of 'no or low' and 'dense' crystal growth. Areas without any crystal growth occurred where strong surface tension prevented the thin-film at the glass centre from dissipating. Black image background and glass edges were accounted for using greyscale values between 0 and 9, while intensity ranges of 10 – 159 and 160 – 255 were assigned to 'no or low' and 'dense' coverage, respectively. These threshold criteria were informed by optical microscopy to achieve the best agreement with verified crystal growth, and in few cases were adjusted to avoid artefacts (*e.g.*, due to reflecting light). For each watch glass, a greyscale digital image was initially adjusted for brightness and

contrast using the in-built auto-adjust function of ImageJ. This automated pixel intensity correction helped to reduce small differences in these parameters between images, which occurred despite consistent camera settings, background, and lighting sources used for photography. The two-dimensional (top view) coverage was determined by multiplying the percentage of pixels by the area of the glass (*e.g.*, 63.6 cm^2 for 90 mm diameter glasses, not accounting for glass curvature).

The most simplistic empirical metric of growth is the total accumulation rate (R_{acc}; in mg day^{-1}) based on the mass of precipitate (m_{prec}; in mg) collected on watch glasses over the deployment time (t; in days). This rate can be normalised to the area available for deposition (A; in cm^2) to give $R_{acc\text{-}norm}$ (in mg cm^{-2} day^{-1}) (Equation 4.2):

$$R_{acc-norm} = \frac{m_{prec}}{t \times A} \tag{4.2}$$

Optical microscopy indicated that areas of 'no or low' coverage primarily hosted sparsely distributed individual crystals with little or no contact between each other. In contrast, areas of 'dense' growth typically comprised multiple layers of tightly packed crystals and crystal aggregates, serving as media for further growth. It is estimated that the vast majority (>95%) of mass is present within areas of 'dense' coverage, and values of R_{acc} were thus normalised to this area (rather than the entire glass surface) to more adequately account for the actual area of precipitation. An example of image-based growth characterisation and subsequent sub-sampling is provided in Figure 4.3.

Beyond the approach outlined above, however, the rate of calcite precipitation (*i.e.*, at crystal level) could not be confidently estimated by empirical means because required crystal surface area measurements (*e.g.*, based on automated particle analysis as proposed by Day et al., 2021) proved unreliable here. Samples were also of insufficient mass for the Brunauer-Emmette-Teller method to infer particle size. Instead, the rate of calcite precipitation (Ca_{acc}) was approximated using the model established by Dreybrodt and Franke (1987) and Dreybrodt (1988), which formulates the mass of calcite deposited from a stagnant solution thin-film at the surface of drip-fed stalagmites (in g m^{-2} s^{-1}, Equation 4.3):

$$Ca_{acc} = \left([Ca^{2+}]_{meas} - [Ca^{2+}]_{eq}\right) \times \left(\frac{\delta}{t}\right) \times \left(1 - \exp^{\frac{-\alpha_p t}{\delta}}\right) \tag{4.3}$$

$[Ca^{2+}]_{meas}$ and $[Ca^{2+}]_{eq}$ are the measured and theoretical equilibrium (w.r.t. calcite) concentrations of Ca in solution (both in g m^{-3}), respectively. The impact of incoming drips at an interval t (in seconds) is assumed to replace the previous thin-film of thickness δ (in m), while α_p presents a rate constant (in m s^{-1}). The latter was calculated using the empirical relationship determined by Baker et al. (1998) as Equation 4.4:

$$\alpha_p = (0.52 + 0.04T + 0.004T^2) \times 10^{-5} \tag{4.4}$$

, in which α_p is solely a function of temperature *T* (in K), and notably independent of δ. This simplified expression of α_p applies when δ is small (0.005 – 0.03 cm), which is the norm for stalagmite tops (typically <0.02 cm; M. Hansen et al., 2013) and assumed to also apply to experimental watch glass deployments. For experiments, PHREEQC was used to derive $[Ca^{2+}]_{eq}$ based on the reservoir solution chemistry and the respective atmospheric pCO_2 and temperature. Total inorganic carbon was specified using the values calculated in PHREEQC for the initial reservoir solution with $SI_{Calcite} < 0$. Calculations of $[Ca^{2+}]_{eq}$ were carried out consistently for a solution pH of 7.0. The assumption of the pH upon dripping inside the enclosure was necessary due to the challenge of obtaining reliable measurements of single drops, but reflects the range of spot observations. This challenge persisted despite degassing of the exposed droplets being negligible on the scale of seconds to minutes (Dreybrodt, 2012), because the thin-film on the pH sensor in turn degasses rapidly (in the order of seconds and tens of seconds). For natural cave waters, monitoring data and dripwater analyses were used to derive $[Ca^{2+}]_{eq}$, drawing on assumptions where measurements were incomplete. The film thickness δ was selected as 0.0001 m (cf. Carlson et al., 2020; Noronha et al., 2017) for both cave-analogue and natural cave settings.

A precipitation rate R_{prec} (in mg day^{-1}) comparable to observed accumulation rates (R_{acc}) is obtained by converting Ca_{acc} according to Equation 4.5:

$$R_{prec} = Ca_{acc} \times 86400 \times \frac{V_{drop}}{\delta} \times 1000 \tag{4.5}$$

, where V_{drop} (in m^3) is the estimated volume of a single drop (here, 1.1×10^{-7} m^3), and 86400 is the number of seconds per day.

4.2.6 Sub-sampling and processing of watch glasses

Targeted sub-sampling of precipitate collected on watch glasses was carried out with the aid of a radial reference grid to enable a spatially consistent collection of material relative to the central drip impact zone (Figure 4.3D). Precipitate was carefully scraped off using Teflon-coated scalpels and razor blades, and stored in acid-clean (10% HNO_3) glass vials. The number and location of sub-samples retrievable varied between glasses depending on the accumulated mass and crystal coverage. Following sub-sampling, further standardised digital photographs were collected of each glass to enable accurate measurement of the width and distance from the glass centre of individual sub-samples using ImageJ.

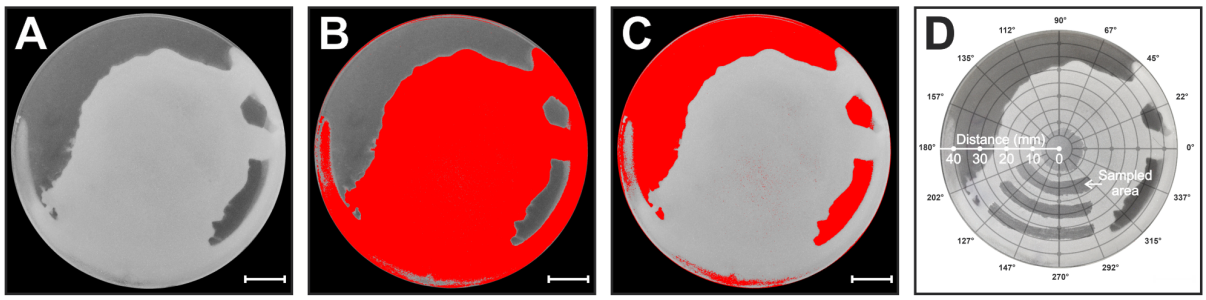

Greyscale digital image | 'Dense' crystal cover | 'No or low' crystal cover | Targeted sub-sampling

Figure 4.3: Example of crystal growth characterisation and sub-sampling of watch glasses. A) Auto-adjusted greyscale image of watch glass Geo-Exp-5-C (inorganic) in preparation for crystal growth characterisation using the ImageJ threshold function. Images **B)** and **C)** show areas (in red) of 'dense' (intensity values 160 – 255) and 'no or low' (intensity values 10 – 159) crystal growth, respectively. Scale bars in each image present 10 mm. **D)** Example of sub-sampling strategy of precipitate. A vector-based radial grid serves as reference for orientation, width, and distance from the drip impact of individual sub-sampled areas.

4.2.7 Analytical techniques

Visual inspection of precipitates

Spatial patterns and properties of crystal growth on watch glasses were initially assessed using an Olympus BX51 optical microscope equipped with an Olympus SC50 attachable digital camera (Olympus Scientific Solutions, Japan). Optical analysis served to select representative areas for sub-sampling and identify any across-glass precipitation patterns. Sub-samples of precipitates were further assessed for crystal microstructures by scanning electron microscopy (SEM). Crystal samples were mounted on taped aluminium stubs and subsequently sputter coated with an ultra-thin cover of platinum and palladium for conductivity. The samples were observed in scanning mode using either a Hitachi S-4700 or Hitachi SU8230 cold field emission microscope at the University of Waikato. The accelerating voltage was normally set to 5.0 kV but was lowered to 3.0 kV to reduce charging effects as necessary.

Analysis of elemental concentrations

Elemental concentrations were quantified at the University of Waikato using an Agilent 8900 inductively-coupled plasma mass spectrometer (ICP-MS; Agilent Technologies, USA), operated by MassHunter WorkStation (Version 4.5) and coupled with an SPS 4 autosampler. The system uses a 0.05 – 0.1 mL min^{-1} MicroMistTM U-Series nebuliser (Glass Expansion, Australia) attached to a quartz cyclonic spray chamber followed by a 2.0 mm injector quartz torch. The plasma torch is followed by Ni sampler and skimmer cones, and ion beam focussing is achieved with an extraction omega lens (Agilent Technologies, USA). The ICP-MS was optimised for maximal sensitivity for each run, ensuring that oxides and divalent ions accounted for less than 2%.

Aqueous samples (GeoMic reservoir solutions and cave waters) were filtered (0.45 µm,

PES membrane) and acidified to 2% (v/v) with double-distilled (Savillex DST-1000 Acid Purification System, USA) HNO_3. Homogenised $CaCO_3$ sub-samples collected from watch glasses or caves were dissolved in 5% (v/v) double-distilled HNO_3 in Milli-Q ultrapure water at a ratio equivalent to 1 mg per 4 mL to achieve consistent concentrations of Ca, and ensure complete dissolution. All samples were handled and prepared in acid-washed (10% HCl, then 10% HNO_3) 15 mL polypropylene Falcon™ tubes. Samples were analysed in triplicate and bracketed with acid blanks of 2% double-distilled HNO_3. Procedural Milli-Q blanks prepared in the same manner as samples were routinely analysed alongside samples to monitor the effectiveness of cleaning protocols.

Trace elements were quantified using five-point calibration curves between 0.1 and 500 µg L^{-1} produced from multi-element standard IV71-A (Inorganic Ventures, USA). Ca and other major elements were calibrated separately against five standards ranging from 100 to 10,000 µg L^{-1} prepared from single-element stocks (Inorganic Ventures, USA). Blank samples were run after every 10 samples to minimise carryover, and check standards analysed every 20 samples were used for drift correction. Re-calibration was carried out after every 100 samples. Instrumental drift and matrix elements were monitored and accounted for using an online internal standard containing Sc, Ge, Rh, Ir, and Tl. Quantification is based consistently on the isotopes ^{24}Mg, ^{59}Co, ^{60}Ni, ^{65}Cu, and ^{88}Sr. ^{44}Ca was used in favour of ^{43}Ca due to overall better precision and the potential matrix interferences of SRFA with ^{43}Ca (cf., Lindeman et al., 2022). Where relevant elemental concentrations were below detection limit but sufficient sample volume was available, a standard addition approach was used to circumvent analytical limits and quantify trace metal concentrations using linear calibration curves based on 4 to 5 sample aliquots spiked with elemental stock solution (Harris, 2010).

Analysis of dissolved organic carbon

Total organic carbon (TOC) in selected cave water samples was quantified by wet chemical oxidation using an Aurora 1030W TOC Analyser (OI Analytical, Texas, USA). Aliquots were filtered prior to analysis using 0.45 µm syringe filters, thereby targeting the dissolved organic carbon (DOC) fraction. The samples were reacted with freshly prepared 5% phosphoric acid (H_3PO_4) and 0.84 M sodium persulfate ($Na_2S_2O_8$). Quantification was achieved using a commercial carbon standard (potassium hydrogen phthalate; Ajax-Finechem, Australia).

Fluorescence measurements

Three-dimensional excitation emission matrices (3D EEM) of reservoir solution and dissolved carbonate samples of SRFA experiments were collected on a Horiba Jobin Yvon Aqualog fluorometer (Horiba, Japan) equipped with a CCD detector for an excitation wavelength (γ_{ex}) range of 240 – 600 nm and an emission wavelength (γ_{em}) range of 245 – 800 nm. Spectra were measured with an integration time of 0.5 seconds and a 3 nm step-size. Post-processing was carried out using the Aqualog data processing suite (Ver. 4.2.0.8, Horiba, Japan), which

included the removal of inner-filter effects, first and second order Rayleigh masking of scatter lines, and normalisation of spectra to the average Raman intensity (peak area) of Milli-Q.

Aliquots of the reservoir solution were acidified to 0.025 M HCl, while sub-samples of precipitate were prepared by dissolving 2 mg of $CaCO_3$ in 4 mL of 0.025 M HCl (cf. Lindeman et al., 2022; Pearson et al., 2020. Samples were quantified against 6 matrix-matched calibration solutions, which were acidified accordingly and adjusted to the reservoir ionic strength of ca. 0.02 with $CaCl_2$.

To statistically relate fluorescent properties to the concentration of SRFA, a parallel factor analysis (PARAFAC; *e.g.*, Fellman et al., 2010; Ishii & Boyer, 2012) was performed on the resulting 3D EEM data. The analysis was carried out using one-component PARAFAC models reflective of the singular prominent humic-like fluorescence peak 'A' (excitation and emission wavelengths of 250 – 260 nm and 380 – 480 nm, respectively; Coble, 1996) produced by the synthetic SRFA solutions. Calibration was achieved based on PARAFAC C1 scores of SRFA standard solutions (linear correlation with $R^2 > 0.99$). Processing of 3D EEM data was carried out using the N-way (Andersson & Bro, 2000) and drEEM (Stedmon & Bro, 2008) toolboxes in MATLAB®2019.

4.2.8 Estimation of apparent partition coefficients

Empirical apparent partition coefficients for experimental and natural couplets of parent solutions and precipitates were calculated according to Equation 4.1. For samples of cave-analogue experiments, the respective averaged GeoMic reservoir concentration of daily sub-samples served as the $X/Ca_{Solution}$ term. For samples derived from natural caves, either discrete or averaged (where applicable) dripwater compositions for corresponding carbonate deposits were used. The same procedure was applied to watch glasses used to collect fresh precipitate, as well as to surficial sub-samples of actively depositing speleothems. Partition coefficients were calculated for each carbonate sub-sample collected from watch glasses, with the value corresponding to the aliquot most central to the drip impact being used throughout statistical analyses (unless stated otherwise). Additional sub-samples collected along transects between the glass centres and edges served to monitor the effect of progressive calcite precipitation, and provide greater confidence in overall D_X estimates. The analytical uncertainty (standard deviations based on triplicate ICP-MS measurements) was propagated throughout the computation of elemental ratios and subsequent estimates of D_X (see the Supplement for details).

The distribution of organic phases between solution and crystals can be expressed analogously to elemental partition coefficients (*e.g.*, Lindeman et al., 2022; Pearson et al., 2020) in form of Equation 4.6, allowing an assessment of direct capture of organics by the precipitate:

$$D_{Ligand} = \frac{\left(\frac{Ligand}{Ca}\right)_{Crystal}}{\left(\frac{Ligand}{Ca^{2+}}\right)_{Solution}} \tag{4.6}$$

Further, elemental D_X normalised to D_{Ligand} provides a measure of the incorporation of metal-ligand complexes in form of ternary complexation (Equation 4.7; Hartland et al., 2014):

$$D_{Ligand-M} = \frac{\left(\frac{M}{Ligand}\right)_{Crystal}}{\left(\frac{M^{2+}}{Ligand}\right)_{Solution}} \tag{4.7}$$

Accordingly, a $D_{Ligand\text{-}M}$ of ca. 1 would indicate that both the ligand and metal ions distribute at the same rate, implying that metal-ligand complexes are included without prior dissociation. In this study, this approach was only applicable to experiments using SRFA because the lack of aromatic functional groups (and thus fluorescent properties) of NTA precluded the measurement of its distribution across phases.

4.3 Results

4.3.1 Cave-analogue experimental conditions

Experimental air temperature, pCO_2, and relative humidity were generally close to respective targets (Table 4.1; Figure 4.2; Supplementary Figure 4.S1 and Figure 4.S2), although the control and/or recording of enclosure air temperature was compromised in several experiments. Specifically, a breakdown of the chiller unit after ca. 60 hours into Experiment 2 resulted in an increase of air temperature by ca. 1.5 °C. Further failures of the chiller prevented accurate automated temperature control in Experiments 4 (run as an open experiment at room conditions) and thereafter. While the enclosure temperature was overall slightly higher and corresponded to diurnal variations in room temperature in these cases, deviations from the mean temperature of ca. 22 °C remained within ca. 1.5 °C. Temperature sensor failures in Experiments 1 and 2 interrupted continuous data logging, but regular spot measurements of reservoir solution and enclosure temperature confirmed an acceptably consistent temperature. The loss of continuous internal temperature recordings was reconciled with the instalment of a HOBO® TidbiT temperature logger (v2; Onset, USA) to the enclosure for all subsequent experiments.

The initial calcite saturation index of experimental reservoir solutions was estimated between -0.22 and -0.01, with variations primarily arising from small differences in pH (controlled solely by CO_2 and N_2 sparging). Sporadic measurements of the pH of falling drips within the enclosure (taken with a HORIBA LAQUAtwin pH22 single-drop meter) typically yielded values of 7.0 to 7.5 (opposed to ca. 6.4 – 6.5 in the reservoir), suggesting slight supersaturation may be reached just prior to drip impact. However, these measurements are seen as indicative only

due to the rapid degassing and pH evolution on the sensor, and inconsistencies between drip rates.

The reservoir solution pH and EC typically remained stable until ca. 8 – 9 L of solution had been drawn from the vessel, at which point the pH increased by up to 0.2 units presumably due to the large volume of headspace. In such case, all remaining drips were stopped immediately to minimise potential impacts of early supersaturation on the final precipitate. During the final hours of Experiments 4 and 5 (both with an initial $SI_{Calcite} \approx 0.01$), considerable decreases in dissolved Ca content by up to ca. 18% and 35%, respectively, imply the precipitation of an appreciable fraction of carbonate within the reservoir. The conditions of both experiments are replicated in Experiments 1 and 9 (both inorganic), and Experiment 10, respectively.

4.3.2 Cave environmental conditions and water chemistry

Water and carbonate samples from natural caves were obtained from a range of environments in Aotearoa New Zealand and Niue, some of which were actively monitored, while others were visited given the opportunity. Across all 11 sampling sites, cave air temperature varied between ca. 4.1 and 24.5 °C, while the atmospheric pCO_2 ranged from ca. 420 to 2150 ppmv. The depositing waters in caves of Aotearoa New Zealand varied in electrical conductivity between ca. 190 and 680 µS cm^{-1}. The lowest conductivity corresponded to waters from Hodge Creek Cave and the alpine Dave's Cave (260 and 290 µS cm^{-1} on average, respectively), while Majumba Cave (entirely located under grazing pastures) dripwaters had an average EC of 564 µS cm^{-1}. With few exceptions, cave waters on Niue were generally more enriched in ions with EC readings in the range of 230 to 1340 µS cm^{-1} (Ulupaka Cave) and 515 to 1700 µS cm^{-1} (Anapala Cave). The pH of all sampled drips was between ca. 7.0 and 8.8.

Spot measurements and Stalagmate™ drip count data recorded a large range of drip intervals between <0.05 and ca. 170 drips min^{-1}, although far lower drip rates and/or temporary cessation of flow were observed at some sites where no water or measurements could be collected. For drip points equipped with drip loggers, the continuous datasets were reduced to the median. For all other sporadically measured drip points, drip rates are reported as the average of spot measurements. Basic information on the environmental conditions at each sampling site is included in Supplementary Table 4.S2 and Table 4.S3, while Chapter 5 details cave monitoring activities of Niuean caves.

The elemental composition of cave waters varied considerably between study locations in terms of both the suite of trace metals of interest to this study, as well as major matrix components. The three studied transition metals exhibited moderate covariation at most study locations (Figure 4.4A to Figure 4.4C), with the most pronounced agreement observed between Ni and Co (Figure 4.4C). Concentrations of Ni, Cu, Co, along with various other transition metals, were consistently close to or below instrumental detection limits (<0.1 µg L^{-1} for the transition metals) in Dave's Cave, located below a thin layer of soil and alpine tussock vegetation. This was particularly the case for Co, for which no water sample yielded reliable quantification. Co

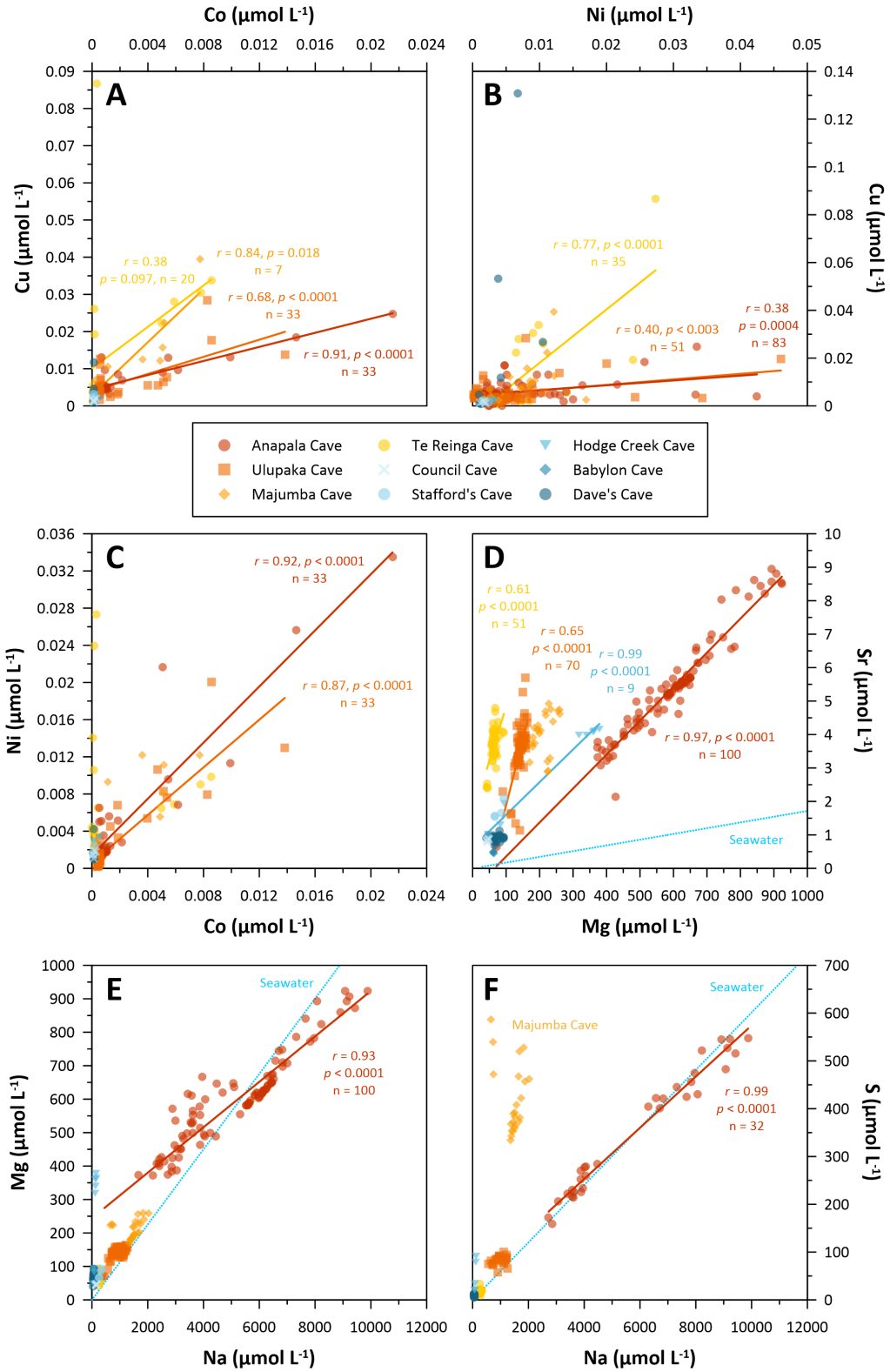

Figure 4.4: Relationships between selected elemental concentrations in natural cave dripwater samples. Linear correlation lines of respective symbol colour are presented where sufficient datapoints were available and variables showed covariance. Due to their significantly higher concentrations in most elements, and distinct environmental contexts, the two Niuean sea caves of Avaiki and Palaha are not included here (see Supplementary Table 4.S4 and Table 4.S5 for data). Dotted light blue lines in panels **D** – **F** represent the typical elemental composition of seawater (values from Pilson, 1998), indicating the contribution of sea spray to the dripwater chemistry. Error bars for elemental measurements are omitted for clarity.

was consistently lower in content compared to Ni (0.006 µmol L^{-1} on average) and Cu (0.008 µmol L^{-1} on average), but quantifiable in at least some samples of all other caves (0.002 µmol L^{-1} on average). Over the course of a year, more frequent sampling at Te Reinga Cave suggested that concentrations at a given drip point varied by ca. 0.003 to 0.004 µmol L^{-1} for both Ni and Co, and by ca. 0.01 µmol L^{-1} for Cu. However, a clear seasonal pattern is not apparent in absence of a longer-term continuous time-series. Similarly, there were no major overall differences in concentrations between dripwaters collected during dry and wet season months in the two Niuean caves.

Mg and Sr concentrations were generally well correlated, but large differences in the slopes of their relationship were evident between caves. Dripwaters of Te Reinga and Ulupaka, especially, showed a much larger variability in Sr compared to Mg. In contrast, the two elements varied more concordantly in Anapala Cave waters, which also exhibited by far the greatest range in respective absolute concentrations (*e.g.*, between ca. 70 and 920 µmol L^{-1} Mg; Figure 4.4D). Ca content varied greatly within each cave between drip points and sampling periods, but was typically between 500 and 1800 µmol L^{-1}. Besides Ca, Na was the dominant matrix element and was particularly abundant in Anapala Cave with concentrations between 2 and 10 mmol L^{-1} (Figure 4.4E and Figure 4.4F). At most sites, Na was well correlated with Mg (and Sr, to a lesser extent), generally coinciding with elevated S concentrations. An exception to the latter was found in Majumba Cave, where the relative proportion of S was notably higher than in any other cave (up to ca. 600 µmol L^{-1}; Figure 4.4F).

The organic matter content of water samples as approximated by their DOC concentration was largely similar within each cave, ranging from an average of ca. 2.9 mg L^{-1} at Dave's Cave to ca. 8.1 mg L^{-1} on average at Te Reinga Cave. Using DOC as a rough measure of organic ligand concentration, and taking only the concentrations of Ni, Cu, and Co into account, these measurements translate to M:L ratios in the order of 10^{-7} to 10^{-4} (mg M)(mg C)$^{-1}$.

4.3.3 Growth and physical properties of experimental and natural precipitates

Experimental precipitates

Analysis of carbonate powder samples by SEM confirmed that the precipitate in all cave-analogue experiments was dominated by the calcite polymorph. While crystal habit, size, and quality varied between experiments, as well as between drip rates and across watch glasses, the vast majority of calcite crystals were euhedral and of rhombohedral configuration (Figure 4.5). Generally, the proportion of growth defects and anhedral crystals increased with higher concentrations of ligands in the solution.

The longest axis of crystals estimated using optical microscopy and SEM was typically between 15 µm and 25 µm within densely covered regions (as defined in Section 4.2.5). In areas of low coverage, individual crystals were found to be either larger or smaller than those

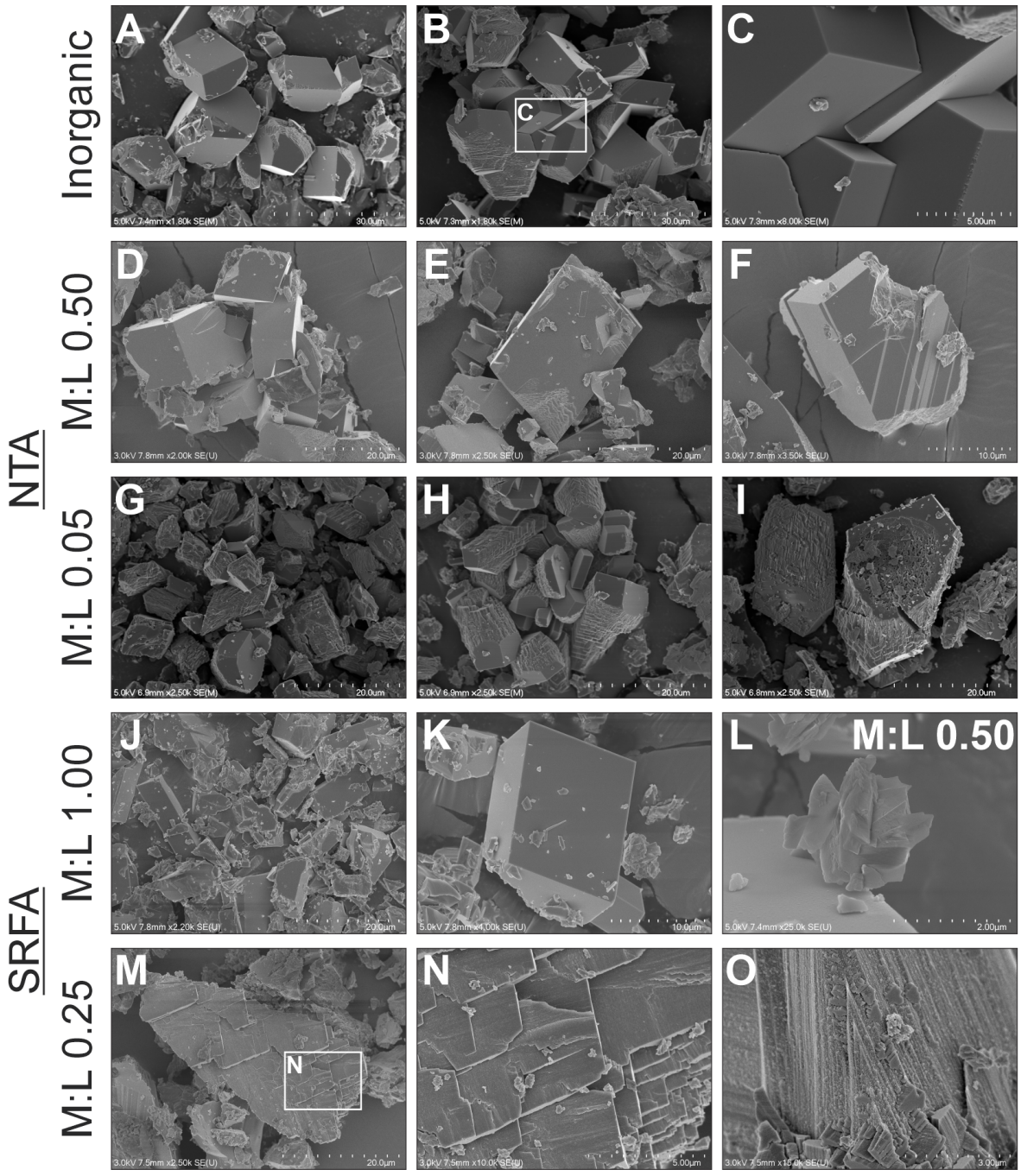

Figure 4.5: Representative scanning electron microscopy images of crystals grown under cave-analogue conditions. M:L refers to the metal:ligand ratio in the GeoMic reservoir solution. Examples of natural farmed carbonates and surficial speleothem samples are shown in Figure 4.7 for comparison.

in densely covered regions, and variable tendencies in crystal size with distance from the centre occurred. Some glasses exhibited clear preferential flow paths of incoming water towards the glass edge (*e.g.*, Supplementary Figure 4.S3K), while narrow bands of microcrystalline (<5 µm) coverage or isolated splash regions with larger crystals (up to ca. 60 µm) were also observed (*e.g.*, Supplementary Figure 4.S3D; Supplementary Figure 4.S4). Narrow circular deposit regions lining the edge of the drip impact were more frequently observed at fast drip rates (>10 drips min^{-1}), whereas most glasses from slow to moderate drip points possessed spatially more coherent coverage.

The accumulated total mass of $CaCO_3$ on watch glasses ranged from 1.5 to 230.3 mg (80.8 mg on average), with normalised accumulation rates ($R_{acc\text{-}norm}$) between 0.3 and 2.2 mg cm^{-2} day^{-1}. Both metrics were weakly positively related with drip rate (r = 0.49, p = 0.004, n= 34 for $R_{acc\text{-}norm}$; Figure 4.6A). Modelled precipitation rates (R_{prec}) were weakly positively related to R_{acc} (r = 0.46, p = 0.003, n = 40), but on average greater by a factor of two to three (Figure 4.6B). The relationship between predicted and observed growth improved greatly for experiments, in which funnels were included to enhance degassing inside the enclosure (r = 0.74, $p < 0.0001$, n = 29).

Natural precipitates

Visual assessment of representative sub-samples indicated that calcite was also consistently the predominant polymorph in natural precipitates. Crystals collected from watch glasses were generally rhombohedral calcite, often in aggregates, and closely resembled those produced from organic experimental solutions. Growth defects were abundant, along with a high density of steps and kinks, incomplete growth, and impurities (Figure 4.7). Surficial scrapings of carbonate included fragments of crystal growth successions opposed to loose crystals, reflecting more maturely developed growth patterns (Figure 4.7G – Figure 4.7L).

Growth rates of natural precipitates could only be constrained for watch glasses that remained *in-situ* for the entire deployment, as some had been displaced from their original location. Where the latter occurred but sufficient mass of calcite had precipitated, the glasses were washed thoroughly with deionised water to remove any visible detritus, and processed according to the normal protocols. Similarly to experimental precipitates, there was an overall moderate positive relationship between drip rate and deposition, particularly evident in Ulupaka samples (r = 0.83, p = 0.003, n = 10; Figure 4.6C). Among Aotearoa New Zealand caves with glass deployments, the fastest accumulation rates with up to 2.1 mg day^{-1} were observed in Te Reinga Cave. Despite continuous dripping throughout the year, most glasses deployed in the alpine Dave's Cave had collected little to no visible material after ca. 11 months, and were consequently left in place. In Hodge Creek Cave, logger data indicated generally slow (<0.5 drips min^{-1}) and/or seasonally inactive dripping. As a result, only 3 and 2 glasses from Dave's Cave and Hodge Creek Cave, respectively, yielded viable quantities of precipitate within the timeframes of this study. Minimal crystal growth and potential chipping or abrasion of glasses resulted in negative mass differences for some deployments upon weighing, and growth rates

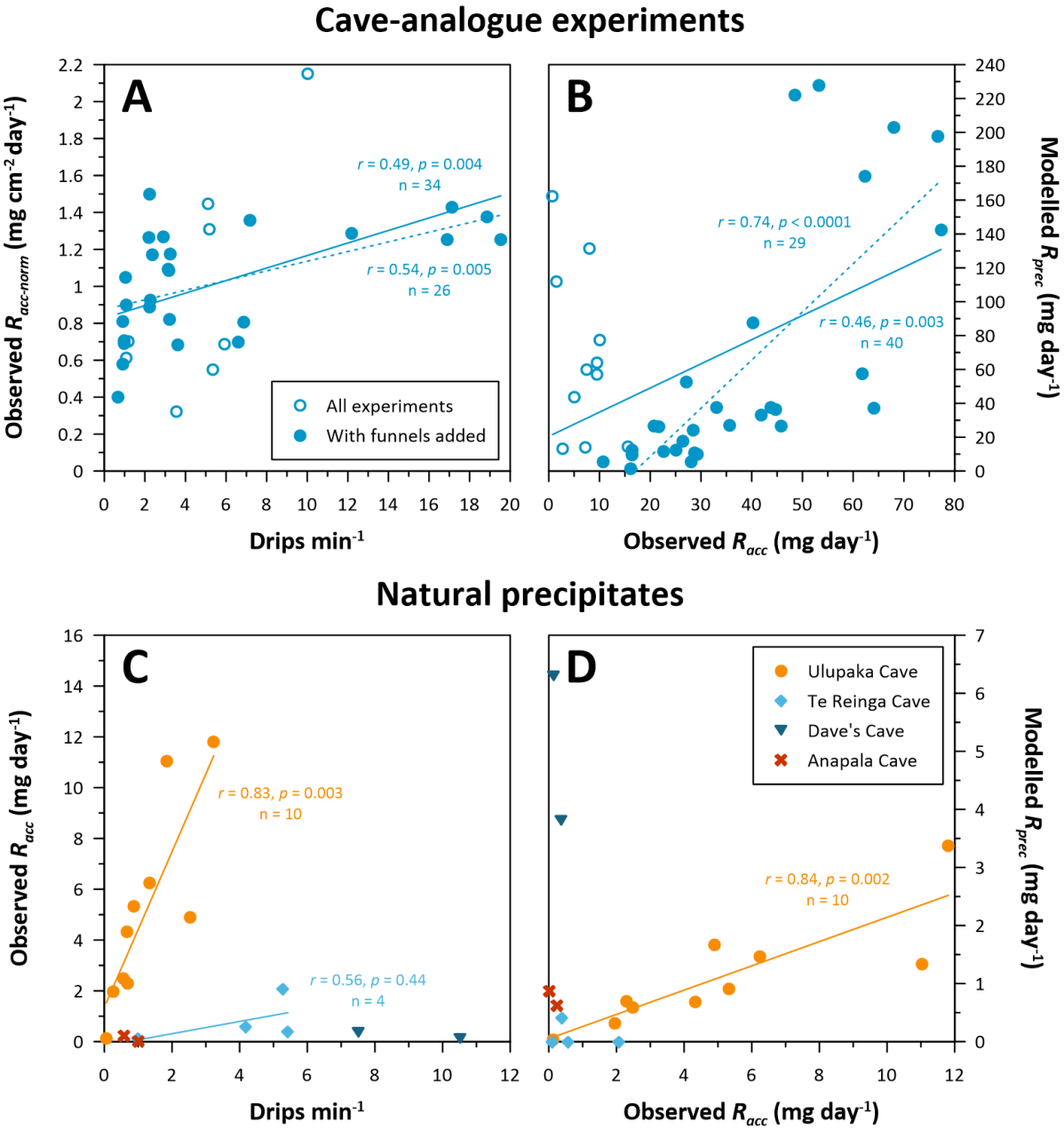

Figure 4.6: Relationships between drip rate and carbonate growth in cave-analogue experiments and natural caves. A) Drip rate related to the total accumulation rate of precipitate on watch glasses, normalised to the area of 'dense' crystal cover ($R_{acc\text{-}norm}$; see Section 4.2.5 for details). **B)** Observed total accumulation rates (R_{acc}) versus predicted rates of precipitation (R_{prec}; calculated for drip pH of 7.0) based on the model described in Dreybrodt and Franke (1987) and Dreybrodt (1988) (see Section 4.2.5 for details). Solid and dashed lines in each plot reflect linear correlations for all cave-analogue experiments and only those experiments with added funnels (Experiments 4 to 10), respectively. **C)** Drip rate related to R_{acc} for watch glasses deployed in natural caves. **D)** Relationship between R_{acc} and theoretical R_{prec} for farmed carbonate. Solid lines in **C)** and **D)** represent linear correlations for all samples of the respective cave. Note that several glasses are excluded from these figures due to implausible growth estimates.

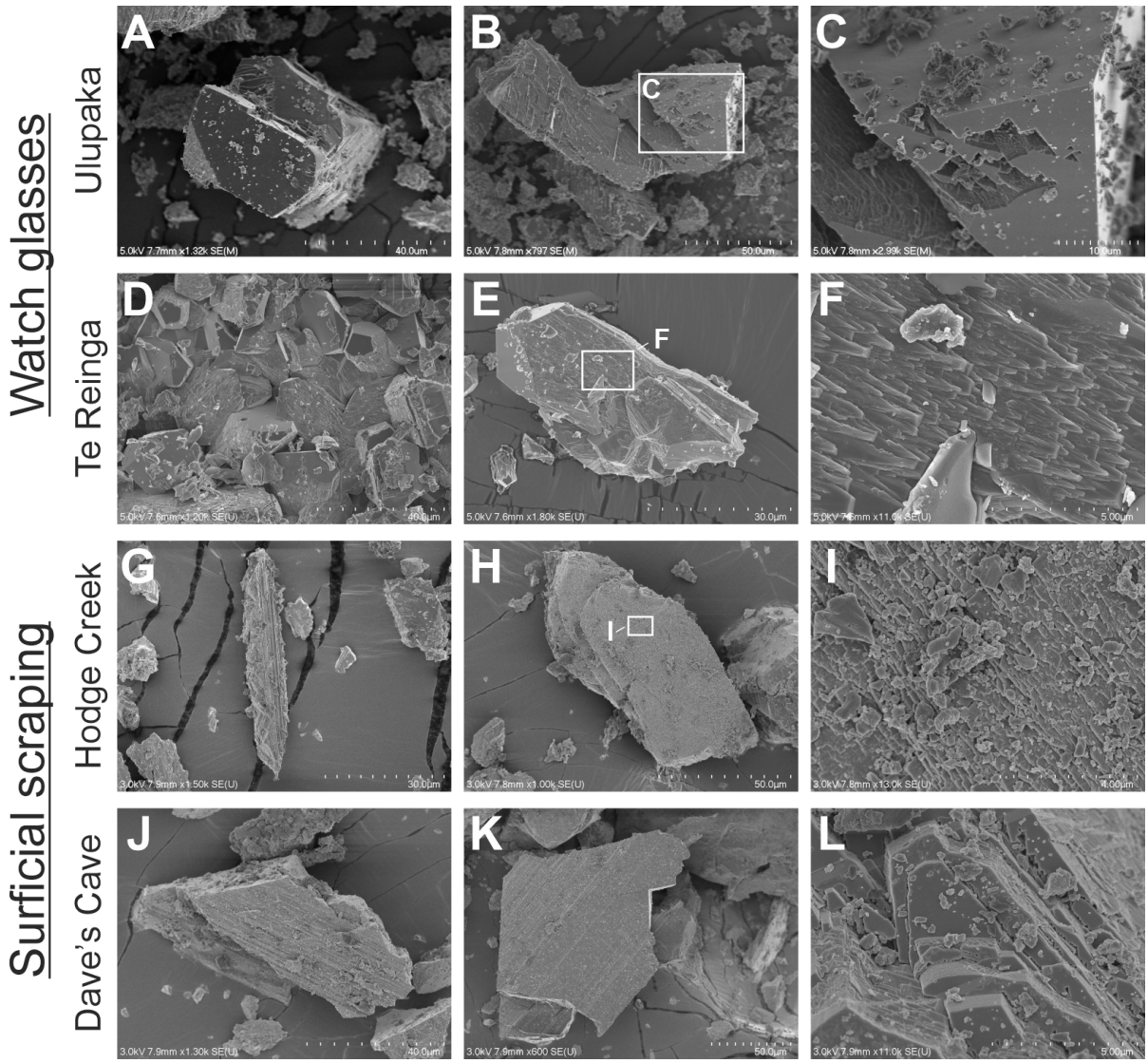

Figure 4.7: Representative scanning electron microscopy images of carbonate samples from natural caves. Crystals were scraped off sand-blasted watch glasses deployed directly under active drip points. Surficial scrapings were collected by carefully removing crystals from modern speleothems using a Teflon-coated scalpel. Rhombohedral calcite crystals were the dominant precipitate on both growth media.

were changed to 0 in these cases. Few glasses remained *in-situ* in Anapala Cave, suggesting minimum growth rates of up to 0.2 mg day^{-1}. In Ulupaka Cave, 14 successful deployments indicated generally faster accumulation at rates of ca. 0.1 to 11.8 mg day^{-1} (5.1 mg day^{-1} on average;). Modelled values of R_{prec} for Ulupaka Cave were well correlated with observed R_{acc} (r = 0.84 , p = 0.002, n = 10; Figure 4.6D), while there were no clear relationships between predicted and observed growth metrics for any other location. Surficial scrapings of speleothems comprise material of unknown age and growth duration, and consequently no attempt was made to constrain precipitation rates for these samples.

Metal systematics in cave-analogue experimental precipitates

Transition metals

The most pronounced variability in concentrations and partition coefficients derived from precipitates was exhibited by Cu (Figure 4.8A and Figure 4.8B; Table 4.3). Cu partition coefficients obtained from within 2 cm of the glass centre (comprising approximately the drip impact and immediate splash zone) varied substantially with solution chemistry, drip rate, and observed accumulation rate.

The three inorganic experiments yielded a wide range of D_{Cu}, however, each exhibiting a consistently positive relationship between D_{Cu} and drip rate (Figure 4.8B). Performed under the same conditions, Experiments 1 and 9 produced values of D_{Cu} varying between 5.83 and 39.25, and 1.83 and 57.40, respectively. In relation to drip rate, the sets of D_{Cu} from these replicate experiments were overall in good agreement (r = 0.95, $p < 0.0001$, n = 13; for linear correlation between drip rate and D_{Cu} when including data from both experiments). Partition coefficients of Cu in the uncontrolled inorganic Experiment 4 were overall considerably lower, ranging between 0.19 and 14.64. A monotonous increase of D_{Cu} with drip rate was likewise evident, albeit with a smaller gradient. With the addition of organic ligands, and an increase in their concentration (*i.e.*, decrease in M:L), D_{Cu} was overall progressively reduced. Nonetheless, D_{Cu} remained positively related with drip rate under most solution chemistries, but the gradient and strength of this relationship declined. This was particularly observed in SRFA experiments, in which an M:L of 1.00 implied only a slight reduction in partitioning compared to the two controlled inorganic experiments. Decreasing the M:L to 0.75 and 0.50 further muted the covariation of partitioning with drip rate, while D_{Cu} remained comparably constant at ca. 6.76 $\pm$ 1.47 (1σ; unless stated otherwise) at an M:L of 0.25 irrespective of drip rate. All three NTA experiments reduced Cu partitioning substantially, with values ranging between 0.55 and 2.98. At an M:L of 0.05, partitioning occurred at a constant, minimal rate with D_{Cu} = 0.72 $\pm$ 0.13. Notably, both Experiment 2 and 5 (M:L = 0.50) include precipitate for which $D_{Cu} < 1$, implying a stark contrast in Cu distribution to all other experimentally derived values of D_{Cu}. A very similar overall pattern to that observed for D_{Cu} was evident in Cu concentrations in relation to drip rate, reflecting an increasing accumulation of Cu in the precipitate with increasing drip rate, and a moderating effect on the latter by added ligands (Figure 4.8A).

Metal concentrations and partitioning were to variable degree also related to carbonate growth (Figure 4.9), expressed using the observed normalised accumulation rate, $R_{acc\text{-}norm}$. The latter is used here as a mathematically independent metric of growth in favour of the modelled precipitation rate (R_{prec}), which is intrinsically linked to drip rate. Cu concentrations were largely unrelated to $R_{acc\text{-}norm}$, with exception of weak to moderate positive correlations in three experiments (Figure 4.9A). Similarly, there were only few datasets of D_{Cu} suggesting a relationship with growth, the strongest of which was at inorganic conditions in Experiment 9 (Figure 4.9B).

Table 4.3: Empirical D_X values based on cave-analogue precipitates. Shown are calculated D_X from the most central sub-samples of each glass. Depending on crystal coverage, some sub-samples were obtained at a distance from the centre. Where values of D_X are missing, measurements were below quantitation limit. Inorganic average values of D_X reflect all centrally obtained (within 2 cm, with exceptions as shown) estimates from the three inorganic experiments.

Experiment	M:L (molar)	Glass ID	Drips min^{-1}	D_{Cu}	D_{Co}	D_{Ni}	D_{Mg}	D_{Sr}	Distance (cm)
1 (Inorganic)	-	Exp-1-B	1.1	6.39	1.78	0.45	0.04	0.11	
		Exp-1-C	5.9	20.22	1.34	0.30	0.03	0.13	3
		Exp-1-D	5.9	39.25	1.32	0.31	0.03	0.14	3
2 (NTA)	0.05	Exp-2-A	3.5	0.66	0.33	-	0.10	0.18	
		Exp-2-B	1.1	0.67	0.28	0.06	0.05	0.17	
		Exp-2-C	5.2	0.63	0.30	-	-	0.17	
		Exp-2-D	10.6	0.83	0.38	-	0.11	0.16	2.4
3 (SRFA)	0.25	Exp-3-A	10.0	4.94	-	-	0.70	0.24	2.5
		Exp-3-B	1.2	7.80	1.49	0.40	0.06	0.28	2.3
		Exp-3-C	5.3	8.94	1.46	0.39	0.13	0.27	2.3
		Exp-3-D	5.1	7.73	1.27	0.38	0.22	0.28	2.6
4 (Inorganic)	-	Exp-4-A	1.1	0.19	1.16	0.12	0.01	0.04	
		Exp-4-B	6.9	6.35	1.81	0.23	0.02	0.04	
		Exp-4-C	3.6	2.72	1.75	0.23	0.02	0.04	
		Exp-4-D	12.2	14.64	1.70	0.22	0.02	0.05	
5 (NTA)	0.50	Exp-5-A	0.7	0.77	0.79	0.07	0.02	0.11	
		Exp-5-B	6.6	1.32	1.76	0.23	0.05	0.09	
		Exp-5-C	7.2	1.25	1.65	0.17	0.04	0.08	
		Exp-5-D	17.8	2.09	1.29	0.29	0.03	0.09	
6 (SRFA)	0.75	Exp-6-A	1.0	4.04	1.04	0.30	0.05	0.19	
		Exp-6-B	2.3	9.59	1.43	0.53	0.04	0.12	
		Exp-6-C	3.2	11.56	1.66	0.50	0.04	0.11	
		Exp-6-D	19.5	36.41	2.15	0.76	0.08	0.13	2.2
7 (SRFA)	0.50	Exp-7-A	1.0	2.13	1.51	0.51	0.07	0.13	
		Exp-7-B	2.2	5.99	1.54	0.38	0.04	0.11	
		Exp-7-C	2.9	8.55	1.50	0.47	0.03	0.11	
		Exp-7-D	15.9	30.19	1.43	0.52	0.04	0.13	3.2
8 (SRFA)	1.00	Exp-8-A	1.0	2.38	1.51	0.36	0.05	0.12	
		Exp-8-B	2.2	6.60	1.71	0.31	0.05	0.11	
		Exp-8-C	3.2	9.65	1.97	0.35	0.05	0.10	
		Exp-8-D	18.9	57.11	2.33	0.53	0.11	0.13	
9 (Inorganic)	-	Exp-9-A	0.9	2.05	1.62	0.48	0.05	0.12	
		Exp-9-B	2.2	5.74	1.94	0.48	0.05	0.11	
		Exp-9-C	3.2	8.96	1.83	0.48	0.04	0.11	
		Exp-9-D	17.1	57.40	2.77	0.75	0.10	0.13	
10 (NTA)	0.50	Exp-10-A	0.9	2.07	1.29	0.23	0.05	0.16	
		Exp-10-B	2.4	1.75	1.18	0.27	0.05	0.14	
		Exp-10-C	3.2	1.72	1.12	0.40	0.05	0.14	
		Exp-10-D	16.9	2.98	1.31	0.17	0.21	0.24	
		Exp-10-E	8.5	2.40	1.02	0.18	-	0.14	
		Inorganic average D_X (n = 21)		12.51 ± 16.52	1.75 ± 0.41	0.37 ± 0.18	0.04 ± 0.02	0.09 ± 0.04	
		Inorganic minimum		0.19	1.16	0.12	0.01	0.04	
		Inorganic maximum		57.40	2.77	0.75	0.10	0.14	

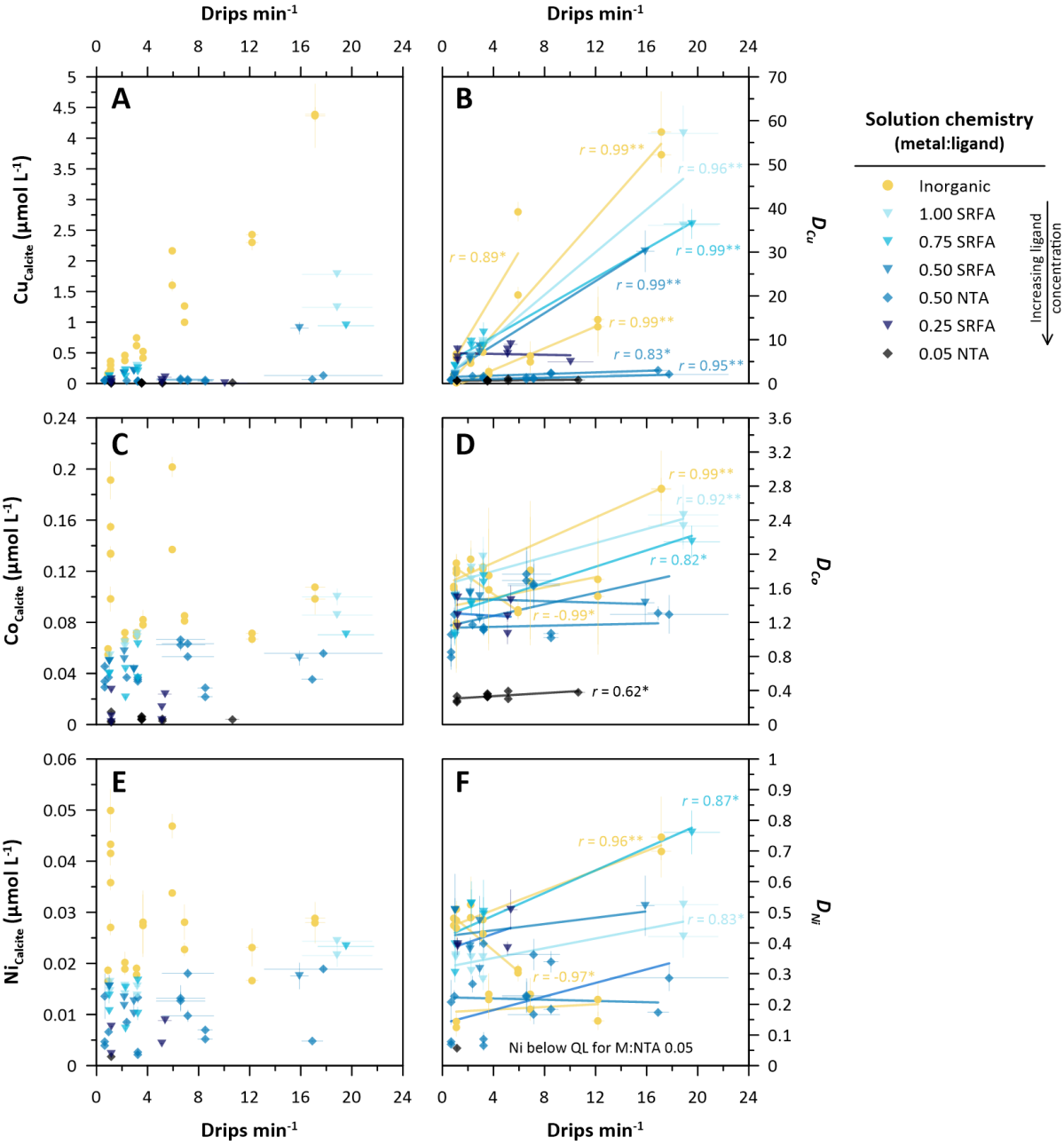

Figure 4.8: Incorporation of Cu, Co, and Ni as a function of drip rate in cave-analogue experiments. Concentrations of each metal are shown in the left column, while their respective apparent partition coefficient is shown in the right panels. Solid lines in the right column represent linear correlations between D_X and drip rate. For clarity, only correlation coefficients (r) are shown where a statistically significant correlation with $p < 0.05$ (denoted with *) was found. Two asterisks (**) are shown where $p < 0.001$. Correlation lines without annotation are shown as visual aids, but do not reflect significant relationships. Horizontal error bars denote 1σ of average drip rate measurements. Vertical error bars represent 1σ of triplicate measurements of concentrations (sub-plots **A**, **C**, and **E**), and the propagated uncertainties of D_X in sub-plots **B**, **D**, and **F**.

Generally, Ni and Co exhibited highly comparable behaviour across most experiments (Figure 4.8C to Figure 4.8F). D_{Ni} and D_{Co} increased slightly with drip rate in most experiments, but opposite and/or incoherent patterns were also observed. The concentrations of both Ni and Co in the precipitate were consistently highest in the three inorganic experiments (Figure 4.8C and Figure 4.8E), and decreased progressively with increasing ligand concentration. However, the differences in D_{Ni} and D_{Co} between inorganic and ligand experiments were less pronounced than for D_{Cu}, with apparently similar partitioning behaviour in absence and presence of SRFA and NTA. The only clear exception was Experiment 2 with an M:NTA of 0.05, in which the Ni concentration in the precipitate (and D_{Ni} by extension) was below quantification limits in most samples. D_{Co} were likewise severely reduced in Experiment 2 to ca. 0.33 $\pm$ 0.04, contrasting most other ligand experiments and all inorganic D_{Co}, which were consistently above 1 ($D_{Co\text{-}inorganic} \approx$ 1.16 to 2.77). Neither Co and Ni concentrations, nor their respective partition coefficients exhibited a clear relationship with $R_{acc\text{-}norm}$ in most experiments (Figures 9C and 9F), with possible exceptions of Experiment 9 and 6 (Figure 4.9D).

Alkaline earth metals

Across all experiments, central partition coefficients of Mg and Sr varied between 0.01 and 0.70, and 0.04 and 0.28, respectively (Figure 4.10B and Figure 4.10D). An overall higher variability was observed in presence of ligands compared to respective inorganic values of D_{Mg} (0.04 $\pm$ 0.02) and D_{Sr} (0.09 $\pm$ 0.04). In contrast to the effect on transition metals, the addition of ligands resulted in consistently higher partition coefficients of Mg and Sr (but always $<$1), reflecting behaviour closer to that of Ca. The highest values of D_{Sr} and lowest Sr concentrations in the precipitate corresponded to an M:SRFA of 0.25 (Experiment 3). The highest D_{Mg} was observed in the same experiment, while several sub-samples had Mg concentrations below instrumental detection. There was no distinct correlation between Mg or Sr with $R_{acc\text{-}norm}$, both in terms of concentrations and partitioning (Supplementary Figure 4.S5).

Metal systematics in precipitates from natural caves

Transition metals

In natural systems, the assessment of transition metal partitioning was challenged by the typically very low native metal concentrations in dripwaters (see Figure 4.4), particularly in the case of Co. Additionally, low growth rates prevented effective sampling of watch glasses in most Aotearoa New Zealand caves, yielding insufficient masses of $CaCO_3$. As a result, a limited number of estimates of D_X with acceptable confidence were achievable from these sites. In contrast, glasses deployed in Ulupaka Cave collected large amounts of precipitate that typically allowed for multiple sub-samples and the collection of abundant material. The magnitude and variability of D_{Ni} in and D_{Cu} in natural precipitates differed considerably from the cave-analogue experiments (Figure 4.11A and Figure 4.11E). D_{Ni} exhibited the overall largest

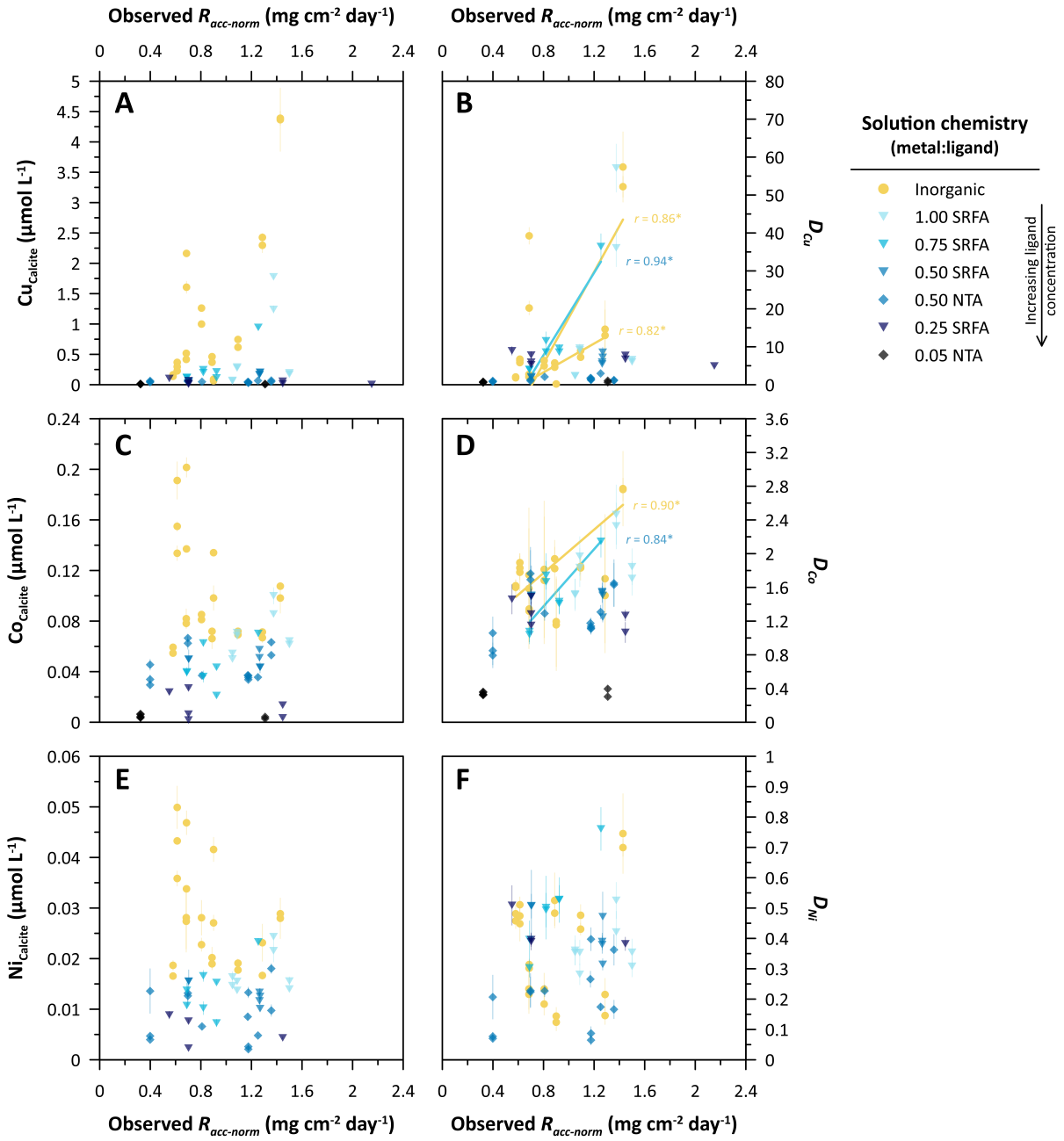

Figure 4.9: Incorporation of Cu, Co, and Ni into calcite as a function of growth rate in cave-analogue experiments. Solid lines represent statistically significant ($p < 0.05$) linear correlations between D_X and the empirical normalised accumulation rate.

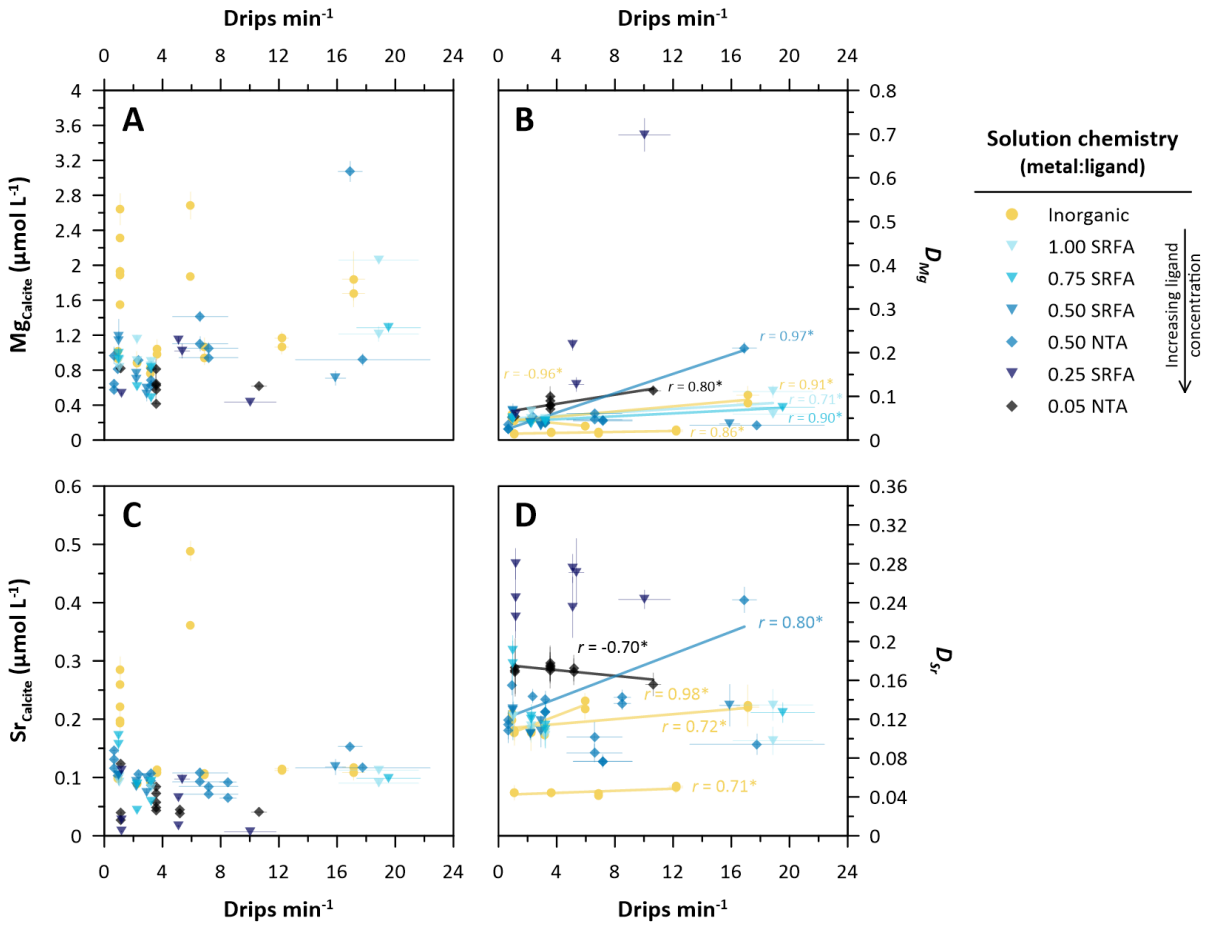

Figure 4.10: Incorporation of Mg and Sr as a function of drip rate in cave-analogue experiments. Concentrations of each metal are shown in the left column, while their respective apparent partition coefficient is shown in the right panels. Solid lines in the right column represent linear correlations between D_X and drip rate. For clarity, only lines and correlation coefficients (r) are shown where a statistically significant correlation with $p < 0.05$ (denoted with *) was found. Horizontal error bars denote 1σ of average drip rate measurements. Vertical error bars represent 1σ of triplicate measurements of concentrations (sub-plots **A**, and **C**), and the propagated uncertainties of D_X in sub-plots **B** and **D**.

range of values between <0.01 and 32.67 (4.13 ± 6.09, n = 114), while D_{Cu} varied between <0.01 and 12.35 (1.84 ± 1.88, n = 137). D_{Ni} and D_{Cu} of <0.01 were exclusively found in Majumba Cave, and indeed only few samples from this location yielded values exceeding 0.01. D_{Co} varied between <0.01 and 24.19 with an average of 1.89 ± 4.23 (n = 57), but estimates could only be achieved for samples from Anapala Cave and Ulupaka Cave. There were no distinct relationships between transition metal inclusion and drip rate or growth metrics.

Alkaline earth metals

Compared to the transition metals, the variation in D_{Mg} (0.05 ± 0.05, n = 183) and D_{Sr} (0.15 ± 0.31, n = 183) was limited among glasses and surficial precipitate samples from natural caves, with total ranges in D_{Mg} and D_{Sr} of 0.01 to 0.45 and 0.04 to 3.75, respectively. Their averages were thereby highly consistent with those obtained under inorganic conditions. Surficial precipitate samples accounted for most of the much higher values for both D_{Mg} and D_{Sr}, but for most of the dataset there was little difference in derived coefficients between the two sampling techniques (Supplementary Figure 4.S6). D_{Ba} measurements were altogether more variable (0.52 ± 1.53, n = 165), coinciding with generally low concentrations in dripwaters (on average ca. 0.01 µmol L^{-1}), including several samples with contents below quantification limits. While on average <1, the observed range included several considerably higher estimates with D_{Ba} in the order of 3 – 18. Growth rate effects on partitioning of the three metals were not evident.

4.4 Discussion

The analysis of trace elements in speleothems and dripwaters is gaining increasing importance for the study of past climates and environments (Fairchild & Treble, 2009; Warken et al., 2018; Ronay et al., 2019), but often rests on statistically derived and potentially ambiguous links between elemental concentrations and environmental drivers. To improve our mechanistic understanding of the incorporation pathways of selected trace elements into speleothems, and thus their reliability as palaeoenvironmental proxies, ten cave-analogue experiments were carried out to provide new insights on trace metal incorporation in presence of organic matter. Specifically, crystal growth experiments set out to test the hypothesis of a drip rate dependency of transition metals in stalagmites due to the kinetic decay of OMCs. These data were integrated with comparable datasets collected from natural caves, and finally compiled with previously reported estimates of partition coefficients to collate the current state of knowledge.

To identify the likely driving mechanisms of metal partitioning in calcite growth studies and ultimately speleothems, it is necessary to acknowledge the complex interplay of several potential controlling factors. In cave-analogue experiments as presented herein, the primary variables of solution chemistry (including concentration of metals and organic ligands, calcite saturation index, temperature, equilibrium speciation) and ambient atmospheric properties (*e.g.*,

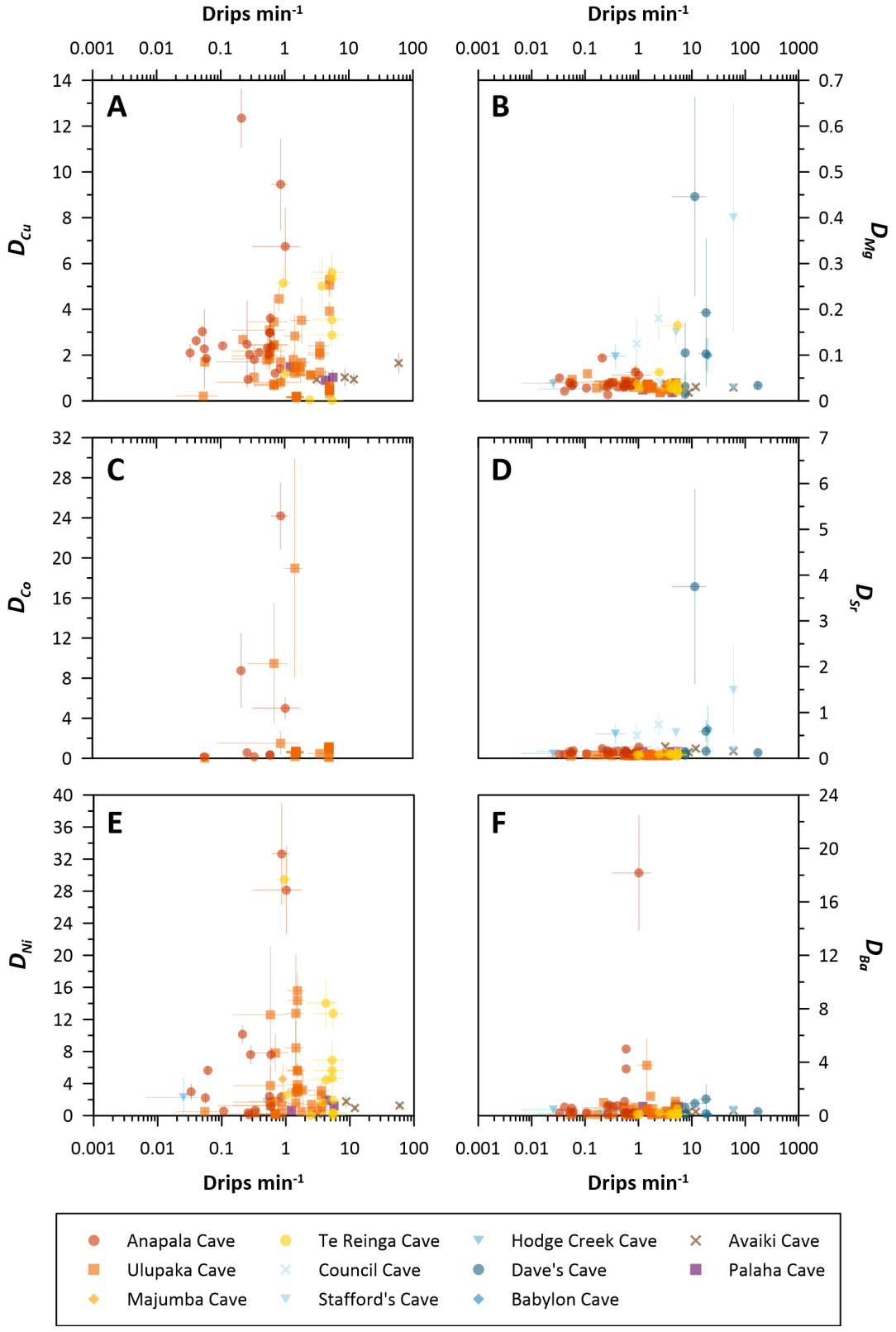

Figure 4.11: In-cave apparent metal partition coefficients as a function of drip rate. Drip rates are the averages of individual measurements during each visit (error bar presents their standard deviation, 1σ). Where drip loggers were deployed, their median drip rate is used instead. Note that drip rate is expressed on a logarithmic scale.

temperature, pCO_2, relative humidity) can largely be constrained. These solution and atmospheric properties are intrinsically linked in the open system of a cave environment or cave-analogue experimental enclosure, and become determinant for fundamental crystal qualities, such as mineralogy (Frisia et al., 2002), growth rate (Baker et al., 1998), and physical characteristics (*e.g.*, crystal habit and fabric; Frisia et al., 2000). Growth properties are further affected by the drip or flow rate (*e.g.*, Riechelmann et al., 2014), which may be hydrologically driven in natural settings, or be controlled in experiments. For this study, the key variables altered were the ligand composition and concentration (between experiments) and drip rate (within experiments), while other solution and atmospheric properties were kept consistent.

4.4.1 Growth properties of experimental and natural $CaCO_3$ precipitates

Relationships between growth metrics and drip rate

To test the hypothesis of a kinetically driven supply of trace metals to stalagmites, cave-analogue carbonate precipitation experiments were conducted with variable drip intervals as the principle independent variable of interest. While drip rate presents a key monitored parameter in cave systems that is often closely linked to karst hydrology, its confounded relationship with growth rate presents a pervasive challenge in studying respective effects on the chemistry of precipitates. Depending on various factors, including dripwater Ca content, pH, atmospheric pCO_2, and temperature, carbonate growth may be positively (*e.g.*, Banner et al., 2007), negatively (*e.g.*, Pu et al., 2016), or hardly at all (*e.g.*, Genty et al., 2001) related to the drip interval. In natural cave systems, the direction and degree of covariance between drip and growth rates may further vary over time (*e.g.*, seasonally; B. Cai et al., 2011), depending on dripwater and cave atmospheric properties that collectively determine the carbonate saturation state of the solution. In controlled experiments, more consistent correlations specific to the generated experimental conditions are achievable. However, these are consequently only representative of certain natural settings. Another important consideration is that crystal growth is enhanced by evaporation, which can increase accumulation rates unnoticed, and favour the formation of aragonite if significant (Frisia et al., 2002; Ryang & Sim, 2019). In the experiments, a relative humidity of $>$90% was maintained to simulate typical humid cave environments with minimal evaporation rates, although the latter were not quantifiable.

The theoretical precipitation rate calculated for cave-analogue experiments was overall linearly related with observed total accumulation rates (r = 0.46, p = 0.003, n = 40), and an improvement of this relationship was evident with the introduction of funnels for enhanced degassing (r = 0.74, $p < 0.0001$, n = 29, including Experiments 4 to 10 only; Figure 4.6B). While principally in good agreement, observed precipitation rates were in many cases considerably higher than predicted. These discrepancies are presumably attributable to the uncertainty in key variables, including the final solution pH, alkalinity, and possible evaporative effects. Simi-

larly, it is plausible that inconsistencies in the image-based characterisation of crystal coverage on glasses contribute to uncertainty in normalised accumulation rates. In this regard, neither growth metric accounts for temporal and crystal-level spatial variations in precipitation rates, for instance related to time required for initial nucleation, or variable size of growth surfaces (see approach in Day et al. (2021) for surface area normalised growth rates). R_{prec} was calculated as an independent and theoretical measure of growth, and to facilitate comparisons with other studies. However, given the direct mathematical dependency of R_{prec} on drip intervals (Equation 4.3 to Equation 4.5), it cannot be used to constrain the relationship between drip rate and crystal development. For this purpose, observed growth metrics were therefore used instead.

Across all cave-analogue experiments presented here, $R_{acc\text{-}norm}$ was overall weakly positively correlated with drip rate (r = 0.49, p = 0.004 for all experiments, n = 34; Figure 4.6A). The strength of this relationship varied considerably between individual experiments ($0.38 < r < 0.94$), with no discernible effect of added funnels (r = 0.54, p = 0.005, n = 26). Accumulation rates similarly increased with drip rate in natural precipitates (Figure 4.6C), although it is noted that these relationships are based on limited and discontinuous information only. Nonetheless, the nature of these relationships presents an analytical predicament in the context of this study, since the varying degree of near-collinearity prevents a statistically robust isolation of the effect of either drip rate or growth rate on the elemental distribution. Therefore, elemental data are considered with respect to both variables, but no attempt of statistically delineating the two was made.

Implications of precipitation rates for crystal development

The rate of precipitation is an important factor determining crystal properties and is often greatly accelerated in experimental studies compared to natural caves. Experimentally produced samples may thus be overall biased towards faster precipitation rates, both in terms of physical and chemical properties. Importantly, this may include an increase in impurities (*e.g.*, Tesoriero & Pankow, 1996) and effects on elemental partitioning (*e.g.*, Sr and Co; Lorens, 1981). Constraining potential effects of experimental growth rates, however, is complicated by the fact that different drip rates under the same atmospheric and initial solution compositions inevitably result in variable precipitation rates. This is due to varying times for thin-film degassing to occur, which in these cases is the determinant variable. Thus, it is not possible to achieve consistent growth rates across a given experiment, and any potential impacts of precipitation rate need to be considered. In this study, experimental accumulation rates ranged from 0.02 to 1.22 mg cm^{-2} day^{-1} (for comparison normalised to the total watch glass area) and closely resembled those in the cave-analogue study of EL-Shenawy et al. (2020), who also used watch glasses to collect precipitate (*e.g.*, 0.03 – 0.24 mg cm^{-2} day^{-1}). Interestingly, Froeschmann (2018) observed far slower growth in the order of 10^{-11} to 10^{-9} mg cm^{-2} day^{-1}, despite using a very similar experimental setup. Compared to accumulation rates observed in four caves (between ca. 0.0003 and 0.2000 mg cm^{-2} day^{-1}), cave-analogue growth was thereby on average ca. 10-fold faster. This magnitude of difference was also found in relation to other in-cave accu-

mulation rates, for instance those compiled in Riechelmann et al. (2014) (ca. 0.0001 – 0.2500 mg cm^{-2} day^{-1}, seven caves in Germany and Morocco). For Ulupaka Cave (ca. 0.08 $\pm$ 0.06 mg cm^{-2} day^{-1} on average), experimental growth was indeed highly representative, however, in turn exceeded rates of slow-depositing caves (*e.g.*, Dave's Cave) by a factor of 100 or higher. Despite this, stark systematic differences in crystal morphology between settings of variable growth rate and/or solution chemistry were not observed (compare for instance Riechelmann et al. (2014) in relation to Mg concentration). Therefore, potential morphological constraints on metal inclusion are assumed to be negligible in this study.

Implications of organic ligands for crystal development

Visual inspection by SEM suggested that precipitates grown under cave-analogue conditions were predominantly composed of calcite, while quantitative methods to characterise the mineralogy (*e.g.*, x-ray powder diffraction) were not feasible due to the low total mass of material obtained. Inorganic experiments generally produced euhedral crystals with pronounced positive and negative rhombohedral forms, and very well-defined edges (Figure 4.5A-C). The addition of NTA and SRFA to growth solutions in organic experiments resulted in noticeable increases in the abundance of growth defects, including incomplete growth, high density of steps, kinks, and pits, and an increased proportion of amorphous crystals (Figure 4.5D-O). Generally, the quality of crystal development appeared to scale with the concentration of ligands in solution, consistent with the observations by (Pearson et al., 2020). However, the naturally derived SRFA was found to cause an overall more pronounced impact on growth quality compared to the synthetic NTA of lower molecular weight and structural complexity. The observed disruptive effects of organic impurities on carbonate crystal habit and growth kinetics are well-documented (*e.g.*, Sangwal, 1996; Hoch et al., 2000). Impurities (*i.e.*, compounds other than those involved in crystallisation; Sangwal, 1996) in solution are typically adsorbed to $CaCO_3$ crystal growth surfaces through electrostatic bonding to anionic functional groups (COO^-, OH^-) and Ca^{2+} (Chalmin et al., 2012). The introduction of foreign species to active crystal growth surfaces may impact step propagation and morphology, for instance by diverting, retarding, or blocking subsequent attachments of ions of the crystallising compounds (Davis et al., 2004; Sangwal, 1996; Yoreo et al., 2009; Xu & Higgins, 2011). Arguably, the observed enhancement of kinks and step density in presence of adsorbed DOM may in fact generate positive feedback, given the increased surface roughness that could favour the inclusion of further impurities (Pearson et al., 2020). Smaller dissolved compounds may in turn be directly included in the crystal lattice, as implied by the experimental findings of Phillips et al. (2016) assessing small P-containing organic molecules. In contrast, larger, particulate substances may occupy space between crystal assemblages through direct entrapment (Belli et al., 2017; Borsato et al., 2021; Frisia et al., 2018) or as fluid inclusions (Ramseyer et al., 1997), rather than adsorbing to sites on individual crystals.

Clearly, the variable crystallisation pathways and NOM inclusion mechanisms warrant a critical control for the partitioning of trace elements, particularly regarding metals that are strongly

complexed by organic ligands. To a degree, disruptions to the classical monomer-to-monomer growth mechanism (Sunagawa, 1999) observed in ideal systems are expected to be the norm in natural cave precipitates, given the omnipresence of organic and inorganic impurities, and variable solution chemistries. Consequently, non-classical crystallisation pathways co-occur (Zhu et al., 2016; Frisia et al., 2022), including crystallisation via amorphous precursor phases and the development of impurity-bearing mesocrystals through nanoparticle/nanocrystal attachment and aggregation (Frisia et al., 2022; Cölfen & Antonietti, 2005). Importantly, excessive impurities can result in the formation of mineral phases other than calcite, such as vaterite (cf. Lindeman et al., 2022), or prevent crystal development altogether. For the latter to occur, Pearson et al. (2020) estimated a threshold DOM concentration in the growth solution of ca. 10 – 15 mg C L^{-1}, although considerably lower (*e.g.*, Inskeep & Bloom, 1986; Hoch et al., 2000) and higher (*e.g.*, Falini et al., 2009) limits were also observed under variable experimental conditions. However, either case of severe growth disruption would complicate the study of metal partitioning, which can be sensitive to crystal morphology and may differ vastly between carbonate polymorphs or other phases (*e.g.*, Y. Wang & Xu, 2001; Mavromatis et al., 2018).

With consideration of inhibitive effects of organic matter, the M:L ratios in experiments were selected based on observations of natural dripwaters (Hartland et al., 2014, and estimates in this study using DOC as indicative measures of ligand concentration) and speciation modelling, aiming to represent a range of natural cave waters. Nonetheless, precipitates formed at a M:SRFA of 0.25 (Experiment 3, corresponding to ca. 2 ppm SRFA in solution) showed evidence of significant growth disruptions, likely attributable to poisoning by the high organic content. The latter was embodied by a slight yellow colouration of material deposited on respective watch glasses (Supplementary Figure 4.S3), suggesting a high proportion of co-precipitated SRFA. Optical microscopy and SEM further depicted a high fraction of amorphous and anhedral material produced in this experiment, which potentially includes vaterite and/or crystallites nucleated from colloidal organics (Figure 4.5). It is reasonable to assume that the latter occurs in the organic experiments, given the absence of euhedral calcite seed crystals available for nucleation. Except for Experiment 3, however, crystals grown under cave-analogue conditions in presence of ligands strongly resembled those collected from watch glasses deployed in natural caves (cf. Figure 4.7). Natural precipitates possessed abundant growth defects as expected due to the diverse composition of infiltrating water, but still exhibited dominant rhombohedral cleavage with well-defined crystal faces.

Nonetheless, it is noteworthy that a truly accurate reproduction of speleothem microstructural properties is unlikely achieved with crystals grown on watch glasses (or other artificial surfaces) in either experimental or indeed natural cave settings. This is largely due to the inherent “template” effect of the substrate on crystal development (*e.g.*, Astilleros et al., 2010), which can only to an extent be approximated by sandblasting (*i.e.*, producing surface roughness, *e.g.*, this study, Mickler et al., 2006; Lindeman et al., 2022), using artificial substrate (*e.g.*, glass fibre, Wiedner et al., 2008), or pre-seeding the collection surface with pure calcite crystals (*e.g.*, Day & Henderson, 2011; Reynard et al., 2011). This caveat is amplified by relatively short growth periods (limited by practicality) and/or low growth rates of precipitate

in carbonate farming studies, which typically prevent the development of mature fabric prior to sample collection. Pre-seeding glass substrates likely yields the most representative crystal development by aiding to overcome the initial thermodynamic barriers of solid precipitation (Steefel & Cappellen, 1990; Stumm & Morgan, 1996; Y.-P. Lin & Singer, 2005), however, also complicates the estimation of partition coefficients. Considering the added uncertainty to D_X calculations due to the need to accurately correct for the seed material composition and mass, simple sandblasting used in this study was seen as a suitable compromise.

The analysis of spatial patterns in elemental partitioning in this study was limited to the comparison of sub-samples from different locations across watch glasses (discussed in detail in Section 4.4.2), with partition coefficients calculated for the integrated sample material from obtained powders. Potential spatial variability of elements within carbonate microstructures are thus not resolved. Regardless, it is important to recognise that the partitioning and spatial distribution of some elements is critically sensitive to the specific carbonate structures, which can change frequently over the growth period of a speleothem. Prominent examples are given by Mg and Sr, which appear to preferentially occupy acute and obtuse step sites, respectively (Frisia et al., 2022). This has the implication of sectoral zoning of certain elements (Paquette & Reeder, 1995; Reeder et al., 1997), which is in cases manifest in lateral (*i.e.*, parallel to growth layers) variability in their concentrations. This may in turn inadvertently introduce noise to speleothem-derived elemental records (Sliwinski & Stoll, 2021). However, the resolution of such patterns on micron to sub-micron scale requires sophisticated analytical techniques (*e.g.*, synchrotron-based x-ray fluorescence or secondary-ion mass spectrometry), to which the farmed carbonate material is not amenable. In contrast to precipitate collected from watch glasses, surficial scrapings of actively growing speleothems retain some information on the *in-situ* structural properties of the carbonate. Samples obtained from Hodge Creek Cave (Aotearoa New Zealand), for instance, include a high proportion of elongate, well-defined calcite assemblages (*e.g.*, Figure 4.7G), which resemble morphologies observed in compact and/or porous columnar fabrics.

4.4.2 Metal incorporation in cave-analogue experimental calcite

The study of metal partitioning into experimental calcite in absence and presence of organic ligands based on a set of ten cave-analogue experiments yielded findings largely at odds with the hypothesised patterns. Specifically, a dominant signal that OMC dissociation kinetics at the water-carbonate interface drive metal concentrations in $CaCO_3$ precipitates was not evident in any of the experiments. Under the assumption of an overriding supply of labile metals by OMC decay, slower and faster drip rates (*i.e.*, longer and shorter OMC residence time in the thin-film, respectively) were predicted to result in higher and lower metal concentrations in precipitated $CaCO_3$, respectively. Instead, higher drip rates resulted in higher transition metal concentrations (*i.e.*, implying enhanced partitioning) in the calcite across most experiments, whereas the predicted trends were absent.

Inclusion of Cu

The pattern of enhanced distribution into calcite with higher drip rate was particularly pronounced for Cu, for which the apparent partition coefficient D_{Cu} (derived from centres of watch glasses) was strongly linearly correlated with drip rate under most solution chemistries (Figure 4.8B). Under inorganic conditions, the experiments yielded partition coefficients between 0.2 and 57.4 (Experiments 1, 4, and 9), reflecting a total of 21 aliquots. These estimates include values both substantially lower and higher than those reported in previous empirical and theoretical studies. For instance, the inorganic cave-analogue experiment of Lindeman et al. (2022) indicated a maximal D_{Cu} of ca. 44 using essentially the same experimental setup and solution properties as this study. This value of D_{Cu} represents the first precipitate collected in the drip solution impact zone, and thus should be comparable with precipitates collected from watch glass centres herein. The high magnitude of D_{Cu} is also in good agreement with theoretical estimates based on thermodynamic principles. For instance, Rimstidt et al. (1998) predict a D_{Cu} of 80.15, whereas Y. Wang and Xu (2001) arrive at a theoretical D_{Cu} of ca. 37.2 based on datasets compiled by Rimstidt et al. (1998) and Curti (1997).

The substantial variability in the magnitude of D_{Cu} in both experimental and theoretical studies is likely attributable to the very strong partitioning of Cu, which challenges an accurate empirical quantification. Specifically, any degree of prior calcite precipitation (PCP; adopting terminology from a karst context) would readily remove Cu from solution and alter the final observed D_{Cu}. By example of the GeoMic experimental setup, this may occur due to initial incomplete dissolution or re-precipitation in the reservoir vessel due to pH changes, or deposition inside the tubing, pipette tips, and funnels. PCP was clearly significant in the open-system Experiment 4, and respective D_{Cu} estimates were consistently lower than those obtained in the controlled Experiments 1 and 9. This susceptibility of Cu to PCP was highlighted under cave-analogue conditions by Lindeman et al. (2022), who noted that the initial aqueous Cu^{2+} in two inorganic drip solutions was reduced to below instrumental detection after $<$15% PCP in one experiment. Indeed, a second experiment in the same study yielded no quantifiable Cu in precipitates inside the experimental enclosure. In practice, however, it is difficult to entirely confine $CaCO_3$ deposition to the desired substrate due to the required delicate balance of reservoir saturation and precipitation of material. Ensuring only a minimal undersaturation of the reservoir is particularly important in experiments where CO_2 degassing drives calcite precipitation (opposed to mixing two feeding solutions), because sufficient supersaturation needs to be achieved within the short time window constrained by drip intervals. Thus, a strongly undersaturated reservoir would likely prevent PCP but could in turn lead to insufficient deposition of $CaCO_3$. The strong impact of PCP implies that higher estimates of D_{Cu} likely present more accurate approximations, and the good agreement between estimates from Experiments 1 and 9 support $D_{Cu} > 50$ (Rimstidt et al., 1998). However, it stands to reason that a far higher resolution of both sample collection and analysis may be required for more accurate quantifications, considering that D_{Cu} may even vary at the micron to sub-micron scale as the result of different crystallisation pathways (Frisia et al., 2022) and spatial distribution (Wasylenki et al., 2005).

The near-linear relationships between D_{Cu} and drip rate observed in most experiments are interpreted as a direct result of the extreme affinity of Cu for calcite. Effectively, any labile Cu^{2+} supplied by drips is readily incorporated into the crystal phase well within the residence time of water at the mineral surface. For realistic drip rates in an inorganic system, the available Cu for inclusion into calcite is thus effectively limited merely by its supply, and may behave non-linearly only at extremely fast drip rates (likely $\gg$1 drip s^{-1}) where the rate of replenishment of labile Cu exceeds that of partitioning. Such limits to sorption of Cu to calcite surfaces both in absence and presence of NOM has been observed in the co-precipitation study of Lee et al. (2005), depicting that an apparent equilibrium after an initially rapid uptake of Cu uptake is reached. The authors further note that the overall uptake of Cu scales inversely with NOM concentration in solution, and Cu partitioning into calcite ceases earlier when complexation of Cu occurs. Accordingly, the addition of ligands (here, SRFA and NTA) and an increase in their concentration relative to that of complexed metals (*i.e.*, decreasing M:L) caused an increasing complexation of Cu as expected. The higher proportion of Cu-L complexes in turn resulted in the slope and strength of the linear correlation between D_{Cu} and drip rate to progressively decrease (Figure 4.8B). At an M:L (SRFA) of 0.25, the slope is essentially 0, and no relation between drip rate and D_{Cu} is evident. However, the value of D_{Cu} remained consistently positive at ca. 7, indicating that a considerable fraction of Cu was nonetheless incorporated into the calcite irrespective of drip rate. In experiments with NTA added to the reservoir, however, Cu partitioning was highly reduced ($D_{Cu} < 3$), and no distinguishable response to drip rate was observed even at the lower M:NTA ratio of 0.5.

To better constrain the distinct behaviour of Cu, as well as Ni and Co, the partitioning of transition metals in presence of organic ligands is discussed in more detail with regard of likely incorporation mechanisms in Section 4.4.2.

Inclusion of Ni and Co

The inorganic partition coefficients of Ni and Co were estimated here as ca. 0.4 $\pm$ 0.2 and 1.8 $\pm$ 0.4, respectively, based on the results of all three inorganic experiments. Compared to D_{Cu}, estimates of both D_{Ni} and D_{Co} varied far less in magnitude between individual experiments, as well as between drip rates. These values were highly consistent with those reported by Lindeman et al. (2022) (D_{Ni} = 1.1 $\pm$ 0.1 and D_{Co} = 4.4 $\pm$ 0.3), Rimstidt et al. (1998) (D_{Co} = 2.51), and Magiera (2018) (D_{Co} = 2.26 at 20 °C). Considering the modelled D_{Ni} and D_{Co} of ca. 3.47 and 9.33, respectively (Y. Wang & Xu, 2001), the empirical estimates were in turn comparably low while also indicating a contrasting phase preference for Ni than predicted. The positive relationships of D_{Ni} and D_{Co} with drip rate in some experiments suggest that metal supply may also govern the inclusion of these elements to an extent, although the slopes of these correlations are much smaller than those for D_{Cu} due to weaker partitioning. Negative correlations and lack of covariance of D_{Ni} and D_{Co} with drip rate were also evident (including the inorganic Experiment 1), suggesting that the supposed effects of drip supply of metals can readily be masked by other processes.

While Lorens (1981) reported a negative relationship between D_{Co} and precipitation rate, a weak positive relation was observed when considering all experiments (Figure 4.9). Ni partitioning did not vary with growth metrics in this study, which in turn differed from a weak negative correlation between D_{Ni} and precipitation rate as observed by Lakshtanov and Stipp (2007). These discrepancies from calcite growth studies performed by solution mixing are not surprising, however, given the distinct variables and uncertainties of each experimental approach. Previously reported growth rate controls on D_{Ni} and D_{Co} are thus likely readily overprinted in this study by various confounding factors, including the complex relationship between drip interval and precipitation rate, kinetic processes during CO_2 degassing, and variable solution chemistries. The partition coefficients close to 1 imply that there is little preference of respective cations for either crystal or solution phase compared to Ca, which may be attributable to kinetic and/or thermodynamic properties in ideal systems (Y. Wang & Xu, 2001). This was supported by the comparably small differences in magnitude of D_{Co} and D_{Ni} between inorganic experiments, including the open-atmosphere Experiment 4. Importantly, this indicates that impacts of PCP on these metals are likely negligible, which in turn could prove valuable to help delineating PCP controls on other chemical proxies. Moreover, the low degree of differentiation between solution and crystal phases for Ni and Co arguably preconditions these metals with view to potentially utilising their concentrations in stalagmites to constrain past drip rates based on their kinetic release from OMCs (Hartland & Zitoun, 2018; Lindeman et al., 2022; Chapter 3).

Similarly to D_{Cu}, however, the overall positive response of D_{Ni} and D_{Co} to drip rate in presence of organic ligands contradicts a hypothesised inverse relationship between transition metal inclusion and thin-film residence time. Furthermore, the magnitudes of D_{Ni} and D_{Co} in SRFA experiments, as well as at an M:NTA of 0.5, were mostly within the range of inorganic estimates (Figure 4.8C and Figure 4.8E). The only clear effect of ligands on these metals was observed at the exaggerated M:NTA of 0.05, at which D_{Co} was substantially reduced to ca. 0.30, while Ni was almost entirely prevented from entering the crystal phase.

This outcome can presumably be attributed to the selection of ligands, which inadvertently created conditions at which only Cu was significantly complexed in SRFA experiments. However, the predicted equilibrium speciation of $<$2.2% Ni and $<$0.4% Co of bound to SRFA in the initial reservoir, respectively (Table 4.2), does not reflect a typical natural system. While the complexed fractions were considerably higher for NTA experiments (81.6% to 98.6% of Ni, and 27.4% to 84.9% of Co), it is possible that site competition with Cu, or effects of precipitation rate (although not observed) mask potential kinetic patterns. In either case, the presence of a ligand-driven dependence of Ni and Co inclusion in calcite remains inconclusive and requires further experimental investigation. A possible approach to reconcile this would be to either identify alternative ligands that possess very similar binding properties for all three metals, or to repeat selected experiments without including Cu in the initial solution.

Inclusion of Mg and Sr

Mg and Sr are the trace elements whose partitioning into calcite is best constrained and regularly exploited as means to assess prior calcite precipitation (Wassenburg et al., 2020; Tremaine & Froelich, 2013; Sinclair, 2011; Stoll et al., 2012). Previous estimates of D_{Mg} and D_{Sr} from laboratory and field-based studies are consistently below 1, indicating their cations' principal tendency to remain in solution relative to Ca as calcite is precipitated. This behaviour was also coherently evident in the cave-analogue experiments of this study, both in terms of overall magnitude, as well as in trends across individual glasses as a function of calcite deposition (see Section 4.4.2 for further discussion).

Inorganic experiments suggested values for D_{Mg} between 0.01 and 0.1 (average D_{Mg} = 0.04 $\pm$ 0.02), with moderate positive correlations of D_{Mg} with drip rate (Figure 4.10B), but not accumulation rate (Supplementary Figure 4.S5). The variations with drip rate had no apparent link to the solution chemistry (cf. transition metals), but are nonetheless noteworthy given that Mg in speleothems is not known to relate with drip interval. The magnitude of these estimates are in excellent agreement with published datasets, which vary between 0.01 (Day & Henderson, 2013) and ca. 0.06 (Gascoyne, 1983) around a commonly cited figure of $\approx$0.03 (Huang & Fairchild, 2001). In presence of SRFA and NTA, the inclusion of Mg was not systematically altered, but slightly reduced on average (organic D_{Mg} = 0.08 $\pm$ 0.10). However, this difference from inorganic estimates primarily arises from sub-samples of Experiments 2 and 3, representing the highest concentrations of NTA and SRFA, respectively. Interestingly, multiple calcite analyses in both experiments measured Mg concentrations below instrumental detection, while the values of D_{Mg} closer to 1 reflect atypically low Mg contents in the remaining samples (Figure 4.10A). Mg was not predicted to be complexed significantly by either ligand, however, suggesting that crystallographic modifications potentially prevent the substitution of Mg ions (*e.g.*, Chalmin et al., 2012).

At large, however, the experiments reiterate that Mg primarily exists in labile hydrated form or simple inorganic complexes (Table 4.2), thus rendering Mg partitioning comparably predictable. Even in light of known environmental and chemical controls on Mg partitioning, such as temperature (*e.g.*, Oomori et al., 1987; Gascoyne, 1983; Wassenburg et al., 2020), growth rate (*e.g.*, Gabitov et al., 2014), and solution Mg/Ca ratio (Mucci & Morse, 1983; constant in experiments herein), the associated variability across realistic scenarios and within a given cave setting can be expected to be marginal in most cases. For instance, the fitted relationship for datasets compiled in Wassenburg et al. (2020) suggests that D_{Mg} increases consistently but by less than 0.04 between 1 °C and 40 °C, varying from ca. 0.013 to 0.053. In this regard, any impact by brief temperature fluctuations ($\pm$1.5 °C) in some experiments presented herein should thus be minimal. Similarly, the negative correlation of D_{Mg} with growth as demonstrated by Gabitov et al. (2014) was observed over 5 orders in magnitude of growth rate ($D_{Mg} \approx$ 0.01 – 0.04), reflecting a far greater range in growth conditions than estimated here (Figure 4.6). Alkhatib et al. (2022) in turn found D_{Mg} (estimates of 0.01 – 0.15) to positively relate to precipitation rate (as well as temperature and Mg/Ca) over a range of ca. 0.1 to 10 mmol h^{-1}. This

implies that controls on Mg partitioning may indeed be more complex, however, vary within a relatively narrow window of magnitude. These dependencies on growth rate and temperature presumably contribute to the variability in D_{Mg} observed within and across experiments, but are largely indistinct and inconsequential within the context of this study.

The partitioning of Sr in inorganic solution chemistries was likewise well constrained with values of centrally derived D_{Sr} ranging from 0.04 to 0.14 (average D_{Sr} = 0.09 $\pm$ 0.04). Previous estimates suggest an average inorganic D_{Sr} in the order of 0.1 (*e.g.*, Huang & Fairchild, 2001; Gabitov & Watson, 2006), but values between 0.02 and 0.35 have been reported (Gabitov & Watson, 2006; Tesoriero & Pankow, 1996). In ligand experiments, D_{Sr} values were consistently slightly elevated (but $<$1) compared to inorganic estimates, reaching ca. 0.28 in Experiment 3 (Figure 4.10D). Given the general tendency of Sr to remain in solution upon calcite precipitation, the greater fraction of dissolved Sr at very high concentrations of SRFA is likely related to an incompatibility of Sr with organics in the precipitate. Sr is understood to effectively not interact with dissolved organics (Hartland et al., 2012), and the apparent exclusion of Sr from calcite in presence of SRFA (and NTA to a lesser extent) supports the notion of inhibitive effects of organic impurities on Sr partitioning (*e.g.*, Baker et al., 1999; Frisia et al., 2003). For instance, elemental and luminescence maps depict contrasting spatial distributions of Sr and organic associations within speleothem fabrics (*e.g.*, Baker et al., 2000; Faraji et al., 2021; Ortega et al., 2005; Sliwinski & Stoll, 2021). In Experiment 3, a high degree of co-precipitation of SRFA (discussed further in Section 4.4.2) may thus block sites suitable for Sr (*e.g.*, obtuse steps) or otherwise prevent Sr from partitioning through modifications of crystal growth (Chalmin et al., 2012). In either case, the increased fractions of both Sr and Mg in solution are not expected to be due to organic complexation (cf. Ni, Cu, Co), as supported by the predicted equilibrium speciation suggesting that less $<$0.1% of Mg and Sr were bound to SRFA (Table 4.2).

In some experiments, particularly under inorganic conditions, Sr partitioning was moderately but incoherently correlated with drip rate (Figure 4.10D). However, D_{Sr} did not vary with observed ($r < 0.01$, $p \approx 1$, n = 69; with $R_{acc\text{-}norm}$) or modelled precipitation rates (r = 0.15, p = 0.2, n = 77; with R_{prec}). The lack of correlation with growth metrics is interesting considering various evidence suggesting otherwise (Gabitov & Watson, 2006; Lorens, 1981; Nehrke et al., 2007). For instance, Gabitov et al. (2014) demonstrated through beaker calcite growth experiments and previously published datasets that D_{Sr} may range between ca. 0.02 and 0.36, increasing with growth rate across ca. 7 orders of magnitude (between 10^{-5} and 100 nm s^{-1}). While pH has also more recently been suggested as a potential superordinate control on D_{Sr} due to the precipitation rate's predicted dependency on carbonate speciation (Jia et al., 2022), Sr concentrations have also been positively related to growth rates in speleothems (*e.g.*, estimated based on layer thickness; Belli et al., 2017; Borsato et al., 2007; Sliwinski et al., 2022). The cave-analogue study of Day and Henderson (2013) in turn did not depict any statistically significant relationship of D_{Sr} with growth, suggesting that the sampling strategy applied in their study and herein may not achieve the resolution required to distinguish growth effects on D_{Sr}. Additionally, the range in growth rates in this study (observed and modelled) was comparably small and potentially insufficient to affect elemental partitioning. Finally, it is also plausible

that the calculated growth metrics inadequately reflect the true precipitation rate, and may be more appropriately approximated using a revised approach. If this were the case, the positive correlations between D_{Sr} and drip rate observed in some experiments may indeed reflect precipitation rate effects gone unnoticed in this study.

Implications of progressive calcite precipitation for trace metal inclusion

In addition to partition coefficients derived by sub-sampling the centre (location of drip impact) of each watch glass, sub-samples were collected along transects from the glass centre to its edge provided sufficient material was present. This strategy allowed for the additional assessment of metal partitioning and spatial distribution across regions of growth coverage, while also providing a means of reproduction of central partition coefficients. With increasing distance from the central drip impact, dispersion and degassing of the thin water film results in the progressive deposition of carbonate. As a result of different partitioning tendencies relative to Ca, elemental concentrations in both the residual solution and precipitate thus continuously evolve in a Rayleigh distillation as a function of the previously deposited carbonate. Equally important for isotopic fractionation, the concept of PCP presents a key process in natural karst systems for the interpretation of speleothem trace element proxies (*e.g.*, Fairchild, Smith, et al., 2006; Sinclair, 2011; Stoll et al., 2012).

Despite the limited distance for solution flow on watch glasses (up to 4.5 cm) compared to glass plates used in most studies specifically investigating effects of PCP (*e.g.*, M. Hansen et al., 2013), the expected trends according to empirical partition coefficients were nonetheless evident. In line with its very high inorganic partition coefficient, Cu was rapidly removed from the solution as calcite precipitated, resulting in a stark drop in Cu concentrations (expressed as relative decrease in D_{Cu}) in calcite away from the first deposit on the glass (Figure 4.12A). The same general pattern was also observed in the presence of SRFA and NTA at low to moderate concentrations. This fast progressive uptake of Cu resembles that in inorganic experiments of Lindeman et al. (2022), who observed that Cu was virtually completely removed from solution following calcite precipitation over a flow distance of $<$17 cm (estimated to reflect ca. 15% PCP). At high NTA concentrations, however, D_{Cu} changed inconsistently across glasses including increasing aqueous Cu fractions, indicative of ligand binding inhibiting the ready partitioning of Cu. Similar but altogether more distinct spatial patterns were observed for the inclusion of Co. Notably, Co progressively distributed into the precipitate in absence of ligands, consistent with an inorganic $D_X > 1$ (Figure 4.12C). Conversely, the opposite trend was evident in most ligand experiments, illustrating that even limited predicted complexation of Co significantly altered its partitioning efficiency. According to its partition coefficients closer to 1, spatial trends were largely absent for Ni (Figure 4.12E). This applied to both inorganic as well as most ligand solution chemistries, although few greater excursions in the magnitude of D_{Ni} across watch glasses occurred at an M:NTA of 0.50.

Interestingly, Mg partitioning was comparably inconsistent between glasses and experiments, showing both relative increases and decreases in D_{Mg} in response to calcite precipi-

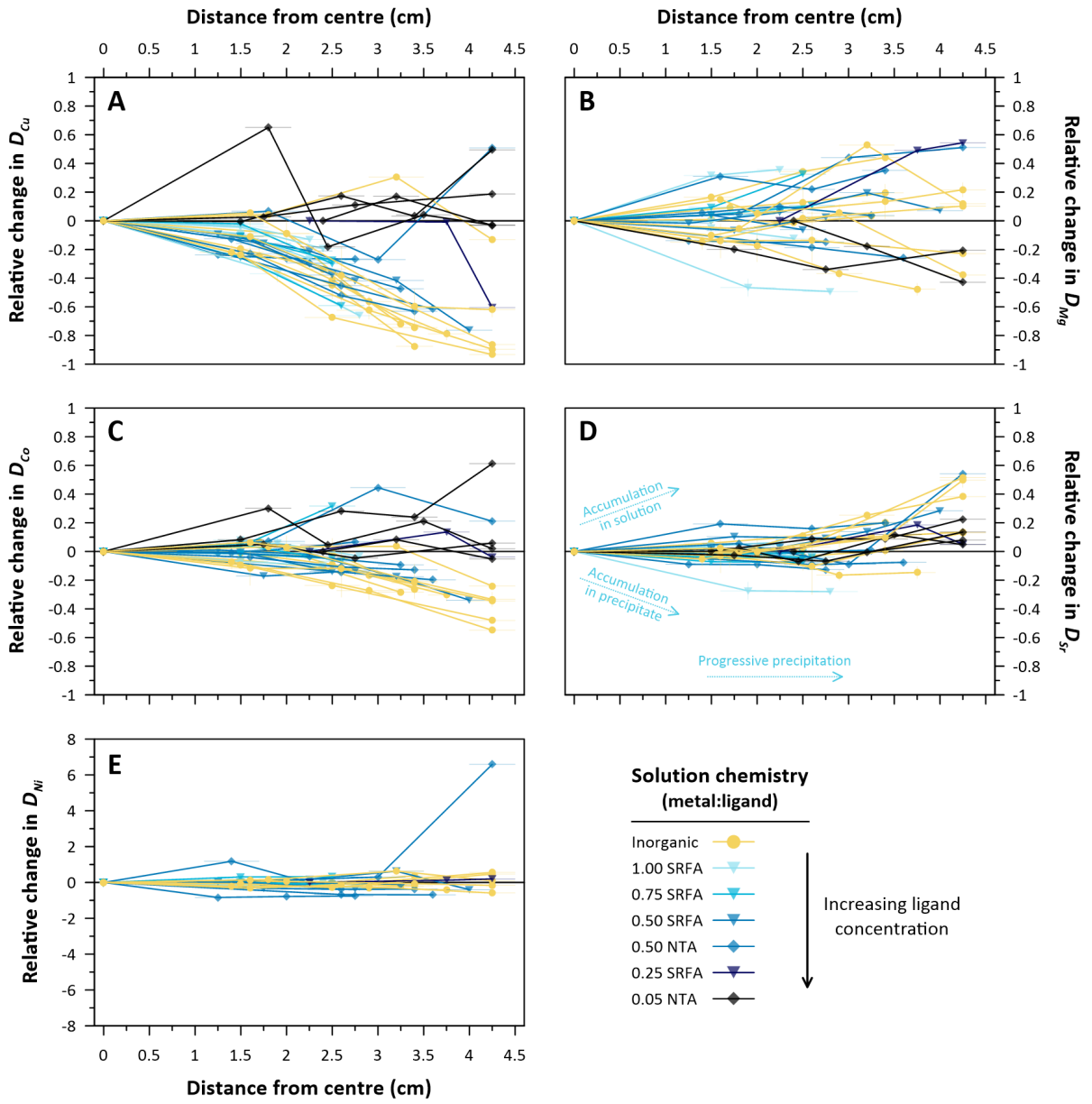

Figure 4.12: Relative change in metal partition coefficients across watch glasses from cave-analogue experiments. Data are included for all glasses from which at least three sub-samples at different distances from the centre were collected. Values of D_X are expressed as the fractional change relative to the central partition coefficient (*i.e.*, at 0 cm distance). Metals with $D_X > 1$ are predicted to accumulate in the precipitate with progressive calcite deposition, whereas a $D_X < 1$ results in an apparent reduction in metal inclusion. Distances from the glass centre were measured from the centre of sub-sampled areas, with horizontal error bars reflecting their extent (width) along the same line of measure (see Figure 4.3 for sub-sampling strategy). Vertical error bars are not included for clarity. Note that scale on the y-axis in sub-plot **E** is adjusted.

tation, seemingly irrespective of solution chemistry (Figure 4.12B). Given that D_{Mg} was consistently <1 in all experiments, the lack of a systematic accumulation in calcite was therefore surprising. In contrast, a monotonous relative increase of D_{Sr} with distance from the drip impact was clearly observable on almost all watch glasses (Figure 4.12D). Nonetheless, some discrepancies from predicted patterns are to be expected, given that the solution flow across the glasses can vary, and may not directly relate with solution residence time. Sub-samples taken from the glass edges present a special case due to surface tension often resulting in drip solution to pool, rather than immediately dripping off the side of the glass. These samples thus reflect prolonged thin-film residence times that are not directly determined by drip rate. However, this provides an additional opportunity to test the assumption of a time-dependent increase of transition metal concentrations due to decaying OMCs. Indeed, there was some evidence of increasing concentrations of Ni and Co in samples collected from the edges of glasses, which stood in contrast to their largely coherent concentrations across glasses under inorganic conditions. These observations are at odds with a sole control by PCP, and may imply that a release of transition metals from more stable OMCs is observable where long residence times permit this. However, this interpretation is based on a limited number of watch glasses where this trend is observed. Further, the same pattern was not observed for Cu, implying suggesting either that OMC decay was negligible or in case of Cu likely overprinted by the strong crystal affinity.

Possible pathways of metal inclusion in cave-analogue experiments

The experimental findings seemingly contradict the reasoning that transition metal cations are released from organic complexes as a function of thin-film residence time during calcite deposition, and should thus increasingly distribute into calcite at slower drip rates. However, the discrepancies between expected and observed trends do not altogether dismiss the OMC decay hypothesis, convincing support for which has been put forward by Hartland and Zitoun (2018), and most recently by Sliwinski et al. (2022). Rather, the observed patterns may be reconciled by closer inspection of elemental and ligand characteristics.

Specifically, the pronounced positive relationship of Cu inclusion with drip rate at variable SRFA concentrations is interpreted to be the product of intrinsic properties of both Cu and SRFA. Cu exhibits an acute thermodynamically founded preference for the crystal phase over solution (Y. Wang & Xu, 2001), and thus distributes readily into calcite upon precipitation. In these experiments, the supply of Cu for inclusion in calcite is dictated almost exclusively by drip rate, thus resulting in an essentially linear increase of Cu concentration in calcite as a function of the drip interval (Figure 4.8B). On the other hand, an increase in the SRFA concentration noticeably yields a higher retention of Cu in OMCs as evident by the overall decrease in D_{Cu} values (Lee et al., 2005; Lindeman et al., 2022), and a reduction in the slope of their relationship with drip rate. This consists with an increased fraction of total Cu predicted to be complexed by SRFA (Table 4.2), in turn limiting freely available or labile Cu. However, SRFA appears to simultaneously co-precipitate with calcite efficiently enough for the relation between drip rate

and D_{Cu} not to diverge from positive linearity for M:SRFA ratios of 1.00 to 0.50. Only at very high concentrations of SRFA (M:SRFA = 0.25), the effect of Cu supply as a function of drip rate is muted, and partitioning of Cu occurs at consistent rates apparently in line with SRFA (Figure 4.8B).

In the flow-channel cave-analogue experiments of Lindeman et al. (2022), D_{SRFA} were estimated between ca. 0.34 and 0.44 at an M:SRFA $\approx$ 0.0025 corresponding to an SRFA concentration of ca. 20 mg L^{-1}, which inadvertently resulted in severe disruptions of calcite development. Although not as pronounced, crystal growth was also impacted in Experiment 3 in this study (M:SRFA = 0.25), with yellow/brown colouration of the precipitate alluding to a significant co-precipitation of SRFA (Supplementary Figure 4.S3). Presumably because of this, the experiment yielded an insufficient mass of precipitate in discrete sub-samples to carry out corresponding elemental and fluorescence analyses, and D_{SRFA} could not be quantified. For the remaining SRFA experiments, D_{SRFA} ranged between ca. 0.03 and 0.23 based on sub-samples taken from within ca. 2 cm of the drip impact on glasses (n = 11). These data represent M:SRFA of 0.5, 0.75, and 1.0, depicting slightly lower partitioning of SRFA than observed by Lindeman et al. (2022). This is expected given the lower absolute concentrations of SRFA in the parent solutions (Pearson et al., 2020).

The magnitude of D_{SRFA} is principally in good agreement with the adsorption of Suwannee River Humic Acid (SRHA) to calcite observed by Lee et al. (2005) in co-precipitation experiments (ca. 20 – 30% of SRHA adsorbed), but also NOM partitioning in natural karst systems. For instance, Hartland et al. (2014) derived values for D_{NOM} of ca. 0.03 in the hyperalkaline Poole's Cavern (UK; pH $\approx$ 11), which is very similar in magnitude to the low estimates of D_{SRFA} in this study. A higher tendency of DOM to co-precipitate with carbonate was observed by Pearson et al. (2020), who estimated D_{DOM} for dripwater and speleothem couplets from several Aotearoa New Zealand caves to be in the order of ca. 2 – 3. Indeed, a tendency of DOM to accumulate in speleothems to some degree is also supported by experimental observations on the inclusion of humic and fulvic substances in calcite growth studies (*e.g.*, Hoch et al., 2000; Pearson et al., 2020). It therefore stands to reason that ternary complexation is likely to occur in most settings to a certain extent, and may present a dominant metal inclusion pathway where M-NOM complexes are stable.

Relating D_X of transition metals to D_{SRFA} yielded $D_{SRFA\text{-}M}$ (Equation 4.6 and Equation 4.7) of ca. 10 – 356 for Cu, 7 – 42 for Co, and 1 – 15 for Ni. These values above 1 imply that transition metals were consistently included at higher rates than SRFA, which is principally in agreement with a combination of their preferential inorganic partitioning into calcite (for Cu and Co; D_{Ni} was estimated $<$1), as well as inclusion of metals via adsorption of SRFA-M complexes without prior dissociation (Lee et al., 2005). The magnitude of these coefficients is similar to in-cave $D_{NOM\text{-}M}$ estimated by Hartland et al. (2014), who report values of ca. 105 and 146 for Ni and Cu, respectively. In their study, $D_{NOM\text{-}Co}$ was estimated to be around 1, implying enhanced stability of complexed Co likely due to the atypically high pH regime of Poole's Cavern.

$D_{SRFA\text{-}Cu} > 1$ (ca. 9.7 on average) were also observed by Lindeman et al. (2022), who

attribute the apparent increase in Cu:SRFA between solution and crystal phases to the decay of SRFA-Cu complexes. However, the same interpretation is not supported by observations in this study because of the dominant positive relation between D_{Cu} and drip rate, which opposes the expected direction of Cu distribution if assumed to be driven by the decay of SRFA-Cu. Indeed, considering the additional variable of drip rate (and precipitation rate by extension), the clear positive relationship between $D_{SRFA\text{-}Cu}$ and drip rate (Figure 4.13) supports the inference that the drip rate control on Cu partitioning outweighs any contribution to D_{Cu} by direct capture of SRFA-Cu complexes at these SRFA concentrations. Although lacking quantitative information on ligand partitioning in Experiment 3, the absence of covariance between D_{Cu} and drip rate in turn suggests that ternary complexation was the primary contributor to Cu inclusion at an M:SRFA of 0.25. In fact, the average D_{Cu} of ca. 6.76 $\pm$ 1.47 is higher than that calculated at low drip rates ($<$6 drips min^{-1}) for most other experiments. This implies that ternary complexation may in fact amplify Cu inclusion in this case, apparently overriding the limits on supply and partitioning of Cu imposed by drip rate under other solution chemistries.

For Ni and Co, incorporation appeared to be largely independent of SRFA, with the absence of pronounced trends presumably arising from an insufficient proportion of complexed Ni and Co species to represent typical dripwater conditions. Indeed, Ni-SRFA and Co-SRFA were predicted to account for up to 0.3% and 2.2% of total Ni and Co, respectively, only marginally exceeding the proportion of organic Mg and Sr complexes (Table 4.2). Considering that both Ni and Co are in fact primarily found complexed by organic ligands in natural aqueous systems (*e.g.*, Qian et al., 1998; Chapter 3), this predicted equilibrium speciation appears counterintuitive. This implies either that SRFA is not adequately parameterised in the user-defined Nica-Donnan model for DOM, or that the extract indeed does not efficiently complex Ni and Co.

To represent more hydrophilic ligands, the well-characterised synthetic polymer NTA was selected given its lack of aromatic structures. In contrast to SRFA, adsorption to calcite was thus predicted to be minimal and favourable for the attempt to isolate kinetic signals of OMC decay. Although not quantifiable by standard methods, the inclusion of NTA into calcite indeed appeared to be negligible as indicated by the virtual absence of Ni in precipitates at an M:NTA of 0.05. Even at exaggerated concentrations of NTA, M-NTA complexes thus remained in solution rather than co-precipitate with calcite. This experiment primarily served to demonstrate the case of extremely strong complexation in a stalagmite-type growth setting, where partitioning is virtually halted. These findings are consistent with the flowstone-type setup of Lindeman et al. (2022), who observed strong metal retention in solution at an M:NTA of ca. 0.25. Nonetheless, this scenario is not unrealistic for natural systems, where a residual fraction of metals is typically retained by highly stable complexes (M. Collins et al., 2010; Chapter 3). In hyperalkaline cave waters, in particular, the stabilising effect of pH on OMCs is likely to considerably limit transition metal partitioning into speleothems compared to typical karst water chemistries with pH $\approx$ 8 (Hartland et al., 2011), while also potentially fostering inclusion of some metals via ternary complexation (*e.g.*, for Co; Hartland et al., 2014).

A lower degree of complexation was simulated in experiments with an M:NTA of 0.50, which

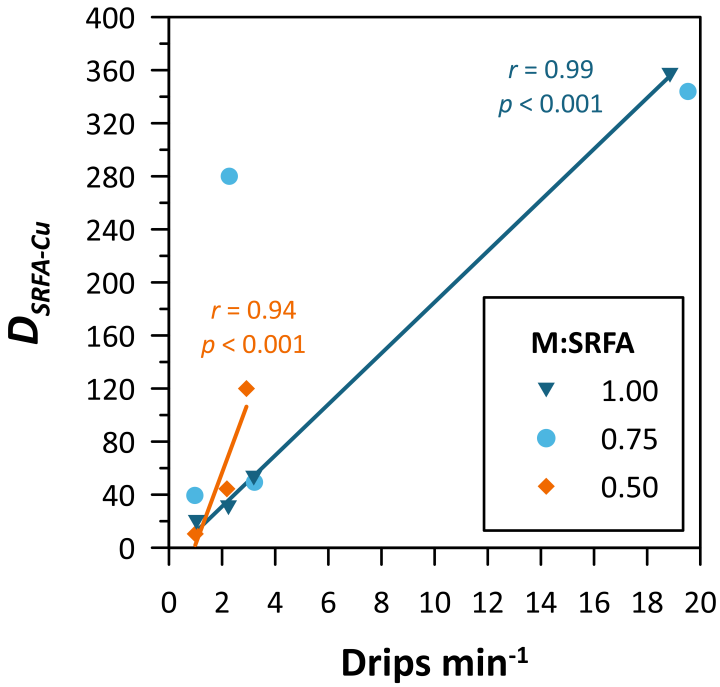

Figure 4.13: Relationship between drip rate and $D_{SRFA-Cu}$ in cave-analogue experiments. Solid lines represent significant linear correlations for experiments with M:SRFA 1.00 and 0.50. Each datapoint stems from a single sub-sample from near the centre of watch glasses.

presents a halving of the relative concentration of NTA compared to the experiment conducted by Lindeman et al. (2022). These experimental conditions were repeated due to small technical problems in Experiment 5, and to include a greater range of drip rates for the same complexing regime. The concentration of NTA was considered sufficiently low to prevent excessive complexation, while ensuring a representative fraction of >80% of Ni and Cu initially bound to NTA (Table 4.2). It is noted that due to distinct binding affinities, the modelled fraction of Co-NTA was considerably lower (ca. 27% of total Co). Regardless, none of the metals exhibited behaviour indicative of a significant influence of OMC decay (Figure 4.8). Although apparent partition coefficients of each metal were noticeably reduced with increasing NTA concentration relative to their inorganic estimates, inverse relationships between D_X and drip rate were consistently absent. Rather, both D_{Cu} and D_{Co} (to a lesser extent) increased with drip rate as under inorganic conditions. Interestingly, the incorporation of Co and Ni was similar in Experiment 5 (r = 0.66, p = 0.4, n = 8; although lacking statistical significance), despite the substantially different predicted speciation at an M:NTA of 0.50. Nonetheless, this subtle covariation between in D_{Co} and D_{Ni} alludes to the possibility that the observed partitioning merely involves the already labile metal fractions, with minimal contribution from M-NTA complexes by either dissociation or adsorption. This would explain the seemingly inorganic behaviour of Cu and Co with respect to drip rate, but operating at overall lower metal concentrations.

These observations differ from the findings of Salmanzadeh et al. (in prep.), who utilised diffusive-gradients in thin-film (DGT) sediment probes (see Li et al. (2018) for an overview of DGT devices) to constrain OMC decay kinetics in synthetic and natural dripwater solutions. By dripping an experimental solution with an M:NTA of 0.50 onto an inclined DGT sediment

probe, the authors observed a considerable accumulation of Ni in the probe's Chelex-100 ion exchange resin (serving as a competing ligand) at greater solution residence times. Attributable to the progressive dissociation of Ni-NTA complexes with time, this approach provides precedent for NTA as a suitable ligand in this study.

However, a likely reconciliation of the different behaviour is that metals possess dissimilar binding affinities for Chelex-100 and calcite, complicating the prediction of metal binding to either phase. For instance, calcite likely presents a weaker competition for Ni and Co than Chelex-100, considering that both elements show a limited affinity (*i.e.*, $D_X \approx 1$) for the crystal phase compared to Cu. Given that complex dissociation is driven by competition (*e.g.*, Davranche et al., 2008), OMC decay may be hampered if calcite presents a less stable sink for a given metal (although evidence for inner-sphere complexation of transition metals in calcite principally suggests otherwise; *e.g.*, Elzinga et al., 2006; Zachara et al., 1991). For NOM-Cu complexes on the other hand, calcite surfaces appear sufficiently competitive to invoke Cu uptake even in presence of high NOM concentrations (Lee et al., 2005). Importantly, the same study demonstrated a preference of Cu for carbonate surfaces (opposed to attaching to or via co-precipitated NOM), thereby potentially facilitating NOM-Cu decay, provided that NOM-Cu decay rates are sufficiently high. Nonetheless, it is noted that these observations are based on adsorption experiments using carbonate seeds, and thus do not reflect additional kinetic constraints posed by active precipitation.

To reveal kinetic signals under cave-analogue conditions, it may be necessary to further increase the M:NTA (*e.g.*, to 1.00 or above) at the compromise of lowering the proportion of complexed metals below that observed in natural caves. Moreover, alternative ligands with overall weaker binding characteristics may also be required to altogether facilitate a greater release of metals for calcite deposition. Regardless of the selection of ligands, however, the active precipitation of calcite under cave-analogue conditions may in itself present a critical caveat possibly precluding the observation of OMC kinetic signals. For instance, it is plausible that the kinetic release of transition metals from OMCs is exceedingly disproportionate to the rapid consumption of cations during calcite precipitation, rendering subtle variations in thin-film residence time inconsequential. A significant reduction in calcite precipitation rates (*e.g.*, by raising pCO_2) may thus additionally be required to enhance the uptake of kinetically-supplied cations relative to cations from the available metal pool, although this approach is limited by feasible experimental time-frames.

4.4.3 In-cave trace metal systematics and synthesis of published datasets

Metal incorporation in natural cave precipitates

In addition to material produced in cave-analogue experiments, modern precipitates and associated dripwaters were sampled from several caves to survey apparent partition coefficients in

various natural cave environments. Carbonate collection on watch glasses analogous to the experimental setups is only feasible where natural growth rates permit the collection of sufficient material for analysis within ca. 6 – 9 months. In most Aotearoa New Zealand caves, however, growth rates are far lower than required to achieve this. An additional critical challenge in obtaining in-cave partition coefficients for elements, such as first-row transition metals, is their typically very low native concentration in dripwaters. Frequently, the concentrations of Ni, Co, or Cu were close to or below instrumental detection limits, rendering their quantification challenging. In fact, in several caves only a limited number of D_{Ni} and D_{Cu} were quantifiable, while robust measurements of Co in both dripwater and precipitate were only possible in the Niuean caves of Anapala and Ulupaka. For most drip points it was possible to obtain coupled carbonate and solution samples for direct comparisons, but extremely slow drip rates prevented this at some locations (especially in Majumba Cave). In these cases, averaged values representative of the chamber dripwater chemistry were used to derive partition coefficients.

To complement data from 31 successful watch glass deployments from five caves, microsampling (*i.e.*, surficial scrapings) of actively forming speleothems was used to provide additional denotative datasets on elemental partitioning. This approach does not provide information on several important variables, such as growth and drip rate (bar spot observations), and the aqueous chemistry end-member (*i.e.*, $(X^{2+}/Ca^{2+})_{solution}$) to derive partition coefficients is only constrained by one or few water samples. Nonetheless, these datasets proved insightful and at large coherent with expected patterns, while reflecting a wide range of native cave water elemental compositions (Figure 4.4).

Considering that the solution chemistry of nearby drip points within a cave chamber was similar in most cases, the modern deposits lend themselves to further test the hypothesis of OMC decay controlling transition metal concentrations. In relation to *in-situ* and logger measurements of drip rate, apparent partition coefficients for Ni (4.13 $\pm$ 6.09, n = 114), Cu (1.84 $\pm$ 1.88, n = 137), and Co (1.89 $\pm$ 4.23, n = 57) varied substantially, but seemingly non-systematically in the natural caves (Figure 4.11). Likewise, a clear, systematic trend in any partition coefficient with growth metrics was absent (Figure 4.9), possibly attributable to large uncertainties and necessary assumptions around growth rate estimates (Section 4.2.5). This wide range in D_X values is in line with the notion of dominating ligand interactions, although some of this variability undoubtedly arises from the far lower native concentrations and overall greater analytical uncertainties, as well as possible detrital contamination. In contrast, apparent partition coefficients derived for Mg (0.05 $\pm$ 0.05, n = 183) and Sr (0.15 $\pm$ 0.31, n = 183) varied comparably little across the entire dataset, and were with few exceptions consistently close to the range observed in cave-analogue experiments and previous studies (Figure 4.11). The alkaline earth metal Ba (not included in experimental solutions) is also frequently used in speleothem science alongside Mg and Sr to assess prior calcite precipitation and pCO_2 dynamics (*e.g.*, Johnson et al., 2006; Stoll et al., 2012), and showed similar, albeit less consistent patterns to these elements. With an average apparent D_{Ba} of ca. 0.52 $\pm$ 1.53 (n = 165), these estimates were comparable to inorganic estimates of ca. 0.16 (Magiera, 2018; measured at 20 °C) and measurements from other natural systems in the order of 0.3 – 0.5 (Z. Wang et al.,

2021). However, far lower values for inorganic D_{Ba} have also been reported (*e.g.*, $D_{Ba} < 0.009$; Mavromatis et al., 2018). Although the vast majority of derived D_{Ba} in this study were below 1 in line with all comparable studies and the expected behaviour of an incompatible cation (Böttcher & Dietzel, 2010), $D_{Ba} > 1$ were observed in a few samples, presumably attributable to localised contamination. In principle, however, Ba is interpreted to present an additional example to Sr and Mg of relatively predictable behaviour in natural abiogenic carbonate systems as supported by many speleothem records (Stoll et al., 2012), where its distribution is primarily governed by thermodynamic constraints as a function of precipitation rate (*e.g.*, Mavromatis et al., 2018) and temperature (*e.g.*, Magiera, 2018).

For Mg and Sr (with exceptions), sub-samples across watch glasses exhibited the expected trends of both metals remaining in solution as calcite was precipitated (Figure 4.14). In fact, patterns of Mg distribution are more distinct in these natural samples than in SRFA and NTA experiments. This implies that co-precipitation of these ligands may indeed have adverse effects on crystal morphology and subsequently Mg partitioning, which in turn appears not to be the case in natural cave deposits. Considering this, some of the counterintuitive variability in Sr and Mg incorporation observed in organic cave-analogue experiments may thus be attributable to ligand properties, but likely not representative for typical in-cave conditions. In agreement with their overall more variable inclusion patterns, transition metals and Ba spatial estimates of D_X were less distinct, although generally coherent within a given glass for Ba. The more complex behaviour of Cu and Ni (insufficient data for Co) is likely reflective of evolving equilibrium constraints (especially M:L) and competitive effects, which clearly preclude simple predictions.

Differences in metal behaviour were also evident between study locations, as well as between growth media (to a lesser extent). Dripwaters from Anapala Cave were strongly enriched in many elements compared to the other cave locations. The concentration of Mg, for instance, was approximately 10 times higher than that observed in Te Reinga Cave, while Sr was up to 10 times more concentrated than in Dave's Cave. The high concentrations also translated into elevated Mg/Ca (320 – 1500 mmol mol^{-1}) and Sr/Ca ratios (2.8 – 8.0 mmol mol^{-1}), reflecting the partly dolomitised Niuean bedrock (Aharon et al., 2006; Tremaine et al., 2016). While the three transition metals were found at similar concentrations to the other caves, Ni and Co appeared to be particularly strongly related here. A comparison to typical seawater ratios suggests that sea spray likely presents the primary source of elements such as Na and S in Anapala Cave with possible contributions to other locations (Figure 4.4E and Figure 4.4F; see Chapter 5 for detailed discussion), whereas the ratios of Mg and Sr indicate that bedrock and/or soil inputs are determinant but distinct for each cave setting (Figure 4.4D, bedrock and soil ratios were not plotted for clarity). Apparent partition coefficients of the transition metals ranged considerably in magnitude within Anapala Cave but were moderately correlated between each of the three metals (linear correlations with $0.68 < r < 0.79$). Most likely, this apparently synchronous inclusion of transition metals across various drip points is attributable to direct capture of OMCs, indicating that ternary complexation may be the dominant pathway for transition metals in this cave. Both D_{Mg} and D_{Sr} were in turn highly consistent across watch glass precipitates and surficial scrapings, with relative standard deviations in D_X of less than 40% and 30%, respectively.

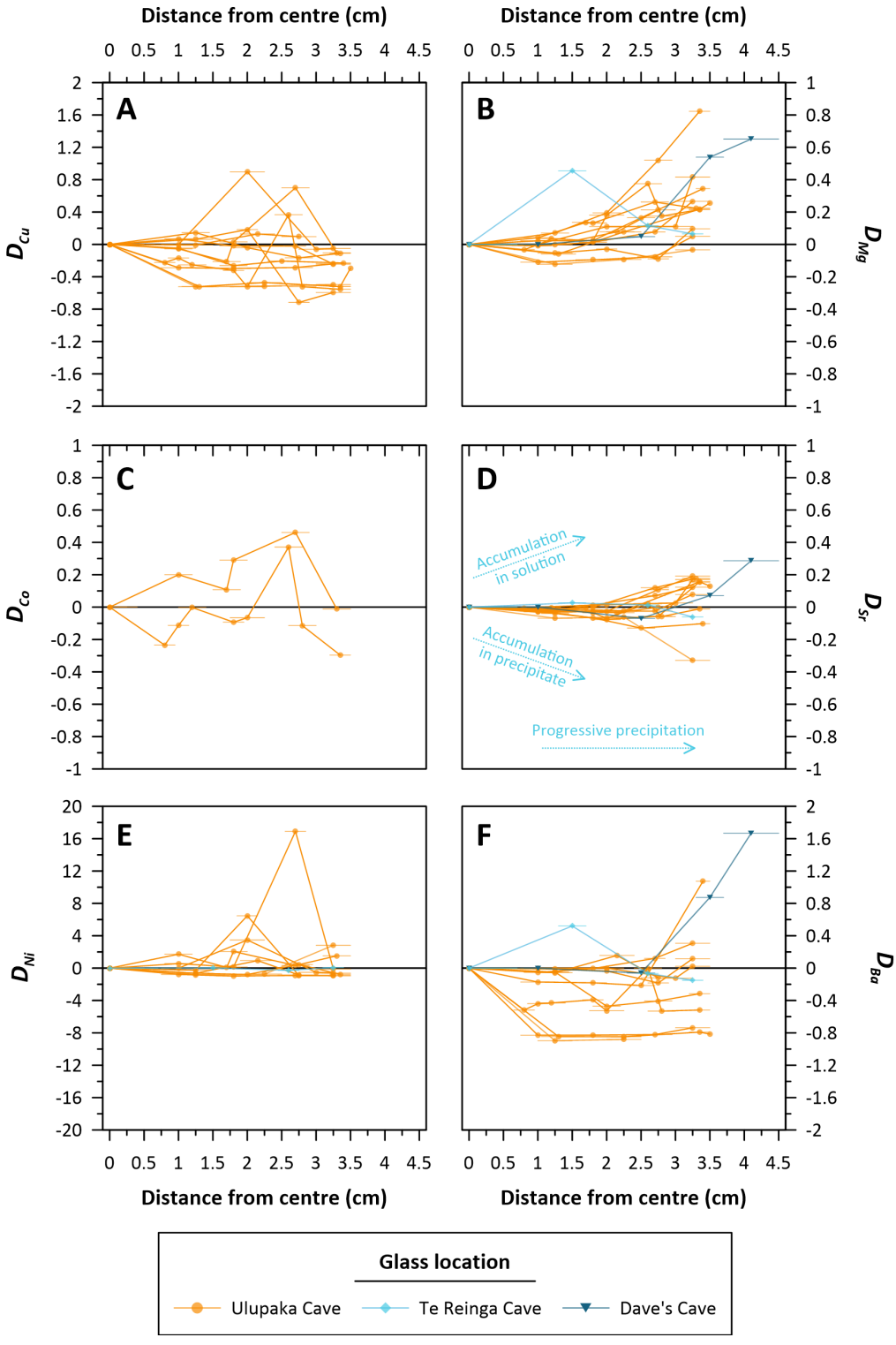

Figure 4.14: Relative changes in metal partition coefficients across watch glasses deployed in natural caves. Data are included for all glasses from which at least three sub-samples at different distances from the centre were collected. Values of D_X are expressed as the fractional change relative to the central partition coefficient (*i.e.*, at 0 cm distance). Metals with $D_X > 1$ are predicted to accumulate in the precipitate with progressive calcite deposition, whereas a $D_X < 1$ results in an apparent reduction in metal inclusion. Co concentrations were frequently below quantification limits (<0.1 µg L^{-1}). Distances from the glass centre were measured from the centre of sub-sampled areas, with horizontal error bars reflecting their extent (width) along the same line of measure (see Figure 4.3 for sub-sampling strategy). Vertical error bars are not included for clarity. Note that scales on the y-axis vary between sub-plots.

These small deviations are particularly noteworthy in light of the substantial range in dripwater chemistry between drip points and sampling periods. The pronounced range in aqueous Mg and Sr concentrations appears effectively muted in the corresponding precipitate, which may more so reflect the average dripwater composition.

Compared to Anapala Cave, dripwaters from Ulupaka Cave were considerably less enriched in most major and trace elements (Figure 4.4). As the location with most watch glass deployments and fastest growth, Ulupaka Cave yielded the most comprehensive compilation of partition coefficients. Within the cave, D_X estimates for Ni, Cu, and Co were comparably coherent for each respective element, with only few sub-samples deviating considerably. A distinct relationship between metal inclusion and drip rate was not evident, and neither did partition coefficients vary with theoretical or observed growth metrics. However, the strongest partitioning of Ni was consistently observed for the lowest M:L in Ulupaka Cave, which is principally in line with an increased stability of OMCs at higher relative ligand concentrations (*e.g.*, Aiken et al., 2011; Figure 4.15). A similar but weaker trend was observed for D_{Cu}, whereas too few values for D_{Co} were reliable for interpretation. However, these possible indications of expected trends were absent or indistinguishable in other datasets, and thus remain largely unsubstantiated.

Dripwater from Te Reinga Cave, situated beneath pine forestry and emergent native vegetation, had amongst the highest DOC (up to ca. 8.1 mg L^{-1}) content in some samples, although most were far lower at around 3.2 mg L^{-1}. Apparent partition coefficients of Ni and Cu were with few exceptions greater than 1 with averages of ca. 5.7 and 3.2, respectively, likely indicating a considerable degree of OMC adsorption. These relatively high rates of Ni and Cu inclusion in turn stood in contrast to those observed in Majumba Cave. Noticeably, all but two water-carbonate couplets from Majumba Cave exhibited D_{Ni} (0.03 ± 0.07) and D_{Cu} (0.006 ± 0.006) far lower than in any other cave, despite similar aqueous concentrations. Although the DOC was not distinctly higher than in other caves (ca. 3.9 mg L^{-1}), it is perceivable that the ligand composition favoured particularly strong complexation of transition metals assessed here. Majumba Cave presents an interesting case due to its location underneath grazed pastureland, which may contribute considerably to the dripwater chemistry. Possibly related to the latter, concentrations of S (ca. 419 µmol L^{-1}) and K (ca. 58 µmol L^{-1}), for instance, were respectively ca. five and two times higher on average than in most other caves (bar Anapala Cave). Concentrations of S also showed a noticeably different relationship with Na (Figure 4F) compared to the similarly enriched dripwaters of Anapala Cave. However, while the elemental abundances in Anapala Cave are explained by a significant and almost exclusive sea spray contribution, the S and Na anomalies in Majumba Cave appear almost entirely locally derived, presumably primarily from the soil.

Precipitates obtained through surficial scraping of speleothems in Dave's Cave included the by far highest values of D_{Mg} (up to 0.45) and D_{Sr} (up to 3.75), while those calculated from watch glasses likewise comprised some of the highest estimates for D_{Mg} (ca. 0.19). With an approximate average temperature of 4 °C, Dave's Cave is the coldest study location considered in this study. However, neither D_{Mg} nor D_{Sr} are explained by temperature based on empirical relationships established by Wassenburg et al. (2020), which predict reduced partitioning of both

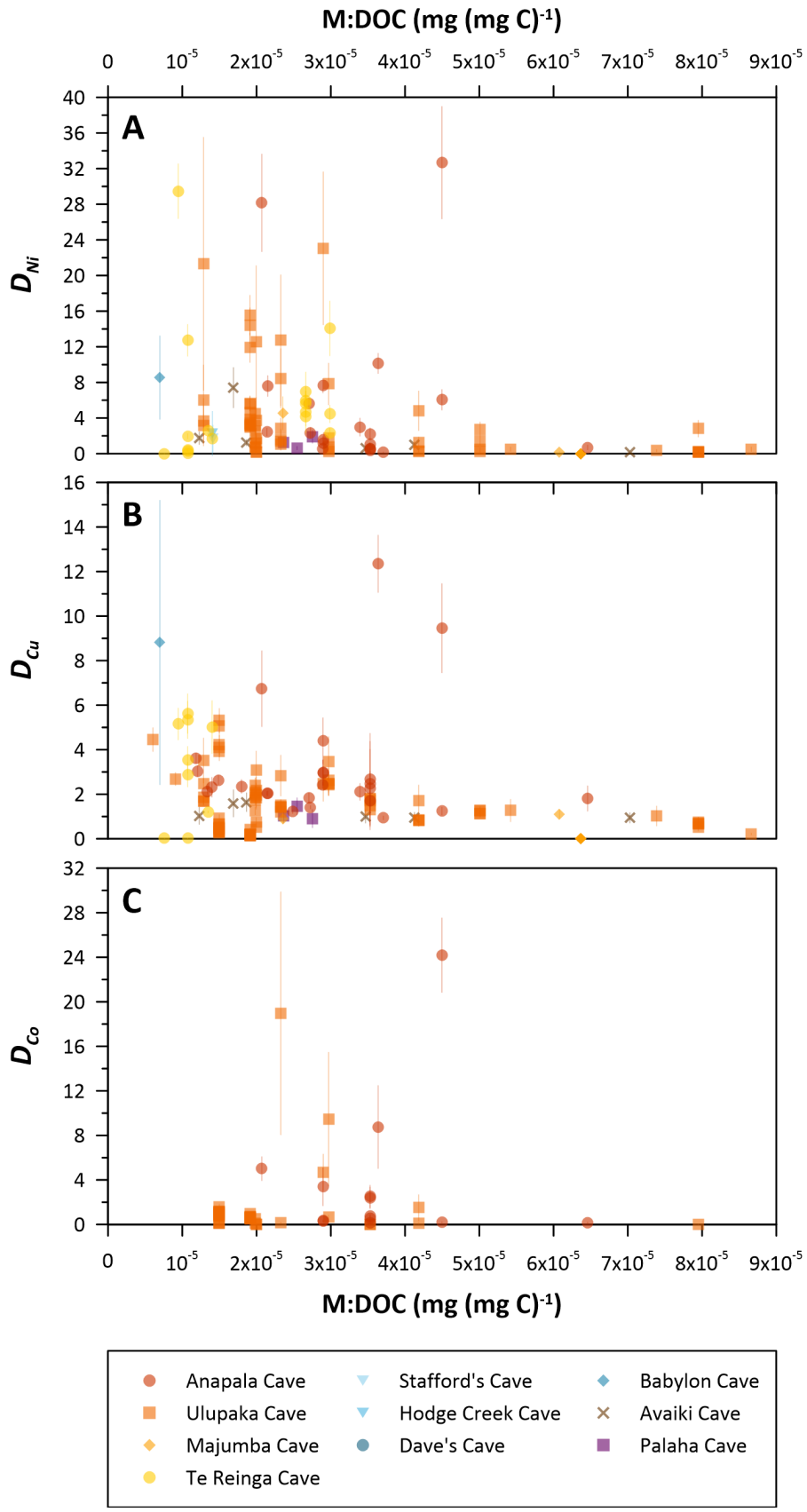

Figure 4.15: In-cave transition metal partition coefficients as a function of M:DOC. Figures include data from watch glass deployments and speleothem micro-sampling. Dripwater DOC analyses serve as crude measures of the ligand concentration. Chamber averages of DOC concentrations were used for drip points at which DOC analysis was not feasible. Vertical error bars denote propagated standard deviations of D_X estimates.

elements at lower temperatures. Similarly, the solution chemistry does not warrant the anomalously high magnitude of D_{Sr}, which moderately scales with aqueous Mg/Ca (Wassenburg et al., 2020). Given that carbonate Mg/Ca, Sr/Ca, as well as Ba/Ca were relatively well related (linear correlations between ratios with $0.66 < r < 0.94$), while respective aqueous end-members were comparably consistent, it is unclear what causes the high D_{Mg} and D_{Sr}.

Discrete sampling periods limit the confidence in partition coefficients derived from study locations that were infrequently visited, particularly Council Cave, Stafford's Cave, and Babylon Cave (all visited only once). At these sites, precipitates were exclusively collected through speleothem micro-sampling. Nonetheless, D_{Mg}, D_{Sr}, and D_{Ba} were in good agreement with those from other caves and previously published datasets, supporting the consideration of these samples despite limited information. However, very few measurements of transition metals proved reliable in these settings, yielding only a few partition coefficient estimates that were inconsistent but within the observed range.

With the possible exception of Ulupaka Cave, there was no apparent relationship between D_X and the derived M:L (as estimated by the measured DOC) across the dataset of in-cave partition coefficients (Figure 4.15). Generally, the stability of OMCs increases as M:L decreases (*e.g.*, Town et al., 2012; Aiken et al., 2011), given the greater number of binding sites and enhanced potential for multidentate binding of cations. While this was evident in cave-analogue experiments with SRFA and NTA (Section 4.4.2), it is likely that variations of in-cave M:L were either not large enough to affect net partitioning (expected to be reduced at lower M:L) or masked by overall variability in drip chemistry and environmental parameters. With regards to their magnitude, in-cave partition coefficients of transition metals included values both well above and below those observed in experiments, reflecting the more heterogeneous ligand composition, varying M:L, and natural chemical and environmental variability. Nonetheless, these values were altogether in good agreement with other natural karst or surface water deposits, including in-cave estimates of Hartland et al. (2014) and tufa deposits described in Z. Wang et al. (2021) (D_{Cu} = 0.83 – 10.22; D_{Ni} = 0.60 – 1.13; D_{Co} = 0.29 – 2.73). The large variability also implies that the selection of SRFA and NTA at the chosen experimental M:L may be representative of some natural ligand binding characteristics, but under- and overestimate others. For instance, D_{Cu} were rather consistent at 6.76 $\pm$ 1.47 (n = 7) at a cave-analogue M:SRFA of 0.25 (Experiment 3), at which crystal development was notably disrupted beyond what is observed in most cave deposits. Although SRFA co-precipitation was excessive at these concentrations, this experimental organic D_{Cu} is only slightly above the average observed in-cave D_{Cu} of ca. 1.84 $\pm$ 1.88 (n = 137). Indeed, for an M:NTA of 0.50 (Experiments 5 and 10), Cu inclusion rates were nearly identical (experimental D_{Cu} = 1.57 $\pm$ 0.64, n = 16). For D_{Ni}, the in-cave average of ca. 4.13 $\pm$ 6.09 (n = 114) was considerably higher than in cave-analogue experiments (ca. 0.34 $\pm$ 0.15, n = 43; all organic experiments), whereas D_{Co} (1.89 $\pm$ 4.23, n = 57) as measured in Anapala Cave and Ulupaka Cave was very close to the D_{Co} estimated in organic experiments (ca. 1.22 $\pm$ 0.56, n = 55). As discussed in Section 4.4.2, however, predicted complexation of Co and Ni by SRFA (but not NTA) was negligible, and SRFA experimental D_{Ni} and D_{Co} were thus close to the inorganic values of 0.37 $\pm$ 0.18 (n = 21) and

1.75 $\pm$ 0.41 (n = 21), respectively.

Uncertainties of in-cave partition coefficients and observations

It is important to recognise that the estimation of in-cave partition coefficients (and indeed other chemical properties) warrants several caveats, foremost including an inevitable sampling bias reflected in the sensitivity to derived partition coefficients to the selected aqueous end-member (Equation 4.1). This uncertainty is amplified by the significant difference in temporal resolutions of dripwater and precipitate samples. For example, precipitate collected on watch glasses or of active speleothems represents material deposited over several months or even years, whereas the aqueous end-member typically only represents a limited number of discrete dripwater samples. Similarly, the dripwater chemistry may respond rapidly (within hours) to processes at the surface or along the flow path, thereby greatly exceeding the temporal resolution captured by (and extractable from) corresponding carbonate precipitates. Contamination presents another potentially compromising factor, which is more likely to go unnoticed in surficial scraping samples than on watch glasses. Together with the uncertain deposition window, detrital contamination likely contributes to the overall slightly larger variation across datasets obtained from surficial carbonate samples (Supplementary Figure 4.S6). In this regard, however, this difference was mostly evident for transition metal partitioning, whereas D_{Mg} and D_{Sr} were highly consistent between growth media. All considered, this remarkable reproducibility of D_{Mg} and D_{Sr} across a wide range of environments and growth conditions therefore encourages the approach of *in-situ* glass deployments and speleothem micro-sampling to further investigate elemental behaviour in cave systems. The study of partition coefficients as a function of environmental parameters, such as growth rate or drip rate, is also complicated by similar constraints of sampling resolution. For instance, empirical growth metrics cannot account for variable precipitation rates over the deployment time or evaporative effects. Further, logistical constraints limit the number of drip counters that can feasibly be deployed for the continuous record of drip rates. These limitations are exacerbated by a high likelihood of logger displacement or loss, for instance through human or animal interferences, ground-shaking, or battery failures. For most drip points, drip rate observations were thus based on very few *in-situ* observations that reflect discrete points in time. While these estimates become more robust as the number of observations increases, it is plausible that the lack of continuous drip rate data of many drip points conceals potentially systematic relationships. In this regard, ongoing cave monitoring and collection of water and precipitate samples are anticipated to improve the datasets presented herein.

Synthesis of new and published metal partition coefficients

The contrasting behaviour of transition metals and alkaline earth metals was further emphasised in the context of a total of 47 previously published experimental and field-based studies in combination with data generated herein, distinguishing between ‘inorganic’ and ‘organic’

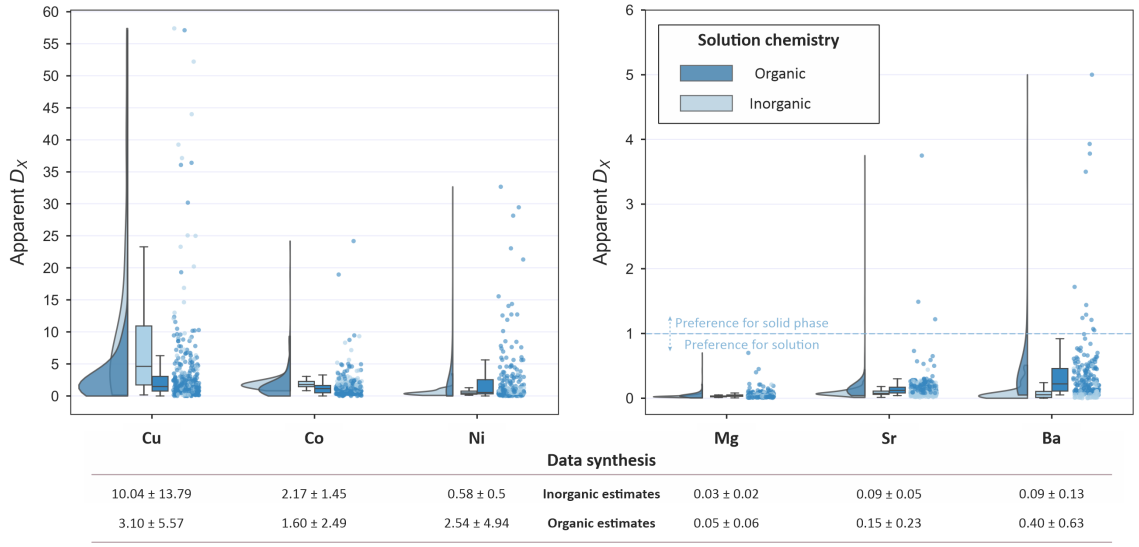

Figure 4.16: Compilation of elemental partition coefficients in calcite for selected transition metals and alkaline earth metals. The compilation includes data collected in this study and a survey of 47 previously published datasets. Data shown are depicted in a raincloud plot (M. Allen et al., 2021; adapting Python code provided within) and are separated into 'inorganic' (light blue) and 'organic' (dark blue) solution chemistries, where the latter category includes both natural settings as well as experiments including organic compounds in the parent solution. The compilation also includes Ba (not included in cave-analogue experiments). Values underneath each element present the respective mean and standard deviation.

systems (Figure 4.16; Table 4.4). This synthesis of comparable datasets of calcite deposits (*i.e.*, excluding other polymorphs) integrates metal partition coefficients derived for a total of between 231 (for Ba) and 593 (for Sr) solution-crystal couplets, including from beaker and cave-analogue experiments, theoretical studies, in-cave calcite farming or micro-sampling, and other abiogenic freshwater calcite deposits, such as tufas. Partition coefficients for biogenic calcite were excluded due to the often uncertain contribution of vital effects (*e.g.*, Saunders et al., 2014).

Notably, the values of D_X of transition metals deviated from their inorganic estimates towards both higher and lower rates of inclusion, including opposing phase preferences ($D_X < 1$). Cu was the only element where organic interactions confined the overall range of apparent D_X, which is attributable to complexation pervasively counteracting the extreme tendency of Cu to distribute into calcite. For both Ni and Co, organic solution chemistries in turn increased variability away from approximate thermodynamic equilibrium, which is expected given their inorganic D_X close to 1. This differential distribution behaviour was largely absent for both Mg and Sr, whose partition coefficients were exclusively between 0 and 1. This compilation constrains apparent D_{Mg} and D_{Sr} applicable to karst systems of 0.04 $\pm$ 0.05 (n = 493) and 0.13 $\pm$ 0.18 (n = 593), respectively, accounting for a large range in growth and environmental conditions.

Because measured (apparent) partition coefficients do not differentiate between pathways of metal capture, but are only based on total cation concentrations as quantified by ICP-MS, these estimates are expected to include metal inclusion by substitution in solid solution, ternary complexation, and kinetically-limited supply. This complexity clearly precludes simple assump-

Table 4.4: Averaged values of inorganic and organic D_X estimates based on the compilation of new and published datasets. Values reported here describe the datasets plotted in Figure 4.16 and comprise a survey of 47 individual studies in addition to estimates produced here. Inorganic estimates reflect experimental and predicted partitioning in absence of organic ligands. Organic solution chemistries include laboratory experiments and field-based estimates of D_X in natural abiogenic calcite precipitates.

		Compiled estimates of D_X			
Solution chemistry	**Element**	**Mean ± 1 SD**	**Min**	**Max**	**n**
Inorganic	Cu	10.04 ± 13.79	0.16	57.40	51
	Co	2.17 ± 1.45	0.82	9.33	84
	Ni	0.58 ± 0.5	0.10	3.47	62
	Mg	0.03 ± 0.02	0.01	0.21	156
	Sr	0.09 ± 0.05	0.01	0.44	245
	Ba	0.09 ± 0.13	0.00	0.51	51
Organic	Cu	3.10 ± 5.57	0.003	57.11	254
	Co	1.60 ± 2.49	0.002	24.19	186
	Ni	2.54 ± 4.94	0.004	32.67	201
	Mg	0.05 ± 0.06	0.01	0.70	338
	Sr	0.15 ± 0.23	0.04	3.75	349
	Ba	0.40 ± 0.63	0.05	5.00	180

tions of transition metal D_X values, warranting an assessment of their likely inclusion pathways conceptualised in Section 4.4.4.

4.4.4 Implications for the interpretation of speleothem records

Recent advances in overcoming analytical challenges in quantifying trace concentrations of transition metals in high-Ca matrices, such as cave waters (Warken, Kuchalski, et al., 2022), have paved the path for more reliable measurements of these elements for palaeoenvironmental applications in karst systems. However, the herein demonstrated complexity of transition metal inclusion into speleothem fabrics currently precludes straightforward and generalisable interpretations.

In cave-analogue experiments, partitioning was interpreted to reflect strong inorganic controls on partitioning (primarily for Cu), while also suggesting that moderate to high degrees of direct capture of OMCs by calcite are likely to result in a dominantly positive relationship between drip rate and transition metal concentrations in the precipitate if OMCs are sufficiently stable and able to co-precipitate. Notably, this pattern contrasts with that predicted in the OMC decay hypothesis, convincing support for which stems from proxy time-series of the prominent HS-4 stalagmite record from Heshang Cave, China (Hartland et al., in prep.) and Dharamjali Cave, India (Giesche et al., 2023), as well as the ubiquitous kinetic limitation of transition metals observed in cave waters (Chapter 3). Explicit support for a kinetic dependence of transition metals inclusion on drip rate has recently also been put forward by Sliwinski et al. (2022), who conceptualised the incorporation of Y (with ion Y^{3+}) as facilitated by OMCs and their dissociation as a function of their surface retention time (*i.e.*, residence time at stalagmite surfaces). Supported by concurrent confocal imaging, the authors were able to constrain contrasting Sr and Y distributions in seasonally banded speleothems, and inversely relate the effective incorporation of Y to drip intervals in modern stalagmites. Importantly, this study also implies that this behaviour may extend to other rare earth elements that share characteristics with Y and

first-row transition metals, including a preferential distribution into calcite (*i.e.*, $D_X > 1$; *e.g.*, Qu et al., 2009; Terakado & Masuda, 1988; Voigt et al., 2017) and significant complexation by NOM (Stern et al., 2007; Sholkovitz, 1995).

All considered, it follows that peak concentration excursions of OMC-associated metals in either direction may be interpreted as either high or low flow rates, depending on which inclusion mechanism is assumed to prevail. This dilemma raises the question to what degree the controls on transition metal partitioning may be system-specific, and discernible if so. Despite the lack of concrete experimental evidence of kinetically-driven metal supply as a function of drip rate, published datasets and the results presented in this study and Chapter 3 allow for the establishment of a preliminary conceptual framework aimed at distinguishing between metal inclusion pathways.

Analogous to the positive correlations between drip rate and partitioning of Cu (and Ni and Co to a lesser extent) found in cave-analogue experiments (Figure 4.8), Warken, Kuchalski, et al. (2022), for instance, found that tropical cyclone activity often coincided with peak transition metal concentrations in dripwaters from Puerto Rico. This was linked to rapid transport of metals complexed in colloidal and particulate matter. Such event-based transition metal mobilisation has been documented previously in dripwater samples (*e.g.*, Hartland et al., 2012; Vesper, 2012; Wynn et al., 2014) and speleothems (*e.g.*, Borsato et al., 2007; Huang & Fairchild, 2001; Fairchild et al., 2001; Richter et al., 2004; Sliwinski et al., 2022), clearly presenting an important pathway for metal supply to speleothems under certain hydrological regimes. It is proposed that this inclusion mechanism through adsorption and/or entrapment may particularly predominate in many shallow cave systems, where the occurrence of ternary complexation is likely significant due to a higher fraction of primary, potentially larger, soil-derived hydrophobic organic compounds in infiltrating water. It is thus perceivable that the concentrations of strongly complexed transition metals in speleothems from such systems primarily record strong flushing events through the adsorption of OMCs, rather than exhibiting kinetic signals. This may especially be the case where infiltration is strongly seasonal and the overburden is relatively thin and porous, as was generally true in studies reporting soil-flushing signals in transition metals (*e.g.*, Warken, Kuchalski, et al., 2022; Borsato et al., 2007; Kost et al., 2022; although not in Wynn et al. (2014) with ca. 70 m cave depth below surface). Similarly, fast accumulation rates may favour the inclusion of impurities (*e.g.*, Tesoriero & Pankow, 1996; Füger et al., 2019), thus facilitating direct capture of OMCs. Conversely, it is argued that hydrophilic (less aromatic) fractions of OM may play a more prominent role as flow paths increase in length, and larger and/or more aromatic components are removed. In consequence, the significance of direct capture of OMCs on metal incorporation under such circumstances is predicted to progressively decrease, while OMC decay kinetics become a dominant supply of labile metals to speleothems in deeper systems.

In practice, these considerations imply that the driving controls on first row transition metals may in fact lie on a continuum of specific settings for a given site, where flow path properties, the evolution of NOM, and possibly growth rate collectively determine the relative significance of adsorption and OMC decay for the inclusion of transition metals in speleothems. Concep-

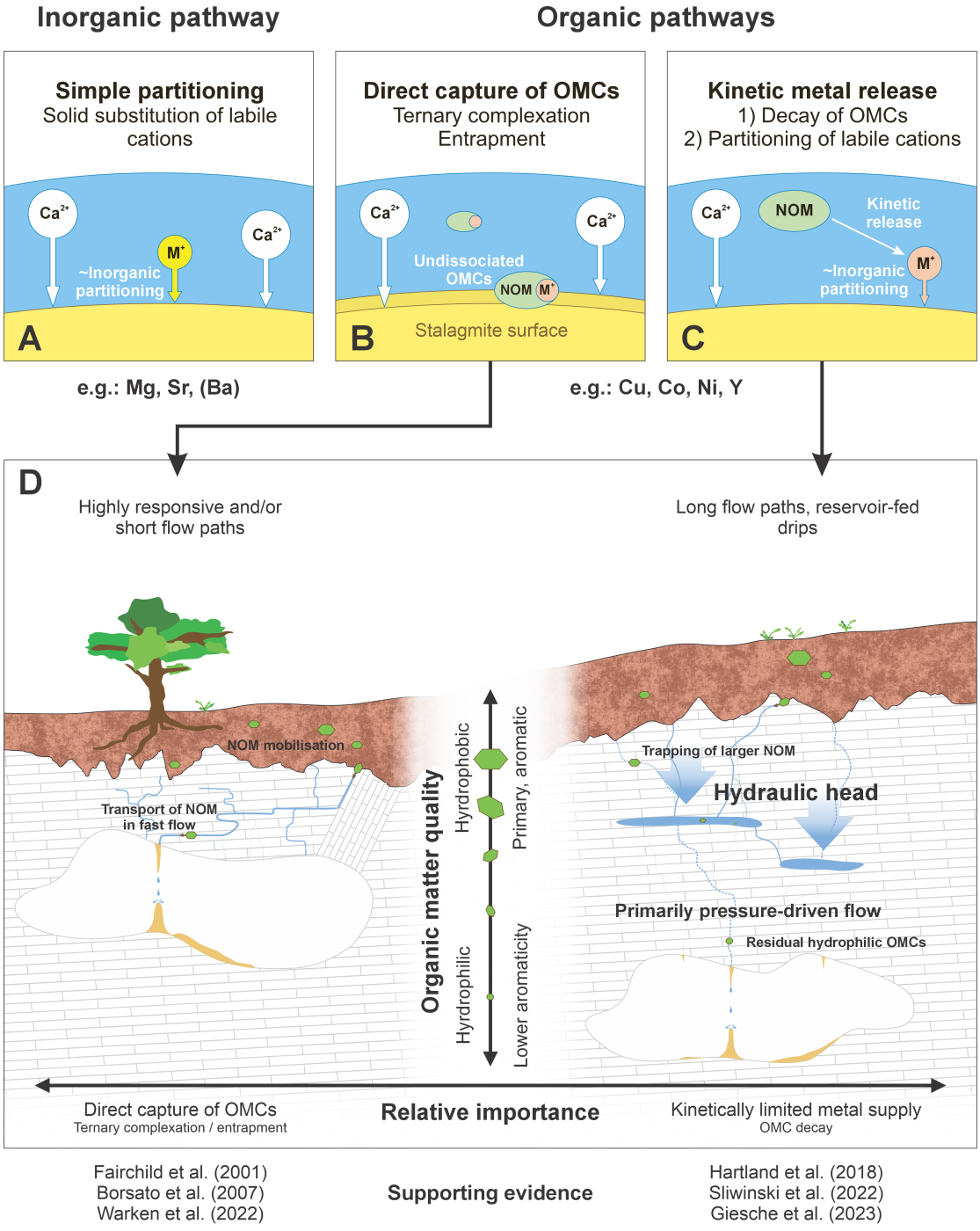

Figure 4.17: Hypothesised metal inclusion pathways and system-specific controls of transition metal incorporation. Experimental and field-based evidence suggest effectively inorganic, simple partitioning of Mg and Sr (**A**). In contrast, first-row transition metals and other organically complexed cations are included through direct capture mechanisms (**B**) or an essentially step-wise rate-dependent release from OMCs, and subsequent partitioning of labile cations according to thermodynamic constraints (**C**). The relative importance of organic pathways is hypothesised to vary along a continuum of organic matter maturity, karst hydrology, and speleothem growth conditions (*e.g.*, growth rate, porosity; not depicted here). Dominant ternary metal supply (left side of **D**): Example of shallow cave systems, direct/responsive dripwater flow paths, immature/primary soil-derived ligands. Favourable conditions for ternary complexation / adsorption of OMCs without prior dissociation. Flushing events likely to cause *increase* in metal concentrations due to colloidal / particulate associated transport. Dominant OMC decay metal supply (right side of **D**): Example of deeper cave systems, longer/reservoir-fed dripwater supply (dependent on hydraulic head), evolved/remnant ligands. Favourable conditions for OMC decay from hydrophilic ligands at stalagmite apex. Increased hydraulic head (higher recharge) likely to cause *decrease* in metal concentrations due to shorter drip intervals and time for OMC decay to occur.

tualised in Figure 4.17, this notion provides grounds for reconciling the contrasting possible hydrological interpretations for metal concentration excursions in a given direction (*e.g.*, peak X/Ca interpreted as reflecting either high or low flow). Careful assessment of the preconditions is thus critical for interpreting transition metals as hydrological proxies, requiring confidence in whether event-like incorporation of transition metals is likely. For instance, if a system is prone to strong infiltration events, it is expected that the perpetual control posed by OMC decay (Chapter 3) is temporarily overridden by the direct capture of complexed metals. Importantly, either of the inclusion mechanisms may provide an opportunity to arrive at (semi-)quantitative rainfall reconstructions based on transition metal time-series in stalagmites, provided the cave system is sufficiently characterised. This in turn reinforces the significance and necessity of conducting at least minimal monitoring of a study location to constrain the site-specific variability in dripwater chemistry, flow regimes, and atmospheric properties in response to surface processes. Regardless, further work is clearly necessary to firstly provide the fundamental experimental evidence that OMC decay kinetics may dominate under certain circumstances. Secondly, distinct (quantifiable) criteria to test for the likely primary control on metal partitioning in a stalagmite are needed, for instance based on other proxy records, microscopic techniques, and statistical constraints. It is further noted that the suggested interpretative framework would apply specifically to stalagmites, where thin-film resident times are primarily governed by the drip interval.

In contrast to transition metals, Mg and Sr were found to overall behave predictably within the limits of known effects of growth rate, solution chemistry (*e.g.*, Mg/Ca), and temperature. As expected, both alkaline earth metals exhibited little or no susceptibility to organic complexation, noting however that Sr partitioning may be slightly reduced in particularly organic-rich precipitates. This behaviour presumably bears particular significance in systems with strongly seasonal infiltration (*e.g.*, Sliwinski et al., 2022). Nonetheless, the overall magnitude of variability in D_{Sr} was comparably limited, and the average D_{Sr} and D_{Mg} are expected to present adequate estimates applicable across most cave environments. In this regard, it is noteworthy that Mg was consistently quantifiable in natural carbonates, implying that the observed exclusion of Mg from precipitates at high experimental concentrations of NTA and SRFA was not representative of natural drip solutions. Altogether, this study thus supports the assumption of D_{Mg} and D_{Sr} values for palaeoenvironmental applications, but suggests the use of appropriate error margins to account for the minor variability observed.

4.5 Conclusions and outlook

The series of ten cave-analogue experiments set out to test the hypothesis of a kinetically-driven supply of transition metals to stalagmite surfaces. The decay of OMCs was predicted to impose an inverse control of drip rate on respective apparent metal partitioning into calcite. Although the addition of SRFA and NTA yielded a clear reduction of partitioning of transition metals compared to inorganic drip solutions, the OMC decay hypothesis was not supported by

the results. Inorganic D_{Cu} exhibited a strong positive linear correlation with drip rate, which persisted but was progressively muted with increasing ligand concentration. A similar but weaker correlation was observed for D_{Co}, whereas Ni partitioning only noticeably deviated from inorganic experiments at a very high NTA concentration. Based on three inorganic experiments, partitioning followed the hierarchy Cu $>$ Co $>$ Ni as consistent with the literature, with average $D_{Cu} \approx 13$, $D_{Co} \approx 1.8$, and $D_{Ni} \approx 0.4$. The experiments further corroborated that Mg and Sr essentially do not interact with organic matter via complexation, yielding average inorganic D_{Mg} and D_{Sr} of ca. 0.04 and 0.09, respectively. D_{Sr} in organic experiments were slightly elevated, which was interpreted to reflect an inhibition of Sr partitioning by a large presence of organic impurities in the crystal phase.

Although in apparent contradiction to the original hypothesis, the experimental findings do not rebut the potential significance of OMC decay under certain circumstances, but are likely explained by the selection of ligands used in this study. Values of up to 0.23 for D_{SRFA} suggested that a considerable fraction of SRFA co-precipitated with calcite, presumably contributing to metal partitioning via ternary complexation rather than OMC decay. Nonetheless, $D_{SRFA\text{-}M}$ consistently above 1 implied that transition metals partitioned at higher rates than SRFA, with inorganic controls seemingly imprinted in the overall reduced partitioning in presence of ligands. Predicted signatures of OMC decay were therefore likely masked by combined effects of increased retention in solution, adsorption of OMCs without dissociation, and thermodynamic partitioning preferences of metals. The structural properties of the more hydrophilic NTA were considered less likely to support direct capture of OMCs, however, simultaneously prevented the measurement of NTA in solution and precipitate. In the experiments, the addition of NTA altogether muted partitioning of transition metals more than the equivalent M:SRFA did, but positive relationships between D_{Cu} and D_{Co} with drip rate likewise dominated.

It is possible that metals were inadvertently complexed too strongly for calcite to invoke the decay of OMCs, thus effectively restricting partitioning pathways to either adsorption or labile 'inorganic' uptake. Further experiments using different ligands less prone to direct capture and/or strong complexation are thus recommended. This would benefit from an initial targeted study to assess partitioning behaviour of a range of ligands with varying degrees of aromaticity and structural complexity with view to identifying ligands with properties most likely to demonstrate OMC decay in precipitation experiments. Subsequent growth studies would need to achieve M:L ratios favourable for moderate kinetic limitation, and could be augmented with the analysis of metal isotope ratios (particularly Ni), which could provide valuable insights into complexation and co-precipitation kinetics (*e.g.*, Alvarez et al., 2021). Future experiments also need to rectify substantial differences in equilibrium complexation between the different metals for a given ligand, possibly requiring separate experimental solutions for each metal. At large, however, the feasibility of cave-analogue precipitation experiments for the identification of OMC decay signals may inherently be limited by a mismatch of ($\sim$slow) metal release from OMCs and the subsequent rapid uptake by calcite at the observed precipitation rates. If these challenges cannot be resolved by altering experimental conditions (*e.g.*, reducing calcite precipitation rates and enhancing OMC decay), alternative experimental approaches may be

required to demonstrate kinetic signatures.

The synthesis of new and published metal partition coefficients served to further illustrate the contrasting controls and pathways determining the inclusion of first-row transition metals and alkaline earth metals in calcite. The wide range of Ni and Co partition coefficients from natural and experimental systems suggested that organic complexation may both significantly reduce or amplify their inclusion. In contrast, Cu partitioning was consistently limited compared to its extreme affinity for the crystal phase under inorganic conditions. For the studied first-row transition metals, inorganic controls observable in ideal systems are thus largely overridden by ligand action. In contrast, the data synthesis indicated that partitioning of alkaline earth metals into calcite generally adheres to first-order thermodynamic and kinetic constraints, providing additional confidence in their use for palaeoclimate applications. Exceptions may include deposits with high concentrations of organic inclusions, which can evidently inhibit Sr and potentially Mg substitution. Based on these datasets and additional observations from several cave systems and experimental studies, a conceptual framework of different inclusion pathways was constructed. Specifically, metal pathways of simple 'inorganic' cation substitution, direct capture of OMCs by adsorption and/or entrapment, and a two-step kinetic inclusion via OMC decay were distinguished. The relative significance of each pathway is suggested to vary across a spectrum of system-specific conditions, but is hypothesised to be largely a function organic matter composition and maturity. Importantly, either organic pathway provides significant prospect for using speleothem transition metal concentrations as hydrological recharge proxies in well-characterised systems. However, despite growing evidence for this concept, additional studies are required to provide more conclusive and experimentally verifiable support for the OMC decay pathway. Ideally, this includes the establishment of widely applicable criteria for the identification and utilisation of each metal partitioning pathway in speleothem science. For instance, future studies may test this concept in natural caves where the cave architecture permits sampling of modern speleothems from a large range in flow path lengths, reflecting a progressive filtration and maturing of NOM. For samples collected in this study, it is also aimed to systematically quantify ligand partitioning in natural precipitates, and characterise ligand properties in relation to $D_{NOM\text{-}M}$. While beyond the scope of this study, the compiled datasets further encourage a re-assessment of metal partitioning under aspects such as temperature, solution chemistry, and growth kinetics.

Supplementary information

Error estimations of derived parameters

Error estimation of data presented herein is achieved by the propagation of uncertainties related to (i) the analytical results, (ii) statistical measures where applicable, and (iii) any subsequent mathematical operations. By example of derived partition coefficients (*e.g.*, D_{Sr}), this specifically includes the standard deviations from triplicate ICP-MS analyses for each element, averaging of multiple aliquots (*e.g.*, multiple GeoMic reservoir sub-samples), and the establishment of ratios (*i.e.*, $(Sr/Ca)_{Crystal}$, $(Sr/Ca)_{Solution}$, as well as their ratio to express D_{Sr} (Equation 4.1)). Error propagation of division applicable to ratios follows the general Equation 4.S1 as:

$$\sigma_z = \sqrt{(\sigma_x)^2 + (\sigma_y)^2} \tag{4.S1}$$

, where σ_z is the propagated uncertainty (either in relative or absolute terms) of the derived ratio, and σ_x and σ_y are the respective original uncertainties of individual concentration measurements (Harris, 2010). The uncertainty of an average composite value $\bar{x}$ (*e.g.*, the average reservoir Sr/Ca based on *k* number of aliquots taken during an experiment) is expressed as its pooled standard deviation according to Equation 4.S2 (Harris, 2010):

$$\sigma_{\bar{x}} = \sqrt{\frac{\sigma_{x,1})^2 + \sigma_{x,2})^2 + ... + \sigma_{x,k})^2}{k}} \tag{4.S2}$$

, where σ_x, k is the propagated standard deviation of $(Sr/Ca)_k$ of each aliquot, based on the individual standard deviations of Sr_k and Ca_k (measured consistently in triplicates for each aliquot).

Supplementary figures and tables

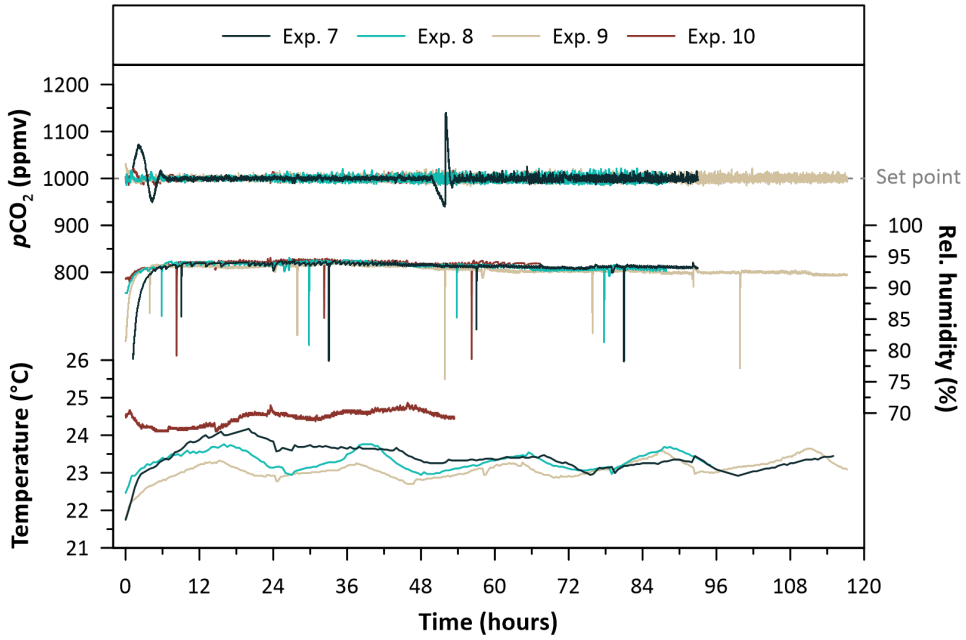

Figure 4.S1: Atmospheric conditions of Experiments 7, 8, 9, and 10. Logged data of pCO_2 (ppmv), relative humidity (%), and air temperature (℃) inside the GeoMic enclosure during Experiments 7 to 10. Data were logged every minute. The brief pCO_2 in Experiment 7 occurred during a change of N_2 tanks, but is not expected to be consequential.

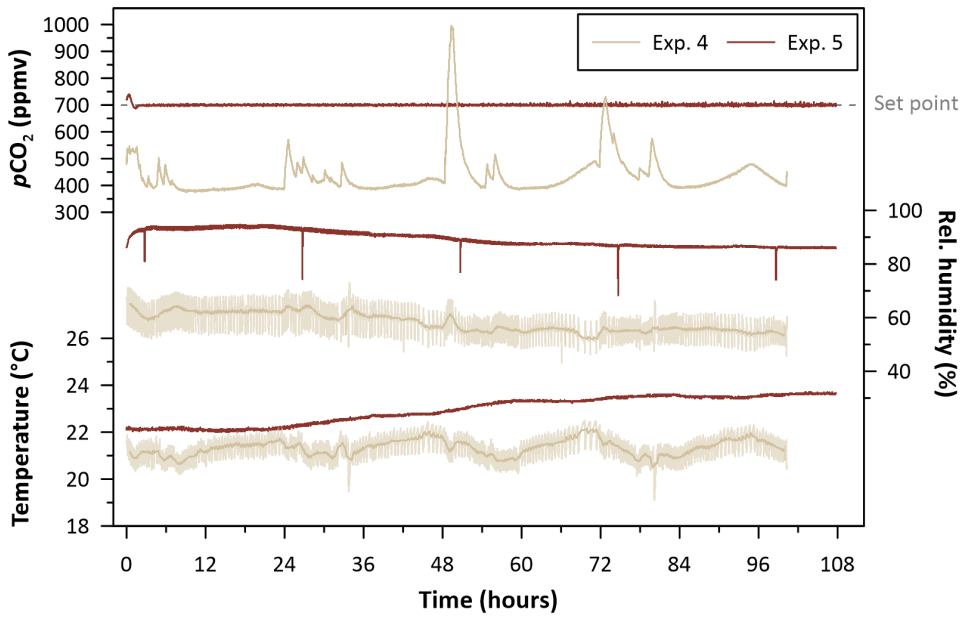

Figure 4.S2: Atmospheric conditions of Experiments 4 and 5. Logged data of pCO_2 (ppmv), relative humidity (%), and air temperature (℃) inside the GeoMic enclosure during Experiments 4 and 5. Data are logged every minute. Experiment 4 was performed without use of the controlled atmosphere, creating conditions akin to a well-ventilated cave chamber. Experiment 5 was carried out with a target pCO_2 of 700 ppmv, opposed to 1000 ppmv in other experiments. This change was made to enhance calcite deposition, but conditions in subsequent experiments were once again set to 1000 ppmv CO_2.

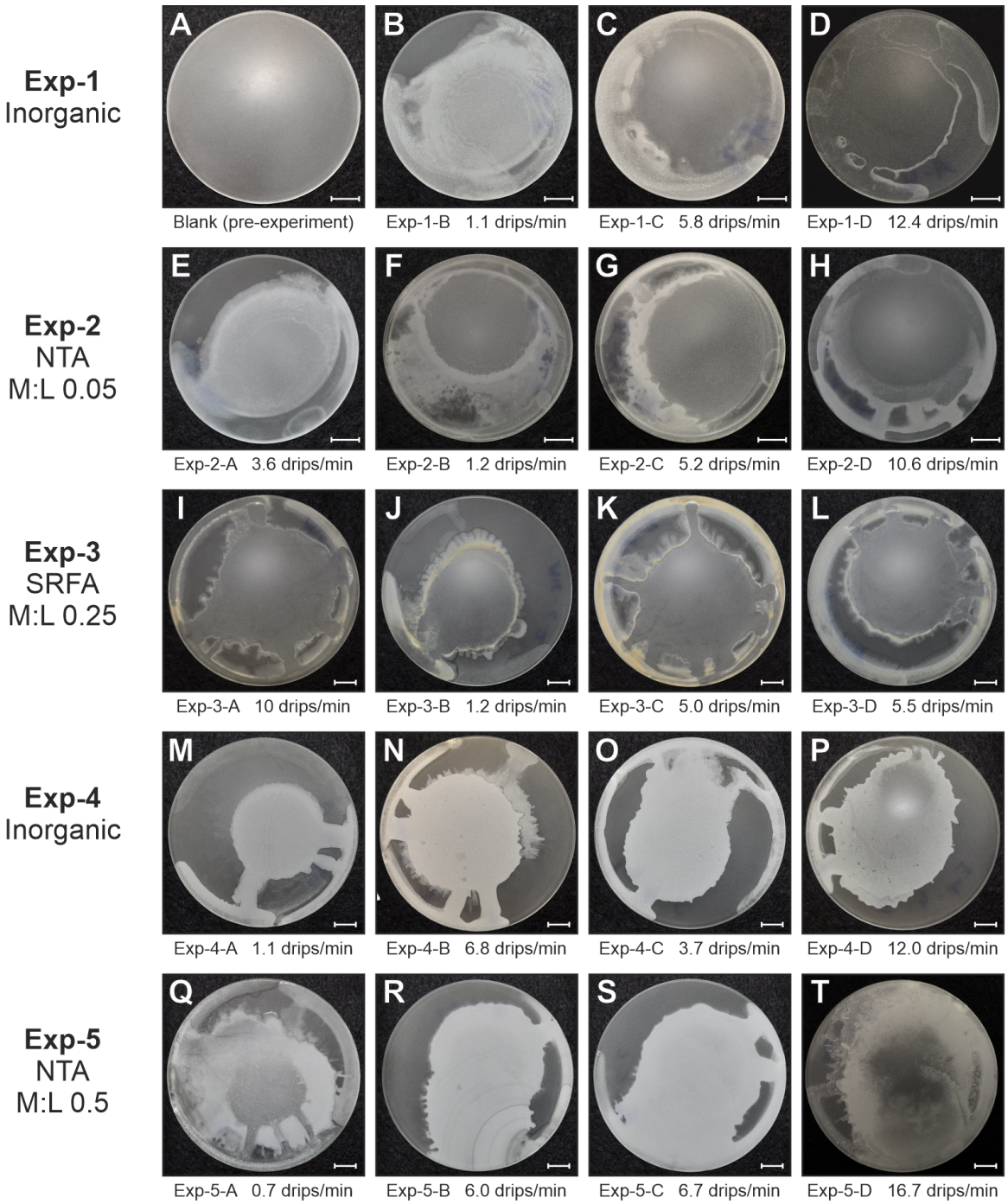

Figure 4.S3: Standardised digital images (RGB versions) of each watch glass used in cave-analogue experiments 1 to 5. Labels below each image include the ID of each glass and the average drip rate at which the precipitate formed. Glass Exp-1-A was discarded due to a pump component breaking early in the experiment. Image A shows a sandblasted glass without any calcite growth for reference, which was used to inform ImageJ threshold criteria in the characterisation of crystal coverage. Blue tints visible in some images (*e.g.*, image C) stem from labelling on the inside of the glasses, and were manually corrected for in ImageJ routines. Note also the slight yellow colouration of precipitates formed in presence of high concentrations of SRFA (images I to L), indicating considerable ternary complexation. All images were auto-corrected for contrast and brightness. The scale bar in each image denotes 10 mm.

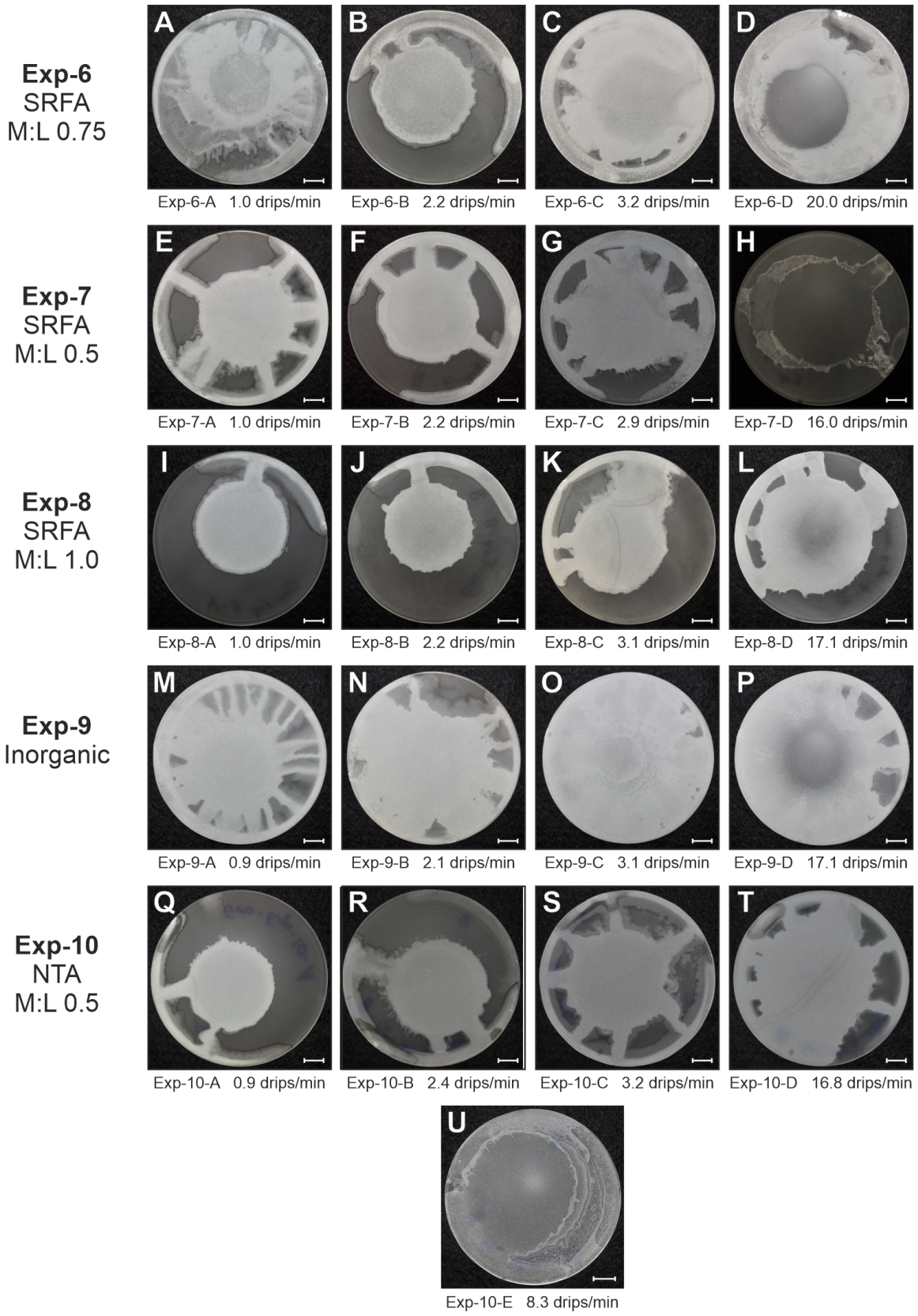

Figure 4.S4: Standardised digital images (RGB versions) of each watch glass used in cave-analogue experiments 6 to 10. Labels below each image include the ID of each glass and the average drip rate at which the precipitate formed. Blue tints visible in some images (*e.g.*, image U) stem from labelling on the inside of the glasses, and were manually corrected for in ImageJ routines. All images were auto-corrected for contrast and brightness. The scale bar in each image denotes 10 mm.

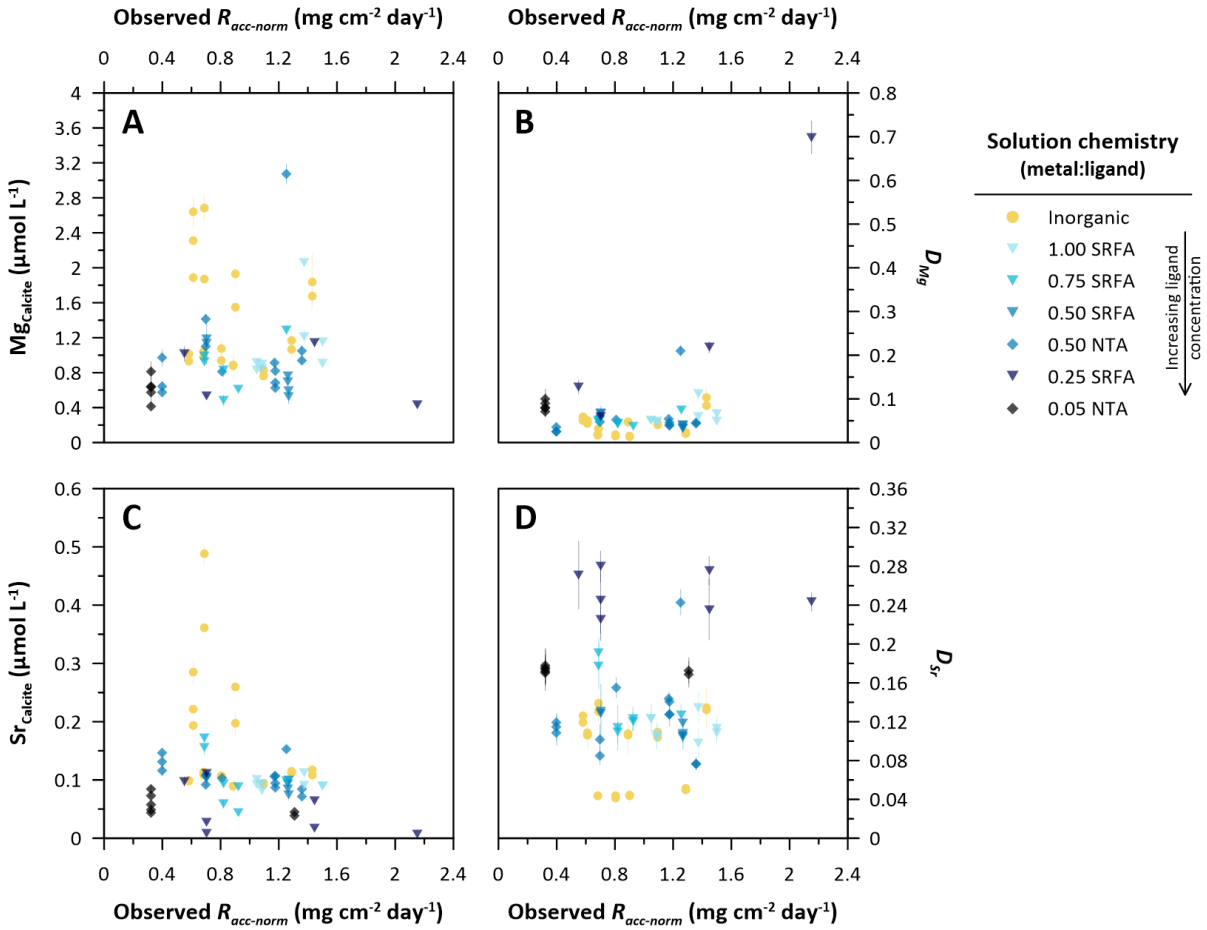

Figure 4.S5: Inclusion of Mg and Sr into calcite as a function of growth rate in cave-analogue experiments. Apparent partition coefficients did not correlate significantly ($p < 0.05$) with empirical growth metrics.

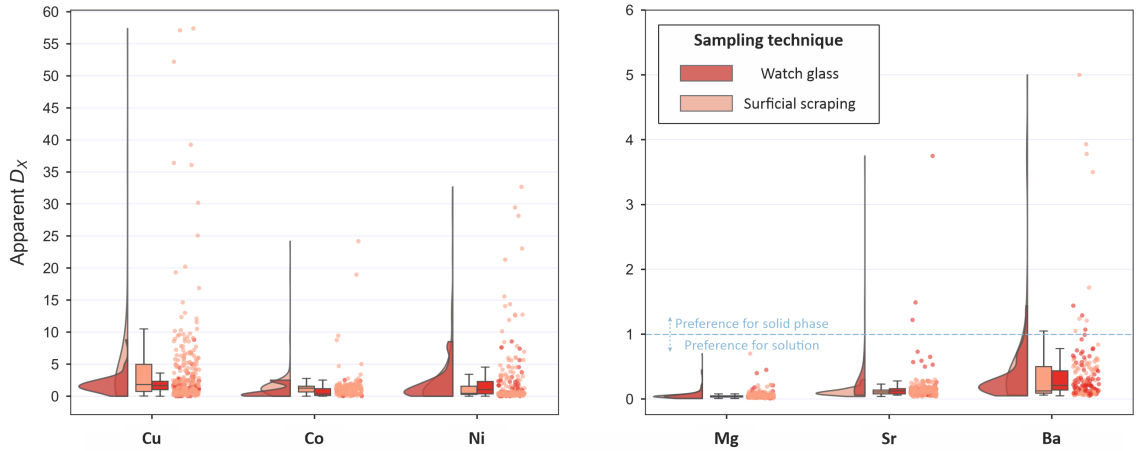

Figure 4.S6: Comparison of elemental partition coefficients in calcite obtained through different sampling techniques. All data generated in this study are shown. Data are depicted in a raincloud plot (M. Allen et al., 2021; adapting Python code provided within) and are separated by the respective sampling technique used to collect precipitate. Surficial scraping refers to the targeted removal (micro-sampling) of precipitate from the surface of actively depositing speleothems, opposed to collecting precipitate on watch glasses.

Table 4.S1: Overview of cave-analogue watch glass and calcite growth properties. Diameter refers to the glass size. Crystal cover was estimated using the threshold function of ImageJ (Rasband, 2012). Information on solution and atmospheric properties of each experiment are found in Table 4.1.

Experiment	Glass ID	Diameter	Drip rate	Low or no crystal cover	Dense crystal cover	Growth time	Total mass on glass	Total mass in funnel	Observed R_{acc}	Observed $R_{acc\text{-}norm}$	Modelled R_{prec}
		mm	drips min^{-1}	% of glass	% of glass	h	mg	mg	mg day^{-1}	mg day^{-1} cm^{-2}	mg day^{-1}
1 (Inorganic)	Exp-1-B	70	1.1	32.5	66.0	79.5	51.6	N/A	15.6	0.6	14.3
	Exp-1-C	70	5.9	62.1	37.9	79.5	33.2	N/A	10.0	0.7	77.4
	Exp-1-D	70	5.9	99.9	0.1	49.7	1.5	N/A	0.7	N/A	162.3
2 (NTA)	Exp-2-A	70	3.5	59.7	40.3	100.8	21.0	N/A	5.0	0.3	43.8
	Exp-2-B	70	1.1	99.7	0.3	100.8	30.1	N/A	7.2	N/A	14.2
	Exp-2-C	70	5.2	81.2	18.8	100.8	39.8	N/A	9.5	1.3	63.9
	Exp-2-D	70	10.6	99.9	0.1	47.8	16.0	N/A	8.0	N/A	131.3
3 (SRFA)	Exp-3-A	90	10.0	98.9	1.1	54.8	3.3	N/A	1.4	2.2	112.1
	Exp-3-B	90	1.2	94.0	6.0	82.0	9.2	N/A	2.7	0.7	13.1
	Exp-3-C	90	5.3	78.7	21.3	92.8	28.8	N/A	7.5	0.6	59.8
	Exp-3-D	90	5.1	89.6	10.4	44.8	17.8	N/A	9.5	1.4	56.9
4 (Inorganic)	Exp-4-A	90	1.1	71.9	28.1	99.1	66.5	7.7	16.1	0.9	1.6
	Exp-4-B	90	6.9	42.9	57.1	72.0	87.7	11.5	29.2	0.8	10.0
	Exp-4-C	90	3.6	35.5	64.5	79.6	93.2	10.1	28.1	0.7	5.2
	Exp-4-D	90	12.2	67.8	32.2	30.0	33.0	2.1	26.4	1.3	17.6
5 (NTA)	Exp-5-A	90	0.7	57.9	42.1	107.1	47.7	8.1	10.7	0.4	5.3
	Exp-5-B	90	6.6	38.8	61.1	37.2	42.0	1.0	27.1	0.7	52.8
	Exp-5-C	90	7.2	28.4	71.6	37.0	95.3	0.6	61.8	1.4	57.3
	Exp-5-D	90	17.8	98.4	1.6	37.1	119.3	0.5	77.3	N/A	142.3
6 (SRFA)	Exp-6-A	90	1.0	48.5	51.5	108.5	102.0	10.4	22.6	0.7	11.4
	Exp-6-B	90	2.3	64.7	35.3	117.8	101.9	3.2	20.7	0.9	26.5
	Exp-6-C	90	3.2	15.9	84.1	117.7	214.9	6.6	43.8	0.8	37.5
	Exp-6-D	90	19.5	33.2	66.8	39.1	86.8	1.3	53.3	1.3	227.8
7 (SRFA)	Exp-7-A	90	1.0	43.9	56.1	90.8	95.1	11.5	25.1	0.7	12.3
	Exp-7-B	90	2.2	55.6	44.4	91.1	135.4	7.3	35.7	1.3	27.1
	Exp-7-C	90	2.9	44.6	55.4	90.7	168.8	9.9	44.7	1.3	36.3
	Exp-7-D	90	15.9	100.0	0.0	48.6	155.2	3.4	76.7	N/A	197.7
8 (SRFA)	Exp-8-A	90	1.0	75.5	24.5	72.3	49.3	3.3	16.4	1.0	12.2
	Exp-8-B	90	2.2	77.3	22.7	65.4	59.0	2.1	21.7	1.5	26.3
	Exp-8-C	90	3.2	52.1	47.9	65.2	90.0	3.1	33.1	1.1	37.6
	Exp-8-D	90	18.9	44.5	55.5	45.3	91.6	1.3	48.5	1.4	222.0
9 (Inorganic)	Exp-9-A	90	0.9	22.2	77.8	93.5	111.9	6.0	28.7	0.6	10.7
	Exp-9-B	90	2.2	18.9	81.1	86.5	165.2	7.2	45.8	0.9	26.4
	Exp-9-C	90	3.2	8.0	92.0	86.3	230.1	3.3	64.0	1.1	37.3
	Exp-9-D	90	17.1	25.2	74.8	46.8	132.6	1.0	68.0	1.4	202.9
10 (NTA)	Exp-10-A	90	0.9	68.1	31.9	67.6	46.3	3.3	16.4	0.8	9.5
	Exp-10-B	90	2.4	61.8	38.2	68.2	80.8	4.4	28.5	1.2	24.2
	Exp-10-C	90	3.2	44.0	56.0	67.7	118.1	3.5	41.9	1.2	33.3
	Exp-10-D	90	16.9	21.8	78.2	32.2	83.5	0.9	62.3	1.3	174.1
	Exp-10-E	80	8.5	90.8	9.2	45.0	75.5	1.2	40.3	N/A	87.6

Table 4.S2: Overview of watch glass deployments and calcite growth in natural caves. Temperature is reported as the average measured over the respective deployment period. $SI_{Calcite}$ is the calcite saturation index, the diameter refers to the size of glasses, and M:L denotes the molar metal:ligand ratio as estimated by the dissolved organic carbon (DOC) concentration. CO_2 is based either on spot measurements during cave visits or continuous monitoring (Anapala Cave). Where no M:L is reported, limited sample volume precluded DOC measurements. Glasses with retrieval dates marked with one asterisk (*) denote that the glass was found displaced from its original position but otherwise intact. Glasses found displaced and damaged are marked with two asterisks. Note that several glasses yielded negative total masses based on pre- and post-deployment weights. This was the case when growth was very slow and/or glasses were eroded.

Cave	Latitude	Longitude	Glass ID	Drip ID	Diameter	Deployed	Retrieved	Growth time	Total mass on glass	Observed R_{acc}	Modelled R_{prec}	Drip rate	Temperature	pH	CO_2	$SI_{Calcite}$	M:L (molar)
					mm			days	mg	mg day^{-1}	mg day^{-1}	drips min^{-1}	°C		ppmv		Co, Ni, Cu only
Te Reinga Cave	38°49'32.2"S	177°32'18.6"E	TR-E	TR-E	80	13/02/2019	31/03/2021	777	N/A	N/A	0.417	5.4	11.3	7.7	850	0.0	1×10^{-5}
Hawke's Bay, NZ			TR-03-21-F	TR-F	90	31/03/2021	22/09/2021	175	<0	N/A	0.000	2.2	11.2	7.8	850	0.1	8×10^{-6}
			TR-03-21-D	TR-D	90	31/03/2021	27/01/2022	302	N/A	N/A	0.000	5.3	11.3	7.7	850	0.0	3×10^{-5}
			TR-01-22-G	TR-G	80	27/01/2022	4/12/2022	311	0.178	0.574	0.000	4.2	11.3	7.7	850	-0.1	3×10^{-5}
			TR-01-22-C	TR-C	80	28/01/2022	4/12/2022	310	0.035	0.113	0.000	1.0	11.6	7.5	850	-0.2	9×10^{-6}
			TR-01-22-E	TR-E	80	27/01/2022	4/12/2022	311	0.122	0.391	0.417	5.4	11.3	7.7	850	0.0	1×10^{-5}
			TR-01-22-D	TR-D	80	27/01/2022	4/12/2022	311	0.646	2.077	0.000	5.3	11.3	7.7	850	0.0	3×10^{-5}
Dave's Cave	45°23'14.6"S	167°37'10.4"E	SI-04-21-A	DC-Core-Drip	90	30/04/2021	13/03/2022	317	<0	N/A	10.840	18.5	4.1	8.4	650	0.6	2×10^{-5}
Southland, NZ			SI-04-21-B	DC-Upper-2	90	30/04/2021	13/03/2022	317	0.113	0.358	3.816	7.5	4.8	8.4	650	0.5	N/A
			SI-04-21-C	DC-Upper-4	90	30/04/2021	13/03/2022	317	0.044	0.137	6.304	10.5	4.8	8.4	650	0.6	2×10^{-5}
Hodge Creek Cave	41°10'12.6"S	172°41'12.7"E	SI-04-21-I	HC-7	90	4/05/2021	24/03/2022	324	<0	N/A	0.185	0.5	6.3	8.4	650	0.5	2×10^{-5}
Tasman, NZ			SI-04-21-J	HC-9	90	4/05/2021	24/03/2022*	324	<0	N/A	0.245	0.5	6.3	8.4	650	0.6	1×10^{-5}
Anapala Cave	19°08'01.1"S	169°50'17.1"W	ANA-LC-5	ANA-LC-5	70	25/09/2019	22/02/2020	150	N/A	N/A	0.774	0.8	23.7	8.2	600	0.7	4×10^{-5}
Niue			ANA-LC-1	ANA-LC-1	70	25/09/2019	22/02/2020*	150	N/A	N/A	0.164	0.2	23.7	8.2	600	0.7	3×10^{-5}
			N-02-20-C	ANA-UC-4	70	22/02/2020	5/11/2022*	987	<0	N/A	0.134	0.2	24.3	7.9	420	0.4	N/A
			N-02-20-B	ANA-UC-6	70	22/02/2020	5/11/2022*	987	0.021	0.021	0.875	1.0	24.3	8.3	420	0.7	2×10^{-5}
			N-02-20-D	ANA-LC-2	70	22/02/2020	5/11/2022*	987	0.235	0.239	0.618	0.6	23.8	8.2	600	0.7	3×10^{-5}
			N-02-20-L	ANA-LC-5	70	23/02/2020	5/11/2022**	986	<0	N/A	0.923	0.9	23.8	8.2	600	0.7	4×10^{-5}
Ulupaka Cave	19°01'13.4"S	169°47'55.8"W	ULU-3	ULU-3	80	26/09/2019	23/02/2020*	150	N/A	N/A	3.690	3.6	23.6	8.3	650	0.8	2×10^{-5}
Niue			ULU-5	ULU-5	80	26/09/2019	23/02/2020	150	N/A	N/A	1.702	1.5	23.6	8.4	650	0.9	2×10^{-5}
			ULU-6	ULU-6	80	26/09/2019	23/02/2020*	150	N/A	N/A	N/A	N/A	23.6	8.3	650	0.8	N/A
			ULU-7	ULU-7	80	26/09/2019	23/02/2020	150	N/A	N/A	0.316	0.3	23.6	8.3	650	0.9	1×10^{-5}
			N-02-20-T	ULU-10	70	23/02/2020	6/11/2022	987	10.893	11.037	1.331	1.8	23.9	8.1	650	0.6	1×10^{-5}
			N-02-20-I	ULU-9	70	23/02/2020	6/11/2022*	987	4.843	4.907	1.671	2.5	23.9	8.3	650	0.6	5×10^{-5}
			N-02-20-F	ULU-3	70	23/02/2020	6/11/2022	987	11.654	11.807	3.379	3.2	23.9	8.3	650	0.8	2×10^{-5}
			N-02-20-P	ULU-2	70	23/02/2020	6/11/2022	987	2.454	2.486	0.588	0.6	23.9	8.4	650	0.9	2×10^{-5}
			N-02-20-H	ULU-8	70	23/02/2020	6/11/2022	987	2.272	2.302	0.696	0.7	23.9	8.4	650	0.8	3×10^{-5}
			N-02-20-K	ULU-11	70	23/02/2020	6/11/2022	987	4.267	4.323	0.683	0.7	23.9	8.2	650	0.7	8×10^{-5}
			N-02-20-E	ULU-4	70	23/02/2020	6/11/2022**	987	6.160	6.241	1.467	1.3	23.9	8.3	650	0.8	2×10^{-5}
			N-02-20-G	ULU-7	70	23/02/2020	6/11/2022	987	1.933	1.958	0.320	0.3	23.9	8.3	650	0.9	1×10^{-5}
			N-02-20-R	ULU-1	70	23/02/2020	6/11/2022	987	5.253	5.322	0.905	0.9	23.9	8.5	650	0.9	4×10^{-5}
			N-02-20-M	ULU-12	70	23/02/2020	6/11/2022	987	0.114	0.115	0.031	0.1	23.9	8.2	650	0.6	9×10^{-5}

Table 4.S3: Overview of surficial carbonate samples collected in natural caves. Temperature is reported as the average measured over the respective deployment period. CO_2 is based either on spot measurements during cave visits or continuous monitoring (Anapala Cave). M:L denotes the metal:ligand ratio as estimated by the dissolved organic carbon (DOC) concentration. Where no M:L is reported, limited sample precluded DOC measurements.

Cave	Latitude	Longitude	Sub-sample ID	Drip ID	Drip rate drips min^{-1}	Temperature ℃	CO_2 ppmv	M:L (molar) Co, Ni, Cu only
Te Reinga Cave Hawke's Bay, NZ	38°49'32.2"S	177°32'18.6"E	MIC-238	TR-K	1.0	11.3	850	1×10^{-5}
			MIC-240	TR-L	3.8	11.3	850	1×10^{-5}
Dave's Cave Southland, NZ	45°23'14.6"S	167°37'10.4"E	MIC-71	DC-CLEM-Core	N/A	4.1	650	3×10^{-5}
			MIC-72	DC-Core-Drips	18.5	4.1	650	2×10^{-5}
			MIC-73	DC-Upper-1	11.4	4.8	650	1×10^{-5}
			MIC-74	DC-Upper-2	7.5	4.8	650	N/A
			MIC-75	DC-Upper-3	170.8	4.8	650	8×10^{-6}
Hodge Creek Cave Tasman, NZ	41°10'12.6"S	172°41'12.7"E	MIC-77	HC-2 (no water)	0.0	6.3	650	1×10^{-5}
			MIC-78	HC-7	0.4	6.3	650	2×10^{-5}
			MIC-79	HC-8	0.2	6.3	650	1×10^{-5}
			MIC-80	HC-5	N/A	6.3	650	2×10^{-5}
			MIC-81	Council-Drips-1	1.0	N/A	650	N/A
			MIC-82	Council-Drips-2	0.9	N/A	650	N/A
			MIC-83	Council-Drips-3	2.6	N/A	650	N/A
			MIC-84	Council-Drips-4	0.9	N/A	650	N/A
			MIC-85	Council-Drips-5	5.6	N/A	650	N/A
			MIC-86	Council-Drips-6	2.4	N/A	650	N/A
Stafford's Cave Tasman, NZ	40°45'57"S	172°37'38"E	MIC-87	Stafford's-Drips-3	60.0	N/A	N/A	1×10^{-5}
			MIC-88	Stafford's-Drips-4	5.0	N/A	N/A	1×10^{-5}
			MIC-89	Stafford's-Drips-5	60.0	N/A	N/A	3×10^{-7}
			MIC-90	Stafford's-Drips-6	0.5	N/A	N/A	1×10^{-5}
Babylon Cave West Coast, NZ	42°02'54.8"S	171°29'33.2"E	B-2	Babylon-Drips-2	N/A	N/A	N/A	7×10^{-6}
			B-3	Babylon-Drips-3	20.0	N/A	N/A	9×10^{-6}
Majumba Cave Waikato, NZ	37°37'26.6"S	174°50'39.3"E	MIC-60	no water - chamber average used	N/A	14.6	N/A	6×10^{-5}
			MIC-63	no water - chamber average used	N/A	14.6	N/A	6×10^{-5}
			MIC-64	no water - chamber average used	N/A	14.6	N/A	6×10^{-5}
			MIC-65	no water - chamber average used	N/A	14.6	N/A	6×10^{-5}
			MIC-66	no water - chamber average used	N/A	14.6	N/A	6×10^{-5}
			MIC-68	no water - chamber average used	N/A	14.6	N/A	6×10^{-5}
			MIC-69	MAJ-6	0.9	14.6	N/A	2×10^{-5}
			MIC-70	MAJ-X	N/A	14.6	N/A	6×10^{-5}
Anapala Cave Niue	19°08'01.1"S	169°50'17.1"W	MIC-218	ANA-UC-2	N/A	24.2	420	4×10^{-5}
			MIC-216	ANA-UC-3	0.3	24.2	420	6×10^{-5}
			MIC-236	ANA-UC-8	0.3	24.2	420	2×10^{-5}
			MIC-215	ANA-UC-11	0.3	24.2	420	4×10^{-5}
			MIC-219	ANA-UC-13	0.0	24.2	420	1×10^{-5}
			MIC-210	ANA-UC-17	N/A	24.2	420	4×10^{-5}
			MIC-197	ANA-UC-17	N/A	24.2	420	4×10^{-5}
			MIC-212	ANA-UC-19	0.1	24.2	420	1×10^{-5}
			MIC-217	ANA-UC-20	0.1	24.2	420	4×10^{-5}
			MIC-211	ANA-UC-21	0.6	24.2	420	1×10^{-5}
			MIC-213	ANA-UC-22	0.3	24.2	420	4×10^{-5}
			MIC-214	ANA-UC-23	0.1	24.2	420	3×10^{-5}
			MIC-222	ANA-LC-11	0.7	23.8	600	2×10^{-5}
			MIC-234	ANA-LC-13	0.5	23.8	600	1×10^{-5}
			MIC-220	ANA-LC-14	0.6	23.8	600	2×10^{-5}
			MIC-235	ANA-LC-15	0.6	23.8	600	2×10^{-5}
			MIC-224	ANA-LC-17	0.8	23.8	600	3×10^{-5}
			MIC-221	ANA-LC-18	0.4	23.8	600	1×10^{-5}
			MIC-223	ANA-LC-19	0.1	23.8	600	3×10^{-5}
			MIC-241	ANA-BC-1	0.0	23.8	600	3×10^{-5}
Ulupaka Cave Niue	19°01'13.4"S	169°47'55.8"W	MIC-203	ULU-13	0.3	23.8	650	7×10^{-5}
			MIC-200	ULU-14	3.3	23.8	650	N/A
			MIC-201	ULU-15	1.7	23.8	650	N/A
			MIC-199	ULU-16	0.8	23.8	650	6×10^{-6}
			MIC-202	ULU-17	0.8	23.8	650	N/A
			MIC-204	ULU-18	0.1	23.8	650	N/A
			MIC-205	ULU-19	1.8	23.8	650	5×10^{-5}
			MIC-206	ULU-20	0.2	23.8	650	9×10^{-6}
			MIC-207	ULU-21	0.3	23.8	650	N/A
			MIC-208	ULU-22	0.2	23.8	650	N/A
			MIC-244	ULU-25	1.7	23.8	650	4×10^{-5}
			MIC-239	ULU-26	0.5	23.8	650	4×10^{-5}
			MIC-248	ULU-27	0.1	23.8	650	4×10^{-5}
			MIC-243	ULU-28	N/A	23.8	650	4×10^{-5}
			MIC-245	ULU-29	1.4	23.8	650	4×10^{-5}
			MIC-198	ULU-2	0.6	23.8	650	2×10^{-5}
Avaiki Cave Niue	18°59'49.9"S	169°54'40.0"W	MIC-229	AV-1-Drip	N/A	24.5	420	2×10^{-5}
			MIC-225	AV-2-Drip	12.0	24.5	420	4×10^{-5}
			MIC-226	AV-3-Drip	60.0	24.5	420	2×10^{-5}
			MIC-228	AV-4-Drip	8.7	24.5	420	1×10^{-5}
			MIC-230	AV-5-Drip	3.2	24.5	420	7×10^{-5}
Palaha Cave Niue	18°59'43.9"S	169°54'33.5"W	MIC-231	PAL-3	1.2	24.5	420	3×10^{-5}
			MIC-233	PAL-4	5.6	24.5	420	2×10^{-5}
			MIC-232	PAL-5	4.3	24.5	420	3×10^{-5}

Table 4.S4: Selected elemental concentrations of natural cave waters. Where applicable, data present averages of multiple water samples from a given drip point. Instrumental quantitation limits are shown for each element in the third row. See also Supplementary Table 4.S5 for data from other caves.

Cave	Drip ID	Na	Mg	K	Ca	P	S	Co	Ni	Cu	Sr	Ba
		µmol L^{-1}	µmol L^{-1}	µmol L^{-1}	µmol L^{-1}	µmol L^{-1}	µmol L^{-1}	µmol L^{-1}	µmol L^{-1}	µmol L^{-1}	µmol L^{-1}	µmol L^{-1}
		0.4	0.4	12.8	2.5	0.03	15.6	0.002	0.002	0.002	0.001	0.001
Te Reinga Cave Hawke's Bay, NZ	TR-A	308	65.7	35.6	926	0.50			0.005	0.005	3.58	0.061
	TR-B	240	43.6	26.9	726	0.41			0.004		2.44	0.016
	TR-C	314	66.5	34.8	989	0.72			0.003	0.003	3.54	0.054
	TR-D	280	60.5	43.9	1064	0.71		0.003	0.005	0.010	4.01	0.038
	TR-E	284	62.5	40.8	1058	0.90			0.005	0.002	3.77	0.045
	TR-F	284	63.3	39.6	1046	0.70			0.003	0.002	3.82	0.042
	TR-G	282	61.0	42.8	1022	0.92		0.004	0.005	0.011	3.98	0.047
	TR-H	281	62.5	43.2	1053	0.97	18.55		0.004		3.70	0.044
	TR-I	287	62.9	41.0	1069	1.18			0.005	0.002	3.63	0.052
	TR-J	276	59.7	42.0	864	0.42			0.003	0.004	3.77	0.043
	TR-K	282	61.2	31.1	947	0.44			0.004	0.005	4.34	0.031
	TR-L	309	67.6	37.2	1407	1.27			0.007	0.002	4.68	0.039
	TR-SYP	318	70.2	35.7	1051	1.30		0.005	0.006	0.022	3.74	0.054
Dave's Cave Southland, NZ	DC-SYP	49	62.4		735	1.08			0.005	0.068	0.90	0.022
	DC-Upper-1	77	90.1		1075						0.90	0.017
	DC-Upper-2	69	87.1		972	0.12					0.84	0.014
	DC-Upper-3	75	93.0		1542						0.93	0.017
	DC-Upper-4	61	75.9		1097	0.74				0.003	0.91	0.018
	DC-Upper-5	61	67.1		950	1.87					0.79	0.015
	DC-Upper-6	52	60.4		987	1.96			0.002		0.96	0.033
	DC-Upper-7	57	72.8		1004	1.18					1.04	0.028
	DC-Upper-8	66	43.5		1015	0.95			0.004	0.012	0.95	0.741
	DC-Upper-9	56	74.9		647	0.84					0.83	0.016
	DC-Upper-10	57	65.4		600	1.22			0.010	0.027	0.70	0.017
	DC-Upper-11	46	57.9		711	1.62					0.89	0.025
	DC-Core-Drips	66	76.5		1093	0.71				0.004	0.98	0.013
Hodge Creek Cave Tasman, NZ	HC-5	130	340.2		1075				0.003	0.002	3.98	0.044
	HC-7	136	368.7	13.6	731	0.11	85.17		0.003	0.003	4.12	0.038
	HC-8	123	341.1	13.5	864	0.33	62.87		0.002	0.002	4.04	0.041
Council Cave Tasman, NZ	Council-Drips-1	146	44.8		1380					0.002	0.77	0.041
	Council-Drips-2	174	46.1		1522				0.010	0.002	0.94	0.051
	Council-Drips-3	155	42.4		1405				0.002		0.83	0.045
	Council-Drips-4	160	45.7		1385				0.002	0.002	0.91	0.044
	Council-Drips-5	147	44.8		1430						0.84	0.045
	Council-Drips-6	168	48.1		1405						0.87	0.047
Stafford's Cave Tasman, NZ	Stafford's-Drips-3	256	66.6		1622				0.002	0.002	1.54	0.048
	Stafford's-Drips-4	277	75.3		1964				0.002	0.002	1.79	0.051
	Stafford's-Drips-5	260	66.6		1734						1.56	0.049
	Stafford's-Drips-6	348	93.0		1687				0.002	0.002	2.10	0.061
Babylon Cave West Coast, NZ	Babylon-Drips-2	212	62.5		988						0.50	0.021
	Babylon-Drips-3	212	60.9		993				0.002		0.47	0.020
Majumba Cave Waikato, NZ	MAJ-X	1466	218.3	23.2	944	0.62	310.10		0.017	0.003	4.58	0.243
	MAJ-A	712	224.3	25.8	1614	0.10	580.95		0.008	0.009	3.00	0.317
	MAJ-3	1440	206.0	23.8	848	0.12	441.23		0.003	0.007	3.77	0.132
	MAJ-4	1726	231.5	27.4	1077	0.12	443.97		0.009	0.011	4.26	0.209
	MAJ-5	1563	199.9	26.7	1101	0.60	397.13		0.003	0.003	4.12	0.220
	MAJ-6	1540	213.9	26.9	983	0.75	385.73		0.002	0.003	4.46	0.219
	MAJ-7	1486	190.9	27.0	1107	0.19	378.27	0.005	0.007	0.012	4.01	0.210
	MAJ-8	1511	194.9	28.8	990	0.24	401.31	0.005	0.006	0.012	4.13	0.207
	MAJ-9	1673	231.2	681.4	696	550.14	587.84	0.008	0.012	0.039	3.29	0.132
	MAJ-10	1386	178.3	41.1	849	23.21	403.89			0.009	3.73	0.186
	MAJ-11	1380	181.0	63.6	878	27.50	428.93			0.010	3.92	0.185
	MAJ-12	1746	226.9	34.4	1067	0.61	472.27	0.004	0.012	0.013	4.93	0.250
	MAJ-13	1444	184.5	28.8	925	0.24	338.46	0.005	0.008	0.016	4.20	0.177

Table 4.S5: Selected elemental concentrations of natural cave waters (continued). Where applicable, data present averages of multiple water samples from a given drip point. Instrumental quantitation limits are shown for each element in the third row. See also Supplementary Table 4.S4 for data from other caves.

Cave	Drip ID	Na	Mg	K	Ca	P	S	Co	Ni	Cu	Sr	Ba
		µmol L^{-1}	µmol L^{-1}	µmol L^{-1}	µmol L^{-1}	µmol L^{-1}	µmol L^{-1}	µmol L^{-1}	µmol L^{-1}	µmol L^{-1}	µmol L^{-1}	µmol L^{-1}
		0.4	0.4	12.8	2.5	0.03	15.6	0.002	0.002	0.002	0.001	0.001
Anapala Cave Niue	ANA-UC-1	4016	493.3	47.6	761	0.28	230.16	0.002	0.005	0.008	4.19	0.016
	ANA-UC-2	4686	549.8	49.3	833	0.15	255.08		0.004	0.005	5.03	0.008
	ANA-UC-3	3526	576.1	22.1	1177	0.33	227.78	0.003	0.005	0.007	5.57	0.003
	ANA-UC-4	4467	646.9	20.5	1268		303.12		0.004	0.005	5.70	
	ANA-UC-5	3960	588.2	21.0	1395		255.22		0.002	0.005	5.58	
	ANA-UC-6	3365	482.1	25.7	1017	0.11	238.06		0.002	0.003	4.27	0.002
	ANA-UC-7	5618	635.0	45.6	956	0.09	297.85		0.002	0.002	5.61	0.003
	ANA-UC-8	3109	471.8	29.4	987	0.23	229.69			0.004	4.46	0.003
	ANA-UC-9	2663	396.9	33.1	1110	0.77	171.15	0.003	0.004	0.009	3.38	0.004
	ANA-UC-10	3287	481.6	49.1	687	0.08	246.31		0.003	0.005	4.12	0.006
	ANA-UC-11	2483	427.0	23.6	284	0.09	200.37		0.002	0.003	2.14	0.005
	ANA-UC-12	447	70.7		191	0.04	37.07		0.014	0.002	0.64	0.003
	ANA-UC-13	2190	372.2	46.1	673	0.63	193.31			0.003	3.61	0.006
	ANA-UC-16	1666	373.6	50.3	772	3.31	118.35		0.002	0.008	3.78	0.006
	ANA-UC-18	3186	451.4	57.9	915	0.04	274.17			0.002	3.97	0.005
	ANA-UC-19	2421	400.3	46.3	926	0.20	170.15			0.003	3.22	0.007
	ANA-UC-21	3233	489.6	30.4	769	0.03	236.08			0.003	4.98	0.010
	ANA-UC-23	2320	408.1	109.9	811	0.09	158.78		0.003	0.004	3.31	0.007
	ANA-UC-24	2862	383.1	87.1	947	0.06	182.32		0.002	0.006	3.08	0.008
	ANA-LC-1	8108	851.4	66.5	1368	0.07	437.05		0.003	0.003	8.25	0.006
	ANA-LC-2	7699	817.6	64.9	1458	0.04	439.62		0.003	0.004	8.30	0.003
	ANA-LC-3	8088	803.4	50.8	1211	0.04	496.48		0.002	0.002	7.37	0.003
	ANA-LC-4	5408	607.0	38.6	988	0.15	440.58		0.002	0.004	5.63	0.004
	ANA-LC-5	8435	827.7	52.8	1441	0.08	611.65		0.003	0.008	7.88	0.002
	ANA-LC-6	6074	671.6	45.9	1232	0.07	428.09			0.003	6.35	0.003
	ANA-LC-8	3045	386.8	27.5	512	0.26	270.36			0.005	3.53	0.005
	ANA-LC-9	3623	552.2	68.8	787	0.17	327.50			0.004	4.79	0.011
	ANA-LC-10	3619	498.8	33.3	802	0.35	287.03			0.004	4.46	0.007
	ANA-LC-11	4681	619.6	68.0	702	0.04	367.80			0.005	5.01	0.007
	ANA-LC-12	2996	536.2	83.8	727	0.31	310.70			0.003	4.07	0.006
	ANA-LC-13	2894	571.6	107.5	777	0.06	287.54			0.004	4.74	0.008
	ANA-LC-14	4439	489.3	32.0	746	0.04	331.47		0.002	0.004	4.37	0.006
	ANA-LC-15	5060	647.6	68.5	921	0.13	393.27			0.005	5.49	0.009
	ANA-LC-16	2399	407.0	50.6	640	0.09	249.45		0.015	0.003	3.83	0.007
	ANA-LC-17	3544	530.2	57.0	759		278.90		0.002	0.005	4.77	0.006
	ANA-LC-18	3882	514.6	41.2	688	0.10	327.82			0.003	4.34	0.006
	ANA-LC-19	3436	615.5	88.4	728	0.11	283.07		0.004	0.004	4.62	0.007
Ulupaka Cave Niue	ULU-1	897	150.5		913	0.25	71.41	0.002	0.003	0.006	3.10	0.002
	ULU-2	851	140.9		1023	0.47	69.13		0.003	0.003	3.18	0.002
	ULU-3	953	150.3		1184	0.07	79.84		0.002	0.003	3.73	0.003
	ULU-4	1174	156.2		1264	0.19	88.07			0.007	4.09	
	ULU-5	1151	141.3		1225	0.44	73.88			0.004	3.59	
	ULU-7	722	141.7		1396	0.31	64.43			0.004	3.57	
	ULU-8	1057	141.8		1031	0.03	70.15		0.003	0.004	3.57	0.002
	ULU-9	1063	131.5		758	0.57	60.79		0.003	0.003	2.70	0.002
	ULU-10	1138	143.6		1107	0.16	76.04			0.004	4.19	0.003
	ULU-11	1236	155.2		1361	0.63	80.74	0.007	0.007	0.011	4.44	0.006
	ULU-12	1030	144.7		748	1.86	82.01	0.004	0.004	0.017	4.81	0.007
	ULU-13	1112	147.5		903	0.05	81.66	0.005	0.011	0.006	3.83	0.008
	ULU-14	835	143.2		1384	0.67	72.53				3.53	0.004
	ULU-15	923	144.5		1351	0.43	71.63				3.79	0.004
	ULU-16	987	148.3		943	0.05	73.11			0.002	3.61	0.004
	ULU-17	950	142.9		1120	0.06	72.04				3.77	0.004
	ULU-18	1045	139.1		1144	0.10	72.42				3.93	0.005
	ULU-19	1033	145.9		962	0.23	74.07	0.004	0.005	0.006	3.97	0.007
	ULU-20	1028	126.4		665	0.32	50.44			0.002	2.77	0.003
	ULU-21	963	134.8		1038	0.23	83.24				3.77	0.005
	ULU-22	678	115.3		451		49.68				1.65	0.002
	ULU-23	1133	132.7		1244	0.08	66.86			0.002	4.27	0.006
	ULU-24	1068	141.4		811	1.65	74.27			0.010	3.72	0.005
Avaiki Cave Niue	AV-1	1026	721.5	20.8	1225	0.10	150.05		0.002	0.008	11.26	0.018
	AV-2	3669	1192.9	132.8	1812	0.07	264.70	0.005	0.007	0.011	16.89	0.011
	AV-3	7550	1542.5	203.9	2380	0.08	471.05		0.003	0.007	23.00	0.007
	AV-4	1121	565.3		551	0.04	117.25		0.002	0.005	6.89	0.006
	AV-5	3675	834.4	113.0	1210	0.32	321.98	0.008	0.012	0.020	12.05	0.020
Palaha Cave Niue	PAL 1	6616	1351.0		987	0.03	198.82		0.005	0.006	24.48	0.015
	PAL-3	4100	1048.0	32.4	1691	0.12	306.05		0.003	0.011	19.03	0.007
	PAL-4	4717	1085.0	17.8	1644	0.03	289.73		0.003	0.009	19.81	0.004
	PAL-5	1606	529.2	18.1	1138	0.28	127.96		0.005	0.011	12.31	0.009

Chapter 5

Trace elemental systematics in dripwater and stalagmites from two Niuean caves – a case study

Chapter notes: The content of this chapter is unplublished. In its current form, this chapter integrates intermittent cave monitoring data from two caves from Niue, South Pacific, as well as preliminary interpretations of elemental and isotopic proxy records of two Holocene stalagmite samples. Sebastian F. M. Breitenbach (Northumbria University) conducted stalagmite isotope analyses, Jeffrey Lang (University of Waikato) performed structure-from-motion imaging and processing, Fernando Gázquez (University of Almería) performed water isotope analyses, John Hellstrom (ca. 80%; University of Melbourne) and Denis Scholz (ca. 20%; University of Mainz) carried out stalagmite radiometric dating, Danielle Blackwell (ca. 70%) and Amanda French (ca. 30%) performed elemental analyses at the University of Waikato.

Abstract

Many of the numerous caves of the South Pacific island of Niue host annually-laminated, relatively fast-growing stalagmites with the potential to provide valuable high-resolution records of major oceanic and atmospheric climate phenomena. However, the interpretation of speleothem proxy records, such as trace element measurements, requires an understanding of modern-day environmental controls of the proxy system. In this study, trace element measurements in cave environments are assessed to further constrain their systematics in the context of a tropical coastal karst system. A particular focus was placed on alkaline earth metals (Mg, Sr), Na, and first-row transition metals (*e.g.*, Co, Ni, Cu, Zn), with the latter receiving increasing attention as potential indicators of dripwater discharge and extreme hydrological events. To this effect, field observations and chemical analyses from intermittent monitoring efforts between September 2019 and November 2022 of two Niuean caves were assessed with regards to hy-

drological controls and processes within the karst system. These data further served to inform a tentative interpretation of two Holocene stalagmite records obtained from one of the study locations. Although both stalagmite records lack reliable absolute chronologies due to problematic radiometric age-depth relationships, their trace elemental and reconnaissance stable isotope analyses permitted preliminary interpretations of environmental drivers and trends. Drawing on dripwater analyses for reference, the most pronounced elemental signal of stalagmite Mg/Ca ratios likely reflected a combined control of water-rock interactions, prior calcite precipitation (PCP), and marine aerosol inputs. Typically independent of these controls, Ni/Ca closely covaried with Mg/Ca, other PCP indicators, as well as $\delta^{18}O$ and $\delta^{13}C$, suggesting that Ni/Ca also reflected the local hydrology. Considering the similar but muted patterns of Cu, Co, and Zn, it is possible that transition metal concentrations exhibited a previously proposed kinetic drip rate signal throughout most of the stalagmite record, with only sporadic short-lived 'soil flushing' signatures in response to heavy rainfall events. However, in light of problematic age control, these proxy records remain indicative only, and require further investigation on absolute time-scales.

5.1 Introduction

In the South Pacific and indeed the Southern Hemisphere, palaeoclimatic records are comparably limited in number and temporal coverage (Knight et al., 2021), and are often limited to marine environmental archives that primarily record oceanic climate signals (*e.g.*, coral records; Linsley et al., 2000; DeLong et al., 2012). Consequently, longer-term dynamics of some major climatic processes (including rainfall variability) in the region remain comparably poorly constrained, and thus do not allow for confident predictions of their likely response to projected climate change scenarios. In this regard, the small island nation of Niue is particularly interesting due to its location in the South Pacific Convergence Zone (SPCZ), and its strong susceptibility to the El Niño-Southern Oscillation (ENSO). Migrations of the SPCZ result in a pronounced seasonality in rainfall with distinct wet and dry seasons, while the ENSO largely drives interannual variability (Wheeler & Aharon, 1997; Rasbury & Aharon, 2006). Niue is furthermore subject to tropical cyclones with at times devastating consequences, the occurrence of which may similarly be expected to change under future scenarios (Pinto et al., 2007). The raised atoll's characteristic karst topography gives rise to numerous chasms and cave systems, many of which are of high cultural significance and host abundant carbonate deposits (Aharon et al., 2006). Their strong potential for reliably recording environmental conditions at sub-annual temporal resolutions has been demonstrated in recent and Holocene records (Rasbury & Aharon, 2006; Murgulet, 2010; Nava-Fernandez et al., 2024). These records have primarily been interpreted based on growth rate estimates and/or stable isotope analyses, both of which provided valuable information on past rainfall dynamics.

A detailed investigation of trace element systematics has been carried out by Tremaine et al. (2016), whose comprehensive monitoring study of a coastal Niuean cave remains the

only one of its kind on the island, and indeed the wider region. The need for at least minimal cave monitoring to boost confidence in speleothem-based climate interpretations is increasingly recognised (*e.g.*, Czuppon et al., 2018; Tadros et al., 2022; Yin et al., 2021), given that different caves and indeed different drip locations within the same cave can exhibit vastly different sensitivity to climatic and environmental processes. This was reiterated in the study of Tremaine et al. (2016), who noted a significant marine contribution to Mg and other trace elements, which are typically interpreted in terms of bedrock processes in continental settings. Specifically, the ratios Mg/Ca and Sr/Ca, in particular, are most commonly interpreted to reflect drying or wetting of the karst. This typically results in a fractionation of Mg and Sr relative to Ca as prior calcite precipitation (PCP) in pore spaces is enhanced or reduced, respectively (*e.g.*, Fairchild et al., 2000; Sinclair et al., 2012). Consistent with a limited number of other studies in coastal settings (*e.g.*, Moreno et al., 2010; L. M. Baldini et al., 2015), however, a significant contribution of marine aerosols (*i.e.*, sea spray) to the dripwater chemistry may considerably alter speleothem elemental concentrations, and complicate conventional approaches to interpret these.

Likewise indicative of hydrological processes, the concentrations of first-row transition metals (*e.g.*, Co, Ni, Cu) have gained increasing attention as potential tracers of past rainfall events in stalagmites (*e.g.*, Warken, Kuchalski, et al., 2022; Ban et al., 2008; Hartland et al., 2014). Due to their association with organic components in the soil zone, peak elevated transition metal contents in speleothems are typically attributed to short-lived extreme events that trigger 'flushing' of the soil zone by meteoric water. At low to moderate drip rates, however, field-based and experimental evidence increasingly supports the existence of an additional and potentially dominant rate-dependent (kinetic) control on transition metal contents in stalagmites, governed by the decay of organic metal complexes (OMCs) at the dripwater-stalagmite interface (Hartland & Zitoun, 2018; Lindeman et al., 2022; Giesche et al., 2023; Sliwinski et al., 2022; Chapter 3 and Chapter 4). Specifically, the time-sensitive release of transition metals by OMC decay is expected to result in lower and higher metal concentrations in the carbonate in response to shorter and longer drip intervals (and water residence time at stalagmite surfaces, by extension), respectively (Chapter 3).

With particular focus on conventional and novel hydrologically-sensitive elemental proxies, this case study aims to investigate modern trace element systematics in dripwaters from tropical cave environments, with view to providing an empirical basis for the eventual interpretation of stalagmite-derived palaeoclimatic records from these. To this effect, preliminary results of an ongoing monitoring study of two Niuean caves carried out intermittently between September 2019 and November 2022 are initially discussed. Secondly, the field observations and analyses of modern dripwaters serve to inform tentative interpretations of two stalagmite samples (ca. 9.51 to 0.48 ka BP) from one of the monitored systems, which are ultimately aimed to provide a rare high-resolution account of Holocene hydroclimate variability in this region.

5.2 Materials and methods

5.2.1 Study sites

Geological context and climate of Niue

The island nation of Niue in the central South Pacific (ca. 19°00'S, 169°50'W; Figure 5.1), home to approximately 1,600 people, presents a typical example of an uplifted "simple carbonate island" according to the classification scheme of Mylroie et al. (2001). The topography is characterised by three main units that are inherent features of the island's coral atoll history (Marsters & Kennedy, 2014). Most of the island's area of ca. 298 km^2 is comprised of the central shallow, flat-bottomed ancient Mutalau Lagoon (ca. 35 m above sea level), which is nearly continuously surrounded by the karstified remnants of the former barrier reef. The Miocene Mutalau Reef crest, ca. 60 to 70 m above sea level, is lined on the seaside by the narrow Alofi Terrace at approximately 20 – 23 m above sea level, which is primarily comprised of Pleistocene fringing reefs (Kennedy et al., 2012).

The karst topography of the island gives rise to numerous chasms and cave systems of various types, which in turn host speleothems with a range of distinct morphologies. Important baseline data in this respect were compiled by Aharon et al. (2006), who characterised different Niuean cave settings by example of the caves Avaiki, Palaha, and Ulupaka, and speleothems obtained from these. Two main types of caves were therein broadly categorised as inland water-table caves (including Ulupaka Cave) and coastal caves, most of which are seaward dipping open systems found along the flank-margin of Alofi Terrace on the leeward side of the island (*e.g.*, Avaiki Cave and Palaha Cave). In addition, several other caves were recently surveyed with a view to recording the cave fauna (Millar, 2017), while earlier studies were primarily concerned with archaeological aspects (Worthy et al., 1998). Detailed information on speleothem development in Niuean caves, however, is largely limited to the work of Aharon et al. (2006). Importantly, petrographic studies of active stalagmites have shown distinct differences between specimens collected from coastal (*i.e.*, flank-margin) caves compared to samples from inland (water-table) caves (Aharon et al., 2006), suggesting that inland caves host generally better developed speleothems than their more exposed and highly-ventilated coastal equivalents. It is noted that cave freshwater pools presented the sole source of drinking water for the island's population until the establishment of first wells, since surface water bodies, such as streams or lakes are absent. Torches made from plant materials used during visits left many caves with varying extent of soot covering the surfaces or forming distinct layers in the sediment in highly frequented sites. Consequently, it is not unlikely that some speleothems may have incorporated soot particles during their growth, which could compromise trace elemental concentrations. However, this was not evident in petrographic analyses carried out by Aharon et al. (2006) on samples from Ulupaka Cave, which was noted to contain substantial amounts of soot by Millar (2017). The region further experiences earthquakes associated with the Tonga

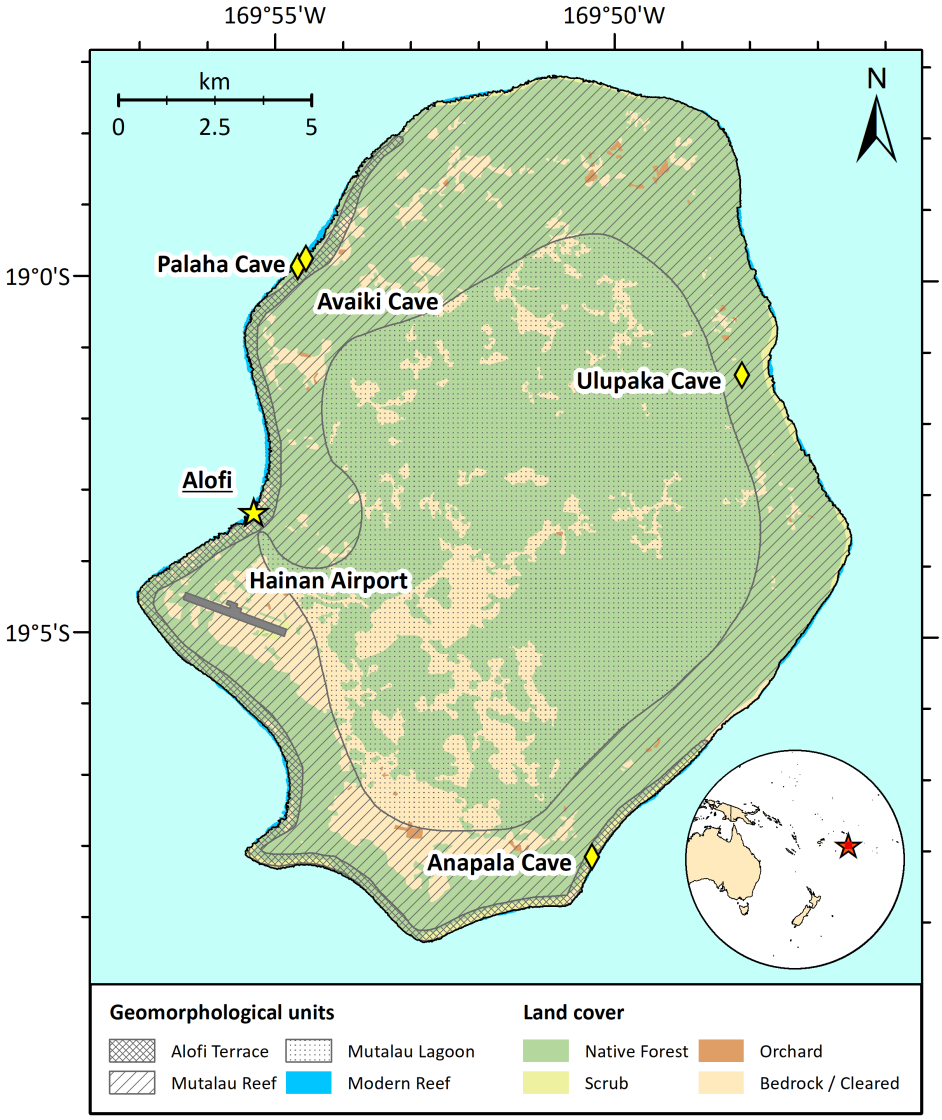

Figure 5.1: Map overview of study sites and main surface features on Niue. The location of Niue in the South Pacific is denoted by the red star in the map inset. The location of the capital and governmental seat of Alofi is marked by the yellow star symbol. Meteorological data from the Niue Meteorological Service were recorded at Hainan International Airport. Anapala Cave and Ulupaka Cave were actively equipped with monitoring instrumentation, while the publicly accessible sea caves of Avaiki and Palaha were visited infrequently. Spatial datasets were obtained from Land Information New Zealand (LINZ; https://data.linz.govt.nz, accessed in January 2020) and processed using the ArcGIS Desktop software suite (ver. 10.5.1; Esri Inc., USA).

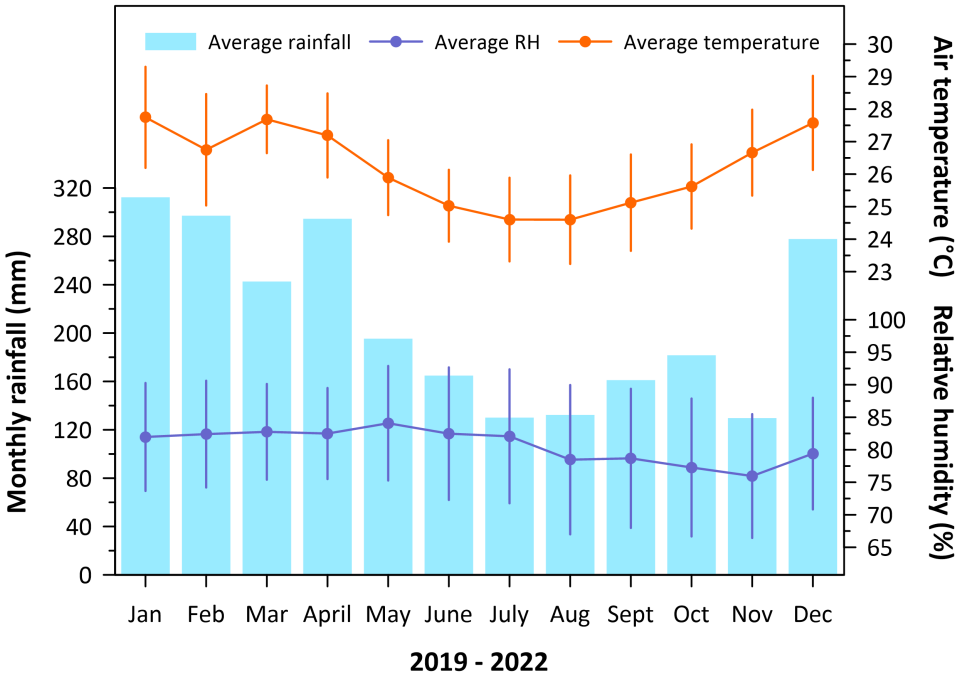

Figure 5.2: Monthly climate statistics of Niue for the study period of 2019 – 2022. Air temperature (top) and relative humidity (RH; bottom) data are the averages of daily measurements for each month. Rainfall is reported as the average total monthly rainfall. Data were provided by the Niue Meteorological Service and collected at Hainan Airport, Alofi. Error bars denote 1 SD of the mean.

Trench, which have verifiably resulted in significant structural changes of some cave systems (*e.g.*, Vaikona Chasm, Willie S., personal communication). Indeed, severe shaking linked to a 7.5 magnitude earthquake between Niue and Tonga during the field campaign of November 2022 resulted in the displacement of several sampling devices, and damage to multiple fragile stalactites in Ulupaka Cave.

The original Niuean reef, fore-reef, and lagoonal facies with a primary calcite and aragonite mineralogy have in many parts of the island been considerably dolomitised, presumably due to interactions with hypersaline (and Mg-rich) brines generated under evaporative conditions during tectonic uplift and low glacio-eustatic sea levels (Terry, 2004; Wheeler et al., 1999). Generally, the carbonate bedrock exhibits high permeability, practically precluding surface runoff and water logging. The comparably pure and readily dissolved carbonate bedrock (>90% $CaCO_3$; Soulsby, 2004) and sediments furthermore limit soil production, which is manifest in the generally shallow soil zones, particularly on the elevated reef plateau and rim formations that host most of the caves. Soils have previously been described and classified in detail (*e.g.*, Leslie, 1986; Fieldes et al., 1960), but are comparably uniform with common traits. For instance, Niuean soils are typically characterised by circum-neutral pH, high permeability, low Si and K contents, and anomalously high natural radioactivity (see Soulsby (2004) and Whitehead et al. (1993) for discussion).

The Niuean climate is oceanic and primarily governed by the intra-annual latitudinal migration of the South Pacific Convergence Zone (SPCZ), resulting in a distinct monsoon season from ca. December to April with a monthly average rainfall of ca. 307 mm, and a dry sea-

son from May to November (ca. 84 mm rainfall/month; Figure 5.2). Relative humidity is high at around 80% largely irrespective of season, and similarly, temperatures remain relatively constant throughout the year with ca. 26 °C and 24 °C on average in the monsoon and dry season, respectively (Rasbury & Aharon, 2006). Inter-annual rainfall variability is largely driven by ENSO, with El Niño events typically entailing relatively dry conditions that may at times result in severe droughts, whereas strong La Niña conditions are commonly associated with enhanced rainfall (Wheeler & Aharon, 1997). At a longer-term scale, ENSO is understood to be modulated by the Inter-Decadal Pacific Oscillation (IPO) (Folland, 2002).

Anapala Cave

Unlike many Niuean caves, which have traditionally been extensively used for freshwater supply or cultural practices, there is little anecdotal or physical evidence of frequent human visits to Anapala Cave. The cave has not been previously described in the academic literature. The system appears to have developed in line with Anapala Chasm (19°08'01.4"S, 169°50'17.3"W; Figure 5.1), a collapsed former cave near the village of Hakupu, ca. 200 m from the island's south-eastern shoreline. The cave's largest opening is located near the top of the chasm, which extends tens of metres down to a freshwater pool of historic significance. Scuba diving in September 2019 confirmed that this rainfall-fed pool comprises a freshwater lens located on top of saltwater due to an apparent connection to the ocean. As such, the chasm water level is modulated by tidal cycles, and varied by several cm over the course of a week-long observation period (although much larger level changes in the order of tens of cm have been observed; Richard Siataga (RS), personal communication). A continuation of the water body was not found within Anapala Cave at the readily accessible depth of the system, but a proximal and potentially connected shaft historically provided freshwater during droughts when other sources had ceased (RS, personal communication).

The herein termed "upper" chamber of the cave is an inclined, narrowing passage extending perpendicularly to the general chasm orientation. The upper part of the cave is shallow, possibly with less than 10 m overburden. Although relatively close (ca. 45 m) to the entrance, a couple of narrowing chambers appear to limit ventilation as suggested by a sudden perceivable change in humidity upon entering. Inside this chamber, several speleothems have developed along the walls and centrally on the ground, most of which are fed by active drips. The chamber includes a few stalagmites of up to ca. 25 cm height, but most vertical formations are short (few cm) and/or wide stumps, often encircled by small pool features and rimstones attesting to occasional significant flow. Many formations possess small central depressions and grooves, possibly indicative of dissolution. Both stalagmites and stalactites are often highly variable in morphology across the same formation, implying diverse and likely discontinuous flow histories. Throughout the cave, surfaces are extensively covered with cave coral, and seemingly inactive speleothems are abundant. Structurally complicated formations, such as helictites, are likewise frequently found. Most formations have strong orange to brownish colourations.

The "lower" chamber is considerably more extensive than the upper part of the system,

opening to a maximum ceiling height and horizontal extent of ca. 15 m and 30 m, respectively. This chamber includes various large boulders associated with the collapsed ceilings and/or ground shaking. Stalagmites have formed on top of some of these boulders as well as on the presently concealed ground underneath, providing the prospect for constraining the timing of the structural damage. The lower chamber narrows vertically, but again opens into a larger chamber located diagonally below. This "bottom" chamber was so-termed as no deeper part of the cave was safely accessible during the visits, although a steep vertical shaft of $<$10 m depth alludes to a continuation of cave. Example three-dimensional renderings of the upper and lower chambers from an ongoing mapping effort are shown in Figure 5.S1.

Ulupaka Cave

The water-table cave of Ulupaka is located near the eastern coast of Niue (19°01'13.4"S, 169°47'55.8"W; Figure 5.1) and has in some detail been described by Aharon et al. (2006) and Millar (2017). The cave has formerly been open to visitors on guided tours, but these had been discontinued before the start of this study. Throughout the cave, substantial damage to decorations attest to frequent human recreational and possibly habitational use, while it historically also served as freshwater supply, burial grounds, and cyclone shelter (Daryn Magatogiia, personal communication). A noticeable feature of Ulupaka Cave is a thin black film coating almost all surfaces of the cave, which was not observed in any other cave visited. Exceptions to the black coating are patches and formations of fresh deposits, and the ground-facing surfaces of multi-layered speleothems. Likely derived from the soil above, the exact nature of the black film is unclear. Some broken speleothems show evidence of episodic events depositing these black layers (*e.g.*, severe rainfall / flooding), while other speleothems are clear throughout.

This study was focussed on a side chamber (denoted Ulupaka Cave "study chamber" in data tables) of the cave, accessible over a small ridge of mostly active deposition. While the cave entrance is virtually at ground level, the cave gains depth at a slight angle before a couple of step changes in elevation perceivably limit its atmospheric connectivity. The study chamber is characterised by a high density of actively depositing stalagmites amongst tall fossil formations, reaching heights of ca. 80 cm. Most of the chamber's deposits are fed by discrete stalactites, many of which are soda straws. Example three-dimensional renderings of the study chamber from an ongoing mapping effort are shown in Figure 5.S2.

5.2.2 Cave monitoring and sample collection

Cave monitoring

To establish a modern reference and increase confidence in speleothem-based climate reconstructions, cave monitoring was initiated in September 2019 at Anapala Cave and Ulupaka Cave. Although anticipated bi-annual visits came to a halt after the second field campaign in February 2020 due to unforeseen circumstances, fieldwork was recommenced in November

2022 to re-establish and expand monitoring efforts.

Anapala Cave

In Anapala Cave, two chambers with actively accreting speleothems were selected for long-term cave monitoring. The herein termed upper chamber (denoted in sample IDs as "UC") was equipped with a custom-built cave atmosphere monitoring station comprising a GMP252 CARBOCAP® carbon dioxide probe, HMP110 HUMICAP® sensor to measure temperature and relative humidity, and a CS106 BAROCAP® barometer (all Vaisala, Finland). The sensors were operated through a CR1000 wiring interface (Campbell Scientific, USA), measuring all parameters every three hours (*i.e.*, eight times per day) for a period of 2 minutes (12 repeat measurements in intervals of 10 seconds). Measurements were preceded by a 10-minute sensor warm-up phase, which ensured that the sensors were at operating temperature. The monitoring station was complemented by a HOBO® TidbiT temperature logger (v2; Onset, USA) for independent temperature measurements, and a CO_2 data logger (Goodsell Systems Ltd, UK) with a nondispersive infrared sensor as of November 2022 (data not available here). The lower chamber ("LC") of Anapala Cave was initially equipped with a single HOBO® TidbiT temperature logger for atmospheric measurements, which was augmented with a Goodsell Systems CO_2 data logger in November 2022. Five Stalagmate® acoustic drop counters (Driptych, UK) were deployed on top of active stalagmites targeted for potential future sampling. Each drip logger was equipped with sandblasted watch glasses to collect fresh precipitates. In addition to in-cave instrumentations, a HOBO® TidbiT was placed above the cave entrance in February 2020, replacing a lost logger installed in September 2019. As of November 2022, a fourth HOBO® TidbiT was installed in the "bottom chamber" ("BC"), which had not been accessed on previous visits. A Syp fluid autosampler (Waikato Scientific, Aotearoa New Zealand; https://www.waikatoscientific.com/syp) was deployed in November 2022 to automatically collect weekly dripwater samples from drip point ANA-LC-5, which had been confirmed to be active throughout the year.

Ulupaka Cave

A second cave monitoring program was established in 2019 in Ulupaka Cave, targeted primarily for in-cave calcite farming experiments. Ulupaka Cave showed evidence of generally faster calcite growth rates amenable to collecting natural precipitates over feasible time-scales, but also hosts stalagmites potentially suitable for palaeoclimatic applications. The study chamber was initially equipped with a HOBO® TidbiT and a Stalagmate® drip counter carrying a watch glass, and three additional watch glasses placed on the tips of stalagmites. The deployment of monitoring equipment and watch glasses was progressively increased during fieldwork in February 2020 and November 2022. As of November 2022, a total of 29 watch glasses are deployed in both established (*i.e.*, previously monitored) and several new drip sites across the chamber. Six of these glasses were placed on top of Stalagmate® drip counters. Atmospheric

monitoring was augmented by the addition of a Goodsell Systems CO_2 data logger and a second HOBO® TidbiT. The latter was placed closer to the cave entrance to evaluate the connectivity of the study chamber to external conditions. A Syp fluid autosampler was installed at drip point ULU-3 to collect weekly samples in temporal synchronisation with the Anapala Cave unit. Owing to a sufficient drip height at both ANA-LC-5 and ULU-3, Stalagmate® drip counters could be attached to the sides of the funnels in a manner that allowed recording of drip impacts inside the funnels. This setup was preferred over placing drip loggers and watch glasses inside the funnels, which would yield modern precipitate, but in the process alter the original drip chemistry due to progressive calcite precipitation.

Dripwater collection and *in-situ* measurements

Drip points for long-term monitoring were surveyed based on flow rate (aiming for a wide range) and quality of associated speleothems (aiming for active deposits). Drip rates were generally very low during initial fieldwork in September 2019 (typically $<$1 drip per 15 minutes), resulting in the identification of relatively few active drips in Anapala Cave. However, further drip points were added to the monitoring program in all sampled caves during follow-up visits.

During cave visits, the atmospheric pCO_2 was measured using a Vaisala GMP252 CO_2 sensor attached to an MI70 handheld measurement indicator prior to commencing work in a cave chamber. Handheld single-drop probes were used to measure *in-situ* pH (LAQUAtwin pH22; HORIBA Advanced Techno Co., Ltd., Japan), electrical conductivity, and temperature (both using a HORIBA LAQUAtwin EC22) of water at each of the selected study sites. Water measurements were typically carried out in triplicate. Drip intervals were determined manually. Supplementary Table 5.S1, Table 5.S2, and Table 5.S3 provide a summary of monitored drip points.

Dripwater samples were collected using acid-clean (10% HCl, then 10% HNO_3) polypropylene Falcon™ centrifuge tubes (15 mL or 50 mL) or 70 mL polypropylene specimen collection beakers, either directly from the drips or with the aid of acid-clean funnels where drips were too high or slow. Samples were subsequently filtered (0.45 µm PES syringe filters) and stored in the fridge at ca. 4 °C. Rainwater was sampled during fieldwork using 4 mL glass vials (filled completely). In line with Aotearoa New Zealand biosecurity requirements, all biological samples (including water and soils) were required to be shipped for import into Aotearoa New Zealand, during which continuous refrigeration could not be guaranteed. However, shipment was timed to minimise transfer times, and samples were refrigerated immediately again upon arrival at the University of Waikato, and processed for analyses as soon as possible.

Daily records of rainfall, temperature, humidity, and atmospheric pressure for the years of 2019 – 2022 were provided by the Niue Meteorological Service (Figure 5.2 and Figure 5.3). These measurements were collected by an automated weather station at Hanan International Airport (19°04'35.1"S, 169°55'38.1"W; Figure 5.1).

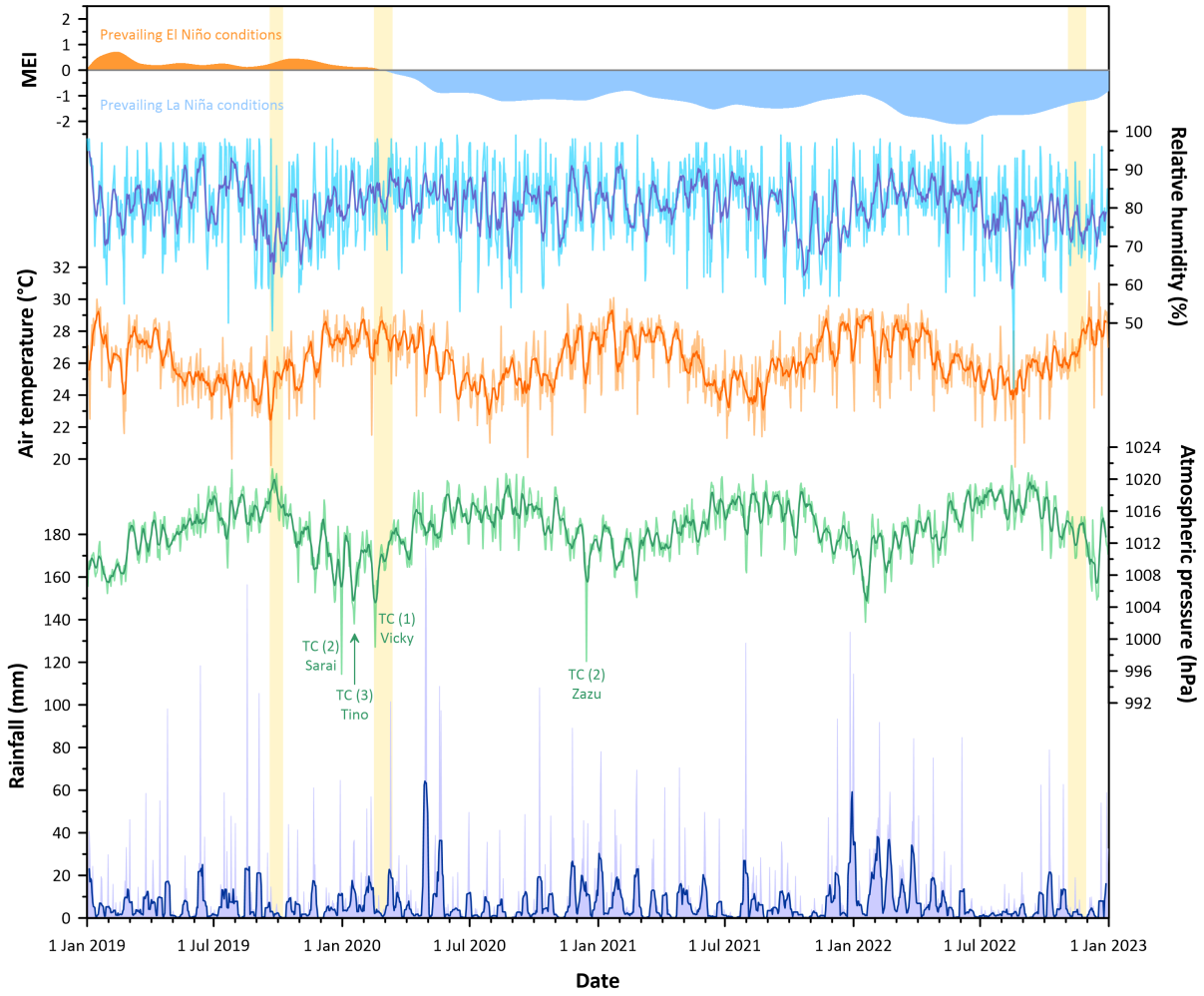

Figure 5.3: Daily meteorological observations of Niue for the years 2019 – 2022. Data were provided by the Niue Meteorological Service and collected at Hainan Airport, Alofi. Solid lines in each plot reflect the 7-day running average. Positive and negative values of the Multivariate El Niño-Southern Oscillation Index Version 2 (MEI.v2; obtained from https://www.psl.noaa.gov/enso/mei, National Oceanic and Atmospheric Administration (NOAA); accessed May 2023) define prevailing El Niño and La Niña conditions, respectively. Vertical yellow bars indicate the three periods of fieldwork, with cave monitoring commencing in September 2019. So-defined tropical cyclones with direct effect on Niue are marked as 'TC' with their maximal category in brackets.

Table 5.1: Overview of watch glass deployments in Anapala Cave and Ulupaka Cave. The observed R_{acc} and modelled R_{prec} denote empirical total accumulation rates and theoretical precipitation rates, respectively (see Chapter 4 for details). Deployment end dates marked by one asterisk (*) indicate that glasses had slid off the original location but were intact. Two asterisks (**) indicate that glasses had fallen and broken, but $CaCO_3$ was retrievable. Drip rate is the average of spot measurements or the median of drip logger continuous data. Temperature is the average derived from hourly logger measurements. The calcite saturation index ($SI_{Calcite}$) was calculated using PHREEQC (Interactive ver. 3.7.3; Parkhurst & Apello, 1999).

Cave	Glass ID	Drip ID	Deployed	Retrieved	Growth time	Total mass	Observed R_{acc}	Modelled R_{prec}	Drip rate	Temperature	pH	CO_2	$SI_{Calcite}$
					days	mg	mg day^{-1}	mg day^{-1}	drips min^{-1}	℃		ppmv	
Anapala Cave	ANA-LC-5	ANA-LC-5	25/09/2019	22/02/2020	150	N/A	N/A	0.774	0.8	23.7	8.2	600.0	0.7
Niue	N-02-20-C	ANA-UC-4	22/02/2020	5/11/2022*	987	<0	N/A	0.134	0.2	24.3	7.9	420.0	0.4
	N-02-20-B	ANA-UC-6	22/02/2020	5/11/2022*	987	0.021	0.021	0.875	1.0	24.3	8.3	420.0	0.7
	N-02-20-D	ANA-LC-2	22/02/2020	5/11/2022*	987	0.235	0.239	0.618	0.6	23.8	8.2	600.0	0.7
	N-02-20-L	ANA-LC-5	23/02/2020	5/11/2022**	986	<0	N/A	0.923	0.9	23.8	8.2	600.0	0.7
Ulupaka Cave	ULU-3	ULU-3	26/09/2019	23/02/2020*	150	N/A	N/A	3.690	3.6	23.6	8.3	650.0	0.8
Niue	ULU-5	ULU-5	26/09/2019	23/02/2020	150	N/A	N/A	1.702	1.5	23.6	8.4	650.0	0.9
	ULU-6	ULU-6	26/09/2019	23/02/2020*	150	N/A	N/A	N/A	N/A	23.6	8.3	650.0	0.8
	ULU-7	ULU-7	26/09/2019	23/02/2020	150	N/A	N/A	0.316	0.3	23.6	8.3	650.0	0.9
	N-02-20-T	ULU-10	23/02/2020	06/11/2022	987	10.893	11.037	1.331	1.8	23.9	8.1	650.0	0.6
	N-02-20-I	ULU-9	23/02/2020	6/11/2022*	987	4.843	4.907	1.671	2.5	23.9	8.3	650.0	0.6
	N-02-20-F	ULU-3	23/02/2020	06/11/2022	987	11.654	11.807	3.379	3.2	23.9	8.3	650.0	0.8
	N-02-20-P	ULU-2	23/02/2020	06/11/2022	987	2.454	2.486	0.588	0.6	23.9	8.4	650.0	0.9
	N-02-20-H	ULU-8	23/02/2020	06/11/2022	987	2.272	2.302	0.696	0.7	23.9	8.4	650.0	0.8
	N-02-20-K	ULU-11	23/02/2020	06/11/2022	987	4.267	4.323	0.683	0.7	23.9	8.2	650.0	0.7
	N-02-20-E	ULU-4	23/02/2020	6/11/2022**	987	6.160	6.241	1.467	1.3	23.9	8.3	650.0	0.8
	N-02-20-G	ULU-7	23/02/2020	06/11/2022	987	1.933	1.958	0.320	0.3	23.9	8.3	650.0	0.9
	N-02-20-R	ULU-1	23/02/2020	06/11/2022	987	5.253	5.322	0.905	0.9	23.9	8.5	650.0	0.9
	N-02-20-M	ULU-12	23/02/2020	06/11/2022	987	0.114	0.115	0.031	0.1	23.9	8.2	650.0	0.6

Collection of modern cave precipitate

Modern cave $CaCO_3$ was collected on a total of 19 sandblasted watch glasses deployed under active drip points in Ulupaka Cave (14 glass deployments) and Anapala Cave (5 glass deployments). Following retrieval, watch glasses were allowed to dry and were subsequently stored in individual softly lined containers. At the laboratory, glasses were oven-dried at 30 ℃, prior to imaging and sub-sampling. The methodology and results of modern calcite analyses are discussed in more detail in Chapter 4 in the context of metal partitioning. Details of glass deployments are provided in Table 5.1.

Collection of speleothem samples

Stalagmite samples ANA-19-1 and ANA-19-9 were collected in September 2019 along with several other carefully selected speleothems from caves identified as suitable for palaeoclimate studies. The majority of samples collected had already been detached from their original base, either by natural events (*i.e.*, ground shaking, flooding) or previous cave visitors. ANA-19-1 was still intact upon collection, while ANA-19-9 was found detached from its base ca. 1 m downslope to ANA-19-1. Both samples originate from the lower chamber of Anapala Cave. Stalagmites found *in-situ* were chiselled off as closely to their base as possible. Further samples were identified as potential future targets following cave monitoring. To this effect, basal cores were obtained of two larger stalagmites for reconnaissance dating using a water-cooled electric

power drill with a 24 mm drill bit.

Collection of soil and bedrock samples

A total of 10 and 12 soil and bedrock samples, respectively, were collected from just above the studied caves and additional sites across the island. All soils were obtained from the A horizon from depths between 5 and 15 cm, discarding larger non-soil components during sampling. Bedrock samples were collected by removing weathered surfaces and chiselling off fresh material.

5.2.3 Sample processing and analysis

Processing and sub-sampling of stalagmites for geochemical analyses

Upon return to the laboratory, stalagmite samples were cut along their central growth axis using a circular saw. A second parallel cut was made to obtain a central slab, as well as two flank pieces. The exposed surfaces of the slab and one flank part of each stalagmite were polished using a sanding belt with fine grit initially, and cork for the final smoothing. The remaining flanks were archived. Prior to any physical alteration to the polished slabs, 2400 dpi scans of the surface facing the centre of the stalagmite were obtained for visual assessments and greyscale analysis. Powdered crystal sub-samples of stalagmites ANA-19-1 and ANA-19-9 were collected for geochemical analyses using a Sherline Model 5410 Mill (Sherline Products Inc., USA) equipped with a digital Sherline Wettroth readout and tachometer. A custom-built LED light stage facilitated the observation of growth layers and macrostructures. All sub-samples were drilled using a 1 mm diameter tungsten drill bit at ca. 750 rpm. Aliquots for dating were obtained by targeted drilling of discrete trenches of 1 mm width and between 5.0 and 10.0 mm length (2.0 mm depth) following visually distinct and coherent growth increments. Sub-samples were collected in acid-clean (10% HNO_3) 2 mL glass vials using a Teflon-coated scalpel and razor blade. Parallel and central to stalagmite growth, a continuous trench was drilled from the youngest to the oldest material at a resolution of 1 mm and a depth of 2.0 mm. The top 0.1 mm of material were discarded prior to sampling to minimise contamination, and drilling was carried out in vertical increments of 0.2 mm. This low-resolution strategy served to produce sufficient mass for several geochemical analyses, and generate reconnaissance data for potential future higher resolution milling (cf. J. U. L. Baldini et al., 2021).

Processing of bedrock and soil samples

To determine the bulk rock composition, dried (48 hours at 100 ℃) rock samples were broken up to expose fresh surfaces, from which multiple powdered sub-samples were collected and homogenised using a dental drill. Powdered sub-samples of 1 – 2 mg were dissolved in

5% (v/v) double-distilled HNO_3, and subsequently filtered (0.45 µm) in preparation for solution ICP-MS. Soil aggregates were manually broken up before oven-drying samples at 100 ℃ for 24 hours. The dried samples were split into three portions, one of which was archived. Representative sub-samples of one of the remaining portions were leached using 1 M ammonium acetate to obtain the exchangeable cation fraction (Ure et al., 1993). Aliquots of the other soil portion were leached using deionised water to mobilise readily soluble components. Both leachates were produced at a ratio of ca. 7.5 g soil in 50 mL solution, and were shaken for 24 hours. Following centrifugation, the supernatant was decanted and filtered using 0.45 µm PES syringe filters. Dilute aliquots of soil leachates were prepared for elemental quantification via ICP-MS (acidified to 2% HNO_3 v/v). The results of soil and bedrock analyses are summarised in Supplementary Table 5.S4 and Table 5.S5, respectively.

5.2.4 Analytical methods

Radiometric dating

Absolute ages of stalagmites ANA-19-1 and ANA-19-9 were determined using the ^{230}Th/U-method on powdered sub-samples obtained by targeted drilling. Initial reconnaissance ages (2 and 3 samples of ANA-19-1 and ANA-19-9, respectively) were determined using a Nu Plasma multi-collector inductively-coupled plasma mass spectrometer at the Max Planck Institute for Chemistry, Mainz, Germany, following protocols detailed by Obert et al. (2016). All activity ratios determined at the Max Planck Institute for Chemistry were corrected for detrital contamination assuming a ^{232}Th/^{238}U weight ratio of 3.8 (translating to an initial activity ratio $(^{230}\text{Th}/^{232}\text{Th})^{a}_{i}$ of 0.8) for the detritus and ^{230}Th, ^{234}U and ^{238}U in secular equilibrium. Additional ^{230}Th/U dating was performed on 9 and 14 samples from ANA-19-1 and ANA-19-9, respectively. These samples were analysed at the University of Melbourne, Australia, using a Nu Instruments Plasma MC-ICP-MS based on the approach detailed in Hellstrom (2003). Activity ratios determined at the University of Melbourne were corrected using an assumed $(^{230}\text{Th}/^{232}\text{Th})^{a}_{i}$ of 1.50 ± 1.50. Final ages are reported in thousands of years before present (ka BP) relative to 1950 AD. Data are summarised in Table 5.2.

Table 5.2: ^{230}Th/U dating results for stalagmites ANA-19-1 and ANA-19-9. The superscript *a* denotes activity ratios. Assumed values of $(^{230}Th/^{232}Th)^{a}_{i}$ were used to correct ages for detrital ^{230}Th. Uncertainties of activity ratios are reported as two standard deviations (2σ). Age errors are reported as 2σ and 1σ for analyses carried out at the University of Melbourne ('Melbourne') and the Max Planck Institute for Chemistry, Mainz ('Mainz'), respectively. Final ages are reported in thousands of years before 1950 AD (ka BP).

Stalagmite	Sample ID	Depth (mm)	^{238}U (ng/g)	$(^{230}Th/^{238}U)^{a}$	$(^{234}U/^{238}U)^{a}$	$(^{230}Th/^{232}Th)^{a}_{i}$	Uncorrected age (ka)	Corrected final age (ka BP)	Laboratory
ANA-19-1	ANA-1-11	1.3	243.0	0.0094 ± 0.0028	1.0257 ± 0.0020	1.5 ± 1.5	1.005 ± 0.299	0.91 ± 0.30	Melbourne
	ANA-1-1	2.9	232.9	0.0077 ± 0.0001	1.0281 ± 0.0005	0.8	0.823 ± 0.014	0.82 ± 0.01	Mainz
	ANA-1-3	5.6	241.8	0.0070 ± 0.0023	1.0254 ± 0.0022	1.5 ± 1.5	0.749 ± 0.249	0.67 ± 0.24	Melbourne
	ANA-1-4	10.9	253.6	0.0053 ± 0.0012	1.0263 ± 0.0023	1.5 ± 1.5	0.565 ± 0.128	0.49 ± 0.13	Melbourne
	ANA-1-5	18.0	233.9	0.0053 ± 0.0011	1.0265 ± 0.0025	1.5 ± 1.5	0.564 ± 0.117	0.48 ± 0.12	Melbourne
	ANA-1-10	22.6	217.1	0.0075 ± 0.0016	1.0250 ± 0.0022	1.5 ± 1.5	0.801 ± 0.171	0.72 ± 0.17	Melbourne
	ANA-1-6	27.0	222.6	0.0075 ± 0.0012	1.0220 ± 0.0023	1.5 ± 1.5	0.803 ± 0.129	0.72 ± 0.13	Melbourne
	ANA-1-7	35.3	267.0	0.0067 ± 0.0009	1.0247 ± 0.0020	1.5 ± 1.5	0.715 ± 0.096	0.63 ± 0.10	Melbourne
	ANA-1-8	42.3	274.3	0.0114 ± 0.0018	1.0223 ± 0.0024	1.5 ± 1.5	1.222 ± 0.195	1.14 ± 0.20	Melbourne
	ANA-1-2	48.1	220.8	0.0101 ± 0.0001	1.0208 ± 0.0005	0.8	1.084 ± 0.014	1.08 ± 0.01	Mainz
	ANA-1-9	54.2	226.7	0.0261 ± 0.0023	1.0158 ± 0.0023	1.5 ± 1.5	2.840 ± 0.253	2.75 ± 0.25	Melbourne
ANA-19-9	ANA-9-1	2.1	146.8	0.0509 ± 0.0005	1.0356 ± 0.0007	0.8	5.518 ± 0.049	5.50 ± 0.06	Mainz
	ANA-9-4	9.0	138.9	0.0349 ± 0.0024	1.0367 ± 0.0023	1.5 ± 1.5	3.733 ± 0.262	3.64 ± 0.26	Melbourne
	ANA-9-5	14.8	151.0	0.0422 ± 0.0021	1.0367 ± 0.0026	1.5 ± 1.5	4.531 ± 0.230	4.43 ± 0.23	Melbourne
	ANA-9-6	20.4	153.0	0.0390 ± 0.0015	1.0422 ± 0.0022	1.5 ± 1.5	4.158 ± 0.165	4.08 ± 0.16	Melbourne
	ANA-9-8	38.0	160.8	0.0479 ± 0.0016	1.0361 ± 0.0025	1.5 ± 1.5	5.161 ± 0.176	5.07 ± 0.18	Melbourne
	ANA-9-9	48.6	161.1	0.0448 ± 0.0016	1.0343 ± 0.0026	1.5 ± 1.5	4.828 ± 0.177	4.75 ± 0.18	Melbourne
	ANA-9-10	61.6	148.0	0.0482 ± 0.0021	1.0388 ± 0.0023	1.5 ± 1.5	5.177 ± 0.232	5.09 ± 0.23	Melbourne
	ANA-9-3	82.9	105.2	0.0594 ± 0.0004	1.0291 ± 0.0009	0.8	6.479 ± 0.054	6.48 ± 0.05	Mainz
	ANA-9-12	90.7	175.0	0.0645 ± 0.0018	1.0379 ± 0.0020	1.5 ± 1.5	6.995 ± 0.202	6.90 ± 0.20	Melbourne
	ANA-9-13	96.2	191.5	0.0517 ± 0.0032	1.0271 ± 0.0019	1.5 ± 1.5	5.634 ± 0.364	5.54 ± 0.35	Melbourne
	ANA-9-14	104.1	159.0	0.0518 ± 0.0016	1.0263 ± 0.0022	1.5 ± 1.5	5.646 ± 0.182	5.56 ± 0.18	Melbourne
	ANA-9-15	112.2	133.9	0.0824 ± 0.0045	1.0301 ± 0.0018	1.5 ± 1.5	9.087 ± 0.516	8.98 ± 0.52	Melbourne
	ANA-9-16	120.0	159.6	0.0590 ± 0.0037	1.0342 ± 0.0024	1.5 ± 1.5	6.401 ± 0.412	6.30 ± 0.41	Melbourne
	ANA-9-2	136.8	82.2	0.0888 ± 0.0007	1.0626 ± 0.0008	0.8	9.517 ± 0.076	9.51 ± 0.08	Mainz

Elemental analysis of solution samples

Elemental concentrations of solution samples were determined at the University of Waikato using an Agilent 8900 triple quadrupole inductively-coupled plasma mass spectrometer (ICP-MS; Agilent Technologies, USA), operated by MassHunter WorkStation (Version 4.5) and coupled with an SPS 4 autosampler. The system uses a 0.05 – 0.1 mL min^{-1} MicroMistTM U-Series nebuliser (Glass Expansion, Australia) attached to a quartz cyclonic spray chamber followed by a 2.0 mm injector quartz torch. The plasma torch is followed by Ni sampler and skimmer cones, and an extraction omega lens (Agilent Technologies, USA) is used for ion beam focussing. The ICP-MS was optimised for maximal sensitivity for each run, ensuring that oxides and divalent ions accounted for less than 2%. Water samples were filtered (0.45 µm, PES membrane) and acidified to 2% (v/v) with double-distilled (Savillex DST-1000 Acid Purification System, USA) HNO_3. $CaCO_3$ sub-samples collected from watch glasses and speleothems were homogenised and dissolved in 5% (v/v) double-distilled HNO_3 in Milli-Q ultrapure water at a ratio equivalent to 1 mg/4 mL. Sample analyses were carried out in triplicate and bracketed with acid blanks of 2% double-distilled HNO_3. Quantification was based on five-point calibration curves between 0.1 and 500 ppb produced from multi-element standard IV71-A (Inorganic Ventures, USA). Five separate standards ranging from 100 to 10,000 ppb prepared from single-element stocks (Inorganic Ventures, USA) were used to calibrate Ca and other major elements. Blank samples were run after every 10 samples to minimise carryover, and check standards analysed every 20 samples were used for drift correction. Re-calibration was carried out after every 100 samples. Instrumental drift and matrix elements were monitored and accounted for using an online internal standard containing Sc, Ge, Rh, Ir, and Tl. To circumvent analytical detection limits (provided sufficient sample volume was available), a standard addition approach was used quantify trace metal concentrations using linear calibration curves based on 4 to 5 sample aliquots spiked with elemental stock solution (Harris, 2010).

Elemental analysis of stalagmite samples

Laser ablation inductively-coupled mass spectrometry (LA-ICP-MS)

The polished surfaces of central slabs of stalagmites ANA-19-1 and ANA-19-9 were analysed for elemental concentrations by laser ablation inductively-coupled plasma mass spectrometry (LA-ICP-MS) at the University of Waikato. The system consists of a RESOlution SE 193 nm excimer laser ablation system with a Laurin Technic S155 ablation cell coupled to an Agilent 8900 triple quadrupole ICP-MS (see details in Section 5.2.4). Sample introduction was achieved using helium as the carrier gas. Ablation was consistently performed using a 50 µm diameter laser spot size and scan speed of 24.3 µm s^{-1}, resulting in a spatial resolution of ca. 25 µm. Ablation tracks were aimed to follow the central growth axis and were adjusted according to changes in growth direction. For each stalagmite, the total length of the sample was ablated in 5 segments, each of which contained two parallel ablation transects with an offset of 50 µm to account for lateral heterogeneity. Measurements were preceded by a brief surface

ablation of the target tracks to minimise potential contamination. Reduction and quantification of raw LA-ICP-MS data against bracketed NIST-610 and NIST-612 glass standards (measured at maximum every 30 minutes of ablation) was achieved using the IOLITE data-processing suite (Paton et al., 2011). Processed data from parallel transects were averaged and the resulting averaged segments were stitched to create one coherent data series per speleothem sample. Stitching was carried out by averaging overlapping regions of transects as determined by microscopy and direct comparison of elemental data. Outliers (*e.g.*, due to porosity or grain inclusions) were identified and interpolated by applying a Hampel filter (written in Python) with an outlier threshold criterion of 4σ and a sliding window size of 5 data points (equating to 125 µm distance). Statistically identified outliers were cross-validated by visual inspection of the data using scanned images and optical microscopy.

Synchrotron radiation micro x-ray fluorescence mapping (SR-µXRF)

Both stalagmites were analysed via synchrotron radiation micro-x-ray fluorescence (SR-µXRF) microscopy using the XFM beamline at the Australian Synchrotron (Howard et al., 2020). Measurements were performed using the Maia 834 detector array at a distance of ca. 10 mm from the polished stalagmite surfaces. Fluorescence spectra were obtained at a monochromatic incident energy of 18.5 keV and setting the beam spot size to 1.5 µm. The beam dwell time was 1.7 ms, which was a compromise between sufficient elemental detection and achievable spatial resolution. These settings enabled the detection of Ca, Br, and Sr, which possess attenuation depths of 6 µm, 150 µm, and 240 µm, respectively. Other elements (*e.g.*, Fe, Y) are theoretically detectable, however, were generally not sufficiently concentrated for feasible dwell times. Reconnaissance scans at a low resolution (100 µm) were initially performed of the entire slab of ANA-19-1, and a region of 125.2 by 42.5 mm of ANA-19-9 that covered most of the ca. 140 mm total length of the sample. Subsequently, targeted high-resolution (2 µm) maps of 57.5 by 2.3 mm (28751 by 1151 pixels) and 136.2 by 1.2 mm (68101 by 601 pixels) were obtained from the central regions of ANA-19-1 and ANA-19-9, respectively. Both maps were aimed to follow the growth axis as best as possible, noting that experimental time constraints only allowed for the collection of a single continuous high-resolution map per sample. Quantification was achieved via single element Mn, Fe, and Pt foils (Micromatter Technologies Inc., Canada), and XFM maps were processed using the GeoPIXE software (Commonwealth Scientific and Industrial Research Organisation (CSIRO), Australia).

Stable isotope analysis of speleothems and water samples

Stable oxygen (δ^{18}O) and carbon (δ^{13}C) isotope ratios of stalagmite sub-samples (dissolved powders, between ca. 95 – 118 µg) were measured at Northumbria University (UK) using a Thermo Delta V Advantage isotope ratio mass spectrometer (IRMS) interfaced with a Gasbench II universal on-line gas preparation and introduction system. External standard deviation with respect to Vienna Pee Dee Belemnite (VPDB) was better than 0.09‰ and 0.07‰ for δ^{18}O

and $\delta^{13}C$, respectively.

Water samples from February 2020 were analysed for stable oxygen ($\delta^{18}O$) and hydrogen ($\delta^{2}H$, or δD) isotope ratios at the Universidad de Almería, Spain, by cavity ring-down spectroscopy coupled with an A0211 high-precision vaporiser. Internal standards consist of JRW, BOTTY and SPIT, and measurements were normalised to VSMOW (Vienna Standard Mean Ocean Water). Samples were bracketed by repeat analyses of an internal standard every six samples, indicating a typical long-term instrumental precision (1 SD) of $\pm 0.06‰$ for $\delta^{18}O$ and $\pm 0.6‰$ for δD.

5.3 Results

5.3.1 Hydrological and atmospheric measurements in caves

Cave monitoring in Anapala Cave and Ulupaka Cave started in September 2019, with the latest data and samples collected in November 2022. However, logger data are discontinuous for the period between February 2020 and November 2022 (no fieldwork possible) due to battery and memory limits. Additionally, several drip loggers and one temperature logger (lost) were misplaced from their original location. Collectively but to varying extent, the available data of atmospheric and drip loggers cover most of two wet seasons and three dry seasons, capturing four tropical cyclones and multiple significant low pressure systems that impacted the island during this period. Interestingly, the monitoring period also included a change in ENSO regime from El Niño conditions to prevailing La Niña conditions (Figure 5.3). Typically, El Niño and La Niña conditions are characterised by lower and greater than average rainfall in this region (Rasbury & Aharon, 2006), respectively, with several historic droughts coinciding with strong El Niño phases (McGree et al., 2016). Between 2019 and 2022, total monthly rainfall was overall slightly higher (2180 – 2720 mm year^{-1}) than the long-term annual average of ca. 2180 mm (The Global Climate Change Alliance Plus Initiative, 2019).

The atmosphere and monitored drip points of Anapala Cave generally responded to cave-external weather conditions, particularly in the upper part of the cave. A comparison of temperature records from the upper (24.2 $\pm$ 0.3 °C) and lower (23.8 $\pm$ 0.1 °C) chambers depicted an increasing disconnection from the surface (24.4 $\pm$ 1.3 °C), noticeable in a progressively muted amplitude of temperature variation with depth (Figure 5.4). Drip rates showed large variability in response to effective rainfall, with baseline flows of $<$1 drip min^{-1} (or inactive dripping) increasing rapidly to up to 244 drips min^{-1} (reflected in an average of $>$70 drips min^{-1} over 24 hours as shown in Figure 5.4). Similarly to temperature, the variability and responsiveness of drip rate decreased from the upper to the lower chamber, with drip point ANA-LC-5, for instance, showing a maximum increase in flow from ca. 0.6 drips min^{-1} to ca. 2.5 drips min^{-1}. The atmospheric pressure recorded in the upper chamber of Anapala Cave closely followed surface pressure, varying between 991 and 1017 hPa. pCO_2 in the upper cave varied between 368 and

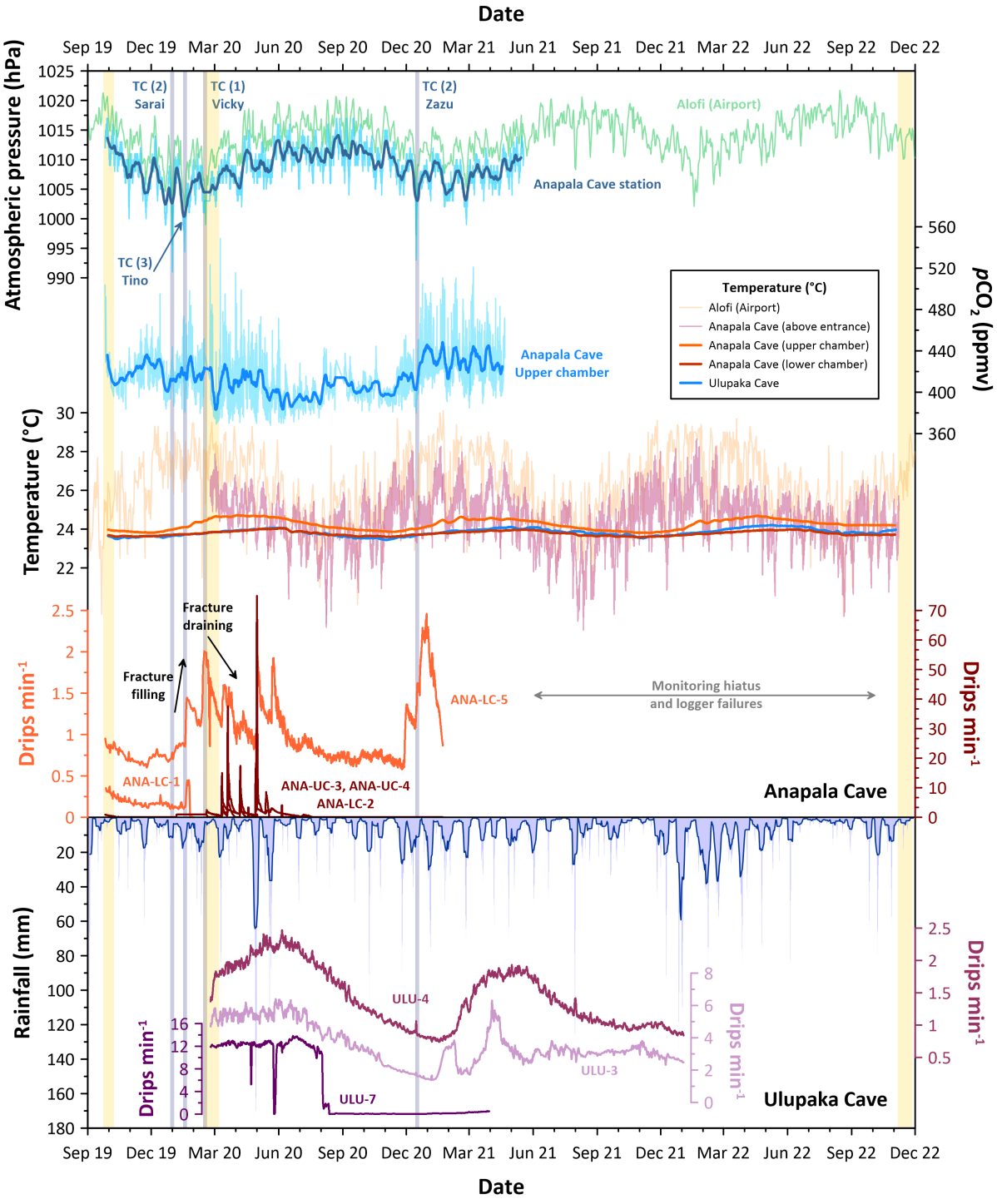

Figure 5.4: Atmospheric and hydrological response of Anapala Cave and Ulupaka Cave to surface conditions. Labels on the x-axes denote the first day of each month. Vertical yellow bars indicate the three periods of fieldwork, with cave monitoring commencing in September 2019. Tropical cyclones with direct effect on Niue are marked by vertical purple bars and as 'TC' with their maximal category in brackets. Thick solid lines of atmospheric pressure and pCO_2 data denote the 7-day running average. Data indicated as 'Alofi (Airport)' were provided by the Niue Meteorological Service and collected at Hainan Airport. For clarity, daily temperature readings from Hainan Airport and from above the entrance of Anapala Cave are shown faintly without a 7-day running average. Thick coloured lines of temperature observations stem from hourly in-cave measurements using HOBO® TidbiT temperature loggers. Drip rates were measured in intervals between 15 and 60 minutes, and are shown consistently as daily running averages. Note that drip rates are displayed on different colour-coded y-axes for clarification. The solid line of rainfall is the 7-day running average of daily observations (note inverted axis).

549 ppmv, with overall lower concentrations and diurnal variability during the months of June to November. Atmospheric monitoring of Ulupaka Cave was limited to in-cave temperature, which was ca. 23.8 ± 0.2 °C on average. Three drip loggers depicted an overall more gradual response of flow rates to rainfall in Alofi, with all drips discharging throughout the year. Drip rates in Ulupaka Cave were generally higher than those in Anapala Cave, ranging in median between 0.27 and 3.23 drips min^{-1}.

5.3.2 Chemical characteristics of modern cave environments

In-situ observations

The pH of cave waters in both Anapala Cave and Ulupaka Cave varied between ca. 7.9 and 8.6, with no discernible trends between locations and field campaigns (Supplementary Table 5.S1, Table 5.S2, and Table 5.S3). Similarly, there was little observed temporal variation in the water temperature of drips in both caves, averaging around 25.6 ± 0.7 (Anapala Cave) and 25.4 ± 0.7 °C (Ulupaka Cave) across all measurements. The difference between dripwater temperature in the lower chamber (25.3 ± 0.5 °C) and upper chamber (25.9 ± 0.8 °C) of Anapala Cave was likewise marginal. On the other hand, electrical conductivity (EC) measurements indicated large differences in total ion content between dripwaters of Anapala Cave and Ulupaka Cave, within each cave, and between sampling periods. With few exceptions, dripwater monitored in Anapala Cave was generally more enriched in ions than in Ulupaka Cave (average EC = 500 ± 161 µS cm^{-1}), with average EC readings of 729 ± 121 µS cm^{-1} and 1064 ± 352 µS cm^{-1} in the upper and lower chambers of Anapala Cave, respectively. EC in Ulupaka was overall highest and most variable in September 2019 (on average 657 ± 404 µS cm^{-1}), coinciding with a total rainfall of 1.4 mm recorded over 5 days preceding the measurements. In February 2020, a total of 19.3 mm rainfall occurred prior to in-cave analyses, which depicted slightly lower EC of 515 ± 53 µS cm^{-1}. Measurements in November 2022 (443 ± 83 µS cm^{-1}) were carried out twice over the course of three weeks, with 9.2 and 11.3 mm rainfall preceding the cave visits. The ionic content of dripwaters from Anapala Cave was likewise lower in November 2022 than in February 2020. In the upper chamber, EC was 837 ± 65 µS cm^{-1} and 633 ± 68 µS cm^{-1}, respectively, while measurements in the lower chamber yielded EC readings of 1457 ± 186 µS cm^{-1} and 855 ± 208 µS cm^{-1}.

Elemental composition of cave waters and modern carbonates

Total cation concentrations in Anapala Cave and Ulupaka Cave as quantified by ICP-MS showed characteristic properties of cave waters, but considerable differences between the two monitored caves were evident in the composition of major components (Figure 5.5 and Figure 5.6).

In line with the generally higher electrical conductivity readings, Anapala Cave possessed considerably greater contents of certain matrix elements, including Na, Mg, Sr, S, and K (Ta-

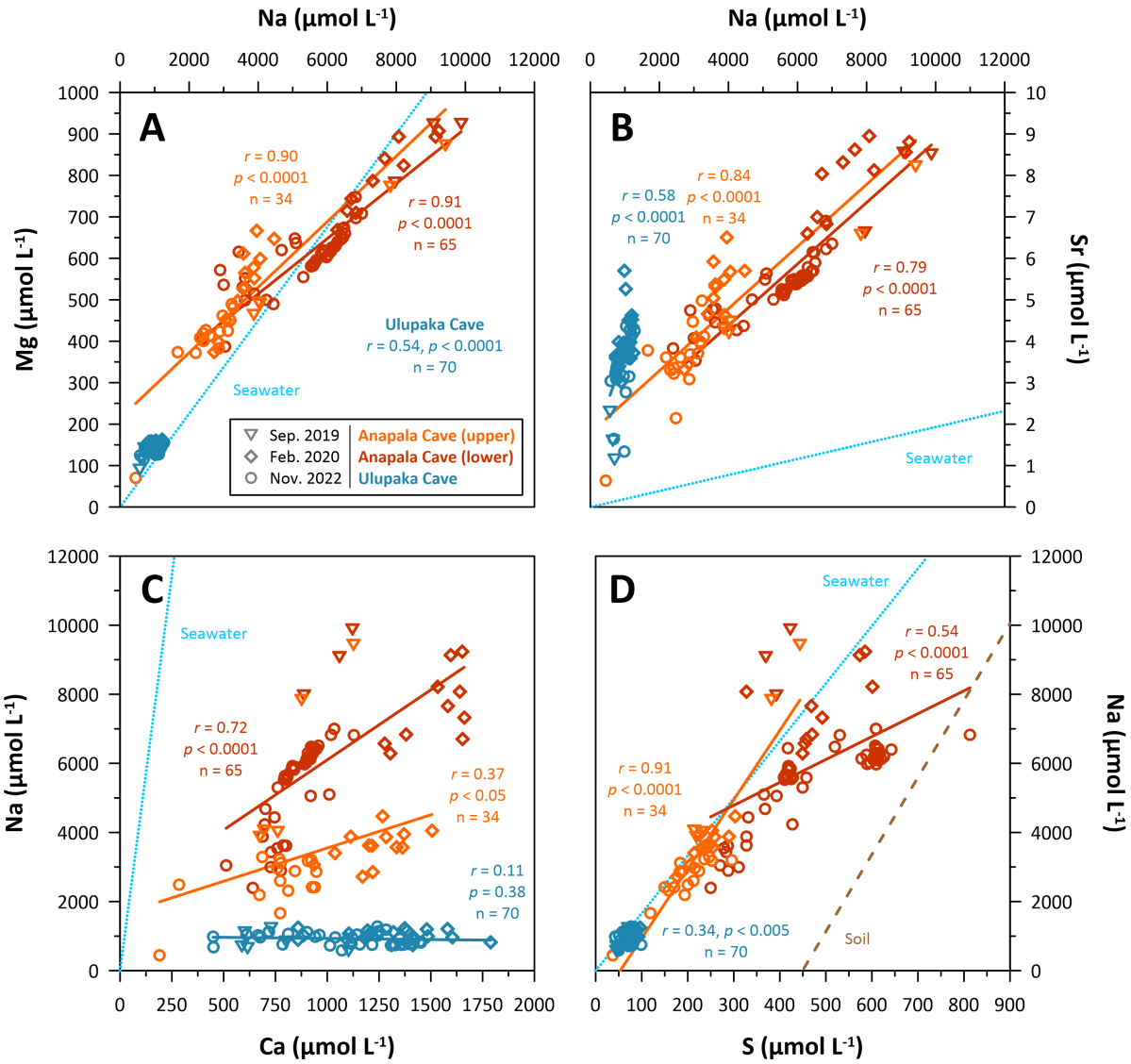

Figure 5.5: Selected relationships of major elements in dripwater indicative of elemental sources. Coloured solid lines in each sub-plot are linear regressions for all data from the respective cave location. The seawater mixing line (blue dotted line) is based on typical elemental contents compiled in Pilson (1998). The dashed brown line in **D** denotes a linear regression of elemental measurements from deionised water leachates of ten soil samples collected across Niue (Supplementary Table 5.S4).

ble 5.3; Figure 5.5), whereas Ca was slightly more concentrated in Ulupaka Cave (1145 ± 304 µmol L^{-1} compared to 963 ± 284 µmol L^{-1} in Anapala Cave). In contrast, Na ranged in concentration between ca. 450 and 9880 µmol L^{-1} with highest concentrations measured in September 2019 and February 2020 sampling periods, compared to concentrations of 569 to 1277 µmol L^{-1} in Ulupaka Cave. Sr and Mg were on average ca. two- and fourfold higher in Anapala Cave (5.36 ± 1.50 µmol L^{-1} and 592 ± 143.26 µmol L^{-1}, respectively) compared to Ulupaka Cave with averages of 3.54 ± 0.74 µmol L^{-1} (Sr) and 141.7 ± 12.2 µmol L^{-1} (Mg). Mg and Sr were well correlated in dripwaters from both caves (and consistently within Anapala Cave), but greater relative variability in Sr was reflected in a considerably steeper slope of this relationship in Ulupaka Cave. Strong positive correlations were also evident between Na and Mg (r = 0.93, $p < 0.0001$, n = 100) and Na and S (r = 0.99, $p < 0.0001$, n = 32) in Anapala Cave, while these correlation were weaker in Ulupaka Cave (r = 0.53 for Na vs. Mg, and r = 0.93 for Na vs. S; Figure 5.5). Na also correlated with Ca in the lower chamber (r = 0.72, $p <$ 0.0001, n = 65) and upper chamber (r = 0.37, $p < 0.05$, n = 34) of Anapala Cave, but not in Ulupaka Cave (r = 0.11, p = 0.38, n = 70). The concentrations of Ni, Cu, and Co were very similar in both caves, averaging at ca. 0.008 µmol L^{-1}, 0.006 µmol L^{-1}, and 0.007 µmol L^{-1}, respectively (Figure 5.6). Likewise, linear regressions suggested largely consistent covariance in concentrations ($0.35 < r < 0.97$; Figure 5.6A, B, C). Elevated concentrations (*e.g.*, beyond 1 SD) of Ni and Co were almost exclusively observed in samples collected in November 2020, while it is noted that most samples were close to or below (not reported) instrumental detection of Co (0.0017 µmol L^{-1}). Normalised elemental ratios to Ca indicated that Mg and Sr were relatively enriched in the lower chamber of Anapala Cave compared to the upper chamber. while Mg/Ca and Sr/Ca were well correlated in both Anapala Cave and Ulupaka Cave (Figure 5.7).

Modern precipitates collected on watch glasses were used to estimate elemental partition coefficients, which are detailed in Chapter 4 and used for prior calcite precipitation calculations in Section 5.4.2. Data relevant to this study are summarised in Table 5.4, depicting highly consistent inclusion of Mg and Sr with partition coefficients of 0.06 ± 0.02 (D_{Mg} in Anapala Cave), 0.04 ± 0.01 (D_{Mg} in Ulupaka Cave), 0.18 ± 0.05 (D_{Sr} in Anapala Cave), and 0.07 ± 0.02 (D_{Sr} in Ulupaka Cave).

Isotopic composition of cave waters and rainfall

$\delta^{18}O$ and δD of cave waters and rainfall collected in February 2020 were well correlated ($r > 0.99$) with a linear regression describing their relationship as $\delta D = 8.7 \times \delta^{18}O + 15.0$ (Figure 5.8A) and $\delta D = 8.2 \times \delta^{18}O + 12.5$ (Figure 5.8B) when including and excluding rainwater samples, respectively. Notwithstanding slight deviations in slope and δD excess, both regression lines are at large consistent with the Global Meteoric Water Line (GMWL; $\delta D = 8.0 \times \delta^{18}O + 10$; Craig, 1961; Dansgaard, 1964) and regional South Pacific Meteoric Water Line (SPMWL; $\delta D = 7.7 \times \delta^{18}O + 9.3$; Aharon et al. 2006). Isotopic ratios of rain samples were highly variable and considerably lower than those of cave samples, with minimal values of -11.03‰ ($\delta^{18}O$) and -80.83‰ (δD) representing torrential rainfall associated with ex-cyclone Wasi (22 to 23

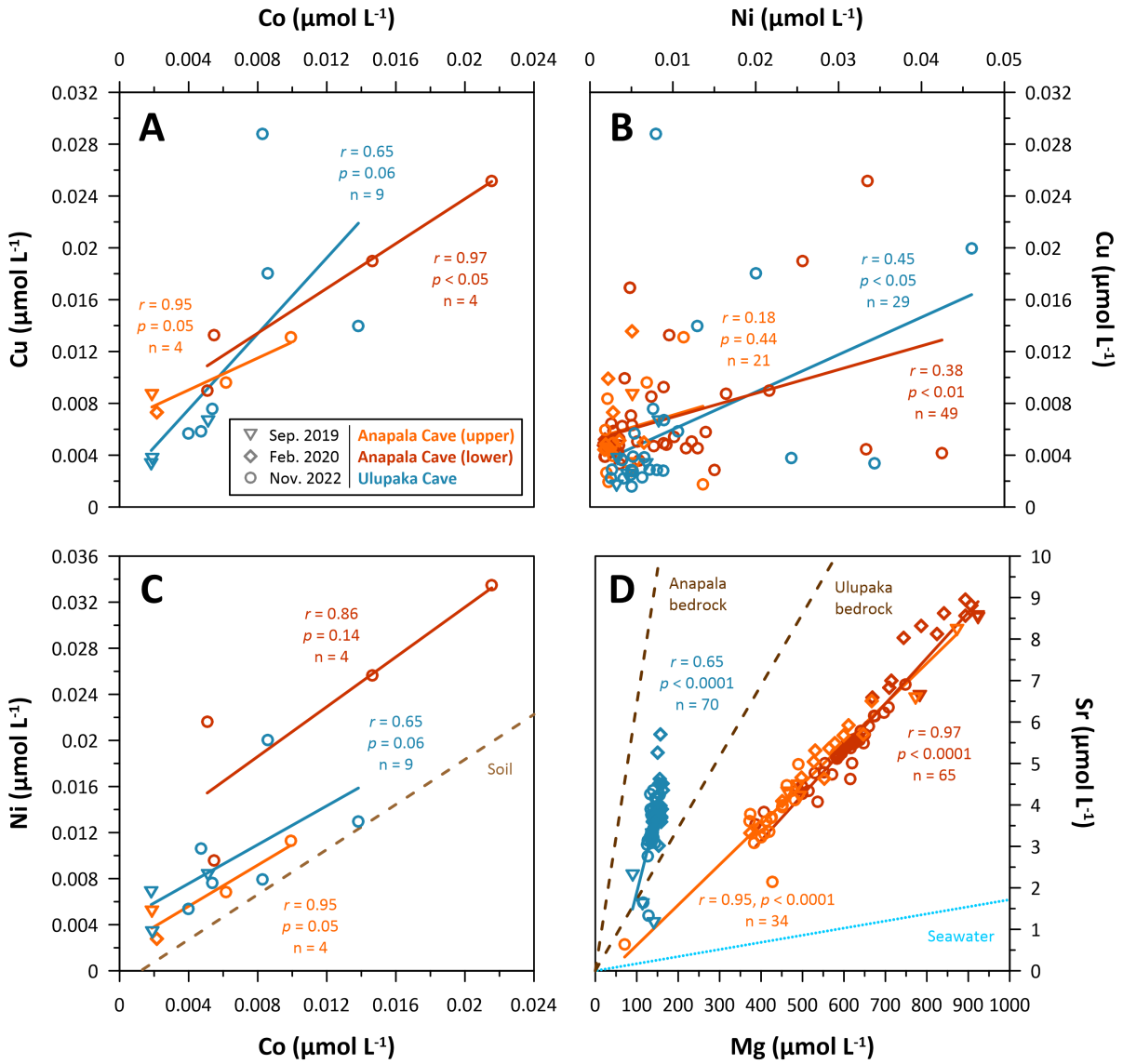

Figure 5.6: Selected relationships of transition metals and alkaline earth metals in dripwater indicative of elemental sources. Coloured solid lines in each sub-plot are linear regressions for all data from the respective cave location. The dashed brown line in **C** denotes a linear regression of elemental measurements from ammonium acetate extracts of ten soil samples collected across Niue (Supplementary Table 5.S4). Note that elements shown in sub-plots **A** and **B** did not fall on this regression line. Dark brown dashed lines in **D** represent the ratio of Mg and Sr based on fresh bedrock samples collected from above Anapala Cave and Ulupaka Cave (Supplementary Table 5.S5). The seawater mixing line (blue dotted line) in **D** is based on typical elemental contents compiled in Pilson (1998).

Table 5.3: Selected elemental concentrations in Niuean cave waters. Values for a given drip point present the average of multiple samples collected during visits. Where data are missing, concentrations were below quantitation limits (shown below in the third row in µmol L^{-1}).

Cave	Drip ID	Na µmol L^{-1}	Mg µmol L^{-1}	K µmol L^{-1}	Ca µmol L^{-1}	P µmol L^{-1}	S µmol L^{-1}	Co µmol L^{-1}	Ni µmol L^{-1}	Cu µmol L^{-1}	Sr µmol L^{-1}	Ba µmol L^{-1}
		0.4	0.4	12.8	2.5	0.03	15.6	0.002	0.002	0.002	0.001	0.001
Anapala	ANA-UC-1	4016	493.3	47.6	761	0.28	230.16	0.002	0.005	0.008	4.19	0.016
Cave	ANA-UC-2	4686	549.8	49.3	833	0.15	255.08		0.004	0.005	5.03	0.008
	ANA-UC-3	3526	576.1	22.1	1177	0.33	227.78	0.003	0.005	0.007	5.57	0.003
	ANA-UC-4	4467	646.9	20.5	1268		303.12		0.004	0.005	5.70	
	ANA-UC-5	3960	588.2	21.0	1395		255.22		0.002	0.005	5.58	
	ANA-UC-6	3365	482.1	25.7	1017	0.11	238.06		0.002	0.003	4.27	0.002
	ANA-UC-7	5618	635.0	45.6	956	0.09	297.85		0.002	0.002	5.61	0.003
	ANA-UC-8	3109	471.8	29.4	987	0.23	229.69			0.004	4.46	0.003
	ANA-UC-9	2663	396.9	33.1	1110	0.77	171.15	0.003	0.004	0.009	3.38	0.004
	ANA-UC-10	3287	481.6	49.1	687	0.08	246.31		0.003	0.005	4.12	0.006
	ANA-UC-11	2483	427.0	23.6	284	0.09	200.37		0.002	0.003	2.14	0.005
	ANA-UC-12	447	70.7		191	0.04	37.07		0.014	0.002	0.64	0.003
	ANA-UC-13	2190	372.2	46.1	673	0.63	193.31			0.003	3.61	0.006
	ANA-UC-16	1666	373.6	50.3	772	3.31	118.35		0.002	0.008	3.78	0.006
	ANA-UC-18	3186	451.4	57.9	915	0.04	274.17			0.002	3.97	0.005
	ANA-UC-19	2421	400.3	46.3	926	0.20	170.15			0.003	3.22	0.007
	ANA-UC-21	3233	489.6	30.4	769	0.03	236.08			0.003	4.98	0.010
	ANA-UC-23	2320	408.1	109.9	811	0.09	158.78		0.003	0.004	3.31	0.007
	ANA-UC-24	2862	383.1	87.1	947	0.06	182.32		0.002	0.006	3.08	0.008
	ANA-LC-1	8108	851.4	66.5	1368	0.07	437.05		0.003	0.003	8.25	0.006
	ANA-LC-2	7699	817.6	64.9	1458	0.04	439.62		0.003	0.004	8.30	0.003
	ANA-LC-3	8088	803.4	50.8	1211	0.04	496.48		0.002	0.002	7.37	0.003
	ANA-LC-4	5408	607.0	38.6	988	0.15	440.58		0.002	0.004	5.63	0.004
	ANA-LC-5	8435	827.7	52.8	1441	0.08	611.65		0.003	0.008	7.88	0.002
	ANA-LC-6	6074	671.6	45.9	1232	0.07	428.09			0.003	6.35	0.003
	ANA-LC-8	3045	386.8	27.5	512	0.26	270.36			0.005	3.53	0.005
	ANA-LC-9	3623	552.2	68.8	787	0.17	327.50			0.004	4.79	0.011
	ANA-LC-10	3619	498.8	33.3	802	0.35	287.03			0.004	4.46	0.007
	ANA-LC-11	4681	619.6	68.0	702	0.04	367.80			0.005	5.01	0.007
	ANA-LC-12	2996	536.2	83.8	727	0.31	310.70			0.003	4.07	0.006
	ANA-LC-13	2894	571.6	107.5	777	0.06	287.54			0.004	4.74	0.008
	ANA-LC-14	4439	489.3	32.0	746	0.04	331.47		0.002	0.004	4.37	0.006
	ANA-LC-15	5060	647.6	68.5	921	0.13	393.27			0.005	5.49	0.009
	ANA-LC-16	2399	407.0	50.6	640	0.09	249.45		0.015	0.003	3.83	0.007
	ANA-LC-17	3544	530.2	57.0	759		278.90		0.002	0.005	4.77	0.006
	ANA-LC-18	3882	514.6	41.2	688	0.10	327.82			0.003	4.34	0.006
	ANA-LC-19	3436	615.5	88.4	728	0.11	283.07		0.004	0.004	4.62	0.007
	UC average $\pm 1\sigma$	3131 ± 1160	457.8 ± 127.1	44.2 ± 23.4	867 ± 294	0.38 ± 0.78	211.84 ± 63.90	0.003 ± 0.001	0.004 ± 0.003	0.005 ± 0.002	4.03 ± 1.29	0.006 ± 0.003
	LC average $\pm 1\sigma$	4857 ± 2005	608.2 ± 140.4	58.1 ± 21.2	916 ± 295	0.12 ± 0.10	364.91 ± 95.42		0.004 ± 0.004	0.004 ± 0.001	5.43 ± 1.54	0.006 ± 0.002
Ulupaka	ULU-1	897	150.5		913	0.25	71.41	0.002	0.003	0.006	3.10	0.002
Cave	ULU-2	851	140.9		1023	0.47	69.13		0.003	0.003	3.18	0.002
	ULU-3	953	150.3		1184	0.07	79.84		0.002	0.003	3.73	0.003
	ULU-4	1174	156.2		1264	0.19	88.07			0.007	4.09	
	ULU-5	1151	141.3		1225	0.44	73.88			0.004	3.59	
	ULU-7	722	141.7		1396	0.31	64.43			0.004	3.57	
	ULU-8	1057	141.8		1031	0.03	70.15		0.003	0.004	3.57	0.002
	ULU-9	1063	131.5		758	0.57	60.79		0.003	0.003	2.70	0.002
	ULU-10	1138	143.6		1107	0.16	76.04			0.004	4.19	0.003
	ULU-11	1236	155.2		1361	0.63	80.74	0.007	0.007	0.011	4.44	0.006
	ULU-12	1030	144.7		748	1.86	82.01	0.004	0.004	0.017	4.81	0.007
	ULU-13	1112	147.5		903	0.05	81.66	0.005	0.011	0.006	3.83	0.008
	ULU-14	835	143.2		1384	0.67	72.53				3.53	0.004
	ULU-15	923	144.5		1351	0.43	71.63				3.79	0.004
	ULU-16	987	148.3		943	0.05	73.11			0.002	3.61	0.004
	ULU-17	950	142.9		1120	0.06	72.04				3.77	0.004
	ULU-18	1045	139.1		1144	0.10	72.42				3.93	0.005
	ULU-19	1033	145.9		962	0.23	74.07	0.004	0.005	0.006	3.97	0.007
	ULU-20	1028	126.4		665	0.32	50.44			0.002	2.77	0.003
	ULU-21	963	134.8		1038	0.23	83.24				3.77	0.005
	ULU-22	678	115.3		451		49.68				1.65	0.002
	ULU-23	1133	132.7		1244	0.08	66.86			0.002	4.27	0.006
	ULU-24	1068	141.4		811	1.65	74.27			0.010	3.72	0.005
	Average $\pm 1\sigma$	1001 ± 139	141.7 ± 9.1		1045 ± 249	0.4 ± 0.48	72.11 ± 9.37	0.004 ± 0.002	0.004 ± 0.003	0.005 ± 0.004	3.63 ± 0.65	0.004 ± 0.002
Avaiki	AV-1	1026	721.5	20.8	1225	0.10	150.05		0.002	0.008	11.26	0.018
Cave	AV-2	3669	1192.9	132.8	1812	0.07	264.70	0.005	0.007	0.011	16.89	0.011
	AV-3	7550	1542.5	203.9	2380	0.08	471.05		0.003	0.007	23.00	0.007
	AV-4	1121	565.3		551	0.04	117.25		0.002	0.005	6.89	0.006
	AV-5	3675	834.4	113.0	1210	0.32	321.98	0.008	0.012	0.020	12.05	0.020
	Average $\pm 1\sigma$	3408 ± 2655	971.3 ± 394.1	117.6 ± 75.4	1435 ± 691	0.12 ± 0.11	265 ± 142.08	0.007 ± 0.002	0.005 ± 0.005	0.01 ± 0.006	14.02 ± 6.15	0.012 ± 0.006
Palaha	PAL 1	6616	1351.0		987	0.03	198.82		0.005	0.006	24.48	0.015
Cave	PAL-3	4100	1048.0	32.4	1691	0.12	306.05		0.003	0.011	19.03	0.007
	PAL-4	4717	1085.0	17.8	1644	0.03	289.73		0.003	0.009	19.81	0.004
	PAL-5	1606	529.2	18.1	1138	0.28	127.96		0.005	0.011	12.31	0.009
	Average $\pm 1\sigma$	4260 ± 2068	1003.3 ± 343.7	22.8 ± 8.3	1365 ± 355	0.12 ± 0.12	230.64 ± 83.13		0.004 ± 0.001	0.009 ± 0.002	18.9 ± 5.01	0.009 ± 0.004

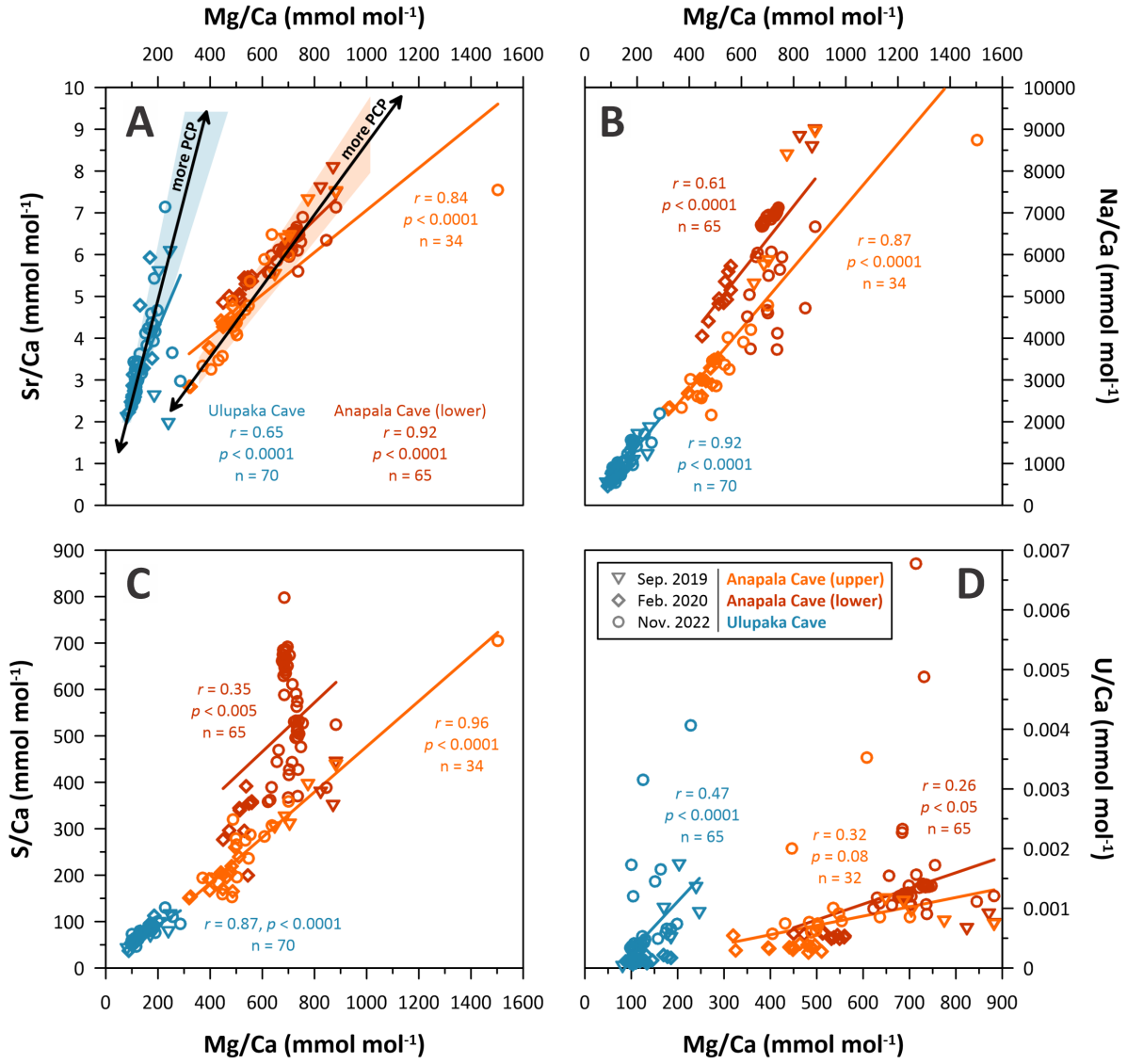

Figure 5.7: Selected relationships of trace elements in dripwater indicative of prior calcite precipitation. Coloured solid lines In sub-plots **A** to **D** denote linear regressions for all data (*i.e.*, including all sampling periods) from the respective cave location. PCP vectors in **A** are modelled using the spreadsheet implementation made available by Tremaine and Froelich (2013). The chemical evolution is predicted based on the lowest measured Sr/Ca of each cave (1.94 mmol mol^{-1} for Ulupaka, 2.84 mmol mol^{-1} for Anapala Cave). For Ulupaka Cave, a bedrock mixture of 8% dolomite and 92% limestone yielded good agreement with the dripwater measurements, whereas the model for Anapala Cave (both chambers) assumes 37% dolomite. D_{Mg} ($\approx$0.04 in both caves) and a D_{Sr} of 0.14 (Anapala Cave) and 0.07 (Ulupaka Cave) were used based on measurements in dripwater and modern precipitates from each cave. $>$95% of data from Ulupaka Cave were explained by varying the dolomite contribution by $\pm$2%, whereas $\pm$4% were required for Anapala Cave. The resulting regions of PCP are indicated by the shaded area around PCP vectors (black arrows).

Table 5.4: Summary of Mg and Sr partition coefficients estimated from watch glass deployments in Anapala Cave and Ulupaka Cave. The number of sub-samples collected from individual glasses and included in the respective glass average value of D_X is given as n.

Cave	Chamber	Glass ID	Drip point	D_{Mg}	1 SD	n	D_{Sr}	1 SD	n
Anapala Cave	Upper chamber	N-02-20-C	ANA-UC-4	0.09	-	1	0.21	-	1
		N-02-20-B	ANA-UC-6	0.06	-	1	0.25	-	1
	Lower chamber	ANA-LC-5	ANA-LC-5	0.06	-	1	0.13	-	1
		N-02-20-D	ANA-LC-2	0.04	0.00	3	0.14	0.01	3
		N-02-20-L	ANA-LC-5	0.04		1	0.16	-	1
			ANA-UC average	0.07	0.03	2	0.23	0.03	2
			ANA-LC average	0.05	0.01	3	0.14	0.01	3
			Cave average	0.06	0.02	5	0.18	0.05	5
Ulupaka Cave	Study chamber	ULU-3	ULU-3	0.02	-	1	0.08	-	1
		ULU-5	ULU-5	0.04	0.00	13	0.08	0.01	13
		ULU-6	ULU-6	0.05	-	1	0.12	-	1
		ULU-7	ULU-7	0.03	0.00	14	0.09	0.00	14
		N-02-20-T	ULU-10	0.03	0.00	5	0.06	0.00	5
		N-02-20-I	ULU-9	0.02	0.00	4	0.06	0.00	4
		N-02-20-F	ULU-3	0.03	0.01	5	0.06	0.01	5
		N-02-20-P	ULU-2	0.04	0.00	5	0.07	0.01	5
		N-02-20-H	ULU-8	0.04	0.00	5	0.06	0.00	5
		N-02-20-K	ULU-11	0.04	0.00	5	0.07	0.00	5
		N-02-20-E	ULU-4	0.04	0.01	6	0.07	0.00	6
		N-02-20-G	ULU-7	0.04	0.01	5	0.08	0.00	5
		N-02-20-R	ULU-1	0.04	0.00	4	0.05	0.01	4
		N-02-20-M	ULU-12	0.04	-	1	0.05	-	1
			Cave average	0.04	0.01	14	0.07	0.02	14

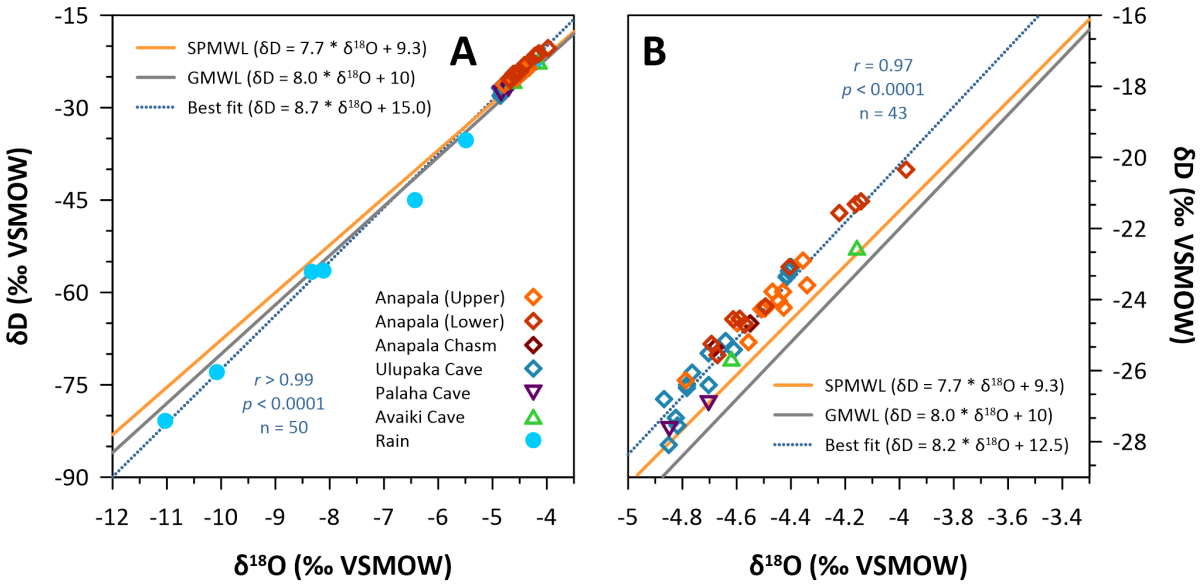

Figure 5.8: Stable oxygen ($\delta^{18}O$) and hydrogen (δD) isotope ratios of rain and cave waters collected on Niue in February 2020. The orange and grey solid lines denote the South Pacific Meteoric Water Line (SPMWL; first derived by Aharon et al., 2006) and Global Meteoric Water Line (GMWL; Craig, 1961; Dansgaard, 1964), respectively. The blue dotted line represents a linear regression of all data shown in each sub-plot. Sub-plot **B** contains the same data as sub-plot **A** but excludes rainwater samples for clarity. The dataset includes dripwater samples collected in the two open sea caves of Avaiki and Palaha (described in Aharon et al., 2006), which were infrequently visited but not equipped for monitoring. Rainwater samples with highly negative isotopic ratios shown in A were collected during substantial downpours associated with cyclone Wasi (22 – 23 February 2020). Note that these data have previously been reported in Nava-Fernandez et al. (2024).

February 2020). Waters from four caves (including the openly accessible sea caves of Avaiki and Palaha) were altogether less variable, ranging between -4.87‰ and -3.97‰ in $\delta^{18}O$, and -28.09‰ and -20.34‰ in δD. Most drip samples from Ulupaka Cave (-4.87‰ to -4.40‰ $\delta^{18}O$; -28.09‰ to -23.09‰ δD) possessed lower isotopic ratios than those from Anapala Cave (-4.79‰ to -3.97‰ $\delta^{18}O$; -26.28‰ to -20.34‰ δD). $\delta^{18}O$ and δD of waters from the upper chamber of Anapala Cave were on average ca. 0.1‰ and 1.0‰ lower than in the lower chamber, respectively.

5.3.3 Stalagmites ANA-19-1 and ANA-19-9

Structural properties and chronological constraints

Stalagmites ANA-19-1 and ANA-19-9 exhibit clearly distinguishable binary laminae throughout the entire record (Figure 5.9). Laminae are generally wide and relatively flat, but small dips potentially indicating splash cups are evident in sections of ANA-19-1. Further, the bottom ca. 1.5 cm and 2.5 cm of ANA-19-1 and ANA-19-9, respectively, are marked by laterally more heterogeneous laminae of the original stump deposit, that reflect the uneven growth surface on which deposition initiated. Throughout formation, slight lateral shifts in growth axis are visible in both stalagmites. ANA-19-1 consists primarily of dark dense calcite (DDC) laminae interlaced with regions of dominant pale porous calcite (PPC) laminae. The latter are proportionally more

abundant in ANA-19-9.

The total of eleven ^{230}Th/U dates obtained for ANA-19-1 provided overall problematic preconditions for chronology building. With ages between 0.48 and 2.75 ka BP across a depth of ca. 53 mm, the age-depth relationship contained several reversals within and beyond analytical uncertainties (Table 5.3; Figure 5.9). In addition, a hiatus likely occurs at a depth of 49.2 mm as identified by jagged Sr laminations observed in XFM maps, rough optical lamina boundaries, and sharp changes in most elemental concentrations (including peak 'detrital' signals with anomalously high Al, Ti, and Si contents). Fourteen ^{230}Th/U measurements for ANA-19-9 indicated an age range of ca. 3.64 to 9.51 ka BP across ca. 135 mm. Similarly to ANA-19-1, however, these data indicate multiple intractable age reversals throughout the stalagmite section, particularly between ca. 90 and 120 mm depth. The sample also presumably contains at least one hiatus at depth of 132.7 mm, with another possibly occurring at 123.1 mm.

Some stalagmites can be challenging for ^{230}Th/U dating due to multiple sources of ^{230}Th or low U concentration (*e.g.*, Hua et al., 2012; Faraji et al., 2023). Although it is noted that robust ^{230}Th/U chronologies have been obtained for another Niuean stalagmite (Nava-Fernandez et al., 2024), it may be that detrital contamination caused inconsistent age estimates with depth, and a closer assessment of the age calculations is required. For instance, existing dates were obtained under the assumption of constant values for $(^{230}\text{Th}/^{232}\text{Th})^{a}_{i}$, which were distinct for samples measured in Mainz (0.8) and in Melbourne (1.5 $\pm$ 1.5). Varying the assumed $^{230}\text{Th}/^{232}\text{Th})^{a}_{i}$ with regards of the stratigraphic context of the stalagmites could be explored (see for example J. U. L. Baldini et al., 2008). Regardless, for this thesis, no adequate age-depth model could be obtained without removing at least a third of the ages from the calculations, or by increasing uncertainties substantially.

Semi-automated lamina counting was performed on SR-µXRF maps of Sr intensity with spatial resolution of 2 µm (compressed to 4 µm and 6 µm for ANA-19-1 and ANA-19-9, respectively) collected from the central region of each stalagmite parallel to the growth direction. Within experimental time limits, it was only feasible to obtain a single high-resolution SR-µXRF Sr map per stalagmite, which was aimed to follow the central growth axis with consideration of axial shifts as best as possible. The central maps measured 57.5 mm by 2.3 mm, and 136.2 mm by 1.2 mm for ANA-19-1 and ANA-19-9, respectively. From each central SR-µXRF map, three evenly-spaced transects were drawn using ImageJ (Rasband, 2012) for the extraction of pixel intensity values (1 pixel equating to 4 by 4 µm in the example of ANA-19-1). To account for lateral heterogeneity in Sr intensity, each transect was initially smoothed with a 4th order Savitzky-Golay filter using the PAST 4 software (Ver. 4.12b; Øyvind Hammer et al., 2001). The size of the sliding window was set to equate to a distance of 100 µm in both stalagmites. Lamina counts were achieved using the *find_peaks* function of the Scientific Computing in Python (SciPy; Virtanen et al., 2020) software, which is designed to identify local maxima in serial datasets based on user-defined criteria. The analysis was carried out in segments across the length of each stalagmite, with peak criteria adjusted to achieve the best agreement with visually identifiable lamina across test regions (Supplementary Figure 5.S3). Peaks were identified using a distance threshold that required peaks to be at minimum 60 – 80 µm apart (equating

to 10 – 20 data points in ANA-19-1; 10 data points in ANA-19-9). This approach yielded a total number of laminae of 663 ± 11 based on triplicate counts on stalagmite ANA-19-1, with an average lamina width 84 ± 2 µm. In ANA-19-9, 1590 ± 19 lamina were counted with an average width of 85 ± 1 µm. Although layer counts were approximately within the range of youngest and oldest radiometric dates (prior to the hiatus) in ANA-19-1, the large inconsistencies between absolute dates particularly within the top 6 mm (difference in ages of ∼240 years, all inverted) rendered anchoring the lamina count data to any particular starting date arbitrary. Furthermore, monitoring observations over the three field campaigns have not conclusively confirmed whether ANA-19-1 was actively depositing or flow had ceased prior to sampling. Because of these uncertainties (applicable to both samples) that could easily result in incorrect assumptions and misleading interpretations, the potential for palaeoclimate reconstructions of the two stalagmites is assessed in terms of depth for the purpose of this study.

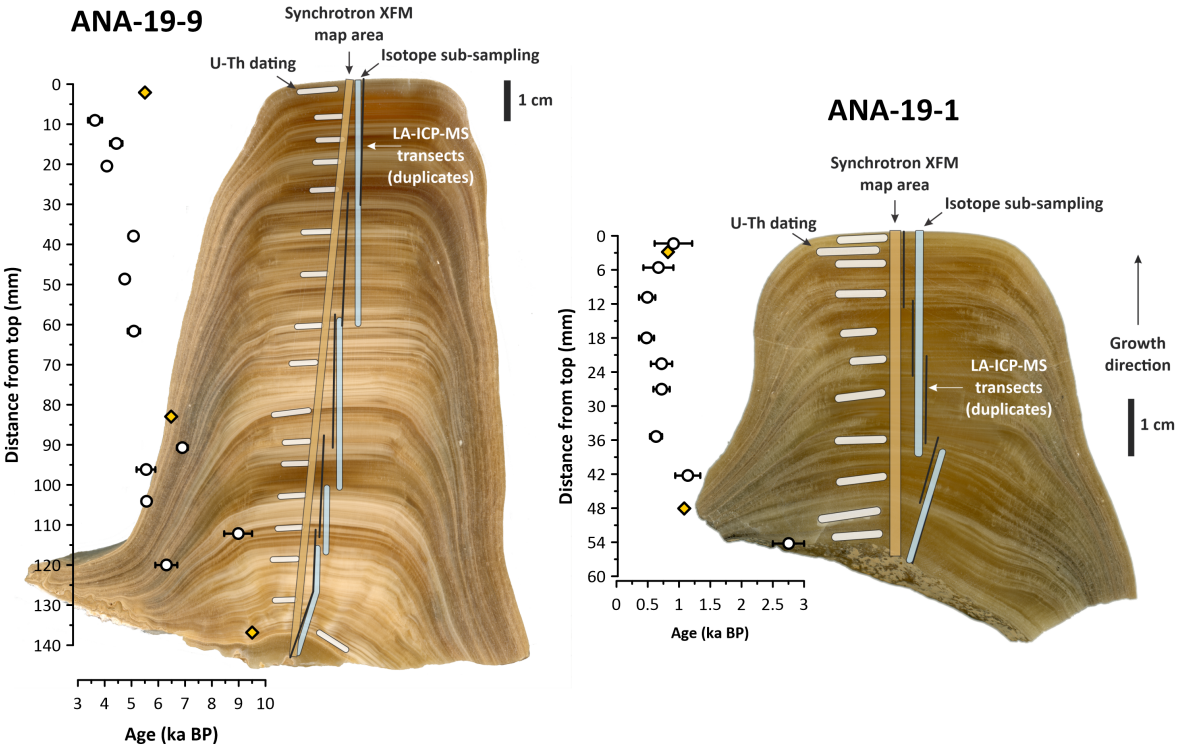

Figure 5.9: Sub-sampling locations and age-depth relationships of stalagmite samples ANA-19-1 and ANA-19-9. Indicated are locations of ^{230}Th/U dating sub-samples (white), sub-sampling tracks for stable isotope analyses (light blue; 1 mm resolution), LA-ICP-MS tracks for elemental analysis (black solid lines, and central regions (light orange) mapped at 2 µm resolution via Synchrotron radiation micro x-ray fluorescence microscopy (XFM). Uncertainties of ^{230}Th/U ages denote $\pm 2\sigma$ and $\pm 1\sigma$ for samples measured at the University of Melbourne (white circles) and University of Mainz (yellow diamonds), respectively. Note that dates for three sub-samples from ANA-19-9 are missing. Ages are reported in Table 5.2.

Stalagmite geochemistry

Trace elements

Most elements quantified along the growth axes of ANA-19-1 and ANA-19-9 exhibited clear trends and/or cyclicity, as well as relationships between each other (Figure 5.10). The strongest signals were observed in Mg/Ca (on average 19.9 $\pm$ 6.2 mmol mol^{-1}), Na/Ca (0.6 $\pm$ 0.2 mmol mol^{-1}), and Sr/Ca (0.49 $\pm$ 0.06 mmol mol^{-1}), which generally showed very similar spatial patterns. Elevated and lower ratios typically coincided with DDC (low greyscale values) and PPC (high greyscale values) laminae, respectively. In ANA-19-9, the most pronounced features in these elemental ratios were found within the top ca. 6 mm, across which Mg, Na, Sr, and Ba, amongst others, were progressively enriched in the stalagmite to approximately threefold their average concentration. Prominent positive elemental excursions also occurred between ca. 76 and 84 mm depth, as well as between ca. 89 and 99 mm depth. The bottommost section below an assumed hiatus at ca. 132 mm depth of the stalagmite was likewise elevated in Mg/Ca and Na/Ca, but less so in other elemental ratios. U/Ca (0.06 $\pm$ 0.02 µmol mol^{-1}) covaried positively with Mg/Ca (and similarly behaving elements) in some regions, while showing opposite trends in others. For instance, U/Ca were near their minimum at the very top and at ca. 134 mm depth of ANA-19-9, where Mg/Ca were highest. In the region between 89 and 99 mm (dominated by DDC), U/Ca were altogether elevated as Mg/Ca, whilst local maxima and minima appear inversely related. The trends of Cu/Ca and Zn/Ca were relatively coherent throughout most of ANA-19-9, showing several periods of elevated concentrations particularly between 54 and 75 mm depth (Figure 5.11). While most elevated alkaline earth metal concentrations did not correspond to synchronous Cu/Ca and Zn/Ca increases, consistent but muted and possibly lagged trends were evident for most major excursions (*e.g.*, top 5 mm). In contrast, Ni/Ca (0.31 $\pm$ 0.09 µmol mol^{-1}) varied rather consistently and positively with Mg/Ca (r = 0.59, $p < 0.0001$) and other alkaline earth metals by extension, exhibiting relative accumulation and depletion in DDC and PPC laminae, respectively. The spatial patterns of Co/Ca (0.02 $\pm$ 0.01 µmol mol^{-1}) were largely distinct from other elemental series and without discernible relation to lamina properties. Exceptions were found within the top and bottom regions of ANA-19-9, where Co was enriched in line with most other elements. Variability in Mn/Ca was altogether less distinct, although most periods of elevated Cu/Ca and Zn/Ca coincided with coherent positive excursions in Mn/Ca. In contrast, Mn/Ca were with few exceptions typically minimal during periods of elevated Mg/Ca.

Trace element systematics in the younger ANA-19-1 (ca. 0.48 to 2.75 ka BP) were less consistent than in ANA-19-9, with lower ranges and variability of elemental concentrations, and fewer distinct features that were evident across different proxy series (Figure 5.10 and Figure 5.S4). An example of the latter was at a distance from the top of ca. 44 to 47 mm, where Mg/Ca (24.5 $\pm$ 3.2 mmol mol^{-1}) and Na/Ca (0.7 $\pm$ 0.2 mmol mol^{-1}) were synchronously at their maxima, whereas all other reported elemental ratios either depict contrasting or distinct patterns. Similarly to ANA-19-9, the normalised ratios of Cu, Zn, and Co showed largely coher-

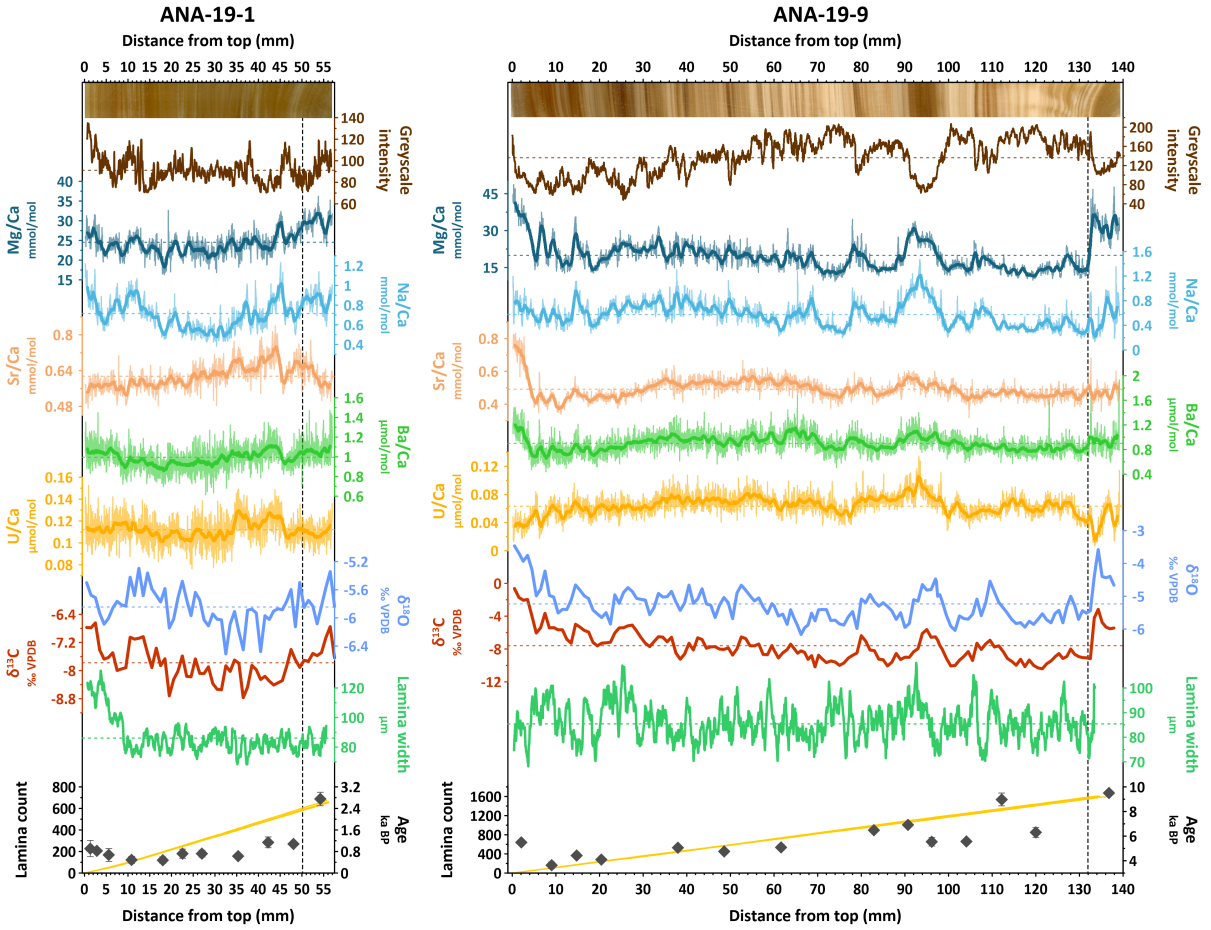

Figure 5.10: Trace elemental and stable isotope proxy series of stalagmites ANA-19-1 and ANA-19-9. The scanned images show the respective central region of the stalagmite section used for sub-sampling (parallel to growth laminae). Greyscale intensity values were extracted from the scanned images. Note that the alignment of proxy data with the scanned images worsens where lateral heterogeneity in laminae increases. Thin and thick solid lines of element:Ca ratios represent the original resolution (25 µm) and a running average across a 1 mm window, respectively. $\delta^{18}O$ and $\delta^{13}C$ series are shown at their original resolution of 1 mm. Lamina width is based on the distance between peaks identified in a semi-automated lamina counting routine. Cumulative lamina counts (solid yellow lines) are shown for three triplicate measurements and are not aligned to age, nor do they account for suspected growth discontinuities (vertical dashed lines). Ages are based on ^{230}Th/U dates, with error bars denoting 2σ (University of Melbourne) and 1σ (University of Mainz) uncertainty estimates (see Table 5.2). Horizontal dashed lines in each plot reflect the total average value.

ent variability, marked by several coinciding short-lived peaks in concentrations (most notably between ca. 31 and 33 mm depth). Ni/Ca (0.32 $\pm$ 0.09 µmol mol^{-1}) showed similarities to both Mg/Ca and Na/Ca, as well as the other transition metals (Figure 5.S4).

Likely due to variable degrees of covariance, LA-ICP-MS elemental datasets proved not amenable for principal component analysis (PCA), which can be useful for the reduction of large datasets and identify potential common forcings (*e.g.*, J. U. L. Baldini et al., 2021; Orland et al., 2014).

Stable oxygen and carbon isotopes

A low resolution (1 mm) sampling track for stable oxygen and carbon isotopes revealed an overall correspondence of δ^{18}O and δ^{13}C to elemental data. In ANA-19-9, δ^{18}O ranged between -6.17 to -3.46‰ VPDB, with highest and lowest values generally coinciding with laminae of DDC and PPC, respectively. The same pattern was observed with regards to Mg/Ca, Na/Ca, and Sr/Ca, amongst other elemental proxies, the regions with greatest enrichment of which corresponded to greater δ^{18}O. The overall maximal value of δ^{18}O (-3.46‰ VPDB) was observed at the very tip of ANA-19-9. Following a steady increase in δ^{18}O by ca. 1.5‰ just prior to growth cessation coincides with various elemental proxies that are likewise progressively enriched (*e.g.*, Mg/Ca, Sr/Ca, Ni/Ca) or depleted (*e.g.*, U/Ca) over the top ca. 5 mm of the stalagmite (Figure 5.10). In ANA-19-1, a much smaller range of δ^{18}O of -6.51 to -5.30‰ VPDB was observed, showing patterns generally consistent with those evident in ANA-19-9. Accordingly, greater values of δ^{18}O coincided with DDC laminae, whereas lower δ^{18}O were primarily found within PPC. Similarly to ANA-19-9, the top (youngest) region of ANA-19-1 was marked by a progressive increase in δ^{18}O by ca. 0.6‰ over the last 5 mm of the record, coinciding with major excursions in trace element ratios. δ^{13}C and δ^{18}O were well correlated in both ANA-19-1 (r = 0.59, $p < 0.0001$, n = 59) and ANA-19-9 (r = 0.85, $p < 0.0001$, n = 145; Supplementary Figure 5.S5). Values of δ^{13}C varied between -8.77 and -6.64‰ VPDB in ANA-19-1, and between -10.41 and -0.63‰ VPDB in ANA-19-9. Given the greater range in magnitude, most features (*e.g.*, the top region of ANA-19-9) are more pronounced in the δ^{13}C record.

5.4 Discussion

Previous monitoring efforts to constrain the present climatic and environmental controls of Niuean caves revealed a significant sensitivity to seasonality and multi-year cyclic climate drivers (Tremaine et al., 2016; Rasbury & Aharon, 2006; Murgulet, 2010; Nava-Fernandez et al., 2024). These studies highlight the potential of cave deposits from the island to record highly-resolved climate information, including on phenomena such as cyclone activity, El Niño-Southern Oscillation (ENSO), the Inter-Decadal Pacific Oscillation (IPO), and positional changes in the South Pacific Convergence Zone (SPCZ). However, it is also clear that caves across the island may differ significantly in their susceptibility to climatic and environmental processes, thus requiring

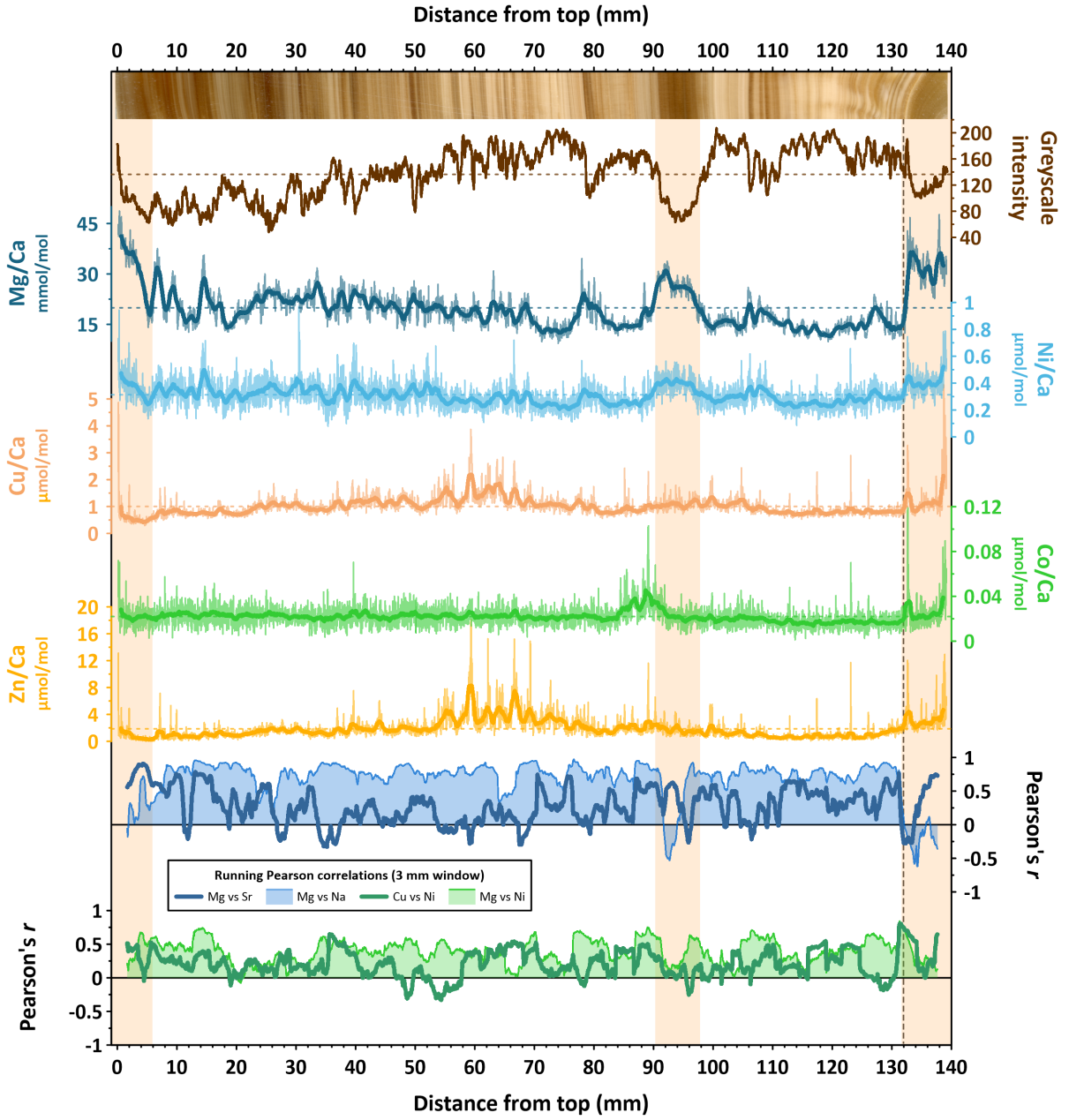

Figure 5.11: Trace elemental proxy series and running correlations in stalagmite ANA-19-9. The scanned image shows the central region of the stalagmite section used for sub-sampling (parallel to growth laminae). Greyscale intensity values were extracted from the scanned image. Note that the alignment of proxy data with the scanned image worsens where lateral heterogeneity in laminae increases. Thin and thick solid lines of element:Ca ratios represent the original resolution (25 µm) and a running average across a 1 mm window, respectively. Horizontal dashed lines in each plot reflect the total average value. Pearson correlations between different element:Ca ratios (for clarity abbreviated to the element normalised to Ca) were performed using a sliding window of 3 mm. The vertical dashed line marks a suspected hiatus. Vertical coloured bars indicate regions of decoupled Mg/Ca and Na/Ca trends, and concurrent increases in the correlation of Mg/Ca and Sr/Ca.

modern observations of cave environments to corroborate speleothem-based interpretations. Here, preliminary data from ongoing cave monitoring of two Niuean caves are presented (Section 5.4.1 and Section 5.4.2), which are ultimately intended to aid in the interpretation of two Holocene stalagmite records (tentatively discussed in Section 5.4.3).

5.4.1 Modern climatic and environmental controls of cave atmosphere, dripwater chemistry, and carbonate deposits

Atmospheric and hydrological sensitivity of cave environments

Three field campaigns and intermittent cave monitoring of Anapala Cave and Ulupaka Cave between September 2019 and November 2022 provide insights into the sensitivity of these caves and respective dripwaters to processes at the surface and in the karst. Temperature recorded just outside Anapala Cave mirrored measurements at Hanan Airport as expected, with a consistent slight offset by ca. -0.8 °C (Figure 5.4). This difference presumably reflects the logger location amongst shaded rocks and canopy, and/or calibration differences. The characteristically low intra-annual variability in air temperature (26.2 °C $\pm$ 1.8 based on data from Hanan Airport) of Niue's tropical climate was consistent but considerably muted inside both caves (and with depth inside of Anapala Cave), with annual cave air temperature varying by less than 0.3 °C and 0.2 °C in Anapala Cave and Ulupaka Cave, respectively. Measured in the upper part of Anapala Cave, the atmospheric pressure was largely in tune but reduced with respect to external measurements, suggesting that the limited overburden in the order of several metres is insufficient to noticeably insulate the cave atmosphere from surface pressure changes. Accordingly, the cave atmosphere was subject to significant low pressure systems, reaching as low as 991 hPa during category 2 tropical cyclone Sarai on 31 December 2019 (recorded as 996 hPa at Hanan Airport). Although in-cave relative humidity is expected to vary slightly in response to lateral air exchange, recordings rapidly became unreliable upon saturation of the sensor.

The pCO_2 measured in the upper part of Anapala Cave was higher and more variable in austral summer (ca. December to May) based on recordings from September 2019 to May 2021, suggesting enhanced CO_2 degassing and/or reduced cave ventilation during these periods. Cave ventilation principally arises from pressure differentials, for instance, linked to temperature and density gradients (Spötl et al., 2005; Kowalczk & Froelich, 2010; Mattey et al., 2010). For example, chimney ventilation is likely enhanced when the in-cave temperature exceeds that at the surface (*e.g.*, Breitenbach et al., 2015), which may be particularly pronounced near cave entrances, where heat exchange between external air and cave walls readily occurs (Mattey et al., 2010). During periods of enhanced ventilation, the influx of surface air with atmospheric pCO_2 ($\approx$400 ppmv) thus effectively dilutes cave air enriched with soil-derived CO_2, whereas low ventilation regimes result in the progressive build-up of pCO_2. In Anapala Cave, diurnal and multi-day variations in in-cave pCO_2 were largely in accord with external

temperature fluctuations during austral summer. During this period, surface temperature was dominantly higher than that recorded inside the cave, presumably limiting lateral air exchange. Conversely, minimal pCO_2 levels during the months of July to September 2020 coincided with surface temperature near or lower than in the upper cave, which is expected to enhance ventilation. Irrespective of cave ventilation, however, the lower pCO_2 observed during the dry period presumably also reflects limited water discharge during austral winter, as evident from drip logger data (Figure 5.4). At large, however, pCO_2 in the upper part of Anapala Cave was typically either at or only slightly above surface levels (368 – 549 ppmv) and very comparable to the Niuean coastal cave (395 – 800 ppmv) studied by Tremaine et al. (2016) (cf. for instance Natural Bridge Caverns with 400 – 37,000 ppmv Wong et al., 2011; Ballynamintra Cave with 400 – 1,700 ppmv J. U. L. Baldini et al., 2008; Mawmluh Cave with 370 – 1049 ppmv; Breitenbach et al., 2015). While the generally shallow depth of Anapala Cave (and indeed all known Niuean caves) in the order of metres to a few tens of metres generally facilitates atmospheric influences, it is also plausible that the limited soil profile above the cave prevents significant enrichment of infiltrating water in soil-derived CO_2. Regardless, these data imply that cave ventilation is likely favoured during the drier months of austral winter, which in turn is expected to enhance prior calcite precipitation (Wong et al., 2011). In the context of speleothem-based climate interpretations (noting that samples discussed in Section 5.4.3 stem from the lower part of Anapala Cave with spot measurements indicating pCO_2 of ca. 700 ppmv), PCP signals imprinted in speleothem geochemical proxies should thus primarily reflect the drier periods of intra- and inter-annual scale. Due to limited water supply during austral winter, however, most of the deposition is in turn expected to occur during the wet period.

A characterisation of drip rates based on Stalagmate® drip count data using the classification scheme of Smart and Friederich (1986) (modified by Baker et al., 1997b; Fairchild, Tuckwell, et al., 2006) suggested that all drip points were either governed primarily by seepage flow or seasonal discharge (Figure 5.12). Compared to seepage flow, seasonal drips are distinguished by increased variation across the drip rate dataset for a given maximal volumetric discharge. Temporal variation was particularly pronounced for the two drip points in the upper chamber of Anapala Cave. These were effectively inactive during dry periods but discharged substantially and presumably in several drips in response to larger rainfall amounts (up to 244 drips min^{-1}). The drip rate timeseries of these and other "seasonal" drips depicted hydrographs typically associated with dominant fracture-flow (*e.g.*, Fairchild, Smith, et al., 2006; Treble et al., 2022). Specifically, flow rates were marked by a sharp initial increase in drip rate within a few hours of strong rainfall events as registered by the Hanan International Airport weather station (Figure 5.4; noting though that rainfall can vary significantly across Niue; Daryn Magatogiia, personal communication). The rapid onset of discharge as fractures fill was typically followed by a slower, more gradual decline in drip rate as fractures were drained (see example annotations in Figure 5.4). This flow pattern was evident in most drips but muted with increasing influence of seepage flow. The constantly active ANA-LC-5 in the lower part of the cave presents an example of dominant seepage flow, which showed pronounced short-lived responsivity in flow only at exceedingly high rainfall amounts.

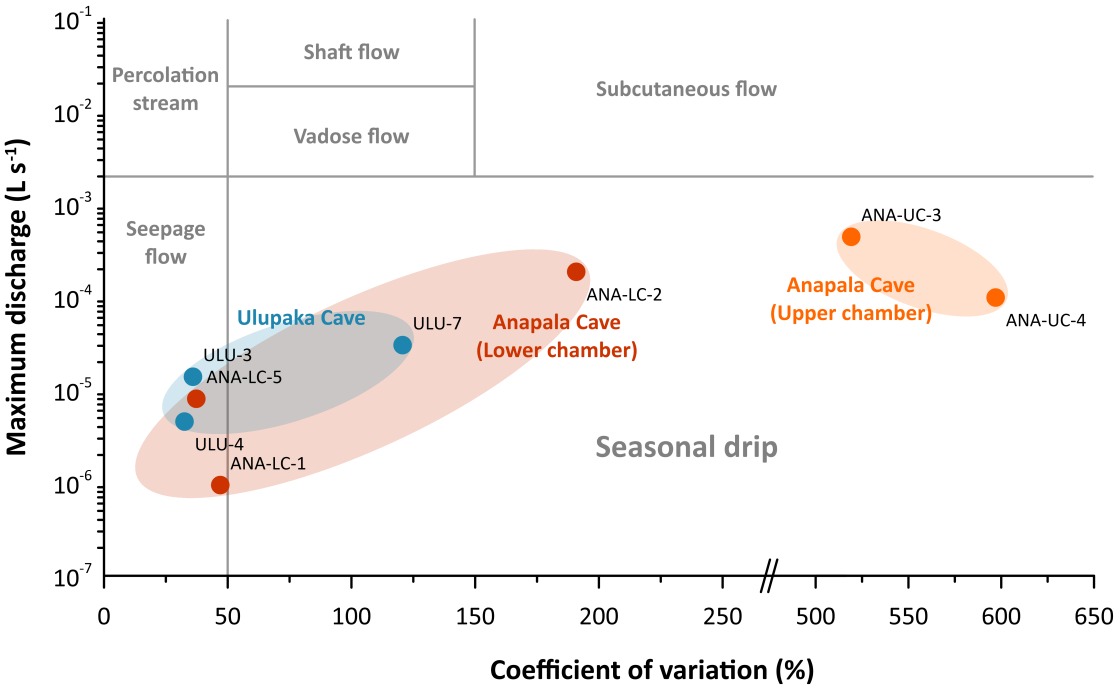

Figure 5.12: Flow characterisation of drip points in Anapala Cave and Ulupaka Cave. Data are only shown for drip points equipped with drip count loggers. Note that the characterisation is inevitably constrained to the respective logged period. The characterisation is based on the approach of Fairchild, Tuckwell, et al. (2006) and Baker et al. (1997a) (after Smart & Friederich, 1986) and assumes a drop volume of 0.11 mL. The x-axis contains an axis break to accommodate for the far greater variation in drip rates in the upper chamber of Anapala Cave.

In Ulupaka Cave, drip points ULU-3 and ULU-4 both exhibited seasonality with an overall gentler rise and fall of flow rates than those observed in Anapala Cave. This was particularly the case for ULU-4, whereas ULU-3 exhibited more short-term variability (order of days to weeks) alongside longer-term (order of months) trends. Compared to drips monitored in Anapala Cave, discharge in Ulupaka Cave was overall less responsive to recharge, while drainage occurred over several months largely irrespective of fresh rainfall. Consistent with dominant soda straw stalactite morphologies in the study chamber, these discharge patterns are interpreted to reflect reservoir effects on drip rates and thresholds on reservoir recharge, while fracture flow is limited (Figure 5.12). ULU-7 depicted an interesting case of persistently high flow rates between March and August 2020 of ca. 12 drips min^{-1}, before a sharp decrease in flow was recorded. Following the step decrease to a new baseline of <1 drip min^{-1}, drip rate continued to exhibit temporal variability, although substantially reduced compared to the previous period. Because the drip logger was equipped with a watch glass that could have potentially caused a sudden reduction in registered drips, it is unclear whether this sudden decrease presents an artefact or true change in flow rate. The latter could arise, for instance, from hydrological re-routing due to flow path clogging or directional changes. However, spot measurements in November 2022 depicted a considerably reduced baseline flow, suggesting that flow paths may indeed have changed suddenly. Alternatively, the feeding reservoir may have ceased, given that the sharp decline coincided with the flow of other drips waning in both Anapala Cave and Ulupaka Cave in response to reduced winter recharge.

5.4.2 Drivers of modern dripwater and carbonate chemistry

Trace element sources and controls

To understand the dominant contributing sources of various trace elements measured in modern dripwaters and speleothem samples, the cave water chemistry was firstly compared to seawater, soil, and bedrock chemical characteristics. Typically, Ca, Mg, and Sr concentrations are primarily attributed to bedrock dissolution (*e.g.*, Tadros et al., 2019; Fairchild et al., 2000). In coastal settings, however, marine aerosols can significantly contribute to the abundance of these and other elements (L. M. Baldini et al., 2015; Tremaine et al., 2016; Kost & Stoll, 2023). In the coastal Niuean cave studied in Tremaine et al. (2016), for instance, the authors reported a substantial marine input accounting for ca. 85%, 19%, and 17%, for Mg, Ca, and Sr, respectively. SO_4 (here approximated by total S) and Na were found to be ca. 93% and 89% of seawater origin. In this study, the comparison of Mg to Na implied that much of the variability in Mg content in Anapala Cave was likewise linked to sea spray inputs, given the strong resemblance of dripwater Mg/Na to that characteristic of ocean water (Figure 5.5) and assuming that negligible amounts of Na are directly derived from the host rock (*e.g.*, Tadros et al., 2016). Ca and Sr were also positively correlated with Na in Anapala Cave, with the different slopes of dripwater and seawater regression lines suggesting that marine aerosols presented an additional source to water-rock interactions. The same assessment of dripwater from Ulupaka Cave in turn suggested a lower influence of seawater on Mg (slope $\approx$0.04 and $\approx$0.11 for Ulupaka Cave and seawater, respectively), and effectively no marine contribution to Ca (Figure 5.4). Mg and Sr exhibited strong covariance in dripwaters from both caves, although the slopes of the relationships were unique. Based on linear regressions of bulk elemental compositions of respective cave host rock, Mg and Sr in Anapala Cave consistently depicted a composition intermediate to that expected of (bulk) bedrock dissolution and seawater. Dripwaters from Ulupaka Cave were in turn highly consistent with the respective host rock composition (considering uncertainties due to heterogeneity in rock formations), with no apparent seawater influence. In this regard, Kost and Stoll (2023) recently demonstrated that the atmospheric concentration of marine aerosols and their impact on cave water chemistry can decrease rapidly with distance to the coast, noting a reduction of ca. 40% – 80% within the first 1400 m at their study location. Marine aerosols derived from wave breaking in surf zones (or in the case of Niue, at the reef crest or upper reef platform during high tide), in particular, are readily deposited within short distance following their mobilisation (Hossain & Easa, 2011; O'Dowd & de Leeuw, 2007). While finer particles are generally transported further, the exact spatial distribution of aerosols ultimately depends largely on wind speed (*e.g.*, Meira et al., 2007). Although seemingly marginal, the sheer difference in distance from the shoreline between Anapala Cave (ca. 250 m) and Ulupaka Cave (ca. 500 m), coupled with different wind regimes, may thus be sufficient to cause the up to ten-fold lower concentrations of Na, K, and S in Ulupaka Cave (Table 5.3), effectively decoupling the cave from major seawater inputs. The difference in Mg/Ca (and Sr/Ca to a lesser degree) between caves is likely in part attributable to different bedrock compositions (*i.e.*, higher proportion of dolomite in Anapala Cave, see

discussion below), although a quantitative assessment of bedrock mineralogy is still required. Within Anapala Cave, an enrichment in elements, such as Mg, Sr, and Na, was noticeable with depth between dripwater collected from the upper and lower chambers. These differences likely reflect longer flow paths and/or prolonged water-rock interactions, which would result in the increase of these elements relative to Ca under the assumption of incongruent dissolution (cf. Fairchild et al., 2000). Similarly, longer flow paths appear to flush out more salt deposits within the karst, thus concentrating seawater-derived elements. However, the persistent elemental enrichment from upper to lower parts of the cave in all three monitored periods may also imply that conditions for much of the year may favour calcite dissolution along flow paths in Anapala Cave, as evidence of speleothem dissolution is present throughout most of the cave, and the upper chamber, in particular.

In contrast to most major matrix elements, the first-row transition metals Ni and Cu were very similarly concentrated in dripwaters of both cave systems, with Co not reliably quantified in most samples due to very low concentrations (note that Zn was consistently below detection). The few available ratios of Co and Ni were similar to those measured in soil extracts collected above the cave, while this was not observed for Cu and Ni (Figure 5.6). However, soil extracts were highly variable in elemental compositions (Supplementary Table 5.S4), presumably in part due to very thin and carbonate-rich soil layer (especially above Anapala Cave) that challenged the characterisation of true 'soil' chemical properties. However, these elements are not typically associated with marine aerosols, nor with bedrock dissolution. Their partial agreement with the soil composition, as well as their coherent relative abundances between study sites, thus support the assumption that Cu and Ni (alongside other transition metals) primarily derive from soil components (cf., Fairchild & Treble, 2009; Hartland et al., 2012; Warken, Kuchalski, et al., 2022; Liao et al., 2021).

The potential of Mg/Ca and Sr/Ca systematics in cave waters as quantitative indicators of water-rock interactions and prior calcite precipitation (PCP) has been the subject of several in-depth investigations (*e.g.*, Fairchild et al., 2000; Sinclair, 2011; Tremaine & Froelich, 2013). A common approach is to assess the covariance of Mg/Ca and Sr/Ca, where the degree of PCP is expressed as the removal of Ca^{2+} from solution. Using the model made available by Tremaine and Froelich (2013), the chemical evolution of Mg/Ca as a function of Ca removal was applied to measurements in dripwaters from the Niuean caves (Figure 5.7A). Here, the lowest and highest Mg/Ca ratios from a total of 12 bedrock samples from across the island served as low-Mg ($\sim$limestone; here Mg/Ca $\approx$ 11.1 mmol mol^{-1}) and high-Mg ($\sim$dolomite; Mg/Ca $\approx$ 838 mmol mol^{-1}) end-members, respectively. For Anapala Cave, this model described the data best assuming a mixture of ca. 37% dolomite and 63% limestone as the host rock, whereas a presence of ca. 8% dolomite yielded an adequate result for Ulupaka Cave. For both caves, fluid evolution was modelled using the respective lowest measured dripwater Sr/Ca. Varying the dolomite contribution by $\pm$2% (while keeping other parameters constant) and $\pm$4% accounted for $>$95% of the data in Ulupaka Cave and Anapala Cave, respectively. Inclusion rates of Mg and Sr were described by empirical partition coefficients (for an element X, defined as: D_X = $(X/Ca)_{Calcite}$ / $(X/Ca)_{Solution}$) obtained by comparing dripwater and modern calcite

precipitates in each cave. Values of D_{Sr} were estimated as 0.14 $\pm$ 0.04 (n = 27) and 0.07 $\pm$ 0.01 (n = 90) in Anapala Cave and Ulupaka Cave, respectively, whereas D_{Mg} was 0.04 $\pm$ 0.01 (n = 107) in both settings (including estimates from watch glasses (Table 5.4) and surficial $CaCO_3$ samples presented in Chapter 4). It is noted, however, that the exact value of D_X has negligible effects on the PCP vector calculated in this model (Fairchild et al., 2000). Regardless of uncertainties related to the preliminary characterisation of bedrock composition, this exercise implies that modern dripwater Mg/Ca and Sr/Ca co-vary largely in response to PCP (Figure 5.7), while absolute contents of Mg appear to be driven also by marine aerosols (Figure 5.5). As noted by Tremaine and Froelich (2013), the seawater-associated elements Na and K likewise preferentially remain in solution upon calcite precipitation (*i.e.*, $D_X < 1$). Accordingly, Na/Ca and K/Ca were similarly positively correlated with Mg/Ca, and affected by PCP in the same direction.

The effectively discrete collection of water samples in September 2019, February 2020, and November 2022 largely prevent robust assessment of temporal variability. According to the findings of Tremaine et al. (2016), however, it is expected that marine salts accumulate within the karst during drier periods, while wetter conditions would more readily mobilise salts within the karst. Hence, it is plausible to expect short-lived 'flushing' signals analogous to those observed for soil-derived elements (*e.g.*, Warken, Kuchalski, et al., 2022), in response to significant rainfall following prolonged dry conditions.

Stable isotopes of cave water and rainfall

The analysis of stable oxygen and hydrogen isotope ratios in cave water and rainfall samples demonstrated their consistent relationship along the South Pacific Meteoric Water Line (SPMWL; $\delta D = 7.7 \times \delta^{18}O + 9.3$; Aharon et al., 2006), deviating slightly from the Global Meteoric Water Line (GMWL; $\delta D = 8.0 \times \delta^{18}O + 10$; Craig, 1961; Dansgaard, 1964) towards heavier (less negative) signals of δD and $\delta^{18}O$ (Figure 5.8). Rainfall on Niue is exclusively of marine origin, and topographic effects are negligible given the limited size (ca. 260 km^2) and elevation (maximum ca. 70 m above sea level) of the geographically remote island. Given that water $\delta^{18}O$ during wet periods did not deviate substantially from the SPMWL, local rainfall amount is considered to present the primary driver of isotopic variation in dripwaters (Tremaine et al., 2016). This was supported by samples collected during heavy convective downpours linked to cyclone Wasi (22 – 23 February 2020) with isotopic ratios as low as -11.0 ($\delta^{18}O$) and -80.9 (δD), which were nonetheless in good agreement with the SPMWL. At the other end of extremes, dripwater samples collected by Tremaine et al. (2016) during a prolonged dry spell in 2012 in turn suggested an evaporative loss of reservoir volume in the unsaturated zone by up to 17%, demonstrating that disequilibrium isotopic fractionation can be significant even in the humid (>95% RH) caves of Niue. This observation implies that evaporation may amplify enrichment of ^{18}O in dripwater (and speleothems by extension) during droughts, leading to higher $\delta^{18}O$ values in response to reservoir drying.

Consistent with previous studies (Tremaine et al., 2016; Aharon et al., 2006; Murgulet,

2010; Rasbury & Aharon, 2006), the range in δD and δ^{18}O observed in Niuean dripwaters was limited relative to rainfall values derived from the Global Network of Isotopes in Precipitation (GNIP) for the wider region (Rarotonga station, Cook Islands; see Tremaine et al., 2016). This suggests that vadose mixing of rainfall inputs on super-seasonal scales may reduce overall isotopic variability, effectively muting rainfall signals (Tremaine et al., 2016; Moerman et al., 2014). As noted by Moerman et al. (2014), however, reduced variability in isotopic variation of infiltrating water may also stem from seasonal bias of recharge, including strongly seasonal baseline rainfall and strong sporadic events. Both constraints on dripwater isotope variability are very likely to operate in the monitored caves, given the overall pronounced rainfall seasonality and susceptibility to extreme rainfall events. In addition, flow rate signatures of many drips depicted multiple magnitudes higher than baseline flow in response to sufficiently strong rainfall, whereas smaller rainfall events were seemingly buffered by karst storage in the studied caves.

5.4.3 Tentative interpretation of stalagmite proxy signals in Anapala Cave

Stalagmite growth and structural properties

While ongoing monitoring and automated weekly water sampling are expected to provide a more comprehensive understanding of the modern cave environments, the available chemical and physical observations of Anapala Cave and Ulupaka Cave suggested a high sensitivity of the cave atmosphere to external weather conditions. Moreover, strong hydrological links between flow regimes and chemistry of infiltrating waters were evident. The latter was particularly the case in Anapala Cave (the source of stalagmite records discussed here), where discharge was more directly related to rainfall through dominant fracture flow. The closest monitored drip points to the bases of sampled stalagmites were ANA-LC-1, ANA-LC-2, and ANA-LC-5. While drip site ANA-LC-2 was classified as a seasonal drip with significant discharge variability, both drips ANA-LC-1 (ca. 20 cm offset from the base of stalagmite ANA-19-1) and ANA-LC-5 showed characteristics of year-round seepage flow punctuated by periods of high discharge after high rainfall (Figure 5.4). Assuming similar intra-annual flow patterns over most of the stalagmite growth periods, it is thus plausible to expect deposits to reflect seasonality with higher and lower extension rates during wet and dry months, respectively. This interpretation was supported by the stalagmite morphology with predominantly broad, binary lamination (Figure 5.9), and variable layer width (Figure 5.10). Both samples comprised alternating laminae of dark dense calcite (DDC; corresponding to lower grey scale intensities) and pale porous calcite (PPC; higher grey scale intensities), interpreted to present $\sim$dry and $\sim$wet periods, respectively (cf. Murgulet, 2010; Rasbury & Aharon, 2006; Nava-Fernandez et al., 2024; Hartland et al., 2014; Boch et al., 2011). During drier periods (*e.g.*, austral winter), cave ventilation in Anapala Cave was enhanced as implied by consistently lower cave air pCO_2 (Figure 5.4). Although not noticeable in water samples analysed in this study, the lower pCO_2 is expected to result in an

increase in dripwater pH, and consequently the saturation of dripwater with respect to calcite. Higher supersaturation during winter months, combined with overall lower drip rates, has been shown to favour the formation of compact columnar fabrics with negligible space between crystals (∼complete lateral coalescence), which appear as dense dark (translucent) calcite laminae at macroscopic scale (Boch et al., 2011). Conversely, low ventilation during summer months results in typically higher pCO_2, lower dripwater pH, and consequently, a lower degree of calcite supersaturation. Coupled with higher drip rates, fabrics developing under these conditions tend to be more porous and microcrystalline, with incomplete lateral coalescence allowing for fluid inclusions and impurities to be incorporated in elongate inter-crystal spaces. The resulting white laminae often vary in thickness in response to changes in ventilation regime and/or drip rate, whereas laminae of DDC are typically more consistent in width. While Boch et al. (2011) found ventilation to be the primary driver of lamina variations in the Austrian Katerloch Cave, the strong seasonality in drip rates observed in Anapala Cave, combined with comparably small variability in cave pCO_2 (368 – 549 ppmv between September 2019 and May 2021), imply that drip rate in this cave may be similarly (or more) important for the definition of fabrics than seasonal ventilation changes.

Although the binary nature of laminae, as well as their counts with respect to the radiometric age ranges, support the assumption of annual banding of both samples, absolute chronologies remain poorly constrained. Consequently, proxy signals could not be confidently interpreted with respect to their exact timing. Nonetheless, the elemental and isotopic patterns provided insights into environmental variability within each record and time window as constrained by the magnitude of radiometric ages. Collectively, both samples covered most of the Holocene, with proxy series representing ca. 2.75 to 0.48 ka BP and 9.51 to 5.84 ka BP in ANA-19-1 and ANA-19-9, respectively.

Drivers of trace elemental trends: karst processes and marine aerosols

By far the strongest trace element signal observed in stalagmites ANA-19-1 and ANA-19-9 was that of Mg (Figure 5.10). Variations in speleothem Mg/Ca, in combination with Sr/Ca (and sometimes Ba/Ca), are most commonly related to karst hydrology through the process of prior carbonate precipitation (PCP) and/or water-rock interactions. Both of these processes drive the ratios in the same direction under varying hydroclimatic conditions. PCP refers to any deposition of carbonate (here, calcite) occurring before formation of the final deposit of interest (Fairchild & Treble, 2009), while water-rock interactions are typically attributed to incongruent calcite dissolution (ICD). The latter describes the partial dissolution of calcite (opposed to congruent/complete dissolution), during which Mg and Sr are preferentially released relative to Ca (*e.g.*, Schroeder, 1969; Fairchild et al., 2000). This in turn results in an evolution of Mg/Ca and Sr/Ca water ratios. Both PCP and ICD along the flow path of infiltrating water are typically enhanced during drier conditions due to a lower saturation of pore spaces and stronger ventilation within the unsaturated zone, promoting water residence time (due to lower flow) and CO_2 degassing (due to higher air:water ratio) (Sinclair, 2011; Sinclair et al., 2012; Wassenburg et

al., 2020). Conversely, a saturated bedrock during periods of frequent recharge limits the exchange between dripwater and air prior to reaching the cave, thus resulting in less carbonate precipitation upstream from speleothems inside the cave.

The sensitivity of Mg and Sr to PCP and ICD (often occurring in rapid succession) originates from their relatively predictable partitioning behaviour into calcite (note that elemental inclusion into aragonite is distinct), which results in their progressive Rayleigh-type enrichment in solution compared to Ca as calcite is precipitated (see Chapter 4). Based on these observations, Sinclair et al. (2012) suggested that the slope of carbonate Sr/Ca versus Mg/Ca in natural log space should fall within close vicinity to 0.88 (irrespective of initial dripwater ratios and bedrock composition) if PCP and/or ICD were the primary drivers. However, it has since been shown that these criteria were too stringent (Wassenburg et al., 2020), and significant PCP (and by reasoning, hydrological forcings) can in fact be reflected in a wide range of relationships between Mg and Sr. Specifically, the authors suggested revised diagnostic slopes of ln(Sr/Ca) versus ln(Mg/Ca) between ca. 0.71 and 1.45. In this context, the slope of this relationship in stalagmite ANA-19-9 was ca. 1.04 (but weakly correlated, with R^2 = 0.17) and thus principally within the range observed across the large number of datasets compiled in Sinclair et al. (2012) and Wassenburg et al. (2020). However, this slope is at the higher end of the observed range reported in Wassenburg et al. (2020), who noted based on a modelling approach that the most likely scenario for a slope of >1 is a progressive increase in D_{Sr} in response to increasing solution and calcite Mg/Ca. For the only three comparable caves discussed in their study, the authors suggested that this behaviour is possibly linked to a mixed limestone-dolomite bedrock composition, causing variable bedrock dissolution rates. As discussed in Section 5.4.2, such an influence of dolomite on the cave water chemistry and chemical evolution is plausible for Anapala Cave. Indeed, it is noted that some sub-samples collected in ANA-19-1 were only partially dissolved during preparation procedures for isotope analysis (yielding lower but acceptable signal). This is noteworthy because the incomplete dissolution of sample powder implies a potential presence of more robust phases within the stalagmite fabric (*e.g.*, dolomite, detrital aluminosilicates; pending quantitative mineralogical analysis). Interestingly, a relationship between ln(Sr/Ca) and ln(Mg/Ca) in the late Holocene / Common Era formed stalagmite ANA-19-1 was virtually absent (slope 0.13, $R^2 < 0.01$), suggesting distinct controls altogether. Notwithstanding that dripwater Mg and Sr relationships largely depicted a sensitivity to PCP (Figure 5.7A), Mg and Sr systematics in Anapala Cave are clearly more complicated and likely not readily attributable to PCP and ICD dynamics alone.

In this regard, modern dripwater analyses also revealed a pronounced contribution of marine aerosols to the concentrations of Mg in dripwater (Figure 5.5), which is argued to vary largely independently of water-rock interactions. Based on observations in this study and monitoring conducted by Tremaine et al. (2016), it is expected that sea spray input to dripwater and stalagmites varies over time, most likely as a function of wind intensity and direction (Kost & Stoll, 2023). Specifically, dripwater analyses by Tremaine et al. (2016) suggested that sea salt aerosols and halite minerals in the unsaturated zone may build up during drier periods, whereas wetter conditions are expected to mobilise salts. Considering the strong contribution

of sea salt to dripwater Mg concentrations, and a far less pronounced marine influence on Sr (Figure 5.5B), the authors further argued that the relationship of Sr and Mg in speleothems should be indicative of the dominant controls at a given time. Accordingly, covariance of Sr and Mg (*i.e.*, ∼constant Sr/Mg) is predicted to reflect hydrological / climatic controls via PCP and water-rock interactions in line with conventional interpretations (Fairchild et al., 2000; Sinclair, 2011), whereas inconsistent variations coupled with strong Mg-Na relationships may relate to changes in flow path and/or the input of sea aerosols (Tremaine et al., 2016). Following this reasoning, and by example of the ANA-19-9 record (given the apparent additional complexity of ANA-19-1), correlations between Mg/Ca, Sr/Ca, and Na/Ca series were assessed with respect to depth within the stalagmite sample. To this effect, a simple Pearson correlation across a sliding window of 3 mm was applied to different elemental series. Tentatively, a moderate to good correlation (∼Pearson $r > 0.5$) of Mg/Ca with Sr/Ca and Na/Ca were regarded to indicate dominant controls of PCP/water-rock interactions and source (*i.e.*, via re-routing or variable aerosol contributions), respectively (Figure 5.11). Throughout 87% of the record, Mg/Ca and Na/Ca (overall $r = 0.59$) were more strongly correlated than Mg/Ca and Sr/Ca (overall $r = 0.44$). In fact, only three distinct regions in the ANA-19-9 stalagmite depicted an effective decoupling of Mg and Na (see vertical bars in Figure 5.11), which coincided with a strengthening of the correlation between Mg/Ca and Mg/Sr.

Notably, all three of these intervals occurred across extended periods of DDC deposition, and coincided with synchronous increases in $\delta^{18}O$ and $\delta^{13}C$ (discussed further in Section 5.4.3), as well as elevated Ba/Ca (also considered sensitive to PCP; *e.g.* Stoll et al., 2012) and U/Ca (in two periods, but anti-correlated at the stalagmite top; Figure 5.10 and Figure 5.11). Considering the simultaneous strengthening and decline of Mg-Sr and Mg-Na covariance, respectively, these segments of the stalagmite likely present a rare part of the record, in which PCP and/or ICD present the primary drivers of Mg and Sr with negligible contributions to dripwater Mg by halites. Mechanistically, the combination of elemental and isotopic signals during these dry periods suggested stronger ventilation and a higher proportion of unsaturated karst, presumably linked to reduced recharge. Distinct from other parts of the record, however, these conditions seemed to additionally coincide with a temporary cessation in aerosol supply. A possible scenario is that accumulated aerosols along flow paths were removed, whilst drier surface conditions limited new sea spray inputs. This could potentially occur during prolonged changes in wind regimes that may reduce onshore aerosol transport, and/or a lack of wet deposition as a key pathway for aerosols to enter the soil zone (*i.e.*, due to reduced rainfall). Under these circumstances, dripwater Mg/Ca would be increasingly decoupled from marine contributions, and in turn increasingly controlled by karst processes. A similar situation has previously been attributed to marked changes in Mg concentrations in a Spanish stalagmite presented by L. M. Baldini et al. (2015), who linked shifts in westerly winds during the Younger Dryas to variable sea spray delivery. In ANA-19-9, one of the three intervals was found at the very top of the sample (Figure 5.11), which appeared to depict a progressively intensifying drying trend, culminating in the terminal growth cessation. Although growth may have stopped for other reasons (*e.g.*, displacement), the geochemical signals are at large consistent with a

dwindling and ultimately ceasing water supply.

Regardless, while the prevailing dominant relationship between Mg and Na generally complicated the interpretation of stalagmite Mg/Ca ratios, Mg and Sr were nonetheless positively related (although to lower degree) throughout most of the ANA-19-9 record. Moreover, it is important to note that Na is expected to also fractionate with respect to Ca in response to PCP, given that $D_{Na} < 1$ (Tremaine & Froelich, 2013). Most likely, PCP and water-rock interactions as driven by rainfall inputs, thus nonetheless exert an important and pertinent control on trace elements in the stalagmite as suggested by dripwater analyses, albeit variable aerosol inputs may conceal these signals. However, the exact relative importance of hydrological forcings and source effects require further investigation, including an assessment at higher temporal resolutions. For instance, it is plausible that source effects and PCP/ICD operate on distinct time-scales, an isolation of which could help differentiate different forcings. Furthermore, semi-quantitative approaches (*e.g.*, Stoll et al., 2012) applied to proxy series may also prove insightful, and aid in more confidently constraining their environmental controls.

Transition metal systematics in stalagmite ANA-19-9

While the systematics of alkaline earth metals and Na were interpreted to be largely driven by sea spray inputs and karst processes, the first-row transition metals Co, Ni, Cu, and Zn appeared to be primarily derived from the thin soil layer and vegetation. In both stalagmites, these metals generally showed similar behaviour across the proxy records, which was most pronounced for Zn and Cu in ANA-19-9. The systematics of first-row transition metals in stalagmites are particularly interesting in light of new convincing support for a proposed drip rate control on the release of these metals from organic metal complexes (OMCs) at the dripwater-stalagmite interface (Giesche et al., 2023; Hartland & Zitoun, 2018; Sliwinski et al., 2022; Chapter 4). In many cave settings, transition metals have been interpreted to primarily reflect short-lived 'flushing' events (*e.g.*, Ban et al., 2008; Warken, Kuchalski, et al., 2022), during which organo-metal associations in particulate or colloidal form are mobilised in the soil zone, and transported to the site of speleothem deposition. At fast growth rates and high porosity, in particular, metals may thereby be incorporated alongside organic components via adsorption or entrapment (see Chapter 4 for discussion). In absence of strong flow events, however, it has been suggested that the rate-dependent kinetic decay of OMCs poses an alternative control. Accordingly, drier and wetter periods are predicted to result in higher and lower transition metal concentrations (normalised to Ca), respectively, if metal release is dictated by OMC residence time at stalagmite surfaces (Hartland & Zitoun, 2018; Giesche et al., 2023; Sliwinski et al., 2022; Chapter 3; Chapter 4).

To assess the behaviour of transition metals in ANA-19-9, the strategy of serial correlation was applied to Mg/Ca with respect to Ni/Ca, as well as between the latter and Cu/Ca (Figure 5.11). Interestingly, Ni/Ca was moderately to strongly positively correlated with Mg/Ca for virtually the entire ANA-19-9 record, showing consistent patterns with almost all major Mg excursions. To some degree, covariance with Mg/Ca was also observable for Cu/Ca, Co/Ca, and

Zn/Ca, however, fewer common features of the Mg/Ca ratios were imprinted in these elements. Importantly, Ni/Ca values are not expected to be sensitive to PCP, given an inorganic partition coefficient of Ni (D_{Ni}) close to 1 (Lindeman et al., 2022; Chapter 4). The latter implies that under equilibrium conditions, Ni distributes between solution and crystal phase effectively at the same rate as Ca, and the removal of Ca from solution during calcite precipitation has no effect on the evolving Ni/Ca. Furthermore, Ni is not typically associated with marine aerosols, as supported by dripwater Ni concentrations depicting no discernible marine origin (Figure 5.6). Thus, the concurrent trends in Mg/Ca and Ni/Ca are unlikely due to water-bedrock interactions (*e.g.*, ICD), PCP, or sea spray inputs.

If accepting that Mg/Ca values trace drying and wetting of the karst in addition to the underlying assumed marine influence, trends of Ni/Ca appear to likewise reflect hydrological forcing in the same direction. By extension, this implies that Ni/Ca are in principle inversely related with dripwater flow rates at the seasonal to inter-annual resolution (assuming annual lamination).

Gradual changes of transition metal concentrations were nonetheless periodically interspersed with extreme deviations from baseline variability. While concurrent strong excursions were absent for the more concentrated elements, this behaviour of transition metals alludes to the superimposed intermittent influence of high-flow events as observed in other systems (*e.g.*, Warken, Kuchalski, et al., 2022; Borsato et al., 2007; Fairchild et al., 2001). However, while short-lived discharge events may thus periodically drive transition metal supply through direct capture of OMCs (*i.e.*, via adsorption or entrapment), this appeared to be the exception rather than the rule in ANA-19-9. Possibly, the generally low drip rates throughout most of the year may in fact favour kinetic OMC pathways. The latter is supported by experimental and modelling approaches (Chapter 3), which indicated that OMC decay of Ni in a range of cave water samples was most sensitive at drip rates $<$40 drips min^{-1} and increasingly sensitive towards longer drip intervals.

It is further noted that during greater excursions of Mg/Ca, the normalised concentrations of Cu, Co, and Zn varied largely in accord, whilst generally not mirroring smaller variations in Mg/Ca. In the context of OMC stability, this seemingly hierarchical covariance of transition metals with Mg/Ca may reflect different OMC binding characteristics for each metal (Chapter 3). This at times contrasting behaviour of transition metals was evident when comparing the running Pearson correlations between Ni and Mg with those of Cu and Mg (all normalised to Ca). Ni-NOM complexes were likely strong enough to facilitate the transport of Ni, while dissociating at sufficiently high rates for Ni to be included in calcite in response to longer-term changes in dripwater discharge at the observed baseline drip rate range in the lower Anapala Cave in the order of 0.1 to 1.0 drips min^{-1}. Following this logic, a greater reduction in flow may be necessary for other metal-NOM complexes to release metals with a discernible effect on carbonate metal:Ca ratios.

These patterns of transition metal concentrations observed in ANA-19-9 are promising with view to reconstructing past hydroclimate variability based on the OMC decay hypothesis, however, would benefit by further assessment in relation to temporally-resolved water sampling

over at least one seasonal cycle. This could, for instance, allow for an analysis of seasonal covariance between transition metals in dripwater, possibly providing further insights into the dominant hydrological responses (*e.g.*, Hartland et al., 2014; Warken, Kuchalski, et al., 2022).

Origin and potential of stable isotope signals

Considering that stable isotope measurements of dripwater and local rainfall consistently followed the South Pacific Meteoric Water Line (Figure 5.8), their variability is expected to primarily reflect the amount of local rainfall. Specifically, lower and higher $\delta^{18}O$ values in the stalagmite records are interpreted as wetter and drier periods, respectively, consistent with monitoring data presented here and in previous studies in Niuean caves (Murgulet, 2010; Rasbury & Aharon, 2006; Tremaine et al., 2016; Nava-Fernandez et al., 2024). Measured only at a low spatial resolution of 1 mm, isotopic records of ANA-19-1 and ANA-19-9 do not resolve seasonal variability as achieved by Nava-Fernandez et al. (2024) and Murgulet (2010), but presumably integrate annual to inter-annual signals. For the purpose of this study, these data primarily served to support trace element interpretations as a mechanistically independent proxy system. In both stalagmites, $\delta^{18}O$ variations broadly agree with major excursions in Mg/Ca, Sr/Ca, and Ba/Ca (Figure 5.10). This apparent covariance supported the assumption that respective elemental abundances were at least partially driven by karst hydrology. Specifically, the observation of lower and higher values of $\delta^{18}O$ in PPC and DDC laminae, respectively, likely reflected enhanced kinetic fractionation at higher precipitation rates (*i.e.*, favouring the inclusion of ^{18}O into the crystal phase) during austral summer.

Stable carbon isotope ratios ($\delta^{13}C$) in turn are typically attributed to soil processes and bedrock properties, with various intricate biogeochemical controls collectively shaping the ultimate speleothem $\delta^{13}C$ record (Fohlmeister et al., 2020; Cruz et al., 2005; Lechleitner et al., 2021). For the Niuean caves of Avaiki and Palaha, Aharon et al. (2006) estimated that dripwater $\delta^{13}C$ was almost entirely ($<$90%) governed by the isotopic composition of soil CO_2 ($\delta^{13}C \approx$ -29.40 $\pm$ 0.09), with carbonate bedrock dissolution ($\delta^{13}C \approx$ -0.40 $\pm$ 0.09) contributing most of the remaining signal. The moderately good correlation of stalagmite $\delta^{13}C$ and $\delta^{18}O$ (Supplementary Figure 5.S5) depicted similar kinetic controls on $\delta^{13}C$ related to the rate of CO_2 degassing, with potential modulations of the relative source contributions (*i.e.*, soil and bedrock). For instance, the relative significance of bedrock-derived carbon for dripwater $\delta^{13}C$ has in other systems been suggested to increase during wet periods, when elevated soil moisture facilitates microbial respiration (*e.g.*, Cruz et al., 2005; Genty et al., 2003). The increased CO_2 production may in turn promote water-bedrock interactions due to a higher acidity of percolating waters (McDermott, 2004), thus increasingly inheriting isotopic values from the bedrock dissolved organic carbon pool. However, given the marginal soil depth, high carbonate content (and thus buffering capacity), and essentially vertical drainage with a negligible water holding capacity of typical Niuean soils, it is questionable whether this effect would be significant. It is thus more likely, that rate-dependent kinetic fractionation at the water-stalagmite interface as a function of CO_2 degassing and controls thereof (*e.g.*, ventilation, drip rate, saturation) drive most of the

observed $\delta^{13}C$ signals.

Consistent with previous studies on Niuean cave deposits Niue (Murgulet, 2010; Rasbury & Aharon, 2006; Tremaine et al., 2016; Nava-Fernandez et al., 2024), the carbonate values of $\delta^{18}O$ and $\delta^{13}C$ show potential for faithfully recording past hydroclimatic variability. While beyond the scope of this study, these data thus encourage further sub-sampling (micro-milling) at higher (sub-annual) resolution as part of the ongoing development of ANA-19-1 and ANA-19-9 palaeoclimatic records, provided that sample age control can be significantly improved.

Prospects of Ulupaka Cave for palaeoclimatic reconstructions

The water-table cave of Ulupaka along the eastern coast of Niue presents one of the most extensive and most decorated systems on the island. As such, it has historically been used for various purposes, including recreation, shelter, water supply, and burial (Daryn Magatogiia, personal communication), as well as tourism in recent decades. As a result, most of the cave has experienced substantial damage to formations. while the historic use of leaf torches has introduced considerable amounts of soot to the cave environment (Millar, 2017). However, petrographic analyses of stalagmite samples from Ulupaka Cave carried out by Aharon et al. (2006) did not reveal significant inclusion of soot, which could otherwise impact radiometric dating methods. Deposition is perceivably fast in many parts of the cave, which was corroborated by estimated total accumulation rates on watch glasses deployed between September 2019 and November 2022 (order of 0.1 to 11.8 mg day^{-1}), while Aharon et al. (2006) observed extension rates of 225 $\pm$ 85 µm $year^{-1}$ in a stalagmite from the cave. Monitoring data further suggested that marine aerosols present a far less prominent and possibly negligible source for trace elements in dripwater of Ulupaka Cave, potentially rendering the interpretation of speleothem records thereof less convoluted than those from Anapala Cave. Moreover, most drip points in Ulupaka Cave were active throughout the year, and responsive to smaller variations in rainfall than Anapala Cave. Although no geochemical analyses of speleothems from this cave have to date been published, the muted influence of seawater (Figure 5.5 and Figure 5.6) and high deposition rates suggest that speleothems could prove amenable to palaeoclimatic interpretations. For instance, the culturally significant cave hosts a vast number of presumably Common Era / Holocene stalagmites, which could provide valuable climatic context to the island's settlement period (ca. 900 AD) and regional Polynesian sailing age. Naturally, palaeoclimatic applications require robust age control, which in recent deposits may prove more feasible via radiocarbon (^{14}C) dating (cf. Faraji et al., 2023; Murgulet, 2010), in favour of the $^{230}Th/U$ method (cf. challenges with Anapala Cave samples).

5.5 Conclusions and outlook

Intermittent field observations from the two Niuean caves of Anapala and Ulupaka confirmed a pronounced sensitivity to external climate in terms of atmospheric conditions, flow rates,

and dripwater chemistry. In Anapala Cave, dripwater Mg appeared strongly related to marine aerosol inputs based on a Mg and Na mixing line, which was not observed in the more inland located Ulupaka Cave. Anapala Cave dripwater alkaline earth metal concentrations were further characterised by a mixed limestone-dolomite bedrock composition compared to the primarily limestone-derived values in Ulupaka Cave. First-row transition metals were interpreted to derive from soil at both locations. Although dripwater Mg and Sr systematics were in line with predicted prior calcite precipitation trends, the marine contribution seemingly complicated their relationship in speleothems from Anapala Cave. Sample ANA-19-9 showed prominent covariance between Mg and Na throughout most of the record, while Mg-Sr correlations were less consistent. These patterns generally precluded classical interpretations of Mg-Sr covariance as karst processes (*e.g.*, prior calcite precipitation and incongruent calcite dissolution), which were potentially overprinted by varying influence of marine aerosol contribution. Regardless, overall correspondence of positive Mg/Ca excursions with other trace elements and $\delta^{18}O$ and $\delta^{13}C$ values in dark dense calcite laminae principally suggested drier conditions, whereas opposite trends were evident for pale porous calcite laminae attributed to wetter conditions. Soil-derived first-row transition metals (Ni, Cu, Co, Zn) were overall positively related with Mg/Ca ratios, with a coupling of Ni and Mg, in particular, alluding to Ni responding inversely to dripwater supply. Importantly, these findings suggested that several first-row transition metals were potentially driven by rate-dependent organic metal complex (OMC) decay, and only sporadically by direct capture in response to 'flushing' events. In principle, the two stalagmites from Anapala Cave thus showed promise for developing valuable new records of South Pacific hydroclimate, but require further deconvolution of environmental controls on proxy signals. Furthermore, both stalagmites exhibited problematic age-depth relationships based on $^{230}Th/U$ dating, precluding confident absolute chronologies. Provided that age control can be significantly improved by a re-assessment of radiometric dates and further lamina counting, it is planned to complement existing proxy datasets with, for instance, higher-resolution stable isotope analyses, detailed fabric analysis via microstratigraphic logging (Frisia, 2015), and confocal fluorescence microscopy to reveal the spatial distribution of organic inclusions (*e.g.*, Baker et al., 2008; Sliwinski & Stoll, 2021). Speleothem-based interpretations are aimed to be further refined by additional cave monitoring, including weekly-resolved automated water sampling.

It is also noted that Anapala Cave potentially presents an opportunity to test the hypothesis outlined in Chapter 4, proposing a spectrum of controls affecting transition metal inclusion in stalagmites as a function of flow characteristics and organic matter evolution. The upper and lower chambers of Anapala Cave showed distinct properties with respect to aqueous chemistry and responsivity to surface processes, while deeper parts of the cave host further formations for comparison to existing material from the cave. Finally, speleothems from Ulupaka Cave are potentially amenable to high-resolution reconstructions of Common Era and Holocene hydroclimate. Stalagmites from monitored drip points are thus aimed to be analysed for inter-cave comparison with Anapala Cave samples, and ultimately the development of a first complete high-resolution Niuean record of Holocene climate history.

Supplementary information

Photometric cave mapping

Three-dimensional images of Anapala Cave and Ulupaka Cave were created by means of Structure-from-Motion (SfM; Figure 5.S1 and Figure 5.S2). These images serve as examples of an ongoing effort to completely map all accessible parts of Anapala Cave and Chasm, and a significant part of Ulupaka Cave. Images have also been collected in Avaiki Cave and Palaha Cave. The final models are eventually intended to be used for outreach and educational purposes, while also providing unique perspectives on the structural properties of each cave.

The SfM approach is based on the collection of a large number of digital images from various perspectives of the object or space of interest, which are subsequently analysed for common pixels, stitched, and textured in dedicated software suites. Here, an Olympus OM-D E-M5 Mark 3 mirrorless digital camera (Olympus, Japan) with an Olympus M.Zuiko Digital ED 8mm f/1.8 Fisheye PRO lens was augmented with a Ledgo LG-R332 (Ledgo Technology Limited, China) ring light to provide consistent lighting. Photogrammetric processing of images was performed using Agisoft Metashape (v.1.8.4; Agisoft LLC, Russia). Initially, photos of different imaging batches (*i.e.*, different parts of a cave and/or collections from multiple imaging sessions) were spatially aligned to facilitate pixel recognition. Based on these images, preliminary low-resolution dense point clouds were created to verify the correct identification of structures, before the remaining images were added for a high-resolution render. Mesh-building based on the dense point clouds yields a coherent three-dimensional surface model, which is manually refined by removing artefacts and visually affirming appropriate connection of points. The model is finally completed by overlaying photographic textures generated and stitched from input images.

Supplementary figures and tables

Figure 5.S1: Example structure-from-motion render of Anapala Cave. Photometric images of the upper (left) and lower (right) chambers of Anapala Cave. Included in the render is a Syp fluid autosampler unit (https://www.waikatoscientific.com/syp) and other monitoring equipment. These images are preliminary outcomes from photometric mapping of the entire cave, eventually aimed for outreach and educational purposes. The methodology is briefly outlined in Section 5.5. Image courtesy of Jeffrey Lang.

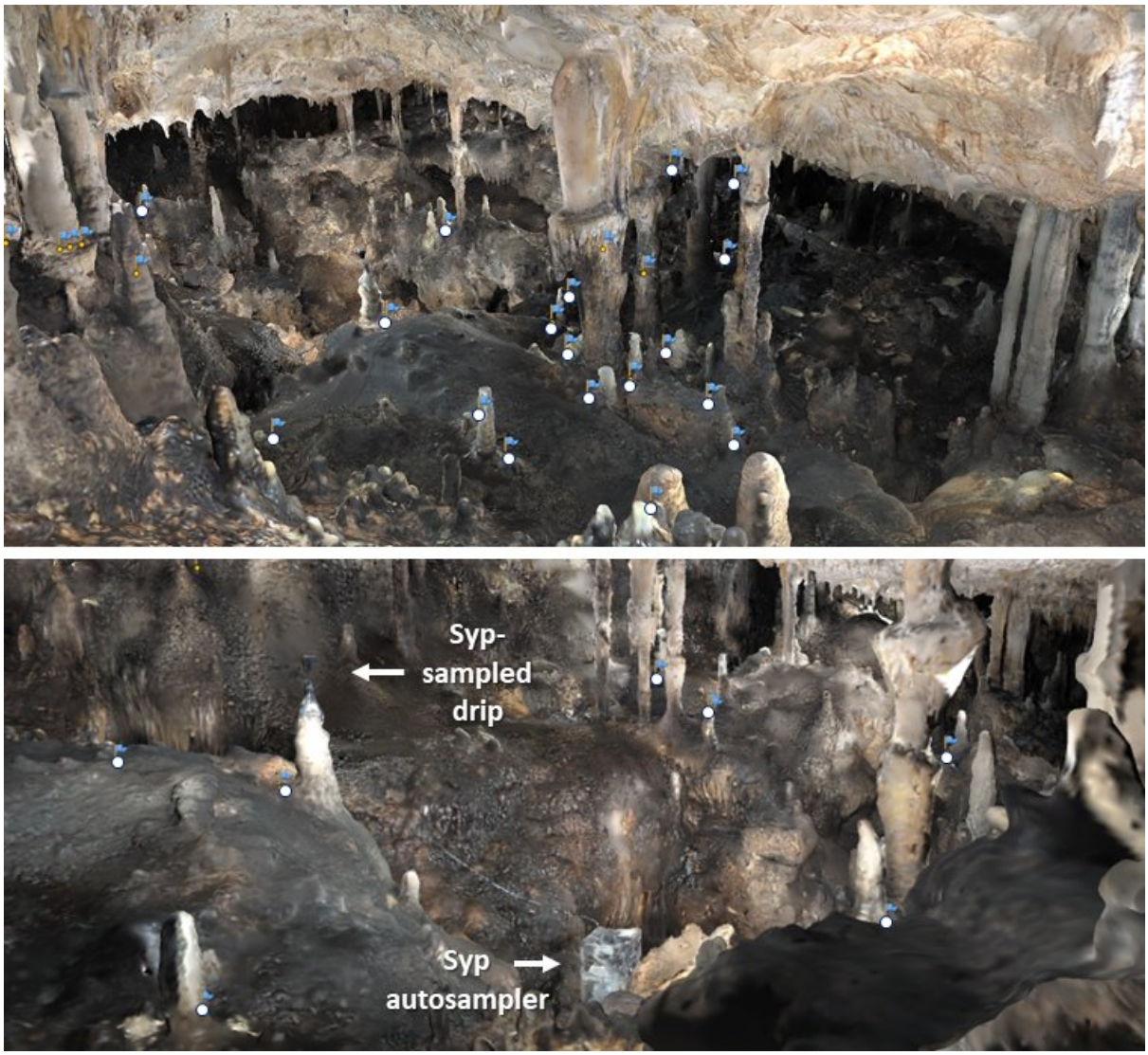

Figure 5.S2: Example three-dimensional structure-from-motion render of Ulupaka Cave. Photometric images of the study chamber in Ulupaka Cave. White dots and blue flags indicate locations of sampled/monitored drip points. Also included in the render is a Syp fluid autosampler unit (https://www.waikatoscientific.com/syp). These images are preliminary outcomes from photometric mapping of the entire cave, eventually aimed for outreach and educational purposes. The methodology is briefly outlined in Section 5.5. Image courtesy of Jeffrey Lang.

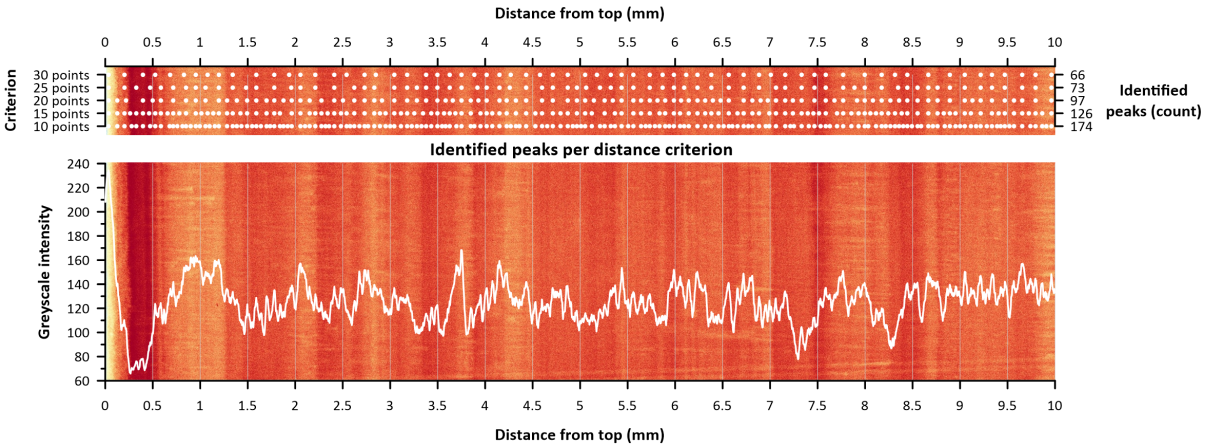

Figure 5.S3: Example of lamina counting via semi-automated peak identification. Intensity peaks in 2 µm resolution synchrotron radiation micro-x-ray fluorescence (SR-µXRF) maps of the central regions of stalagmite samples ANA-19-1 and ANA-19-9 were identified using the *find_peaks* Python function (SciPy; Virtanen et al., 2020) applied to a 100 µm sliding window. The distance criterion was adjusted to obtain the best agreement with visually identified laminae (see top panel for results using different minimum distances between neighbouring peaks). Shown are the top 10 mm of stalagmite ANA-19-1.

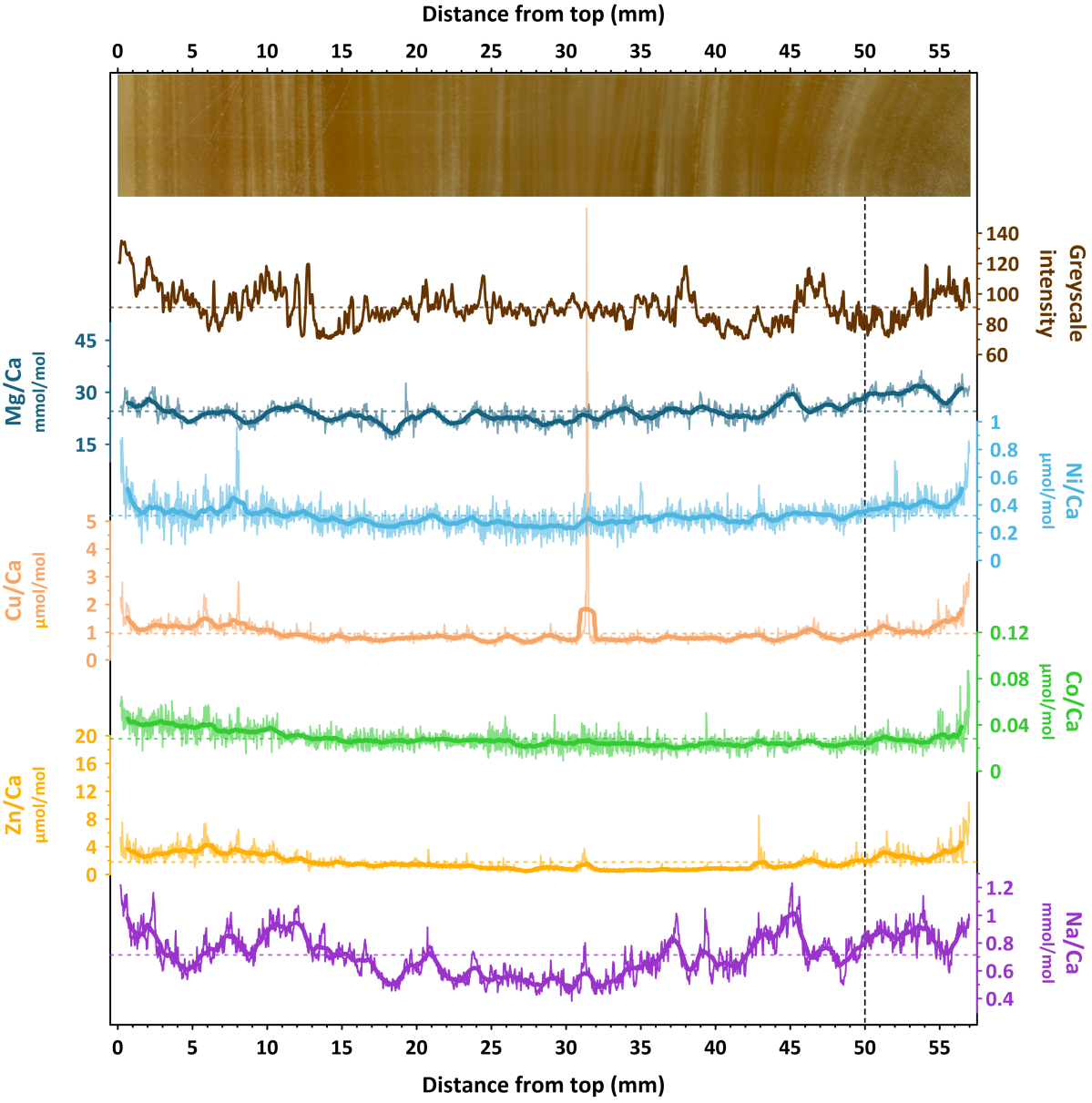

Figure 5.S4: Trace elemental proxy series in stalagmite ANA-19-1. The scanned image shows the central region of the stalagmite section used for sub-sampling (parallel to growth laminae). Greyscale intensity values were extracted from the scanned image. Note that the alignment of proxy data with the scanned image worsens where lateral heterogeneity in laminae increases. Thin and thick solid lines of element:Ca ratios represent the original resolution (25 µm) and a running average across a 1 mm window, respectively. Horizontal dashed lines in each plot reflect the total average value. The vertical dashed line marks a suspected hiatus.

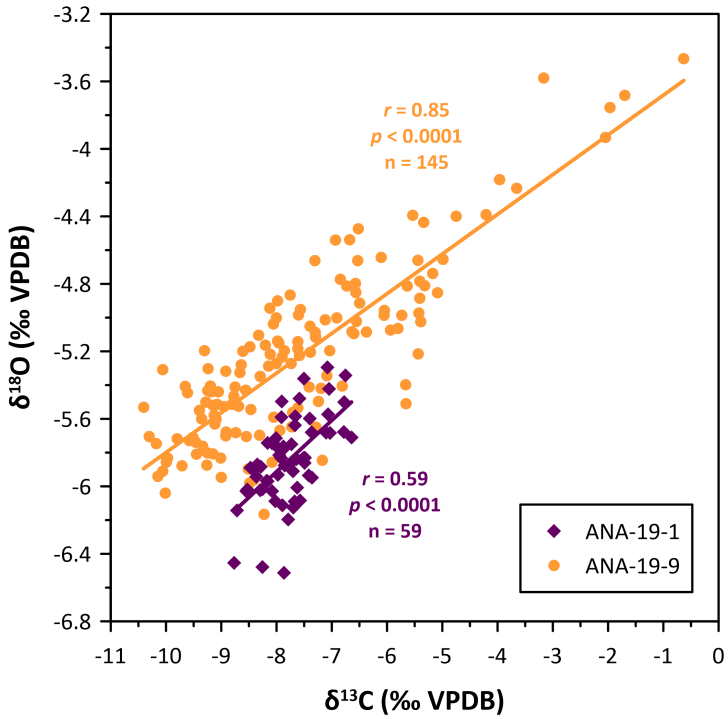

Figure 5.S5: Correlation between stable oxygen and carbon isotope ratios in stalagmite samples ANA-19-1 and ANA-19-9. Coloured solid lines represent respective linear regressions. Measurements were performed at a spatial resolution of 1 mm in both stalagmites.

Table 5.S1: Summary of *in-situ* dripwater measurements in Anapala Cave between September 2019 and November 2022. Data are the averages and 1 SD of repeat (typically at least triplicate) spot measurements during cave visits, reported in chronological order. EC denotes electrical conductivity. See also Supplementary Table 5.S2 and Table 5.S3 for data from other Niuean caves.

Cave	Location	Site ID	Date	pH		EC (µS cm^{-1})		Temperature (°C)		Drip rate (drips min^{-1})
			GMT -11 (Niue)	Average	1 SD	Average	1 SD	Average	1 SD	Average
Anapala Cave	Lower chamber	ANA-LC-1	15/02/2020	8.17	0.01	1514.0	3.6	24.8	0.1	1.0
	Lower chamber	ANA-LC-2	15/02/2020	8.15	0.06	1350.0	0.0	25.0	0.2	2.3
	Lower chamber	ANA-LC-3	15/02/2020	8.22	0.04	1482.0	21.5	24.7	0.1	1.0
	Lower chamber	ANA-LC-4	15/02/2020	8.18	0.05	1215.3	11.0	25.8	0.2	4.3
	Lower chamber	ANA-LC-5	15/02/2020	8.16	0.02	1634.3	2.3	26.0	0.3	2.0
	Lower chamber	ANA-LC-6	15/02/2020	8.25	0.05	1240.3	2.1	26.0	0.2	46.3
	Upper chamber	ANA-UC-1	15/02/2020							0.0
	Upper chamber	ANA-UC-3	15/02/2020	8.13	0.03	857.7	6.1	26.0	0.1	4.7
	Upper chamber	ANA-UC-4	15/02/2020	7.88	0.16	916.5	16.3	26.1	0.1	2.3
	Upper chamber	ANA-UC-6	15/02/2020	8.12	0.02	850.0	2.6	25.9	0.1	2.0
	Lower chamber	ANA-LC-2	18/02/2020							2.0
	Lower chamber	ANA-LC-5	18/02/2020	8.12	0.10	1700.5	49.8	25.5	0.1	
	Upper chamber	ANA-UC-3	18/02/2020	8.31	0.05	812.3	37.5	26.0	0.1	2.3
	Upper chamber	ANA-UC-4	18/02/2020	7.92	0.12	954.7	3.5	26.0	0.2	0.7
	Upper chamber	ANA-UC-6	18/02/2020	8.12	0.05	854.0	6.0	25.8	0.1	1.0
	Upper chamber	ANA-UC-5	20/02/2020	8.31	0.01	849.7	9.7	26.4	0.2	0.6
	Upper chamber	ANA-UC-7	20/02/2020	8.41	0.02	760.0	9.6	27.1	0.3	0.1
	Lower chamber	ANA-LC-1	22/02/2020							0.5
	Lower chamber	ANA-LC-5	22/02/2020	8.29	0.03	1666.3	4.2	25.9	0.2	1.9
	Lower chamber	ANA-LC-6	22/02/2020	8.39	0.02	1312.0	1.7	25.6	0.2	25.0
	Upper chamber	ANA-UC-3	22/02/2020	8.21	0.01	855.5	11.9	26.7	0.2	
	Upper chamber	ANA-UC-5	22/02/2020	8.53	0.01	844.7	9.5	26.1	0.1	0.3
	Upper chamber	ANA-UC-6	22/02/2020	8.23	0.00	863.7	2.1	26.5	0.2	0.7
	Upper chamber	ANA-UC-7	22/02/2020	8.27	0.01	719.7	3.2	27.5	0.1	
	Upper chamber	ANA-UC-8	22/02/2020	8.48	0.01	849.3	6.4	28.0	0.2	2.2
	Upper chamber	ANA-UC-9	22/02/2020	8.19	0.05	724.3	9.7	26.5	0.1	1.3
	Lower chamber	ANA-LC-4	05/11/2022	8.12	0.04	772.7	1.2	25.2	0.4	2.1
	Lower chamber	ANA-LC-5	05/11/2022	8.15	0.02	1198.7	4.5	25.0	0.2	1.2
	Lower chamber	ANA-LC-6	05/11/2022	8.26	0.03	955.0	1.7	24.6	0.1	11.3
	Lower chamber	ANA-LC-7	05/11/2022							
	Lower chamber	ANA-LC-8	05/11/2022	7.90	0.10	702.7	0.6	25.0	0.1	1.4
	Lower chamber	ANA-LC-9	05/11/2022	8.09	0.03	778.0	0.0	25.1	0.2	0.7
	Upper chamber	ANA-UC-10	07/11/2022	8.21	0.03	699.7	0.6	25.1	0.2	0.0
	Upper chamber	ANA-UC-11	07/11/2022	8.35	0.01	554.0	1.0	26.0	0.2	0.3
	Upper chamber	ANA-UC-12	07/11/2022	8.44	0.03	612.3	2.5	25.1	0.1	1.1
	Upper chamber	ANA-UC-13	07/11/2022	8.44	0.04	514.3	0.6	25.3	0.2	0.0
	Upper chamber	ANA-UC-16	07/11/2022	8.54	0.06	586.0	1.7	25.0	0.1	0.2
	Upper chamber	ANA-UC-18	07/11/2022	8.40	0.03	739.0	1.7	25.5	0.1	0.2
	Upper chamber	ANA-UC-19	07/11/2022	8.47	0.03	628.0	1.0	25.5	0.1	0.1
	Upper chamber	ANA-UC-20	07/11/2022	8.54	0.03	556.3	0.6	24.9	0.1	0.1
	Upper chamber	ANA-UC-21	07/11/2022	8.29	0.01	711.7	2.3	25.8	0.1	0.6
	Upper chamber	ANA-UC-22	07/11/2022	8.40	0.02	570.0	1.0	25.5	0.2	0.3
	Upper chamber	ANA-UC-23	07/11/2022	8.37	0.02	607.3	1.2	25.7	0.2	0.1
	Upper chamber	ANA-UC-24	07/11/2022	8.49	0.04	677.7	1.5	25.4	0.2	0.0
	Upper chamber	ANA-UC-3	07/11/2022	8.49	0.01	709.7	1.2	24.8	0.1	0.3
	Upper chamber	ANA-UC-6	07/11/2022	8.53	0.01	664.3	1.5	25.0	0.1	0.4
	Upper chamber	ANA-UC-9	07/11/2022	8.35	0.03	601.3	0.6	25.1	0.0	0.0
	Lower chamber	ANA-LC-12	10/11/2022	8.33	0.01	675.7	2.5	24.9	0.2	1.7
	Lower chamber	ANA-LC-13	10/11/2022	8.28	0.02	674.3	8.6	25.4	0.2	0.5
	Lower chamber	ANA-LC-14	10/11/2022	8.45	0.02	841.3	0.6	24.5	0.1	0.6
	Lower chamber	ANA-LC-18	10/11/2022	8.22	0.04	738.0	3.0	25.5	0.6	0.4
	Lower chamber	ANA-LC-1	13/11/2022	8.27	0.03	1262.7	3.1	24.9	0.2	0.1
	Lower chamber	ANA-LC-10	13/11/2022	8.24	0.05	743.7	2.9	25.0	0.2	0.4
	Lower chamber	ANA-LC-11	13/11/2022	8.30	0.01	899.3	2.5	25.0	0.2	0.7
	Lower chamber	ANA-LC-15	13/11/2022	8.36	0.03	962.7	1.5	25.3	0.2	0.6
	Lower chamber	ANA-LC-16	13/11/2022	8.37	0.05	549.7	0.6	25.7	0.2	0.2
	Lower chamber	ANA-LC-17	13/11/2022	8.36	0.02	765.3	1.2	24.8	0.3	0.8
	Lower chamber	ANA-LC-19	13/11/2022	8.04	0.01	776.3	1.2	26.3	0.4	0.1
	Lower chamber	ANA-LC-2	13/11/2022	8.26	0.02	1246.3	0.6	25.7	0.1	
	Upper chamber	ANA-UC-2	13/11/2022	8.24	0.03	689.3	3.2	25.5	0.1	
	Upper chamber	ANA-UC-8	21/11/2022	7.94	0.03			25.9	0.3	0.3
Anapala Chasm	Anapala Chasm	ANA-Chasm	15/02/2020	8.19	0.04	921.7	3.8	26.3	0.1	
	Anapala Chasm	ANA-Chasm	22/02/2020	8.23	0.02	995.7	6.4	26.8	0.3	
	Anapala Chasm	ANA-Chasm	07/11/2022	7.83	0.02	862.3	0.6	24.0	0.1	

Table 5.S2: Summary of *in-situ* dripwater measurements in Ulupaka Cave between September 2019 and November 2022. Data are the averages and 1 SD of repeat (typically at least triplicate) spot measurements during cave visits, reported in chronological order. EC denotes electrical conductivity. See also Supplementary Table 5.S1 and Table 5.S3 for data from other Niuean caves.

Cave	Location	Site ID	Date	pH		EC (µS cm^{-1})		Temperature (°C)		Drip rate (drips min^{-1})
			GMT -11 (Niue)	Average	1 SD	Average	1 SD	Average	1 SD	Average
Ulupaka Cave	Study chamber	ULU-E	25/09/2019	8.13	0.01	403.7	26.0	24.6		
		ULU-1	26/09/2019	8.62	0.01	1343.0				1.2
		ULU-3	26/09/2019	8.32		231.0				5.7
		ULU-4	26/09/2019	8.56		567.0	4.2	24.2		3.0
		ULU-5	26/09/2019							1.8
		ULU-7	26/09/2019	8.36	0.02	493.0		24.7		8.0
		ULU-8	26/09/2019							0.9
		ULU-A	26/09/2019							
		ULU-B	26/09/2019	8.51		910.0				3.9
		ULU-C	26/09/2019							2.2
		ULU-D	26/09/2019							1.8
		ULU-Pool-A	26/09/2019							
		ULU-Pool-B	26/09/2019							
		ULU-1	21/02/2020	8.47	0.03	488.8	1.6	26.5	0.1	1.0
		ULU-10	21/02/2020	8.08	0.09	568.0	1.7	24.9	0.2	1.0
		ULU-11	21/02/2020	8.01	0.07	591.0	1.7	25.5	0.4	1.0
		ULU-12	21/02/2020							
		ULU-2	21/02/2020	8.38	0.01	499.0	1.7	26.1	0.2	1.0
		ULU-3	21/02/2020	8.35	0.01	532.3	4.3	26.1	0.6	4.0
		ULU-4	21/02/2020	8.41	0.04	562.8	4.5	25.7	0.3	1.0
		ULU-5	21/02/2020	8.38	0.04	526.0	6.2	25.2	0.1	1.0
		ULU-6	21/02/2020							
		ULU-7	21/02/2020	8.29	0.06	511.5	20.8	26.1	0.5	13.0
		ULU-8	21/02/2020	8.41	0.02	487.7	2.1	25.4	0.1	1.0
		ULU-9	21/02/2020	8.37	0.01	547.3	0.6	26.0	0.0	4.7
		ULU-1	23/02/2020	8.53	0.01	469.3	1.5	26.4	0.1	1.9
		ULU-10	23/02/2020	7.95	0.05	563.3	0.6	25.9	0.1	2.5
		ULU-11	23/02/2020	8.18	0.03	591.0	4.0	25.7	0.3	0.9
		ULU-12	23/02/2020							0.1
		ULU-2	23/02/2020	8.44	0.02	498.0	6.1	26.3	0.3	0.9
		ULU-3	23/02/2020	8.33	0.06	506.0	0.0	26.2	0.2	4.0
		ULU-4	23/02/2020	8.38	0.03	545.0	3.5	27.0	0.1	1.5
		ULU-5	23/02/2020	8.33	0.05					1.7
		ULU-7	23/02/2020	8.19	0.01	495.0	1.0	25.6	0.1	14.0
		ULU-8	23/02/2020							1.0
		ULU-9	23/02/2020	8.27	0.01	543.7	1.5	25.3	0.1	2.4
		ULU-pool-1	23/02/2020	8.39	0.01	489.7	0.6			
		ULU-pool-2	23/02/2020	8.53	0.02	364.0	3.5			
		ULU-pool-3	23/02/2020	8.46	0.03	437.7	2.9			
		ULU-1	14/09/2022							0.2
		ULU-10	14/09/2022							1.9
		ULU-11	14/09/2022							0.3
		ULU-12	14/09/2022							0.1
		ULU-2	14/09/2022							0.3
		ULU-3	14/09/2022							2.6
		ULU-4	14/09/2022							0.6
		ULU-7	14/09/2022							0.1
		ULU-8	14/09/2022							0.4
		ULU-9	14/09/2022							1.9
		ULU-1	06/11/2022	8.41	0.02	317.3	1.5	25.1	0.1	0.0
		ULU-10	06/11/2022	8.17	0.02	560.0	1.0	24.8	0.1	1.9
		ULU-11	06/11/2022	8.30	0.03	559.7	0.6	25.0	0.3	0.5
		ULU-12	06/11/2022	8.23	0.04	306.3	1.5	26.0	0.6	0.0
		ULU-13	06/11/2022	8.44	0.02	423.7	3.2	25.7	0.2	0.3
		ULU-14	06/11/2022	8.10	0.00	513.0	1.0	24.7	0.2	3.3
		ULU-15	06/11/2022	8.14	0.02	515.0	0.0	24.9	0.2	1.7
		ULU-16	06/11/2022	8.44	0.03	404.3	2.1	24.9	0.2	0.8
		ULU-17	06/11/2022	8.40	0.02	512.3	0.6	24.9	0.2	0.8
		ULU-18	06/11/2022	8.25	0.02	472.7	1.5	26.5	0.2	0.1
		ULU-19	06/11/2022	8.49	0.03	442.0	1.0	24.7	0.1	1.8
		ULU-2	06/11/2022	8.40	0.01	397.3	1.2	25.0	0.1	0.1
		ULU-20	06/11/2022	8.46	0.01	463.7	4.6	25.8	0.2	0.2
		ULU-21	06/11/2022	8.29	0.02	422.7	0.6	25.0	0.1	0.3
		ULU-22	06/11/2022	8.45	0.00	320.3	2.5	24.6	0.1	0.2
		ULU-23	06/11/2022	8.22	0.03	525.7	0.6	24.6	0.2	3.2
		ULU-3	06/11/2022	8.22	0.03	483.7	0.6	25.0	0.2	2.0
		ULU-4	06/11/2022	7.85	0.23	534.0	2.6	25.2	0.2	1.0

Table 5.S3: Summary of *in-situ* dripwater measurements in Niuean caves between September 2019 and November 2022. Data are the averages and 1 SD of repeat (typically at least triplicate) spot measurements during cave visits. The data are firstly sorted by cave location, and then in chronological order. EC denotes electrical conductivity. See also Supplementary Table 5.S1 and Table 5.S2 for data from other Niuean caves.

Cave	Location	Site ID	Date	pH		EC (µS cm^{-1})		Temperature (°C)		Drip rate (drips min^{-1})
			GMT -11 (Niue)	Average	1 SD	Average	1 SD	Average	1 SD	Average
Ulupaka Cave	Study chamber	ULU-7	06/11/2022	8.29	0.02	425.0	1.0	25.0	0.1	0.1
		ULU-8	06/11/2022	8.39	0.01	317.0	0.0	26.2	0.3	0.1
		ULU-9	06/11/2022	8.28	0.01	507.0	0.0	24.8	0.1	1.2
		ULU-Pool-1	06/11/2022	8.04	0.06	341.0	1.0	24.1	0.1	
		ULU-24	22/11/2022							0.2
		ULU-25	22/11/2022							1.7
		ULU-26	22/11/2022							0.5
		ULU-27	22/11/2022							0.1
		ULU-29	22/11/2022							1.4
Avaiki Cave	Upper gallery (climb up)	AV-2	18/02/2020	8.11	0.03	1579.0	4.5	26.1	0.2	1.4
	Upper gallery (climb up)	AV-3	19/02/2020	7.97	0.04	4036.7	20.8	27.3	0.1	0.5
	Upper gallery (climb up)	AV-3-Pool	19/02/2020	8.38	0.03	27175.0	221.7	26.7	0.4	
	King's Pool	AV-1-Drip	08/11/2022	8.08	0.03	774.7	5.5	24.3	0.1	
	Upper gallery (climb up)	AV-2-Drip	08/11/2022	8.38	0.02	892.0	2.6	25.1	0.1	12.0
	Upper gallery (climb up)	AV-2-Pool	08/11/2022	8.90	0.00	422666.7	577.4	24.4	0.2	
	Upper gallery (climb up)	AV-3-Drip	08/11/2022	7.70	0.01	979.3	4.2	26.5	0.2	60.0
	Upper gallery (climb up)	AV-4-Drip	08/11/2022	8.22	0.01	734.0	1.0	25.4	0.1	8.7
	King's Pool	AV-5-Drip	08/11/2022	8.25	0.00	995.7	1.2	23.8	0.2	3.2
Palaha Cave	Back gallery	PAL-3	18/02/2020	7.87	0.03	1431.3	3.8	26.5	0.1	5.0
		PAL-3-Pool	18/02/2020	8.36	0.01	46300.0	173.2	28.1	0.1	
		PAL-4	18/02/2020	7.89	0.01	1650.3	3.1	26.5	0.2	6.7
		PAL-4-Pool	18/02/2020	8.09	0.01	51400.0	600.0	27.5	0.4	
		PAL-3	09/11/2022	7.78	0.03	1266.8	18.6	25.0	0.4	1.2
		PAL-3-Pool	09/11/2022							
		PAL-4	09/11/2022	7.47	0.04	1325.3	2.3			5.6
		PAL-4-Pool	09/11/2022							
		PAL-5	09/11/2022	7.84	0.01	986.7	9.0			4.3
		PAL-Pool-large	09/11/2022	8.72	0.02	1789333.3	1154.7	24.2	0.1	

Table 5.S4: Summary of elemental concentrations (normalised to Ca) in Niuean soils. Each sample as shown in the table reflects several sub-samples of soil collected from the site. Data shown are based on analyses of the respective homogenised bulk sample. AA in sample IDs refers to an extraction via 1 M ammonium acetate, whereas DI denotes a leaching with deionised water. Given the inconsistencies across samples, soil ratios shown in Figure 5.5 and Figure 5.6 are based on linear regressions of all DI extracts (selected because of stronger covariance than AA extracts).

ID	Location	Na/Ca	Mg/Ca	Al/Ca	K/Ca	P/Ca	S/Ca	Mn/Ca	Fe/Ca	Co/Ca	Ni/Ca	Cu/Ca	Zn/Ca	Sr/Ca	Ba/Ca	U/Ca
		mmol mol^{-1}	mmol mol^{-1}	µmol mol^{-1}	mmol mol^{-1}	mmol mol^{-1}	mmol mol^{-1}	µmol mol^{-1}	µmol mol^{-1}	µmol mol^{-1}	µmol mol^{-1}	µmol mol^{-1}	µmol mol^{-1}	mmol mol^{-1}	µmol mol^{-1}	µmol mol^{-1}
AA-1	Anapala Cave	76.5	510.6	32.9	32.7	11.2	31.0	235.1	3.1	1.4	0.7	6.9	2.9	5.8	2.5	0.05
AA-2	Anapala Cave 2	274.1	802.5	0.0	63.6	78.4	58.6	1489.0	0.0	0.6	1.0	2.8	99.1	4.5	8.7	0.03
AA-3	Inland road	36.8	480.0	1020.2	43.9	7.7	29.6	10361.8	297.9	7.6	6.9	30.7	14.5	1.0	10.1	2.54
AA-4	Avaiki Cave	11.2	209.2	352.5	37.6	8.4	19.0	1402.3	74.4	2.5	1.8	18.0	21.1	3.4	24.6	0.63
AA-5	Togo Chasm	86.6	459.3	24.0	71.7	35.0	50.4	2665.1	0.0	0.6	0.7	5.9	1.2	1.1	3.2	0.04
AA-6	Tagalahi Sea Track	348.3	1418.4	443.0	108.7	56.3	83.1	1868.6	245.1	3.3	5.0	42.1	477.8	6.8	191.4	0.64
AA-7	Avatale – Alofi Road	540.3	1169.9	161.9	164.0	49.2	122.7	8253.2	25.0	4.9	1.9	9.0	45.5	4.9	28.9	0.09
AA-8	Ulupaka Cave	68.7	299.7	685.5	66.9	2.4	30.9	2403.4	249.8	8.3	7.3	28.3	9.3	1.4	14.5	1.34
AA-9	Palaha Cave	149.6	714.7	464.5	64.8	27.3	108.4	1542.2	251.6	6.2	3.0	41.7	52.6	6.1	14.8	0.44
AA-10	Limu Pools	22.9	252.2	314.3	37.7	7.9	30.0	3425.9	89.5	4.8	2.4	14.9	6.3	5.7	14.6	0.37
DIL-1	Anapala Cave	373.8	837.4	124.3	129.0	15.5	146.9	246.0	0.0	6.3	3.7	41.1	0.0	6.5	2.7	0.39
DIL-2	Anapala Cave 2	1254.1	1249.3	435.2	213.6	374.7	298.1	1570.2	408.2	21.0	23.9	35.4	226.4	4.7	15.9	4.63
DIL-3	Inland road	130.1	811.5	2121.2	179.7	28.7	194.0	6842.5	324.9	19.8	26.1	117.8	53.4	1.1	5.3	1.62
DIL-4	Avaiki Cave	52.2	366.3	613.8	149.7	12.8	84.4	707.9	0.0	6.6	6.3	48.2	8.2	3.5	13.3	1.42
DIL-5	Togo Chasm	232.1	694.0	147.9	170.7	80.6	145.2	2237.2	0.0	1.3	1.6	12.8	0.0	1.2	2.5	0.12
DIL-6	Tagalahi Sea Track	1436.3	2379.5	1015.1	383.1	90.7	410.6	997.6	347.5	8.3	9.8	121.9	370.3	7.3	135.9	1.48
DIL-7	Avatale – Alofi Road	1856.3	1779.8	389.4	487.1	128.4	483.2	6100.0	0.0	10.8	5.8	27.6	28.5	5.3	17.9	0.29
DIL-8	Ulupaka Cave	232.3	363.7	710.6	280.1	5.1	117.5	872.8	0.0	10.5	7.5	50.9	99.9	1.0	6.3	0.64
DIL-9	Palaha Cave	344.3	722.9	896.4	107.0	16.4	176.2	947.0	2351.8	153.1	149.7	197.4	175.1	4.9	64.6	36.60
DIL-10	Limu Pools	107.5	448.5	448.7	148.9	12.2	139.4	2006.8	35.4	12.7	8.9	40.8	4.7	6.1	7.8	0.79

Table 5.S5: Summary of elemental concentrations (normalised to Ca) in Niuean bedrock samples. Each sample as shown in the table reflects several sub-samples of host rock (freshly exposed surfaces) collected from the site. Data shown are based on analyses of the respective homogenised bulk sample. Representative samples collected at Anapala Cave (average of two sample sets from two field campaigns) and Ulupaka Cave served to constrain bedrock ratios as shown in Figure 5.6. Also shown are the ratios of Mg/Sr and Mg/Na (dimensionless).

Sample	Na/Ca	Mg/Ca	P/Ca	Sr/Ca	Ba/Ca	U/Ca	Mg/Sr	Mg/Na	Comment
	mmol mol^{-1}	mmol mol^{-1}	mmol mol^{-1}	mmol mol^{-1}	µmol mol^{-1}	µmol mol^{-1}			
Anapala Cave	43.0	113.8	38.1	0.8	12.4	5.7	145.8	2.6	used in PCP vector calculations in Figure 5.7A
Anapala Cave 2	15.8	25.1	2.9	8.3	3.9	1.4	3.0	1.6	used in PCP vector calculations in Figure 5.7A
Ulupaka Cave	8.5	31.0	4.6	0.5	1.9	0.4	58.1	3.7	used in PCP vector calculations in Figure 5.7A
Palaha Cave	26.5	17.6	5.9	10.7	8.5	1.5	1.6	0.7	
Limu Pools	27.6	20.6	1.9	4.6	4.6	0.9	4.5	0.7	
Niue quarry	23.9	37.9	0.8	10.2	11.3	1.8	3.7	1.6	
Avaiki Cave	22.4	18.2	4.0	8.5	7.6	1.9	2.1	0.8	
Inland road	23.9	837.5	39.9	0.9	4.1	6.8	914.5	35.1	
Avatale-Alofi Road	10.5	35.9	3.7	0.9	2.3	1.2	40.5	3.4	
Tangalaki Sea track	38.2	11.1	1.9	12.9	15.7	3.5	0.9	0.3	
Togo Chasm	7.4	35.8	4.2	0.4	2.0	0.7	85.0	4.8	
Togo Chasm 2	35.7	26.0	3.4	13.2	14.7	2.1	2.0	0.7	
Average	23.6	100.9	9.3	6.0	7.4	2.3	105.1	4.7	
1 SD	11.6	233.5	14.0	5.2	5.0	2.0	258.9	9.7	

Chapter 6

Summary and conclusions

With view to advancing the establishment of a novel (semi-)quantitative proxy for cave flow rates, and hydroclimate by extension, this thesis aimed to contribute new fundamental information on the underlying processes governing the transport, lability, and inclusion of selected 'kinetic' first-row transition metals into stalagmites. Specifically, this work addressed a lack of systematic understanding of the equilibrium interactions between different trace metals with organic ligands ubiquitous to natural waters, and their implications for speleothem metal concentrations and environmental information encoded in these.

To this effect, the thesis applied a 'bottom-up' approach, assessing firstly the processes determining metal behaviour in presence of natural organic matter in dripwater (Chapter 3), followed by a study investigating metal inclusion pathways at the dripwater-calcite interface as a function of organic complexation (Chapter 4). Finally, the potential of stalagmite metal contents to inform past hydrological conditions in light of findings from Chapter 3 and Chapter 4 was investigated by example of a case study of two South Pacific cave systems (Chapter 5).

6.1 Chapter-wise major findings and significance

6.1.1 Chapter 3 – The perpetual control of organic complexation on first-row transition metals

This chapter sought to provide first systematic quantitative estimates of the decay rate constants (k_d) of different organic metal complexes (OMCs) in natural caves based on water and soil solutions collected from a range of Aotearoa New Zealand cave environments. By means of competitive ligand exchange (CLE) experiments using Chelex-100 as the competing ligand, this study firstly demonstrated the pertinent susceptibility of first-row transition metals (by example of Co, Ni, Cu) to organic complexation, and the effective lack thereof of alkaline earth metals (here: Mg, Sr). Across the eight different cave water samples, kinetic modelling of OMC

decay suggested a hierarchy of complex stability of Cu $\approx$ Co $>$ Ni, with k_d estimates in the order of 8.5×10^{-4} to 6.9×10^{-3} s^{-1} (Cu), 4.4×10^{-5} to 1.7×10^{-2} s^{-1} (Co), and 9.2×10^{-2} to 1.0×10^{-1} s^{-1} (Ni). For all three transition metals, a considerable 'inert' fraction of 15.8% to 46.2% remained complexed after 2 hours. The observed variability amongst water samples was not explained by DOC content or quality but was distinct compared to the far more consistent and overall stronger complexation regimes depicted in experiments on three soil extracts with substantially higher native organic content. A caveat of this study was that the planned description of kinetic parameters according to the continuous log-normal model of Rate et al. (1992) was not reliably achieved, and thus requires re-assessment to more adequately account for the heterogeneous composition of ligand binding sites. Regardless, a simple forward modelling exercise served to demonstrate that, using empirical k_d estimates derived for Ni, OMC decay theoretically imposes a significant rate-dependent control on the availability of transition metals for inclusion into calcite. Importantly, this was predicted to be most sensitive for drip rates of $<$40 drips min^{-1} representative of typical baseline flows, with exponentially increasing sensitivity towards lower drip rate. These findings support the notion that OMC decay may be particularly significant in absence of high-flux 'flushing' inputs of OMCs, resulting in an increasingly enhanced ($\sim$exponential) inclusion of transition metals in the limit of ceasing discharge.

6.1.2 Chapter 4 – Testing for kinetic signals in cave-analogue and in-cave calcite precipitates

This chapter was aimed to test whether signals of kinetic OMC decay as evident in experiments of Chapter 3 were identifiable and sensitive to drip rate in experimentally and naturally precipitated calcite. Ten cave-analogue experiments were carried out to simulate stalagmite growth at variable drip rate and solution chemistries, adding the organic ligands Suwannee River Fulvic Acid (SRFA) and nitrilotriacetic acid (NTA) in varying concentrations. The findings suggested that organic complexation of Co, Ni, and Cu was pertinent and dependent on ligand quality and quantity, primarily modulating the inclusion of transition metals into calcite by increasing retention of metals in solution with increasing ligand concentration. SRFA, in particular, was found to co-precipitate considerably, implying that much of the observed metal inclusion was facilitated by direct capture of OMCs without prior dissociation. NTA experiments resulted in a strong reduction of partitioning at higher ligand concentrations due to overly strong complexation. Inorganic experiments yielded average $D_{Cu} \approx 13$, $D_{Co} \approx 1.8$, and $D_{Ni} \approx 0.4$, with the extreme affinity of Cu resulting in a pronounced positive linear relationship between Cu partitioning into calcite and drip rate under almost all organic complexation regimes. Cu inclusion was interpreted to thus reflect both the strong inorganic preference of Cu for the crystal phase, as well as considerable adsorption of Cu-SRFA complexes. Patterns of Ni and Co incorporation were overall less consistent, largely attributable to unfavourable complexation regimes achieved with the selected ligands. Concurrent analysis of inclusion behaviour of the alkaline earth metals Mg and Sr suggested little effect of organic complexation on their partitioning into calcite (overall $D_{Mg} \approx 0.04$, $D_{Sr} \approx 0.13$), although the data alluded to increasing organic impu-

rities in the precipitate potentially interfering with the accommodation of Mg and Sr cations in the calcite lattice. At large, however, the cave-analogue experiments did not demonstrate drip rate sensitive metal inclusion in response to OMC decay, which was likely due to a mismatch of calcite precipitation rate and the rate of kinetic metal release that would readily mask kinetic contributions of metals to the precipitate.

The second part of the chapter presented a synthesis of new and published metal partition coefficients to further highlight the contrasting controls and pathways determining the inclusion of first-row transition metals and alkaline earth metals in calcite. This study contributed a large dataset of in-cave partition coefficients derived from watch glass deployments ('calcite farming') and *in-situ* micro-sampling of active speleothems from a total of ten Aotearoa New Zealand and Niuean caves. The data compilation revealed an extensive range of Ni and Co partition coefficients from natural and experimental systems with organic complexation both significantly reducing and enhancing their inclusion. Cu partitioning was in turn consistently limited compared to its extreme inorganic affinity for the crystal phase. In contrast to transition metals, partitioning of alkaline earth metals into calcite was found to generally adhere to first-order thermodynamic and kinetic constraints, supporting the use of D_{Mg} and D_{Sr} estimates for palaeoclimate applications.

The findings of this chapter allowed for the conceptual differentiation of different inclusion pathways of trace metals into speleothems, distinguishing between (i) simple 'inorganic' cation substitution (*e.g.*, alkaline earth metals), (ii) direct capture of OMCs by adsorption and/or entrapment, and (iii) a two-step kinetic inclusion via OMC decay and subsequent $\sim$inorganic sorption. The relative importance of each pathway was suggested to vary across a continuum of system-specific conditions, with organic matter composition and maturity likely presenting the decisive variable. Importantly, both organic pathways present significant prospect for using speleothem transition metal concentrations as (semi-)quantitative hydrological recharge proxies.

6.1.3 Chapter 5 – Assessing trace element systematics in two South Pacific cave systems

The final research chapter presents a case study of trace element systematics in two modern cave environments on Niue island, as well as two Holocene stalagmite samples from one of the caves. This chapter aimed to apply insights from Chapter 3 and Chapter 4 to the interpretation of trace metal concentrations in stalagmites, as corroborated by intermittent cave monitoring conducted between September 2019 and November 2022. Field observations demonstrated a pronounced response of atmosphere and dripwaters in Anapala Cave and Ulupaka Cave to external weather conditions. In both caves, dripwater elemental contents largely reflected respective bedrock and soil compositions, while Anapala Cave was found to receive additional significant inputs from marine aerosols. The variable but overall dominant effect of the latter on Mg contents was reflected a strong covariance between Mg and Na in both dripwater and

carbonate, generally complicating the identification of controls of Mg/Ca ratios in the two Anapala Cave stalagmite records. As supported by other elemental proxies (*e.g.*, Sr/Ca, Ba/Ca), Mg/Ca ratios were considered to reflect a combination of source effects (depending on flow path and/or sea spray supply), prior calcite precipitation, and water-rock interactions (both dependent on bedrock saturation). These interpretations were further corroborated by the good correspondence of the suite of hydrologically-sensitive trace metals with alternating laminae of dark dense calcite (DDC; ∼drier growth conditions) and pale porous calcite (PPC; ∼wetter growth conditions), as well as low-resolution δ^{18}O and δ^{13}C measurements. Stable oxygen and carbon isotopes were likewise interpreted to ultimately reflect temporal variations in recharge and cave atmosphere, as supported by isotopic analysis of dripwater and rainwater.

Notably, stalagmite ANA-19-9 (9.51 to 5.84 ka BP) seemingly recorded trends in the abundance of Ni (and Cu, Co, Zn to a lesser extent) consistent with predominant kinetic controls, despite originating from the comparably shallow and responsive Anapala Cave. Ni/Ca ratios were almost exclusively positively correlated with Mg/Ca, and thus interpreted to similarly, but by other mechanisms, reflect recharge variations. Although not strictly expected based on the hypothesised system-specific controls conceptualised in Section 4.4.4 of Chapter 4, OMC decay may in fact typically be favoured in this cave over direct capture pathways (*i.e.*, via adsorption or entrapment) due to ligand quality and quantity derived from a limited soil profile (speculated), as well as low baseline drip rates as indicated by cave monitoring. Inclusion of transition metals via direct capture appeared only sporadically significant in response to substantial recharge events. Although challenged by the additional sea spray control on Mg/Ca and some other elements, the stalagmites generally show promise for valuable high-resolution palaeoenvironmental reconstructions. However, these require that robust absolute chronologies can be established, which was precluded by problematic age-depth relationships with several intractable age reversals. Together with additional cave monitoring, potential stalagmite sampling in Ulupaka Cave, and a major revision of stalagmite chronology building, the findings of this chapter could provide valuable field-based support for the development of the proposed transition metal proxies based on OMC decay, whilst also presenting an opportunity to shed new light on South Pacific Holocene climatic conditions.

6.2 Overarching implications for the interpretation of stalagmite metal concentrations

This thesis demonstrated via experimental and field-based approaches the ubiquitous control that organic complexation poses on the systematics of first-row transition metals in typical limestone cave environments. The transport and lability of organically-complexed metals are defined by the stability of OMCs, which generally exert a kinetic limitation to the partitioning of respective metal cations between dripwater and precipitate. However, this perpetual kinetic control is likely overridden when either, or a combination of, NOM properties (*e.g.*, high aromaticity), fast discharge (*e.g.*, soil flushing), high precipitation rates, and porous fabrics, facili-

tate the direct capture of OMCs without sufficient retention of OMCs at the water-calcite interface to drive their dissociation. Regardless of the exact preconditions for either mechanism, a key implication is that transition metal concentrations in stalagmites may either be negatively or positively related to cave flow rates, depending on whether OMC decay or direct capture pathways dominate, respectively. By the very nature of high-flux events, however, these are inherently expected to present short periods of deposition only. Where temporal resolution is high enough to isolate the often extreme concentrations of metals associated with organic inclusions, it is thus plausible to expect the remaining signal to primarily reflect kinetic controls sensitive to the residence time of OMCs at stalagmite surfaces. Despite the lack of concrete experimental demonstration, important field-based precedent exists for this hypothesis. Notably, Sliwinski et al. (2022) recently discussed the highly comparable behaviour of Y in a detailed account of Y-Sr relationships in modern stalagmite samples, explicitly linking Y inclusion in stalagmites to the residence (in their study, 'retention') time of OMCs in contact with the crystal phase as limited by incoming drips. These observations suggest that other rare earth elements may also be susceptible to kinetic controls, thus increasing the suite of elements with premise for exhibiting kinetic behaviour applicable to palaeoclimatic interpretations. While experiments were consistently conducted using calcite, the same directional response of transition metal inclusion was also evident in the aragonitic sections of the Indian DHAR-1 stalagmite (Giesche et al., 2023). Presenting the first published direct application of the herein investigated transition metal proxy alongside established proxy systems, the authors were able to demonstrate an increased frequency of prolonged droughts associated with the 4.2-kiloyear event, which coincided with significant societal changes in the Indus Civilisation.

Importantly, modelling exercises in Chapter 3 in principle allude to the possibility of relating stalagmite metal concentrations to cave drip rates (as approximated by thin-film residence times) in a quantitative or semi-quantitative matter, thus increasing their value as hydrological proxies substantially. However, this requires that OMC dissociation rate constants can be accurately constrained for a given cave system, which may be possible using a refined methodology for *in-situ* characterisation of k_d, and/or modelling approaches calibrated against cave monitoring observations.

Regardless, the work presented herein strongly encourages the analysis of stalagmite transition metal concentrations in light of potentially contrasting but meaningful hydrological controls, including a re-assessment of previously published records that currently lack interpretation of these data.

6.3 Recommendations for further research

The findings and caveats of this work suggest a number of potential avenues for further research of direct relevance to advancing the applicability of transition metals as palaeoenvironmental proxies in speleothems.

An inevitable caveat of kinetic experiments as presented in Chapter 3 is that derived kinetic parameters are strongly sensitive to the methodology. Although conditions in CLE experiments were kept close to respective in-cave conditions, these experiments can only approximate the true kinetic constraints imposed by organic complexation in incoming drips of cave waters. One possible approach could be to utilise modified setups based on the diffusive-gradients in thin-films (DGT) method (*e.g.*, Sigg et al., 2006), which could be deployed *in-situ* and retain native metal concentrations, pH, temperature, and ionic strength. Another important question is as to how much kinetic variability within a given cave is, which could be addressed by temporally resolving kinetic measurements (by CLE, DGT, or otherwise). This could be particularly interesting in highly seasonal systems, where ligand quantity and quality are likely more variable in response to large variations in recharge.

Cave-analogue experiments as performed in Chapter 4 have proven useful to investigate controls of various trace elemental and isotopic proxies under controlled conditions (*e.g.*, Huang & Fairchild, 2001; M. Hansen et al., 2013; Day & Henderson, 2011; Lindeman et al., 2022). In this study, the experiments depicted the inclusion mechanisms of direct capture by either adsorption or entrapment, however, were likely inadequate for demonstrating drip rate sensitive contributions of metals via OMC decay. This is plausible when considering that the rate of precipitation (and thus cation consumption) is accelerated at feasible experimental conditions, greatly exceeding the rate of metal release from OMCs. To successfully resolve and quantify kinetic metal release in presence of calcite, it may thus be necessary to instead target OMC decay signatures during metal sorption to already precipitated crystals in an adapted experimental design (*e.g.*, similar to experiments by Lee et al. (2005)). Considering that Ni isotopes evidently fractionate during inclusion into calcite (Alvarez et al., 2021), experimental studies on OMC decay and calcite sorption could further benefit from metal isotope analyses. Additionally, it is recommended to further investigate the variable degree of organic matter inclusion into calcite representative of temporal variations of organic inputs in typical cave environments.

Finally, it is clear that the establishment of diagnostic criteria would greatly facilitate the development and applicability of transition metals as routine hydrological proxy systems. This in turn requires further holistic assessments of metal behaviour in natural cave systems, including within the soil, karst, infiltrating water, and carbonate components, in addition to experimental studies as outlined above.

Bibliography

Affolter, S., Fleitmann, D., & Leuenberger, M. (2014). New online method for water isotope analysis of speleothem fluid inclusions using laser absorption spectroscopy (WS-CRDS). *Climate of the Past*, *10*(4), 1291–1304. doi: 10.5194/cp-10-1291-2014

Affolter, S., Häuselmann, A., Fleitmann, D., Edwards, R. L., Cheng, H., & Leuenberger, M. (2019). Central Europe temperature constrained by speleothem fluid inclusion water isotopes over the past 14,000 years. *Science Advances*, *5*(6). doi: 10.1126/sciadv.aav3809

Aharon, P., Rasbury, M., & Murgulet, V. (2006). Caves of Niue Island, South Pacific: Speleothems and water geochemistry. In *Perspectives on Karst Geomorphology, Hydrology, and Geochemistry - A Tribute Volume to Derek C. Ford and William B. White.* Geological Society of America. doi: 10.1130/2006.2404(24)

Aiken, G. R., Hsu-Kim, H., & Ryan, J. N. (2011). Influence of Dissolved Organic Matter on the Environmental Fate of Metals, Nanoparticles, and Colloids. *Environmental Science & Technology*, *45*(8), 3196–3201. doi: 10.1021/es103992s

Alkhatib, M., Qutob, M., Alkhatib, S., & Eisenhauer, A. (2022). Influence of precipitation rate and temperature on the partitioning of magnesium and strontium in calcite overgrowths. *Chemical Geology*, *599*, 120841. doi: 10.1016/j.chemgeo.2022.120841

Allen, H. B., & Hansen, D. J. (1996). The Importance of Trace Metal Speciation to Water Quality Criteria. *Water Environment Research*, *68*(1), 42–54.

Allen, M., Poggiali, D., Whitaker, K., Marshall, T. R., van Langen, J., & Kievit, R. A. (2021). Raincloud plots: a multi-platform tool for robust data visualization. *Wellcome Open Research*, *4*, 63. doi: 10.12688/wellcomeopenres.15191.2

Allison, J. D., Brown, D. S., & Novo-Gradac, K. J. (1991). *MINTEQA2/PRODEFA2, a geochemical assessment model for environmental systems: Version 3.0 user's manual* (Tech. Rep.). Environmental Protection Agency, Athens, GA (United States). Environmental Research Lab.

Alvarez, C. C., Quitté, G., Schott, J., & Oelkers, E. H. (2021). Nickel isotope fractionation as a function of carbonate growth rate during Ni coprecipitation with calcite. *Geochimica et*

Cosmochimica Acta, *299*, 184–198. doi: 10.1016/j.gca.2021.02.019

Amery, F., Degryse, F., Cheyns, K., Troyer, I. D., Mertens, J., Merckx, R., & Smolders, E. (2008). The UV-absorbance of dissolved organic matter predicts the fivefold variation in its affinity for mobilizing Cu in an agricultural soil horizon. *European Journal of Soil Science*, *59*(6), 1087–1095. doi: 10.1111/j.1365-2389.2008.01078.x

Amery, F., Degryse, F., Moorleghem, C. V., Duyck, M., & Smolders, E. (2010). The dissociation kinetics of Cu-dissolved organic matter complexes from soil and soil amendments. *Analytica Chimica Acta*, *670*(1-2), 24–32. doi: 10.1016/j.aca.2010.04.047

Anderegg, G. (1982). Critical survey of stability constants of NTA complexes. *Pure and Applied Chemistry*, *54*(12), 2693–2758. doi: 10.1351/pac198254122693

Andersson, C. A., & Bro, R. (2000). The N-way Toolbox for MATLAB. *Chemometrics and Intelligent Laboratory Systems*, *52*(1), 1–4. doi: 10.1016/s0169-7439(00)00071-x

Arienzo, M. M., Swart, P. K., & Vonhof, H. B. (2013). Measurement of δ^{18}O and δ^{2}H values of fluid inclusion water in speleothems using cavity ring-down spectroscopy compared with isotope ratio mass spectrometry. *Rapid Communications in Mass Spectrometry*, *27*(23), 2616–2624. doi: 10.1002/rcm.6723

Artinger, R., Buckau, G., Geyer, S., Fritz, P., Wolf, M., & Kim, J. I. (2000). Characterization of groundwater humic substances: influence of sedimentary organic carbon. *Applied Geochemistry*, *15*(1), 97–116. doi: 10.1016/s0883-2927(99)00021-9

Astilleros, J. M., Fernández-Díaz, L., & Putnis, A. (2010). The role of magnesium in the growth of calcite: An AFM study. *Chemical Geology*, *271*(1-2), 52–58. doi: 10.1016/j.chemgeo.2009.12.011

Atsawawaranunt, K., Comas-Bru, L., Mozhdehi, S. A., Deininger, M., Harrison, S. P., Baker, A., ... Scroxton, N. (2018). The SISAL database: a global resource to document oxygen and carbon isotope records from speleothems. *Earth System Science Data*, *10*(3), 1687–1713. doi: 10.5194/essd-10-1687-2018

Babst, F., Bodesheim, P., Charney, N., Friend, A. D., Girardin, M. P., Klesse, S., ... Evans, M. E. K. (2018). When tree rings go global: Challenges and opportunities for retro- and prospective insight. *Quaternary Science Reviews*, *197*, 1–20. doi: 10.1016/j.quascirev.2018.07.009

Bajo, P., Hellstrom, J., Frisia, S., Drysdale, R., Black, J., Woodhead, J. D., ... Haese, R. (2016). "Cryptic" diagenesis and its implications for speleothem geochronologies. *Quaternary Science Reviews*, *148*, 17–28. doi: 10.1016/j.quascirev.2016.06.020

Baken, S., Degryse, F., Verheyen, L., Merckx, R., & Smolders, E. (2011). Metal Complexation Properties of Freshwater Dissolved Organic Matter Are Explained by Its Aromaticity and by Anthropogenic Ligands. *Environmental Science & Technology*, *45*(7), 2584–2590. doi: 10.1021/es103532a

Baker, A., Barnes, W. L., & Smart, P. L. (1997a). Stalagmite drip discharge and organic matter

fluxes in Lower Cave, Bristol. *Hydrological Processes*, *11*, 1541–1555.

Baker, A., Barnes, W. L., & Smart, P. L. (1997b). Variations in the discharge and organic matter content of stalagmite drip waters in Lower Cave, Bristol. *Hydrological Processes*, *11*(11), 1541–1555. doi: 10.1002/(sici)1099-1085(199709)11:11<1541::aid-hyp484>3.0.co;2-z

Baker, A., & Genty, D. (1998). Environmental pressures on conserving cave speleothems: effects of changing surface land use and increased cave tourism. *Journal of Environmental Management*, *53*(2), 165–175. doi: 10.1006/jema.1998.0208

Baker, A., Genty, D., & Fairchild, I. J. (2000). Hydrological characterisation of stalagmite dripwaters at Grotte de Villars, Dordogne, by the analysis of inorganic species and luminescent organic matter. *Hydrology and Earth System Sciences*, *4*(3), 439–449. doi: 10.5194/hess-4-439-2000

Baker, A., Genty, D., & Smart, P. L. (1998). High-resolution records of soil humification and palaeoclimate change from speleothem luminescence excitation-emission wavelength variations. *Geology*, *26*, 903–906.

Baker, A., Jex, C. N., Rutlidge, H., Woltering, M., Blyth, A. J., Andersen, M. S., ... Khan, S. J. (2016). An irrigation experiment to compare soil, water and speleothem tetraether membrane lipid distributions. *Organic Geochemistry*, *94*, 12–20. doi: 10.1016/j.orggeochem.2016.01.005

Baker, A., Mockler, N. J., & Barnes, W. L. (1999). Fluorescence intensity variations of speleothem-forming groundwaters: Implications for paleoclimate reconstruction. *Water Resources Research*, *35*(2), 407–413. doi: 10.1029/1998wr900057

Baker, A., Smart, P. L., Edwards, R. L., & Richards, D. A. (1993). Annual growth banding in a cave stalagmite. *Nature*, *364*(6437), 518–520. doi: 10.1038/364518a0

Baker, A., Smith, C., Jex, C., Fairchild, I., Genty, D., & Fuller, L. (2008). Annually laminated speleothems: a review. *International Journal of Speleology*, *37*(3), 193–206. doi: 10.5038/1827-806x.37.3.4

Baldini, J. U. L., Lechleitner, F. A., Breitenbach, S. F. M., van Hunen, J., Baldini, L. M., Wynn, P. M., ... Fohlmeister, J. (2021). Detecting and quantifying palaeoseasonality in stalagmites using geochemical and modelling approaches. *Quaternary Science Reviews*, *254*, 106784. doi: 10.1016/j.quascirev.2020.106784

Baldini, J. U. L., McDermott, F., Baldini, L. M., Ottley, C. J., Linge, K. L., Clipson, N., & Jarvis, K. E. (2012). Identifying short-term and seasonal trends in cave drip water trace element concentrations based on a daily-scale automatically collected drip water dataset. *Chemical Geology*, *330-331*, 1–16. doi: 10.1016/j.chemgeo.2012.08.009

Baldini, J. U. L., McDermott, F., & Fairchild, I. J. (2006). Spatial variability in cave drip water hydrochemistry: Implications for stalagmite paleoclimate records. *Chemical Geology*, *235*(3-4), 390–404. doi: 10.1016/j.chemgeo.2006.08.005

Baldini, J. U. L., McDermott, F., Hoffmann, D. L., Richards, D. A., & Clipson, N. (2008). Very

high-frequency and seasonal cave atmosphere pCO_2 variability: Implications for stalagmite growth and oxygen isotope-based paleoclimate records. *Earth and Planetary Science Letters*, *272*(1-2), 118–129. doi: 10.1016/j.epsl.2008.04.031

Baldini, L. M., McDermott, F., Baldini, J. U. L., Arias, P., Cueto, M., Fairchild, I. J., ... Richards, D. A. (2015). Regional temperature, atmospheric circulation, and sea-ice variability within the Younger Dryas Event constrained using a speleothem from northern Iberia. *Earth and Planetary Science Letters*, *419*, 101–110. doi: 10.1016/j.epsl.2015.03.015

Ban, F., Pan, G., Zhu, J., Cai, B., & Tan, M. (2008). Temporal and spatial variations in the discharge and dissolved organic carbon of drip waters in Beijing Shihua Cave, China. *Hydrological Processes*, *22*(18), 3749–3758. doi: 10.1002/hyp.6979

Banner, J. L., Guilfoyle, A., James, E. W., Stern, L. A., & Musgrove, M. (2007). Seasonal Variations in Modern Speleothem Calcite Growth in Central Texas, U.S.A. *Journal of Sedimentary Research*, *77*(8), 615–622. doi: 10.2110/jsr.2007.065

Bar-Matthews, M., Ayalon, A., Kaufman, A., & Wasserburg, G. J. (1999). The Eastern Mediterranean paleoclimate as a reflection of regional events: Soreq cave, Israel. *Earth and Planetary Science Letters*, *166*(1-2), 85–95. doi: 10.1016/s0012-821x(98)00275-1

Barton, H. A., & Northup, D. E. (2007). Geomicrobiology in cave environments: Past, current and future perspectives. *Journal of Cave and Karst Studies*, *69*(1), 163–178.

Battarbee, R. W., & Binney, H. A. (Eds.). (2008). *Natural Climate Variability and Global Warming*. Wiley Blackwell. doi: 10.1002/9781444300932

Belli, R., Borsato, A., Frisia, S., Drysdale, R., Maas, R., & Greig, A. (2017). Investigating the hydrological significance of stalagmite geochemistry (Mg, Sr) using Sr isotope and particulate element records across the Late Glacial-to-Holocene transition. *Geochimica et Cosmochimica Acta*, *199*, 247–263. doi: 10.1016/j.gca.2016.10.024

Bichet, V., Gauthier, E., Massa, C., & Perren, B. B. (2014). Lake Sediments as an Archive of Land use and Environmental Change in the Eastern Settlement, Southwestern Greenland. *Journal of the North Atlantic*, *601*, 47–63. doi: 10.3721/037.002.sp606

Bjerknes, J. (1966). A possible response of the atmospheric Hadley circulation to equatorial anomalies of ocean temperature. *Tellus*, *18*, 820.

Black, K. H., Archer, M., Hand, S. J., & Godthelp, H. (2010). First comprehensive analysis of cranial ontogeny in a fossil marsupial – from a 15-million-year-old cave deposit in northern Australia. *Journal of Vertebrate Paleontology*, *30*(4), 993–1011. doi: 10.1080/02724634.2010.483567

Blyth, A. J., Asrat, A., Baker, A., Gulliver, P., Leng, M. J., & Genty, D. (2007). A new approach to detecting vegetation and land-use Change using high-resolution lipid biomarker records in stalagmites. *Quaternary Research*, *68*(3), 314–324. doi: 10.1016/j.yqres.2007.08.002

Blyth, A. J., & Frisia, S. (2008). Molecular Evidence for Bacterial Mediation of Calcite Formation in Cold High-Altitude Caves. *Geomicrobiology Journal*, *25*(2), 101–111. doi: 10.1080/

01490450801934938

Blyth, A. J., Hartland, A., & Baker, A. (2016). Organic proxies in speleothems – New developments, advantages and limitations. *Quaternary Science Reviews*, *149*, 1–17. doi: 10.1016/j.quascirev.2016.07.001

Blyth, A. J., Jex, C. N., Baker, A., Khan, S. J., & Schouten, S. (2014). Contrasting distributions of glycerol dialkyl glycerol tetraethers (GDGTs) in speleothems and associated soils. *Organic Geochemistry*, *69*, 1–10. doi: 10.1016/j.orggeochem.2014.01.013

Blyth, A. J., & Schouten, S. (2013). Calibrating the glycerol dialkyl glycerol tetraether temperature signal in speleothems. *Geochimica et Cosmochimica Acta*, *109*, 312–328. doi: 10.1016/j.gca.2013.02.009

Blyth, A. J., Smith, C. I., & Drysdale, R. N. (2013). A new perspective on the δ^{13}C signal preserved in speleothems using LC–IRMS analysis of bulk organic matter and compound specific stable isotope analysis. *Quaternary Science Reviews*, *75*, 143–149. doi: 10.1016/j.quascirev.2013.06.017

Boch, R., Spötl, C., & Frisia, S. (2011). Origin and palaeoenvironmental significance of lamination in stalagmites from Katerloch Cave, Austria. *Sedimentology*, *58*(2), 508–531. doi: 10.1111/j.1365-3091.2010.01173.x

Bond, G. (1997). A Pervasive Millennial-Scale Cycle in North Atlantic Holocene and Glacial Climates. *Science*, *278*(5341), 1257–1266. doi: 10.1126/science.278.5341.1257

Borsato, A., Frisia, S., Fairchild, I. J., Somogyi, A., & Susini, J. (2007). Trace element distribution in annual stalagmite laminae mapped by micrometer-resolution X-ray fluorescence: Implications for incorporation of environmentally significant species. *Geochimica et Cosmochimica Acta*, *71*(6), 1494–1512. doi: 10.1016/j.gca.2006.12.016

Borsato, A., Frisia, S., Howard, D., & Greig, A. (2021). A guide to synchrotron hard X-ray fluorescence mapping of annually laminated stalagmites: Sample preparation, analysis and evaluation. *Spectrochimica Acta Part B: Atomic Spectroscopy*, *185*, 106308. doi: 10.1016/j.sab.2021.106308

Borsato, A., Frisia, S., Wynn, P. M., Fairchild, I. J., & Miorandi, R. (2015). Sulphate concentration in cave dripwater and speleothems: long-term trends and overview of its significance as proxy for environmental processes and climate changes. *Quaternary Science Reviews*, *127*, 48–60. doi: 10.1016/j.quascirev.2015.05.016

Böttcher, M. E., & Dietzel, M. (2010). Metal-ion partitioning during low-temperature precipitation and dissolution of anhydrous carbonates and sulphates. In *Ion partitioning in ambient-temperature aqueous systems* (pp. 139–187). Mineralogical Society of Great Britain & Ireland. doi: 10.1180/emu-notes.10.4

Bradl, H. B. (2004). Adsorption of heavy metal ions on soils and soil constituents. *Colloidal Interf. Science*, *277*, 1–18.

Breitenbach, S. F. M., Lechleitner, F. A., Meyer, H., Diengdoh, G., Mattey, D., & Marwan,

N. (2015). Cave ventilation and rainfall signals in dripwater in a monsoonal setting – a monitoring study from NE India. *Chemical Geology*, *402*, 111–124. doi: 10.1016/j.chemgeo.2015.03.011

Broecker, W. S., Olson, E. A., & Orr, P. C. (1960). Radiocarbon Measurements and Annual Rings in Cave Formations. *Nature*, *185*(4706), 93–94. doi: 10.1038/185093a0

Brown, M. (1977). Transmission spectroscopy examinations of natural waters. *Estuarine and Coastal Marine Science*, *5*(3), 309–317. doi: 10.1016/0302-3524(77)90058-5

Bruland, K. W., Rue, E. L., Donat, J. R., Skrabal, S. A., & Moffett, J. W. (2000). Intercomparison of voltammetric techniques to determine the chemical speciation of dissolved copper in a coastal seawater sample. *Analytica Chimica Acta*, *405*(1-2), 99–113. doi: 10.1016/s0003-2670(99)00675-3

Buffle, J., Wilkinson, K. J., Stoll, S., Filella, M., & Zhang, J. (1998). A Generalized Description of Aquatic Colloidal Interactions: The Three-colloidal Component Approach. *Environmental Science & Technology*, *32*(19), 2887–2899. doi: 10.1021/es980217h

Burba, P. (1994). Labile/inert metal species in aquatic humic substances: an ion-exchange study. *Fresenius' Journal of Analytical Chemistry*, *348*(4), 301–311. doi: 10.1007/bf00324039

Cabaniss, S. E. (1990). pH and Ionic Strength Effects on Nickel-Fulvic Acid Dissociation Kinetics. *Environmental Science & Technology*, *24*, 583–588.

Cai, B., Zhu, J., Ban, F., & Tan, M. (2011). Intra-annual variation of the calcite deposition rate of drip water in Shihua Cave, Beijing, China and its implications for palaeoclimatic reconstructions. *Boreas*, *40*(3), 525–535. doi: 10.1111/j.1502-3885.2010.00201.x

Cai, W., Borlace, S., Lengaigne, M., van Rensch, P., Collins, M., Vecchi, G., ... Jin, F.-F. (2014). Increasing frequency of extreme El Niño events due to greenhouse warming. *Nature Climate Change*, *4*(2), 111–116. doi: 10.1038/nclimate2100

Campbell, M., McDonough, L., Treble, P. C., Baker, A., Kosarac, N., Coleborn, K., ... Schmitt, A. K. (2023). A Review of Speleothems as Archives for Paleofire Proxies, With Australian Case Studies. *Reviews of Geophysics*, *61*(2). doi: 10.1029/2022rg000790

Carlson, P. E., Noronha, A. L., Banner, J. L., Jenson, J. W., Moore, M. W., Partin, J. W., ... Bautista, K. K. (2020). Constraining speleothem oxygen isotope disequilibrium driven by rapid CO_2 degassing and calcite precipitation: Insights from monitoring and modeling. *Geochimica et Cosmochimica Acta*, *284*, 222–238. doi: 10.1016/j.gca.2020.06.012

Chakrabarti, C. L., Lu, Y., Gregoire, D. C., Back, M. H., & Schroeder, W. H. (1994). Kinetic Studies of Metal Speciation Using Chelex Cation Exchange Resin: Application to Cadmium, Copper, and Lead Speciation in River Water and Snow. *Environmental Science & Technology*, *28*(11), 1957–1967. doi: 10.1021/es00060a029

Chalmin, E., Perrette, Y., Fanget, B., & Susini, J. (2012). Investigation of Organic Matter Entrapped in Synthetic Carbonates – A Multimethod Approach. *Microscopy and Micro-*

analysis, *19*(1), 132–144. doi: 10.1017/s1431927612013773

Charlson, R. J., & Rodhe, H. (1982). Factors controlling the acidity of natural rainwater. *Nature*, *295*(5851), 683–685. doi: 10.1038/295683a0

Chen, F. H., Bloemendal, J., Wang, J. M., Li, J. J., & Oldfield, F. (1997). High-resolution multi-proxy climate records from Chinese loess: evidence for rapid climatic changes over the last 75 kyr. *Palaeogeography, Palaeoclimatology, Palaeoecology*, *130*(1-4), 323–335. doi: 10.1016/s0031-0182(96)00149-6

Chen, J., Rao, Z., Liu, J., Huang, W., Feng, S., Dong, G., ... Chen, F. (2016). On the timing of the East Asian summer monsoon maximum during the Holocene – Does the speleothem oxygen isotope record reflect monsoon rainfall variability? *Science China Earth Sciences*, *59*(12), 2328–2338. doi: 10.1007/s11430-015-5500-5

Cheng, H., Edwards, R. L., Shen, C.-C., Polyak, V. J., Asmerom, Y., Woodhead, J. D., ... Alexander, E. C. (2013). Improvements in ^{230}Th dating, ^{230}Th and ^{234}U half-life values, and U–Th isotopic measurements by multi-collector inductively coupled plasma mass spectrometry. *Earth and Planetary Science Letters*, *371-372*, 82–91. doi: 10.1016/j.epsl.2013.04.006

Cobb, K. M., Charles, C. D., Cheng, H., Kastner, M., & Edwards, R. L. (2003). U/Th-dating living and young fossil corals from the central tropical Pacific. *Earth and Planetary Science Letters*, *210*(1-2), 91–103. doi: 10.1016/s0012-821x(03)00138-9

Coble, P. G. (1996). Characterization of marine and terrestrial DOM in seawater using excitation-emission matrix spectroscopy. *Marine Chemistry*, *51*(4), 325–346. doi: 10.1016/0304-4203(95)00062-3

Cole, J. E., Rind, D., Webb, R. S., Jouzel, J., & Healy, R. (1999). Climatic controls on interannual variability of precipitation δ^{18}O: Simulated influence of temperature, precipitation amount, and vapor source region. *Journal of Geophysical Research: Atmospheres*, *104*(D12), 14223–14235. doi: 10.1029/1999jd900182

Cölfen, H., & Antonietti, M. (2005). Mesocrystals: Inorganic Superstructures Made by Highly Parallel Crystallization and Controlled Alignment. *Angewandte Chemie International Edition*, *44*(35), 5576–5591. doi: 10.1002/anie.200500496

Collins, M., An, S.-I., Cai, W., Ganachaud, A., Guilyardi, E., Jin, F.-F., ... Wittenberg, A. (2010). The impact of global warming on the tropical Pacific Ocean and El Niño. *Nature Geoscience*, *3*(6), 391–397. doi: 10.1038/ngeo868

Collins, R. N., & Kinsela, A. S. (2010). The aqueous phase speciation and chemistry of cobalt in terrestrial environments. *Chemosphere*, *79*(8), 763–771. doi: 10.1016/j.chemosphere.2010.03.003

Columbu, A., Drysdale, R., Hellstrom, J., Woodhead, J. D., Cheng, H., Hua, Q., ... Edwards, R. L. (2019). U-Th and radiocarbon dating of calcite speleothems from gypsum caves (Emilia Romagna, North Italy). *Quaternary Geochronology*, *52*, 51–62. doi: 10.1016/

j.quageo.2019.04.002

Craig, H. (1961). Isotopic variations in meteoric waters. *Science*, *133*(3465), 1702–1703.

Crossley, P. C. (1988). *The New Zealand Cave Atlas: North Island, New Zealand.*

Cruz, F. W., Burns, S. J., Karmann, I., Sharp, W. D., & Vuille, M. (2006). Reconstruction of regional atmospheric circulation features during the late Pleistocene in subtropical Brazil from oxygen isotope composition of speleothems. *Earth and Planetary Science Letters*, *248*(1-2), 495–507. doi: 10.1016/j.epsl.2006.06.019

Cruz, F. W., Karmann, I., Viana, O., Burns, S. J., Ferrari, J. A., Vuille, M., ... Moreira, M. Z. (2005). Stable isotope study of cave percolation waters in subtropical Brazil: Implications for paleoclimate inferences from speleothems. *Chemical Geology*, *220*(3-4), 245–262. doi: 10.1016/j.chemgeo.2005.04.001

Cumberland, S. A., & Baker, A. (2007). The freshwater dissolved organic matter fluorescence - total organic carbon relationship. *Hydrological Processes*, *21*, 2093–2099.

Curl, R. L. (1972). Minimum diameter stalagtites. *Bulletin of the National Speleological Society*.

Curl, R. L. (1973). Minimum diameter stalagmites. *Bulletin of the National Speleological Society*.

Curti, E. (1997). *Coprecipitation of radionuclides: basic concepts, literature review and first applications* (No. 97-10). Paul Scherrer Institute.

Curti, E. (1999). Coprecipitation of radionuclides with calcite: estimation of partition coefficients based on a review of laboratory investigations and geochemical data. *Applied Geochemistry*, *14*(4), 433–445. doi: 10.1016/s0883-2927(98)00065-1

Czuppon, G., Demény, A., Leél-Őssy, S., Óvari, M., Molnár, M., Stieber, J., ... Haszpra, L. (2018). Cave monitoring in the Béke and Baradla caves (Northeastern Hungary): implications for the conditions for the formation cave carbonates. *International Journal of Speleology*, *47*(1), 13–28. doi: 10.5038/1827-806x.47.1.2110

Dahlqvist, R., Zhang, H., Ingri, J., & Davison, W. (2002). Performance of the diffusive gradients in thin films technique for measuring Ca and Mg in freshwater. *Analytica Chimica Acta*, *460*(2), 247–256. doi: 10.1016/s0003-2670(02)00248-9

Dansgaard, W. (1964). Stable isotopes in precipitation. *Tellus*, *16*(4), 436–468. doi: 10.1111/j.2153-3490.1964.tb00181.x

Dansgaard, W., Johnsen, S. J., Clausen, H. B., Dahl-Jensen, D., Gundestrup, N. S., Hammer, C. U., ... Bond, G. (1993). Evidence for general instability of past climate from a 250-kyr ice-core record. *Nature*, *364*(6434), 218–220. doi: 10.1038/364218a0

Davis, K. J., Dove, P. M., Wasylenki, L. E., & Yoreo, J. J. D. (2004). Morphological consequences of differential Mg^{2+} incorporation at structurally distinct steps on calcite. *American Mineralogist*, *89*(5-6), 714–720. doi: 10.2138/am-2004-5-605

Davison, W., & Zhang, H. (1994). In situ speciation measurements of trace components in natural waters using thin-film gels. *Nature*, *367*(6463), 546–548. doi: 10.1038/367546a0

Davranche, M., Pourret, O., Gruau, G., Dia, A., Jin, D., & Gaertner, D. (2008). Competitive binding of REE to humic acid and manganese oxide: Impact of reaction kinetics on development of cerium anomaly and REE adsorption. *Chemical Geology*, *247*(1-2), 154–170. doi: 10.1016/j.chemgeo.2007.10.010

Day, C. C., & Henderson, G. M. (2011). Oxygen isotopes in calcite grown under cave-analogue conditions. *Geochimica et Cosmochimica Acta*, *75*(14), 3956–3972. doi: 10.1016/j.gca.2011.04.026

Day, C. C., & Henderson, G. M. (2013). Controls on trace-element partitioning in cave-analogue calcite. *Geochimica et Cosmochimica Acta*, *120*, 612–627. doi: 10.1016/j.gca.2013.05.044

Day, C. C., von Strandmann, P. A. E. P., & Mason, A. J. (2021). Lithium isotopes and partition coefficients in inorganic carbonates: Proxy calibration for weathering reconstruction. *Geochimica et Cosmochimica Acta*, *305*, 243–262. doi: 10.1016/j.gca.2021.02.037

Debret, M., Bout-Roumazeilles, V., Grousset, F., Desmet, M., McManus, J. F., Massei, N., ... Trentesaux, A. (2007). The origin of the 1500-year climate cycles in Holocene North-Atlantic records. *Climate of the Past*, *3*(4), 569–575. doi: 10.5194/cp-3-569-2007

DeLong, K. L., Quinn, T. M., Taylor, F. W., Lin, K., & Shen, C.-C. (2012). Sea surface temperature variability in the southwest tropical Pacific since AD 1649. *Nature Climate Change*, *2*(11), 799–804. doi: 10.1038/nclimate1583

deMenocal, P., Ortiz, J., Guilderson, T., Adkins, J., Sarnthein, M., Baker, L., & Yarusinsky, M. (2000). Abrupt onset and termination of the African Humid Period: rapid climate responses to gradual insolation forcing. *Quaternary Science Reviews*, *19*(1-5), 347–361. doi: 10.1016/s0277-3791(99)00081-5

deMenocal, P., Ortiz, J., Guilderson, T., & Sarnthein, M. (2000). Coherent High- and Low-Latitude Climate Variability During the Holocene Warm Period. *Science*, *288*(5474), 2198–2202. doi: 10.1126/science.288.5474.2198

Demény, A., Rinyu, L., Kern, Z., Hatvani, I. G., Czuppon, G., Surányi, G., ... Koltai, G. (2021). Paleotemperature reconstructions using speleothem fluid inclusion analyses from Hungary. *Chemical Geology*, *563*, 120051. doi: 10.1016/j.chemgeo.2020.120051

Densem, G. (2017). *Golden Bay/Mohua Landscape Project - Additional Landscape Assessments* (Tech. Rep.). Tasman District Council.

Détroit, F., Mijares, A. S., Corny, J., Daver, G., Zanolli, C., Dizon, E., ... Piper, P. J. (2019). A new species of Homo from the Late Pleistocene of the Philippines. *Nature*, *568*(7751), 181–186. doi: 10.1038/s41586-019-1067-9

Diamond, H. J., Lorrey, A. M., & Renwick, J. A. (2013). A Southwest Pacific Tropical Cyclone Climatology and Linkages to the El Niño–Southern Oscillation. *Journal of Climate*, *26*(1),

3–25. doi: 10.1175/jcli-d-12-00077.1

Dong, B., Dai, A., Vuille, M., & Timm, O. E. (2018). Asymmetric Modulation of ENSO Teleconnections by the Interdecadal Pacific Oscillation. *Journal of Climate*, *31*(18), 7337–7361. doi: 10.1175/jcli-d-17-0663.1

Dorale, J. A., Edwards, R. L., Alexander, E. C., Shen, C.-C., Richards, D. A., & Cheng, H. (2004). Uranium-Series Dating of Speleothems: Current Techniques, Limits, & Applications. In *Studies of cave sediments* (pp. 177–197). Springer US. doi: 10.1007/978-1-4419-9118-8_10

Dredge, J., Fairchild, I. J., Harrison, R. M., Fernandez-Cortes, A., Sanchez-Moral, S., Jurado, V., ... Grassineau, N. (2013). Cave aerosols: distribution and contribution to speleothem geochemistry. *Quaternary Science Reviews*, *63*, 23–41. doi: 10.1016/j.quascirev.2012.11.016

Dreybrodt, W. (1988). *Processes in Karst Systems*. Springer Berlin Heidelberg. doi: 10.1007/978-3-642-83352-6

Dreybrodt, W. (2008). Chemical kinetics, speleothem growth and climate. *Boreas*, *28*(3), 347–356. doi: 10.1111/j.1502-3885.1999.tb00224.x

Dreybrodt, W. (2012). Comment on “Oxygen isotopes in calcite grown under cave-analogue conditions” by C.C. Day and G.M. Henderson. *Geochimica et Cosmochimica Acta*, *85*, 383–387. doi: 10.1016/j.gca.2012.01.047

Dreybrodt, W., & Franke, H. W. (1987). Wachstumsgeschwindigkeiten und Durchmesservon Kerzenstalagmiten. *Die Höhle - Zeitschrift für Karst- und Höhlenkunde*(1).

Drysdale, R. N., Zanchetta, G., Baneschi, I., Guidi, M., Isola, I., Couchoud, I., ... Hellstrom, J. C. (2019). Partitioning of Mg, Sr, Ba and U into a subaqueous calcite speleothem. *Geochimica et Cosmochimica Acta*, *264*, 67–91. doi: 10.1016/j.gca.2019.08.001

Duplessy, J. C., Labeyrie, J., Lalou, C., & Nguyen, H. V. (1970). Continental Climatic Variations between 130,000 and 90,000 Years BP. *Nature*, *226*(5246), 631–633. doi: 10.1038/226631a0

Edwards, R. L., Chen, J. H., & Wasserburg, G. J. (1987). ^{238}U-^{234}U-^{230}Th-^{232}Th systematics and the precise measurement of time over the past 500,000 years. *Earth and Planetary Science Letters*, *81*(2-3), 175–192. doi: 10.1016/0012-821x(87)90154-3

Edwards, R. L., Taylor, F. W., & Wasserburg, G. J. (1988). Dating earthquakes with high-precision thorium-230 ages of very young corals. *Earth and Planetary Science Letters*, *90*(4), 371–381. doi: 10.1016/0012-821x(88)90136-7

Eigen, M., & Wilkins, R. G. (1965). The Kinetics and Mechanism of Formation of Metal Complexes. In R. K. Murmann, R. T. M. Fraser, & J. Bauman (Eds.), *Mechanisms of Inorganic Reactions* (pp. 55–80). American Chemical Society. doi: 10.1021/ba-1965-0049.ch003

Elliott, H. A., & Brown, G. A. (1989). Comparative evaluation of NTA and EDTA for extractive

decontamination of Pb-polluted soils. *Water, Air, and Soil Pollution*, *45*(3-4). doi: 10.1007/bf00283464

EL-Shenawy, M. I., Kim, S.-T., & Schwarcz, H. P. (2020). Carbon and oxygen isotope systematics in cave environments: Lessons from an artificial cave "McMaster Cave". *Geochimica et Cosmochimica Acta*, *272*, 137–159. doi: 10.1016/j.gca.2019.12.009

Elzinga, E. J., & Reeder, R. J. (2002). X-ray absorption spectroscopy study of Cu^{2+} and Zn^{2+} adsorption complexes at the calcite surface. *Geochimica et Cosmochimica Acta*, *66*(22), 3943–3954. doi: 10.1016/s0016-7037(02)00971-7

Elzinga, E. J., Rouff, A. A., & Reeder, R. J. (2006). The long-term fate of Cu^{2+}, Zn^{2+}, and Pb^{2+} adsorption complexes at the calcite surface: An X-ray absorption spectroscopy study. *Geochimica et Cosmochimica Acta*, *70*(11), 2715–2725. doi: 10.1016/j.gca.2006.02.026

Emiliani, C. (1971). The Last Interglacial: Paleotemperatures and Chronology. *Science*, *171*(3971), 571–573. doi: 10.1126/science.171.3971.571

Epure, L., Meleg, I. N., Munteanu, C.-M., Roban, R. D., & Moldovan, O. T. (2014). Bacterial and Fungal Diversity of Quaternary Cave Sediment Deposits. *Geomicrobiology Journal*, *31*(2), 116–127. doi: 10.1080/01490451.2013.815292

Fairchild, I. J., & Baker, A. (2012). *Speleothem Science*. John Wiley & Sons, Ltd. doi: 10.1002/9781444361094

Fairchild, I. J., Baker, A., Borsato, A., Frisia, S., Hinton, R. W., McDermott, F., & Tooth, A. F. (2001). Annual to sub-annual resolution of multiple trace-element trends in speleothems. *Journal of the Geological Society*, *158*(5), 831–841. doi: 10.1144/jgs.158.5.831

Fairchild, I. J., Borsato, A., Tooth, A. F., Frisia, S., Hawkesworth, C. J., Huang, Y., ... Spiro, B. (2000). Controls on trace element (Sr–Mg) compositions of carbonate cave waters: implications for speleothem climatic records. *Chemical Geology*, *166*(3-4), 255–269. doi: 10.1016/s0009-2541(99)00216-8

Fairchild, I. J., Smith, C. L., Baker, A., Fuller, L., Spötl, C., Mattey, D., ... E.I.M.F. (2006). Modification and preservation of environmental signals in speleothems. *Earth-Science Reviews*, *75*(1-4), 105–153. doi: 10.1016/j.earscirev.2005.08.003

Fairchild, I. J., Spötl, C., Frisia, S., Borsato, A., Susini, J., Wynn, P. M., ... EIMF (2010). Petrology and geochemistry of annually laminated stalagmites from an Alpine cave (Obir, Austria): seasonal cave physiology. *Geological Society, London, Special Publications*, *336*(1), 295–321. doi: 10.1144/sp336.16

Fairchild, I. J., & Treble, P. C. (2009). Trace elements in speleothems as recorders of environmental change. *Quaternary Science Reviews*, *28*(5-6), 449–468. doi: 10.1016/j.quascirev.2008.11.007

Fairchild, I. J., Tuckwell, G. W., Baker, A., & Tooth, A. F. (2006). Modelling of dripwater hydrology and hydrogeochemistry in a weakly karstified aquifer (Bath, UK): Implications for climate change studies. *Journal of Hydrology*, *321*(1-4), 213–231. doi: 10.1016/j.jhydrol.2005.08

.002

Falini, G., Fermani, S., Tosi, G., & Dinelli, E. (2009). Calcium Carbonate Morphology and Structure in the Presence of Seawater Ions and Humic Acids. *Crystal Growth & Design*, *9*(5), 2065–2072. doi: 10.1021/cg8002959

Faraji, M., Borsato, A., Frisia, S., Hellstrom, J. C., Lorrey, A., Hartland, A., ... Mattey, D. P. (2021). Accurate dating of stalagmites from low seasonal contrast tropical Pacific climate using Sr 2D maps, fabrics and annual hydrological cycles. *Scientific Reports*, *11*(1). doi: 10.1038/s41598-021-81941-x

Faraji, M., Frisia, S., Hua, Q., Borsato, A., & Markowska, M. (2023). Accurate chronological construction for two young stalagmites from the tropical South Pacific. *Quaternary Geochronology*, *74*, 101415. doi: 10.1016/j.quageo.2022.101415

Fasfous, I. I., Yapici, T., Murimboh, J., Hassan, N. M., Chakrabarti, C. L., Back, M. H., ... Grégoire, D. C. (2004). Kinetics of Trace Metal Competition in the Freshwater Environment: Some Fundamental Characteristics. *Environmental Science & Technology*, *38*(19), 4979–4986. doi: 10.1021/es035427v

Fauchereau, N., Fedaeff, N., & Pearce, P. (2018). *Regional climate mode impacts on the Wellington Region. Part A: Introduction, Background, and Methodology* (NIWA Client report No. 2018259AK). National Institute of Water & Atmospheric Research Ltd (NIWA), Auckland, New Zealand.

Fedaeff, N., & Fauchereau, N. (2015). *Relationship between climate modes and Hawke's Bay seasonal rainfall and temperature. NIWA Client Report prepared for Hawke's Bay Regional Council* (NIWA Client Report No. AKL2015-016). NIWA.

Fein, J. B. (2002). The effects of ternary surface complexes on the adsorption of metal cations and organic acids onto mineral surfaces. In R. Hellmann & S. A. Wood (Eds.), *Water-Rock Interactions, Ore Deposits, and Environmental Geochemistry: A Tribute to David A. Crerar* (pp. 365–378). The Geochemical Society.

Fellman, J. B., Hood, E., & Spencer, R. G. M. (2010). Fluorescence spectroscopy opens new windows into dissolved organic matter dynamics in freshwater ecosystems: A review. *Limnology and Oceanography*, *55*(6), 2452–2462. doi: 10.4319/lo.2010.55.6.2452

Ferreira, C. M. H., Pinto, I. S. S., Soares, E. V., & Soares, H. M. V. M. (2015). (Un)suitability of the use of pH buffers in biological, biochemical and environmental studies and their interaction with metal ions – a review. *RSC Advances*, *5*(39), 30989–31003. doi: 10.1039/c4ra15453c

Fieldes, M., Bealing, G., Claridge, G. G. C., et al. (1960). Mineralogy and radioactivity of Niue Island soils. *New Zealand Journal of Science*, *3*, 658–675.

Filella, M., Town, R. M., & Buffle, J. (2002). Chemical Speciation in the Environment. In A. M. Ure & C. M. Davidson (Eds.), (Second Edition ed., p. 188 - 236). Blackwell Science Ltd.

Fleitmann, D., Matter, A., Burns, S. J., Al-Subbary, A., & Al-Aowah, M. A. (2004). Geology and Quaternary climate history of Socotra. *Fauna of Arabia*, *20*, 27–43.

Flores, O., Gritti, E. S., & Jolly, D. (2009). Climate and CO_2 modulate the C3/C4 balance and $\delta^{13}C$ signal in simulated vegetation. *Climate of the Past*, *5*(3), 431–440. doi: 10.5194/cp-5-431-2009

Fohlmeister, J., & Lechleitner, F. A. (2019). STAlagmite dating by radiocarbon (star): A software tool for reliable and fast age depth modelling. *Quaternary Geochronology*, *51*, 120–129. doi: 10.1016/j.quageo.2019.02.008

Fohlmeister, J., Plessen, B., Dudashvili, A. S., Tjallingii, R., Wolff, C., Gafurov, A., & Cheng, H. (2017). Winter precipitation changes during the Medieval Climate Anomaly and the Little Ice Age in arid Central Asia. *Quaternary Science Reviews*, *178*, 24–36. doi: 10.1016/j.quascirev.2017.10.026

Fohlmeister, J., Voarintsoa, N. R. G., Lechleitner, F. A., Boyd, M., Brandtstätter, S., Jacobson, M. J., & Oster, J. L. (2020). Main controls on the stable carbon isotope composition of speleothems. *Geochimica et Cosmochimica Acta*, *279*, 67–87. doi: 10.1016/j.gca.2020.03.042

Folland, C. K. (2002). Relative influences of the Interdecadal Pacific Oscillation and ENSO on the South Pacific Convergence Zone. *Geophysical Research Letters*, *29*(13). doi: 10.1029/2001gl014201

Ford, D., & Williams, P. (2007). *Karst Hydrogeology and Geomorphology*. John Wiley & Sons Ltd.

Frappier, A. B. (2008). A stepwise screening system to select storm-sensitive stalagmites: Taking a targeted approach to speleothem sampling methodology. *Quaternary International*, *187*(1), 25–39. doi: 10.1016/j.quaint.2007.09.042

Friedman, I. (2002). Stable isotope composition of waters in the Great Basin, United States 1. Air-mass trajectories. *Journal of Geophysical Research*, *107*(D19). doi: 10.1029/2001jd000565

Frisia, S. (2015). Microstratigraphic logging of calcite fabrics in speleothems as tool for palaeoclimate studies. *International Journal of Speleology*, *44*(1). doi: 10.5038/1827-806x.44.1.1

Frisia, S., Borsato, A., Drysdale, R. N., Paul, B., Greig, A., & Cotte, M. (2012). A re-evaluation of the palaeoclimatic significance of phosphorus variability in speleothems revealed by high-resolution synchrotron micro XRF mapping. *Climate of the Past*, *8*(6), 2039–2051. doi: 10.5194/cp-8-2039-2012

Frisia, S., Borsato, A., Fairchild, I. J., & McDermott, F. (2000). Calcite Fabrics, Growth Mechanisms, and Environments of Formation in Speleothems from the Italian Alps and Southwestern Ireland. *Journal of Sedimentary Research*, *70*(5), 1183–1196. doi: 10.1306/022900701183

Frisia, S., Borsato, A., Fairchild, I. J., McDermott, F., & Selmo, E. M. (2002). Aragonite-Calcite Relationships in Speleothems (Grotte De Clamouse, France): Environment, Fabrics, and Carbonate Geochemistry. *Journal of Sedimentary Research*, *72*(5), 687–699. doi: 10 .1306/020702720687

Frisia, S., Borsato, A., Hartland, A., Faraji, M., Demeny, A., Drysdale, R. N., & Marjo, C. E. (2022). Crystallization pathways, fabrics and the capture of climate proxies in speleothems: Examples from the tropics. *Quaternary Science Reviews*, *297*, 107833. doi: 10.1016/j.quascirev.2022.107833

Frisia, S., Borsato, A., & Hellstrom, J. (2018). High spatial resolution investigation of nucleation, growth and early diagenesis in speleothems as exemplar for sedimentary carbonates. *Earth-Science Reviews*, *178*, 68–91. doi: 10.1016/j.earscirev.2018.01.014

Frisia, S., Borsato, A., Preto, N., & McDermott, F. (2003). Late Holocene annual growth in three Alpine stalagmites records the influence of solar activity and the North Atlantic Oscillation on winter climate. *Earth and Planetary Science Letters*, *216*(3), 411–424. doi: 10.1016/s0012-821x(03)00515-6

Frisia, S., Borsato, A., & Susini, J. (2008). Synchrotron radiation applications to past volcanism archived in speleothems: An overview. *Journal of Volcanology and Geothermal Research*, *177*(1), 96–100. doi: 10.1016/j.jvolgeores.2007.11.010

Froeschmann, M.-L. (2018). *The influence of drip interval and temperature on the C and O isotope composition of DIC and $CaCO_3$ – a novel laboratory approach* (Unpublished master's thesis). Johannes Gutenburg University Mainz.

Füger, A., Konrad, F., Leis, A., Dietzel, M., & Mavromatis, V. (2019). Effect of growth rate and pH on lithium incorporation in calcite. *Geochimica et Cosmochimica Acta*, *248*, 14–24. doi: 10.1016/j.gca.2018.12.040

Gabitov, R. I., Sadekov, A., & Leinweber, A. (2014). Crystal growth rate effect on Mg/Ca and Sr/Ca partitioning between calcite and fluid: An in situ approach. *Chemical Geology*, *367*, 70–82. doi: 10.1016/j.chemgeo.2013.12.019

Gabitov, R. I., & Watson, E. B. (2006). Partitioning of strontium between calcite and fluid. *Geochemistry, Geophysics, Geosystems*, *7*(11). doi: 10.1029/2005gc001216

Gagan, M. K. (2009). Paleo-El Niño-Southern Oscillation (Enso) Records. In *Encyclopedia of earth sciences series* (pp. 721–728). Springer Netherlands. doi: 10.1007/978-1-4020 -4411-3_172

Gałuszka, A., Migaszewski, Z. M., & Namieśnik, J. (2017). The role of analytical chemistry in the study of the Anthropocene. *TrAC Trends in Analytical Chemistry*, *97*, 146–152. doi: 10.1016/j.trac.2017.08.017

Gams, I. (1981). Contribution to morphometrics of stalagmites. In *Proceedings of the 8th International Congress of Speleology* (pp. 276–278).

Gascoyne, M. (1983). Trace-element partition coefficients in the calcite-water system and their

paleoclimatic significance in cave studies. *Journal of Hydrology*, *61*(1-3), 213–222. doi: 10.1016/0022-1694(83)90249-4

Gat, J. R., Mook, W. G., & Meijer, H. A. J. (2001). Environmental isotopes in the hydrological cycle. *Principles and Applications UNESCO/IAEA Series*, *2*, 63–7.

Genty, D., Baker, A., Massault, M., Proctor, C., Gilmour, M., Pons-Branchu, E., & Hamelin, B. (2001). Dead carbon in stalagmites: carbonate bedrock paleodissolution vs. ageing of soil organic matter. Implications for ^{13}C variations in speleothems. *Geochimica et Cosmochimica Acta*, *65*(20), 3443–3457. doi: 10.1016/s0016-7037(01)00697-4

Genty, D., Blamart, D., Ouahdi, R., Gilmour, M., Baker, A., Jouzel, J., & Van-Exter, S. (2003). Precise dating of Dansgaard–Oeschger climate oscillations in western Europe from stalagmite data. *Nature*, *421*(6925), 833–837. doi: 10.1038/nature01391

Genty, D., & Deflandre, G. (1998). Drip flow variations under a stalactite of the Père Noël cave (Belgium). Evidence of seasonal variations and air pressure constraints. *Journal of Hydrology*, *211*(1-4), 208–232.

Genty, D., & Massault, M. (1999). Carbon transfer dynamics from bomb-^{14}C and $\delta^{13}C$ time series of a laminated stalagmite from SW France – modelling and comparison with other stalagmite records. *Geochimica et Cosmochimica Acta*, *63*(10), 1537–1548. doi: 10 .1016/s0016-7037(99)00122-2

Gerringa, L. J. A., Gledhill, M., Ardiningsih, I., Muntjewerf, N., & Laglera, L. M. (2021). Comparing CLE-AdCSV applications using SA and TAC to determine the Fe-binding characteristics of model ligands in seawater. *Biogeosciences*, *18*(19), 5265–5289. doi: 10.5194/bg-18-5265-2021

Giesche, A., Hodell, D. A., Petrie, C. A., Haug, G. H., Adkins, J. F., Plessen, B., . . . Breitenbach, S. F. M. (2023). Recurring summer and winter droughts from 4.2-3.97 thousand years ago in north India. *Communications Earth &Environment*, *4*(1). doi: 10.1038/s43247-023 -00763-z

Gillieson, D. S. (2011). Management of Caves. In P. E. van Beynen (Ed.), *Karst Management* (pp. 141–158). Springer Netherlands. doi: 10.1007/978-94-007-1207-2_6

Goede, A., & Vogel, J. C. (1991). Trace element variations and dating of a Late Pleistocene Tasmanian speleothem. *Palaeogeography, Palaeoclimatology, Palaeoecology*, *88*(1-2), 121–131. doi: 10.1016/0031-0182(91)90018-m

Goldberg, P., & Sherwood, S. C. (2006). Deciphering human prehistory through the geoarcheological study of cave sediments. *Evolutionary Anthropology: Issues, News, and Reviews*, *15*(1), 20–36. doi: 10.1002/evan.20094

Goswami, B. N., Madhusoodanan, M. S., Neema, C. P., & Sengupta, D. (2006). A physical mechanism for North Atlantic SST influence on the Indian summer monsoon. *Geophysical Research Letters*, *33*(2). doi: 10.1029/2005gl024803

Gregusova, M., & Docekal, B. (2011). New resin gel for uranium determination by diffusive

gradient in thin films technique. *Analytica Chimica Acta*, *684*(1-2), 142–146. doi: 10.1016/j.aca.2010.11.002

Grenthe, I., Fuger, J., Konings, R. J. M., Lemire, R. J., Muller, A. B., Nguyen-Trung, C., & Wanner, H. (1992). *Chemical thermodynamics of uranium* (Vol. 1). North-Holland Amsterdam.

Griffiths, M. L., Fohlmeister, J., Drysdale, R. N., Hua, Q., Johnson, K. R., Hellstrom, J. C., ... x. Zhao, J. (2012). Hydrological control of the dead carbon fraction in a Holocene tropical speleothem. *Quaternary Geochronology*, *14*, 81–93. doi: 10.1016/j.quageo.2012.04.001

Guan, Y., Huang, B., Zhu, J., Hu, Z.-Z., & Kinter, J. L. (2014). Interannual variability of the South Pacific Ocean in observations and simulated by the NCEP Climate Forecast System, version 2. *Climate Dynamics*, *43*(3-4), 1141–1157. doi: 10.1007/s00382-014-2148-y

Güngör, E. B. O., & Bekbölet, M. (2010). Zinc release by humic and fulvic acid as influenced by pH, complexation and DOC sorption. *Geoderma*, *159*, 131–138.

Gupta, A. K., Anderson, D. M., & Overpeck, J. T. (2003). Abrupt changes in the Asian southwest monsoon during the Holocene and their links to the North Atlantic Ocean. *Nature*, *421*(6921), 354–357. doi: 10.1038/nature01340

Guthrie, J. W., Mandal, R., Salam, M. S. A., Hassan, N. M., Murimboh, J., Chakrabarti, C. L., ... Grégoire, D. C. (2003). Kinetic studies of nickel speciation in model solutions of a well-characterized humic acid using the competing ligand exchange method. *Analytica Chimica Acta*, *480*(1), 157–169. doi: 10.1016/s0003-2670(02)01590-8

Halverson, G. P. (2013). Marine Isotope Stratigraphy. In *Encyclopedia of Scientific Dating Methods* (pp. 1–17). Springer Netherlands. doi: 10.1007/978-94-007-6326-5_130-1

Hansen, A. M., Kraus, T. E. C., Pellerin, B. A., Fleck, J. A., Downing, B. D., & Bergamaschi, B. A. (2016). Optical properties of dissolved organic matter (DOM): Effects of biological and photolytic degradation. *Limnology and Oceanography*, *61*(3), 1015–1032. doi: 10.1002/lno.10270

Hansen, M., Dreybrodt, W., & Scholz, D. (2013). Chemical evolution of dissolved inorganic carbon species flowing in thin water films and its implications for (rapid) degassing of CO_2 during speleothem growth. *Geochimica et Cosmochimica Acta*, *107*, 242–251. doi: 10.1016/j.gca.2013.01.006

Hansen, M., Scholz, D., Froeschmann, M.-L., Schöne, B. R., & Spötl, C. (2017). Carbon isotope exchange between gaseous CO_2 and thin solution films: Artificial cave experiments and a complete diffusion-reaction model. *Geochimica et Cosmochimica Acta*, *211*, 28–47. doi: 10.1016/j.gca.2017.05.005

Harmon, R. S., Schwarcz, H. P., & O'Neil, J. R. (1979). D/H ratios in speleothem fluid inclusions: A guide to variations in the isotopic composition of meteoric precipitation? *Earth and Planetary Science Letters*, *42*(2), 254–266. doi: 10.1016/0012-821x(79)90033-5

Harris, D. C. (2010). *Quantitative chemical analysis 8th Edition*. W. H. Freeman and Co.

Hartland, A., Fairchild, I. J., Lead, J. R., Borsato, A., Baker, A., Frisia, S., & Baalousha, M. (2012). From soil to cave: Transport of trace metals by natural organic matter in karst dripwaters. *Chemical Geology*, *304-305*, 68–82. doi: 10.1016/j.chemgeo.2012.01.032

Hartland, A., Fairchild, I. J., Lead, J. R., Zhang, H., & Baalousha, M. (2011). Size, speciation and lability of NOM–metal complexes in hyperalkaline cave dripwater. *Geochimica et Cosmochimica Acta*, *75*(23), 7533–7551. doi: 10.1016/j.gca.2011.09.030

Hartland, A., Fairchild, I. J., Müller, W., & Dominguez-Villar, D. (2014). Preservation of NOM-metal complexes in a modern hyperalkaline stalagmite: Implications for speleothem trace element geochemistry. *Geochimica et Cosmochimica Acta*, *128*, 29–43. doi: 10.1016/j.gca.2013.12.005

Hartland, A., & Zitoun, R. (2018). Transition metal availability to speleothems controlled by organic binding ligands. *Geochemical Perspectives Letters*, 22–25. doi: 10.7185/geochemlet.1824

Heidke, I., Hartland, A., Scholz, D., Pearson, A., Hellstrom, J., Breitenbach, S. F. M., & Hoffmann, T. (2021). Lignin oxidation products in soil, dripwater and speleothems from four different sites in New Zealand. *Biogeosciences*, *18*(7), 2289–2300. doi: 10.5194/bg-18-2289-2021

Hellstrom, J. (2003). Rapid and accurate U/Th dating using parallel ion-counting multi-collector ICP-MS. *Journal of Analytical Atomic Spectrometry*, *18*(11), 1346. doi: 10.1039/b308781f

Hellstrom, J., McCulloch, M., & Stone, J. (1998). A Detailed 31,000-Year Record of Climate and Vegetation Change, from the Isotope Geochemistry of Two New Zealand Speleothems. *Quaternary Research*, *50*(2), 167–178. doi: 10.1006/qres.1998.1991

Helms, J. R., Stubbins, A., Ritchie, J. D., Minor, E. C., Kieber, D. J., & Mopper, K. (2008). Absorption spectral slopes and slope ratios as indicators of molecular weight, source, and photobleaching of chromophoric dissolved organic matter. *Limnology and Oceanography*, *53*(3), 955–969. doi: 10.4319/lo.2008.53.3.0955

Henderson, G. M. (2002). New oceanic proxies for palaeoclimate. *Earth and Planetary Science Letters*, *203*, 1–13.

Hendy, C. H. (1971). The isotopic geochemistry of speleothems - 1. The calculation of the effects of different modes of formation on the isotopic composition of speleothems and their applicability as palaeoclimatic indicators. *Geochimica et Cosmochimica Acta*, *35*(8), 801–824. doi: 10.1016/0016-7037(71)90127-x

Hering, J. G., & Morel, F. M. M. (1990). Kinetics of Trace Metal Complexation: Ligand-Exchange Reactions. *Environmental Science & Technology*, *24*, 242–252.

Hill, C., & Forti, P. (1995). The classification of cave minerals and speleothems. *International Journal of Speleology*, *24*(1/4), 77–82. doi: 10.5038/1827-806x.24.1.5

Hoch, A. R., Reddy, M. M., & Aiken, G. R. (2000). Calcite crystal growth inhibition by humic substances with emphasis on hydrophobic acids from the Florida Everglades. *Geochimica et Cosmochimica Acta*, *64*(1), 61–72. doi: 10.1016/s0016-7037(99)00179-9

Hoffmann, S. R., Shafer, M. M., & Armstrong, D. E. (2007). Strong Colloidal and Dissolved Organic Ligands Binding Copper and Zinc in Rivers. *Environmental Science & Technology*, *41*(20), 6996–7002. doi: 10.1021/es070958v

Holden, G. (2018). *Cosmogenic nuclide dating of thesediments of Bulmer Cavern: implications for the uplift history of southern Northwest Nelson, South Island New Zealand* (Unpublished master's thesis). Victoria University of Wellington.

Hossain, K. M. A., & Easa, S. M. (2011). Spatial distribution of marine salts in coastal region using wet candle sensors. *International Journal of Research and Reviews in Applied Sciences*, *7*(3), 228–235.

Howard, D. L., de Jonge, M. D., Afshar, N., Ryan, C. G., Kirkham, R., Reinhardt, J., ... Paterson, D. J. (2020). The XFM beamline at the Australian Synchrotron. *Journal of Synchrotron Radiation*, *27*(5), 1447–1458. doi: 10.1107/s1600577520010152

Hu, C., Henderson, G. M., Huang, J., Xie, S., Sun, Y., & Johnson, K. R. (2008). Quantification of Holocene Asian monsoon rainfall from spatially separated cave records. *Earth and Planetary Science Letters*, *266*(3-4), 221–232. doi: 10.1016/j.epsl.2007.10.015

Hua, Q., Cook, D., Fohlmeister, J., Penny, D., Bishop, P., & Buckman, S. (2017). Radiocarbon Dating of a Speleothem Record of Paleoclimate for Angkor, Cambodia. *Radiocarbon*, *59*(6), 1873–1890. doi: 10.1017/rdc.2017.115

Hua, Q., McDonald, J., Redwood, D., Drysdale, R., Lee, S., Fallon, S., & Hellstrom, J. (2012). Robust chronological reconstruction for young speleothems using radiocarbon. *Quaternary Geochronology*, *14*, 67–80. doi: 10.1016/j.quageo.2012.04.017

Huang, Y., & Fairchild, I. J. (2001). Partitioning of Sr^{2+} and Mg^{2+} into calcite under karst-analogue experimental conditions. *Geochimica et Cosmochimica Acta*, *65*(1), 47–62. doi: 10.1016/s0016-7037(00)00513-5

Huang, Y., Fairchild, I. J., Borsato, A., Frisia, S., Cassidy, N. J., McDermott, F., & Hawkesworth, C. J. (2001). Seasonal variations in Sr, Mg and P in modern speleothems (Grotta di Ernesto, Italy). *Chemical Geology*, *175*(3-4), 429–448. doi: 10.1016/s0009-2541(00)00337-5

Informatics - Manaaki Whenua Landcare Research. (2020). *Soils Map Viewer.* Manaaki Whenua Landcare Research. doi: 10.26060/9VFZ-HW43

Inskeep, W. P., & Bloom, P. R. (1986). Kinetics of Calcite Precipitation in the Presence of Water-soluble Organic Ligands. *Soil Science Society of America Journal*, *50*(5), 1167–1172. doi: 10.2136/sssaj1986.03615995005000050015x

Irving, H., & Williams, R. J. P. (1953). The stability of transition-metal complexes. *Journal of the Chemical Society (Resumed)*, 3192. doi: 10.1039/jr9530003192

Ishii, S. K. L., & Boyer, T. H. (2012). Behavior of Reoccurring PARAFAC Components in Fluorescent Dissolved Organic Matter in Natural and Engineered Systems: A Critical Review. *Environmental Science and Technology*, *46*(4), 2006–2017. doi: 10.1021/es2043504

James, J. M. (2005). Condensation Corrosion. In D. C. Culver & W. B. White (Eds.), *Encyclopedia of Caves* (pp. 492–494). Elsevier Academic Press, London, United Kingdom.

Jia, Q., Zhang, S., Lammers, L., Huang, Y., & Wang, G. (2022). A model for pH dependent strontium partitioning during calcite precipitation from aqueous solutions. *Chemical Geology*, *608*, 121042. doi: 10.1016/j.chemgeo.2022.121042

Jiang, N., Griffiths, G., & Lorrey, A. (2012). Influence of large-scale climate modes on daily synoptic weather types over New Zealand. *International Journal of Climatology*, *33*(2), 499–519. doi: 10.1002/joc.3443

Jo, K., Woo, K. S., Hong, G. H., Kim, S. H., & Suk, B. C. (2010). Rainfall and hydrological controls on speleothem geochemistry during climatic events (droughts and typhoons): An example from Seopdong Cave, Republic of Korea. *Earth and Planetary Science Letters*, *295*(3-4), 441–450. doi: 10.1016/j.epsl.2010.04.024

Johnson, K., Hu, C., Belshaw, N., & Henderson, G. (2006). Seasonal trace-element and stable-isotope variations in a Chinese speleothem: The potential for high-resolution paleomonsoon reconstruction. *Earth and Planetary Science Letters*, *244*(1-2), 394–407. doi: 10.1016/j.epsl.2006.01.064

Juillet-Leclerc, A., Thiria, S., Naveau, P., Delcroix, T., Bec, N. L., Blamart, D., & Corrège, T. (2006). SPCZ migration and ENSO events during the 20th century as revealed by climate proxies from a Fiji coral. *Geophysical Research Letters*, *33*(17). doi: 10.1029/2006gl025950

Karkanas, P., Shahack-Gross, R., Ayalon, A., Bar-Matthews, M., Barkai, R., Frumkin, A., ... Stiner, M. (2007). Evidence for habitual use of fire at the end of the Lower Paleolithic: Site-formation processes at Qesem Cave, Israel. *Journal of Human Evolution*, *53*(2), 197–212. doi: 10.1016/j.jhevol.2007.04.002

Kaufmann, G. (2003). Stalagmite growth and palaeo-climate: the numerical perspective. *Earth and Planetary Science Letters*, *214*(1-2), 251–266. doi: 10.1016/s0012-821x(03)00369-8

Kemp, J., Radke, L. C., Olley, J., Juggins, S., & Deckker, P. D. (2012). Holocene lake salinity changes in the Wimmera, southeastern Australia, provide evidence for millennial-scale climate variability. *Quaternary Research*, *77*(1), 65–76. doi: 10.1016/j.yqres.2011.09.013

Kennedy, D. M., Marsters, T. H., Woods, J. L. D., & Woodroffe, C. D. (2012). Shore platform development on an uplifting limestone island over multiple sea-level cycles, Niue, South Pacific. *Geomorphology*, *141-142*, 170–182. doi: 10.1016/j.geomorph.2011.12.041

Kidston, J., Renwick, J. A., & McGregor, J. (2009). Hemispheric-Scale Seasonality of the

Southern Annular Mode and Impacts on the Climate of New Zealand. *Journal of Climate*, *22*(18), 4759–4770. doi: 10.1175/2009jcli2640.1

Kidwell, A., Lee, T., Jo, Y.-H., & Yan, X.-H. (2016). Characterization of the Variability of the South Pacific Convergence Zone Using Satellite and Reanalysis Wind Products. *Journal of Climate*, *29*(5), 1717–1732. doi: 10.1175/jcli-d-15-0536.1

Klimchouk, A. (2005). Gypsum caves. In D. C. Culver & W. B. White (Eds.), *Encyclopedia of Caves* (p. 674). Elsevier Academic Press, London, United Kingdom.

Knight, J., Shulmeister, J., & Petherick, L. (2021). Introduction to the SHeMax thematic set and prospects for LGM research in the Southern Hemisphere. *Quaternary Research*, *102*, 1–4. doi: 10.1017/qua.2021.39

Kost, O., González-Lemos, S., Rodriguez-Rodriguez, L., Sliwinski, J., Endres, L., Haghipour, N., & Stoll, H. (2022). Relationship of seasonal variations in drip water $\delta^{13}C_{DIC}$, $\delta^{18}O$ and trace elements with surface and physical cave conditions of La Vallina Cave, NW Spain. *in review*. doi: 10.5194/hess-2022-386

Kost, O., & Stoll, H. (2023). Marine aerosols in coastal areas and their impact on cave drip water – A monitoring study from Northern Spain. *Atmospheric Environment*, *302*, 119730. doi: 10.1016/j.atmosenv.2023.119730

Kottek, M., Grieser, J., Beck, C., Rudolf, B., & Rubel, F. (2006). World Map of the Köppen-Geiger climate classification updated. *Meteorologische Zeitschrift*, *15*(3), 259–263. doi: 10.1127/0941-2948/2006/0130

Kowalczk, A. J., & Froelich, P. N. (2010). Cave air ventilation and CO_2 outgassing by radon-222 modeling: How fast do caves breathe? *Earth and Planetary Science Letters*, *289*(1-2), 209–219. doi: 10.1016/j.epsl.2009.11.010

Kowalczuk, P., Stoń-Egiert, J., Cooper, W. J., Whitehead, R. F., & Durako, M. J. (2005). Characterization of chromophoric dissolved organic matter (CDOM) in the Baltic Sea by excitation emission matrix fluorescence spectroscopy. *Marine Chemistry*, *96*(3-4), 273–292. doi: 10.1016/j.marchem.2005.03.002

Lachniet, M. S. (2009). Climatic and environmental controls on speleothem oxygen-isotope values. *Quaternary Science Reviews*, *28*(5-6), 412–432. doi: 10.1016/j.quascirev.2008.10.021

Lachniet, M. S., & Patterson, W. P. (2009). Oxygen isotope values of precipitation and surface waters in northern Central America (Belize and Guatemala) are dominated by temperature and amount effects. *Earth and Planetary Science Letters*, *284*(3-4), 435–446. doi: 10.1016/j.epsl.2009.05.010

Lakshtanov, L. Z., & Stipp, S. L. S. (2007). Experimental study of nickel(II) interaction with calcite: Adsorption and coprecipitation. *Geochimica et Cosmochimica Acta*, *71*(15), 3686–3697. doi: 10.1016/j.gca.2007.04.006

Lam, M. T., Murimboh, J., Hassan, N. M., & Chakrabarti, C. L. (1999). Competitive ligand

exchange/adsorptive cathodic stripping voltammetry (CLE/AdCSV) for kinetic studies of nickel speciation in aqueous environmental samples containing heterogeneous, macromolecular, organic complexants. *Analytica Chimica Acta*, *402*, 195–209.

Larive, C. K., Rogers, A., Morton, M. D., & Carper, W. R. (1996). ^{113}Cd NMR binding studies of Cd-fulvic acid complexes: evidence of fast exchange. *Environmental Science & Technology*, *30*(9), 2828–2831.

Lavigne, J. A., Langford, C. H., & Mak, M. K. S. (1987). Kinetic Study of Speciation of Nickel(II) Bound to a Fulvic Acid. *Analytical Chemistry*, *59*, 2616–2620.

Lead, J. R., & Wilkinson, K. J. (2006). Aquatic Colloids and Nanoparticles: Current Knowledge and Future Trends. *Environmental Chemistry*, *3*(3), 159. doi: 10.1071/en06025

Lechleitner, F. A., Day, C. C., Kost, O., Wilhelm, M., Haghipour, N., Henderson, G. M., & Stoll, H. M. (2021). Stalagmite carbon isotopes suggest deglacial increase in soil respiration in western Europe driven by temperature change. *Climate of the Past*, *17*(5), 1903–1918. doi: 10.5194/cp-17-1903-2021

Lee, Y. J., Elzinga, E. J., & Reeder, R. J. (2005). Cu(II) adsorption at the calcite–water interface in the presence of natural organic matter: Kinetic studies and molecular-scale characterization. *Geochimica et Cosmochimica Acta*, *69*(1), 49–61. doi: 10.1016/j.gca.2004.06.015

Leenheer, J. A., Brown, G. K., MacCarthy, P., & Cabaniss, S. E. (1998). Models of Metal Binding Structures in Fulvic Acid from the Suwannee River, Georgia. *Environmental Science & Technology*, *32*(16), 2410–2416. doi: 10.1021/es9708979

Leermakers, M., Gao, Y., Navez, J., Poffijn, A., Croes, K., & Baeyens, W. (2009). Radium analysis by sector field ICP-MS in combination with the Diffusive Gradients in Thin Films (DGT) technique. *Journal of Analytical Atomic Spectrometry*, *24*(8), 1115. doi: 10.1039/b821472g

LeGrande, A. N., & Schmidt, G. A. (2006). Global gridded data set of the oxygen isotopic composition in seawater. *Geophysical Research Letters*, *33*(12). doi: 10.1029/2006gl026011

Lehmann, J., & Kleber, M. (2015). The contentious nature of soil organic matter. *Nature*, *528*(7580), 60–68. doi: 10.1038/nature16069

Lenton, T. M., Held, H., Kriegler, E., Hall, J. W., Lucht, W., Rahmstorf, S., & Schellnhuber, H. J. (2008). Tipping elements in the Earth's climate system. *Proceedings of the National Academy of Sciences*, *105*(6), 1786–1793. doi: 10.1073/pnas.0705414105

Leslie, D. M. (1986). *Soil taxonomic unit description for Niue Island* (Tech. Rep.). New Zealand Soil Bureau, Department of Scientific and Industrial Research.

Levy, J. L., Zhang, H., Davison, W., Galceran, J., & Puy, J. (2012). Kinetic Signatures of Metals in the Presence of Suwannee River Fulvic Acid. *Environmental Science & Technology*, *46*(6), 3335–3342. doi: 10.1021/es2043068

Lewis, S. L., & Maslin, M. A. (2015). Defining the Anthropocene. *Nature*, *519*(7542), 171–180. doi: 10.1038/nature14258

Li, X., Cui, X., He, D., Liao, J., & Hu, C. (2018). Evaluation of the Heshang Cave stalagmite calcium isotope composition as a paleohydrologic proxy by comparison with the instrumental precipitation record. *Scientific Reports*, *8*(1). doi: 10.1038/s41598-018-20776-5

Liao, J., Hu, C., Li, X., & Ruan, J. (2021). Drying increases organic colloidal mobilization in the karst vadose zone: Evidence from a 15-year cave-monitoring study. *Hydrological Processes*, *35*(4). doi: 10.1002/hyp.14163

Lin, Y., Jochum, K. P., Scholz, D., Hoffmann, D. L., Stoll, B., Weis, U., & Andreae, M. O. (2017). In-situ high spatial resolution LA-MC-ICPMS ^{230}Th/U dating enables detection of small-scale age inversions in speleothems. *Solid Earth Sciences*, *2*(1), 1–9. doi: 10.1016/j.sesci.2016.12.003

Lin, Y.-P., & Singer, P. C. (2005). Effects of seed material and solution composition on calcite precipitation. *Geochimica et Cosmochimica Acta*, *69*(18), 4495–4504. doi: 10.1016/j.gca.2005.06.002

Lindeman, I., Hansen, M., Scholz, D., Breitenbach, S. F. M., & Hartland, A. (2022). Effects of organic matter complexation on partitioning of transition metals into calcite: Cave-analogue crystal growth experiments. *Geochimica et Cosmochimica Acta*, *317*, 118–137. doi: 10.1016/j.gca.2021.10.032

Linsley, B. K., Wellington, G. M., & Schrag, D. P. (2000). Decadal Sea Surface Temperature Variability in the Subtropical South Pacific from 1726 to 1997 A.D. *Science*, *290*(5494), 1145–1148. doi: 10.1126/science.290.5494.1145

Liu, Z., Bowen, G. J., & Welker, J. M. (2010). Atmospheric circulation is reflected in precipitation isotope gradients over the conterminous United States. *Journal of Geophysical Research*, *115*(D22). doi: 10.1029/2010jd014175

Liu, Z., Kutzbach, J., & Wu, L. (2000). Modeling climate shift of El Niño variability in the Holocene. *Geophysical Research Letters*, *27*(15), 2265–2268. doi: 10.1029/2000gl011452

Lorens, R. B. (1981). Sr, Cd, Mn and Co distribution coefficients in calcite as a function of calcite precipitation rate. *Geochimica et Cosmochimica Acta*, *45*(4), 553–561. doi: 10.1016/0016-7037(81)90188-5

Ludwig, K. R., Simmons, K. R., Szabo, B. J., Winograd, I. J., Landwehr, J. M., Riggs, A. C., & Hoffman, R. J. (1992). Mass-Spectrometric ^{230}Th-^{234}U-^{238}U Dating of the Devils Hole Calcite Vein. *Science*, *258*(5080), 284–287. doi: 10.1126/science.258.5080.284

Lundelius, E. L. (2006). Cave site contributions to vertebrate history. *Alcheringa: An Australasian Journal of Palaeontology*, *30*, 195–210. doi: 10.1080/03115510609506863

Lyvén, B., Hassellöv, M., Turner, D. R., Haraldsson, C., & Andersson, K. (2003). Competition between iron- and carbon-based colloidal carriers for trace metals in a freshwater as-

sessed using flow field-flow fractionation coupled to ICPMS. *Geochimica et Cosmochimica Acta*, *67*(20), 3791–3802. doi: 10.1016/s0016-7037(03)00087-5

Macara, G. R. (2018). *The Climate and Weather of New Zealand* (NIWA Science and Technology Series No. 74). NIWA, New Zealand.

Magiera, M. (2018). *Controls On Trace Element Partitioning In Calcite Under Cave Analogue Conditions* (M.Sc Thesis). Ruhr-University Bochum.

Mandal, R., Sekaly, A. L. R., Murimboh, J., Hassan, N. M., Chakrabarti, C. L., Back, M. H., ... Schroeder, W. H. (1999a). Effect of the competition of copper and cobalt on the lability of Ni(II)–organic ligand complexes, Part II: in freshwaters (Rideau River surface waters). *Analytica Chimica Acta*, *395*(3), 323–334. doi: 10.1016/s0003-2670(99)00351-7

Mandal, R., Sekaly, A. L. R., Murimboh, J., Hassan, N. M., Chakrabarti, C. L., Back, M. H., ... Schroeder, W. H. (1999b). Effect of the competition of copper and cobalt on the lability of Ni(II)–organic ligand complexes. Part I. In model solutions containing Ni(II) and a well-characterized fulvic acid. *Analytica Chimica Acta*, *395*(3), 309–322. doi: 10.1016/s0003-2670(99)00350-5

Mariethoz, G., Kelly, B. F. J., & Baker, A. (2012). Quantifying the value of laminated stalagmites for paleoclimate reconstructions. *Geophysical Research Letters*, *39*(5). doi: 10.1029/2012gl050986

Markowska, M., Baker, A., Treble, P. C., Andersen, M. S., Hankin, S., Jex, C. N., ... Roach, R. (2015). Unsaturated zone hydrology and cave drip discharge water response: Implications for speleothem paleoclimate record variability. *Journal of Hydrology*, *529*, 662–675. doi: 10.1016/j.jhydrol.2014.12.044

Marsters, T. H., & Kennedy, D. M. (2014). Beach development on an uplifted coral atoll: Niue, south west Pacific. *Geomorphology*, *222*, 82–91. doi: 10.1016/j.geomorph.2014.03.003

Martín-García, R., Alonso-Zarza, A. M., & Martín-Pérez, A. (2009). Loss of primary texture and geochemical signatures in speleothems due to diagenesis: Evidences from Castañar Cave, Spain. *Sedimentary Geology*, *221*(1-4), 141–149. doi: 10.1016/j.sedgeo.2009.09.007

Mash, H. E., Chin, Y.-P., Sigg, L., Hari, R., & Xue, H. (2002). Complexation of Copper by Zwitterionic Aminosulfonic (Good) Buffers. *Analytical Chemistry*, *75*(3), 671–677. doi: 10.1021/ac0261101

Mattey, D. P., Fairchild, I. J., Atkinson, T. C., Latin, J.-P., Ainsworth, M., & Durell, R. (2010). Seasonal microclimate control of calcite fabrics, stable isotopes and trace elements in modern speleothem from St Michaels Cave, Gibraltar. *Geological Society, London, Special Publications*, *336*(1), 323–344. doi: 10.1144/sp336.17

Matthews, A., Ayalon, A., & Bar-Matthews, M. (2000). D/H ratios of fluid inclusions of Soreq cave (Israel) speleothems as a guide to the Eastern Mediterranean Meteoric Line relationships in the last 120 ky. *Chemical Geology*, *166*(3-4), 183–191. doi:

10.1016/s0009-2541(99)00192-8

Mavromatis, V., Goetschl, K. E., Grengg, C., Konrad, F., Purgstaller, B., & Dietzel, M. (2018). Barium partitioning in calcite and aragonite as a function of growth rate. *Geochimica et Cosmochimica Acta*, *237*, 65–78. doi: 10.1016/j.gca.2018.06.018

McCulloch, M. T., & Mortimer, G. E. (2008). Applications of the ^{238}U - ^{230}Th decay series to dating of fossil and modern corals using MC-ICPMS. *Australian Journal of Earth Sciences*, *55*(6-7), 955–965. doi: 10.1080/08120090802097435

McDermott, F. (2004). Palaeo-climate reconstruction from stable isotope variations in speleothems: a review. *Quaternary Science Reviews*, *23*(7-8), 901–918. doi: 10.1016/j.quascirev.2003.06.021

McDonald, J., Drysdale, R., & Hill, D. (2004). The 2002-2003 El Niño recorded in Australian cave drip waters: Implications for reconstructing rainfall histories using stalagmites. *Geophysical Research Letters*, *31*(22). doi: 10.1029/2004gl020859

McDonough, L. K., Treble, P. C., Baker, A., Borsato, A., Frisia, S., Nagra, G., ... Paterson, D. (2022). Past fires and post-fire impacts reconstructed from a southwest Australian stalagmite. *Geochimica et Cosmochimica Acta*, *325*, 258–277. doi: 10.1016/j.gca.2022.03.020

McGillen, M. R., & Fairchild, I. J. (2005). An experimental study of incongruent dissolution of $CaCO_3$ under analogue glacial conditions. *Journal of Glaciology*, *51*(174), 383–390. doi: 10.3189/172756505781829223

McGree, S., Schreider, S., & Kuleshov, Y. (2016). Trends and Variability in Droughts in the Pacific Islands and Northeast Australia. *Journal of Climate*, *29*(23), 8377–8397. doi: 10.1175/jcli-d-16-0332.1

McGregor, H. V., & Gagan, M. K. (2004). Western Pacific coral δ^{18}O records of anomalous Holocene variability in the El Niño-Southern Oscillation. *Geophysical Research Letters*, *31*(11), n/a–n/a. doi: 10.1029/2004gl019972

McKnight, D., Boyer, E., Westerhoff, P., Doran, P., Kulbe, T., & Andersen, D. (2001). Spectrofluorometric characterization of dissolved organic matter for indication of precursor organic material and aromaticity. *Limnology and Oceanography*, *46*(1), 38–48.

McMillan, E. A., Fairchild, I. J., Frisia, S., Borsato, A., & McDermott, F. (2005). Annual trace element cycles in calcite-aragonite speleothems: evidence of drought in the western Mediterranean 1200-1100 yr BP. *Journal of Quaternary Science*, *20*(5), 423–433. doi: 10.1002/jqs.943

Meira, G. R., Andrade, C., Alonso, C., Padaratz, I. J., & Jr, J. C. B. (2007). Salinity of marine aerosols in a Brazilian coastal area—Influence of wind regime. *Atmospheric Environment*, *41*(38), 8431–8441. doi: 10.1016/j.atmosenv.2007.07.004

Meyer, K. W., Feng, W., Breecker, D. O., Banner, J. L., & Guilfoyle, A. (2014). Interpretation of speleothem calcite δ^{13}C variations: Evidence from monitoring soil CO_2 , drip water, and

modern speleothem calcite in central Texas. *Geochimica et Cosmochimica Acta*, *142*, 281–298. doi: 10.1016/j.gca.2014.07.027

Meyer, M. C., Spötl, C., & Mangini, A. (2008). The demise of the Last Interglacial recorded in isotopically dated speleothems from the Alps. *Quaternary Science Reviews*, *27*(5-6), 476–496. doi: 10.1016/j.quascirev.2007.11.005

Mickler, P. J., Stern, L. A., & Banner, J. L. (2006). Large kinetic isotope effects in modern speleothems. *Geological Society of America Bulletin*, *118*(1-2), 65–81. doi: 10.1130/b25698.1

Millar, I. (2017). *Niue Cave Fauna: Report on a survey for subterranean species, October-November 2017. Report of Niue's Ridge to Reef Project: "Application of Ridge to Reef Concept for Biodiversity Conservation and for the Enhancement of Ecosystem Services and Cultural Heritage in Niue."* (Tech. Rep.). Global Environmental Facility.

Moerman, J. W., Cobb, K. M., Partin, J. W., Meckler, A. N., Carolin, S. A., Adkins, J. F., ... Tuen, A. A. (2014). Transformation of ENSO-related rainwater to dripwater δ^{18}O variability by vadose water mixing. *Geophysical Research Letters*, *41*(22), 7907–7915. doi: 10.1002/2014gl061696

Moffett, J. W. (1995). Temporal and spatial variability of copper complexation by strong chelators in the Sargasso Sea. *Deep Sea Research Part I: Oceanographic Research Papers*, *42*(8), 1273–1295. doi: 10.1016/0967-0637(95)00060-j

Morel, F. M. M., & Hering, J. G. (1993). *Principles and applications of aquatic chemistry*. Wiley, New York.

Moreno, A., Stoll, H., Jiménez-Sánchez, M., Cacho, I., Valero-Garcés, B., Ito, E., & Edwards, R. L. (2010). A speleothem record of glacial (25–11.6 kyr BP) rapid climatic changes from northern Iberian Peninsula. *Global and Planetary Change*, *71*(3-4), 218–231. doi: 10.1016/j.gloplacha.2009.10.002

Morioka, Y., Ratnam, J. V., Sasaki, W., & Masumoto, Y. (2013). Generation Mechanism of the South Pacific Subtropical Dipole. *Journal of Climate*, *26*(16), 6033–6045. doi: 10.1175/jcli-d-12-00648.1

Morse, J. W., & Bender, M. L. (1990). Partition coefficients in calcite: Examination of factors influencing the validity of experimental results and their application to natural systems. *Chemical Geology*, *82*, 265–277. doi: 10.1016/0009-2541(90)90085-l

Moy, C. M., Seltzer, G. O., Rodbell, D. T., & Anderson, D. M. (2002). Variability of El Niño/Southern Oscillation activity at millennial timescales during the Holocene epoch. *Nature*, *420*(6912), 162–165. doi: 10.1038/nature01194

Mucci, A., & Morse, J. W. (1983). The incorporation of Mg^{2+} and Sr^{2+} into calcite overgrowths: influences of growth rate and solution composition. *Geochimica et Cosmochimica Acta*, *47*(2), 217–233. doi: 10.1016/0016-7037(83)90135-7

Murgulet, V. (2010). *Paleoclimate reconstructions over the last century from a tropical*

speleothem on Niue Island, South Pacific (PhD Thesis). Department of Geological Sciences, The University of Alabama.

Mylroie, J. E., Jenson, J. W., Taborosi, D., Jocson, J. M. U., Vann, D. T., & Wexel, C. (2001). Karst features of Guam in terms of a general model of carbonate island karst. *Journal of Cave and Karst Studies*, *63*(1), 9–22.

Nava-Fernandez, C. E., Braun, T., Fox, B., Hartland, A., Kwiecien, O., Pederson, C., ... Breitenbach, S. F. M. (2022). Mid-Holocene rainfall changes in the southwestern Pacific. doi: 10.5194/cp-2021-172

Nava-Fernandez, C. E., Braun, T., Pederson, C. L., Fox, B., Hartland, A., Kwiecien, O., ... Breitenbach, S. F. M. (2024). Mid-Holocene rainfall seasonality and ENSO dynamics over the south-western Pacific. *The Depositional Record*. doi: 10.1002/dep2.268

Nehrke, G., Reichart, G. J., Cappellen, P. V., Meile, C., & Bijma, J. (2007). Dependence of calcite growth rate and Sr partitioning on solution stoichiometry: Non-Kossel crystal growth. *Geochimica et Cosmochimica Acta*, *71*(9), 2240–2249. doi: 10.1016/j.gca.2007.02.002

Newman, M., Alexander, M. A., Ault, T. R., Cobb, K. M., Deser, C., Lorenzo, E. D., ... Smith, C. A. (2016). The Pacific Decadal Oscillation, Revisited. *Journal of Climate*, *29*(12), 4399–4427. doi: 10.1175/jcli-d-15-0508.1

Niggemann, S., Mangini, A., Mudelsee, M., Richter, D. K., & Wurth, G. (2003). Sub-Milankovitch climatic cycles in Holocene stalagmites from Sauerland, Germany. *Earth and Planetary Science Letters*, *216*(4), 539–547. doi: 10.1016/s0012-821x(03)00513-2

Nimmo, M., & Fones, G. R. (1997). The potential pool of Co, Ni, Cu, Pb and Cd organic complexing ligands in coastal and urban rain waters. *Atmospheric Environment*, *31*(5), 693–702. doi: 10.1016/s1352-2310(96)00243-9

Noronha, A. L., Hardt, B. F., Banner, J. L., Jenson, J. W., Partin, J. W., James, E. W., ... Bautista, K. K. (2017). Trade winds drive pronounced seasonality in carbonate chemistry in a tropical Western Pacific island cave-Implications for speleothem paleoclimatology. *Geochemistry, Geophysics, Geosystems*, *18*(1), 384–399. doi: 10.1002/2016gc006644

Noronha, A. L., Johnson, K. R., Southon, J. R., Hu, C., Ruan, J., & McCabe-Glynn, S. (2015). Radiocarbon evidence for decomposition of aged organic matter in the vadose zone as the main source of speleothem carbon. *Quaternary Science Reviews*, *127*, 37–47. doi: 10.1016/j.quascirev.2015.05.021

Northup, D. E. (2011). Managing Microbial Communities in Caves. In P. van Beynen (Ed.), *Karst Management* (pp. 225–240). Springer Netherlands. doi: 10.1007/978-94-007-1207-2_10

Novello, V. F., Cruz, F. W., Vuille, M., Stríkis, N. M., Edwards, R. L., Cheng, H., ... Santos, R. V. (2017). A high-resolution history of the South American Monsoon from Last Glacial Maximum to the Holocene. *Scientific Reports*, *7*(1). doi: 10.1038/srep44267

Obert, J. C., Scholz, D., Felis, T., Brocas, W. M., Jochum, K. P., & Andreae, M. O. (2016). ^{230}Th/U dating of Last Interglacial brain corals from Bonaire (southern Caribbean) using bulk and theca wall material. *Geochimica et Cosmochimica Acta*, *178*, 20–40. doi: 10 .1016/j.gca.2016.01.011

O'Dowd, C. D., & de Leeuw, G. (2007). Marine aerosol production: a review of the current knowledge. *Philosophical Transactions of the Royal Society A: Mathematical, Physical and Engineering Sciences*, *365*(1856), 1753–1774. doi: 10.1098/rsta.2007.2043

Oomori, T., Kaneshima, H., Maezato, Y., & Kitano, Y. (1987). Distribution coefficient of Mg^{2+} ions between calcite and solution at 10 - 50 °C. *Marine Chemistry*, *20*(4), 327–336. doi: 10.1016/0304-4203(87)90066-1

Orland, I. J., Burstyn, Y., Bar-Matthews, M., Kozdon, R., Ayalon, A., Matthews, A., & Valley, J. W. (2014). Seasonal climate signals (1990 - 2008) in a modern Soreq Cave stalagmite as revealed by high-resolution geochemical analysis. *Chemical Geology*, *363*, 322–333. doi: 10.1016/j.chemgeo.2013.11.011

Ortega, R., Maire, R., Devès, G., & Quinif, Y. (2005). High-resolution mapping of uranium and other trace elements in recrystallized aragonite–calcite speleothems from caves in the Pyrenees (France): Implication for U-series dating. *Earth and Planetary Science Letters*, *237*(3-4), 911–923. doi: 10.1016/j.epsl.2005.06.045

Oster, J. L., Montañez, I. P., Guilderson, T. P., Sharp, W. D., & Banner, J. L. (2010). Modeling speleothem δ^{13}C variability in a central Sierra Nevada cave using ^{14}C and ^{87}Sr/^{86}Sr. *Geochimica et Cosmochimica Acta*, *74*(18), 5228–5242. doi: 10.1016/j.gca.2010.06.030

Owen, R. A., Day, C. C., Hu, C.-Y., Liu, Y.-H., Pointing, M. D., Blättler, C. L., & Henderson, G. M. (2016). Calcium isotopes in caves as a proxy for aridity: Modern calibration and application to the 8.2 kyr event. *Earth and Planetary Science Letters*, *443*, 129–138. doi: 10.1016/j.epsl.2016.03.027

Paquette, J., & Reeder, R. J. (1995). Relationship between surface structure, growth mechanism, and trace element incorporation in calcite. *Geochimica et Cosmochimica Acta*, *59*(4), 735–749. doi: 10.1016/0016-7037(95)00004-j

Parkhurst, D. L., & Apello, C. A. J. (1999). *User's Guide to PHREEQC (Version 2) –A Computer Program for Speciation, Batch-Reaction, One-Dimensional Transport, and Inverse Geochemical Calculations* (Tech. Rep. No. Water Resources Investigations Report 99). U.S. Geological Survey (USGS).

Paton, C., Hellstrom, J., Paul, B., Woodhead, J., & Hergt, J. (2011). Iolite: Freeware for the visualisation and processing of mass spectrometric data. *Journal of Analytical Atomic Spectrometry*, *26*(12), 2508. doi: 10.1039/c1ja10172b

Pearson, A. R., Hartland, A., Frisia, S., & Fox, B. R. S. (2020). Formation of calcite in the presence of dissolved organic matter: Partitioning, fabrics and fluorescence. *Chemical Geology*, *539*, 119492. doi: 10.1016/j.chemgeo.2020.119492

Pédrot, M., Dia, A., Davranche, M., Coz, M. B.-L., Henin, O., & Gruau, G. (2008). Insights into colloid-mediated trace element release at the soil/water interface. *Journal of Colloid and Interface Science*, *325*(1), 187–197. doi: 10.1016/j.jcis.2008.05.019

Perkins, S. E., Irving, D. B., Brown, J. R., Power, S. B., Moise, A. F., Colman, R. A., & Smith, I. (2012). CMIP3 ensemble climate projections over the western tropical Pacific based on model skill. *Climate Research*, *51*(1), 35–58. doi: 10.3354/cr01046

Perrin, C., Prestimonaco, L., Servelle, G., Tilhac, R., Maury, M., & Cabrol, P. (2014). Aragonite-Calcite Speleothems: Identifying Original and Diagenetic Features. *Journal of Sedimentary Research*, *84*(4), 245–269. doi: 10.2110/jsr.2014.17

Perrin, J. (2003). *A conceptual model of flow and transport in a karstaquifer based on spatial and temporal variations ofnatural tracers* (PhD Thesis). University of Lausanne, France.

Phillips, B. L., Zhang, Z., Kubista, L., Frisia, S., & Borsato, A. (2016). NMR spectroscopic study of organic phosphate esters coprecipitated with calcite. *Geochimica et Cosmochimica Acta*, *183*, 46–62. doi: 10.1016/j.gca.2016.03.022

Pilson, M. E. Q. (1998). *An Introduction to the Chemistry of the Sea*. Prentice Hall.

Pinto, J. G., Ulbrich, U., Leckebusch, G. C., Spangehl, T., Reyers, M., & Zacharias, S. (2007). Changes in storm track and cyclone activity in three SRES ensemble experiments with the ECHAM5/MPI-OM1 GCM. *Climate Dynamics*, *29*, 195–210.

Poulain, A., Watlet, A., Kaufmann, O., Camp, M. V., Jourde, H., Mazzilli, N., ... Hallet, V. (2018). Assessment of groundwater recharge processes through karst vadose zone by cave percolation monitoring. *Hydrological Processes*, *32*(13), 2069–2083. doi: 10.1002/hyp.13138

Pu, J., Wang, A., Shen, L., Yin, J., Yuan, D., & Zhao, H. (2016). Factors controlling the growth rate, carbon and oxygen isotope variation in modern calcite precipitation in a subtropical cave, Southwest China. *Journal of Asian Earth Sciences*, *119*, 167–178. doi: 10.1016/j.jseaes.2015.12.010

Qian, J., Xue, H. B., Sigg, L., & Albrecht, A. (1998). Complexation of Cobalt by Natural Ligands in Freshwater. *Environmental Science & Technology*, *32*(14), 2043–2050. doi: 10.1021/es971018l

Qu, C., Liu, G., & Zhao, Y. (2009). Experimental study on the fractionation of yttrium from holmium during the coprecipitation with calcium carbonates in seawater solutions. *Geochemical Journal*, *43*(6), 403–414. doi: 10.2343/geochemj.1.0036

Quiers, M., Perrette, Y., Chalmin, E., Fanget, B., & Poulenard, J. (2015). Geochemical mapping of organic carbon in stalagmites using liquid-phase and solid-phase fluorescence. *Chemical Geology*, *411*, 240–247. doi: 10.1016/j.chemgeo.2015.07.012

Ramseyer, K., Miano, T. M., D'orazio, V., Wildberger, A., Wagner, T., & Geister, J. (1997). Nature and origin of organic matter in carbonates from speleothems, marine cements and coral skeletons. *Organic Geochemistry*, *26*(5-6), 361–378. doi: 10.1016/s0146-6380(97)

00008-9

Rasband, W. S. (2012). *ImageJ* (Tech. Rep.). National Institutes of Health, Bethesda, Maryland, USA.

Rasbury, M., & Aharon, P. (2006). ENSO-controlled rainfall variability records archived in tropical stalagmites from the mid-ocean island of Niue, South Pacific. *Geochemistry, Geophysics, Geosystems*, *7*(7). doi: 10.1029/2005gc001232

Rate, A. W., McLaren, R. G., & Swift, R. S. (1992). Evaluation of log-normal distribution first-order kinetic model for copper(II)-humic acid complex dissociation. *Environmental Science & Technology*, *26*(12), 2477–2483. doi: 10.1021/es00036a021

Rate, A. W., McLaren, R. G., & Swift, R. S. (1993). Response of copper(II)-humic acid dissociation kinetics to factors influencing complex stability and macromolecular conformation. *Environmental Science & Technology*, *27*(7), 1408–1414. doi: 10.1021/es00044a017

Ravelo, A. C., Dekens, P. S., & McCarthy, M. (2006). Evidence for El Niño–like conditions during the Pliocene. *GSA Today*, *16*(3), 4. doi: 10.1130/1052-5173(2006)016<4:efenlc>2.0.co;2

Reeder, R. J., & Grams, J. C. (1987). Sector zoning in calcite cement crystals: Implications for trace element distributions in carbonates. *Geochimica et Cosmochimica Acta*, *51*(2), 187–194. doi: 10.1016/0016-7037(87)90230-4

Reeder, R. J., Valley, J. W., Graham, C. M., & Eiler, J. M. (1997). Ion microprobe study of oxygen isotopic compositions of structurally nonequivalent growth surfaces on synthetic calcite. *Geochimica et Cosmochimica Acta*, *61*(23), 5057–5063. doi: 10.1016/s0016-7037(97)00309-8

Reimer, P. J., Bard, E., Bayliss, A., Beck, J. W., Blackwell, P. G., Ramsey, C. B., ... van der Plicht, J. (2013). IntCal13 and Marine13 Radiocarbon Age Calibration Curves 0–50,000 Years cal BP. *Radiocarbon*, *55*(4), 1869–1887. doi: 10.2458/azu_js_rc.55.16947

Reynard, L. M., Day, C. C., & Henderson, G. M. (2011). Large fractionation of calcium isotopes during cave-analogue calcium carbonate growth. *Geochimica et Cosmochimica Acta*, *75*(13), 3726–3740. doi: 10.1016/j.gca.2011.04.010

Richards, D. A., Bottrell, S. H., Cliff, R. A., Ströhle, K., & Rowe, P. J. (1998). U-Pb dating of a speleothem of Quaternary age. *Geochimica et Cosmochimica Acta*, *62*(23-24), 3683–3688. doi: 10.1016/s0016-7037(98)00256-7

Richards, D. A., & Dorale, J. A. (2003). Uranium-series Chronology and Environmental Applications of Speleothems. *Reviews in Mineralogy and Geochemistry*, *52*(1), 407–460. doi: 10.2113/0520407

Richter, D. K., Gotte, T., Niggemann, S., & Wurth, G. (2004). REE^{3+} and Mn^{2+} activated cathodoluminescence in lateglacial and Holocene stalagmites of central Europe: evidence for climatic processes? *The Holocene*, *14*(5), 759–768. doi: 10.1191/0959683604hl754rp

Riechelmann, S., Schröder-Ritzrau, A., Wassenburg, J. A., Schreuer, J., Richter, D. K., Riechelmann, D. F. C., ... Immenhauser, A. (2014). Physicochemical characteristics of drip waters: Influence on mineralogy and crystal morphology of recent cave carbonate precipitates. *Geochimica et Cosmochimica Acta*, *145*, 13–29. doi: 10.1016/j.gca.2014.09.019

Rieuwerts, J. S., Thornton, I., Farago, M. E., & Ashmore, M. R. (1998). Factors influencing metal bioavailability in soils: preliminary investigations for the development of a critical loads approach for metals. *Chemical Speciation & Bioavailability*, *10*(2), 61–75. doi: 10.3184/095422998782775835

Rimstidt, J. D., Balog, A., & Webb, J. (1998). Distribution of trace elements between carbonate minerals and aqueous solutions. *Geochimica et Cosmochimica Acta*, *62*(11), 1851–1863. doi: 10.1016/s0016-7037(98)00125-2

Roberts, M. S., Smart, P. L., & Baker, A. (1998). Annual trace element variations in a Holocene speleothem. *Earth and Planetary Science Letters*, *154*(1-4), 237–246. doi: 10.1016/s0012-821x(97)00116-7

Roebroeks, W., & Villa, P. (2011). On the earliest evidence for habitual use of fire in Europe. *Proceedings of the National Academy of Sciences*, *108*(13), 5209–5214. doi: 10.1073/pnas.1018116108

Romanov, D., Kaufmann, G., & Dreybrodt, W. (2008). Modeling stalagmite growth by first principles of chemistry and physics of calcite precipitation. *Geochimica et Cosmochimica Acta*, *72*(2), 423–437. doi: 10.1016/j.gca.2007.09.038

Ronay, E. R., Breitenbach, S. F. M., & Oster, J. L. (2019). Sensitivity of speleothem records in the Indian Summer Monsoon region to dry season infiltration. *Scientific Reports*, *9*(1). doi: 10.1038/s41598-019-41630-2

Rose, A. L., & Waite, T. D. (2003). Kinetics of iron complexation by dissolved natural organic matter in coastal waters. *Marine Chemistry*, *84*(1-2), 85–103. doi: 10.1016/s0304-4203(03)00113-0

Rutlidge, H., Andersen, M. S., Baker, A., Chinu, K. J., Cuthbert, M. O., Jex, C. N., ... Rau, G. C. (2015). Organic characterisation of cave drip water by LC-OCD and fluorescence analysis. *Geochimica et Cosmochimica Acta*, *166*, 15–28. doi: 10.1016/j.gca.2015.05.042

Ryang, H.-M., & Sim, H.-C. (2019). Formation of $CaCO_3$ varieties from a carbonated aqueous solution. *Carbonates and Evaporites*, *34*(4), 1619–1626. doi: 10.1007/s13146-019-00510-6

Salati, E., Dall'Olio, A., Matsui, E., & Gat, J. R. (1979). Recycling of water in the Amazon Basin: An isotopic study. *Water Resources Research*, *15*(5), 1250–1258. doi: 10.1029/wr015i005p01250

Sanders, J. R., & Bloomfield, C. (1980). The influence of pH, ionic strength and reactant concentrations on copper complexing by humified organic matter. *Journal of Soil Science*,

31(1), 53–63. doi: 10.1111/j.1365-2389.1980.tb02064.x

Sangwal, K. (1996). Effects of impurities on crystal growth processes. *Progress in Crystal Growth and Characterization of Materials*, *32*(1-3), 3–43. doi: 10.1016/0960-8974(96)00008-3

Saunders, P., Rogerson, M., Wadhawan, J. D., Greenway, G., & Pedley, H. M. (2014). Mg/Ca ratios in freshwater microbial carbonates: Thermodynamic, kinetic and vital effects. *Geochimica et Cosmochimica Acta*, *147*, 107–118. doi: 10.1016/j.gca.2014.10.014

Sawagaki, T., Miura, H., & Iwasaki, S. (2008). Discovery of an ice cave in the Yatude Valley, Langhovde, Dronning Maud Land, East Antarctica. *Polar Science*, *2*(4), 287–294. doi: 10.1016/j.polar.2008.10.002

Scally, S., Davison, W., & Zhang, H. (2003). *In Situ* Measurements of Dissociation Kinetics and Labilities of Metal Complexes in Solution Using DGT. *Environmental Science & Technology*, *37*, 1379–1384.

Schaetzl, R. J., Bettis, E. A., Crouvi, O., Fitzsimmons, K. E., Grimley, D. A., Hambach, U., ... Zech, R. (2018). Approaches and challenges to the study of loess – Introduction to the LoessFest Special Issue. *Quaternary Research*, *89*(3), 563–618. doi: 10.1017/qua.2018.15

Scholz, D., & Hoffmann, D. L. (2008). ^{230}Th/U-dating of fossil corals and speleothems. *Quaternary Science Journal*, *57*(1–2), 52–76.

Schroeder, J. H. (1969). Experimental Dissolution of Calcium, Magnesium, and Strontium from Recent Biogenic Carbonates: A Model of Diagenesis. *SEPM Journal of Sedimentary Research*, *Vol. 39*. doi: 10.1306/74d71d98-2b21-11d7-8648000102c1865d

Schwarcz, H. P., Harmon, R. S., Thompson, P., & Ford, D. C. (1976). Stable isotope studies of fluid inclusions in speleothems and their paleoclimatic significance. *Geochimica et Cosmochimica Acta*, *40*(6), 657–665. doi: 10.1016/0016-7037(76)90111-3

Sekaly, A. L. R., Mandal, R., Hassan, N. M., Murimboh, J., Chakrabarti, C. L., Back, M. H., ... Schroeder, W. H. (1999). Effect of metal/fulvic acid mole ratios on the binding of Ni(II), Pb(II), Cu(II), Cd(II), and Al(III) by two well-characterized fulvic acids in aqueous model solutions. *Analytica Chimica Acta*, *402*(1-2), 211–221. doi: 10.1016/s0003-2670(99)00534-6

Sekaly, A. L. R., Murimboh, J., Hassan, N. M., Mandal, R., Younes, M. E. B., Chakrabarti, C. L., ... Grégoire, D. C. (2003). Kinetic Speciation of Co(II), Ni(II), Cu(II), and Zn(II) in Model Solutions and Freshwaters: Lability and the d Electron Configuration. *Environmental Science & Technology*, *37*(1), 68–74. doi: 10.1021/es025805g

Shafaei Arvajeh, M. R., Lehto, N., Garmo, Ø. A., & Zhang, H. (2012). Kinetic Studies of Ni Organic Complexes Using Diffusive Gradients in Thin Films (DGT) with Double Binding Layers and a Dynamic Numerical Model. *Environmental Science & Technology*, *47*(1), 463–470. doi: 10.1021/es301371b

Shen, C.-C., Li, K.-S., Sieh, K., Natawidjaja, D., Cheng, H., Wang, X., ... Kilbourne, K. H. (2008). Variation of initial $^{230}Th/^{232}Th$ and limits of high precision U–Th dating of shallow-water corals. *Geochimica et Cosmochimica Acta*, *72*(17), 4201–4223. doi: 10.1016/j.gca.2008.06.011

Shi, Z., Wang, P., Peng, L., Lin, Z., & Dang, Z. (2016). Kinetics of Heavy Metal Dissociation from Natural Organic Matter: Roles of the Carboxylic and Phenolic Sites. *Environmental Science & Technology*, *50*(19), 10476–10484. doi: 10.1021/acs.est.6b01809

Sholkovitz, E. R. (1995). The aquatic chemistry of rare earth elements in rivers and estuaries. *Aquatic Geochemistry*, *1*(1), 1–34. doi: 10.1007/bf01025229

Siegenthaler, U. (1979). Stable Hydrogen and Oxygen Isotopes in the Water Cycle. In E. Jäger & J. C. Hunziker (Eds.), *Lectures in Isotope Geology* (pp. 264–273). Berlin, Heidelberg: Springer Berlin Heidelberg.

Sigg, L., & Behra, R. (2005). Metal Ions In Biological Systems. In A. Sigel, H. Sigel, & R. K. O. Sigel (Eds.), (Vol. 44, chap. Speciation and Bioavailability of Trace Metals in Freshwater Environments). CRC Press.

Sigg, L., Black, F., Buffle, J., Cao, J., Cleven, R., Davison, W., ... Zhang, H. (2006). Comparison of Analytical Techniques for Dynamic Trace Metal Speciation in Natural Freshwaters. *Environmental Science & Technology*.

Sinclair, D. J. (2011). Two mathematical models of Mg and Sr partitioning into solution during incongruent calcite dissolution. *Chemical Geology*, *283*(3-4), 119–133. doi: 10.1016/j.chemgeo.2010.05.022

Sinclair, D. J., Banner, J. L., Taylor, F. W., Partin, J., Jenson, J., Mylroie, J., ... Miklavič, B. (2012). Magnesium and strontium systematics in tropical speleothems from the Western Pacific. *Chemical Geology*, *294-295*, 1–17. doi: 10.1016/j.chemgeo.2011.10.008

Sivry, Y., Riotte, J., & Dupre, B. (2006). Study of exchangeable metal on colloidal humic acids and particulate matter by coupling ultrafiltration and isotopic tracers: Application to natural waters. *Journal of Geochemical Exploration*, *88*, 144–147.

Sliwinski, J. T., Kost, O., Endres, L., Iglesias, M., Haghipour, N., González-Lemos, S., & Stoll, H. M. (2022). Exploring soluble and colloidally transported trace elements in stalagmites: the strontium-yttrium connection. *Geochimica et Cosmochimica Acta*. doi: 10.1016/j.gca.2022.12.023

Sliwinski, J. T., & Stoll, H. M. (2021). Combined fluorescence imaging and LA-ICP-MS trace element mapping of stalagmites: Microfabric identification and interpretation. *Chemical Geology*, *581*, 120397. doi: 10.1016/j.chemgeo.2021.120397

Smart, P. L., & Friederich, H. (1986). Water movement and storage in the unsaturated zone of a maturely karstified aquifer..

Smith, A. J., Nelson, T., Ratnarajah, L., Genovese, C., Westwood, K., Holmes, T. M., ... Lannuzel, D. (2022). Identifying potential sources of iron-binding ligands in coastal Antarc-

tic environments and the wider Southern Ocean. *Frontiers in Marine Science*, *9*. doi: 10.3389/fmars.2022.948772

Smith, C. L., Baker, A., Fairchild, I. J., Frisia, S., & Borsato, A. (2006). Reconstructing hemispheric-scale climates from multiple stalagmite records. *International Journal of Climatology*, *26*(10), 1417–1424. doi: 10.1002/joc.1329

Soulsby, J. A. (2004). Niue Island, Geographical Perspectives on the Rock of Polynesia. In J. P. Terry & W. E. Murray (Eds.), (pp. 89–112). International Scientific Council For Island Development.

Spötl, C., & Boch, R. (2019). Uranium series dating of speleothems. In *Encyclopedia of Caves* (pp. 1096–1102). Elsevier. doi: 10.1016/b978-0-12-814124-3.00128-x

Spötl, C., Fairchild, I. J., & Tooth, A. F. (2005). Cave air control on dripwater geochemistry, Obir Caves (Austria): Implications for speleothem deposition in dynamically ventilated caves. *Geochimica et Cosmochimica Acta*, *69*(10), 2451–2468. doi: 10.1016/j.gca.2004.12.009

Spötl, C., & Mangini, A. (2007). Speleothems and paleoglaciers. *Earth and Planetary Science Letters*, *254*(3-4), 323–331. doi: 10.1016/j.epsl.2006.11.041

Staddon, P. L. (2004). Carbon isotopes in functional soil ecology. *Trends in Ecology & Evolution*, *19*(3), 148–154. doi: 10.1016/j.tree.2003.12.003

Stedmon, C. A., & Bro, R. (2008). Characterizing dissolved organic matter fluorescence with parallel factor analysis: a tutorial. *Limnology and Oceanography: Methods*, *6*(11), 572–579. doi: 10.4319/lom.2008.6.572

Stedmon, C. A., Markager, S., & Kaas, H. (2000). Optical Properties and Signatures of Chromophoric Dissolved Organic Matter (CDOM) in Danish Coastal Waters. *Estuarine, Coastal and Shelf Science*, *51*(2), 267–278. doi: 10.1006/ecss.2000.0645

Steefel, C. I., & Cappellen, P. V. (1990). A new kinetic approach to modeling water-rock interaction: The role of nucleation, precursors, and Ostwald ripening. *Geochimica et Cosmochimica Acta*, *54*(10), 2657–2677. doi: 10.1016/0016-7037(90)90003-4

Stern, J. C., Sonke, J. E., & Salters, V. J. M. (2007). A capillary electrophoresis-ICP-MS study of rare earth element complexation by humic acids. *Chemical Geology*, *246*, 170–180.

Stoll, H. M., Müller, W., & Prieto, M. (2012). I-STAL, a model for interpretation of Mg/Ca, Sr/Ca and Ba/Ca variations in speleothems and its forward and inverse application on seasonal to millennial scales. *Geochemistry, Geophysics, Geosystems*, *13*(9). doi: 10.1029/2012gc004183

Stolpe, B., Hassellöv, M., Andersson, K., & Turner, D. R. (2005). High resolution ICPMS as an on-line detector for flow field-flow fractionation; multi-element determination of colloidal size distributions in a natural water sample. *Analytica Chimica Acta*, *535*(1-2), 109–121. doi: 10.1016/j.aca.2004.11.067

Stumm, W., & Morgan, J. J. (1996). *Aquatic chemistry*. Wiley.

Sunagawa, I. (1999). Growth and Morphology of Crystals..

Swart, N. C., Fyfe, J. C., Gillett, N., & Marshall, G. J. (2015). Comparing Trends in the Southern Annular Mode and Surface Westerly Jet. *Journal of Climate*, *28*(22), 8840–8859. doi: 10.1175/jcli-d-15-0334.1

Swindles, G. T., Patterson, R. T., Roe, H. M., & Galloway, J. M. (2012). Evaluating periodicities in peat-based climate proxy records. *Quaternary Science Reviews*, *41*, 94–103. doi: 10.1016/j.quascirev.2012.03.003

Tadros, C. V., Markowska, M., Treble, P. C., Baker, A., Frisia, S., Adler, L., & Drysdale, R. N. (2022). Recharge variability in Australia's southeast alpine region derived from cave monitoring and modern stalagmite δ^{18}O records. *Quaternary Science Reviews*, *295*, 107742. doi: 10.1016/j.quascirev.2022.107742

Tadros, C. V., Treble, P. C., Baker, A., Fairchild, I., Hankin, S., Roach, R., ... McDonald, J. (2016). ENSO - cave dripwater hydrochemical relationship: a 7-year dataset from SE Australia. *Hydrology and Earth System Sciences Discussions*, 1–27. doi: 10.5194/hess-2016-201

Tadros, C. V., Treble, P. C., Baker, A., Hankin, S., & Roach, R. (2019). Cave drip water solutes in south-eastern Australia: Constraining sources, sinks and processes. *Science of The Total Environment*, *651*, 2175–2186. doi: 10.1016/j.scitotenv.2018.10.035

Tan, M., Baker, A., Genty, D., Smith, C., Esper, J., & Cai, B. (2006). Applications of stalagmite laminae to paleoclimate reconstructions: Comparison with dendrochronology/climatology. *Quaternary Science Reviews*, *25*(17-18), 2103–2117. doi: 10.1016/j.quascirev.2006.01.034

Tang, J., & Johannesson, K. H. (2003). Speciation of rare earth elements in natural terrestrial waters: assessing the role of dissolved organic matter from the modeling approach. *Geochimica et Cosmochimica Acta*, *67*(13), 2321–2339. doi: 10.1016/s0016-7037(02)01413-8

Tebo, B. M., Davis, R. E., Anitori, R. P., Connell, L. B., Schiffman, P., & Staudigel, H. (2015). Microbial communities in dark oligotrophic volcanic ice cave ecosystems of Mt. Erebus, Antarctica. *Frontiers in Microbiology*, *6*. doi: 10.3389/fmicb.2015.00179

Terakado, Y., & Masuda, A. (1988). The coprecipitation of rare-earth elements with calcite and aragonite. *Chemical Geology*, *69*(1-2), 103–110. doi: 10.1016/0009-2541(88)90162-3

Terry, J. P. (2004). Niue Island, Geographical Perspectives on the Rock of Polynesia. In J. P. Terry & W. E. Murray (Eds.), (pp. 75–88). International Scientific Council For Island Development.

Tesoriero, A. J., & Pankow, J. F. (1996). Solid solution partitioning of Sr^{2+}, Ba^{2+}, and Cd^{2+} to calcite. *Geochimica et Cosmochimica Acta*, *60*(6), 1053–1063. doi: 10.1016/0016-7037(95)00449-1

The Global Climate Change Alliance Plus Initiative. (2019). *Climate change profile: Niue*

(Version 1) (Tech. Rep.). Author.

Tipping, E. (2002). *Cation binding by humic substances*. Cambridge University Press, Cambridge.

Tomczyk-Żak, K., & Zielenkiewicz, U. (2016). Microbial Diversity in Caves. *Geomicrobiology Journal*, *33*(1), 20–38. doi: 10.1080/01490451.2014.1003341

Tomkins, P. (2009). Domesticity by default. Ritual, ritualization and cave-use in the Neolithic Aegean. *Oxford Journal of Archaeology*, *28*(2), 125–153. doi: 10.1111/j.1468-0092.2009.00322.x

Tooth, A. F., & Fairchild, I. J. (2003). Soil and karst aquifer hydrological controls on the geochemical evolution of speleothem-forming drip waters, Crag Cave, southwest Ireland. *Journal of Hydrology*, *273*(1-4), 51–68. doi: 10.1016/s0022-1694(02)00349-9

Town, R. M. (2008). Metal Binding by Heterogeneous Ligands: Kinetic Master Curves from SSCP Waves. *Environmental Science & Technology*, *42*(11), 4014–4021. doi: 10.1021/es703236b

Town, R. M., van Leeuwen, H. P., & Buffle, J. (2012). Chemodynamics of Soft Nanoparticulate Complexes: Cu(II) and Ni(II) Complexes with Fulvic Acids and Aquatic Humic Acids. *Environmental Science & Technology*, *46*(19), 10487–10498. doi: 10.1021/es3018013

Treble, P. C., Baker, A., Abram, N. J., Hellstrom, J. C., Crawford, J., Gagan, M. K., ... Paterson, D. (2022). Ubiquitous karst hydrological control on speleothem oxygen isotope variability in a global study. *Communications Earth and Environment*, *3*(1). doi: 10.1038/s43247-022-00347-3

Treble, P. C., Chappell, J., & Shelley, J. M. G. (2005). Complex speleothem growth processes revealed by trace element mapping and scanning electron microscopy of annual layers. *Geochimica et Cosmochimica Acta*, *69*(20), 4855–4863. doi: 10.1016/j.gca.2005.06.008

Treble, P. C., Fairchild, I. J., Baker, A., Meredith, K. T., Andersen, M. S., Salmon, S. U., ... McGuire, E. (2016). Roles of forest bioproductivity, transpiration and fire in a nine-year record of cave dripwater chemistry from southwest Australia. *Geochimica et Cosmochimica Acta*, *184*, 132–150. doi: 10.1016/j.gca.2016.04.017

Treble, P. C., Fairchild, I. J., Griffiths, A., Baker, A., Meredith, K. T., Wood, A., & McGuire, E. (2015). Impacts of cave air ventilation and in-cave prior calcite precipitation on Golgotha Cave dripwater chemistry, southwest Australia. *Quaternary Science Reviews*, *127*, 61–72. doi: 10.1016/j.quascirev.2015.06.001

Treble, P. C., Shelley, J. M. G., & Chappell, J. (2003). Comparison of high resolution sub-annual records of trace elements in a modern (1911–1992) speleothem with instrumental climate data from southwest Australia. *Earth and Planetary Science Letters*, *216*(1-2), 141–153. doi: 10.1016/s0012-821x(03)00504-1

Tremaine, D. M., & Froelich, P. N. (2013). Speleothem trace element signatures: A hydrologic geochemical study of modern cave dripwaters and farmed calcite. *Geochimica et*

Cosmochimica Acta, *121*, 522–545. doi: 10.1016/j.gca.2013.07.026

Tremaine, D. M., Sinclair, D. J., Stoll, H. M., Lagerström, M., Carvajal, C. P., & Sherrell, R. M. (2016). A two-year automated dripwater chemistry study in a remote cave in the tropical south Pacific: Using [Cl^-] as a conservative tracer for seasalt contribution of major cations. *Geochimica et Cosmochimica Acta*, *184*, 289–310. doi: 10.1016/j.gca.2016.03.029

Tudhope, A. W. (2001). Variability in the El Niño-Southern Oscillation Through a Glacial-Interglacial Cycle. *Science*, *291*(5508), 1511–1517. doi: 10.1126/science.1057969

Uemura, R., Nakamoto, M., Asami, R., Mishima, S., Gibo, M., Masaka, K., … Shen, C.-C. (2016). Precise oxygen and hydrogen isotope determination in nanoliter quantities of speleothem inclusion water by cavity ring-down spectroscopic techniques. *Geochimica et Cosmochimica Acta*, *172*, 159–176. doi: 10.1016/j.gca.2015.09.017

Ummenhofer, C. C., & England, M. H. (2007). Interannual Extremes in New Zealand Precipitation Linked to Modes of Southern Hemisphere Climate Variability. *Journal of Climate*, *20*(21), 5418–5440. doi: 10.1175/2007jcli1430.1

Ure, M., Thomas, R., & Littlejohn, D. (1993). Ammonium Acetate Extracts and Their Analysis for the Speciation of Metal Ions in Soils and Sediments. *International Journal of Environmental Analytical Chemistry*, *51*(1-4), 65–84. doi: 10.1080/03067319308027612

Valladas, H., Clottes, J., Geneste, J.-M., Garcia, M. A., Arnold, M., Cachier, H., & Tisnérat-Laborde, N. (2001). Evolution of prehistoric cave art. *Nature*, *413*(6855), 479–479.

van Leeuwen, H. P., & Buffle, J. (2009). Chemodynamics of Aquatic Metal Complexes: From Small Ligands to Colloids. *Environmental Science & Technology*, *43*(19), 7175–7183. doi: 10.1021/es900894h

van Leeuwen, H. P., & Jansen, S. (2005). Dynamic aspects of metal speciation by competitive ligand exchange–adsorptive stripping voltammetry (CLE–AdSV). *Journal of Electroanalytical Chemistry*, *579*(2), 337–342. doi: 10.1016/j.jelechem.2005.03.006

Vesper, D. J. (2012). Contamination of Cave Waters by Heavy Metals. In *Encyclopedia of caves* (pp. 161–166). Elsevier. doi: 10.1016/b978-0-12-383832-2.00024-4

Virtanen, P., Gommers, R., Oliphant, T. E., Haberland, M., Reddy, T., Cournapeau, D., … Vázquez-Baeza, Y. (2020). SciPy 1.0: Fundamental Algorithms for Scientific Computing in Python. *Nature Methods*, *17*, 261–272. doi: 10.1038/s41592-019-0686-2

Vogel, J. C., Lerman, J. C., Mook, W. G., & Roberts, F. B. (1972). Natural isotopes in the groundwater of the Tulúm Valley, San Juan, Argentina. *Hydrological Sciences Bulletin*, *17*(1), 85–96. doi: 10.1080/02626667209493805

Voigt, M., Mavromatis, V., & Oelkers, E. H. (2017). The experimental determination of REE partition coefficients in the water-calcite system. *Chemical Geology*, *462*, 30–43. doi: 10.1016/j.chemgeo.2017.04.024

Vonhof, H. B., van Breukelen, M. R., Postma, O., Rowe, P. J., Atkinson, T. C., & Kroon, D.

(2006). A continuous-flow crushing device for on-line δ^2H analysis of fluid inclusion water in speleothems. *Rapid Communications in Mass Spectrometry*, *20*(17), 2553–2558. doi: 10.1002/rcm.2618

Vuille, M., & Werner, M. (2005). Stable isotopes in precipitation recording South American summer monsoon and ENSO variability: observations and model results. *Climate Dynamics*, *25*(4), 401–413. doi: 10.1007/s00382-005-0049-9

Wang, C., Deser, C., Yu, J.-Y., DiNezio, P., & Clement, A. (2016). El Niño and Southern Oscillation (ENSO): A Review. In *Coral reefs of the eastern tropical pacific* (pp. 85–106). Springer Nature. doi: 10.1007/978-94-017-7499-4_4

Wang, R., & Chakrabarti, C. L. (2008). Copper speciation by competing ligand exchange method using differential pulse anodic stripping voltammetry with ethylenediaminetetraacetic acid (EDTA) as competing ligand. *Analytica Chimica Acta*, *614*(2), 153–160. doi: 10.1016/j.aca.2008.03.007

Wang, X., Auler, A. S., Edwards, R. L., Cheng, H., Cristalli, P. S., Smart, P. L., ... Shen, C.-C. (2004). Wet periods in northeastern Brazil over the past 210 kyr linked to distant climate anomalies. *Nature*, *432*(7018), 740–743. doi: 10.1038/nature03067

Wang, Y., & Xu, H. (2001). Prediction of trace metal partitioning between minerals and aqueous solutions: a linear free energy correlation approach. *Geochimica et Cosmochimica Acta*, *65*(10), 1529–1543. doi: 10.1016/s0016-7037(01)00551-8

Wang, Z., Chen, J., Cai, H., Yuan, W., & Yuan, S. (2021). Coprecipitation of metal ions into calcite: an estimation of partition coefficients based on field investigation. *Acta Geochimica*, *40*(1), 67–77. doi: 10.1007/s11631-020-00443-1

Wanner, H., Beer, J., Bütikofer, J., Crowley, T. J., Cubasch, U., Flückiger, J., ... Widmann, M. (2008). Mid- to Late Holocene climate change: an overview. *Quaternary Science Reviews*, *27*(19-20), 1791–1828. doi: 10.1016/j.quascirev.2008.06.013

Wanner, H., Mercolli, L., Grosjean, M., & Ritz, S. P. (2014). Holocene climate variability and change; a data-based review. *Journal of the Geological Society*, *172*(2), 254–263. doi: 10.1144/jgs2013-101

Wanner, H., Solomina, O., Grosjean, M., Ritz, S. P., & Jetel, M. (2011). Structure and origin of Holocene cold events. *Quaternary Science Reviews*, *30*(21-22), 3109–3123. doi: 10.1016/j.quascirev.2011.07.010

Warken, S. F., Fohlmeister, J., Schröder-Ritzrau, A., Constantin, S., Spötl, C., Gerdes, A., ... Scholz, D. (2018). Reconstruction of late Holocene autumn/winter precipitation variability in SW Romania from a high-resolution speleothem trace element record. *Earth and Planetary Science Letters*, *499*, 122–133. doi: 10.1016/j.epsl.2018.07.027

Warken, S. F., Kuchalski, L., Schröder-Ritzrau, A., Vieten, R., Schmidt, M., Höpker, S. N., ... Frank, N. (2022). The impact of seasonal and event-based infiltration on transition metals (Cu, Ni, Co) in tropical cave drip water. *Rapid Communications in Mass Spectrometry*,

36(10). doi: 10.1002/rcm.9278

Warken, S. F., Weißbach, T., Kluge, T., Vonhof, H., Scholz, D., Vieten, R., ... Frank, N. (2022). Last glacial millennial-scale hydro-climate and temperature changes in Puerto Rico constrained by speleothem fluid inclusion δ^{18}O and δ^{2}H values. *Climate of the Past*, *18*(1), 167–181. doi: 10.5194/cp-18-167-2022

Warnken, K. W., Davison, W., Zhang, H., Galceran, J., & Puy, J. (2007). *In Situ* Measurements of Metal Complex Exchange Kinetics in Freshwater. *Environmental Science & Technology*, *41*(9), 3179–3185. doi: 10.1021/es062474p

Wassenburg, J. A., Riechelmann, S., Schröder-Ritzrau, A., Riechelmann, D. F. C., Richter, D. K., Immenhauser, A., ... Scholz, D. (2020). Calcite Mg and Sr partition coefficients in cave environments: Implications for interpreting prior calcite precipitation in speleothems. *Geochimica et Cosmochimica Acta*, *269*, 581–596. doi: 10.1016/j.gca.2019.11.011

Wasylenki, L. E., Dove, P. M., & Yoreo, J. J. D. (2005). Effects of temperature and transport conditions on calcite growth in the presence of Mg^{2+}: Implications for paleothermometry. *Geochimica et Cosmochimica Acta*, *69*(17), 4227–4236. doi: 10.1016/j.gca.2005.04.006

Watanabe, T., Winter, A., Oba, T., Anzai, R., & Ishioroshi, H. (2002). Evaluation of the fidelity of isotope records as an environmental proxy in the coral Montastraea. *Coral Reefs*, *21*(2), 169–178.

Watson, E. B. (2004). A conceptual model for near-surface kinetic controls on the trace-element and stable isotope composition of abiogenic calcite crystals. *Geochimica et Cosmochimica Acta*, *68*(7), 1473–1488. doi: 10.1016/j.gca.2003.10.003

Weishaar, J. L., Aiken, G. R., Bergamaschi, B. A., Fram, M. S., Fujii, R., & Mopper, K. (2003). Evaluation of Specific Ultraviolet Absorbance as an Indicator of the Chemical Composition and Reactivity of Dissolved Organic Carbon. *Environmental Science & Technology*, *37*(20), 4702–4708. doi: 10.1021/es030360x

Welikala, D., Hucker, C., Hartland, A., Robinson, B. H., & Lehto, N. J. (2018). Trace metal mobilization by organic soil amendments: insights gained from analyses of solid and solution phase complexation of cadmium, nickel and zinc. *Chemosphere*, *199*, 684–693. doi: 10.1016/j.chemosphere.2018.02.069

Wheeler, C. W., & Aharon, P. (1997). Geology and Hydrogeology of Niue. In *Developments in Sedimentology* (pp. 537–564). Elsevier. doi: 10.1016/s0070-4571(04)80039-6

Wheeler, C. W., Aharon, P., & Ferrell, R. E. (1999). Successions of late Cenozoic platform dolomites distinguished by texture, geochemistry, and crystal chemistry; Niue, South Pacific. *Journal of Sedimentary Research*, *69*(1), 239–255. doi: 10.2110/jsr.69.239

Whitehead, N. E., Hunt, J., Leslie, D., & Rankin, P. (1993). The elemental content of Niue Island soils as an indicator of their origin. *New Zealand Journal of Geology and Geophysics*, *36*(2), 243–254. doi: 10.1080/00288306.1993.9514572

Whittaker, T. E. (2008). *High-resolution speleothem-based palaeoclimate records from New*

Zealand reveal robust teleconnections to North Atlantic during MIS 1-4 (PhD Thesis). University of Waikato.

Wiedner, E., Scholz, D., Mangini, A., Polag, D., Mühlinghaus, C., & Segl, M. (2008). Investigation of the stable isotope fractionation in speleothems with laboratory experiments. *Quaternary International*, *187*(1), 15–24. doi: 10.1016/j.quaint.2007.03.017

Williams, P. W. (2008). The role of the epikarst in karst and cave hydrogeology: a review. *International Journal of Speleology*, *37*(1), 1–10.

Wong, C. I., Banner, J. L., & Musgrove, M. (2011). Seasonal dripwater Mg/Ca and Sr/Ca variations driven by cave ventilation: Implications for and modeling of speleothem paleoclimate records. *Geochimica et Cosmochimica Acta*, *75*(12), 3514–3529. doi: 10.1016/j.gca.2011.03.025

Wong, C. I., & Breecker, D. O. (2015). Advancements in the use of speleothems as climate archives. *Quaternary Science Reviews*, *127*, 1–18. doi: 10.1016/j.quascirev.2015.07.019

Woodhead, J. D., Hellstrom, J., Maas, R., Drysdale, R., Zanchetta, G., Devine, P., & Taylor, E. (2006). U–Pb geochronology of speleothems by MC-ICPMS. *Quaternary Geochronology*, *1*(3), 208–221. doi: 10.1016/j.quageo.2006.08.002

Woodhead, J. D., Reisz, R., Fox, D., Drysdale, R., Hellstrom, J., Maas, R., ... Edwards, R. L. (2010). Speleothem climate records from deep time? Exploring the potential with an example from the Permian. *Geology*, *38*(5), 455–458. doi: 10.1130/g30354.1

Woodhead, J. D., Sniderman, J. M. K., Hellstrom, J., Drysdale, R. N., Maas, R., White, N., ... Devine, P. (2019). The antiquity of Nullarbor speleothems and implications for karst palaeoclimate archives. *Scientific Reports*, *9*(1). doi: 10.1038/s41598-018-37097-2

Worthy, T. H. (1997). Fossil deposits in the Hodges Creek Cave System, on the northern foothills of Mt Arthur, Nelson, South Island, New Zealand. *Notornis*, *44*(2), 111–124.

Worthy, T. H., & Holdaway, R. N. (1993). Quaternary fossil faunas from caves in the Punakaiki area, West Coast, South Island, New Zealand. *Journal of the Royal Society of New Zealand*, *23*(3), 147–254. doi: 10.1080/03036758.1993.10721222

Worthy, T. H., Walter, R., & Anderson, A. J. (1998). Fossil and archaeological avifauna of Niue Island, Pacific Ocean. *Notornis*, *45*, 177–190.

Wynn, P. M., Fairchild, I. J., Spötl, C., Hartland, A., Mattey, D., Fayard, B., & Cotte, M. (2014). Synchrotron X-ray distinction of seasonal hydrological and temperature patterns in speleothem carbonate. *Environmental Chemistry*, *11*(1), 28. doi: 10.1071/en13082

Xiao, Y.-H., Sara-Aho, T., Hartikainen, H., & Vähätalo, A. V. (2013). Contribution of ferric iron to light absorption by chromophoric dissolved organic matter. *Limnology and Oceanography*, *58*(2), 653–662. doi: 10.4319/lo.2013.58.2.0653

Xu, M., & Higgins, S. R. (2011). Effects of magnesium ions on near-equilibrium calcite dissolu-

tion: Step kinetics and morphology. *Geochimica et Cosmochimica Acta*, *75*(3), 719–733. doi: 10.1016/j.gca.2010.10.018

Xue, H. B., Jansen, S., Prasch, A., & Sigg, L. (2000). Nickel Speciation and Complexation Kinetics in Freshwater by Ligand Exchange and DPCSV. *Environmental Science and Technology*, *35*(3), 539–546. doi: 10.1021/es0014638

Yang, H., Ding, W., Zhang, C. L., Wu, X., Ma, X., He, G., ... Xie, S. (2011). Occurrence of tetraether lipids in stalagmites: Implications for sources and GDGT-based proxies. *Organic Geochemistry*, *42*(1), 108–115. doi: 10.1016/j.orggeochem.2010.11.006

Yao, Y., Wang, P.-F., Wang, C., Hou, J., & Miao, L.-Z. (2017). The Evaluation on the Cadmium Net Concentration for Soil Ecosystems. *International Journal of Environmental Research and Public Health*, *14*(3), 297.

Yapici, T., Fasfous, I. I., Murimboh, J., & Chakrabarti, C. L. (2008). Investigation of DGT as a metal speciation technique for municipal wastes and aqueous mine effluents. *Analytica Chimica Acta*, *622*, 70–76.

Yapici, T., Fasfous, I. I., Zhao, J., & Chakrabarti, C. L. (2009). Effects of various competing ligands on the kinetics of trace metal complexes of Laurentian Fulvic Acid in model solutions and natural waters. *Analytica Chimica Acta*, *636*, 6–12.

Yin, J.-J., Tang, W., Wang, Z., Pu, J., Lan, G., Yang, H., ... Li, J. (2021). Deciphering the hydroclimatic significance of dripwater $\delta^{13}C_{DIC}$ variations in monsoonal China based on modern cave monitoring. *Journal of Hydrology*, *603*, 126882. doi: 10.1016/j.jhydrol.2021.126882

Yoreo, J. J. D., Zepeda-Ruiz, L. A., Friddle, R. W., Qiu, S. R., Wasylenki, L. E., Chernov, A. A., ... Dove, P. M. (2009). Rethinking Classical Crystal Growth Models through Molecular Scale Insights: Consequences of Kink-Limited Kinetics. *Crystal Growth & Design*, *9*(12), 5135–5144. doi: 10.1021/cg900543g

Yun, Y., Xiang, X., Wang, H., Man, B., Gong, L., Liu, Q., ... Wang, R. (2015). Five-Year Monitoring of Bacterial Communities in Dripping Water from the Heshang Cave in Central China: Implication for Paleoclimate Reconstruction and Ecological Functions. *Geomicrobiology Journal*, *33*(7), 1–11. doi: 10.1080/01490451.2015.1062062

Øyvind Hammer, Harper, D. A. T., & Ryan, P. D. (2001). PAST: Paleontological Statistics Software Package for Education and Data Analysis. *Palaeontologia Electronica*, *4*(1).

Zachara, J. M., Cowan, C. E., & Resch, C. T. (1991). Sorption of divalent metals on calcite. *Geochimica et Cosmochimica Acta*, *55*(6), 1549–1562. doi: 10.1016/0016-7037(91)90127-q

Zhang, H., & Davison, W. (1995). Performance Characteristics of Diffusion Gradients in Thin Films for the in Situ Measurement of Trace Metals in Aqueous Solution. *Analytical Chemistry*, *67*(19), 3391–3400. doi: 10.1021/ac00115a005

Zhao, J., fu Yu, K., & xing Feng, Y. (2009). High-precision ^{238}U–^{234}U–^{230}Th disequilibrium

dating of the recent past: a review. *Quaternary Geochronology*, *4*(5), 423–433. doi: 10.1016/j.quageo.2009.01.012

Zhu, G., Yao, S., Zhai, H., Liu, Z., Li, Y., Pan, H., & Tang, R. (2016). Evolution from Classical to Non-classical Aggregation-Based Crystal Growth of Calcite by Organic Additive Control. *Langmuir*, *32*(35), 8999–9004. doi: 10.1021/acs.langmuir.6b01594

Zolitschka, B., Francus, P., Ojala, A. E. K., & Schimmelmann, A. (2015). Varves in lake sediments – a review. *Quaternary Science Reviews*, *117*, 1–41. doi: 10.1016/j.quascirev.2015.03.019

Appendix

THE UNIVERSITY OF WAIKATO
Te Whare Wānanga o Waikato

Co-Authorship Form

Postgraduate Studies Office
Student and Academic Services Division
Wahanga Ratonga Matauranga Akonga
The University of Waikato
Private Bag 3105
Hamilton 3240, New Zealand
Phone +64 7 838 4439
Website: http://www.waikato.ac.nz/sasd/postgraduate/

This form is to accompany the submission of any PhD that contains research reported in published or unpublished co-authored work. **Please include one copy of this form for each co-authored work**. Completed forms should be included in your appendices for all the copies of your thesis submitted for examination and library deposit (including digital deposit).

Please indicate the chapter/section/pages of this thesis that are extracted from a co-authored work and give the title and publication details or details of submission of the co-authored work.

Chapter 3: "Characterising the decay of organic metal complexes in speleothem-forming cave waters" (under review in *Geochimica et Cosmochimica Acta* at the time of final thesis submission)

Nature of contribution by PhD candidate	Collaboration on study conception, study design and development, sample collection and analysis, data analysis and interpretation, manuscript writing and editing
Extent of contribution by PhD candidate (%)	90

CO-AUTHORS

Name	Nature of Contribution
Adam Hartland	Study conception, design and development, sample collection, advice on data interpretation, manuscript feedback
Sebastian F. M. Breitenbach	Study conception, advice on data interpretation, manuscript feedback
Megan Grainger	Inputs to study design, advice on sample analyses, manuscript feedback
Claudine Stirling	Sample analysis, advice on analytical matters, manuscript feedback
Danielle Blackwell	Sample analysis

Certification by Co-Authors

The undersigned hereby certify that:

- the above statement correctly reflects the nature and extent of the PhD candidate's contribution to this work, and the nature of the contribution of each of the co-authors; and

Name	Signature	Date
Adam Hartland	A Hartland	20/2/24
Sebastian F. M. Breitenbach	S. Bth	09.02.2024
Megan Grainger		16/02/24
Claudine Stirling	C Stirling	07 February 2024
Danielle Blackwell		13.02.2024

THE UNIVERSITY OF WAIKATO
Te Whare Wānanga o Waikato

Co-Authorship Form

Postgraduate Studies Office
Student and Academic Services Division
Wahanga Ratonga Matauranga Akonga
The University of Waikato
Private Bag 3105
Hamilton 3240, New Zealand
Phone +64 7 838 4439
Website: http://www.waikato.ac.nz/sasd/postgraduate/

This form is to accompany the submission of any PhD that contains research reported in published or unpublished co-authored work. **Please include one copy of this form for each co-authored work.** Completed forms should be included in your appendices for all the copies of your thesis submitted for examination and library deposit (including digital deposit).

Please indicate the chapter/section/pages of this thesis that are extracted from a co-authored work and give the title and publication details or details of submission of the co-authored work. Chapter 4: "Trace metal incorporation into calcite in caves and cave-analogue experiments: assessing the role of organic complexation"	
Nature of contribution by PhD candidate	Collaboration on study conception, study design and development, sample collection and analysis, data analysis and interpretation, manuscript writing and editing
Extent of contribution by PhD candidate (%)	90

CO-AUTHORS

Name	Nature of Contribution
Adam Hartland	Study conception, design and development, sample collection, advice on data interpretation, manuscript feedback
Sebastian F. M. Breitenbach	Collaboration on study conception and design
Megan Grainger	Advice on analytical matters, manuscript feedback
Amanda French	Sample analysis, advice on analytical matters
Danielle Blackwell	Sample analysis
Daryn Magatogiia	Help with sample collection, enabling of fieldwork

Certification by Co-Authors

The undersigned hereby certify that:

- the above statement correctly reflects the nature and extent of the PhD candidate's contribution to this work, and the nature of the contribution of each of the co-authors; and

Name	Signature	Date
Adam Hartland		20/2/24
Sebastian F. M. Breitenbach	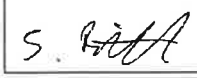	**09.02.2024**
Megan Grainger		16/02/24
Amanda French		09.02.2024

Danielle Blackwell	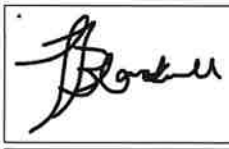	13.02.2024
Daryn Magatogiia		11 February 2024

THE UNIVERSITY OF WAIKATO
Te Whare Wānanga o Waikato

Co-Authorship Form

Postgraduate Studies Office
Student and Academic Services Division
Wahanga Ratonga Matauranga Akonga
The University of Waikato
Private Bag 3105
Hamilton 3240, New Zealand
Phone +64 7 838 4439
Website: http://www.waikato.ac.nz/sasd/postgraduate/

This form is to accompany the submission of any PhD that contains research reported in published or unpublished co-authored work. **Please include one copy of this form for each co-authored work.** Completed forms should be included in your appendices for all the copies of your thesis submitted for examination and library deposit (including digital deposit).

Please indicate the chapter/section/pages of this thesis that are extracted from a co-authored work and give the title and publication details or details of submission of the co-authored work. Chapter 5: Trace elemental signatures in dripwater and stalagmites from two Niuean caves – a case study	
Nature of contribution by PhD candidate	Collaboration on study design and development, sample collection and analysis, data analysis and interpretation, manuscript writing and editing
Extent of contribution by PhD candidate (%)	90

CO-AUTHORS

Name	Nature of Contribution
Adam Hartland	Study conception, design and development, sample collection, advice on data interpretation, manuscript feedback
Sebastian F. M. Breitenbach	Study conception, design and development, sample collection and analysis, advice on data interpretation
Megan Grainger	Inputs to study design, advice on sample analyses, manuscript feedback
Jeffrey Lang	Help with data collection and processing
Fernando Gázquez	Sample analysis
Denis Scholz	Sample analysis, advice on data interpretation
John Hellstrom	Sample analysis, advice on data interpretation
Danielle Blackwell	Sample analysis
Amanda French	Sample analysis
Daryn Magatogiia	Help with sample and data collection, facilitating of fieldwork

Certification by Co-Authors

The undersigned hereby certify that:

- the above statement correctly reflects the nature and extent of the PhD candidate's contribution to this work, and the nature of the contribution of each of the co-authors; and

Name	Signature	Date
Adam Hartland	Adam Hartland	20/2/24
Sebastian F. M. Breitenbach	S. Breitenbach	09.02.2024
Megan Grainger	Megan Grainger	16/02/24
Jeffrey Lang	Jeffrey Lang	11 Feb 2024

Fernando Gázquez	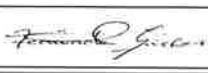	11 February 2024
Denis Scholz	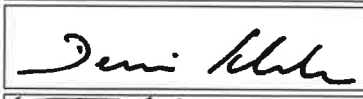	6 February 2024
John Hellstrom		
Danielle Blackwell	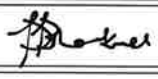	13.02.2024
Amanda French	Amanda French	09-02-2024
Daryn Magatogiia	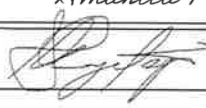	11-02-2024